

Integrated Earthquake Risk Evaluation for Mega-Thrust Earthquakes

Eri Ito

Contents

Preface

Acknowledgements

Chapter 1. General Introduction

1.1 Background of This Study	1- 1
1.1.1 Review of studies on source characteristics of mega-thrust earthquakes.....	1- 2
1.1.2 Review of studies for the damage prediction models of buildings.....	1- 3
1.1.3 Review of studies on site characteristics.....	1- 4
1.1.4 Review of studies of human casualty and evacuation simulation for Tsunami...	1- 7
1.1.5 Summary of the research background.....	1- 9
1.2 Purpose and Strategy of This Study.....	1-11
1.2.1 Strong motion simulation method.....	1-11
1.2.2 The representation of the complex fault rupture process	1-12
1.2.3 Delineation of the past earthquake rupture process.....	1-12
1.2.4 Site amplification based on the vertical amplification correction.....	1-13
1.2.5 Site amplification based on the correction to theoretical amplification.....	1-13
1.2.6 Earthquake-to-Microtremor Ratio as a site-specific parameter.....	1-14
1.2.7 Tsunami evacuation simulation considering structural damage and extraction of the difficult-to-evacuate areas.....	1-14
1.3 Organization of the Thesis.....	1-15
References.....	1-16

Part I Research on Site Amplification Evaluation Methods

Chapter 2. A Method to Directly Estimate S-Wave Site Amplification Factor from Horizontal-to-Vertical Spectral Ratio of Earthquakes (EHVR)

Abstract.....	2- 1
2.1 Introduction.....	2- 2
2.2 Issues on Horizontal-to-Vertical Spectral Ratios: EHVR and HSAF.....	2- 4
2.3 Issues on Horizontal-to-Vertical Spectral Ratios: MHVR and EHVR.....	2- 6

2.4 Diffuse Wavefield Theory and GIT Formulation for EHVR.....	2- 6
2.5 Proposed HSAF Calculation Method.....	2- 8
2.6 Results of Application.....	2- 9
2.7 Validation.....	2-22
2.8 Discussions.....	2-25
2.8.1 Primary cause of site effects in consideration.....	2-25
2.8.2 Basin response in coda.....	2-26
2.8.3 One-dimensionality in S-wave portion.....	2-28
2.8.4 Reference site.....	2-28
2.9 Conclusions.....	2-29
References.....	2-31
Appendix	2-37

Chapter 3. Estimation of Velocity Structures Using Pseudo Earthquake Horizontal-to-Vertical Spectral Ratio from Microtremors

Abstract.....	3- 1
3.1 Introduction.....	3- 2
3.2 Empirical EMR Correction in Japan.....	3- 3
3.3 Previous Studies in the Target Basin.....	3- 5
3.4 EMR _G Specific for the Target Basin.....	3- 8
3.5 Comparison of pHVSR from EMR _G with Other HVSRs.....	3-12
3.6 Validation of pHVSR from EMR _G	3-14
3.7 Improvement of the Reference Model.....	3-20
3.8 Validation of the New Reference Models for OG-Series Site.....	3-26
3.9 Application of EMR _G and New Reference Models to the G-Series Sites.....	3-29
3.10 Discussion.....	3-32
3.11 Conclusions and Future Perspectives.....	3-40
References.....	3-42
Appendix	3-47

Chapter 4. S-Wave Site Amplification Factors from Observed Ground Motions in Japan: Validation of Delineated Velocity Structures and Proposal for Empirical Correction

Abstract.....	4- 1
4.1 Introduction.....	4- 2
4.2 Observed SAF from GIT.....	4- 3
4.3 Unified Velocity Model of NIED.....	4- 4

4.4 Observed and Theoretical SAF	4- 8
4.5 Frequency and Amplitude Modification Ratio.....	4-10
4.5.1 Grid search scheme.....	4-11
4.5.2 Evaluated FMR and AMR.....	4-12
4.5.3 Correlation and residual improvement.....	4-13
4.5.4 Spatial interpolation.....	4-15
4.5.5 Validation.....	4-17
4.6 Conclusions.....	4-20
References.....	4-21

Part II Research on Complex Source Modeling for Predicting Realistic Strong Ground Motions

Chapter 5. Strong Motion Simulation for the 1944 Tonankai Earthquake Based on the Statistical Green's Function Method and Stochastic Representation of Complex Source Process

Abstract.....	5- 1
5.1 Introduction.....	5- 2
5.2 Statistical Green's function.....	5- 3
5.2.1 Outline of GIT.....	5- 3
5.2.2 WSR to account for basin effects.....	5- 5
5.2.3 Tgr modeling.....	5- 7
5.3 Stochastic Source Model.....	5- 8
5.4 Results of Parametric Study.....	5-10
5.4.1 Scenario with variable slip and constant rupture velocity (CASE1).....	5-10
5.4.2 Scenario with constant slip and constant rupture velocity (CASE2).....	5-14
5.4.3 Scenario with variable slip and variable rupture velocity (CASE3).....	5-16
5.5 Discussion.....	5-18
5.5.1 Effects of slip variation on PGA and PGV.....	5-18
5.5.2 Effects of rupture velocity variation on PGA and PGV.....	5-19
5.5.3 Effects of nonlinearity on PGA and PGV.....	5-20
5.6 Conclusions.....	5-23
References.....	5-24

Chapter 6. Complex Source Characterization of the 1944 Tonankai Earthquake from Simulated Damage Ratios based on the Simulated Strong Motions

Abstract.....	6- 1
---------------	------

6.1 Introduction.....	6- 2
6.2 Reviews of the 1944 Tonankai Earthquake Disaster Reports.....	6- 3
6.3 Kinematic Heterogeneous Source Modeling.....	6- 5
6.4 Reproduced Strong Motions at Damaged Cities and Towns.....	6-17
6.5 Damage Evaluation by the Damage Prediction Model of Old Houses.....	6-31
6.6 Conclusions.....	6-49
References.....	6-50

Part III Research on Tsunami Evacuation Simulation

Chapter 7. Tsunami Evacuation Simulation Considering Road Blockage by Collapsed Buildings Evaluated from Predicted Strong Ground Motion

Abstract.....	7- 1
7.1 Introduction.....	7 -2
7.2 Target District for This Study.....	7- 4
7.3 Predicting Building Collapse.....	7- 6
7.4 Tsunami Evacuation Simulation Using Agent Methodology.....	7-10
7.4.1 Summary of the tsunami evacuation evaluation system.....	7-10
7.4.2 Geographical space information.....	7-11
7.5 Summary of the Tsunami Evacuation Simulation.....	7-13
7.5.1 Patterns for evacuation sites.....	7-13
7.5.2 Road blockages caused by collapsed buildings.....	7-14
7.5.3 Time required for evacuation.....	7-16
7.6 Tsunami Evacuation Simulation Results and Discussions.....	7-18
7.6.1 Evaluation of designated evacuation sites.....	7-18
7.6.2 Change in the number of successful evacuees as earthquake resistance reinforcement rates improve.....	7-19
7.6.3 Change in the time required to complete the evacuation of 90% of the population by improving the earthquake resistance.....	7-21
7.7 Summary and Future Tasks.....	7-22
References.....	7-23

Chapter 8. Detailed Estimation of Strong Ground Motion Using Microtremor Observation and Tsunami Evacuation Simulation Considering Road Blockage by Collapsed Houses in a Village with Stiff Soil Layers

Abstract.....	8- 1
---------------	------

8.1 Background of This Study.....	8- 2
8.2 Microtremor Observation and Analysis.....	8- 2
8.2.1 Microtremor observation.....	8- 2
8.2.2 Analysis for observation recordings.....	8- 3
8.3 Identification of the Ground Structure.....	8- 4
8.3.1 Identification of the initial velocity structure model.....	8- 4
8.3.2 Identification of the modified velocity structure models.....	8- 7
8.4 Estimation of the Strong Ground Motions.....	8- 8
8.5 Prediction of Collapse of Wooden Houses.....	8-12
8.5.1 Outline of building damage prediction method.....	8-12
8.5.2 Building damage prediction method.....	8-12
8.5.3 Damage ratio in the entire target research district.....	8-14
8.6 Tsunami Evacuation Simulation Using Agent Methodology.....	8-18
8.6.1 Overview of simulation system.....	8-18
8.6.1.1 Simulation system.....	8-18
8.6.1.2 Simulation conditions.....	8-18
8.6.1.3 Setting of parameters.....	8-20
8.6.1.4 Simulation patterns.....	8-20
8.6.2 Simulation results.....	8-20
8.6.3 Analysis of simulation results.....	8-21
8.7 Conclusions.....	8-22
References.....	8-24

Chapter 9. A Method to Extract Difficult-to-Evacuate Areas by Using Tsunami Evacuation Simulation and Numerical Analysis

Abstract.....	9- 1
9.1 Introduction.....	9- 2
9.2 Target Area for Tsunami Evacuation Simulation.....	9- 3
9.2.1 Vulnerability of the target area to an earthquake and tsunami.....	9- 4
9.2.2 Estimation of tsunami inundation area for the tsunami evacuation planning..	9- 5
9.3 Evaluation System for Tsunami Evacuation.....	9- 8
9.4 Simulation Settings.....	9- 9
9.4.1 Environmental settings.....	9- 9
9.4.2 Parameters for agents.....	9-11
9.5 Simulation Models and Results.....	9-13
9.6 Summary of the Whole Simulation Procedure.....	9-22

9.7 Discussion.....	9-24
9.8 Conclusions.....	9-28
References.....	9-29

Chapter 10. General Conclusions.....	10- 1
---	--------------

Preface

Late January 1995, several days after the 1995 Hyogo-ken Nanbu earthquake

An announcer on the TV was reading out the names of the victims and missing people endlessly. What was projected on the blue background screen was only a group of names written in inorganic katakana, which was changing one by one.

A girl, who just turned four, seemed to understand what it meant, also understood it happened in the area relatively close to her house. But she was so overwhelmed to see the situation that she remained seated for a long time in front of the TV, or more precisely on the kotatsu desk in front of the TV, feeling a kind of "indigestion" which came from the total difference between the area suffering from the disaster and the warm and safe room where she was staying.

23rd January 1998

In the year she entered elementary school, on the day of an annual school event called the Art Appreciation Day, she watched an animated film in the gymnasium that was based on a true story of the days immediately after the 1995 Hyogo-ken Nanbu earthquake that had occurred three years earlier.

The main character was a boy in the 6th grade at the time, who went out with his friends to check on the survival of his classmates. Many of his classmates were confirmed to be alive, but he was unable to get in touch with one girl. They all struggled to reach her apartment and finally found it. The apartment was still standing! Then someone said, "I think she is okay!" But an uncle said to them, "Look, the first floor is a mess." The apartment was projected from the top floor to the ground on the screen. The first floor of the apartment building, which at first glance appeared to be undamaged, was completely crushed. "She was gone," he said.

It was totally shocking. It was the first time she was aware of the destructive power of an earthquake. She did not cry, probably the shock got the better.

For a long time, she could not forget the "digestion" and shock she felt. Then, more than a decade later, when she chose what to learn in a university, she decided to choose a faculty that she could learn knowledge on earthquake after a long consideration.

11th March 2011 at 2:30 p.m.

She became a university student in the spring of the previous year. After experiencing a "fulfilling" spring vacation that included helping the senior students with their graduation projects, a trip abroad, and a trip to Tokyo, she was home all day that day.

She had a late lunch with her mother and was waiting for their favorite drama to start at 3:00 p.m. seated in the kotatsu. Then an emergency earthquake alert went off, but they did not

feel the shaking. Before they knew it, the drama was cancelled and replaced by the emergency news. The expected arrival time and height of the tsunami was announced. Based on what little knowledge she had at the time, she thought that people in that region were used to tsunamis and so would be fine, which was a very careless thought.

As the evening approached, however, on the TV she saw cars being swallowed up, and the death toll was updated one after another. Some part of her brain was telling her that this was out of the ordinary, but it was completely beyond her comprehension. She was seated in the warm kotatsu, while people are dying all over the screen. The same “indigestion” as she experienced when she was four, she felt.

Late August 2012

She went to the area damaged by the tsunami of the 2011 off the Pacific coast of Tohoku Earthquake. A vast view that completely deprives people of the will to rebuild made her feel incredibly helpless. She even felt that she, who was neither a victim nor an acquaintance of a victim and did not experience how it was difficult to survive, should not get involved in the reconstruction of damaged area, or even in disaster prevention. By this experience she got so shocked and mentally drained that she spent her time without taking any concrete action to contribute to the damaged areas although she was assigned in a laboratory of earthquake engineering the next year. She once chose to stay away from earthquake engineering. However, the Kumamoto earthquake, which struck just after she began to work, gave her an opportunity to come back to the laboratory again.

All "she" in the above indicate the author of this thesis. In summarizing this thesis, I was looking back again at my memories on earthquake disasters. I am still struggling to figure out how to face earthquake disaster prevention and earthquake disasters as a researcher. I still cannot cope with the “indigestion” and the sense of helplessness I felt when I faced the threat of earthquakes. Despite this situation, however, I was able to summarize this thesis because of two driving forces. One is the “indigestion” I felt twice in my life, as I mentioned above. The other is the word that “we need opinions from the third party, who have the different perspective from us in order to rebuild our town”, which a man who lost his daughter by the tsunami told me when I visited Tohoku area in 2012. These are not directly related to the content of this paper, but I would like to note that these two things were the underlying motivation.

The title of this thesis is “Integrated Earthquake Risk Evaluation for Mega-Thrust Earthquakes”, and the motivation for this should be mentioned. After 2011 off the Pacific coast of Tohoku Earthquake, the damage predictions for the next mega-thrust earthquakes along Nankai trough have been re-examined. After the Fukushima nuclear accident, the result of worst-case scenario is being well featured, which I feel is so desperate that people are giving up on preparing for the disaster. Not only the worst-case scenario, but also a realistic scale scenario that considers well and integrates all the element affecting the result of damage prediction should also be given importance, since the ultimate goal of damage prediction is not to make people give up on living and preparing, but to save people and encourage them to take action to save themselves.

This thesis is one proposal for earthquake damage prediction to save people's lives, which arose from the author's awareness of the problems that mentioned.

Acknowledgments

Never have I realized how I have been supported by the people around me and how important they are for me more than during my Ph.D. journey which is now almost ending. If I could tell something to myself early spring in 2007, who took a lot of time deciding which to learn in a university, I would want to say: the decision you would make may be the harder one for you, but you can meet the wonderful people that you never expect.

Firstly, I would like to thank the professors who helped me to finish my Ph.D. thesis. Without their help I could not have summarized this thesis which is interdisciplinary and that long.

I would like to express my deepest gratitude to Professor Shinichi Matsushima, who has been a great help to me since I was in the undergraduate and master's course, and who gave me the detailed advice.

I would like to thank Professor Izuru Takewaki and Professor Norio Maki, who provided me the suggestions and opinions from various viewpoints. And I would like to thank Professor Yasuhiro Hayashi for not only advising on the contents but also discussing how to face the disaster prevention. I would like to thank Professor Yuki Sakai for his advice that made me realize what I need to understand until the defense.

I would like to express my gratitude to Professor Michinori Hatayama, for teaching me the tsunami evacuation simulation from the basic. This thesis could have not been such interdisciplinary without his support. I would also like to Haruko Sekiguchi, for providing her program which is the basis for Part II in my thesis.

I owe a deep sense of gratitude and respect to Professor Hiroshi Kawase, for having been a great help to me since I was in the undergraduate and master's course and giving me many opportunities to build my confidence as a researcher. I appreciate his understanding what I wanted to do just after I was assigned to his laboratory when I was an undergraduate student and leading me to manage to embody the essence of what I wanted to do as a Ph.D. thesis. I also learned the attitude toward research from him.

My thanks also go to Assistant professor Fumiaki Nagashima for giving his program and to-the-point advice on my research, in addition to his help for leading daily life in the office. I also thank Kenichi Nakano, not only for giving his program but also for the careful and detailed advice and gentle encouragement during my last few months before application. I would like to thank Haruko Ito for helping all the administrative matters around me and her talk that always makes me feel relaxed.

During the Ph.D. journey I had many opportunities to collaborate with international researchers, which is the greatest experience for me, and I would like to thank all of those whom I met through the opportunities. I am grateful to Professor Cécile Cornou, who took care of me

during my stay in Grenoble. I totally respect her toughness and being energetic all the time. My appreciation also goes to Professor Pierre-Yves Bard, who accepted me to stay in Grenoble and gave advice for research and kindly helped me regarding the administrative matters. My thanks also go to Rouba Iskandar, for being truly kind to me in Grenoble, her kind treatment from the moment we firstly met to the last moment we say good-bye made me feel very comfortable and relaxed.

I would like to thank those who visited DPRI. Especially I would like to express my gratitude to Alan Yong, who gave me the incredibly detailed advice and discussion, and I was influenced by his regular life and healthy eating habits. Thanks also go to Daniela Famiani, who were always cheerful and made me think what really matters in life.

People I met in DPRI in the past three years after coming back here are also those whom I would like to thank: Lexin Lin and Ryoko Araki. Thank you for sharing your values and happy time with me, which colored my daily life in DPRI.

My gratitude also goes to my friends from my university days: Ayaka Ushiyama, Yuki Sudo, and Ayane Hamaguchi, who have to-the-point opinions on many topics and update me whenever we meet each other. Special thanks go to my friends from my junior high school days: Yuki Ishihara, Ayaka Kitagawa, and Kana Yamada, thank you for always understanding my situation and supporting me. I feel as if you were at the core of my heart. Besides them, I thank my friends who are active in many fields but treat me the same as my school days. They all always give me inspiration and energy.

Finally, I am extremely grateful to my father and my mother, who are the greatest supporters of me. I cannot be what I am today without your understanding my decision and encouragement with full of love at any time. My greatest appreciation also goes to my grandmother, who helped me to develop a natural interest in “learning” from my childhood. You are sure to be the best teacher for me in many ways.

The period of 2020 - 2021, during which I am writing this thesis, is undoubtedly the period when the people need to change their lifestyle drastically, and it must be the most challenging time for those who do not know the life during World War II. Through this challenging time, I realize from the bottom of my heart that anyone will not live forever, and a life would be taken away suddenly, and that is also true for me. This experience made me feel more than ever that the existence of all the people who are involved with me, including those mentioned above, is invaluable. That is why I would like to show my deep gratitude to all of you again “here and now”, as closing this page.

With much appreciation,

Eri Ito

February 2021

Chapter 1

General Introduction

1.1 Background of This Study

After the 1995 Hyogo-ken Nanbu earthquake, the southwestern Japan is turned out to have entered an active period, and mega-thrust earthquakes along the Nankai and Sagami Troughs may occur at any time. In order to prepare and mitigate the devastating damage caused by these earthquakes as much as possible, it is necessary to predict the damage impact in advance with high accuracy and take appropriate countermeasures.

All disasters are complex and inter-dependent disasters, and necessarily their estimation can only be achieved through the integrated use of technologies that span cross many different disciplines. Therefore, in this thesis we consider the occurrence of complex disasters associated with future earthquakes as “the earthquake risk” as a whole, including the large variations in the damage caused by earthquakes depending on the assumed scenarios. We aim to propose an integrated approach to evaluate earthquake risk as quantitatively as possible. Here we mainly focus on the building damage and subsequent human losses from building damage and tsunamis caused by the mega-thrust earthquakes in near future as a part of the complex disasters.

In the following, we will examine the current situation in our country. Looking back to the past 25 years, we should note that the M7.3 (Mw6.9) Hyogo-ken Nanbu earthquake of January 17, 1995 killed more than 6,000 people (Fire and Disaster Management Agency, 2006), which was the largest number of casualties since the 1944 Tonankai and 1946 Nankai earthquakes. It had been clarified that a particular velocity pulse generated by a heterogeneous source specific to crustal earthquakes, which is not considered in the current building code, was generated and greatly amplified by the three-dimensional basin structure specific to the Kobe area to form the so called “the damaged belt” where more than 30% of wooden houses were heavily damaged or collapsed (Kawase, 1996).

Then the M9.0 Mega-thrust earthquake of March 11, 2011, that is, the Off the Pacific Coast of Tohoku earthquake along the subducting Pacific Plate towards the Tohoku (northeastern) region of Japan caused extensive tsunami damage to the coastal areas on the Pacific side of the Tohoku region, with more than 16,000 people either killed or missing (Fire and Disaster Management Agency, 2020). However, this earthquake caused very limited damage to structures. On the other hand, the April 16, 2016 Kumamoto earthquake of M7.3 (Mw6.8), along the Futagawa-Hinagu fault system in central Kumamoto Prefecture, caused a lot of damage to wooden houses at specific sites near the fault, and 273 people were killed, including related deaths (Fire and Disaster Management Agency, 2019). These earthquakes provided us a lot of data on the distribution of building damage as well as many strong motion

records. The results of the analysis revealed several issues regarding the applicability of the strong-motion prediction methods used in the past. It is also revealed that there is a high degree of uncertainty in the quantitative evaluation of source and site characteristics important in forecasting strong motions. Since then, various methods for accurately identifying those characteristics have been explored.

Looking into the future, a mega-thrust earthquake along the Nankai Trough, which is expected to occur in the near future (Headquarters for Earthquake Research Promotion, 2020), will certainly cause extensive building damage and human casualties. The damage to buildings is caused by a complex interaction of many factors such as the vibration characteristics of buildings and those of the strong ground motions, which should be quantitatively evaluated. Also, it is obvious that the damage to buildings has a significant impact on the evacuation of residents from the subsequent tsunami immediately after such mega-thrust earthquakes.

Thus, it is our clear and present challenges 1) to recognize that the characteristics of strong ground motions, building damage, and human casualties are tightly linked to each other, 2) to upgrade each evaluation method as sophisticated as possible, 3) to integrate them for quantitative risk evaluation which will lead to countermeasures, and 4) to reduce human suffering as much as possible in the event of such mega-thrust earthquakes. It is our responsibility those who are living in a new active period of Japan Island. In the following subsections, reviews on the selected previous studies in the specific areas of research will be summarized.

1.1.1 Review of studies on source characteristics of mega-thrust earthquakes

For proper damage estimation of mega-thrust earthquakes, it is necessary to evaluate the three characteristics, i.e., source characteristics, propagation path characteristics, and site amplification characteristics. As for the source characteristics, a complex model that takes into account the heterogeneity of the source properties is necessary. For the heterogeneity of source model for mega-thrust earthquakes, analyses of the 2011 off the Pacific coast of Tohoku earthquake have shown that there is a large slip area along the trench that contributes to the generation of tsunamis but does not generate short-periods, and that there is a short-period strong motion generation area deeper near the coast (e.g., Asano and Iwata, 2012; Kurahashi and Irikura, 2013), which means two types of heterogeneity are needed to realistically reproduce the rupture process of this type of earthquake. If the short-period strong motion generation areas of Tonankai, Nankai, and Kanto earthquakes, which will happen in the near future, will be located in the area near the coast, they will be closer to cities than in the case of the 2011 off the Pacific coast of Tohoku earthquake, and the structural damage in the area near the coast will be more severe than the Tohoku case. Therefore, it is an urgent issue to grasp the sources of short-period generation including their locations, sizes, and amount of their stress drops.

However, the prediction of damage by strong ground motion and tsunami predictions using M 9 class earthquake scenarios published by the Central Disaster Management Council (CDMC) after the 2011 off the Pacific coast of Tohoku earthquake (CDMC, 2013) does not

reflect the latest knowledge on the distribution of short-period strong motion generation areas and rupture propagation on faults, which was delineated only from the 2011 off the Pacific coast of Tohoku earthquake.

1.1.2 Review of studies for the damage prediction models of buildings

Under the current condition of scarcity of the delineated rupture process during the mega-thrust earthquakes, a detailed understanding of the source rupture process of past earthquakes in our history of observation is important as a basis for predicting damage from future mega-thrust earthquakes. For the three major subduction-zone earthquakes during the early 1900s, that is, in the last seismically-active period, namely the Kanto earthquake in 1923, the Tonankai earthquake in 1944, and the Nankai earthquake in 1946, the long-period ground motion generation areas with periods ranging from several seconds to 100 seconds are understood to some extent from crustal movements, tsunamis height, and reproduced records with long-period seismometers in distant places. On the other hand, short-period ground motion generation areas with a period of two seconds or less that are directly related to building damage have been assumed to be located in the long-period generation areas, but their nature has not been fully validated. One reason for this lack of investigation is that there was no building damage evaluation model which can reproduce the damage of old buildings quantitatively at the time of the earthquake and so the accuracy of the damage evaluation was considered to be low. Another reason was that there were no observed strong-motion waveforms in the severely damaged areas (the first nation-wide strong motion network was installed in 1987), so only inversions from the estimated seismic intensities obtained from the post-earthquake building damage survey can be performed to delineate the locations of the short-period ground motion generation areas by using the attenuation function of the seismic intensities derived from the current strong-motion data (e.g., Kanda et al., 2004). The accuracy of the delineated short-period ground motion generation areas seems to be quite limited because of the inherent insensitivity of the seismic intensity.

There are currently three major methods for predicting building damage. The first one is based on measured seismic intensity. Before the current measured seismic intensity of JMA based on the observed strong motion time-history was established, the seismic intensity was a human- or damage-based seismic intensity, and the relation between the reported seismic intensity and the building damage around the observed location were roughly the same. However, the current seismic intensity is based on the instrumental filtered peak ground acceleration (PGA), which is roughly proportional to the square-root of the product of PGA and the peak ground velocity (PGV) (Karim and Yamazaki, 2002), therefore it is an index to the maximum value of observed ground motion, not an index of observed damage. The seismic intensity up to the seismic intensity 5 was validated with the human-based intensity when JMA changed the intensity measurement procedure in 1996, but the seismic intensity above the seismic intensity 6+ is an extrapolated value, and it is clear that the seismic intensity above seismic intensity 6+ would be overestimated for most of the cases (e.g., Sakai et al., 2002), which is a problem with this method.

The second method uses a vulnerability function that is empirically established from

the building damage ratio around the observation point using the maximum value of the ground motion (PGA, PGV, JMA seismic intensity, and the averaged response spectra in a certain range of period) as an indicator of the ground motion strength (e.g., Yamaguchi and Yamazaki, 2001; Hayashi and Miyakoshi, 1998). This method is based a single maximum value indicator of ground motion, therefore a single function would be difficult to predict damage to all building types with different characteristics. In addition, there are still relatively small number of data obtained, especially at severely damaged areas. Because the surveyed building damage is inevitably based on the past damaging earthquake, the resultant empirical function is dependent on the characteristics of the damaged buildings by a specific earthquakes and sites used.

The third method is based on building damage prediction models using the nonlinear structural response analyses (e.g., Nagato and Kawase, 2002a,b; Yoshida et al., 2004). Nagato and Kawase (2002 a, b) developed a building damage prediction model that reproduces the observed damage by inputting the strong ground motions of the 1995 Hyogo-ken Nanbu earthquake reproduced by the physical modelling of source, path, and site (Matsushima and Kawase, 2000) into a building damage prediction model and tuning it until the calculated damage ratio matches the observed damage ratio in Kobe. Yoshida et al. (2004) upgraded the model by following the procedure of the Nagato-Kawase model to consider the four construction periods based on the damage survey for the property-tax evaluation for a more detailed damage estimation of Japanese wooden houses. The novelty of these models is that it can reflect the spectral and temporal characteristics of strong ground motions and can take into account the construction age of the building if we can properly estimate the building strength with respect to the shear deformation. In order to predict observed structural damage in the past, we need to expand these building damage prediction models for much older buildings.

1.1.3 Review of studies on site characteristics

Among the three major characteristics of ground motions, namely, the source term, propagation path term, and site amplification, the last one is the most influential term in Japan because of the strong variability in the local underground conditions. Therefore, it is most important to deduce the horizontal site amplification factor (hereafter HSAF, a spectral value as a function of frequency) in the main S-wave part for evaluating the site-specific design of earthquake ground motions and elucidating the relationship between the subsurface structures and their amplification effects. The methods to obtain HSAF include a theoretical calculation method based on the well-defined subsurface structure (e.g., Takahashi and Hirano, 1941; Aki, 1988, Kawase, 2003), an empirical method based on the spectral ratio between borehole and surface sensors (e.g., Kitagawa et al., 1988 and Satoh et al., 1995 for Sendai, Japan; Archuleta et al., 1992, Steidl et al., 1996, and Bonilla et al., 2002 for California, USA), and another empirical method based on the spectral ratio of a sedimentary site with a nearby site on rock (e.g., Borcherdt, 1970; Lermo and Chávez-García, 1993, Field and Jacob, 1995, Steidl et al., 1996). Nevertheless, the theoretical method has difficulty in determining a velocity structure at the site down to the seismological bedrock and validating the adequacy of the velocity structure. We also need damping factors of the structure, which are more difficult to evaluate quantitatively. The empirical method that uses borehole observation data has difficulty in

eliminating the effects of reflected waves contained in the observed borehole seismograms (e.g., Steidl et al, 1996; Tao and Rathje, 2020). The empirical method of using data observed at a rock site for input into the denominator often has difficulty in finding such a nearby site where the intact rock is exposed, and there is an issue of whether such a rock site can really be viewed as a site without soil amplification (e.g., Steidl et al, 1996).

Meanwhile, the generalized spectral inversion technique (GIT, Andrews, 1986; Iwata and Irikura, 1988; Castro et al., 1988; Kato et al., 1992) allows for determining, on a stable basis, the HSAF for appropriately selected reference site or sites, when there are many earthquakes observed at many sites. Fortunately, Japan has a couple of dense strong-motion observation networks of K-NET, KiK-net, and the JMA Seismic Intensity (Shindo-kei) network installed after the 1995 Hyogo-ken Nanbu earthquake, which are nationwide networks of strong-motion observation already containing many strong-motion records. Kawase and Matsuo (2004) have used observation records obtained from 1996 until 2002 to separately perceive and elucidate the basic properties of the source, propagation path, and site amplification. A subsequent study by Kawase (2006) has focused on the nonlinear site amplification effect in the records with high peak ground acceleration. Oth et al. (2011a, 2011b) analyzed both KiK-net's surface and borehole data separately and reported several comparisons of HSAF with horizontal-to-vertical and surface-to-borehole spectral ratios. By following the strategy of Kawase and Matsuo (2004) with recent data added, Nakano et al. (2015) conducted spectral inversion analyses for Fourier spectra of more than 77,000 source-station pairs to find the stress drop dependence on magnitude and depth. A significant feature of the inversions common to Kawase and Matsuo (2004), Kawase (2006), and Nakano et al. (2015) is that they determined HSAFs with respect to the outcrop equivalent of the seismological bedrock at a reference site with an estimated S-wave velocity of 3,450 m/s. To do so they got the spectra by eliminating the effect of weathered rock layers from the surface records observed at the reference site before GIT. Such a clear definition of the reference site with the S-wave velocity higher than 3.0 km/s is indispensable to obtain stable site factors without any trade-offs with source spectra.

However, GIT analysis requires earthquake ground motions from many earthquakes observed at many locations. On the other hand, only three components of earthquake ground motion observed at a single station are required to determine the horizontal-to-vertical spectral ratio of earthquakes (eHVSR). Nakamura (1989) proposed that the HSAF can be estimated directly by using the horizontal-to-vertical ratio of microtremors (mHVSR). Since then, many researchers have studied the following two issues based on either observation or theory: (a) whether the mHVSR and eHVSR are the same; (b) whether the eHVSR and HSAF are the same. Although discussions are still ongoing, the majority of researchers have concluded the following: the mHVSR and eHVSR are similar to each other but not the same; and in both the mHVSR and eHVSR, their peak frequencies are about the same as that of the HSAF, but the amplitudes are underestimated. As a quantitative answer to the issue (a), Kawase, Mori, et al. (2018) have already derived empirical spectral ratios between eHVSR and mHVSR for 100 sites in Japan, defined as EMR. However, the applicability of the method to the site in a different tectonic environment far from Japan is not proved yet. When we apply the EMR method to the mHVSR data in a region with different tectonic settings, it is better to use EMR specific for the region, rather than to directly substitute the Japanese EMR, because EMR depends on the velocity structure as the theory for mHVSR (Sanchez-Sesma et al., 2011) and

eHVSR (Kawase et al., 2011) suggest. However, unless we have plenty of earthquake and microtremor data in a target region, we cannot obtain EMR specific for the region as Kawase, Mori, et al. (2018) did for K-NET and KiK-net sites in Japan. Therefore, it would be quite useful to propose a systematic procedure to determine EMR for a seismically quiet region outside of Japan.

We also need to provide a quantitative answer to the issue (b), by deriving an empirical correction function between HSAF and eHVSR. Let us assume that a sufficient number of small earthquakes have been observed at a certain site. Because it is too laborious to determine HSAF using GIT every time, there is a real need to use the eHVSR that can be determined from only one site. In particular, it is difficult to apply GIT to earthquakes so small that their magnitude or source locations cannot be determined accurately, or their seismograms cannot be recorded simultaneously at different sites. We, therefore, need to propose a simple method to correct the vertical site amplification factor (VSAF, the spectral value as a function of frequency), which represents the largest challenge in determining the HSAF from the observed eHVSR. Contamination with surface waves is eliminated if we use only the main S-wave part.

As described above, if strong ground motion data or microtremor data are available, we can propose a method utilizing the best of their spectral characteristics based on the empirical technique. However, what if we want to predict strong ground motion over a wide area or at arbitrary sites without data? In that case we can use a theoretical Green's function method (TGF) in which wave generation at the source, propagation from the source to the site, and amplification near the site are represented by the numerical modeling for the whole process from the source to the site (e.g., Matsushima and Kawase, 2000). In this method we need a physical model of the medium to represent the wave propagation in the whole path. In other words, we need to calculate the theoretical Green's function for a point source on the fault surface. The problem associated for the TGF is that the accuracy of the reproduced waveform strongly depends on the accuracy of the velocity structure used to represent the seismic wave propagation in the whole path from the source to the site.

The other method of predicting strong motions is an empirical method in which we use observed ground motions of a small earthquake as a substitute for the Green's function and sum up all the contributions from the elemental sources on the fault surface. It is called the empirical Green's function method (EGF). If there are no appropriate small earthquake records to be used as the empirical Green's function, we first generate synthetic waveforms based on many records of small earthquakes. It is called the statistical Green's function method (SGF). Because the frequency range for the theoretical approach with coherent nature is limited to the lower end, usually below 1 Hz or lower, while the effective frequency range of EGF or SGF with inherent nature of stochasticity should be higher than that, a hybrid scheme with TGF and EGF or TGF and SGF are used naturally, as has been used in the current national project for strong motion predictions with specific sources.

As mentioned above, after the deployment of the dense national strong motion observation networks, namely K-NET, KiK-net, and JMA Shindohei (Instrumental Seismic Intensity) network in Japan, a significant number of data has been accumulated. We can use these data to construct a model of SGF in a broadband frequency range. As long as we can generate the SGF for an arbitrary size of a small earthquake at an arbitrary location of a site in the frequency range of engineering interest, namely from 0.1 Hz to 20 Hz, we need not use

a hybrid scheme. Thus, we have been analyzing these strong-motion data in Japan by using the generalized spectral inversion technique (GIT) initially developed in 1980's to delineate statistical properties of the three major terms, namely, the source term, path term, and site term (Kawase and Matsuo, 2004; Kawase, 2006; Nakano et al., 2015) conducted spectral inversion analyses for Fourier spectra of a lot of source-station pairs to be used in the SGF. As emphasized above, the novelty of their approach is that the hypothesized seismological bedrock spectra at a reference site, YMGH01, are used as a reference to calculate site amplification factors at all the other observed sites. Such a separation of observed spectra into three major terms is sufficient to generate SGF at these observed sites. However, strong-motion simulations for the whole region near the seismogenic fault would be still difficult by SGF because we cannot estimate the site term at an arbitrary location other than the observed sites used in GIT. Thus, we need to develop a method to evaluate the site term at an arbitrary location as precisely as possible.

When we look at the site term, HSAF, as a function of frequency evaluated at K-NET, KiK-net, and JMA Shindohei network, we found that they show strong spectral fluctuations from 1 to 10 as a normal range of fluctuations and from 1 to 50 at tens of extraordinary sites with various peak frequencies. Several attempts have been made to correlate the primary characteristics of the observed HSAF with a site proxy or proxies such as the S-wave velocity (V_s) averaged over top xx m, V_s_{xx} (e.g., $Vs30$) or the depth to the layer with the S-wave velocity higher than $y.y$ km/s, $Z_y.y$ (e.g., $Z1.0$), trying to reproduce primary characteristics of SAF such as the fundamental peak frequency f_0 and its peak amplitude A_0 . Unfortunately, these extracted characteristics are not sufficient to reproduce synthetic seismograms needed in the SGF summation. We should find a different strategy to interpolate observed HSAF to obtain HSAF at an arbitrary point as quantitatively as possible.

1.1.4 Review of studies of human casualty and evacuation simulation for Tsunami

A mega-thrust earthquake, like the 2011 Tohoku earthquake, is characterized by a tsunami that causes significant human loss. In order to reduce the human casualties, it is necessary to understand the damage potential to the people and the built environment under the current situation at the time of the earthquake and tsunami. Agent-based simulations of tsunami evacuation, which can reflect the road congestion and detailed behavior of the people, are one of the effective means for estimating the human loss due to tsunami. Recently, many papers on tsunami evacuation simulation have been published, however, the history of tsunami evacuation simulation research is relatively short, and the research is still in the development stage. Therefore, there are several problems necessary to solve toward the more quantitative and realistic simulation. We will focus on two of them in this thesis. The first is that the building damage was not taken into account on the simulation, and the second is that the method of extracting the areas where the evacuation from tsunami is difficult (hereafter DEA, difficult-to-evacuate area) has not been well established yet by using the tsunami evacuation simulations.

As far as we have surveyed, one of the first papers related to tsunami evacuation simulation using agents seems to be Usuzawa et al. (1997). They performed the tsunami

evacuation simulation in the area damaged by the 1993 Hokkaido Nansei-Oki earthquake for future evacuation planning and they showed that the result was validated by the detailed surveys just after the earthquake. Since then, many papers have been published, mainly focusing on the parameters used in the simulation in order to make them more realistic. For instance, the interaction between pedestrians and motorcycles or cars has been considered (e.g., Goto et al. 2012; Mas et al. 2012, 2013; Makinoshima et al. 2016). Among them, Goto et al. (2012) assumed that the walking speed as well as the motorcycle speed decreased with increased density and then simulated the cases with different ratios between pedestrians and motorcycles. They also presented the simulation to the elementary, middle, and high school students in the target area as a course of disaster education and proved that their simulations made easy for students to understand the appropriate evacuation procedure. Mas et al. (2012) introduced a new approach to model the starting time of evacuation based on the sigmoid curve, as they thought that the starting time may have a significant effect on congestions and bottlenecks during evacuation. Thus, progress of tsunami evacuation simulation has been made and these simulations provides various tools for the evacuation planning. Based on such progress, Hori et al. (2015) considered that there remains uncertainty in these tsunami evacuation simulations and suggested a way to evaluate the quality of the simulation.

As for the effects of building damage on evacuation routes, we found only a few reports of the tsunami simulation considering building collapse and subsequent road blockage. For example, Sato et al. (2002) adopted the vulnerability function developed by Murao et al. (1999) for the damage estimate. Tamura et al. (2005) adopted a probability distribution model that predicts the width of the debris depend on the JMA seismic intensity estimated by Akakura et al. (2000). Later Sakata and Teraki (2009) predicted in their tsunami evacuation simulations which buildings would collapse by surveying their ages or observing building exteriors. They proposed a model that can vary the rubble flow distance based on the probabilistic distribution of collapsed directions (i.e., randomly distributed to all directions).

In these pioneering studies, their focus was not primarily on the quantification of expected building damage. The structural damage that buildings are likely to incur depends on a complex combination of multiple factors, including the building's vibration characteristics, seismic input motion characteristics, and the softness of the surrounding ground. Damages should therefore be quantitatively estimated using an up-to-date technology in earthquake engineering. Since traditional methods have not considered the seismic motion characteristic and the ground characteristics, it is likely that the real outcome will differ from the simulation results. In contrast to the Off the Pacific Coast of Tohoku earthquake of 2011, in which building damages were relatively small, there is a strong concern that building damages caused by the seismic motions in the coastal areas will be greater for an earthquake along the Nankai Trough, due to the fact that the hypocentral region will be closer to the shore (e.g., Central Disaster Management Council 2003; Ho and Kawase 2008). Road blockages caused by collapsed buildings are expected to pose a greater obstacle for residents trying to evacuate before the tsunami hits.

If the estimates of building damages used in an evacuation simulation undertaken for the purpose of disaster impact analysis and subsequent development of countermeasures for disaster reduction deviates greatly from the actual outcome, countermeasures based on that inaccurate estimate may not be quite effective. In order to avoid this, the tsunami evacuation simulations should be incorporated with the predicted building damage with the consideration

on three influential factors, that is, the buildings themselves, ground characteristics, and input ground motions, using the up-to-date knowledge available in earthquake engineering.

After the 2011 Great East Japan Earthquake Disaster, which caused devastating damage in the Tohoku region in Japan, related legislatures were rapidly enacted or revised in areas susceptible to tsunami damage all over Japan. In light of this trend, studies on evaluating the safety of each district using the existing evacuation destination distribution and studies on evaluating the distribution itself began to appear in the 2000s. Ministry of Land, Infrastructure, Transport, and Tourism (MLIT, 2013) outlined the following procedure to extract the DEA, which is the fundamental information for evacuation destination planning. First, the “time available for evacuation” is simply calculated by subtracting the “time unavailable for evacuation”, which is the time where people cannot move because of the shaking of an earthquake, from the estimated tsunami arrival time after the earthquake happens. The “maximum evacuation distance” is obtained by multiplying the “time available for evacuation” and the walking speed of evacuees, and the DEA is defined as areas where there is no evacuation destination within the maximum evacuation distance. Minato et al. (2016) studied the 1993 Southwest-off Hokkaido Earthquake. The “time unavailable for evacuation” because of shaking by the earthquake was derived in detail using the characteristics of the strong ground motion, and the maximum evacuation distances from 112 representative sites were obtained using walking experiments. The DEA was identified by combining this information and the estimated tsunami arrival time, and the validity of the method was evaluated by comparing it with the record. However, people will most likely be confused immediately after the occurrence of an earthquake in a real situation, thus the evacuation time will be longer than the minimum time necessary for evacuation calculated based on the simple relation between the distance and walking speed, or the time necessary for evacuation from walking experiments at normal times. Indeed, Minato et al. (2016) concluded that, based on comparison of their result with geological distribution of actual casualties, a “margin” time is necessary in addition to the time necessary for evacuation based on walking experiments. Walking experiments are more realistic than the minimum time necessary for evacuation obtained from geometrical relations, but collecting participants with various walking speeds in an experiment is difficult even though there are evacuees with various walking speeds in a real evacuation situation. Therefore, agent-based simulations that can reflect the behavior of evacuees during evacuation and the variability in walking speeds would be effective for extracting DEA for planning evacuation destinations. We need further explore the potential of the agent-based evacuation simulations on this aspect.

1.1.5 Summary of the research background

In summary, the challenges that we are facing in integrated earthquake risk assessment for the mega-thrust earthquakes in future can be described in detail as:

- (1) Establish a method for quantitatively predicting strong motions of future mega-thrust earthquakes based on the observed records;
- (2) Take into account realistic spatial variability characteristics of fault parameters in setting up rupture scenarios on the fault surface;
- (3) In setting the spatial variability characteristics, extract the source information of past mega-thrust earthquakes and utilize them for prediction;

- (4) For site characteristics that have a significant impact on the prediction of strong ground motions, establish effective and accurate evaluation methods for a wider range of frequency bands based on observed records and subsurface structural information;
- (5) Conduct a realistic tsunami evacuation simulation analysis and extract the DEA based on the simulation in order to utilize them for planning countermeasures.

All of them are important and urgent issues that needs to be addressed as soon as possible. Especially in the southwestern side of Japan, the possibility of one or a couple of mega-thrust earthquakes along the Nankai Trough is estimated to be high, around 60 to 80 %, within the next 30 years, and new efforts are urgently needed for the advancement of integrated earthquake risk evaluation methods to prepare for such an event.

1.2 Purpose and Strategy of This Study

Based on the urgent needs for the integrated earthquake risk evaluation as identified in the previous section, this study aims to improve the integrated risk assessment system for earthquake disasters associated with the increasingly complex mega-thrust earthquakes and their mitigation, based on the investigation of past earthquakes and their associated damage and geophysical surveys and observations. The purpose of this study is to provide a solution to the above problems. Specifically, the following features are presented for the issues raised in this study.

- (1) We use the statistical Green's function, which reflects the characteristics of the observed ground motions over a wide frequency range, to calculate the strong-motion waveforms of mega-thrust earthquakes in a wide area using the conventional waveform summation method.
- (2) Both the asperities or SMGAs, which contribute to long-period ground motions radiated from a fraction of areas in the large fault plane, and the random variations inside and outside of the asperities with high stress drop specifications, which contribute to short-period ground motions, are taken into account in setting up the rupture on the fault plane.
- (3) The source properties of the past mega-thrust earthquake are clarified by matching the estimated damage ratios of buildings from the strong-motion waveforms reproduced by the above prediction method with the observed damage ratios.
- (4) A couple of new methods for quantitative site amplification evaluation are proposed by using the vertical amplification correction function, the theoretical amplification factor correction, and the region-specific earthquake-to-microtremor ratio correction.
- (5) Evacuation simulation analyses considering the building damage due to strong ground motions are carried out which should be reflected in the integrated risk assessment.

In what follows, we will describe our purpose and strategy of the investigation for each specific subject.

1.2.1 Strong motion simulation method

In this research we use the broad-band SGF for quantitative prediction of ground motions in the area near the mega-thrust fault because of its accuracy in predicting detailed characteristics of ground motions without investing the heavy resources needed to delineate the accurate underground structures for the broad-band TGF. The method is also easy to incorporate with the very heterogeneous (kinematic) rupture process if we can prescribe them. We first introduce fundamental characteristics of the SGF derived from the GIT applied to the strong motion records by K-NET, KiK-net, and the JMA Shindo-kei network (Nakano et al., 2015; Nakano, 2020). Then, we introduce a stochastic representation in a kinematic source model for a complex rupture scenario of Tonankai earthquake with the size of 1944 event based on the strong-motion generation areas (SMGAs) with spatially-random perturbation in both slip and rupture velocity. Finally, we calculate synthetic waveforms in the vicinity of the fault area and confirm their appropriateness in term of their average characteristics in the strength indices.

1.2.2 The representation of the complex fault rupture process

As mentioned in Section 1.1, it is indispensable to account for the heterogeneous fault rupture process in the quantitative strong motion simulations for a mega-thrust scenario earthquake. A broadband heterogeneous source model is generated for a plate boundary earthquake along the Nankai Trough by introducing fractal heterogeneity into a characterized source model consisting of a background region and strong-motion generation areas.

In this study first the gross ruptured area (i.e., the assumed whole fault plane) of the fault map of the Central Disaster Management Council (CDMC, 2003) is projected on the upper surface of the Philippine Sea plate of the Japan Integrated Velocity Structure Model (JIVSM; Koketsu et al., 2012) and adjusted the size to be compatible to the fault size of CDMC and to be able to include the strong-motion generation areas (SMGAs) of the Cabinet Office (2015). For the assumed SMGAs in this study, their areas, moments, stress parameters, rise time, and center positions are adopted from those by the Cabinet Office (2015) as the basic model. However, the shape of the SMGA is assumed to be circular or a part of a circle, unlike those of the Cabinet Office (2015). We assumed as such because we want to use an automatic generation system for a large number of parametric studies with various locations and areas of SMGAs. The parameters of the background region of the basic model are based on CDMC (2003). The amount of the average slip is calculated from the total moment and the fault area, similar to the method used by CDMC (2003).

The broadband source heterogeneity is calculated by randomly adding heterogeneity from about one half of the SMGA areas to several km² in size to the basic source parameter distribution, as described in Sekiguchi and Yoshimi (2010). The amplitude of fluctuation is proportional to the size of heterogeneity. We adjust the power of the fall-off in the spatial distribution of the slip heterogeneity is equal to the value obtained by Mai and Beroza (2002), that is, -1.75. The stress parameter distribution was given in proportion to the variation of the slip distribution. The rupture velocity distribution was started from a uniform distribution of 2.7 km/s and a constant amount of variation regardless of the area of the inhomogeneous patch were added and finally adjusted so that the standard deviation of the spatial variation is equivalent to the level obtained by Miyakoshi and Petukhin (2005) in their analysis of the source-inversion model. The distribution of rupture initiation times at an arbitrary point on the fault was obtained through the wave propagation analysis based on an ordinary two-dimensional finite difference method.

Note that this kind of complex source representation is not the original work of this thesis but this is the first attempt to combine such a source representation with the SGF derived from GIT.

1.2.3 Delineation of the past earthquake rupture process

As mentioned in Section 1.1, we have not sufficient information yet on the detailed source process of the past mega-thrust earthquakes because of the lack of observed strong motion records. It is indispensable to delineate the detailed rupture process from the existing observed building damage distribution, instead of strong motion records. We reproduce the building damage ratio during the 1944 Tonankai earthquake by inputting the strong motion

waveforms into the building damage evaluation models as of 1944. The strong ground motion waveforms are obtained from the statistical Green's function and the heterogeneous source model as described above. The site characteristic, which is important for the evaluation of the strong ground motion, is obtained by the method of converting the theoretical S-wave characteristic from the unified velocity model (UVM) by integrating shallower- and deeper-parts of the structures above the seismological bedrock in the Kanto and Tokai regions, to the empirical site characteristics. The detailed description of the site amplification evaluation will follow.

First, we prepare the heterogeneous source model with the four asperities as a standard model, and prepare 36 heterogeneous source models in total, of which varying parameters are the location of hypocenters, the location of asperities (SMGAs), and their stress drops. Then we calculate the strong ground motions from the prescribed complex source models and estimate the building damage ratios using the building damage evaluation models, then compared it with the observed damage ratio during the 1944 Tonankai earthquake by Takemura and Toraya (2015). Second, based on the model with the estimated damage ratio best corresponding with the observed one as the new standard model, we investigate additional five heterogeneous source models with different stress drop and area of SMGA No.1 and No.2 to seek the better source model.

1.2.4 Site amplification based on the vertical amplification correction

Based on the diffuse field concept together with the generalized spectral inversion technique (GIT), we propose a method to directly estimate the HSAF of the S-wave portion from the horizontal-to-vertical spectral ratio of earthquakes (EHVR). As the vertical amplification is included in the denominator of EHVR, it cannot be viewed as HSAF without correction. We use GIT to determine the vertical site amplification factor (VSAF) from strong-motion data observed by the strong motion networks in Japan by Nakano et al. (2015), and then deduce the log-averaged vertical amplification correction function (VACF) from a total of 1,678 sites where ten or more earthquakes have been observed. This is a natural extension of the famous “Nakamura method” in which EHVR is used as a direct substitute of HSAF.

1.2.5 Site amplification based on the correction to theoretical amplification

We compare the observed HSAFs with the 1D theoretical site amplification factors calculated from the recently established unified velocity model (UVM) of the National Research Institute for Earth Science and Disaster Resilience (NIED) in the Kanto and Tokai regions and find significant discrepancies between them different from site to site. Then, we obtain the modification ratios to reduce the gap between them at the observation points and propose a scheme to evaluate HSAF at an arbitrary point by using the theoretical HSAF and the interpolated modification ratios, named FMR as the frequency modification ratio and AMR as the amplitude modification ratio. Finally, we propose an interpolation scheme to get HSAF

in every 250 m grid point and validate the scheme at selected sites.

1.2.6 Earthquake-to-Microtremor Ratio as a site-specific parameter

We establish a systematic procedure to estimate the velocity structure from microtremors and delineate the fundamental characteristics of the velocity structures with a different tectonic environment. We first calculate the EMR specific for the Grenoble Basin (EMR_G) with much stiffer nature than the average basin in Japan and calculate pseudo eHVSR (pHVSR) from EMR_G and mHVSR . We compare the pHVSRs with the eHVSRs at five sites and find sufficient similarity to each other. Then, we invert velocity structures from eHVSRs , pHVSRs , and mHVSRs to prove that our proposed scheme is effective to a basin with totally different characteristics.

1.2.7 Tsunami evacuation simulation considering structural damage and extraction of the difficult-to-evacuate areas

In order to clarify the effect of building collapse and subsequent road blockage to a tsunami evacuation, we first estimate the strong ground motion considering the site characteristic of the target site and predicted building damage based on the nonlinear response analysis for a realistic strong ground motion by using the building damage prediction model of Nagato and Kawase (2002a, b). Then we simulate a tsunami evacuation considering road blockage due to the collapsed buildings by using an agent-based simulation method.

We also try to establish a new scheme to extract the area where the evacuation from the tsunami is difficult (DEA) by conducting tsunami evacuation simulation and performing analyses of the simulated results as follows: First, the initial model is delineated and the location of casualties at the estimated tsunami arrival time is captured by using the simulation images, and improved models are constructed by repeatedly adding evacuation destinations while considering the feasibility. Second, the detailed numerical analyses are performed on the most feasible case with fewest causality among the models in the first step. The target area is divided into small sub-districts and a couple of numerical analyses for grasping the evacuation difficulty of each sub-district are performed. The evacuation difficulty of each sub-district is comprehensively evaluated from the proposed three indices, and the DEAs are effectively extracted.

1.3 Organization of the Thesis

The following is the outline of each chapter.

In Chapter 1, we introduce the background and purpose of this study. First, we address that all disasters are complex, and inevitably their prediction can only be accomplished through the integrated use of technologies that cross many disciplines. We emphasize the importance of reducing the human casualties of earthquakes by sophisticating the evaluation method on the characteristics of strong motion, building damage, and human casualties and by integrating them into countermeasures. We review the status of each evaluation method and explain how they can be sophisticated in this study.

Part I consists of Chapter 2, 3, and 4, where three sophisticated methods related to the estimation of the site characteristic are proposed.

In Chapter 2, we propose a simple method to deduce the horizontal site amplification factor (HSAT) in the S-wave portion from the EHVR of observed earthquake ground motion and vertical amplification correction function (VACF).

In Chapter 3, we propose a method to calculate the Earthquake-to-Microtremor Ratio (EMR) specific for the region where the velocity structure is different from those in Japan based on the Japanese EMR, and estimate the velocity structure using pseudo earthquake horizontal-to-vertical spectral ratio (pHCSR) calculated from microtremor horizontal-to-vertical ratio (mHCSR) and EMR.

In Chapter 4, we propose an interpolation scheme to get S-wave site amplification factor in every 250 m grid point and validate the scheme at selected sites by converting the theoretical S-wave characteristic from the unified velocity model (UVM) by integrating shallower- and deeper-parts of the structures above the seismological bedrock in the Kanto and Tokai regions, into the empirical site characteristic.

Part II consisting Chapter 5 and 6, explains the method for characterizing complex rupture process reflected the knowledge accumulated after the 2011 Off the Pacific Coast of Tohoku earthquake.

In Chapter 5, we first report the basic features of our statistical Green's functions used for summation. We then show how to construct a kinematic source model with distinctive strong-motion generation areas with the spatially random slip and rupture velocity variations.

In Chapter 6, we first calculate strong ground motion waveforms from the statistical Green's function and the heterogeneous source models targeted for the 1944 Tonankai earthquake. Then we reproduce the observed building damage ratios during the 1944 Tonankai earthquake by inputting the strong motion waveforms into the building damage evaluation models reflecting the characteristics of buildings as of 1944. Through two steps forward modelling, we determine the best scenario that can reproduce observed damage ratios during the 1944 Tonankai earthquake.

Part III consisting Chapter 7, 8, and 9, explains three different sophisticated approaches for evaluating human loss by using agent-based tsunami evacuation simulation.

In Chapter 7, focusing on an urbanized area, we perform the tsunami evacuation

simulation by considering building damage ratios from the building damage prediction model, and evaluate the human loss by changing the ratios and locations of earthquake-resistant buildings in the target area.

In Chapter 8, focusing on a village with stiff soil layers, we perform the tsunami evacuation simulation considering the building damage ratios obtained by the building damage prediction model specific for the area and explore the best strategy of the evacuation plan in the target area.

In Chapter 9, we propose a method to extract the areas where the evacuation is difficult using the agent-based tsunami evacuation simulation and performing three different numerical analyses based on the result of the simulations.

In Chapter 10, we conclude this study after summarizing the important findings from each chapter. Future directions of research are also presented.

References

- Akakura Y, Takahashi H, Nakamoto T (2000) An attempt to model street blockage for prediction of earthquake damage in urban coastal area, Report of Port and Harbor Research Institute, Vol.39, No.4, pp.19-41 [in Japanese].
- Aki, K. (1988). Local site effects on strong ground motion, Earthquake Engineering and Soil Dynamics II -Recent Advances in Ground Motion Evaluation, 103-155, ASCE.
- Andrews, D.J. (1986). Objective determination of source parameters and similarity of earthquakes of different size, Earthquake Source Mechanics (eds. S. Das, J. Boatwright and C. H. Scholz), American Geophysical Union, Washington, D.C., 1986. doi: 10.1029/GM037p0259.
- Archuleta, R. J., S. H. Seale, P. V. Sangas, L. M. Baker, and S. T. Swain (1992). Garner Valley downhole array of accelerometers: instrumentation and preliminary data analysis, Bull. Seism. Soc. Am. 82, 1592–1621.
- Asano, K. and Iwata, T. (2012), Source model for strong ground motion generation in the frequency range 0.1-10 Hz during the 2011 Tohoku earthquake, Earth Planets Space, Vol.64, 1111-1123.
- Bonilla, L.F., J.H. Steidl, J.-C. Gariel, and R.J. Archuleta (2002). Borehole response studies at the Garner Valley Downhole Array, Southern California, Bull. Seism. Soc. Am., Vol.92, No.8, 3165–3179.
- Borcherdt, R.D. (1970). Effects of local geology on ground motion near San Francisco Bay, Bull. Seism. Soc. Am., Vol.60, No.1, 29–61.
- Cabinet Office (2015): Report on Long-period Ground Motion Due to a Nankai Trough Megaquake, Committee for Modeling a Nankai Trough Megaquake, December 17, 2015, http://www.bousai.go.jp/jishin/nankai/nankaitrough_report.html, (in Japanese, last accessed, 2020/8/29).

- Castro R.R., S.K. Singh, and E. Mena (1988) An empirical model to predict Fourier amplitude spectra of horizontal ground motion. The Mexico Earthquake of September 19, 1985, *Earthquake Spectra* 4:675–685.
- Central Disaster Management Council, (2003): Strong motions and Tsunami heights, Figures and Tables, Vol.3, http://www.bousai.go.jp/kaigirep/chuobou/senmon/tounankai_nankaijishin/16/pdf/siryou3zuhyou_2.pdf
- Central Disaster Management Council (2013), Report on the measures for the mega-thrust earthquake along the Nankai Trough (Final Report). http://www.bousai.go.jp/jishin/nankai/taisaku_wg/pdf/20130528_houkoku_s1.pdf
- Field, E.H., and K.H. Jacob (1995). A comparison and test of various site-response estimation techniques, including three that are not reference-site dependent, *Bull. Seism. Soc. Am.* Vol.85, No.4, 1127-1143.
- Fire and Disaster Management Agency (2006), Summery of the Great Hanshin-Awaji Earthquake (Final Report). <https://www.fdma.go.jp/disaster/info/assets/post1.pdf>
- Fire and Disaster Management Agency (2020), Summery of The 2011 off the Pacific coast of Tohoku Earthquake (Great East Japan Earthquake) (The 160th Report). <https://www.fdma.go.jp/disaster/higashinihon/items/160.pdf>
- Fire and Disaster Management Agency (2019), Summery of the Earthquake with Epicenter in Kumamoto Area, Kumamoto Prefecture (The 121st Report). <https://www.fdma.go.jp/disaster/info/items/kumamoto.pdf>
- Goto Y, Affan M, Agussabti, Nurdin Y, Yuliana DK, Ardiansyah (2012) Tsunami evacuation simulation for disaster education and city planning, *Journal of Disaster Research*, Vol.7, No.1, pp.92-101.
- Hayashi, Y. and Miyakoshi, J. (1998), Fragility curve based on Hyogo-ken Nanbu earthquake, *Disaster section PD, AIJ*, pp.15-20.
- Headquarters for Earthquake Research Promotion (2020), Probabilistic tsunami assessment of large earthquakes occurring along the Nankai Trough. https://www.jishin.go.jp/main/chousa/20jan_tsunami/nankai_tsunami.pdf
- Ho N and Kawase H (2008) Damage prediction and earthquake risk management strategy for environmental load by the next Nankai earthquake, *Comprehensive Journal of AIJ*, No.6, 87-92 [in Japanese with English abstract].
- Hori M, Sueatsu T, Araki H, Okumura Y, Dohi Y (2015) Verification and validation of tsunami evacuation simulation models, *J of Japan Association for Earthquake Engineering*, Vol.15, No.4, 2015, pp.144-157 [in Japanese with English abstract].
- Iwata, T., and K. Irikura (1988). Source parameters of the 1983 Japan-Sea earthquake sequence, *J. Phys. Earth*, 36, 155-184.
- Kawase, H. (1996). The cause of the damage belt in Kobe: "The basin-edge effect", Constructive interference of the direct S-wave with the basin-induced

- diffracted/Rayleigh waves, *Seismological Research Letters*, 67, 25-34.
- Kawase, H. (2003). Site effects on strong ground motions, *International Handbook of Earthquake and Engineering Seismology*, Part B, W.H.K. Lee, and H. Kanamori (eds.), Academic Press, London, 1013-1030.
- Kawase, H. and H. Matsuo (2004). Amplification characteristics of K-NET, KiK-NET, and JMA Shindo-kei network sites based on the spectral inversion technique, 13th World Conf. on Earthquake Engineering, Vancouver, Canada, Paper No. 454.
- Kawase, H. (2006). Site effects derived from spectral inversion method for K-NET, KiK-net, and JMA strong-motion network with special reference to soil nonlinearity in high PGA records, *Bull. Earthq. Res. Inst., Tokyo Univ.* 81, 309–315.
- Kawase H., F.J. Sánchez-Sesma, and S. Matsushima (2011). The optimal use of horizontal-to-vertical spectral ratios of earthquake motions for velocity inversions based on diffuse-field theory for plane waves. *Bull. Seism. Soc. Am.*, 101, 2011-2014.
- Kawase, H., Y. Mori, and F. Nagashima (2018). Difference of horizontal-to-vertical spectral ratios of observed earthquakes and microtremors and its application to S-wave velocity inversion based on the diffuse field concept, *Earth, Planets, and Space*, Vol.70, No.1, Open Access, doi: 10.1186/s40623-017-0766-4
- Kanda, K., Takemura, M. and Usami, T. (2004), Short-Period Wave Radiation Zones of a Megathrust Fault alongh the Nankai Trough Dededuced from Inversion Analysis of Seismic Intensity Data, *Earthquake*, The Seismological Society of Japan, Part 2, Vol.57, pp.153-170.
- Karim, K.R. and Yamazaki, F. (2002), Correlation of JMA instrumental seismic intensity with strong motion parameters *Earthquake Engng Struct. Dyn.* 2002; 31:1191–1212 (DOI: 10.1002/eqe.158)
- Kato, K., M. Takemura, T. Kieura, K. Urano, and T. Uetake (1992). Preliminary analysis for evaluation of local site effects from strong motion spectra by an inversion method, *J. Phys. Earth*, 40, 175-191.
- Kitagawa Y., I. Ohkawa, and T. Kashima (1988). Dense strong motion earthquake seismometer array at site with different topographic and geologic conditions in Sendal, *Proc. 9th WCEE*, 2, 215-220.
- Koketsu K., Miyake H., Suzuki H., (2012) Japan integrated velocity structure model version 1. *Proceedings of the 15th world conference on earthquake engineering*, Lisbon, Portugal, September, 24-28.
- Kurahashi, S., and Irikura, K. (2013): Short-period source model of the 2011 Mw 9.0 off the Pacific coast of Tohoku earthquake, *Bull. Seismol. Soc. Am.*, Vol.103, 1317-1393.
- Lermo, J. and F. J. Chávez-García (1993). Site effect evaluation using spectral ratios with only one station, *Bull. Seism. Soc. Am.*, Vol.83, No.5, 1574-1594.
- Mai, P.M. and Beroza, G.C. (2002): A spatial random field model to characterize complexity in earthquake slip, *Journal of Geophysical Research*, 107(B11), 2308,

doi:10.1029/2001JB000588.

- Makinoshima F, Imamura F, Abe Y (2016) Behavior from tsunami recorded in the multimedia sources at Kesennuma City in the 2011 Tohoku tsunami and its simulation by using the evacuation model with pedestrian-car interaction, Coastal Engineering Journal, Japan Society of Civil Engineers, Vol. 58, No. 4, pp.1640023-1-28.
- Mas E, Suppasri A, Imamura F, Koshimura S (2012) Agent-based Simulation of the 2011 Great East Japan earthquake/tsunami evacuation: An integrated model of tsunami inundation and evacuation, Journal of Natural Disaster Science, Vol. 34, No. 1, 2012, pp.41-57.
- Mas E, Suppasri A, Srivihok P, Koshimura S (2013) Feasibility of evacuation at the Pakarang Cape in Thailand based on tsunami inundation model and human evacuation simulation, 10th International Conference on Urban Earthquake Engineering, Tokyo, Japan, pp.1-6.
- Matsushima, S. and Kawase, H. (2000) Multiple asperity source model of the Hyogo-Ken Nanbu earthquake of 1995 and strong motion simulation in Kobe, Journal of Structural and Construction Engineering (Transactions of AIJ), No. 534, pp.33-40 [in Japanese with English abstract].
- Minato, F., Hata, Y., Nakashima, T., Koyama, M., Kuwata, Y., Yamada, M, and Tokida, K. (2016), Evaluation of difficult area for tsunami evacuation in Aonae district Okushiri Island, Japan, based on strong ground motion estimation and walking experiment during the 1993 Southwest Hokkaido earthquake, Journal of Japan Society of Civil Engineers, Ser. B3 (Ocean Engineering), Vol.72, no.2, I_509-I_514 [in Japanese].
- Ministry of Land, Infrastructure, Transport, and Tourism (MLIT) (2013), A guideline for community planning for tsunami disaster mitigation [in Japanese].
<https://www.mlit.go.jp/common/001000488.pdf>
- Miyakoshi, K. and Petukhin, A. (2005), Delineation of rupture velocity of heterogeneous source model extracted from source inversion results of inland earthquakes, Proc. of 2005 Japan Earth and Planetary Science Joint Meeting, May, 22-26, 2005, Chiba, Japan, S046P-002.
- Murao O (1999) Study on the vulnerability function based on the observed damage statistics in 1995 Hyogoken Nambu earthquake, Dissertation, the University of Tokyo, <http://hdl.handle.net/2261/51136> [in Japanese].
- Nagato K and Kawase H (2002a), A set of dynamic models of steel buildings for damage evaluation, Journal of Structural and Construction Engineering (Transactions of AIJ), No. 559, pp.101–106 [in Japanese with English abstract].
- Nagato K and Kawase H (2002b), A set of wooden house models for damage evaluation based on observed damages statistics and non-linear response analysis and its application to strong motions of recent earthquakes, Japan Earthquake Engineering Symposium, Japan Association for Earthquake Engineering, No.11, vo.2, pp.1315-1320 [in Japanese with English abstract].
- Nakamura Y. (1989). A method for dynamic characteristics estimation of subsurface using

- microtremor on the ground surface, Railway Tech. Res. Inst., Q. Rep. 30(1): 25-30.
- Nakano, K., S. Matsushima, and H. Kawase (2015). Statistical properties of strong ground motions from the generalized spectral inversion of data observed by K-NET, KiK-net, and the JMA Shindo-kei Network in Japan, Bull. Seism. Soc. Am., Vol.105, 2662-2680, doi:10.1785/0120140349.
- Oth, A., S. Parolai, and D. Bindi (2011a). Spectral analysis of K-NET and KiK-net data in Japan, part I: Database compilation and peculiarities, Bull. Seism. Soc. Am., Vol.101, 652-666, doi:10.1785/0120100134.
- Oth, A., D. Bindi, S. Parolai, and D. Di Giacomo (2011b). Spectral analysis of K-NET and KiK-net data in Japan, part II: On attenuation characteristics, source spectra, and site response of borehole and surface stations, Bull. Seism. Soc. Am., Vol.101, 667-687, doi:10.1785/0120100135.
- Sakai, Y., Kanno, T. and Koketsu, K. (2002), Proposal of the Destructive Power Index of Strong Ground Motion for Prediction of Building Damage Ratio, J. Struct. Constr. Eng., AJJ, No . 555, pp.85-91.
- Sakata T and Teraki A (2009) A study about simulations for road blockage considering directions of rubble flow, Proceedings from the Institute of Social Safety Science, No. 25, 2009 [in Japanese].
- Sánchez-Sesma, F.J., M. Rodríguez, U. Iturrarán-Viveros, F. Luzón, M. Campillo, L. Margerin, A. García-Jerez, M. Suárez, M.A. Santoyo, and A. Rodríguez-Castellanos (2011). A theory for microtremor H/V spectral ratio: Application for a layered medium, Geophys. J. Int. Exp. Lett., 186: 221-225, doi: 10.1111/j.1365-246X.2011.05064. x.
- Sato H, Murakami H, Shimada T, Kozuki Y, Kurata K, Otani H (2002) A study on the evacuation from tsunami considering building collapses by the earthquake, Coastal Engineering Journal, Japan Society of Civil Engineers, Vol.49, 2002, pp.311-315 [in Japanese].
- Satoh, T., H. Kawase, and T. Sato (1995). Evaluation of local site effects and their removal from borehole records observed in the Sendai Region, Japan, Bull. Seism. Soc. Am., Vol.85, 1770-1789.
- Sekiguchi, H. and Yoshimi, M. (2010): Broadband Ground Motion Reconstruction for the Kanto Basin during the 1923 Kanto Earthquake, Pure and Applied Geophysics, doi:10.1007/s00024-010-0142-9.
- Steidl, J.H., Tumarkin, A.G., and Archuleta, R.J. (1996). What is a reference site?, Bull. Seism. Soc. Am., Vol.86, No.6, 1733–1748.
- Takahashi, R., and K. Hirano (1941). Seismic vibration of soft ground, Bull. Earthq. Res. Inst., Tokyo Univ. Vol.19, No.3, 534-543 (in Japanese with English abstract).
- Takemura, M. and Toraya, K. (2015), Re-Evaluation of Seismic Intensity Distribution from the 1944 Tonankai Earthquake and Its Disaster Characteristics, Journal of Japan Association for Earthquake Engineering, Special Issue, Volume 15 Issue 7 Pages 7_2-

7_21. DOI: https://doi.org/10.5610/jaee.15.7_2

- Tamura T, Nishihata T, Moriya Y, Takimoto K, Miura F (2005) Application of evacuation simulation method during tsunami inundation considering road blockage, Coastal Engineering Journal, Japan Society of Civil Engineers, Vol.52, 2005, pp.1286-1290 [in Japanese].
- Tao, Y., and E. Rathje (2020). Taxonomy for evaluating the site-specific applicability of one-dimensional ground response analysis, Soil Dyn. Earthq. Eng., Vol.128, 105865, doi: 10.1016/j.soildyn.2019.105865.
- Usuzawa H, Imamura F, Shuto N (1997) Development of the method for evacuation numerical simulation for tsunami events, Annual Meeting of the Tohoku Branch Technology Research Conference, Japan Society of Civil Engineers, pp.430–431 [In Japanese].
- Yamaguchi, N. and Yamazaki, F. (2001), Estimation of Strong Motion Distribution in the 1995 Kobe Earthquake Based on Building Damage Data, Earthquake Engng Struct. Dyn. 2001; 30:787–801 (DOI: 10.1002/eqe.33)
- Yoshida, K. (2004), Construction of Dynamic Models of Japanese Wooden Houses for Evaluating Earthquake Damage by Considering Building Age and Proposal of the Destructive Power Index, Summery of master thesis of Department of Architecture, Graduate School of Engineering, Kogakuin University [in Japanese with English abstract].

Part I

Research on Site Amplification Evaluation Methods

This part explains three different methods for quantitatively estimating site amplification characteristics.

Chapter 2

A Method to Directly Estimate S-Wave Site Amplification Factor from Horizontal-to-Vertical Spectral Ratio of Earthquakes (EHVR)

Abstract

The main purpose of the site classification or velocity determination at a target site is to obtain or estimate the horizontal site amplification factor (HSAF) at that site during future earthquakes because HSAF would have significant effects on the strong-motion characteristics. To that end, we have been investigating various kinds of methods to delineate the S-wave velocity structures and the subsequent HSAF as precisely as possible. After the advent of the diffuse field concept, we have derived a simple formula based on the equipartitioned energy density observed in the layered half-space for incident body waves. In this study, based on the diffuse field concept together with the generalized spectral inversion technique (GIT), we propose a method to directly estimate the HSAF of the S-wave portion from the horizontal-to-vertical spectral ratio of earthquakes (EHVR). As the vertical amplification is included in the denominator of EHVR, it cannot be viewed as HSAF without correction. We used GIT to determine the vertical site amplification factor (VSAF) from strong-motion data observed by the networks in Japan, and then deduced the log-averaged vertical amplification correction function (VACF) from a total of 1,678 sites where ten or more earthquakes have been observed. The VACF without a category has a constant amplitude of about 2 in the frequency range from 1 to 15 Hz. By multiplying EHVR by VACF, we obtained the simulated HSAF. We verified the effectiveness of this correction method by using data from observation sites not used in the above-mentioned averaging.

2.1 Introduction

It is important to deduce the horizontal site amplification factor (hereafter HSAF, a spectral ratio as a function of frequency) in the main S-wave part for evaluating the site-specific design of earthquake ground motions and elucidating the relationship between the subsurface structures and their amplification effects. The methods to obtain HSAF include a theoretical calculation method based on the well-defined subsurface structure (e.g., the first deconvolution analysis by Takahashi and Hirano, 1941; see reviews in Aki, 1988, as well as Kawase, 2003), an empirical method based on the spectral ratio between borehole and surface sensors (e.g., Kitagawa et al., 1988 and Satoh et al., 1995 for Sendai, Japan; Archuleta et al., 1992, Steidl et al., 1996, and Bonilla et al., 2002 for California), and another empirical method based on the spectral ratio of a sedimentary site with a nearby site on rock (e.g., the first spectral ratio analysis by Borcherdt, 1970; then early applications can be found in Lermo and Chávez-García, 1993, Field and Jacob, 1995, and also Steidl et al., 1996). Nevertheless, the theoretical method has difficulty in determining a velocity structure at the site down to the seismological bedrock and validating the adequacy of the velocity structure. We also need damping factors of the structure, which are more difficult to evaluate quantitatively. The empirical method that uses borehole observation data has difficulty in eliminating the effects of reflected waves contained in the observed borehole seismograms (e.g., Steidl et al., 1996; Tao and Rathje, 2020). The empirical method of using data observed at a rock site for input into the denominator often has difficulty in finding such a nearby site where the intact rock is exposed, and there is an issue of whether such a rock site can really be viewed as a site without soil amplification (e.g., Steidl et al., 1996).

Meanwhile, the generalized spectral inversion technique (GIT, Andrews, 1986; followed by studies with different constraints in Iwata and Irikura, 1988, Castro et al., 1988, and Kato et al., 1992) allows for determining, on a stable basis, HSAF for appropriately selected reference site or sites, when there are many earthquakes observed at many sites. Fortunately, Japan has a couple of dense strong-motion observation networks of K-NET, KiK-net, and the JMA Seismic Intensity (Shindo-kei) network, which are nationwide networks of strong-motion observation already containing many strong-motion records. Kawase and Matsuo (2004) have used observation records obtained from 1996 until 2002 to separately perceive and elucidate the basic properties of the source, propagation path, and site amplification. A subsequent study by Kawase (2006) has focused on the nonlinear site amplification effect in the records with high peak ground acceleration. Oth et al. (2011a, 2011b) analyzed both KiK-net's surface and borehole data separately and reported several comparisons of HSAF with horizontal-to-vertical and surface-to-borehole spectral ratios. By following the strategy of Kawase and Matsuo (2004) with recent data added, Nakano et al. (2015) conducted spectral inversion analyses for Fourier spectra of more than 77,000 source-station pairs to find the stress drop dependence on magnitude and depth. A significant feature of the inversions common to Kawase and Matsuo (2004), Kawase (2006), and Nakano et al. (2015) is that they determined HSAF with respect to the outcrop equivalent of the seismological bedrock at a reference site with an estimated S-wave velocity of 3,450 m/s, by eliminating the effect of weathered rock layers from the surface records. Such a clear definition of the reference site with the S-wave velocity higher than 3.0 km/s is indispensable to obtain

stable site factors without any trade-offs with source spectra.

However, the GIT analysis requires the earthquake ground motions of many earthquakes observed at many locations. On the other hand, only three components of earthquake ground motion observed at a single station are required to determine the horizontal-to-vertical spectral ratio of earthquakes (hereinafter referred to as EHVR, a spectral ratio as a function of frequency). Nakamura (1989) proposed that the HSAF (he called it QTS, Quasi-Transfer Spectra) can be estimated directly by using the horizontal-to-vertical ratio of microtremors (MHVR, a spectral ratio as a function of frequency). Since then, many researchers have studied the following issues based on either observation or theory: (a) whether the MHVR and EHVR are the same; (b) whether the EHVR and HSAF are the same. Although discussions are still ongoing, the majority of researchers have concluded the following: the MHVR and EHVR are similar to each other but not the same; and in both the MHVR and EHVR, their peak frequencies are about the same as that of the HSAF, but the amplitudes are underestimated. Even though we deal with EHVR in the present paper, we do not adopt Nakamura's interpretation. We will discuss briefly the problem at issue (b) based on the published reports with special reference to the recent opinion article by Nakamura (2019). As a quantitative answer to the issue (a), we have already shown the empirical spectral ratios, EMR, between EHVR and MHVR for 100 sites in Japan (Kawase et al., 2018a). This paper will provide a quantitative answer to issue (b), the empirical correction function between HSAF and EHVR.

Let us assume that a sufficient number of small earthquakes have been observed at a certain site. Because it is too laborious to determine HSAF using GIT every time, there is a real need to use the EHVR that can be determined from only one site. In particular, it is difficult to apply GIT to earthquakes so small that their magnitude or source locations cannot be determined accurately, or their seismograms cannot be recorded simultaneously at different sites. We, therefore, propose in this study a simple method to correct the vertical site amplification factor (VSAF, the spectral ratio as a function of frequency), which represents the largest challenge in determining the HSAF from the observed EHVR. Contamination with surface waves is eliminated throughout this paper because we use only the main S-wave part as extracted.

Please note that the concept of the VSAF correction to EHVR has already been proposed in Kawase et al. (2018b) for the pseudo EHVR, which is the modified MHVR using the ratio between EHVR and MHVR (EMR in Kawase et al., 2018a). However, the number of the sites used was only 100 in total and less than 20 for the category-specific average. Therefore, the reliability of the correction functions that they proposed does not seem sufficiently high.

In what follows, we first review briefly the history of development and validation on the use of EHVR as a direct substitute for HSAF. We conclude that a major source of the complicated results on the validity of EHVR is coming from either the site-dependent amplification in the vertical component or the site-dependent amplification at the reference site. Then we explain the fundamental formula of EHVR based on the diffuse field concept, as well as those from GIT established in the previous studies (i.e., Kawase et al., 2011 and Nakano et al., 2015). After combining these two concepts and performing the averaging operation for the sites used, we derive a simple formula to transform EHVR into HSAF. Based on the GIT results for both HSAF and VSAF, first we show examples of HSAF, VSAF, and EHVR and then we show relationships for the maximum and average values between HSAF and VSAF and between HSAF and EHVR

to confirm their amplitude differences. Next, by using the separated VSAF (multiplied by the EHVR at the seismological bedrock) from GIT, we calculate three different types of VCAF with and without categories and recommend the simplest one without category. Finally, we check the validity of the correction method at 103 sites not used to calculate VACF.

2.2 Issues on Horizontal-to-Vertical Spectral Ratios: EHVR and HSAF

Nakamura (2019) has recently expressed that the so-called Nakamura method is not just a method to calculate the horizontal-to-vertical spectral ratio of earthquakes or microtremors, but it includes an interpretation that the horizontal-to-vertical spectral ratio can be viewed as HSAF (QTS in their term). Therefore, care should be taken when quoting the Nakamura method. More specifically, we should use the “Nakamura method” to refer to the method in which the horizontal-to-vertical spectral ratio of ground motion is interpreted as the direct substitute of HSAF, not to refer to the method just taking the horizontal-to-vertical spectral ratio. However, if we separate the Nakamura method into two steps, first to take the horizontal-to-vertical spectral ratio of ground motion, and then to use it as a direct substitute of HSAF, we think that the latter would be called the “Nakamura interpretation” since it is the interpretation, not the method.

In this section, we would like to review several papers regarding the relationships between EHVRs and observed and theoretical HSAFs to see the concrete facts reported in the past. Then we will make a couple of comments on some issues related to the interpretation of Nakamura (1989, 2019).

The first comparison of EHVR of the S-wave part with the conventional horizontal-to-horizontal (at a reference site) spectral ratio method (HHR method, sometimes called host-to-target correction) was reported by Lermo and Chavez-Garcia (1993) for several sites in three regions in Mexico, including four sites inside the Mexico City basin. They showed favorable results on the correlation between HHR and EHVR, both in frequency and amplitude at least for the fundamental mode. Then Field and Jacob (1995) investigated the difference of site terms from HHR as conventional spectral ratios or site factor in the generalized spectral inversion (Andrew, 1986), EHVR labeled the receiver function type estimate, and MHVR labeled the Nakamura method in their paper. They found favorable results for the first two estimates and smaller (1.6 times) amplitude results in EHVR at two sediment sites, but MHVR was reported to be valid only for the fundamental peak frequency. Similar conclusions can be found in Lachet et al. (1996) and Riepl et al. (1998) for EURO-SEISTEST, Theodoulidis et al. (1996) for Garner Valley, and Bonilla et al. (1997) for the aftershocks of the 1994 Northridge earthquake, who were very critical about the correlation between the amplitudes of EHVR and those of HHR. Parolai et al. (2000) also reported a deficiency in amplitude for EHVR in comparison to HHR obtained by GIT.

Then Satoh et al. (2001) performed very complete comparisons on the relationship between HHR and EHVR for the S-wave part, P-wave part, S-coda part, and P-coda part, in addition to the comparison with MHVR by using 20 stations in Sendai, Japan. Their conclusions

are similar to those mentioned above, namely, peak frequencies of EHVR and MHVR are similar to those of HHR if they are less than 1.0 Hz and their amplitudes are higher than 3, but peak amplitudes of EHVR and MHVR are not well correlated to those of HHR. Satoh et al. (2001) also provided VVR, the vertical-to-vertical (at a reference site) spectral ratios, showing 2 to 4 times amplification in the high-frequency range. Satoh et al. (2001) also provided a theoretical explanation of the difference between HHR and EHVR by using oblique incidence of SV-waves to one-dimensional structures, as in Lermo and Chavez-Garcia (1993) but with much better matching. Their results were followed (independently) by the results by Bonilla et al. (2002) by using the Garner Valley vertical array, who also showed similar results and provided the reason why EHVR is deficient in terms of amplitude; it is (quote) “because the vertical component has significant site response due to S-to-P conversions that begin in the weathered granite boundary at 87-m depth”. A similar report on the vertical component amplification was made by Parolai et al. (2004) for aftershocks of the 1999 Izmit earthquake.

As for the vertical component amplification, we should refer to Castro et al. (1997) who obtained relative amplification of the vertical component of the S-wave part of small earthquakes for the first time. Although they mentioned that the relative amplification in the vertical component was found to be small and thus supported the hypothesis of Nakamura (1989, 2019), the site amplification factors that they got were relative to the average site amplification for all the sites, not to a specific rock outcrop site. Since there exists a site with amplification much less than 1.0, the site amplification factors relative to the smallest site should be much higher.

For readers who need further literature surveys on the MHVR and EHVR amplitude characteristics, we would like to refer to three interesting reports which summarize many investigations performed mainly in Europe from the late 90s until the early 2000s, namely Bonnefoy-Claudet et al. (2006) for MHVR, and Haghshenas et al. (2008) and Cultrera et al. (2014) for both EHVR and MHVR. Since these papers are quite complete in reviewing on-going research until their publication dates, we do not cover the content any further, but basically our conclusions mentioned above need not be revised.

However, we found that the majority of our observations were different from those that Rodriguez and Midorikawa (2003) reported, including higher EHVR values than HHR values from 150 sites in Yokohama City. Other reports also showed mixed results. The reason why we have sometimes smaller HHR and higher EHVR in amplitude is because HHR depends on the amplification at the reference site, while EHVR depends on the amplification on the vertical component. As always warned, and as seen in Castro et al. (1997), it is very difficult to find a good rock outcrop site with the S-wave velocity higher than 3 km/s. In the case of the network used by Rodriguez and Midorikawa (2003), all of the stations are inside Yokohama City in the close vicinity of Tokyo Bay, and so it is impossible to find a good rock outcrop site within these urbanized areas. If the reference station is not on a hard rock, then the horizontal amplification at the reference station would be larger than the vertical amplification of soil sites, and therefore HHR could be lower than EHVR. This explains why researchers are reporting that EHVR sometimes works as a substitute for HHR and sometimes does not.

In summary, it is clear that we should pay careful attention to both the vertical amplification factors as a site-dependent parameter and the reference site characteristics used to derive HHR as a target to predict the behavior of the horizontal component of ground motions.

2.3 Issues on Horizontal-to-Vertical Spectral Ratios: MHVR and EHVR

Nakamura's opinion (Nakamura, 2019), as well as his original paper (Nakamura, 1989), did not rigorously distinguish HVRs from microtremors and earthquake ground motions. Since the dominant wave types are significantly different, this negligence cannot be overlooked. Especially after the advent of the theoretical solutions based on the diffuse field concept (Sanchez-Sesma et al., 2011 for MHVR and Kawase et al., 2011 for EHVR), it is no longer possible to consider that they give us the same HVRs. Nakamura (1989, 2019) referred to their comparison of MHVRs and EHVRs at several sites in Mexico City, but they should be considered as a special case where the shallow soil layers are so soft (with low Q values) that they absorb the energy of reverberated S-waves and therefore EHVRs there can only show contributions within shallow soft soil layers and thus no significant high-frequency peaks, as Salinas et al. (2014) showed at one site in the lake-bed zone in Mexico City (Also very high Poisson's ratios of these shallow layers are quite extraordinary but we do not know at this moment how much they contribute to the similarity in MHVRs and EHVRs). For ordinary sediment sites in Japan, we have already shown that we need Earthquake/Microtremor Ratio (EMR) of HVR to correct the amplitude of MHVR (Kawase et al., 2018a).

Nakamura's opinion on his interpretation of MHVR is difficult to follow, but one misinterpretation is apparent: he mentioned that the amplitude of the vertical component at the peak frequency of MHVR is zero or close to zero and therefore there is no surface wave contribution near the peak (which brings the interpretation that we can extract the S-wave amplification at least around the peak of MHVR). This is not true. The surface (in this case, Rayleigh) wave contribution appears not only in the vertical component but also in the horizontal component, irrespective of frequency, even though the percentage of contribution is frequency dependent. It is well known that the horizontal peak frequency will coincide for S-wave, Love-wave, and Rayleigh wave if the impedance contrast between the bedrock and the sediment is sufficiently large. As seen in the theoretical solution based on the diffuse field concept for microtremors (e.g., Sánchez-Sesma et al., 2011), as well as a conventional mode-superposition of surface waves (e.g., Arai and Tokimatsu, 2004), a major source of peaks in MHVR is the amplification in the horizontal component as a result of surface (Love and Rayleigh) wave amplification with soft sediments, while a major source of troughs in MHVR is the amplification in the vertical component from the Rayleigh wave.

2.4 Diffuse Wavefield Theory and GIT Formulation for EHVR

The theoretical background of the proposed method is based on the theory of diffuse wavefield. When observing earthquake ground motion propagated as S-waves from various

seismic sources to one location, the Fourier transform of the autocorrelation function of normalized ground motion u , or the power spectrum at a point P for a circular frequency ω , is given as follows, as shown by Kawase et al. (2011):

$$\left\langle \frac{|u(P, \omega)|^2}{\int |u(P, \varpi)|^2 d\varpi} \right\rangle = K \times |TF(\omega)|^2 = -K \times \rho_H c_H \omega \text{Im}[G^{Eq}(P, P, \omega)] \quad (2.1).$$

where $G^{Eq}(P, P, \omega)$ is the Green's function of seismic motion observed at P for the source at P , ρ_H and c_H is the density and the propagating velocity of the medium, $TF(\omega)$ is the transfer function of the medium in either the horizontal or vertical component, and K is a constant. The corresponding EHVR on the surface is given by

$$EHVR = \frac{H(\omega)}{V(\omega)} = \sqrt{\frac{\text{Im}[G_{\text{horizontal}}^{Eq}(0, 0; \omega)]}{\text{Im}[G_{\text{vertical}}^{Eq}(0, 0; \omega)]}} \quad (2.2).$$

$$= \sqrt{\frac{\alpha_H}{\beta_H}} \frac{|TF_{\text{horizontal}}(\omega)|}{|TF_{\text{vertical}}(\omega)|} \quad (2.3).$$

Here, α_H and β_H are the P- and S-wave velocities of the seismological bedrock (that is the semi-infinite medium), respectively, and $TF_{\text{horizontal}}(\omega)$ and $TF_{\text{vertical}}(\omega)$ are the transfer functions in the horizontal and vertical component for the vertically incident wave from the seismological bedrock to the surface, respectively. We need not consider the incidence angles of individual P- and S-waves in equation (2.3) because we take the average of multiple events with different azimuth and incident angles under the diffuse wavefield assumption. Refer to Kawase et al. (2011) for further explanations and numerical verifications. In the diffuse field theory, a diffuse wavefield is assumed to be formed in the entire propagation path from the hypocenter to the seismological bedrock immediately below the observation site, and energy is assumed to be uniformly distributed in the semi-infinite uniform medium including the hypocenter. A resulting characteristic of the theory is that the amplitude of the incident wave to the bedrock is uniquely determined by the square root of the ratio of the P-wave velocity to the S-wave velocity as shown in equation (2.3), thanks to the equipartition of energy. This theoretical prediction of the bedrock spectral ratio between horizontal and vertical components should correspond to the reciprocal of the observed bedrock spectral ratio, $V_B H_B R$, as mentioned below. From the diffuse wavefield concept, the seismological bedrock corresponds to the surface of the half-space where all the wave propagation and scattering from the source are taking place. This means that we need to estimate strong motion spectra observed on a hypothesized outcrop of the upper crust, with the S-wave velocity at least 3.0 km/s or higher.

According to the GIT concept that has been well-established in previous studies (e.g., Andrews, 1986; Iwata and Irikura, 1988; Castro et al., 1988; Kato et al., 1992; Kawase and Matsuo, 2004), the S-wave Fourier spectrum of horizontal motion, $F_{S_{-ij}}$, of earthquake i observed

at site j is decomposed into the logarithmic sum of the source term S_{S_i} , the path term P_{S_ij} , and the horizontal site amplification factor at site j H_{S_j} , as shown in the following equation:

$$\log F_{S_ij} = \log S_{S_i} + \log P_{S_ij} + \log H_{S_j} \quad (2.4).$$

All the above variables are spectra having mutually independent frequency components. Likewise, the S-wave Fourier spectra of vertical motion, G_{S_ij} , is decomposed into the following equation:

$$\log G_{S_ij} = \log S_{S_i} + \log P_{S_ij} + \log V_B H_B R + \log V_{S_j} \quad (2.5).$$

This assumes that ground motion is propagated as S-waves until reaching the seismological bedrock immediately below the observation site and then these S-waves are converted to P-waves, which are observed as vertical motion on the ground surface. Here, V_{S_j} is the vertical site amplification factor for site j . The third term in equation (2.5), $V_B H_B R$, is a coefficient for converting horizontal (S-wave) amplitude into vertical (P-wave) amplitude, and theoretically it corresponds to the inverse of the aforementioned horizontal-to-vertical amplitude ratio of the incident wave at the bedrock in the diffuse wavefield on the seismological bedrock (i.e., the square-root term in equation (2.3)). This coefficient arises because the main subject being addressed here is the S-waves propagated and scattered through the medium from the hypocenter to the point on the seismological bedrock immediately below the site, whereas V_{S_j} represents the vertical (P-wave) amplification factor from the seismological bedrock to the surface. Please note that HSAF and VSAF are the general terms referring to the site amplifications in the horizontal and vertical directions, while H_{S_j} and V_{S_j} are the specific terms derived from GIT.

2.5 Proposed HSAF Calculation Method

With the above preparation, we now discuss the relationship between the observed EHVR and HSAF. From equations (2.4) and (2.5), the observed EHVR is given by

$$EHVR = \left\langle \frac{F_{S_ij}}{G_{S_ij}} \right\rangle = \left\langle \frac{H_{S_ij}}{V_{S_ij} * V_B H_B R} \right\rangle = \langle H_{S_ij} \rangle / \langle V_{S_ij} * V_B H_B R \rangle \quad (2.6).$$

Then the observed HSAF is therefore given by

$$HSAF = \langle H_{S_ij} \rangle = EHVR * \langle V_{S_ij} * V_B H_B R \rangle \quad (2.7).$$

Here, $\langle \rangle$ represents the averaging operation in the logarithmic space for all the observed events. Throughout the paper, the average is always taken in the logarithmic space. Please note that in the logarithmic space (i.e., for a geometrical mean) the average of ratios in the first formula of equation (2.6) is the same as a ratio of the averages in the last formula, as shown in Appendix. Without GIT analysis we usually use the average of ratios in the first formula of equation (2.6).

Equation (2.7) means that HSAF can be obtained by multiplying EHVR by both VSAF and the inverse of the horizontal-to-vertical spectral ratio on the seismological bedrock, $V_B H_B R$.

From equation (2.3), the theoretical transfer function of a vertically-incident P-wave can be used for VSAF if we know the P-wave velocity structure with the damping factor from the seismological bedrock to the surface. Because it is unrealistic to assume that only the P-wave velocity and its damping are known whereas the S-wave velocity and its damping are unknown, we would like to use the empirical VSAF, that is, $\langle V_{S,j} \rangle$ in equation (2.5) obtained by the GIT analysis.

Since applying equation (2.7) to the same site is a circular argument (or the obvious relationship) as long as we use EHVR in the last formula of equation (2.6), we determine an empirical correction function averaged over multiple sites as in Kawase et al. (2018b) for MHVR. Expressing this vertical amplification correction function as VACF (as a function of frequency) after the log-averaged operation for all the selected sites, we obtain the S-wave amplification ratio at an arbitrary site by the following simple equation.

$$HSAF = EHVR * VACF \quad (2.8).$$

In this equation, VACF means the log-averaged spectral ratio of the vertical amplitude on the ground surface with respect to the horizontal amplitude on the outcrop of the seismological bedrock. It is possible to determine VACF directly by using the GIT for the vertical component on the surface with respect to the horizontal component on the reference bedrock, as shown in equation (2.5).

2.6 Results of Application

The conditions and method of seismic wave analysis using the GIT are not detailed in this paper (see Nakano et al., 2015), but only introduce their basic aspects here. They restricted events and sites with JMA magnitude $M_{JMA} \geq 4.5$; source depth ≤ 60 km; hypocentral distance ≤ 200 km; peak ground acceleration ≤ 2 m/s; and number of observation sites triggered simultaneously for one event ≥ 3 . These selection criteria resulted in 77,213 event-station pairs (three times in terms of the number of accelerograms) at 2,105 sites for 967 events. Only a duration of 5 sec to 15 sec from the onset of the S-wave is analyzed according to the magnitude (5 s for $4.5 < M_{JMA} \leq 6$; 10 s for $6 < M_{JMA} \leq 7$; 15 s for $7 < M_{JMA} \leq 8$). They used a Parzen window of 0.1 Hz for a minimum level of smoothing. The most important feature of their GIT is that before the GIT analysis they determined the S-wave velocity structure at the reference site using the transfer function (the spectral ratio and the phase difference) between the surface and the borehole 200 m below and that the observed Fourier spectra on the surface were corrected (deconvolved) to obtain the hypothesized outcrop spectra of the seismological bedrock with an S-wave velocity of 3,450 m/s.

While no limit was set to the number of earthquakes at one site in GIT, in category-specific averaging, we only use 1,678 sites where ten or more earthquakes had been observed. For verification purposes, we use 103 sites where the number of earthquakes observed ranged from seven to nine.

First, we address the vertical-to-horizontal spectral ratio $V_{BH_B}R$ on the seismological bedrock, that is, the averaged ratio of the corrected vertical spectra with respect to the corrected horizontal spectra as the outcrop motion equivalent to the seismological bedrock at the reference site. In Figure 2.1a the observed EVHR on the surface at YMGH01 and its average and average \pm one standard deviation in the logarithmic space over frequency are shown. This is the observed spectral ratio of the vertical component with respect to the horizontal one, the reciprocal of the EHVR at YMGH01. To estimate $V_{BH_B}R$ we need to correct both HSAF and VSAF in the observed EVHR as:

$$V_{BH_B}R = EVHR/VSAF^*HSAF \quad (2.9).$$

Figure 2.1b shows thus obtained $V_{BH_B}R$ and its average and average \pm one standard deviation over frequency. We can see that the ratio fluctuates slightly around unity except in the frequency range higher than 15 Hz. In the range between 0.12 and 15 Hz, the average minus one standard deviation (lower-side dotted line) is in good agreement with the square root of the ratio of the S-wave velocity to the P-wave velocity on the bedrock (line with circles), which is expected from the diffuse wavefield theory as shown in equation (2.3). As this value is about 0.76 in the case of a Poisson solid, it can be said that the vertical motion is nearly equal to the horizontal motion in the seismological bedrock.

The frequency range of the validity in our analysis from this point should be considered to be in between 0.12 to 15 Hz since we see a conspicuous peak in the higher frequency range. As shown in Figure 2.1b, this conspicuous peak observed in $V_{BH_B}R$ would be coming from the theoretical HSAF used for the site correction at YMGH01 (dot-dash line). We will further investigate the appropriateness of the theoretical correction function at YMGH01 in the frequency range higher than 15 Hz.

We should note that $V_{BH_B}R$ in Figure 2.1b is different from EVHR in Figure 2.1a as the value of the theoretical HSAF shown in Figure 2.1b (dot-dash line). Theoretically speaking, we need also to correct the theoretical VSAF at YMGH01 as in equation (2.9), however, the theoretical VSAF based on the boring data at YMGH01 is found to be almost unity for the whole frequency range of interest. The importance of connecting the formulas from the diffuse field concept, namely equations (2.1) to (2.3), with those from GIT, namely equations (2.4) to (2.7), is that we can confirm the qualification of the reference site condition in GIT through the comparison of $V_{BH_B}R$ derived from the observed EVHR at the reference site and the theoretical prediction in equation (2.3), as is shown in Figure 2.1b. We should note that the correspondence of $V_{BH_B}R$ to the theoretical value in equation (2.3) is considered to be a requirement for the seismological bedrock.

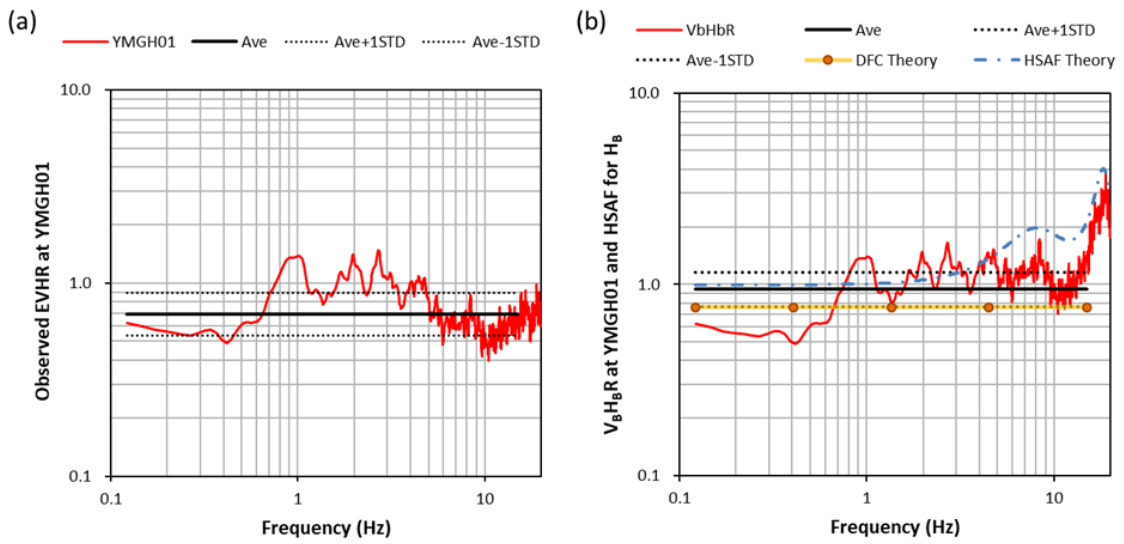


Figure 2.1. (a) The observed EVHR, that is the reciprocal of the EHVR, on the surface at the reference KiK-net site YMGH01 (red line) and its geometrical mean (black line) and the mean \pm one standard deviation (dotted lines) in the frequency range from 0.12 to 15 Hz with equal sampling. (b) The calculated (red line) and geometrical mean (black line) values of $V_B H_B R$ at the reference KiK-net site YMGH01, the mean \pm one standard deviation (dotted lines), the theoretical solution of the diffuse field (line with circles), and the theoretical HSAF used for the outcrop bedrock-motion correction at YMGH01 (dot-dash line). The predominant peak in the frequency range higher than 15 Hz observed in $V_B H_B R$ would be primarily coming from the theoretical HSAF used for the site correction at YMGH01.

Then we would like to show several examples of HSAF, VSAF, and EHVR to let readers understand their relative contributions and general frequency fluctuations. Figure 2.2 shows eight sites among those with nine observed earthquakes. These are the sites used for validation later. In each panel, we compared the observed HSAF and VSAF, together with the observed EHVR. These are all log-averaged spectral values derived from GIT, although EHVR can also be directly calculated as the geometrical mean of the observed spectra as shown in the first formula of equation (2.6). The observed VSAF here is actually $VSAF^* V_B H_B R$, the vertical site amplification relative to the same horizontal reference as HSAF, as shown in equation (2.7), and so we used $VSAF^*$ as its abbreviation. Please note that VACF as the correction function for vertical amplification in equation (2.8) is the geometrical mean of the $VSAF^*$ for selected sites among the 1,678 sites used. As we can see, the HSAFs are almost always higher than the EHVRs and the difference can be quite significant if we have high amplitude in $VSAF^*$. YMN011 is the exception where the EHVR is a little higher than the HSAF, however, both the HSAF and the $VSAF^*$ at this site are basically small.

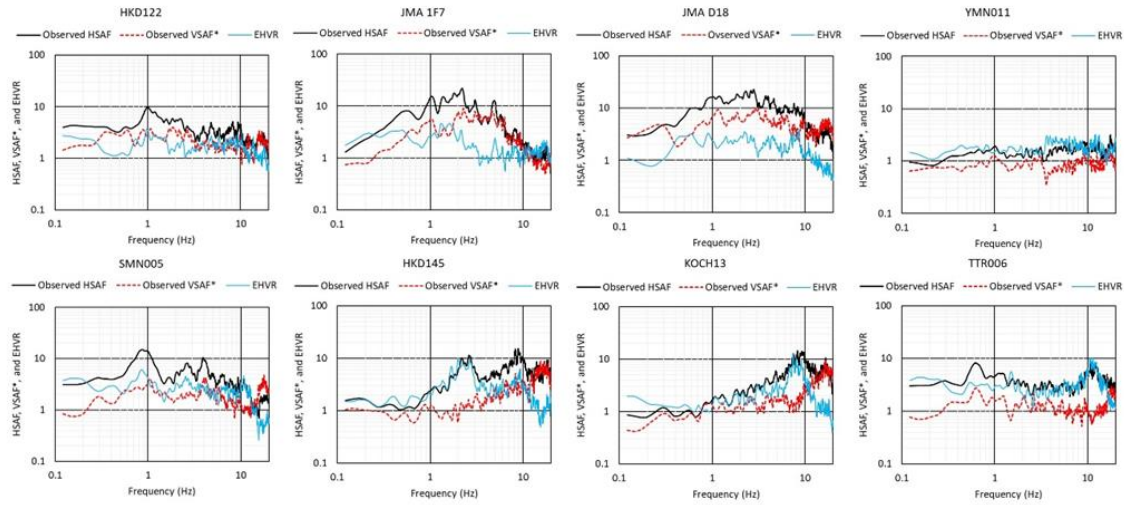


Figure 2.2. HSAF (black line), VSAF* (red broken line), and EHVR (right blue line) at eight sites arbitrarily selected from the sites with nine observed earthquakes and later used for validation (Figure 2.8). The plotted VSAF* here is actually VSAF* V_{BHBR} , the vertical amplification factor relative to the same horizontal bedrock motion. Thus, HSAF is equal to EHVR times VSAF* at each site. At most of the sites the VSAF* is much smaller than the HSAF in amplitude so that EHVR tends to be close to HSAF, however, the VSAF* at JMA D18 is larger than those at the other sites so that the EHVR is smaller not only than the HSAF but also than the VSAF* there.

The next issue is the general correlation characteristics of amplitudes between HSAF and VSAF. Figure 2.3a shows the correlation of the maximum (peak) amplitudes between HSAF in the horizontal axis and VSAF in the vertical axis in the range between 0.12 and 20 Hz, while Figure 2.3b shows the correlation of the average amplitudes over the same frequency range. Note that the VSAFs here are those without V_{BHBR} . These diagrams show that the VSAF is about 30% to 40% of the HSAF, and their correlation is lower in the maximum (peak) amplitude and higher in the average amplitude. The averaged VSAF values of 1 or smaller are found mainly at observation sites where HSAF values are smaller than about 3.

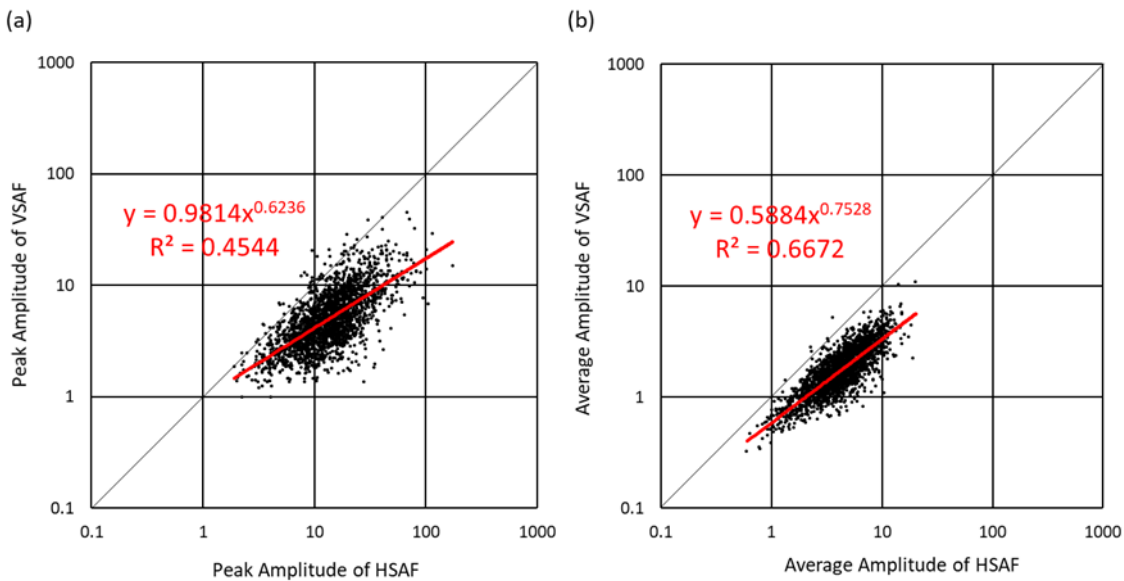


Figure 2.3. The relationship between the HSAF (horizontal axis) and the VSAF (vertical axis) in terms of (a) the maximum (peak) amplitudes and (b) the average amplitudes (the geometrical mean over the frequency), obtained by GIT. The linear regression lines with their coefficients are also plotted.

The relationship between EHVR and HSAF is investigated in a similar manner. Figure 2.4 likewise shows the maximum (peak) and average amplitudes of EHVR (horizontal axis) and those of HSAF (vertical axis). We also add here the direct comparisons of the Fourier spectral amplitudes of EHVR and HSAF at 0.5, 1, 2, and 5 Hz. Although the figure indicates a minor correlation between HSAF and EHVR, they do not correlate apparently on a one-on-one basis (thin solid line). In general, the HSAF is greater than the EHVR by a factor of about 2. The figure clearly indicates that the EHVR cannot be viewed as an effective substitute for the HSAF at the majority of the sites.

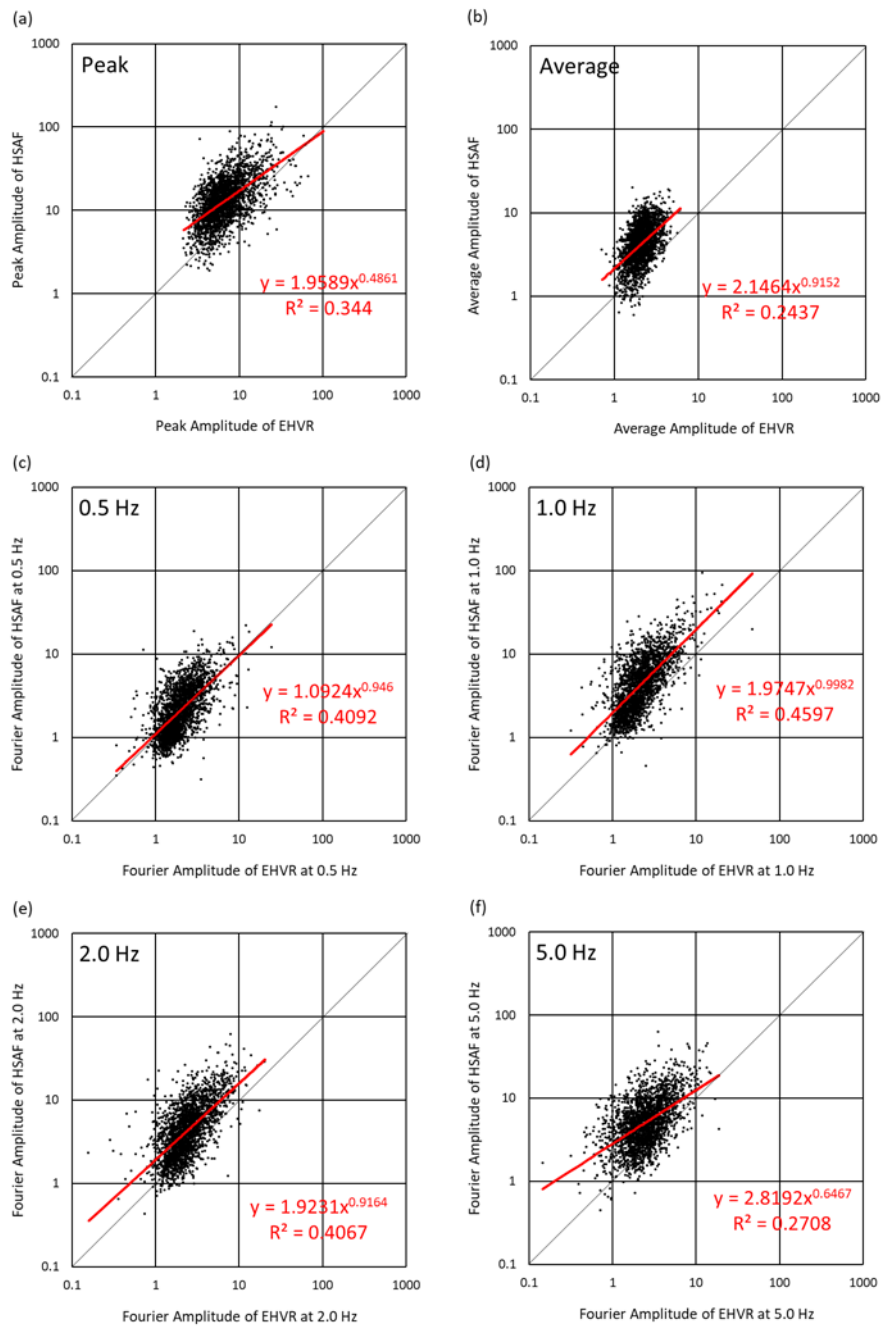


Figure 2.4. The relationships between EHVR in the horizontal axis and HSAF in the vertical axis in terms of (a) the maximum (peak) amplitudes and (b) the average amplitudes (the geometrical mean over the frequency) obtained by GIT. The linear regression lines with coefficients are also plotted. From panels (c) to (f) the Fourier spectral amplitudes of EHVR versus HSAF at 0.5, 1, 2, and 5 Hz are also compared. It is clear that the HSAF is about two times larger than the EHVR, except for the spectra at 0.5 Hz where we can see the 1:1 relationship.

As the above discussion points to the necessity to correct VSAF in obtaining HSAF from the EHVR, we try to correct the EHVR by using the VSAF obtained by the simultaneous GIT analysis for both vertical and horizontal motions. Equation (2.7) suggests that the correction through $V_{\text{SAF}} \times V_{\text{BHBR}}$ is necessary. Since the only constraint condition (the reference point) in the GIT analysis of Nakano et al. (2015) is the horizontal motion spectrum at the outcrop equivalent to the extracted seismological bedrock at YMGH01, the VACF in equation (2.8) is directly determined from the vertical site factors obtained by GIT (i.e., we get V_{SAF}^*). If the GIT analysis is conducted only for the vertical components, V_{BHBR} should be corrected because the vertical component at the reference point will be used as a norm in that case (i.e., we get VSAF).

The 1,678 observation sites where ten or more seismic spectra were available are grouped into two categories divided by whether the peak amplitude of the EHVR was not less than 5 or less than 5. The sites are further classified into four categories according to different peak frequency ranges (1 Hz or less, between 1 and 5 Hz, between 5 and 10 Hz, and 10 Hz or more) to determine the log-averaged VACF over all the sites in each category. The number of the sites in each category is tabulated in Table 2.1 to confirm that a sufficient number of sites exist in all the categories. The results are shown in Figure 2.5 (their digital values of the averages, as well as the standard deviations, are listed in Tables A2.1 and A2.2 in the Appendix to this article). The figure indicates that there are only negligible differences due to peak amplitude; there are relatively small differences due to peak frequency; the amount of correction increases as peak frequency decreases; the correction amplitude is by a factor of about 3 at around 1 Hz and by a factor of 2.5 in the range between 1 and 5 Hz. While the finding that spectra are not significantly affected by the characteristics of EHVR may appear unexpected given that the EHVR is correlated with both the P- and S-wave transfer functions, we should note that there exist several observation sites showing V_{SAF}^* values deviated strongly from the average. The standard deviations are close to and sometimes larger than the differences between the averages of two categories. Therefore, the similarity in the average characteristics does not necessarily mean that the P-wave velocity structure is similar throughout the nation. Nevertheless, it is evident that the fluctuation with frequency is smaller in the V_{SAF}^* than in the HSAF as seen in Figure 2.2.

Table 2.1. Number of sites in each category used for VACF calculation shown in Figure 2.5 and the averages (the geometrical means) of peak frequency fp and peak amplitude Ap of EHVR in each category.

Range of Peak Frequency fp (Hz)	Range of Peak Amplitude Ap	Parameters in each category		
		No. Site	Geometrical mean of peak frequency fp (Hz)	Geometrical mean of peak amplitude Ap
$fp \leq 1$	$Ap < 5$	71	0.55	3.84
	$Ap \geq 5$	54	0.75	7.28
$1 < fp \leq 5$	$Ap < 5$	224	2.52	3.99
	$Ap \geq 5$	540	2.52	7.49
$5 < fp \leq 10$	$Ap < 5$	182	7.00	4.00
	$Ap \geq 5$	337	7.17	7.93
$10 < fp \leq 20$	$Ap < 5$	104	13.35	3.80
	$Ap \geq 5$	166	12.71	7.66
All	-	1,678	4.08	6.07

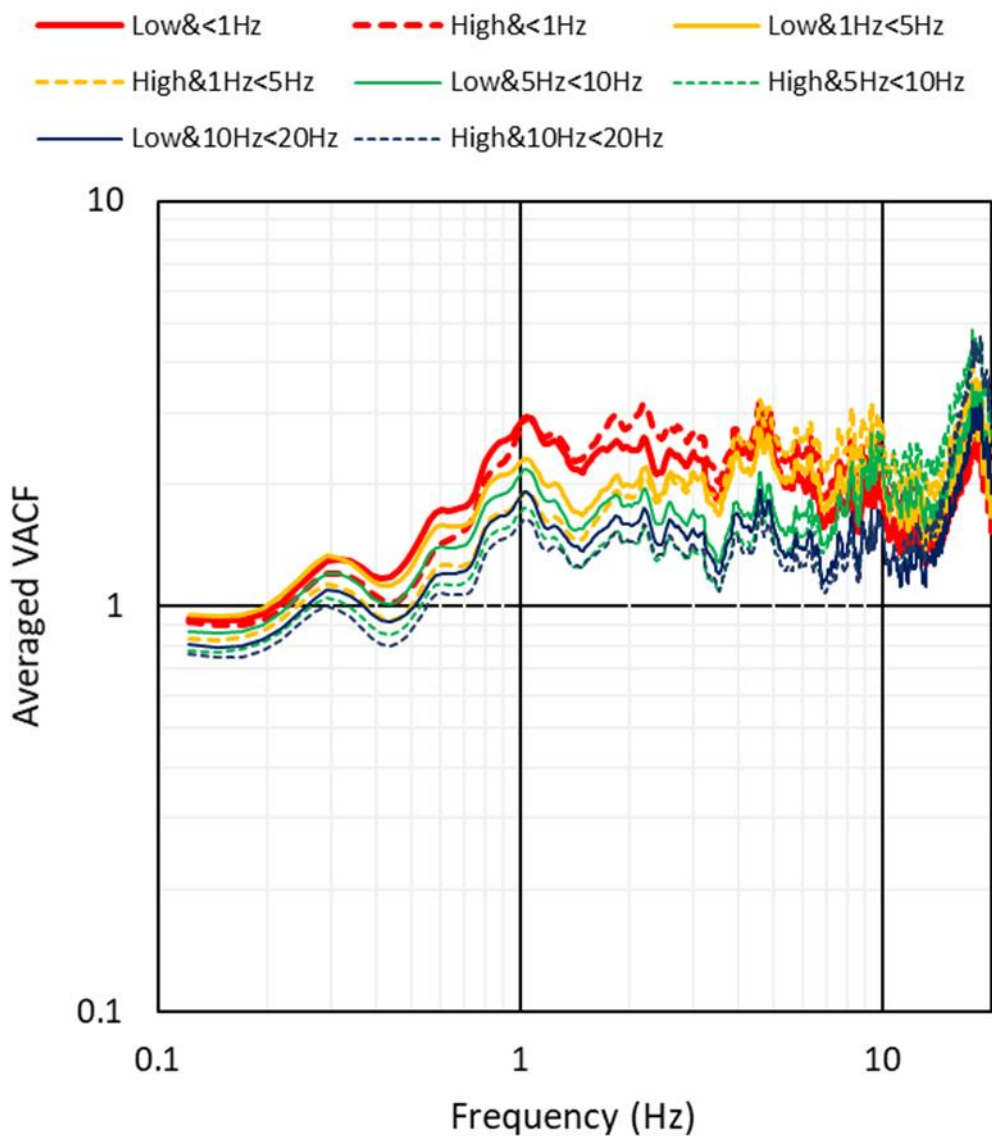


Figure 2.5. The average (geometrical mean) vertical amplification correction functions (VACF) for each of eight site categories classified by the peak EHVR values. The peak amplitude threshold used is 5 and the peak frequency ranges are 0.1 to 1 Hz, 1 to 5 Hz, 5 to 10 Hz, and 10 to 20 Hz. The number of sites in each category and its average peak amplitude and frequency are tabulated in Table 2.1. Note that the common significant peaks in the frequency range higher than 15 Hz should be due to the peak in $V_B H_B R$ shown in Figure 2.1b, which may be an artifact coming from the theoretical amplification correction at YM GH01. Digital values of the averages, as well as the standard deviations, are listed in Tables A2.1 and A2.2 in the Appendix from 0.12 to 15 Hz.

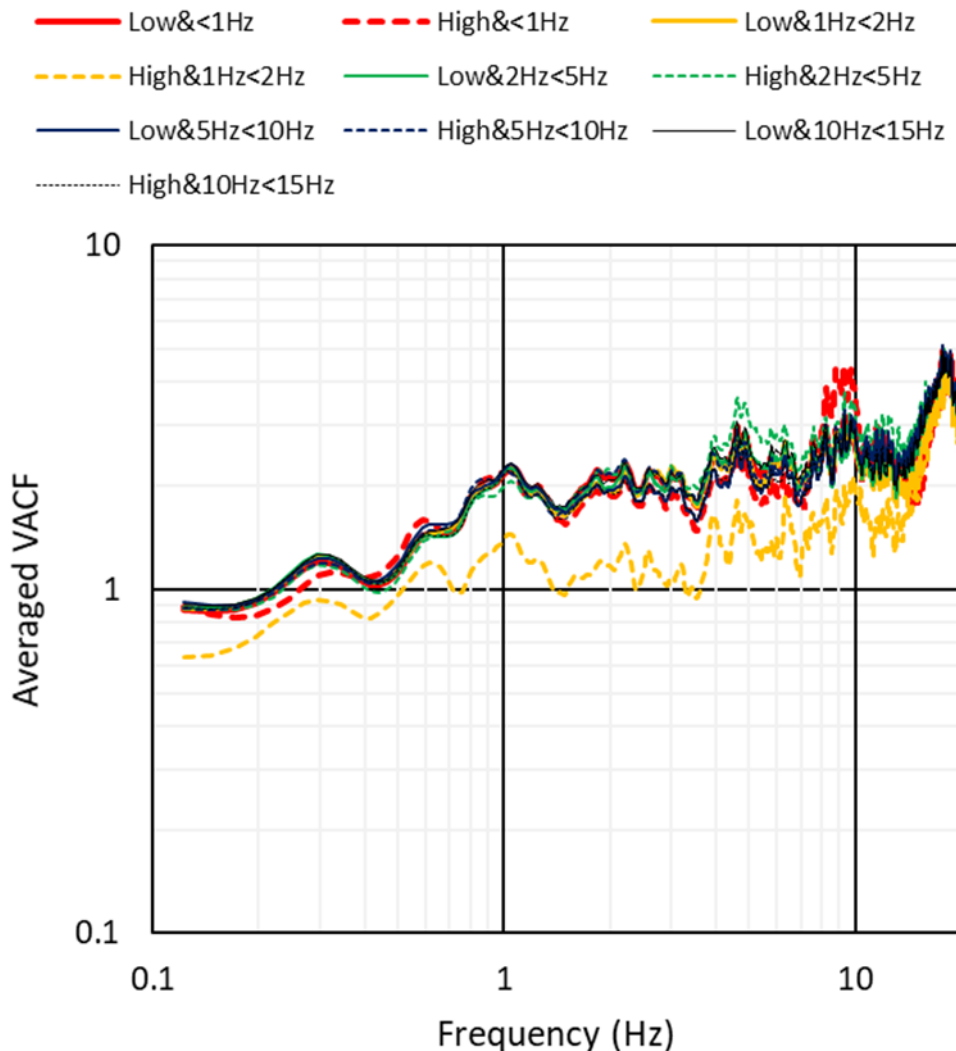


Figure 2.6. The average vertical amplification correction functions (VACF) for each of the ten categories classified by the peak EVHR values, the reciprocal of EHVR. The peak-amplitude threshold used is 1.5 and the peak- frequency ranges used are 0.1 to 1 Hz, 1 to 2 Hz, 2 to 5 Hz, 5 to 10 Hz, and 10 to 20 Hz. The number of sites in each category and its average peak amplitude and frequency are tabulated in Table 2.2.

To categorize the VACF, however, it is thought to be desirable that the categorization would be based on differences in the vertical amplification factor. We, therefore, determine the EVHR, which is the reciprocal of the EHVR, to obtain the VACF through the classification based on the frequency and peak amplitude of the EVHR. The threshold amplitude is chosen as 1.5 at this time. The results are given in Figure 2.6, which unexpectedly shows that the correction functions were nearly identical except when there is an amplitude peak of 1.5 or more in the frequency range between 1 and 2 Hz. As there are only seven sites where an amplitude peak of 1.5 or more existed in the 1 to 2 Hz range as shown in Table 2.2, the difference in the average value appears to reflect the different characteristics of these seven sites. In fact, by eliminating the amplitude-based classification and adopting only the peak frequency-based classification, we can obtain functions having the same form regardless of the peak frequency in EVHR.

As discussed above, it is possible to use the VACF in Figure 2.5 to take the EHVR characteristics into account. However, considering the large standard deviations in comparison to the average differences in the categorized VACFs (Table A2.2), the efficiency of the categories used in Figure 2.5 may not be so significant. Therefore, in the verification given below, we use the average VACF of all sites without categorization for the sake of simplicity, which is shown in Figure 2.7 (the digital values of the average, as well as the standard deviation, are listed in Table A2.3 in the Appendix). The VACF without a category shows the following frequency characteristics: no amplification up to 0.5 Hz, linearly increasing amplitude up to 1.0 Hz, and constant amplitude of about 2.0 up to 15 Hz. We can use this VACF to correct EHVR in the frequency range from 0.12 to 15 Hz as long as the inevitable variability of about 1.5 times (Table A2.3) is acceptable.

Table 2.2. Number of sites in each category used for VACF calculation shown in Figure 6 and the averages (the geometrical means) of peak frequency fp and peak amplitude Ap of EVHR in each category.

Range of Peak Frequency fp (Hz)	Range of Peak Amplitude Ap	Parameters in each category		
		No. Site	Geometrical mean of peak frequency fp (Hz)	Geometrical mean of peak amplitude Ap
$fp \leq 1$	$Ap < 1.5$	346	0.34	0.94
	$Ap \geq 1.5$	12	0.49	2.10
$1 < fp \leq 2$	$Ap < 1.5$	119	1.40	0.99
	$Ap \geq 1.5$	7	1.45	2.30
$2 < fp \leq 5$	$Ap < 1.5$	151	3.03	1.02
	$Ap \geq 1.5$	24	3.55	2.52
$5 < fp \leq 10$	$Ap < 1.5$	156	7.37	1.09
	$Ap \geq 1.5$	74	7.44	2.20
$10 < fp \leq 15$	$Ap < 1.5$	393	13.5	1.10
	$Ap \geq 1.5$	396	13.7	2.30
All	-	1,678	4.12	1.31

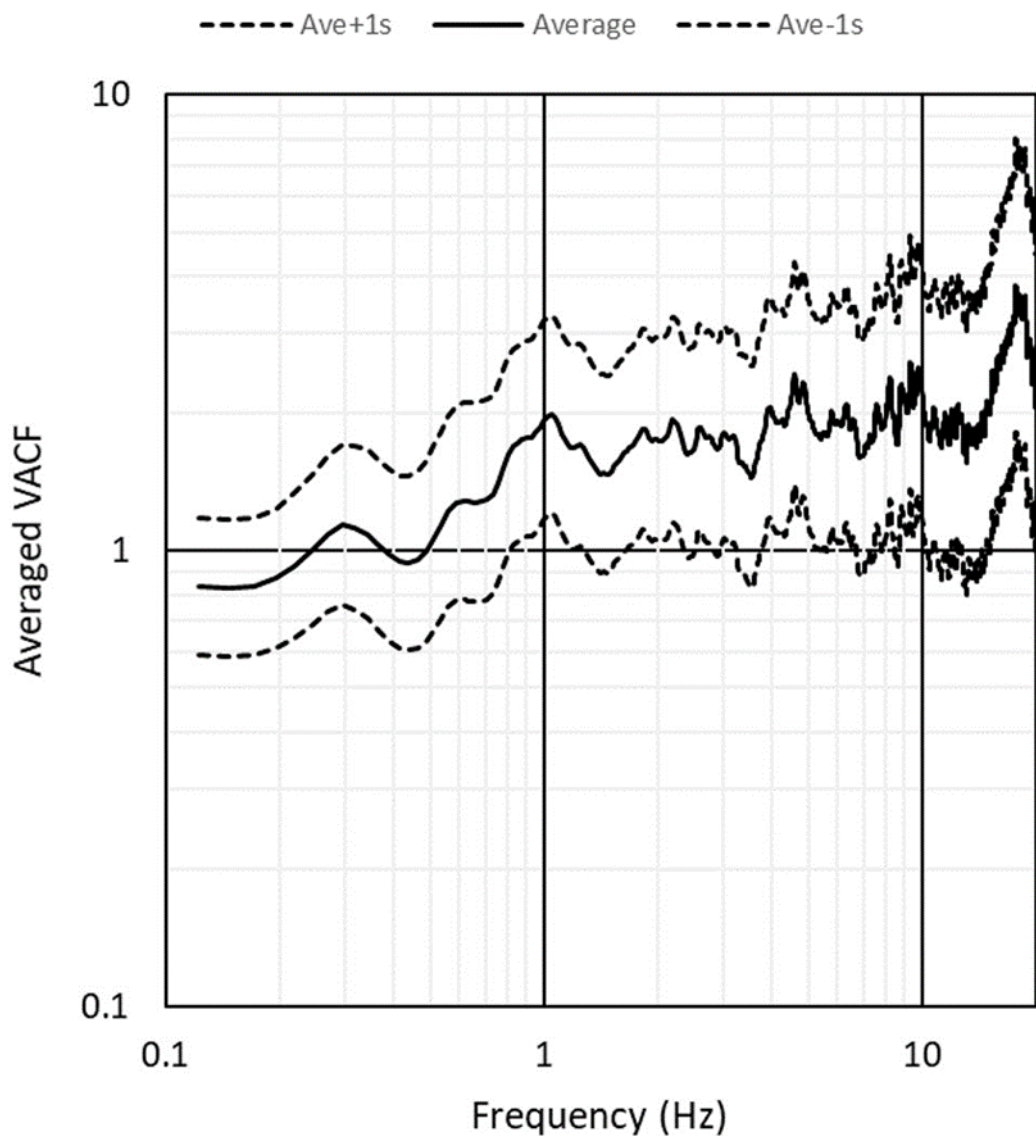


Figure 2.7. The vertical amplification correction function (VACF) obtained as the average (the geometrical mean) of all the 1,678 sites with ten or more events recorded, as well as the functions corresponding to the average \pm one standard deviation. Digital values of the averages, as well as the standard deviations, are listed in Table A2.3 in the Appendix for the valid frequency range from 0.12 to 15 Hz.

2.7 Validation

Lastly, we verify the capability of the proposed method in reproducing the observed HSAF from the EHVR. While we have obtained average values (Figures 2.5 to 2.7) by using only the sites whose number of earthquakes was 10 or more, we have separately made a comparison using sites whose numbers of earthquakes are in the range from seven to nine, which have not been subjected to the aforementioned averaging. As shown in the eight examples given in Figure 2.8 for the same sites shown in Figure 2.2, the HSAFs obtained by GIT are reproduced successfully even though a simple correction function in Figure 2.7 (the average one) is used. Among these examples, the difference in estimation is particularly large at JMA D18 (See "Res" in the title of the panel, which is the average log-residual, and is mathematically equivalent to the geometrical mean of the spectral ratio over frequency up to 15 Hz), and this is so because the actual VSAF* at this site was extraordinarily greater than the average. As long as this method is used, it is inevitable that such sites will be found with a certain probability. When a conservative HSAF estimate is required, it is desirable to use the average correction function plus one standard deviation shown in Figure 2.7 (tabulated in Table A3.3) as a multiplication factor.

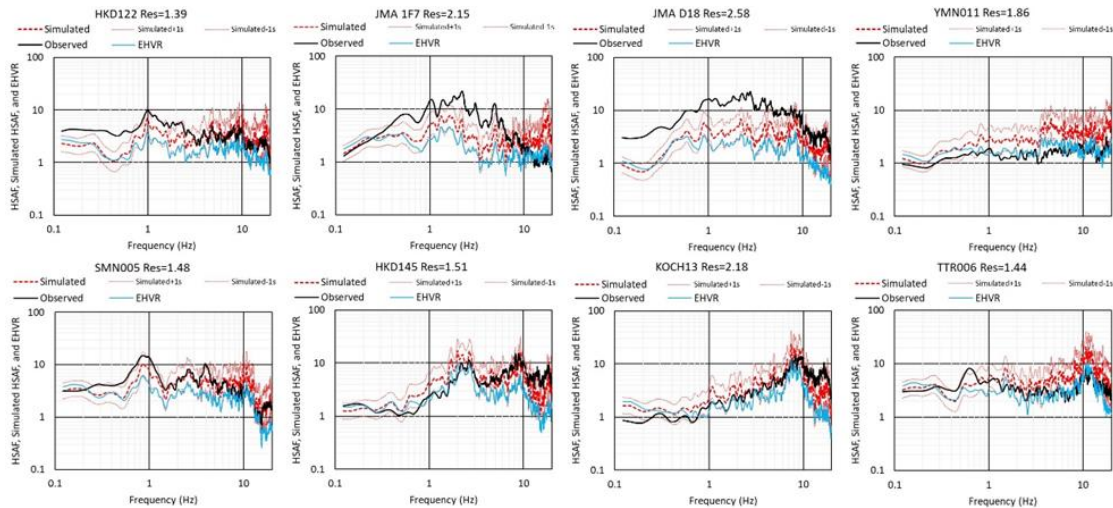


Figure 2.8. Comparison of the observed HSAF (black line) and the simulated HSAF (red broken line) obtained from the EHVR multiplied by the empirical VACF in Figure 2.7 (the average one). The dotted lines represent the simulated HSAFs using the average \pm one standard deviation, and the light blue line represents the EHVR used. These are the same sites shown in Figure 2.2. The numbers “Res” in the titles of these panels equal to the log-averaged residuals between the simulated HSAF and the observed HSAF. It is calculated as the arithmetic average of the differences of all the spectra from 0.12 to 15 Hz in log and then converted to the ratio as a power of 10, which is equivalent to the geometrical mean of the ratio over the frequency. If and only if we have a perfect match, then Res=1, and if they are either twice or one half of each other on average, Res=2. The reproduction capability of VACF in Figure 2.7 seems satisfactory except for the site JMA D18, where the VSAF* is extraordinarily large as shown in Figure 2.2.

To grasp the average trend of our simulation results, we have compared the simulated HSAF obtained by using the average VACF (Figure 2.7) and the EHVR with the observed HSAF for a total of 103 sites whose numbers of observed earthquakes ranged from seven to nine. We have also compared the uncorrected EHVR directly with the HSAF (i.e., Nakamura interpretation). Figure 2.9 shows the maximum and average values (\bullet : synthesized HSAF, \circ : EHVR) on the left and right sides, respectively, with respect to the observed HSAF. We also plot comparisons of Fourier amplitude spectral values at 0.5, 1, 2, and 5 Hz in the panels from (c) to (f). Figure 2.10 shows the log-residuals averaged over frequency (left: with EHVR, right: with simulated HSAF). The average operation is performed in the frequency range from 0.12 to 15 Hz. Note that the average of the modulus of log-residuals is reverted to a real number (ratio) with the power of 10, meaning perfect matching when the ratio is unity. Whereas amplitude is obviously underestimated in the EHVR as already seen in Figure 2.4, data points become more closely distributed around the line of 1:1 after the correction. The log-residual data also indicates the improvement of matching in more than 60% of the sites. More than half of the remaining sites have small residuals in both the EHVR and the simulated HSAF, and the percentage of sites in which errors increased significantly after the correction is only about 14% (14 sites out of 103). We found that at a couple of sites where the degrees of matching are significantly worsened after the correction, such as JMA BE9 and JMA D03, their amplitudes in the high-frequency range of both HSAF and VSAF* are abnormally smaller than those of the ordinary sites. These sites may be under special conditions like a velocity inversion, and this is a subject of future investigation.

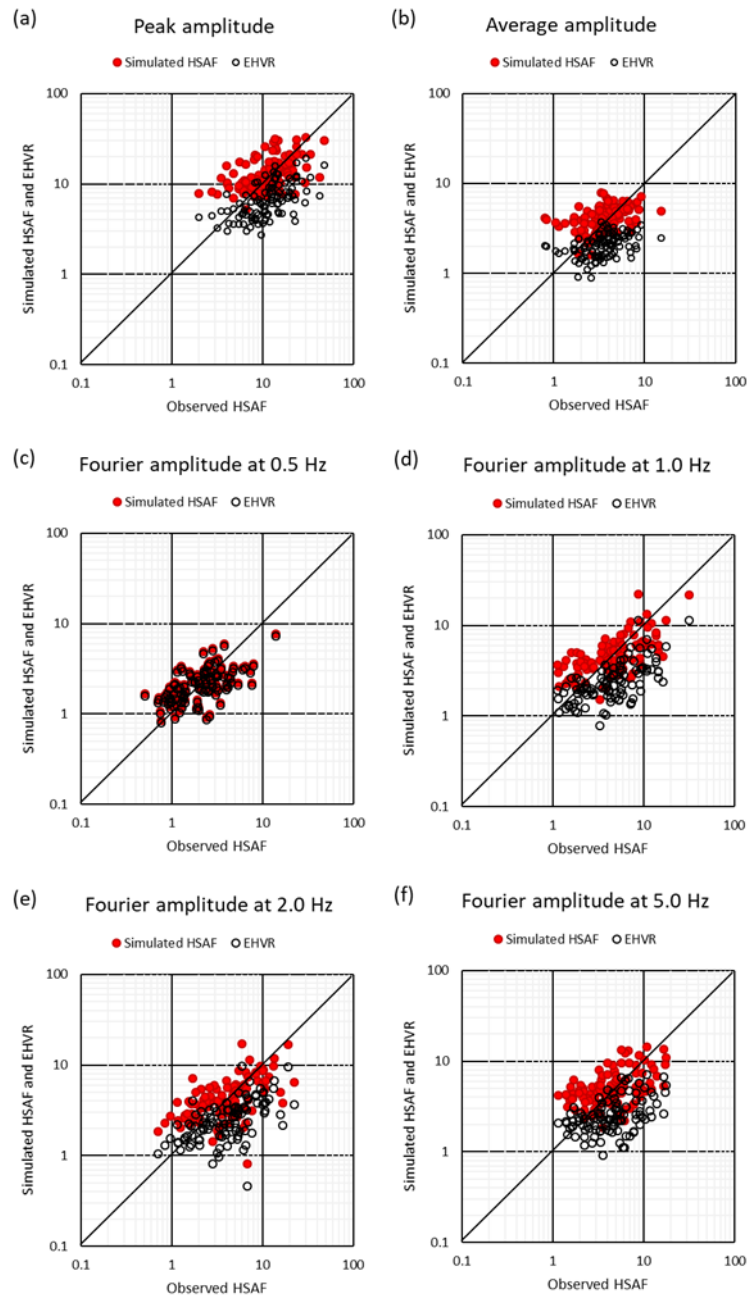


Figure 2.9. Comparisons of the simulated HSAF (red dot) or the observed EHVR (open circle) on the vertical axis plotted against the observed HSAF on the horizontal axis for (a) maximum (peak) amplitude, (b) average amplitude (geometrical mean over the frequency). Comparisons in the Fourier spectral amplitudes at (c) 0.5 Hz, (d) 1.0 Hz, (e) 2.0 Hz, and (f) 5.0 Hz are also shown. Only the difference at 0.5 Hz is negligible because the VACF at 0.5 Hz is close to unity, while at other frequencies the VCAF works to make EHVR closer to the observed HSAF.

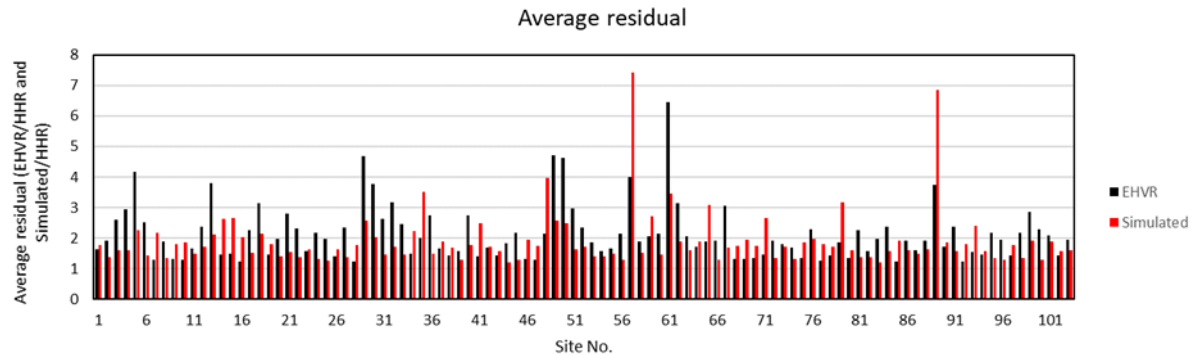


Figure 2.10. The log-residuals between the observed EHVR and the observed HSAF on the left, compared with the log-residuals between the simulated HSAF and the observed HSAF on the right for all the 103 sites. Two sites with extraordinary high residuals in the simulated HSAFs are those of the JMA Seismic Intensity network, namely BE9 and D03, where significant decreases in the high-frequency range were found in both HSAFs and VSAFs. We found fourteen sites in total where we have a significant increase of the residuals from the direct substitution of EHVR to HSAF and end up having a residual higher than 2.

2.8 Discussions

2.8.1 Primary cause of site effects in consideration

As mentioned in the introduction section, there are various ways to evaluate site effects. Therefore, we need to choose the best method that can evaluate quantitatively the most important characteristics of the observed site effects. Since our approach here is fully empirical, we need not (and we cannot) specify the primary cause of the site effects in consideration. Because we focus our attention on the S-wave portion and on the amplification relative to the seismological bedrock, one can say that our study is mainly looking for the seismic amplification due to S-wave resonances from the interfaces with high impedance contrasts. That may be true for the majority of the sites. We use only earthquake ground motions. We select only S-wave portions. We assume a basic idea of linear “separation of variables” for the Fourier amplitude spectra (a requisite for GIT). We implicitly assume fully-scattered body wave incidence from the source to the seismological bedrock beneath the site (a requisite for the diffuse field concept). However, we do not try to exclude any specific types of site amplification by focusing of rays, due to topography, by edge effects, from mode conversions within S-wave portions, and so on. Anything included in the observed EHVR can be evaluated in the synthesized HSAF derived by the correction of VACF in one way or another. The resultant HSAF may not be a correct S-wave amplification factor in a physical sense, because we do not know how to scrutinize the site. The actual primary cause of the observed site factor at a specific site may not be anything from any of the above physical wave-propagation phenomena that we know at present. Even for such an extreme case our synthesized HSAF can reflect the site effects included in the observed EHVR.

Thus, the accuracy of the synthesized HSAF in our proposed method solely depends on

the accuracy of the VACF used, because any site under such a peculiar condition as focusing, topography, edge effects, mode conversion, and so on would have a peculiar VSAF*, different from the average VACF and so the synthesized HSAF would not be correct if we substitute that peculiar VSAF* with the average VACF. However, we have been observing that HSAF should suffer more significantly from such a peculiar condition than VSAF* since S-waves always show stronger effects of interaction with the complex underground structure (e.g., Aki, 1988). This means that the synthesized HSAF here may reflect the fundamental (i.e., most important) characteristics of the S-wave amplification no matter what the primary cause of the actual site effects would be.

It is human's interpretation either to say that the observed HSAF is caused by a resonance of layers with high impedance contrasts, focusing, or edge effects, and so on. Such interpretation can only be made after we delineate the velocity structure down to the seismological bedrock and calculate a theoretical S-wave site amplification factor comparable to the observed HSAF. In this study, we never use any of the velocity structures around a site to delineate what is the real cause of the observed HSAF, except for the reference station YMGH01. On one hand, it is advantageous to just estimate the HSAF at a target site without considering its cause. On the other hand, it is difficult to estimate the reliability of the predicted HSAF even for a nearby site if no data are observed.

2.8.2 Basin response in coda

In this study, we focus our attention on the S-wave portion only with a relatively short duration of motion (5 to 15 s depending on the magnitude). In the later part of the observed strong motions, that is, the early and late codas, we should have significant contributions of the basin-induced surface waves of various types and modes (e.g., Bard and Bouchon, 1980; Kawase and Aki, 1989), in addition to the multiple-scattering body waves (e.g., Sato 1994). It is interesting to see the evolution of EHVRs from the onset of the S-wave till the end of the late coda for sites inside the basin, but it is beyond the scope of this paper to fully investigate such time-evolving characteristics of EHVRs. However, we should note that equation (2.3) could be valid if we consider the whole basin responses in both horizontal and vertical components for the incident S-wave as the transfer functions appeared in this equation.

So we compute HSAF and VSAF* for the whole duration of motion from the onset of the S-wave until the end of the record (called "for full waves" hereinafter) by using the bedrock S-wave spectra effectively estimated from the source and path terms in equations (2.4) and (2.5). This means that we can get the site amplification for full waves relative to the site amplification for S-wave. As an example, Figure 2.11 shows the comparisons of HSAF and VSAF* for full waves with those for S-wave (as in Nakano and Kawase, 2019) at two sites in Figures 2.2 and 2.8, namely, HKD122 and SMN005. We see much larger amplitudes in HSAF and VSAF* for full waves than those for S-wave in the frequency range below 2 Hz. This means that the fundamental expectation to have the same HSAF for both S-wave portion and coda (e.g., Phillips and Aki, 1986; Kato et al., 1995) seems valid only in the frequency range higher than 2 Hz. However, if we compare EHVRs for full waves and S-wave as shown in Figure 2.12, we found that they are remarkably similar to each other. The similarity is stronger in SMN005, which is inside a

relatively shallow and narrow sedimentary basin, and therefore smaller contributions of the basin-induced surface waves in the low-frequency range should be expected. On the other hand, the site HKD122 is located inside the much deeper and larger Ishikari Basin so that stronger contributions of the basin-induced surface waves should be expected (e.g., Sasatani et al., 2006; Yoshida et al., 2007). Although we can notice a small discrepancy in the frequency range around 0.5 Hz at HKD122, the fundamental characteristics of EHVRs for S-wave and full waves are similar to each other. We do not know why this is the case at this moment, however, it is apparent that we need to use different VACFs for S-wave and full waves. We are now investigating VACFs for full waves which will be reported in a separate paper.

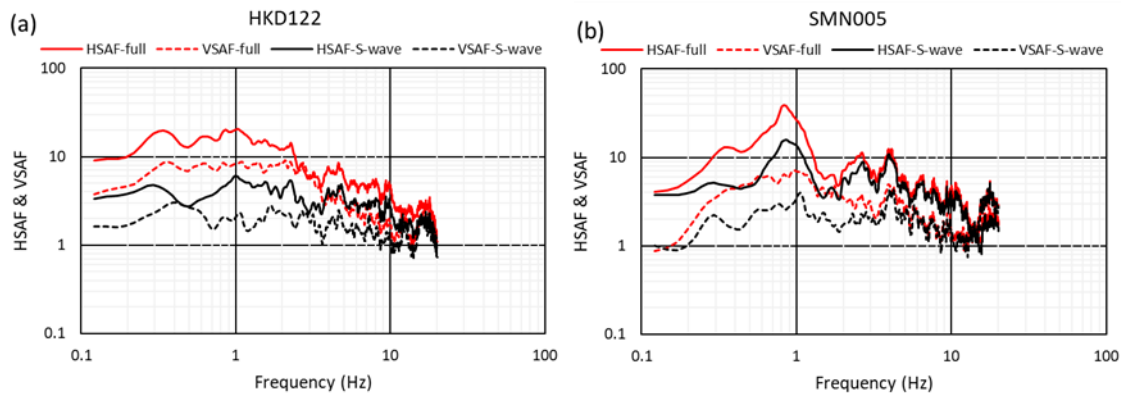


Figure 2.11. Comparisons of HSAF (solid line) and VSAF* (dotted line) for full waves in red with those for S-wave in black at (a) HKD122 and (b) SMN005. We see much larger amplitudes in HSAF and VSAF* for full waves than those for S-wave in the frequency range below 2 Hz at both sites. The degree of similarity in the high-frequency range is higher in SMN005.

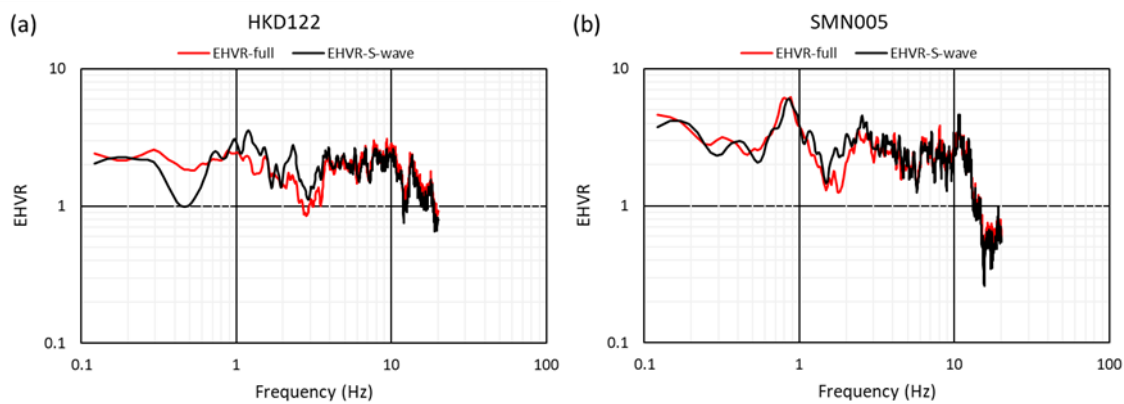


Figure 2.12. Comparisons of EHVRs for full waves in red with those for S-wave in black at (a) HKD122 and (b) SMN005. They are remarkably similar to each other, especially at SMN005 where the width and thickness of the basin are relatively smaller compared to the Ishikari Basin for HKD122.

2.8.3 One-dimensionality in S-wave portion

A similar but fundamentally different issue is the one-dimensional assumption implicitly adopted in this study (although it is not a requisite of the VACF method, as discussed above). After the observed “damage belt” in Kobe and subsequent theoretical studies, nowadays it is well known that near the edge of the basin we would have a strong constructive interference of the incident S-wave with the horizontally-emitted diffracted and surface waves, as called “the edge effect” (e.g., Kawase 1996; Pitarka and Irikura, 1996; Motosaka and Nagano 1996; also Graves and Pitarka, 1998 for the Northridge earthquake). We also see the effects of surface topography in the observed strong ground motions (e.g., Kawase and Aki, 1990; Spudich et al., 1996). Differently from the basin-induced surface waves observed in the middle of the basin, these two- and three-dimensional effects will show up in the S-wave window and therefore they are difficult to separate by a simple time-window scheme.

However, we can see these three-dimensional effects in a directional dependence of EHVR, because in principle the theoretical prediction of equation (2.3) derived from the diffuse field concept is valid for different horizontal components under the three-dimensional response of the ground above the seismological bedrock and that three-dimensional response would usually be directionally dependent. Although an application of the three-dimensional theoretical response to EHVR is under preparation, applications to MHVRs showed quite a nice qualitative correspondence, if not fully quantitative (Matsushima et al., 2014; Matsushima et al., 2017). If it is the case, then we can apply a one-dimensional model for the site where we could not see strong directionality in the observed EHVR. In our preliminary analysis, we found that only about 15% of the sites show non-negligible directionality between NS/UD and EW/UD ratios among the sites used. We need to study further to differentiate the sites with a one-dimensional nature from those with two- or three-dimensional natures.

2.8.4 Reference site

As mentioned in the first part of the section “Results of application”, it is a requisite to use the outcrop spectra on the seismological bedrock as a reference site, where we need not consider any site amplification, for EHVR in equation (2.3) in the diffuse field formulas, as well as EHVR in equation (2.6) in the GIT formulas. The use of such a reference condition makes everything simple and physical. The reason why we do not frequently use the seismological bedrock as a reference is primarily due to the difficulty to reach that level of rock formation with an S-wave velocity higher than 3 km/s. Thanks to the advent of the diffuse field concept and the S-wave velocity inversion scheme based on that (e.g., Nagashima et al., 2014, 2017), it is now relatively easy to obtain the velocity structure from the surface down to the seismological bedrock.

In the GIT analysis equations (2.4) to (2.6) are valid even if the engineering bedrock with an arbitrary definition is used as a reference. However, equation (2.3) becomes no longer valid because the horizontal-to-vertical spectral ratio on the reference bedrock as the incident body wave becomes not a constant as in equation (2.3) but a complex function of frequency. This also means that the HSAF (and VSAF) at a target site derived from GIT will also become a complex function of frequency owing to the HSAF at the reference engineering bedrock. Under such a

condition it is impossible to compare the HSAF derived from GIT with one definition of a reference site with the HSAF with another definition of a different reference site. As reviewed in the section “Issues on Horizontal-to-Vertical spectral ratios: EHVR and HSAF”, the primary cause of conflicting and confusing results reported in the past could be attributed to their arbitrarily chosen definitions of the reference site. Therefore, we cannot place too much emphasis on the importance of using the seismological bedrock as a reference condition in the analysis for quantitative evaluation of site effects.

2.9 Conclusions

We have proposed in this study a simple method to deduce the horizontal site amplification factor (HSAF) in the S-wave portion directly from the EHVR of observed earthquake ground motion. In this method, we have formulated a correction procedure based on formulas from the diffuse field concept and GIT; confirmed the adequacy of the used reference condition as the seismological bedrock; focused on observation records from 1,678 sites where ten or more earthquakes have been observed in the strong-motion networks of K-NET, KiK-net, and JMA seismic intensity network; used the GIT results to determine the vertical site amplification factor VSAF (to be precise, $VSAF^* = VSAF \times V_{BHBR}$); and then averaged over all 1,678 sites to obtain the empirical vertical amplification correction function (VACF). A schematic diagram of these flows of analysis is shown in Figure 2.13.

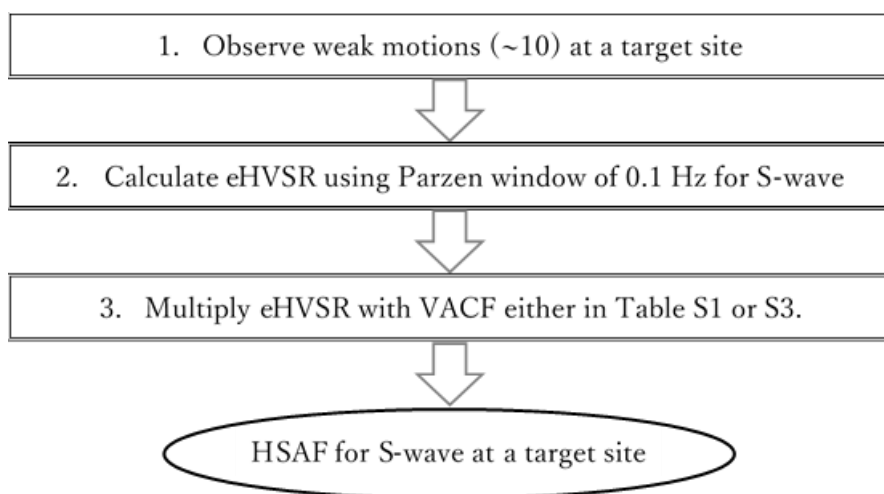


Figure 2.13. A schematic diagram that shows the basic flows of the application to a new target site.

The major findings obtained are as follows:

- 1) The vertical-to-horizontal spectral ratio at the reference observation site ($V_B H_B R$) was nearly unity and agreed with the theoretical solution of 0.76 within the range of variation.
- 2) The amplitude of the VSAF, on average, was 30% to 40% of the HSAF obtained by GIT. While there was a weak correlation between the EHVR and HSAF, the EHVR was obviously smaller than the HSAF in amplitude. Using the EHVR with no correction in place of the HSAF as proposed by Nakamura (1989, 2019) will result in underestimation of HSAF.
- 3) It was possible to obtain the VACF on a very stable basis by reading out the peak amplitude and peak frequency of the EHVR at each site and averaging the data in the corresponding category; there were only negligible differences due to peak amplitude; there were relatively small differences due to peak frequency; the amount of correction increased as the peak frequency decreased; and the VACF was the largest when EHVR peak frequency was 1 Hz or less, where the factor of about 3 was needed. Since the deviations in each category are equal to or larger than the difference between averages in two categories, the effectiveness of using these VACFs with eight categories may not be so significant, even if not negligible.
- 4) We averaged the data in each category classified based on the peak amplitude and peak frequency of the EVHR to obtain nearly identical average values, except for a category having a too small amount of data. For the sake of simplicity, we have deduced a single VACF value by averaging the data of all 1,678 sites without categorization. The resultant uncategorized VACF shows a linearly increasing amplitude up to 1.0 Hz, above which it shows a constant amplitude of about 2.0 up to 15 Hz. We can use this VACF to correct EHVR considering the variability of 1.5 times.
- 5) For the validation exercise of applicability, we applied the obtained VACF to 103 sites whose number of observed earthquakes ranged from seven to nine, which have not been used in the above-mentioned averaging. As a result, the observed HSAF has been successfully reproduced in 86% of the sites, although a couple of sites have shown nearly doubled the differences.

In summary, this paper proposes a new simple method, in which the main S-wave part of earthquake ground motion is extracted, the average horizontal-to-vertical spectral ratio of this portion is determined, and this ratio is multiplied by the empirical correction function to obtain the horizontal S-wave site amplification factor. Although this method inevitably entails errors in the VACF estimation due to its site-specific characteristics, it is capable of evaluating site effects of S-waves based on observed values in a wide frequency range from 0.12 to 15 Hz. The flows of the application procedure for a new target site are quite simple as shown in Figure 2.14. It should be noted that the proposed method obtains the horizontal S-wave amplification factor from the seismological bedrock, rather than the engineering bedrock, to the ground surface. For the sake of reliability, it is advisable to determine the average horizontal-to-vertical ratio of at least about ten earthquakes.

In the future, we will verify the adequacy of this method by applying it to blind test sites,

and we would like to propose a correction method that takes not only the extracted EHVR characteristics but also the nonlinearity of soil into account for large input levels. While this study has focused on the site effects of only the main S-wave part, it is well-known that basin-induced surface waves arrive at observation sites within the basin and cause a large spectral amplitude, in particular in the low-frequency range as basin effects as shown in Figure 2.11. By taking this effect into account, we will also propose a simple method to simulate site amplification for full waves.

Data and Resources

This study has used the strong-motion observation records from the K-NET and KiK-net of the National Research Institute for Earth Science and Disaster Resilience (doi:10.17598/NIED.0004) as well as the Seismic Intensity (Shindo-kei) network of the Japan Meteorological Agency (<https://www.jma.go.jp/jma/indexe.html>, last accessed November 25, 2019). All the digital values up to 15 Hz of the VACFs shown in Figure 2.5 and their standard deviations are listed in Tables A2.1 and A2.2 and those in Figure 2.7 are listed in Table A2.3 in the Appendix.

Acknowledgment

A part of this study was supported by the JSPS Kakenhi Grant-in-Aid for Basic Research (A) No.26242034 and Grant-in-Aid for Basic Research (B) No.19H02405. Information provided by and discussions done with Drs. Pierre-Yves Bard, Cecile Cornou, and Alan Yong for related works are highly appreciated. Very thorough and constructive review comments of the Associate Editor in charge, Dr. Sheri Molnar, and two anonymous reviewers significantly contributed to improve the manuscript.

References

- Aki, K. (1988). Local site effects on strong ground motion, *Earthquake Engineering and Soil Dynamics II -Recent Advances in Ground Motion Evaluation*, 103-155, ASCE.
- Andrews, D.J. (1986). Objective determination of source parameters and similarity of earthquakes of different size, *Earthquake Source Mechanics* (eds. S. Das, J. Boatwright and C. H. Scholz), American Geophysical Union, Washington, D.C., 1986. doi: 10.1029/GM037p0259.
- Arai, H., and K. Tokimatsu (2004). S-wave velocity profiling by inversion of microtremor H/V spectrum, *Bull. Seism. Soc. Am.* Vol.94, No. 1, 53–63.
- Archuleta, R. J., S. H. Seale, P. V. Sangas, L. M. Baker, and S. T. Swain (1992). Garner Valley downhole array of accelerometers: instrumentation and preliminary data analysis, *Bull. Seism. Soc. Am.* 82, 1592–1621.

- Bard, P.-Y. and M. Bouchon (1980). Seismic response of sediment-filled valleys, Part I: The case of incident SH waves, Bull. Seism. Soc. Am., 70, 1263–1286.
- Bonilla, L.F., J.H. Steidl, G.T. Lindley, A.G. Tumarkin, and R.J. Archuleta (1997). Site amplification in the San Fernando Valley, California: Variability of site-effect estimation using the S-wave, coda, and H/V methods, Bull. Seism. Soc. Am., Vol.87, No.3, 710–730.
- Bonilla, L.F., J.H. Steidl, J.-C. Gariel, and R.J. Archuleta (2002). Borehole response studies at the Garner Valley Downhole Array, Southern California, Bull. Seism. Soc. Am., Vol.92, No.8, 3165–3179.
- Bonnefoy-Claudet, S., C. Cornou, P.-Y. Bard, F. Cotton, P. Moczo, J. Kristek, and D. Fäh (2006). H/V ratio: a tool for site effects evaluation. Results from 1D noise simulations. Geophys. J. Int. 167, 2006, 827–837.
- Borcherdt, R.D. (1970). Effects of local geology on ground motion near San Francisco Bay, Bull. Seism. Soc. Am., Vol.60, No.1, 29–61.
- Castro R.R., S.K. Singh, and E. Mena (1988) An empirical model to predict Fourier amplitude spectra of horizontal ground motion. The Mexico Earthquake of September 19, 1985, Earthquake Spectra 4:675–685.
- Castro, R.R., M. Mucciarelli, F. Pacor, and C. Petrungaro (1997). S-wave site-response estimates using horizontal to vertical spectral ratios, Bull. Seism. Soc. Am. Vol.87, 256–260.
- Cultrera, G., V. De Rubeis, N. Theodoulidis, H. Cadet, and P.-Y. Bard (2014). Statistical correlation of earthquake and ambient noise spectral ratios, Bull. Earthq. Eng. Vol.12, 1493–1514, doi: 10.1007/s10518-013-9576-7.
- Field, E.H. and K.H. Jacob (1995). A comparison and test of various site-response estimation techniques, including three that are not reference-site dependent, Bull. Seism. Soc. Am. Vol.85, No.4, 1127–1143.
- Graves, R.W., A. Pitarka, and P.G. Somerville (1998). Ground-motion amplification in the Santa Monica area: Effects of shallow basin-edge structure, Bull. Seism. Soc. Am. Vol.88, No.5, 1224–1242.
- Haghshenas, E., P.-Y. Bard, N. Theodoulidis, and SESAME WP04 Team (2008). Empirical evaluation of microtremor H/V spectral ratio, Bull. Earthquake. Eng., 6, 2008, 75–108, doi:10.1007/s10518-007-9058-x.
- Iwata, T. and K. Irikura (1988). Source parameters of the 1983 Japan-Sea earthquake sequence, J. Phys. Earth, 36, 155–184.
- Kato, K., M. Takemura, T. Kieura, K. Urano, and T. Uetake (1992). Preliminary analysis for evaluation of local site effects from strong motion spectra by an inversion method, J. Phys. Earth, 40, 175–191.
- Kato, K., K. Aki, and M. Takemura (1995). Site amplification from coda waves: Validation and application to S wave site response, Bull. Seism. Soc. Am., Vol.85, 467–477.

- Kawase, H. and K. Aki (1989). A study on the response of a soft basin for incident S, P, and Rayleigh waves with special reference to the long duration observed in Mexico City, Bull. Seism. Soc. Am., Vol.79, 1361-1382.
- Kawase, H. and K. Aki (1990). Topography effect at critical SV-wave incidence: possible explanation of damage pattern by the Whittier Narrows, California, earthquake of 1 October 1987, Bull. Seism. Soc. Am., Vol.80, 1-22.
- Kawase, H. (1996). The cause of the damage belt in Kobe: "The basin-edge effect", Constructive interference of the direct S-wave with the basin-induced diffracted/Rayleigh waves, Seismological Research Letters, 67, 25-34.
- Kawase, H. (2003). Site effects on strong ground motions, International Handbook of Earthquake and Engineering Seismology, Part B, W.H.K. Lee and H. Kanamori (eds.), Academic Press, London, 1013-1030.
- Kawase, H. and H. Matsuo (2004). Amplification characteristics of K-NET, KiK-NET, and JMA Shindo-kei network sites based on the spectral inversion technique, 13th World Conf. on Earthquake Engineering, Vancouver, Canada, Paper No. 454.
- Kawase, H. (2006). Site effects derived from spectral inversion method for K-NET, KiK-net, and JMA strong-motion network with special reference to soil nonlinearity in high PGA records, Bull. Earthq. Res. Inst., Tokyo Univ. 81, 309–315.
- Kawase H., F.J. Sánchez-Sesma, and S. Matsushima (2011). The optimal use of horizontal-to-vertical spectral ratios of earthquake motions for velocity inversions based on diffuse-field theory for plane waves. Bull. Seism. Soc. Am., 101, 2011-2014.
- Kawase, H., Y. Mori, and F. Nagashima (2018a). Difference of horizontal-to-vertical spectral ratios of observed earthquakes and microtremors and its application to S-wave velocity inversion based on the diffuse field concept, Earth, Planets, and Space, Vol.70, No.1, Open Access, doi: 10.1186/s40623-017-0766-4.
- Kawase, H., F. Nagashima, K. Nakano, and Y. Mori (2018b). Direct evaluation of S-wave amplification factors from microtremor H/V ratios: Double empirical corrections to “Nakamura” method, Soil Dyn. Earthquake Eng., Open Access, doi: 10.1016/j.soildyn.2018.01.049.
- Kitagawa Y., I. Ohkawa, and T. Kashima (1988). Dense strong motion earthquake seismometer array at site with different topographic and geologic conditions in Sendai, Proc. 9th WCEE, 2, 215-220.
- Lachet C., D. Hatzfeld, P.-Y. Bard, N. Theodoulidis, C. Papaioannou, and A. Savvaidis (1996). Site effects and microzonation in the city of Thessaloniki (Greece): comparison of different approaches. Bull. Seism. Soc. Am., 86, 1692–1703.
- Lermo, J. and F. J. Chávez-García (1993). Site effect evaluation using spectral ratios with only one station, Bull. Seism. Soc. Am., Vol.83, No.5, 1574-1594.
- Matsushima, S., T. Hirokawa, F. De Martin, H. Kawase, and F.J. Sánchez-Sesma (2014). The

effect of lateral heterogeneity on horizontal-to-vertical spectral ratio of microtremors inferred from observation and synthetics, Bull. Seism. Soc. Am., Vol.104, 381-393, doi:10.1785/0120120321.

Matsushima, S., H. Kosaka, and H. Kawase (2017). Directionally dependent horizontal-to-vertical spectral ratios of microtremors at Onahama, Fukushima, Japan, Earth, Planets, and Space, 69:96, 2017, doi:10.1186/s40623-017-0680-9.

Motosaka, M. and M. Nagano (1996). Analysis of ground-motion amplification characteristics in Kobe City considering a deep irregular underground structure, Interpretation of heavily damaged belt zone during the 1995 Hyogo-ken Nanbu earthquake, J. Phys. Earth, 44, No.5, 577-590.

Nakamura Y. (1989). A method for dynamic characteristics estimation of subsurface using microtremor on the ground surface, Railway Tech. Res. Inst., Q. Rep. 30(1): 25-30.

Nakamura Y. (2019). What is the Nakamura Method, Seism. Res. Lett. Vol.90, No.4, 1437-1443.

Nakano, K., S. Matsushima, and H. Kawase (2015). Statistical properties of strong ground motions from the generalized spectral inversion of data observed by K-NET, KiK-net, and the JMA Shindo-kei Network in Japan, Bull. Seism. Soc. Am., Vol.105, 2662-2680, doi:10.1785/0120140349.

Nakano, K. and H. Kawase (2019). Source parameters and site amplifications estimated by generalized inversion technique: focusing on the 2018 Hokkaido Iburi-Tobu earthquake, Earth, Planets, and Space, 71: 66, 2019.1, 10.1186/s40623-019-1047-1.

Oth, A., S. Parolai, and D. Bindi (2011a). Spectral analysis of K-NET and KiK-net data in Japan, part I: Database compilation and peculiarities, Bull. Seism. Soc. Am., Vol.101, 652-666, doi:10.1785/0120100134.

Oth, A., D. Bindi, S. Parolai, and D. Di Giacomo (2011b). Spectral analysis of K-NET and KiK-net data in Japan, part II: On attenuation characteristics, source spectra, and site response of borehole and surface stations, Bull. Seism. Soc. Am., Vol.101, 667-687, doi:10.1785/0120100135.

Parolai, S., D. Bindi, and P. Augliera (2000). Application of the Generalized Inversion Technique (GIT) to a microzonation study: numerical simulations and comparison with different site-estimation techniques, Bull. Seism. Soc. Am., Vol.90, No.2, 286-297.

Parolai, S., D. Bindi, M. Baumbach, H. Grosser, C. Milkereit, S. Karakisa, and S. Zünbül (2004). Comparison of different site response estimation techniques using aftershocks of the 1999 Izmit Earthquake. Bull. Seism. Soc. Am., 94-3, 2004, 1096-1108. doi: 10.1785/0120030086.

Phillips, W.S. and K. Aki (1986). Site amplification of coda waves from local earthquakes in central California, Bull. Seism. Soc. Am., 76, 627-648.

Riepl, J., P.-Y. Bard, D. Hatzfeld, C. Papaioannou, and S. Nechtschein (1998). Detailed Evaluation of Site-Response Estimation Methods across and along the sedimentary valley of Volvi (EURO-SEISTEST), Bull. Seism. Soc. Am., Vol.88, No.2, 488-502.

- Pitarka, A., K. Irikura, T. Iwata, and T. Kagawa (1996). Basin structure effects in the Kobe area inferred from the modeling of ground motions from two aftershocks of the January 17, 1995, Hyogoken-nanbu earthquake, *J. Phys. Earth*, 44, 563-576.
- Rodriguez, V.H.S. and S. Midorikawa (2003). Comparison of spectral ratio techniques for estimation of site effects using microtremor data and earthquake motions recorded at the surface and in boreholes, *Earthq. Eng. Struct. Dyn.* Vol.32, 1691–1714, doi: 10.1002/eqe.296.
- Salinas, V., F. Luzón, A. García-Jerez, F.J. Sánchez-Sesma, H. Kawase, S. Matsushima, M. Suárez, A. Cuellar, and M. Campillo (2014). Using diffuse field theory to interpret the H/V spectral ratio from earthquake records in Cibeles seismic station, Mexico City, *Bull. Seism. Soc. Am.*, 104: 995–1001, doi: 10.1785/01201302.
- Sánchez-Sesma, F.J., M. Rodríguez, U. Iturrarán-Viveros, F. Luzón, M. Campillo, L. Margerin, A. García-Jerez, M. Suárez, M.A. Santoyo, and A. Rodríguez-Castellanos (2011). A theory for microtremor H/V spectral ratio: Application for a layered medium, *Geophys. J. Int. Exp. Lett.*, 186: 221-225, doi: 10.1111/j.1365-246X.2011.05064.x.
- Sasatani, T., T. Maeda, and N. Takai (2006). Long-period ground motion and deep subsurface structure in Hokkaido: A review, *BUTSURI-TANSA*, Vol.59, No.4, 315-326 (in Japanese with English abstract).
- Sato, H. (1994). Multiple isotropic scattering model including P-S conversions for the seismogram envelope formation, *Geophys. J. Int.*, Vol.117, Issue 2, 487-494, <https://doi.org/10.1111/j.1365-246X.1994.tb03946.x>
- Satoh, T., H. Kawase, and T. Sato (1995). Evaluation of local site effects and their removal from borehole records observed in the Sendai Region, Japan, *Bull. Seism. Soc. Am.*, Vol.85, 1770-1789.
- Satoh, T., H. Kawase, and S. Matsushima (2001). Differences between site characteristics obtained from microtremors, S-waves, P-waves, and cudas, *Bull. Seism. Soc. Am.*, Vol.91, No.2, 313–334.
- Spudich O., M. Hellweg, and W.H.K. Lee (1996). Directional topographic site response at Tarzana observed in aftershocks of the 1994 Northridge, California, earthquake: Implications for mainshock motions, *Bull. Seism. Soc. Am.*, Vol.86, No.1B, S193–S208.
- Steidl, J.H., Tumarkin, A.G., and Archuleta, R.J. (1996). What is a reference site?, *Bull. Seism. Soc. Am.*, Vol.86, No.6, 1733–1748.
- Takahashi, R. and K. Hirano (1941). Seismic vibration of soft ground, *Bull. Earthq. Res. Inst., Tokyo Univ.* Vol.19, No.3, 534-543 (in Japanese with English abstract).
- Theodulidis, N., P.-Y. Bard, R. Archuleta, and M. Bouchon (1996). Horizontal-to-vertical spectral ratio and geological conditions: the case of Garner Valley Downhole Array in Southern California, *Bull. Seism. Soc. Am.*, Vol.86, No.2, 306-319.
- Tao, Y. and E. Rathje (2020). Taxonomy for evaluating the site-specific applicability of one-

dimensional ground response analysis, Soil Dyn. Earthq. Eng., Vol.128, 105865, doi: 10.1016/j.soildyn.2019.105865.

Yoshida, K., M. Yoshimi, H. Suzuki, M. Morino, F. Takizawa, H. Sekiguchi, and H. Horikawa (2007). 3D velocity structure model of the Ishikari and Yufutsu sedimentary basins, Annual Report on Active Fault and Paleoearthquake Researches, No.7, 1-29 (in Japanese with English abstract).

Appendix

The geometrical mean of the horizontal spectra for $H_1, H_2, \dots, H_i, \dots, H_n$ for different events from 1 to n (normalized with the common denominator for V_i in i-th event) is

$$H_{ave}=10^{(\log(H_1*H_2*\dots*H_n)/n)}, \quad (A2.1)$$

where 10^x means the power of 10. Similarly, the geometrical mean of the vertical spectra for $V_1, V_2, \dots, V_i, \dots, V_n$ is

$$V_{ave}=10^{(\log(V_1*V_2*\dots*V_n)/n)}. \quad (A2.2)$$

Then the ratio of these geometrical means, HVR_a will be:

$$\begin{aligned} HVR_a &= H_{ave}/V_{ave}=10^{(\log(H_1*H_2*\dots*H_n)/n)} / 10^{(\log(V_1*V_2*\dots*V_n)/n)} \\ &= 10^{((\log(H_1*H_2*\dots*H_n)-\log(V_1*V_2*\dots*V_n))/n)}. \end{aligned} \quad (A2.3)$$

On the other hand, the average of the individual HVRs, HVR_b (=the geometrical mean of the ratios) will be

$$\begin{aligned} HVR_b &= 10^{((\log(H_1/V_1)+\log(H_2/V_2)+\dots+\log(H_n/V_n))/n)} \\ &= 10^{((\log(H_1*H_2*\dots*H_n)-\log(V_1*V_2*\dots*V_n))/n)} \\ &= HVR_a. \end{aligned} \quad (A2.4)$$

Chapter 3

Estimation of Velocity Structures Using Pseudo Earthquake Horizontal-to-Vertical Spectral Ratio from Microtremors

Abstract

Based on the diffuse field concept for a horizontal-to-vertical spectral ratio of earthquakes (eHVSR), the effectiveness of eHVSRs to invert P- and S-wave velocity structures down to the seismological bedrock (with the S-wave velocity of 3 km/s or higher) has been shown in several published works. An empirical method to correct the difference between eHVSR and a horizontal-to-vertical ratio of microtremors (mHVSR), which is called earthquake-to-microtremor ratio (EMR), has also been proposed for strong-motion sites in Japan. However, the applicability of EMR outside of Japan may not be warranted. We test EMR applicability for the Grenoble Basin in France with plentiful microtremor data together with observed weak-motion recordings at five sites. We thereby establish a systematic procedure to estimate the velocity structure from microtremors and delineate the fundamental characteristics of the velocity structures. We first calculate the EMR specific for the Grenoble Basin (EMR_G) and calculate pseudo eHVSR (pHVSR) from EMR_G and mHVSR. We compare the pHVSRs with the eHVSRs at five sites and find sufficient similarity to each other. Then, we invert velocity structures from eHVSRs, pHVSRs, and mHVSRs. The velocity structures from eHVSRs are much closer to those from pHVSRs than those from mHVSRs. We need to introduce a number of layers with gradually increasing S-wave velocities below the geological basin boundary from a previous gravity study because the theoretical eHVSR of the model with a large velocity contrast has larger peak amplitudes than the observed. The depth of the S-wave velocity of 1.3 km/s (Z1.3) shows a strong, linear correlation with the geological boundary depth. Finally, we apply our validated methodology and invert velocity structures using pHVSRs at fourteen sites where there are no observed earthquakes. The overall picture of Z1.3 at a cross-section in the northeastern part of the basin corresponds to the geological boundary.

3.1 Introduction

It is quite important to determine velocity structures that can explain the characteristics of S-wave amplification from observed earthquake motions, because it may directly lead to the structural damage caused by earthquakes. Nagashima et al. (2014) proposed a method to invert one-dimensional S-wave velocity structure down to the seismological bedrock (with the S-wave velocity equal to or higher than 3 km/s) from earthquake horizontal-to-vertical spectral ratios (eHVSRs) based on the formula proposed by Kawase et al. (2011) derived from the diffuse field concept (DFC). They suggested that by applying the method we can obtain the velocity structure from the surface down to the seismological bedrock that explains the characteristics of the site amplification at several sites in Miyagi Prefecture, Japan. However, that method is applicable only when we have a sufficient number of observed earthquake recordings. Earthquake observation is more costly and time-consuming than microtremor observation and therefore, it is difficult to apply the eHVSR method without a long-term commitment dedicated to the earthquake hazard analysis to the target region. It is also difficult to apply the method in low to moderate seismicity regions.

Kawase, Mori, et al. (2018) proposed a method to transform horizontal-to-vertical spectral ratios of microtremors (mHVSRs) to eHVSR by multiplying mHVSR with the averaged ratio between eHVSR and mHVSR, termed EMR. They derived the EMRs empirically from 100 sites in Japan. The resultant horizontal-to-vertical spectral ratio is called pseudo eHVSR or simply pHVSR. Please note that EHVR, MHVR, and pEHVR in Kawase, Mori, et al. (2018) correspond to eHVSR, mHVSR, and pHVSR here. They demonstrated that the spectral shapes of pHVSRs better agree with eHVSRs than mHVSRs do and that the S-wave velocity structures inverted from pHVSRs through the eHVSR method of Nagashima et al. (2014) are quite similar to those from the observed eHVSRs. We will briefly introduce this EMR method later.

When we apply the EMR method to the mHVSR data in a region with different tectonic settings, it is better to use EMR specific for the region, rather than to directly substitute the Japanese EMR, because EMR depends on the velocity structure as the theory for mHVSR (Sanchez-Sesma et al., 2011) and eHVSR (Kawase et al., 2011) suggest. However, unless we have plenty of earthquake and microtremor data in a target region, we cannot obtain EMR specific for the region as Kawase, Mori, et al. (2018) did for K-NET and KiK-net sites in Japan.

The purpose of this study is to propose a systematic procedure to determine EMR for a seismically quiet region outside of Japan and to delineate the velocity structures from pHVSR using the obtained EMR specific for the region. To this end, we select the Grenoble Basin in France where we already have plenty of microtremor recordings as well as earthquake ground-motion recordings at several sites inside the basin. Although the number of observed sites (five) and earthquakes (less than 10 per site) are not so large, the observed earthquake data could be sufficient to check the validity of a Grenoble specific EMR, called EMR_G hereafter. However, because of the narrow and elongated 2D/3D shape of the basin, it is challenging to delineate velocity structures down to the seismological bedrock based on the piecewise 1D assumption inherent in the inversion. We first calculate EMR_G by assuming the multiplicative factor, α , to be

similar to the Japanese EMR of Kawase, Mori, et al. (2018). We also check the validity of EMR_G by comparing pHVSR with eHVSR and the velocity structures inverted from pHVSR with those from eHVSR. Then we estimate the velocity structures at the sites where we only have microtremor recordings and compare with the geological basin depths determined by Vallon (1999) using the gravity anomaly. Although eHVSR and pHVSR reflects the horizontal site amplification characteristics as the DFC theory suggests (Kawase et al. 2011; Kawase, Nagashima, et al., 2018; Ito et al., 2020), the primary objective of this paper is to establish a methodology to evaluate the S-wave velocity structures inside the Grenoble Basin, which is the first step of the series of analyses towards predicting seismic responses of the basin.

3.2 Empirical EMR Correction in Japan

Here we introduce briefly the EMR method proposed by Kawase, Mori, et al. (2018) for 100 Kyoshin Network (K-NET) and Kiban Kyoshin Network (KiK-net) sites in Japan (Aoi et al., 2000). The motivation for the empirical correction of mHVSR to pHVSR in Kawase, Mori, et al. (2018) is to apply an efficient inversion method based on eHVSR (Nagashima et al., 2014) to microtremor data, which is easier to obtain than earthquake data. The effectiveness of the proposed inversion method using eHVSR has been shown in several papers (e.g., Nagashima et al. 2014, Fukihara et al. 2015, Nagashima et al. 2017). Because the fundamental sources of energy for earthquakes and microtremors are totally different as has been shown in Sanchez-Sesma et al. (2011) and Kawase et al. (2011), the frequency characteristics of mHVSR and eHVSR could be different, especially for frequencies beyond the fundamental resonance frequency. Therefore, Kawase, Mori, et al. (2018) proposed a method to transform mHVSR to pHVSR based on the observed spectral ratio between eHVSR and mHVSR, which they called EMR. EMRs were calculated from the microtremor and strong ground motion recordings at 100 K-NET and KiK-net sites in Japan. They categorized EMRs at 100 sites into five categories with the fundamental peak frequencies of microtremors for 0.2 to 1 Hz, 1 to 2 Hz, 2 to 5 Hz, 5 to 10 Hz, and 10 to 20 Hz. The resultant pHVSRs showed quite similar characteristics to the observed eHVSRs and so the inverted velocity structures from pHVSRs were also quite similar to those from the observed eHVSRs. The details of the method to obtain empirical EMRs and the effectiveness of the EMR method to determine velocity structures from inversion of pHVSRs at several Japanese sites not included in calculating the EMRs can be found in Kawase, Mori, et al. (2018). We show in Figure 3.1 EMRs for five categories in Japan and in Figure 3.2 three examples of the resultant pHVSRs with the observed eHVSRs and mHVSR. We can see how the characteristics of mHVSRs are different from those of eHVSRs and how the proposed EMR can effectively fill the gap. The merit of using pHVSR to invert velocity structures based on the theoretical formula for S-waves (e.g., Nagashima et al., 2014) in comparison to using mHVSR based on the point-source solution on the surface (e.g., Garcia-Jerez et al., 2017) lies in the effectiveness to delineate velocity structures from the surface down to the interface of the seismological bedrock with the S-wave velocity (V_s) of 3 km/s or higher (Kawase, Mori, et al., 2018). The point-source solution would have smaller spectral fluctuations in the high-frequency range due to its limited energy of the reverberated waves between the surface and the seismological bedrock (García-Jerez et al, 2013).

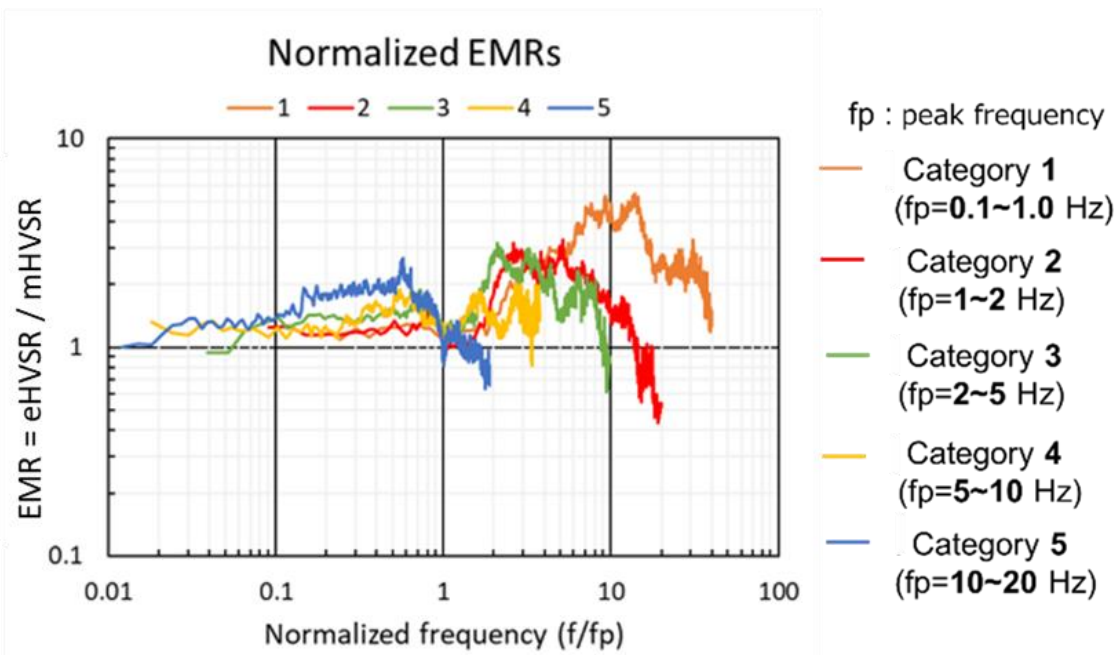


Figure 3.1. Japanese EMRs for all five categories based on the fundamental peak frequency (fp) of mHVSR (after Kawase, Mori, et al., 2018). The horizontal axis is the normalized frequency with respect to fp so that we will expand or shrink the horizontal axis according to fp for a target site before applying EMR to mHVSR.

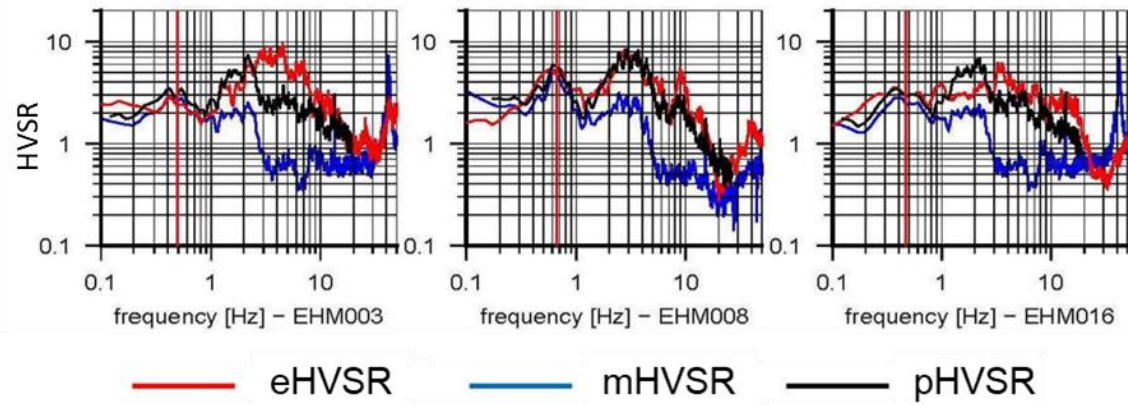


Figure 3.2. Comparison of pHvsr calculated from mHVSR and the Japanese EMR (Category 1), with mHVSR and observed eHVSR at three sites in Japan (after Kawase, Mori, et al., 2018). Vertical red lines show fundamental peak frequencies of mHVSRs, which are very close to those of the observed eHVSRs.

3.3 Previous Studies in the Target Basin

The geological structure of the Grenoble Basin, described in Chaljub et al. (2010), is composed of Quaternary fluvial and postglacial deposits overlaying a Jurassic limestone at the junction of three large valleys of the French Alps, surrounded by three mountain ranges, namely, the Belledonne crystalline massif to the east and old sedimentary limestone to the north (Chartreuse) and the southwest (Vercors). The alluvial deposits consist of sandy and clayey silts as well as sand and gravel layers, typical soil sediments of glacial valleys.

In previous studies about the Grenoble Basin, Lebrun et al. (2001) reported a high site amplification estimated in the frequency range from 0.25 to 10 Hz for both earthquakes and microtremors and the correlation of the predominant frequency of mHVSR with the depth of the geological boundary (basin sediments over rock) by Vallon (1999). Later Gueguen et al. (2007) produced a detailed predominant frequency contour map using the microtremor recordings performed at more than 300 sites, as reproduced in Figure 3.3. Vallon (1999) used gravity data inside the basin to delineate the geological boundary depth contour map which is also shown in Figure 3.3. He used a two-layered model with the assumed homogeneous density of 2.2×10^3 kg/m³ for the basin sediments and 2.70×10^3 kg/m³ for the surrounding rock formation and inverted the geological boundary depths at 3,721 grid points by iteration starting from the 1D approximation. He confirmed agreement between his delineated basin depths with those from seismic reflection surveys (reproduced in Dietrich et al., 2009), as well as that from a deep borehole, within 20 to 60 m uncertainty. Although the geological boundary depth contour of Vallon (1999) was carefully calibrated with the existing basin depth information, uncertainties inherent in the assumptions used by Vallon (1999) would be reflected in the depth contour, especially near the edge of the basin or the measured area.

Guillier et al. (2007) studied the stability of mHVSR by using the data recorded in the Grenoble Basin. They concluded that the fundamental and higher-mode peak frequencies are stable over time and neither affected by human nor natural (weather) activities, but the higher-mode peak frequencies are not as stable as the fundamental one. They also concluded that the amplitude of mHVSR should be applied with caution because it varied depending on the cycle of human activities. They also mentioned that the boundary between anthropic and natural noise was site-dependent, while Bonnefoy-Claudet et al. (2006) proposed that the boundary seems to exist generally around 1 Hz based on the numerical simulation of microtremors. Then Cornou et al. (2008, 2009) compared observed and synthetic mHVSRs to establish a general correlation, although there exist places with significant differences near the edge of the basin. Also, Cornou et al. (2003a, 2003b, 2004) used array measurements of microtremors to delineate the velocity structures. Chaljub et al. (2009, 2010) and Stupazzini et al. (2009) calculated theoretical 3D basin responses for hypothesized earthquake sources based on the velocity structure constructed by various geophysical methods to confirm the validity of the velocity model as well as the simulation methods.

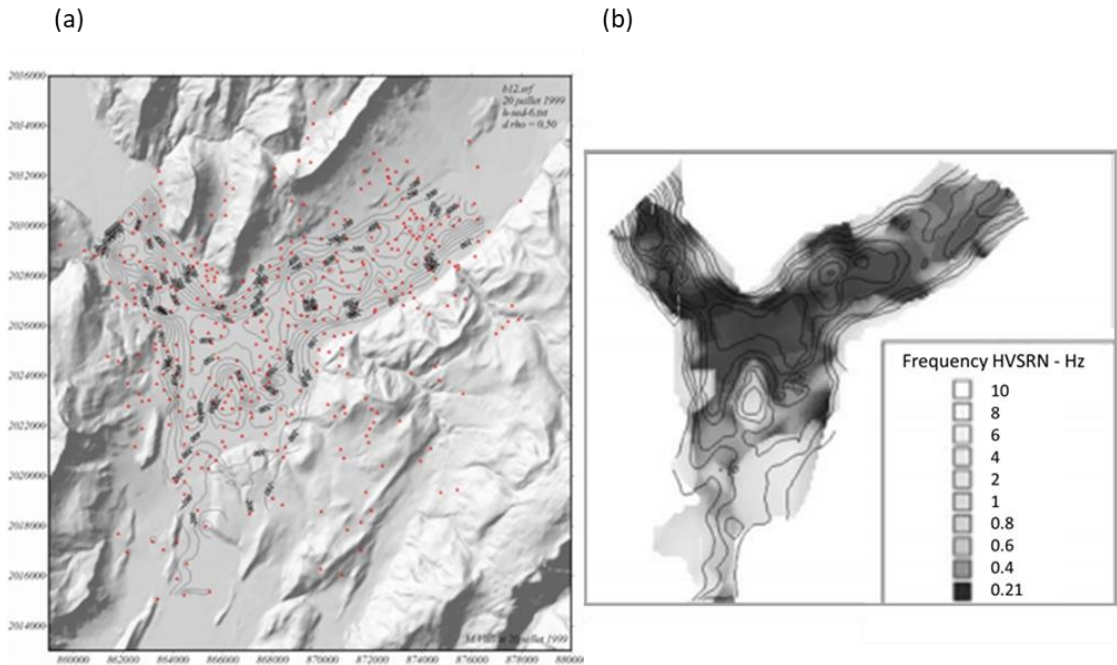


Figure 3.3. Maps of (a) geological basin depth contours in 100 m increment from the gravity anomaly by Vallon (1999); red circles correspond to gravity measurements locations, and (b) fundamental peak frequency distributions by Gueguen et al. (2007).

These studies focused primarily on the distribution of the fundamental peak frequencies of mHVSRs and their subsurface velocity models are composed of the predefined stack of layers in the sediment part and the homogeneous bedrock as an underlying half-space. In these previous studies, eHVSRs and mHVSRs were not effectively utilized to constrain the whole basin structure because the full-use of eHVSR and mHVSR theories based on DFC had not been tested yet at that time. Therefore, detailed velocity structures with multiple layers both in the sediment part and the deeper part above and below the geological boundary were not identified. Because the characteristics of S-wave amplification are controlled by the interaction of all of the layers above the seismological bedrock, we perform in this study the velocity structure inversion by using the observed mHVSRs, together with the EMR_G, to estimate the velocity structures composed of multiple layers down to the seismological bedrock. As explained above, we can expect to obtain a detailed deeper structure if we use pHVSR, which can effectively constrain the velocity structure of the whole basin.

Figure 3.4 shows our overall procedure which will be explained step by step in the following sections. Our final goal is to delineate the velocity structures only from EMR_G and mHVSR. To that end, we first analyze the observed earthquake and microtremor recordings at five sites (termed OG-series) to obtain observed eHVSR and mHVSR. Then we determine the multiplication factor α for EMR_G and calculate the subsequent pHVSRs from mHVSRs. We confirm that pHVSRs are sufficiently similar to eHVSRs. We will validate the proposed EMR_G by comparing the inverted velocity structures from pHVSRs with those from eHVSR. We can then invert the velocity structures from pHVSR at the sites without earthquake data (termed G-

series) and check the validity of the inverted structures by comparing them with basin depth estimates from the gravity-based study of Vallon (1999).

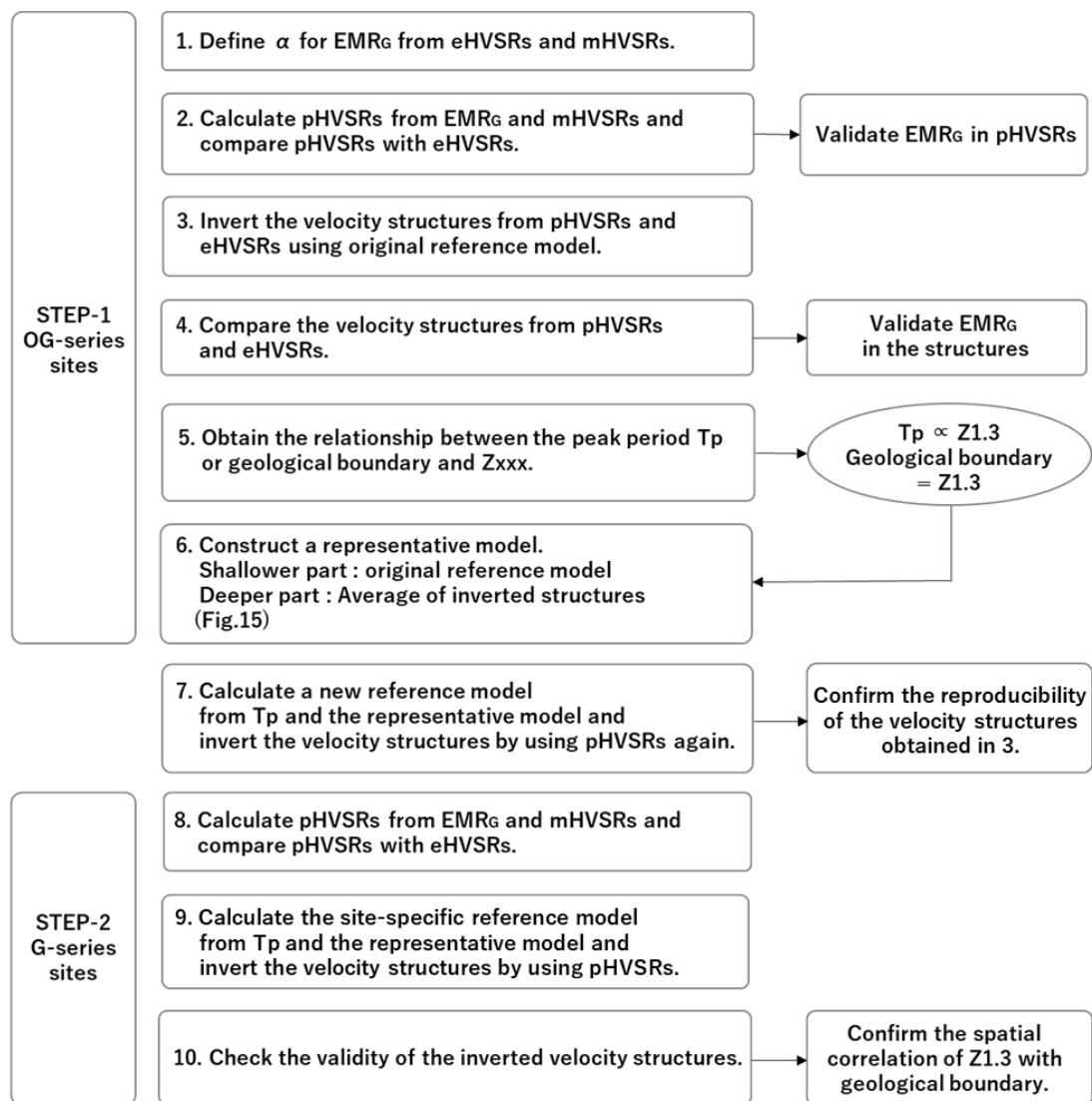


Figure 3.4. Overall procedure in this study to obtain the velocity structures in the Grenoble Basin. Step-1 is the procedure to develop the EMR method specific for the Grenoble Basin based on the earthquake and microtremor data observed at five sites (OG-series), whereas Step-2 is the procedure to apply the developed method at 14 sites with only microtremor data (G-series).

3.4 EMR_G Specific for the Target Basin

We calculate EMR specific for the Grenoble Basin, EMR_G, using the Japanese EMR of Kawase, Mori, et al. (2018) as a template (reference) because we do not have a sufficient number of earthquake observation sites in the Grenoble Basin. We calculate mHVSRs and eHVSRs at five sites in the Grenoble Basin. Strong ground motion data from the French permanent accelerometric network (Traversa et al., 2020) was provided through the Engineering Strong Motion (ESM) database (see Data and Resources section). Table 3.1 lists details of the earthquakes from which we calculate the eHVSR at five sites. Microtremor data were collected by Hollender et al. (2018) at stations coded as OGDH, OGPC, and OGFO; we collect 30 minute durations of microtremor data at OGPS and OGCU using a Lennartz-5s velocimeter connected to a Cityshark digitizer. The peak frequency of mHVSR at each site is within Category 1 in the Japanese EMR, where the peak frequency of mHVSR is within 0.2 to 1 Hz. Figure 3.5 shows the location of our investigated five sites in the Grenoble Basin, and Figure 3.6 shows the Japanese EMR in Category 1 that we use as a template to calculate EMR_G, together with the range of variation. Herein, we refer to these five sites as the OG-series.

Table 3.1. Specification of the events used for calculating EHVRs at OG-series sites. In the left-hand side columns, the epicentral distances to the five OG-series sites are shown only if the event was observed at the site (after ESM Engineering Strong Motion Database).

E Q N O.	DATE (YY MM DD)	TIME (HH MM SS)	LAT.	LON.	DEP	Mw	M _L	EPICENTRAL DISTANCE (KM)				
								OG CU	OG DH	OG FO	OG PC	OG PS
								125	138			
1	2005 0908	112716	46.104	6.8115	10	4.5	4.0					
2	2011 0725	123120	45.016	7.365	11	4.3	4.3	126	129			132
3	2011 0803	013612	44.325	4.4032	18.4		4.3	145	142			141
4	2012 0226	223756	44.52	6.6939	13.1	4.2	4.3	104	105	103	104	109
5	2012 0227	163121	44.49	6.6375	5.6		4.1	104	104	102		108
6	2012 0302	071551	44.492	6.706	8.2		4.1	107	108	106		112
7	2012 0520	020350	44.896	11.2635	9.5	6.1	5.9	433		430	439	439
8	2012 0529	070002	44.842	11.0657	8.1	6.0	5.8	418	421	415	424	424
9	2014 0407	192701	44.604	6.7073	8.1	4.9	4.9	99.0	100	97.1		
10	2014 0407	192701	44.57	6.62	10	4.9	5.1				96.3	101
11	2015 1106	040305	44.47	6.72	5	4.0	4.3	110	110		109	114
12	2016 1024	144411	46.33	7.58	2		4.2	188		185		
13	2016 1110	024812	44.29	6.24	2		4.2	107	106	107	103	110
14	2016 1203	090142	47.09	5.41	2		4.1			211		210
TOTAL NUMBER OF EARTHQUAKES AT EACH SITE								11	9	10	7	11

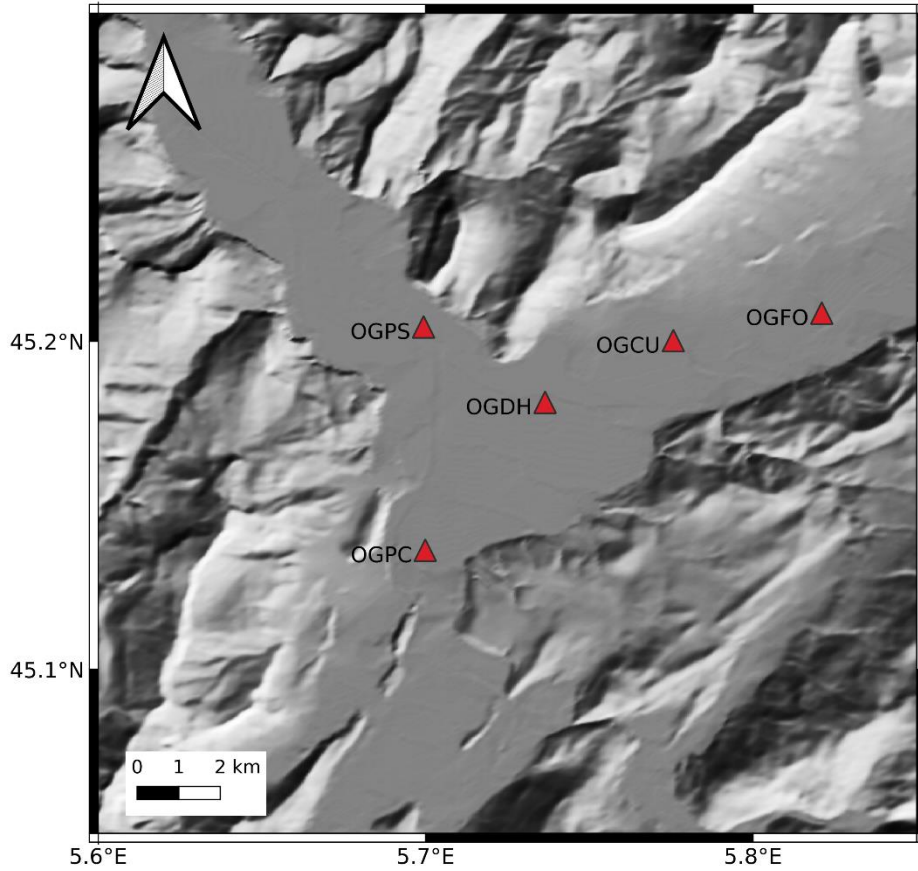


Figure 3.5. The location of the five OG-series sites used to develop EMR_G with both available earthquake and microtremor data in the Grenoble Basin.

In order to make pHVSR closer to the observed eHVSR for five sites, we assume that the spectral shape of EMR_G should follow the shape of the Japanese EMR and only the amplitude would be different with a modification factor α . The rationale for the assumption is the fact that the individual ratios of eHVSRs and mHVSRs at five OG-series are remarkably similar to the shape of the Japanese EMR in Category 1, especially that of the average minus one standard deviation shown in Figure 3.6. This suggests that the average frequency dependence of EMR in the Grenoble Basin would be similar to those for the Japanese sites with much stiffer sediments than the average. With this assumption, we can determine EMR_G by comparing the shape of pHVSR from the Japanese EMR raised to the power of the amplification factor α to the observed eHVSR. For a small number of target sites, it is easier and more stable to determine a single parameter α than to determine the EMR as a function of frequency.

First, we calculate EMR_G using a grid search for α following equations (3.1) and (3.2),

$$\text{EMR}_G = \text{EMR}^\alpha, \quad (3.1)$$

$$\begin{aligned}
\text{pHVSR} &= \text{mHVSR} * \text{EMR}_G \\
&= \text{mHVSR} * \text{EMR}^\alpha.
\end{aligned} \tag{3.2}$$

Then we determine α such that the sum of logarithmic residuals between pHVSRs and observed eHVSRs at the five sites is minimum for equally sampled frequencies f , following equation (3.3),

$$R = \sum_{\text{site}=1}^5 \frac{\sum_{f=f_{\min}}^{f_{\max}} (\log(\text{eHVSR}) - \log(\text{pHVSR}))^2 / f}{\sum_{f=f_{\min}}^{f_{\max}} (\log(\text{eHVSR})^2) / f} \tag{3.3}$$

Here we use a frequency range from about 0.1 Hz to 10 or 20 Hz depending on the effective frequency range from EMR_G during the grid search. In the first step of the grid search, we search the best α from 0.1-0.5 at an interval of 0.1 because we realize through preliminary analysis that EMR_G seems significantly smaller than the Japanese EMR. We find that the optimal α is between 0.2 and 0.3. Then, in the second step of the grid search, we search the optimal α from 0.2-0.3 with an interval of 0.01. We find that the optimal α is 0.28. Figure 3.7 shows the variation in the sum of the logarithmic residuals between pHVSRs and observed eHVSRs at the five sites with respect to α from 0.2 to 0.3.

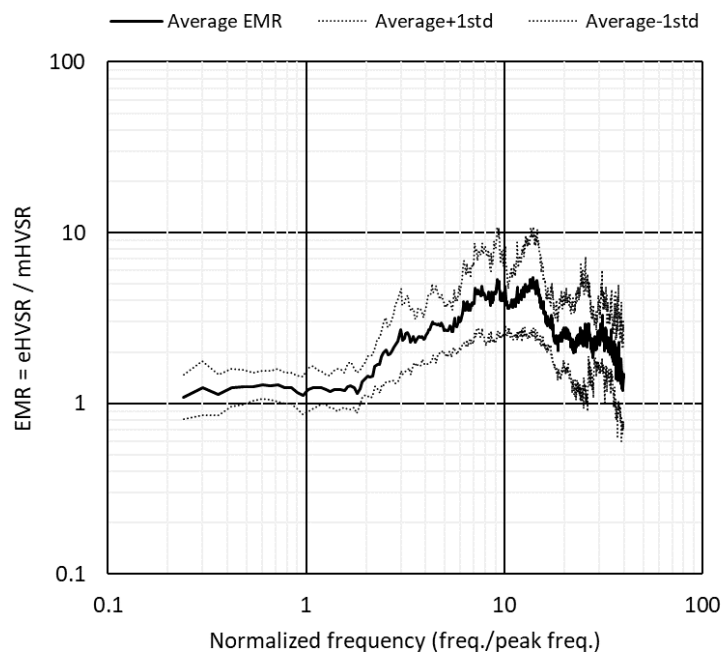


Figure 3.6. Japanese EMR of Category 1 used as a template. To see the range of deviation we plot the average and average \pm one standard deviation.

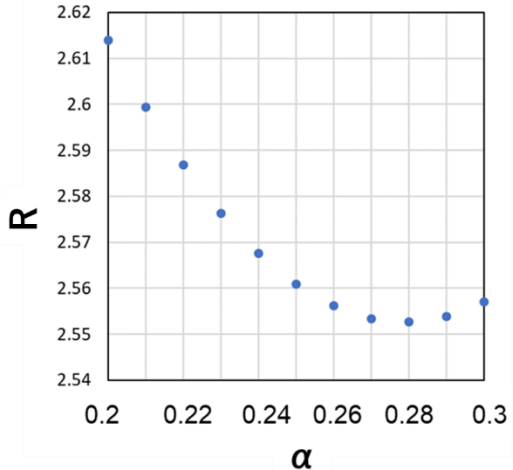


Figure 3.7. The sum of the logarithmic residuals for the amplitudes between pHVSRs and observed eHVSRs at five sites for α from 0.2 to 0.3. We found that α equal to 0.28 corresponds to the minimum residual.

3.5 Comparison of pHVSR Calculated from EMR_G with Other HVSRs

For our five selected OG-series sites, we compare pHVSRs calculated from the local mHVSR and EMR_G with $\alpha=0.28$ or Japanese EMR Category 1 with the observed eHVSR in Figure 3.8.

We find that the pHVSR from EMR_G shows a stronger correlation with observed eHVSR, compared to the correlation of either pHVSR from the full Japanese EMR or mHVSR with no EMR correction. The pHVSR from the Japanese EMR provides larger values than pHVSR from EMR_G, especially in the frequency range higher than the fundamental peak frequency. This reflects the Japanese EMR to be related to the average basin structure in Japan, which is likely to be significantly softer than the structure in the Grenoble Basin to produce greater amplification above the peak frequency. We remind the reader that the Japanese EMR in the frequency range higher than the fundamental peak frequency is high in amplitude on the average but there exist a certain number of sites with much less amplitude as the amplitude of the average minus one standard deviation shows (Figure 3.6). This result suggests the need to calculate an EMR specific for the target region if the tectonic settings are significantly different from those in Japan; Japan is an island arc due to active subduction zones and the Grenoble Basin is due to continental collision producing the Alps. Note that both the frequency and the amplitude at the fundamental peak frequency are the same for eHVSR and mHVSR, as found in Japan (Kawase Mori, et al., 2018).

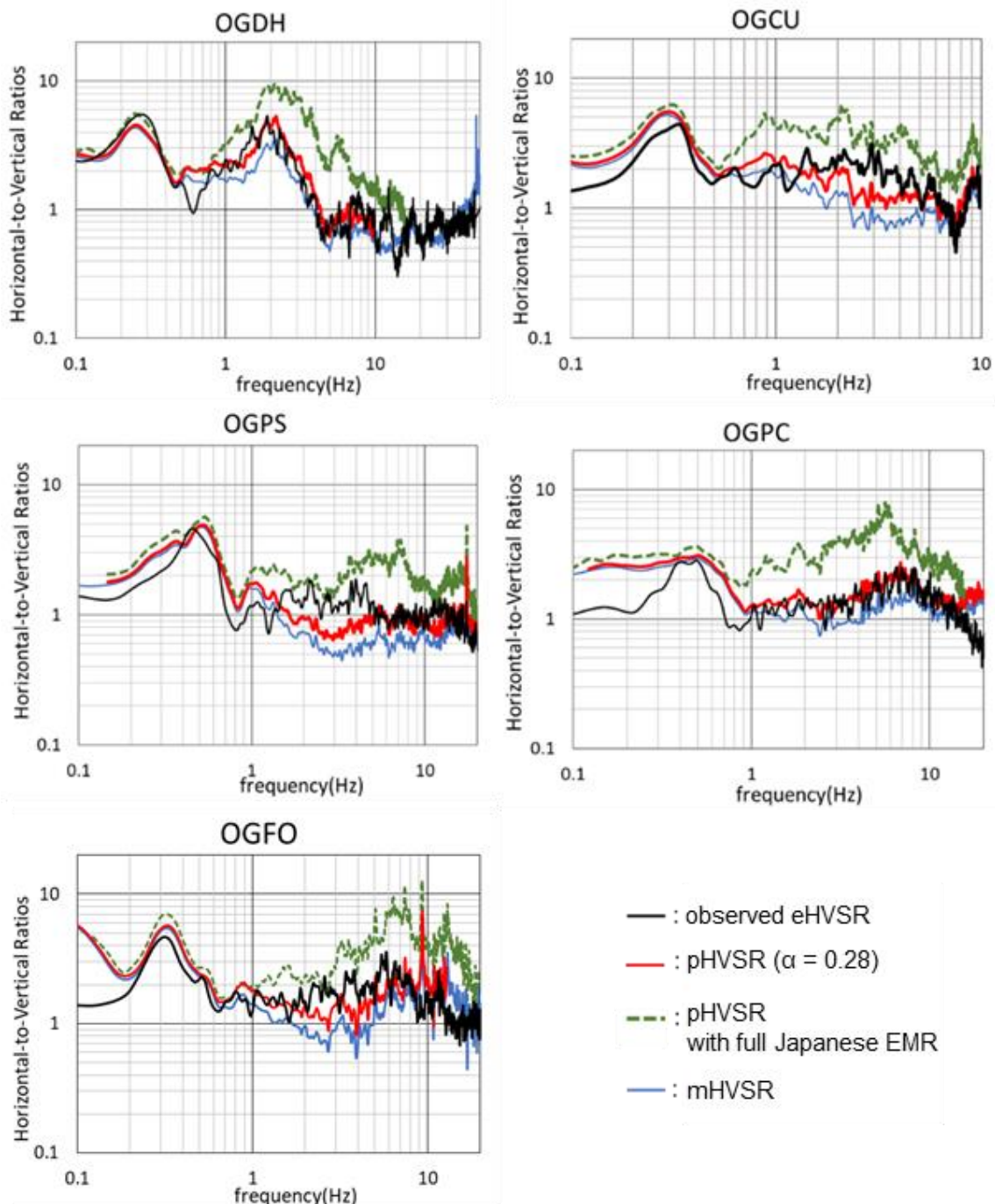


Figure 3.8. Comparison of pHvsRs calculated from EMRG and full Japanese EMR Category 1 with the observed eHVSR and mHVSR at the five OG-Series sites.

3.6 Validation of pHVSR from EMR_G

We invert the one-dimensional velocity structures using pHVSR (from EMR_G with $\alpha=0.28$) or observed eHVSR at our five OG-series sites to confirm whether the velocity structures inverted from pHVSRs are similar to those inverted from observed eHVSRs. We also compare the inverted velocity structures using mHVSRs as a direct substitute without any correction. Please note that this comparison of the inverted velocity structures from mHVSRs does not intend to show the validity of the direct substitute of mHVSR for the eHVSR inversion.

The inversion method here is the one proposed by Nagashima et al. (2014, 2017), where the one-dimensional S-wave velocity structure from the surface to the seismological bedrock can be obtained from eHVSR through the Hybrid Heuristic Search (HHS) method, under the assumption of the diffuse field concept proposed by Kawase et al. (2011). Here is a brief introduction of the inversion scheme adopted in this paper. The HHS method combines genetic algorithm and simulated annealing methods to search the optimal P- and S-wave velocities and thicknesses. The density ρ is converted from the S-wave velocity, V_s , in m/s by

$$\rho = 1.4 + 0.67 * (V_s / 1000)^{1/2}. \quad (3.4)$$

The damping is assumed to be 1.1% for both P-and S-waves as a hysteresis damping type for all the layers. Because eHVSR depends not only on S-wave velocity but also on P-wave velocity, both velocities are equally weighted. However, the contribution of P-wave velocity to eHVSR is not as significant as that of S-wave velocity in general, primarily because of its smaller variation. Besides, in the actual soil and rock materials, there is a certain range of variations between S- and P-wave velocities. To perform a stable inversion, Nagashima et al. (2017) developed a new P-wave velocity conversion formula from PS logging data obtained by borings at K-NET and KiK-net stations in Japan to restrict the searching range of P-wave velocity in relation to the inverted S-wave velocity in each step. The average P-wave velocity (V_{pAve}) and its standard deviation (V_{pStd}) in the logarithmic space (assuming a log-normal distribution) can be evaluated from the V_s by

$$V_{pAve} = 1.93 * V_s + 380 \quad (depth \leq 10m), \quad (3.5)$$

$$V_{pStd} = -6.65 * 10^{-4} * V_s + 1.79 \quad (depth \leq 10m), \quad (3.6)$$

$$V_{pAve} = 1.39 * V_s + 1189 \quad (depth > 10m), \quad (3.7)$$

$$V_{pStd} = -6.63 * 10^{-5} * V_s + 1.25 \quad (depth > 10m), \quad (3.8)$$

where we need to use different formulas depending on the depth of the layer.

We do not allow a low-velocity zone inside a higher velocity layer. Thus, the S-wave velocity will increase gradually with depth. We assume fixed P- and S-wave velocities of 5.6 km/s

and 3.2 km/s for the seismological bedrock (Cornou, 2002). We set our genetic algorithm's variables of generation, population, crossing ratio, and mutation ratio to 200, 400, 0.7, and 0.1, respectively. We identify the subsurface structures ten times changing a seed number for pseudo-random number generation for the initial population to minimize the residual calculated by equation (3.9) where f is frequency, and consider the minimum residual model in those ten results as the optimal model.

$$\text{Residual} = \sum (\text{HVSR}_{\text{observed}} - \text{HVSR}_{\text{theory}})^2 / f \quad (3.9)$$

We weight the residual by the inverse of frequency to evaluate the residual on the logarithmic frequency axis.

For the searching parameter settings in the inversion, we assume that the S-wave velocity of each layer is restricted to vary in the range of $\pm 100\%$ of the reference model, and the thickness of each layer is identified without restriction. The reference model is used only to decide the searching range for the inversion. P-wave velocity is calculated as a function of S-wave velocity (equations (3.5) or (3.7)) and restricted within the range defined by ± 2 times of geometric standard deviation in equation (3.6) or (3.8). We fix the frequency range for the residual computation (equation (3.9)) from 0.1 to 20 Hz at OGDH, OGCU, and OGPS, while we fix the lower frequency limit to 0.2 Hz at OGFO and 0.3 Hz at OGPC because mHVSRs at these two sites appear contaminated by low-frequency noise as seen in Figure 3.8. A reference model for the velocity structure was constructed from the VSP logging at OGFO; this is the deepest (available) borehole to 554 m depth (Gueguen et al. 2007; Dietrich et al., 2009). Figure 3.9 shows the velocity structure at OGFO both directly from the boring measurement (interval velocities from VSP logging) and the reference model inferred as a fourteen-layered structure. Table 3.2 reports the velocity structure used as the reference model for the inversion.

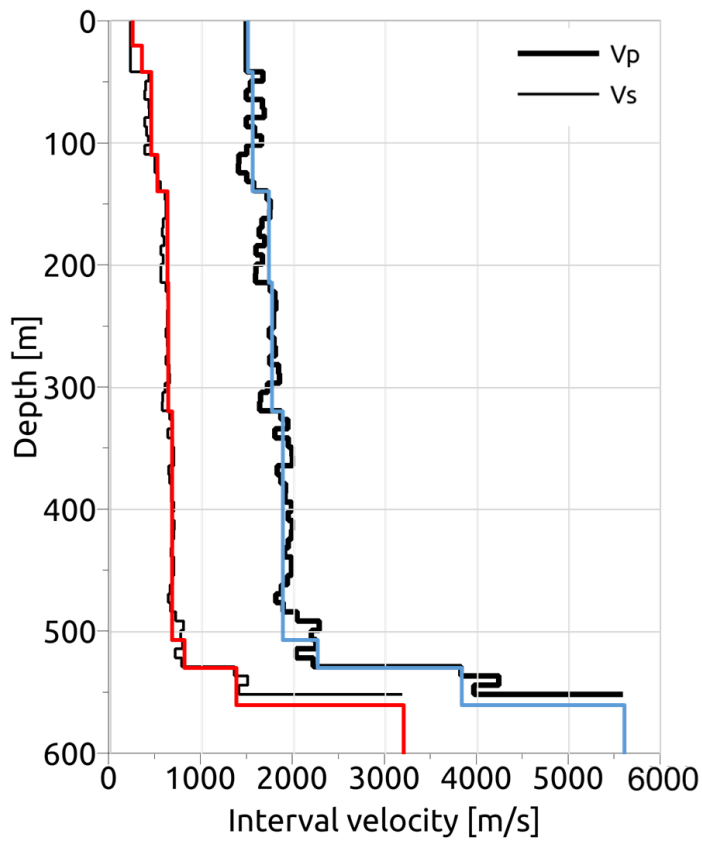


Figure 3.9. The velocity structure from borehole data (VSP logging with 2 m interval) at OGFO (after Gueguen et al., 2007). The red and blue lines are the modeled S- and P- wave velocity profiles used as the reference model in Step-1. The location of OGFO is shown in Figure 3.5.

Table 3.2. The velocity structure at OGFO used as the reference model for the inversion (Step-1).

Layer No.	Thickness(m)	Depth(m)	Vp(m/s)	Vs(m/s)	Density (10^3 kg/m^3)
1	20.0	20.0	1500	240	1.73
2	22.0	42.0	1500	340	1.79
3	67.5	109.5	1550	442	1.79
4	30.0	139.5	1550	507	1.88
5	75.0	214.5	1727	617	1.93
6	105.0	319.5	1760	629	1.93
7	187.5	507.0	1876	670	1.95
8	22.5	529.5	2257	806	2.00
9	30.5	560.0	3834	1369	2.18
10	0	560.0	5600	3200	2.60

Figures 3.10, 3.11, and 3.12 show the results of the inversion for P- and S-wave velocity structures from eHVSR, pHVSR, and mHVSR, respectively, at OGCU as an example. The results at the other sites are shown in Figures A3.2 to A3.5 in the Appendix. In Figure 3.10 we can see that the minimum residual (“best”) inverted structure matches quite well the detailed fluctuations of the observed eHVSR in a wide frequency range. In contrast, the reference model based on the detailed VSP logging yields much higher fluctuations in amplitudes, although the fundamental peak frequency matches the observed one. The inverted S-wave velocity of the topmost layer is about 350 m/s, while the deeper layers show a gradual increase in S-wave velocities from about 500 m down to the seismological bedrock at about 1.3 km. We can see similar characteristics in Figure 3.11 when pHVSR is used as the target. The matching of the best structure to the observed eHVSR in Figure 3.12 is also not so bad in which mHVSR is used as a direct substitute in the inversion, although the inverted S-wave velocity of the topmost layer becomes about 260 m/s. The stabilities among ten trials in terms of the convergence rate with the generation are similar in eHVSR and pHVSR, but it is not as good in mHVSR. From Figures 3.10 to 3.12, we observe that theoretical HVSRs from the best-fit models have high reproducibility of the targeted HVSRs, which suggests that the inversion scheme proposed by Nagashima et al. (2014, 2017) has a strong ability to reproduce the targeted HVSRs, even if we use mHVSR as a direct substitute for eHVSR (Figure 3.12). However, it is not a good practice to directly substitute mHVSR for eHVSR because the resultant velocity structures from mHVSR are not as close as those from pHVSR to those from eHVSR as shown below for all the five sites.

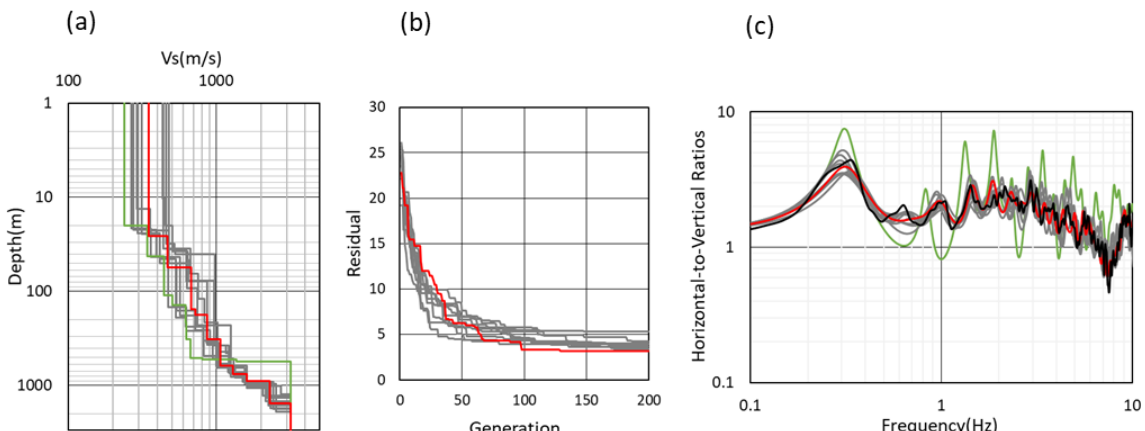


Figure 3.10. Comparison of (a) the obtained S-wave velocities, (b) convergence with respect to the generation in HHS, and (c) the best-fit model (red line) among ten trials (gray lines) with the target eHVSR (black line) observed at OGCU. The reference model and its theoretical eHVSR is shown in green.

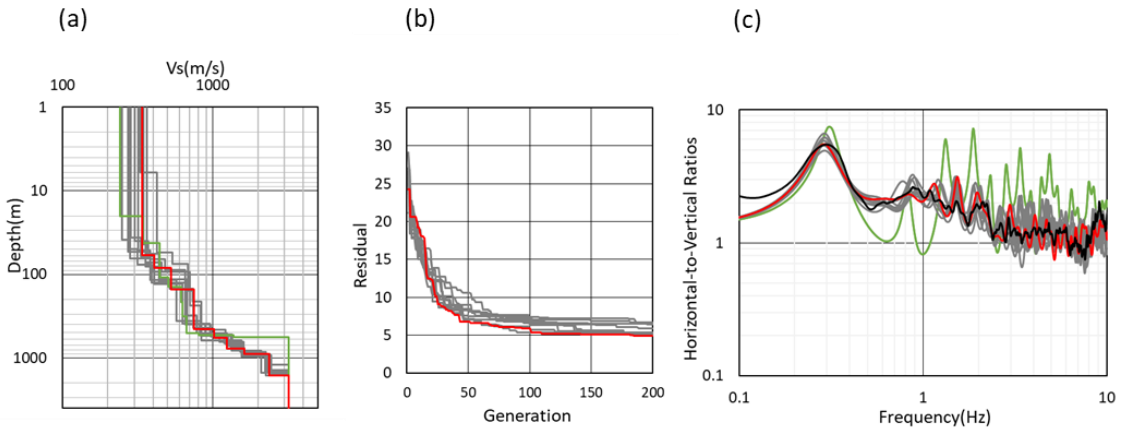


Figure 3.11. Comparison of (a) the obtained S-wave velocities, (b) convergence with respect to the generation in HHS, and (c) the best-fit model (red line) among ten trials (gray lines) with the target pHVSR (black line) calculated from the EMR_G and observed mHVSR at OGCU. The reference model and its theoretical eHVSR is shown in green.

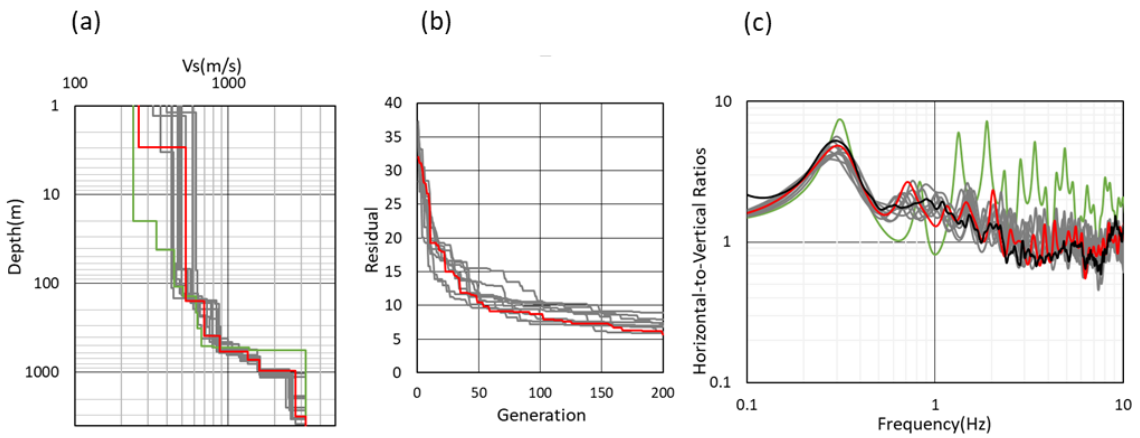


Figure 3.12. Comparison of (a) the obtained S-wave velocities, (b) convergence with respect to the generation in HHS, and (c) the best-fit model (red line) among ten trials (gray lines) with the target mHVSR (black line) observed at OGCU. The reference model and its theoretical eHVSR is shown in green.

The same comparisons for the other four sites are shown in the Appendix (Figures A3.2 to A3.5) for those from eHVSR and pHVSR. Although the amplitude in the EMR_G is not so large, the EMR correction to mHVSR really enhances the peak amplitudes in the frequency range higher than the fundamental peak frequency and contributes to successfully invert similar structures from pHVSR to those from eHVSR.

Figure 3.13 shows the comparison of the best velocity structures inverted from eHVSR, pHVSR, and mHVSR, together with the reference models at all five sites. We observe that the velocity structures from pHVSRs are closer to those of observed eHVSRs than those from

mHVSRs, especially in the upper 30 m. Because the EMR_G correction is effective only in the higher frequency range, it is natural to see the difference mainly in the shallow part. The amount of difference between the inverted structures and the reference model depends on the site, but the differences below the bottommost layer of the reference model at 550 m are all common. Overall a gradual increase of the S-wave velocities from 550 m down to the seismological bedrock is required to improve agreement with the observed fundamental peak frequency amplitude, as seen in Figure 3.10.

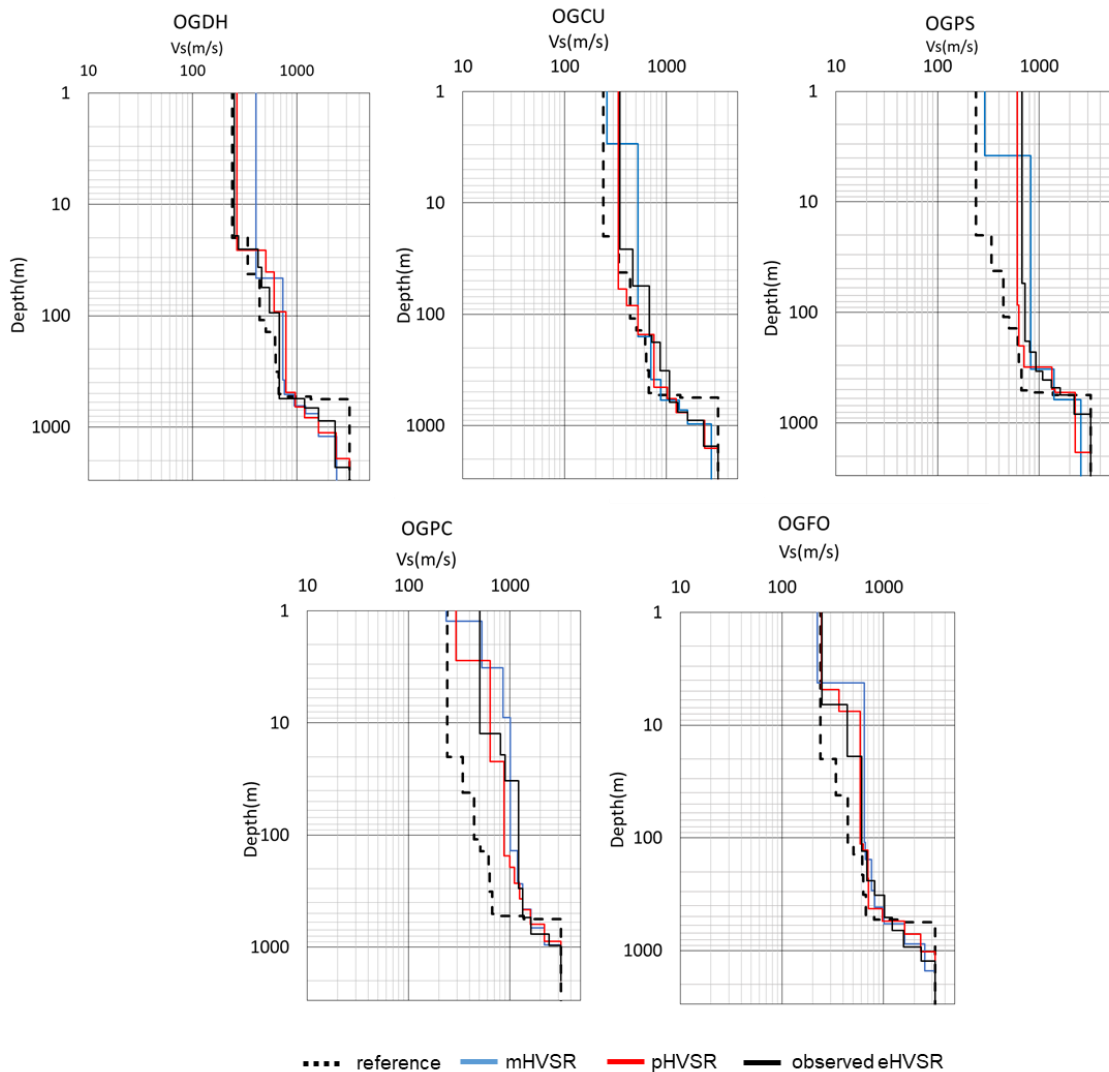


Figure 3.13. Comparisons of the velocity structures inverted from eHVSRs (black lines), pHVSRs (red lines), and mHVSRs (blue lines) at five sites. The reference model is also shown (black dotted line).

Up until this point, we establish the EMR specific for the Grenoble Basin, EMR_G , from five sites with both observed earthquakes and microtremors and demonstrate that pHVSR derived from mHVSR and EMR_G is an effective substitute for eHVSR to invert the S-wave velocity structure. We designate the process explained so far as Step-1 (Figure 3.4). We now apply this

EMR_G to other sites where only microtremors are observed to invert velocity structures, which we term Step-2.

3.7 Improvement of the Reference Model

Here we introduce a scheme for getting more detailed reference models for the velocity structure inversion at the sites where the observed eHVSRs are not available, which is one of the purposes in this study. Therefore, in the process, we focus on and use only the characteristic of the pHVSR, not the observed eHVSR. The reference model that we use for the inversion in Step-1 is made from the borehole data at OGFO (Figure 3.5). At OGFO, Gueguen et al. (2007) and Dietrich et al. (2009) revealed that through borehole measurements the sedimentary layers were found down to 531.5 m and the rock formation was found from 531.5 m to 554 m. However, they stopped the borehole measurement at 554 m, and below 554 m the P-wave velocity was determined from a 6 km long refraction profile, and the S-wave velocity of 3.2 km/s was converted from the P-wave velocity using a Poisson ratio of 0.25 (Cornou, 2002). However, we find that a couple of layers with increasing S-wave velocities below the interface between the sediments and the rock (i.e., the geological basin boundary) would be necessary to reproduce the observed eHVSR as shown in Figures 3.10 and 3.13 (as well as Figures A3.2 and A3.3 in the Appendix). In general, the peak amplitude of the fundamental frequency becomes larger in proportion to the impedance contrast between the layer that corresponds to its frequency and the layer below. When there is a strong impedance contrast at the interface, the peak amplitudes become larger at the peak frequencies to which the upper layers contribute. Thus, a velocity gradient should be introduced in the inverted velocity structures because the observed amplitude at the fundamental frequency seems too small for the structure with such a high-impedance contrast as the reference model in Step-1. Therefore, it would be better to modify the reference model in the deeper part in Step-2 in order to better constrain the searching range in the inversion for the sites where we do not have observed eHVSR. To this end, we try to construct a scheme to improve the reference model of the deeper part based on the fundamental peak frequency at a target site. This modification of the deeper part would be reflected in the shallower part of the reference model, too. We combine the deeper and shallower parts to make a new reference model for inversion. Henceforth, we call this reference model based on the empirical relationship of the inverted structures in Step-1 the new reference model, and call the reference model used in Step-1 the original reference model.

In order to make a detailed deeper part in a new reference model, we need first to define the boundary between the shallower and deeper parts at each G-series site. We would like to know which depth is controlling the fundamental peak frequency inside the Grenoble Basin. So, we compare the observed fundamental peak period (T_p) with the theoretical T_p , which is defined as the inverse of the average S-wave velocity to a certain depth Z , Avs_z , multiplied by 4 times the depth Z , that is $(4*Z/\text{Avs}_z)$. This is the one-quarter wavelength theory for the resonance period T_p of an equivalent two-layered structure (e.g., Kramer, 1996; Kawase, 2003). We use the period T_p here because of this proportionality to the depth Z . We test the threshold S-wave velocity for Z to be either 0.8 km/s, 1.3 km/s, or 3.2 km/s. Figure 3.14 shows the three relationships between

observed Tp from the pHVSR and theoretical Tp when we use the averaged Vs above the bottommost layer with the Vs of 0.8 km/s, 1.3 km/s, or 3.2 km/s by using the inverted velocity structures from eHVSRs. It turns out that observed Tp is controlled by the depth down to the layer with the S-wave velocity of 1.3 km/s, that is, Z1.3. From that result, we regard Z1.3 as the appropriate boundary between the shallower and deeper parts of the new reference model, which would be the effective depth of the basin boundary. Later we would like to show that Z1.3 also corresponds to the geological boundary through comparison with basin depths determined by Vallon (1999).

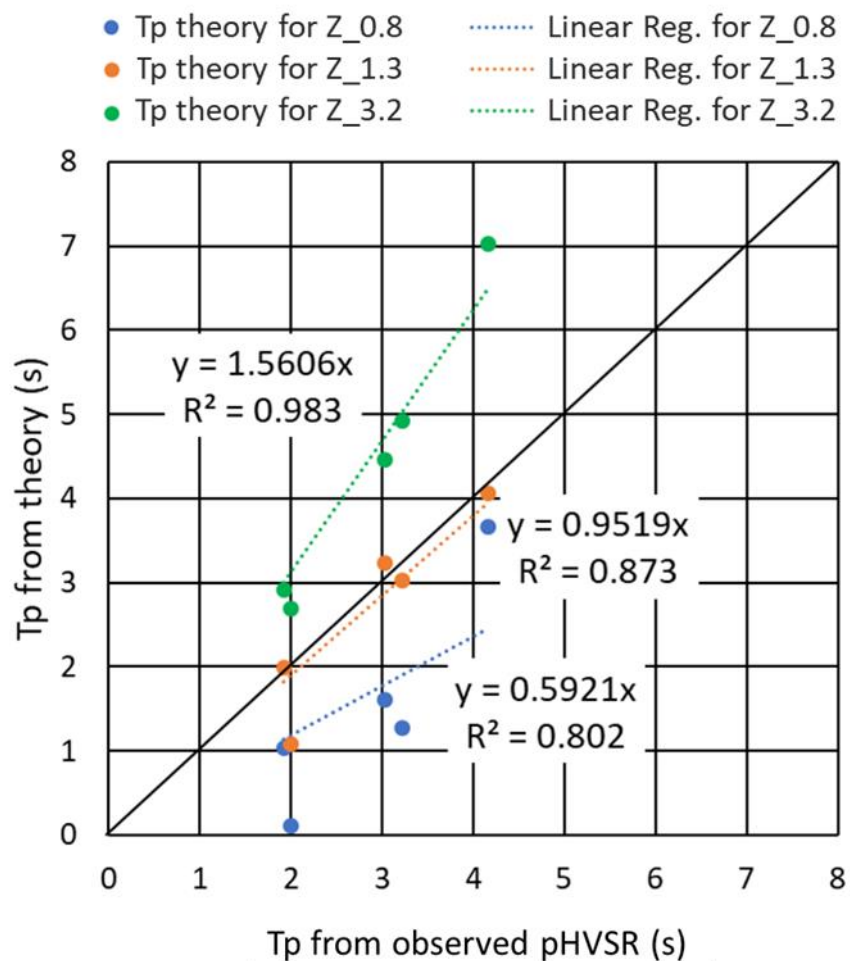


Figure 3.14. Relationship between Tp from observed pHVSR and theoretical Tp from the one-quarter wavelength theory for three different depths at five sites.

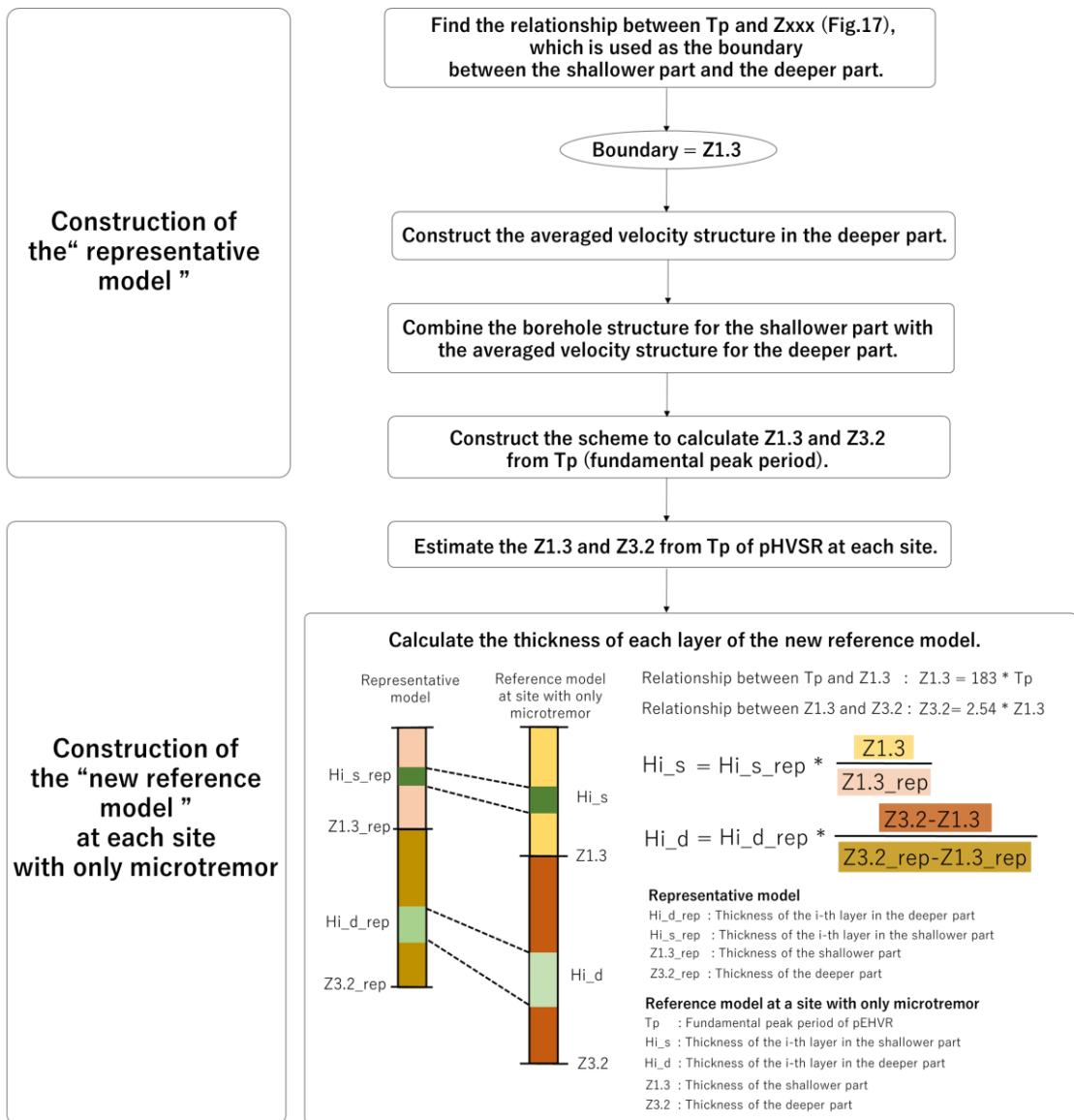


Figure 3.15. Schematic procedure to calculate a reference model at a site with only microtremors.

The upper half corresponds to the procedure to construct the representative model from the results of the OG-series sites, whereas the lower half does to construct a site-specific reference model at each G-series site.

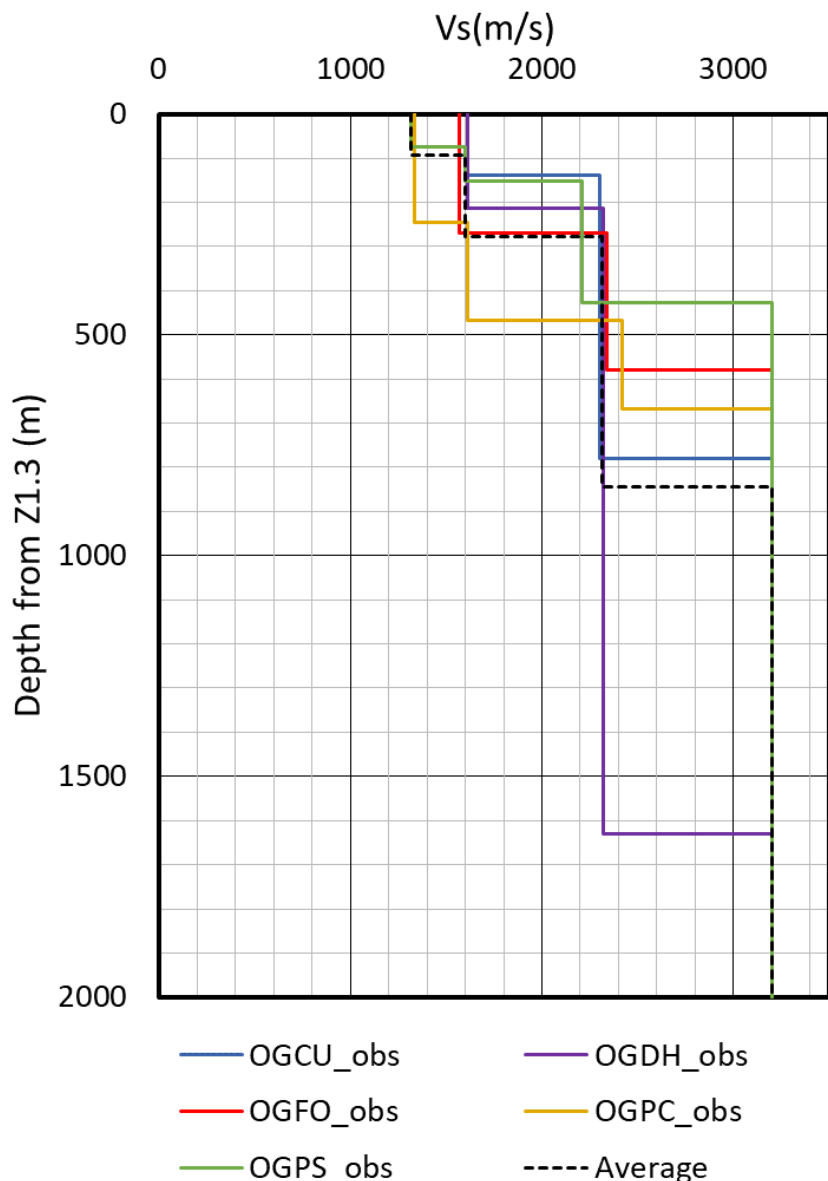


Figure 3.16. Deeper velocity structures (solid lines) after the averaging operation for three groups of layers from the inverted velocity structures in Step-1 at five sites and their average (black dotted line).

The scheme of the new reference model in Step-2 at a target G-series site is shown in Figure 3.15. For the deeper part, we first construct a detailed deeper part model by averaging the velocity structures in the deeper part in Step-1, assuming only three layers. In this first step of the averaging operation, we calculate the averaged S-wave velocity by using the travel-time average for three grouped layers, where the S-wave velocities are in the ranges from 1.3 km/s to 1.5 km/s, from 1.5 km/s to 2.2 km/s, and from 2.2 km/s to 3.2 km/s. The number of layers at each site categorized into each Vs range is zero or one in the lowest Vs range, and one each in the middle and highest Vs ranges. In the second step, we calculate the averaged thickness for each of these

deeper layers at five OG-series sites. As a result of these two averaging steps in the deeper S-wave velocities at the five sites, we obtain a 1.32 km/s layer, a 1.60 km/s layer, and a 2.32 km/s layer. Figure 3.16 shows the velocity structures as the average of the three grouped layers from the inverted structures in Step-1 and the depth- and thickness-averaged deeper velocity structure calculated from those averaged structures, which will be used as a representative model for the deeper part to calculate a reference model at each site in Step-2. Please note that this representative model is not directly used as a reference model at each site.

In order to construct a new reference model, we first need to estimate Z1.3 at each site where we want to analyze because we regard Z1.3 as the bottom of the shallower part. We also need the depth of the seismological bedrock Z3.2, when we construct the deeper part at each site based on the representative model shown in Figure 3.16.

To calculate Z1.3 and Z3.2 at each G-series site as per our described methodology (Figure 3.15), we first check the correlation between observed Tp from pHVSR and the depth down to the threshold Vs layer. Figure 3.17 shows the relationships between Tp from the observed pHVSRs (which is the same as the observed mHVSRs) and Z0.8, Z1.3, and Z3.2 at the five OG-series sites. We find that Z1.3 and Z3.2 are linearly correlated with Tp, and that the regression coefficient of 183 m/s can be used to translate the observed Tp into the estimated Z1.3. The average coefficient of 183 m/s suggests that the average S-wave velocity of the basin above the layer with the S-wave velocity of 1.3 km/s is 4 times this value, that is, 732 m/s from the quarter-wavelength theory, which would be quite reasonable. In addition, we find that the gravity boundary depth by Vallon (1999) is nearly equal to Z1.3. We also calculate the average ratio between Z3.2 and Z1.3 to be 2.54, so that we can estimate Z3.2 from Z1.3 at each site. The correlation between the basin depth of Vallon (1999) and Z1.3 will be used in the validation of the inversion procedure proposed in this paper after performing the velocity structure inversions for the G-series sites in Step-2.

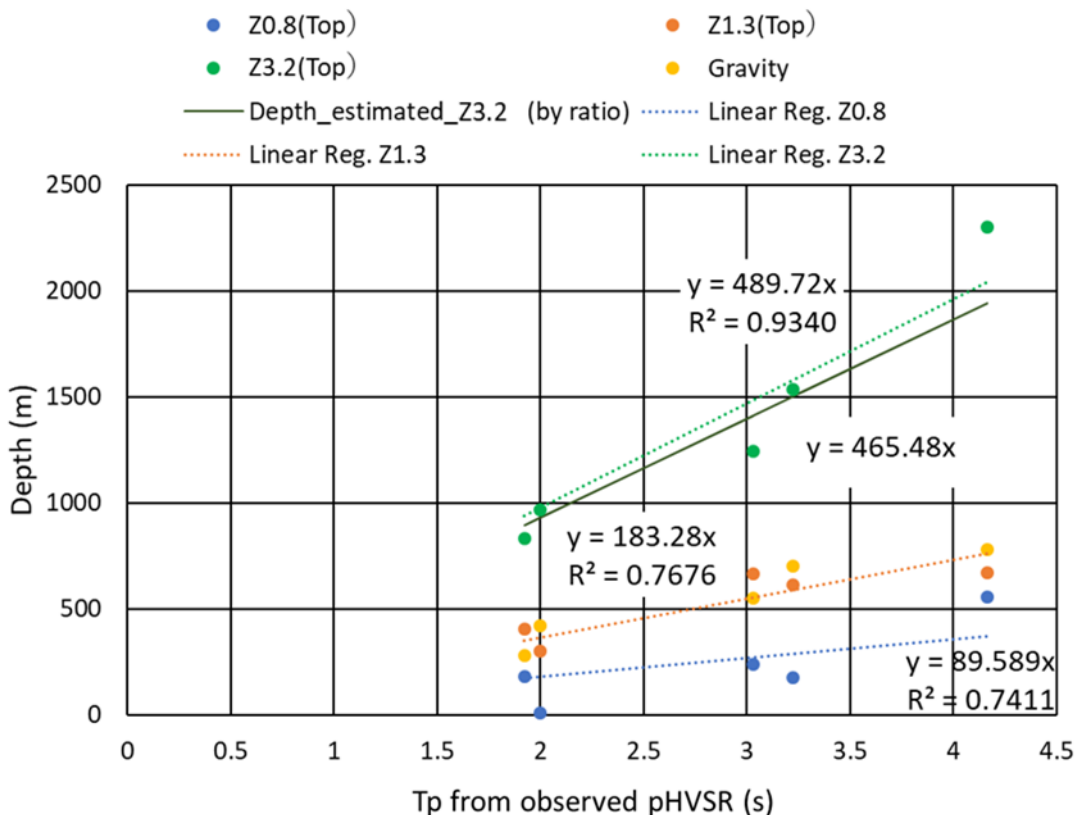


Figure 3.17. Relationship between T_p from observed pHVSR and Z0.8, Z1.3, and Z3.2 at five OG-series sites. The relationship between T_p from observed pHVSR and the geological basin depth from gravity (Vallon, 1999) is also shown. A black line corresponds to the relationship of Z3.2 based on the constant ratio to Z1.3 ($y = 465.48x = 2.54 \cdot Z1.3$).

Based on the relationships as developed above, the new site-specific reference model at each G-series site is constructed as follows. After assessing T_p at a site, Z1.3 and Z3.2 are estimated by

$$Z1.3 = 183 \cdot T_p, \quad (3.10)$$

$$Z3.2 = 2.54 \cdot Z1.3. \quad (3.11)$$

The thickness of the i-th layer in the deeper part below Z1.3 (termed H_i_d in Figure 3.15) is calculated by proportionally distributing the total thickness of the deeper part (Z3.2-Z1.3) using the thicknesses ratio of the i-th layer in the representative model (Figure 3.16). Thus, once we estimate Z1.3 and Z3.2 from equations (3.10) and (3.11) at each site, we can determine H_i_d by

$$H_i_d = H_i_d_{rep} * (Z3.2 - Z1.3) / (Z3.2_{rep} - Z1.3_{rep}), \quad (3.12)$$

where $H_i_d_{rep}$ is the thickness of the i -th layer of the deeper part from the representative model, $Z3.2_{rep}$ and $Z1.3_{rep}$ are 1374.5 m and 529.5 m from the representative model, respectively. The last panel in Figure 3.15 shows the schematic procedure of this operation, while Table 3.3 shows the parameters (i.e., $H_i_d_{rep}/845.0$) necessary for the reference model construction.

Table 3.3. Parameters necessary for a new reference model (Step-2).

Layer No.	Ratio of each layer to (Z3.2-Z1.3)	Vs(m/s)
Deep 1	0.11	1319
Deep 2	0.22	1598
Deep 3	0.67	2315

The representative model for the shallower part is the same as the original reference model, which is the borehole data at OGFO (Figure 3.9). The thickness of the i -th layer in the shallower part H_i_s is calculated by proportionally distributing the thicknesses in the shallower part of this representative model (Figure 3.15), depending on the total thickness of the shallower part at each site obtained from equation (3.10). Thus, from the estimated $Z1.3$ at each site, H_i_s is calculated by

$$H_i_s = H_i_s_{rep} * Z1.3 / Z1.3_{rep}, \quad (3.13)$$

where $H_i_s_{rep}$ is the thickness of i -th layer in the representative model. Figure A3.6 in the supplemental material is an example of the new reference model at OGCU calculated from the construction procedure in Figure 3.15.

3.8 Validation of the New Reference Models for OG-Series Sites

In order to check the validity of the proposed scheme to develop new reference models, we construct new reference models at the OG-series sites following the above scheme, and then we again invert the velocity structures using pHVSR as the target with these new reference models. Figure 3.18 shows comparisons of the velocity structures inverted from pHVSR using the original

reference model in Step-1, those from pHVSR using the new reference model, and those from the observed eHVSR using the original reference model. Figure 3.19 shows the corresponding theoretical eHVSRs of the velocity structures shown in Figure 3.18, in comparison to the pHVSR used as the target. We can see that the velocity structures and the resultant eHVSRs from the new reference models are very close to those from the original reference models.

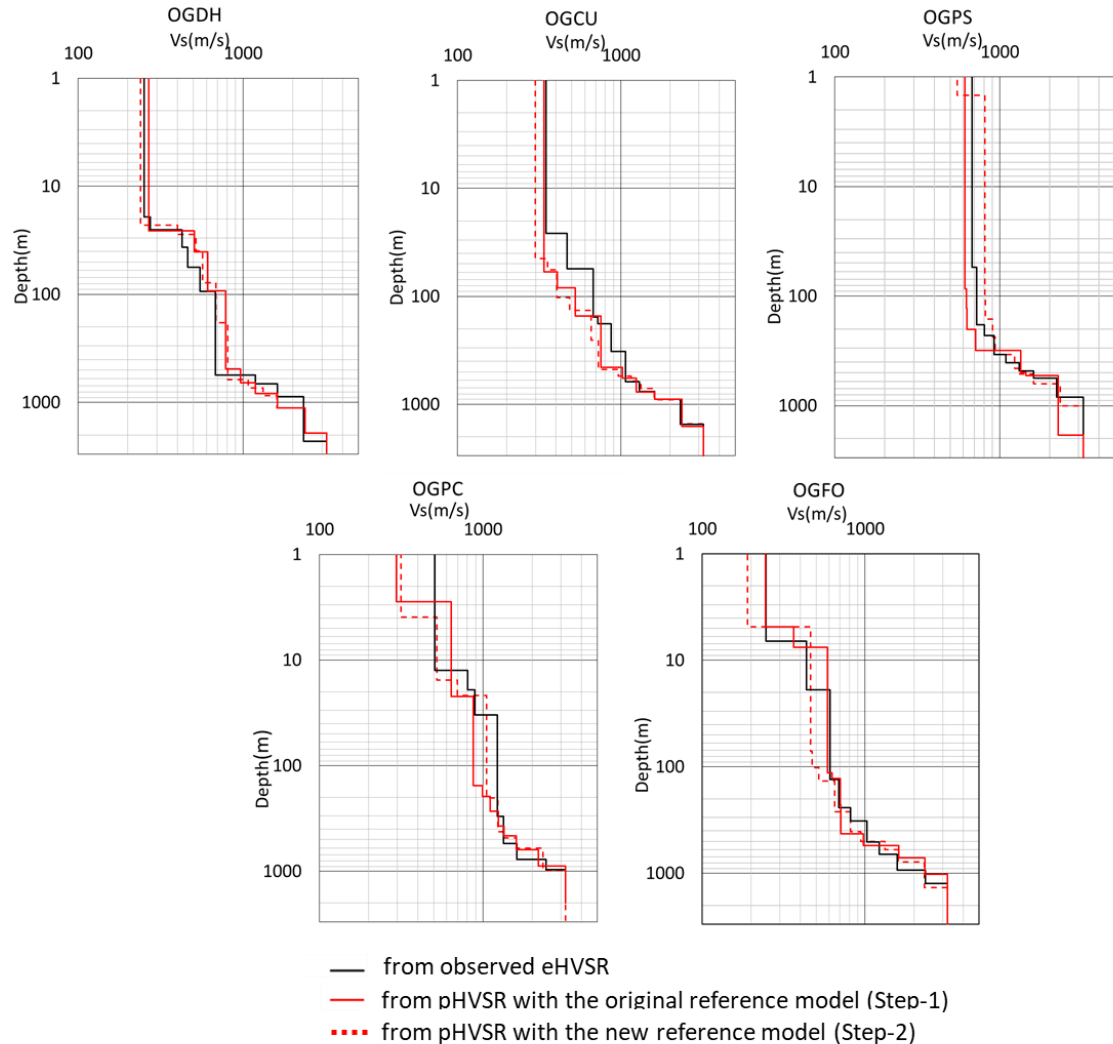


Figure 3.18. Comparison of the velocity structures inverted from pHVSRs using the original reference model and those from pHVSRs using the new reference models specific for each site, together with those from the observed eHVSRs inverted from the original reference model.

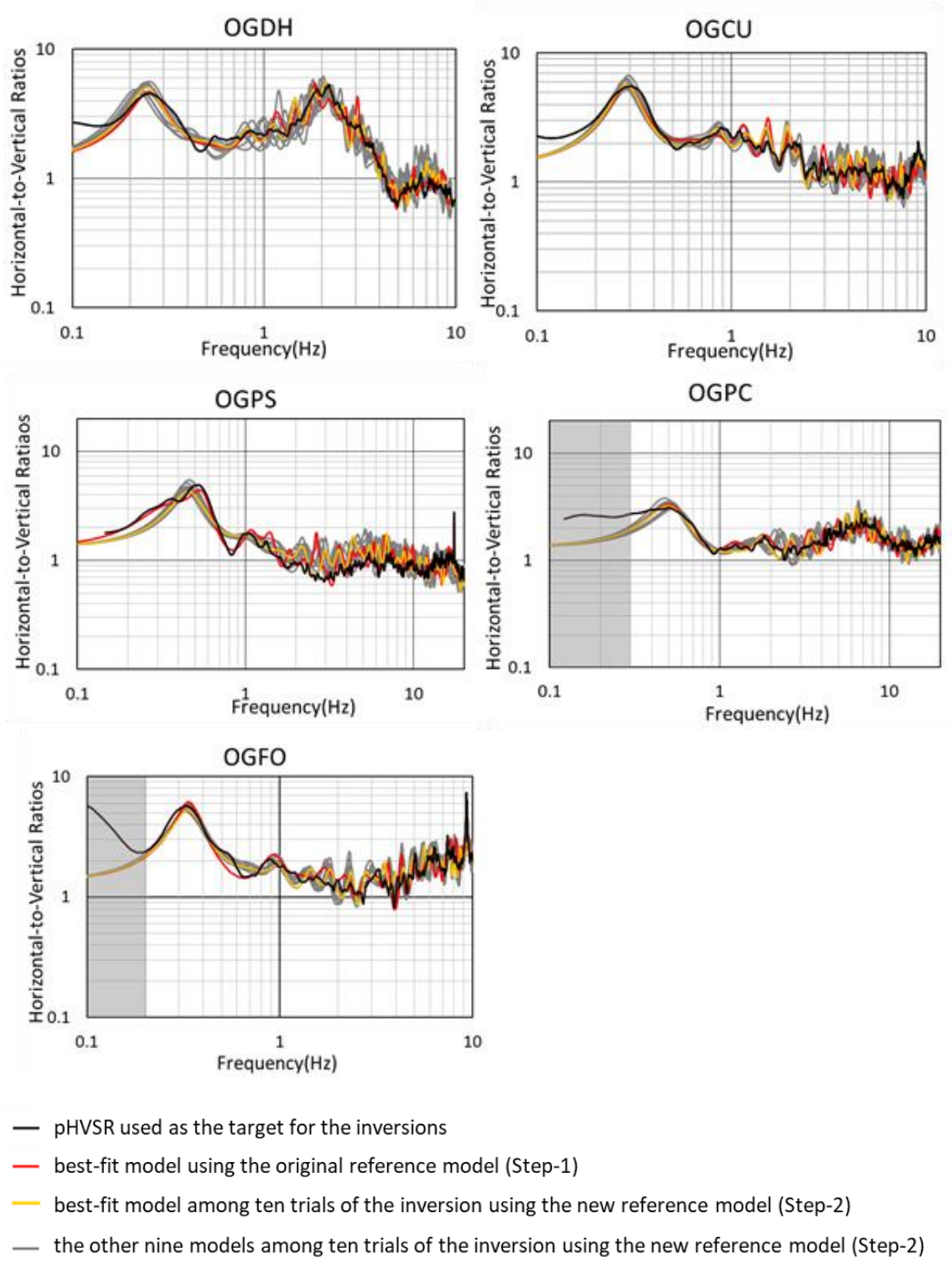


Figure 3.19. Comparison of the theoretical eHVSRs for the inverted velocity structures from the original and new reference models, together with the transformed pHVSRs used as targets. Gray shades show the frequency ranges not used in the inversion.

3.9 Application of EMR_G and New Reference Models to the G-Series Sites

Towards the goal to delineate the whole basin structure, we apply EMR_G, calculated in the section “EMR_G specific for the Grenoble Basin”, together with the new reference models calculated by the scheme mentioned in the section “Reference model construction from the inversion results in Step-1”, to fourteen G-series sites (the sites with the name of “G-xx” in Cornou et al., 2009). We select the G-series sites whose fundamental peak frequencies are in Category 1 in the Japanese EMR (<1.0 Hz). There are microtremor data from several hundred sites in the Grenoble Basin. Among them, we choose the G-series sites because the microtremors at these sites are relatively recent measurements made with broadband sensors that are reliable at low frequencies. Figure 3.20 shows the locations of the G-series sites that we use for the analysis. Among 20 sites, sites outside the basin or very close to the basin edge, namely, G1, G10 to G12, and G17 were excluded because of their fundamental peak frequencies. G16 was excluded because of its lower sampling rate (about 8 Hz). G04 is collocated with OGFO, but hereafter it is treated as one of the other G-series sites.

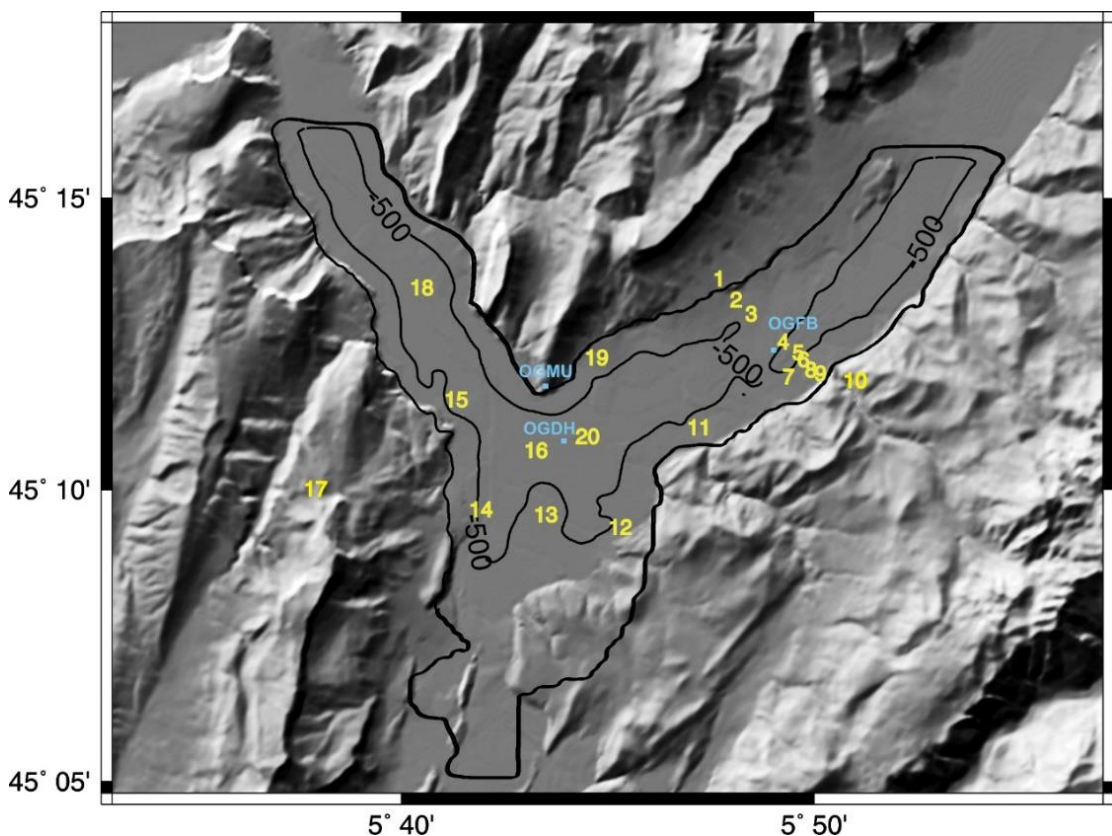


Figure 3.20. Locations of the G-series sites (yellow numbers) used for the analysis of Step-2 (after Cornou et al., 2009). The lines are the 500 m increment contours for the geological basin depth. OGFB is the same as OGFO in this paper, whereas OGMU is another OG-series site outside of the basin.

For the G-series sites, we have five months of continuous microtremor records. These sites are ideal mHVSR sites to check validity of the EMR method for the velocity inversion that we propose in this paper. Figure 3.21 shows the mHVSRs and pHVSRs calculated by multiplying the observed mHVSR with EMR_G at four of the G-series sites as examples of all fourteen sites. The corrections by EMR_G look effective only in the frequency range higher than 0.7 Hz.

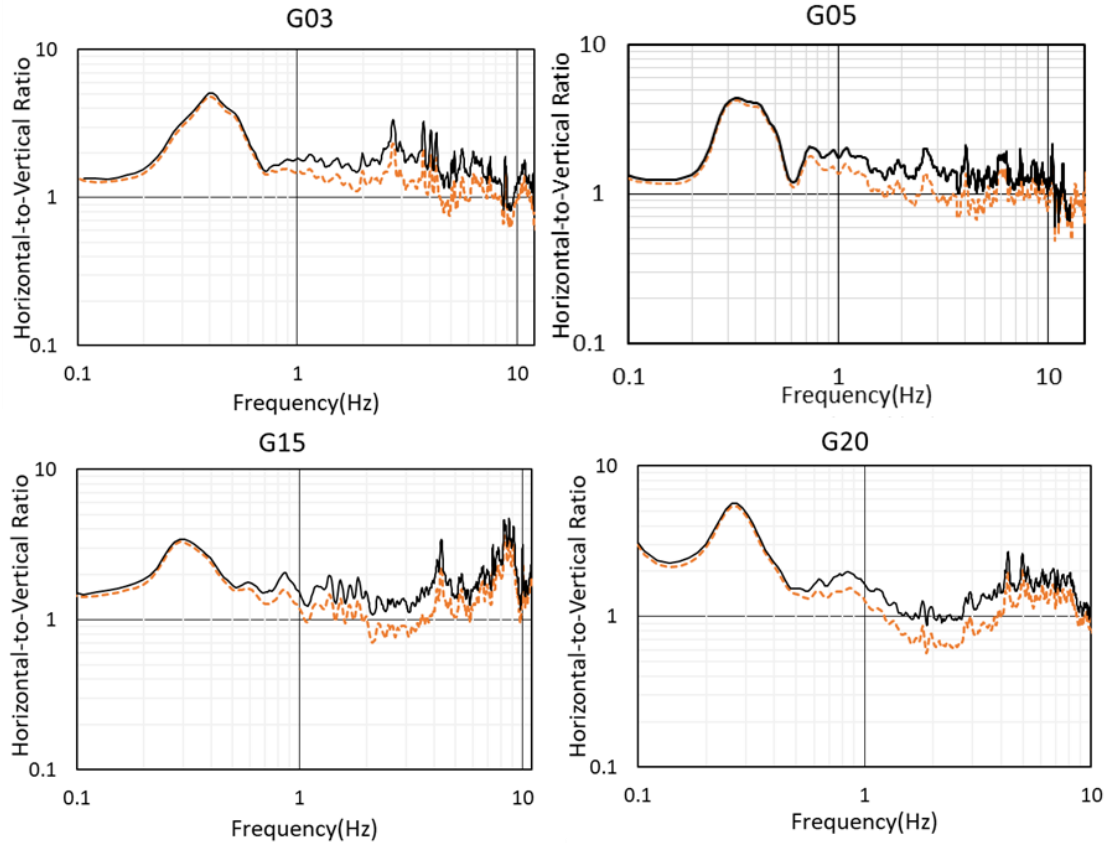


Figure 3.21. Comparison of mHVSRs (orange dotted lines) and pHVSRs calculated by multiplying the observed mHVSRs with EMR_G (black lines) at four representative sites among the G-series sites.

After developing new reference models for the velocity structures following the steps shown in the section “Reference model construction from the inversion results in Step-1”, we obtain the inverted velocity structures and the corresponding theoretical eHVSRs at these sites by using the inversion scheme proposed by Nagashima et al. (2014, 2017). For the parameter settings in the first inversion, the S-wave velocity of each layer was restricted to vary in the range of $\pm 100\%$ of the value of the new reference model in the shallower part and totally fixed in the deeper part. The thickness of each layer is set free in the shallower part and restricted in the deeper part to the range between 50% and 200% of the value of the new reference model. The searching range in the latter is set to be smaller because the fundamental peak period T_p is already reflected in the new reference model.

The results of the initial inversion show a very thin, soft surface layer whose thickness

is less than 1 m at five sites, namely G08, G13, G14, G18, and G19. For the inversion results, we check that almost no difference can be seen between the theoretical eHVSRs from the inverted velocity structure with and without the thin low-velocity layer near the surface because such a thin surface layer affects the eHVSR characteristics only in a very high-frequency range, which is outside of the target frequency range. Therefore, at these sites, we perform the second inversions by restricting the thickness of the first layer to be in the range of $\pm 90\%$ of the new reference model to prevent the emergence of such a very thin layer near the surface.

Figure 3.22 shows the results of ten trials of the velocity structure inversion using our described parameter settings for four example sites, after which we choose the best result that has the lowest residual to the target pHVSR. The results at the other sites are shown in Figures A3.7 to A3.11 in the Appendix. At each site shown in Figure 3.22, the theoretical eHVSR obtained from the best-fit velocity structure is similar to the target pHVSR, indicating that the best-fit model reproduces the characteristics of the target pHVSR at each site quite nicely. The convergence at each site is rapid and smooth as in the case of five sites in Step-1 and the stability of the inverted velocities among the ten solutions are quite good except for the third layer at G20.

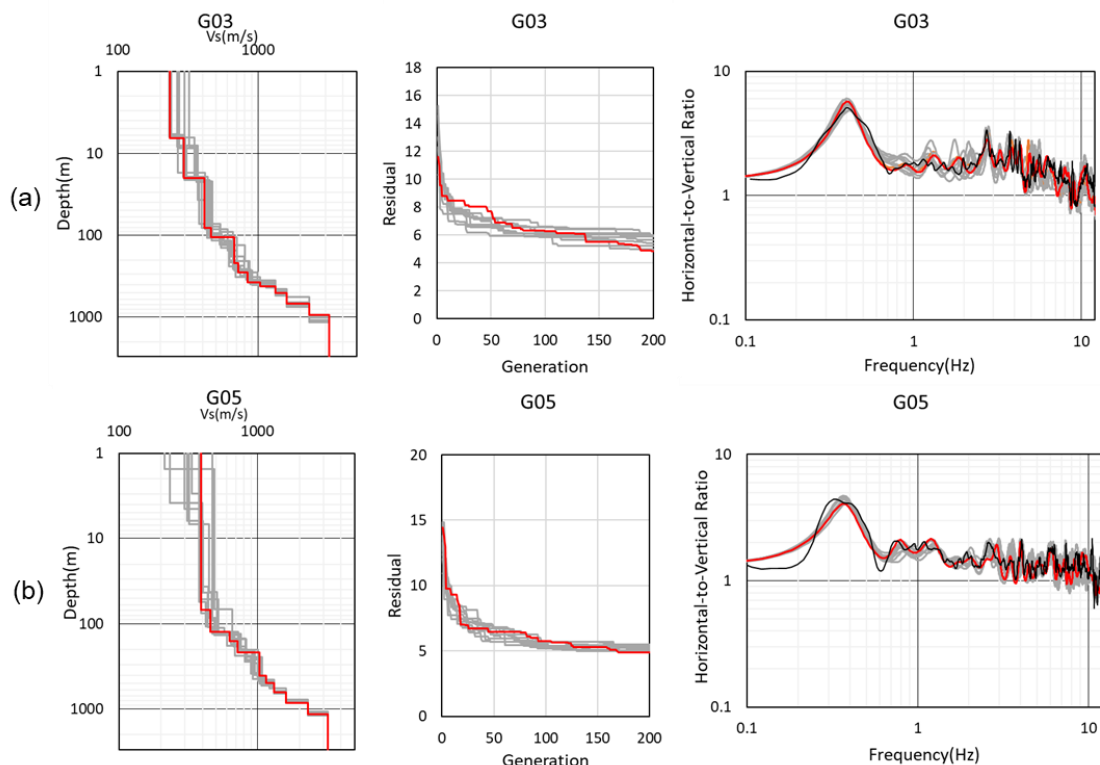


Figure 3.22. Comparison of the best-fit model (red line) of the obtained S-wave velocities among ten trials (gray lines) in the left panel, convergence with respect to the generation in the middle panel, and the theoretical eHVSR of the best-fit model among ten trials in comparison with the transformed pHVSR in the right panel at four sites. The results of the other nine trials are shown by gray lines. (a) G03, (b) G05 (c) G15, (d) G20.

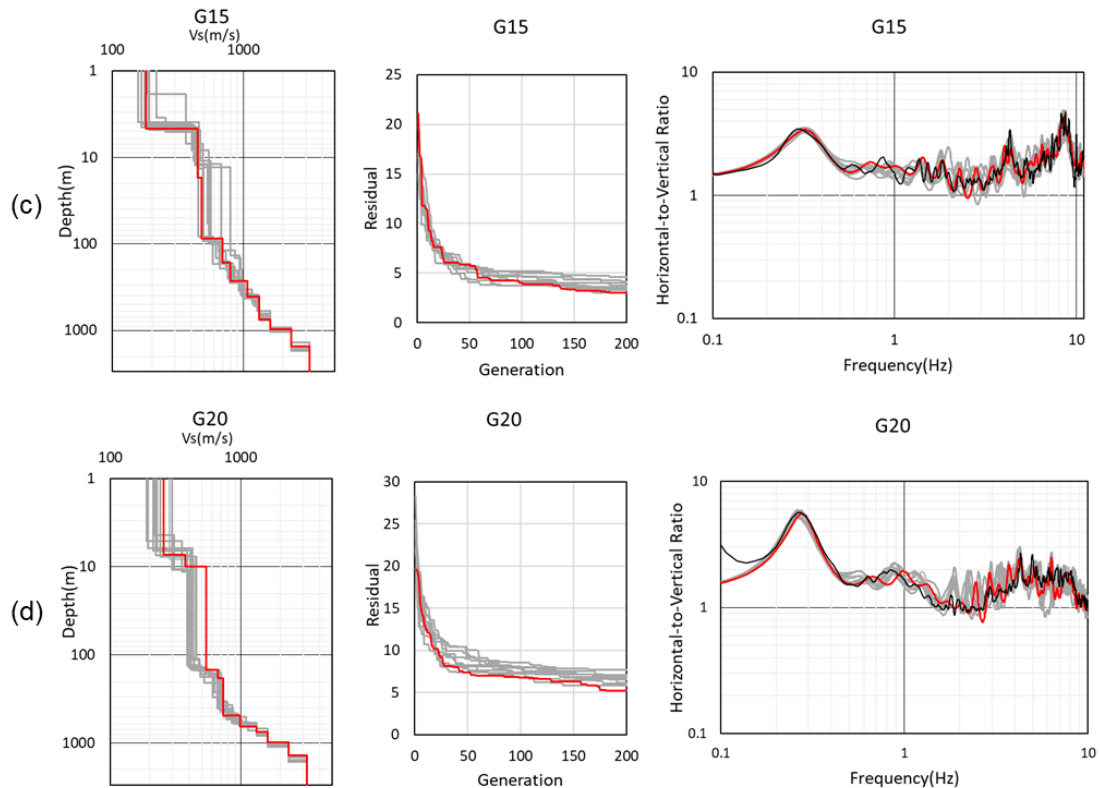


Figure 3.22 (Cont.). Comparison of the best-fit model (red line) of the obtained S-wave velocities among ten trials (gray lines) in the left panel, convergence with respect to the generation in the middle panel, and the theoretical eHVSR of the best-fit model among ten trials in comparison with the transformed pHVSR in the right panel at four sites. The results of the other nine trials are shown by gray lines. (a) G03, (b) G05 (c) G15, (d) G20.

3.10 Discussion

We estimate the EMR specific for the Grenoble Basin and calculate the velocity structures at fourteen sites in the Grenoble Basin by using only the observed mHVSR and the EMR specific for this region. Our motivation for proposing the EMR method is to apply the inversion method for the P- and S-wave velocity structures using mHVSR to sites where there are no earthquake data. Considering the difficulty in observing sufficient numbers of earthquake ground motions in areas that are not seismically active, the method to estimate velocity structures and subsequent amplification factors without using earthquake data would be quite useful.

In this paper, the most important finding from our analysis is the requirement of a velocity gradient near the sediment-to-rock geological boundary reported in the gravity anomaly (Vallon, 1999) and borehole data. Because the bedrock of the Grenoble Basin is Jurassic limestone (Dietrich et al., 2009; Chaljub et al., 2010), it is at first natural to consider the direct contact of

the seismological bedrock at the geological basin boundary. On the contrary, we obtain a thick stack of layers with a strong velocity gradient below Z1.3, which is intended to correspond to the geological boundary obtained by the gravity anomaly (Vallon, 1999), as mentioned in the section “Reference model construction from the inversion in Step-1”. Our empirical relationship in equation (3.11) suggests that the seismological bedrock as represented by Z3.2 is 2.5 times deeper than the geological bedrock, Z1.3. The reason why we need such a thick stack of layers below the geological boundary in the inversion for eHVSRs, as well as pHVSRs, is because the fundamental peak amplitude of these observed HVSRs (Figures 3.10 and 3.11) are not as high as the theoretical eHVSRs from the velocity model (Figure 3.9) with direct contact of the seismological bedrock. Because the average S-wave velocity of the whole basin is on the order of 700 to 800 m/s, the impedance contrast between the basin layers and the seismological bedrock could be more than 6 times. The observed peak amplitude at the fundamental peak frequency is in the range from 4 to 5 as seen in Figures 3.8 and 3.21, which is too small if such a high-impedance contrast at the boundary were a reality.

To show the validity of the above hypothesis we perform a sensitivity analysis of the velocity structure at OGFO, which is the only site inside the Grenoble Basin with the deep borehole data (Figure 3.9). The purpose of this analysis is to demonstrate that: (1) the theoretical eHVSR of the inverted structure, which is closer to the targeted pHVSR, cannot be reproduced by the borehole data, and (2) the inverted velocity structure is well constrained by the target pHVSR. In our sensitivity analysis, we study two cases to test the effects of varying the velocity structure of both the shallower (Case-1) and deeper parts (Case-2) to the amplitude of the calculated eHVSR. In each case, we construct four models for which we calculate theoretical eHVSRs by the same diffuse field theory.

In Case-1 as a parametric study for the shallower part, which means the layers above Z1.3, we set these parameters starting from the values of the inverted velocity structure at OGFO and then bring them closer to those of the borehole via

$$\begin{aligned} Vs_x &= Vs_inverted + (Vs_borehole - Vs_inverted) * x / 100 \\ &= Vs_inverted * (1 - x / 100) + Vs_borehole * x / 100, \end{aligned} \quad (3.14)$$

$$\begin{aligned} Vp_x &= Vp_inverted + (Vp_borehole - Vp_inverted) * x / 100 \\ &= Vp_inverted * (1 - x / 100) + Vp_borehole * x / 100. \end{aligned} \quad (3.15)$$

Here $Vs_inverted$ and $Vp_inverted$ are the S- and P- wave velocity of a certain layer in the inverted velocity structure respectively and $Vs_borehole$ and $Vp_borehole$ are the S- and P- wave velocity of a certain layer in the borehole data respectively, and x is the percentage (weight) of borehole velocities mixed with inverted velocities. For instance, in the case of the velocity structure labeled as 25% in Figure 3.23a, the S-wave velocity of each layer is calculated by equation (3.14) with $x=25$. For the deeper part below Z1.3, we fix the P- and S-wave velocities and the thickness of each layer with the values of the inverted velocity structure at OGFO as shown in Figure 3.23a.

In Case-2 as a parametric study for the deeper part, we set the S-wave velocities starting from the values of the inverted velocity structure and then bring them closer to those of the borehole data every 25% as in Case-1. For the shallower part, we fix parameters with the values of the inverted velocity structure at OGFO again as shown in Figure 3.23b.

Figure 3.23 summarizes the results of our Case-1 and Case-2 sensitivity analyses. eHVSR from the inverted velocity structure (0%) reproduces the targeted pHVSR quite well, while eHVSRs from the other models (25 to 100%) become much different from the target pHVSR. The closer to the borehole data (towards 100%), the worse the matching between the theoretical eHVSR and the target pHVSR in both Case-1 and Case-2. We observe that the S-wave velocity in the top 20 m primarily controls the amplitude of eHVSR within 1 - 3 Hz, while those below Z1.3 primarily controls the amplitude from 0.2 to 2 Hz, considering the frequency range of influence from the quarter-wavelength theory. The sensitivity analysis indicates that the inverted velocity structure is well constrained by the target pHVSR and the strong velocity gradient in the deeper part of the basin required to better predict fundamental peak amplitude is real as long as the observed eHVSR and pHVSR provide us reliable information of the basin response.

Next, we use the geological boundary depth determined by the gravity anomaly (Vallon, 1999) to check the reliability of the velocity structures estimated in this paper. In Figure 3.17 we already checked the relationship between Z1.3 and the geological boundary depth by Vallon (1999) and found that both correspond well to each other at the five sites in Step-1. In order to check the validity of the inverted velocity structures in Step-2, we compare Z1.3 of the inverted velocity structure and the geological boundary depth estimated by Vallon (1999) at each G-series site. We refer to the original Vallon's data of the geological boundary at 250 m by 250 m grid points. For comparison, we calculate the inverse-distance weighted average of the geological boundary depth from the nearest four grid points of Vallon (1999) for G-series sites in addition to the maximum and minimum depths among those nearest four points. Table 3.4 reports the comparison of Z1.3 from the inverted velocity structure with the averaged geological boundary depth. Figure 3.24 shows a cross-section diagram of these sediment basin depths from G02 to G08; the location of each site can be found in Figure 3.20. In Table 3.4 we can see that our estimated Z1.3 depths at five sites are within the minimum and maximum depths of Vallon's (1999) geological boundary depth and at three other sites they are very close to the maximum depths.

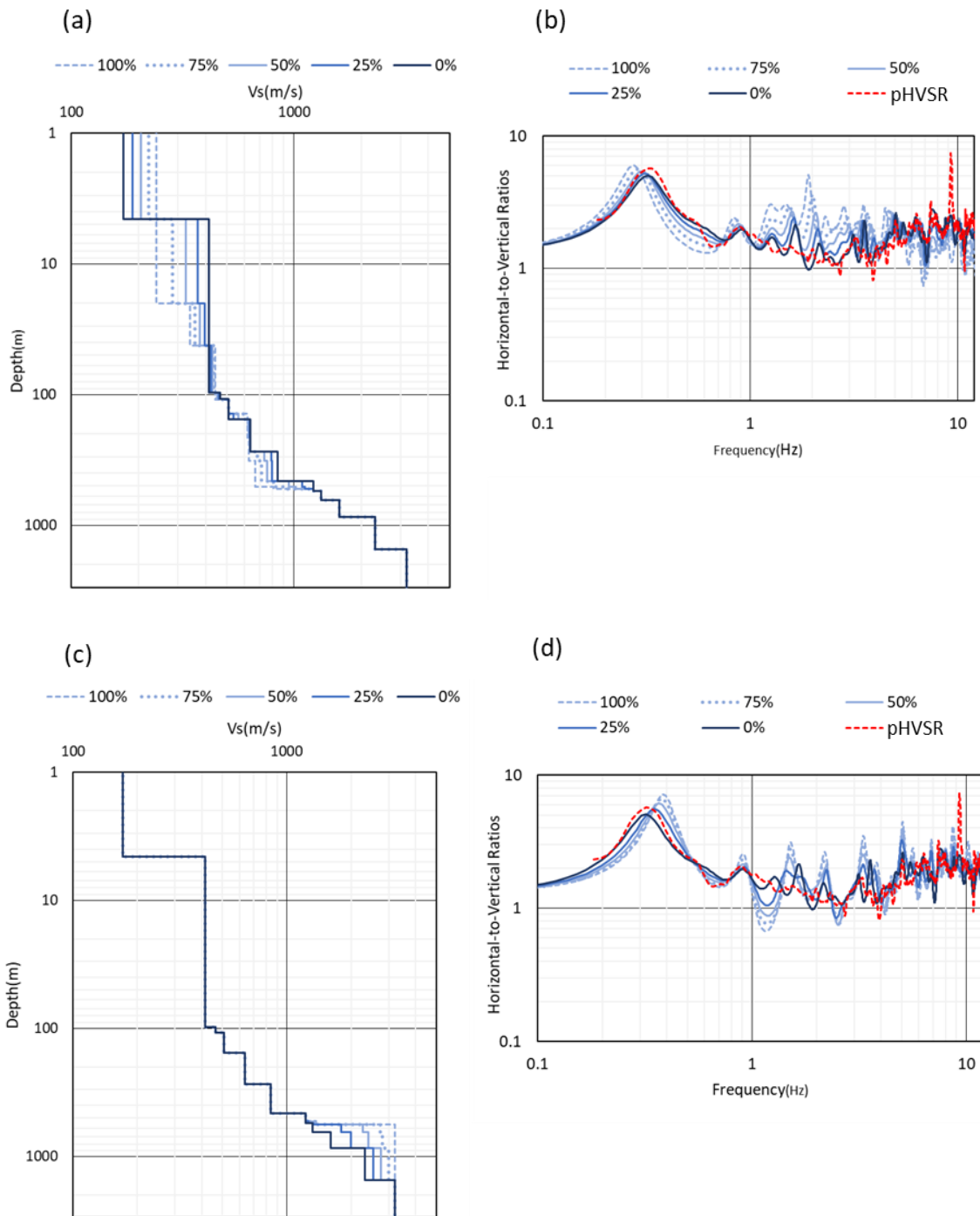


Figure 3.23. Results of the sensitivity analyses in Case-1 for the shallower part and Case-2 for the deeper part. Panels (a) and (c) show each velocity structure model, whereas panels (b) and (d) show the comparison of the theoretical eHVSR obtained from each velocity structure model shown in (a) and (c). Red dotted lines in (b) and (d) correspond to the observed pHVSRs.

Table 3.4. Comparison of Z1.3s from the inverted velocity structures at all the G-series sites with the inverse-distance weighting averages of the nearest four grid points and the maximum and minimum depths from the depth information at 250 m grid by Vallon (1999).

Site name	Estimated Z1.3 (m)	Maximum depth (m)	Average depth (m)	Minimum depth (m)	Ratio of Z1.3/Average
G02	328	181	144	92	2.28
G03	418	407	347	288	1.20
G04	546	541	488	425	1.12
G05	493	577	544	475	0.91
G06	458	475	382	254	1.20
G07	276	487	372	265	0.74
G08	108	254	163	81	0.66
G12	247	455	428	374	0.58
G13	234	378	270	79	0.87
G14	236	659	571	527	0.41
G15	407	779	712	608	0.57
G18	710	1063	992	926	0.72
G19	195	192	115	62	1.70
G20	647	819	811	799	0.80

At the rest of the sites, they are not within the variation between the maximum and minimum depths among the nearest sites. However, when we calculate the ratio between Z1.3 and the inverse-distance weighted average depth (Table 3.4), the average ratio amongst the 14 sites is 1.0. Therefore, we successfully obtain reasonable sediment depths of the Grenoble Basin by the proposed method, as a first attempt toward the final goal to delineate the whole basin structure.

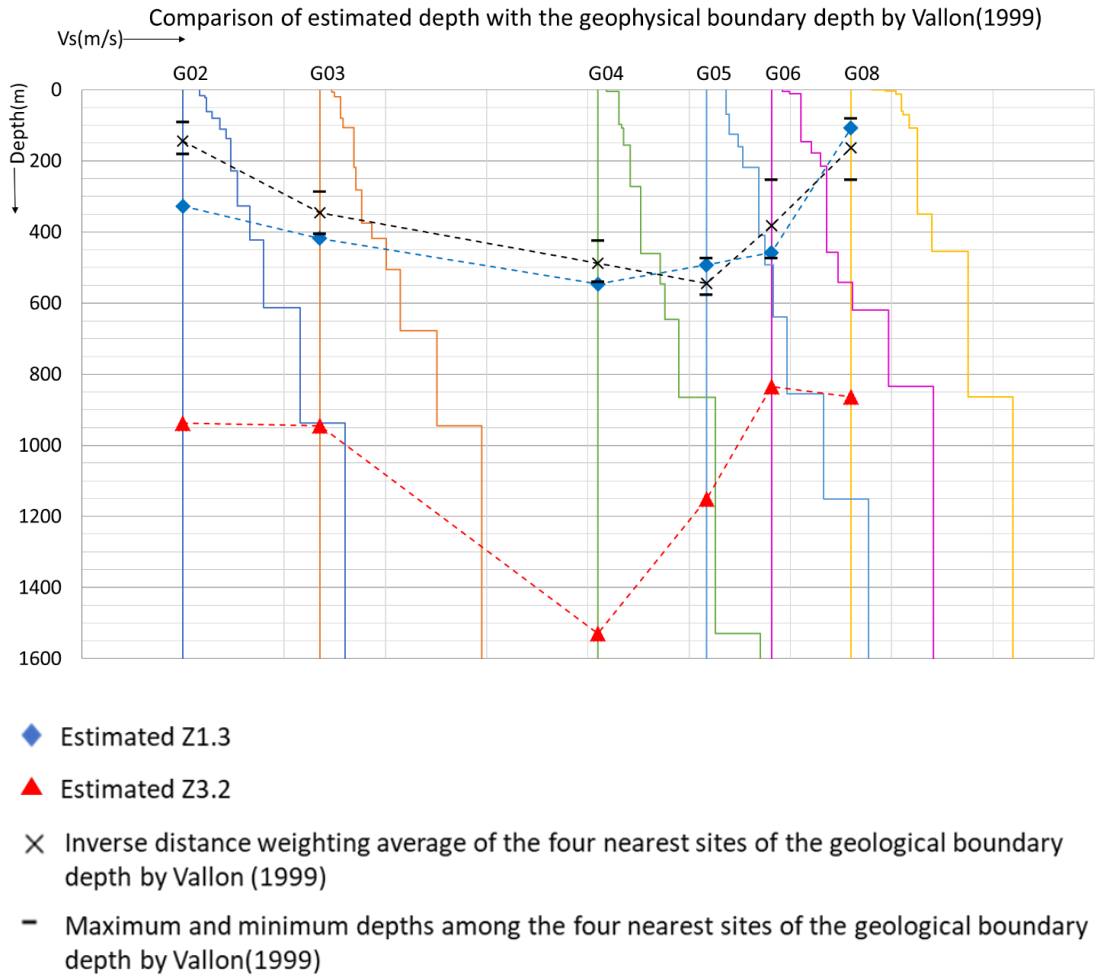


Figure 3.24. Inverted velocity structures (thin solid lines) along the cross-section from G02 to G08 with Z1.3, Z3.2, and the geological boundary depth by Vallon (1999) plotted at the corresponding depth below each site.

Gueguen et al. (2007) compared the theoretical basin depth calculated based on the one-quarter wavelength theory by using the peak frequency of mHVSR with the geological depth by Vallon (1999), as shown in Figure 3.11 of their paper. The significant difference in the basin depth between these two studies occurred near the edge of the basin compared to the center part in the basin. Gueguen et al. (2007) noted that this was probably because of the effect of the 2D/3D valley shape on the peak frequency of mHVSR. Cornou et al. (2008, 2009) also reported that observed and synthetic mHVSRs showed significant differences near the edge of the basin. Figure 3.25 shows the relationship between Z1.3 from the inverted velocity structures and the geological boundary depths by Vallon (1999) at fourteen G-Series sites, together with the ranges of deviation in both axes. Nine sites show good matching to each other. Among the remaining five sites, G02, G12, G14, and G15 are near the edge of the basin (see Figure 3.20). Because our Z1.3 comes from the inversion result using pHVSR under the assumption of 1D soil amplification, we can say that the reason for the difference at these sites could be 2D/3D effects of the valley shape, as Gueguen et al. (2007) inferred, or reliability of Vallon's gravimetric data inversion near the edge of the

basin due to lack of measurement points (Figure 3). We also infer that reliability in the Vallon's gravimetric data would be low if the site is close to the border of the gravity measurement, such as G18 where only a few observed gravity data constrained the depth. Near the edge of the basin, we would need to use 2D/3D representation of the site responses based on the DFC proposed by Matsushima et al. (2014, 2017).

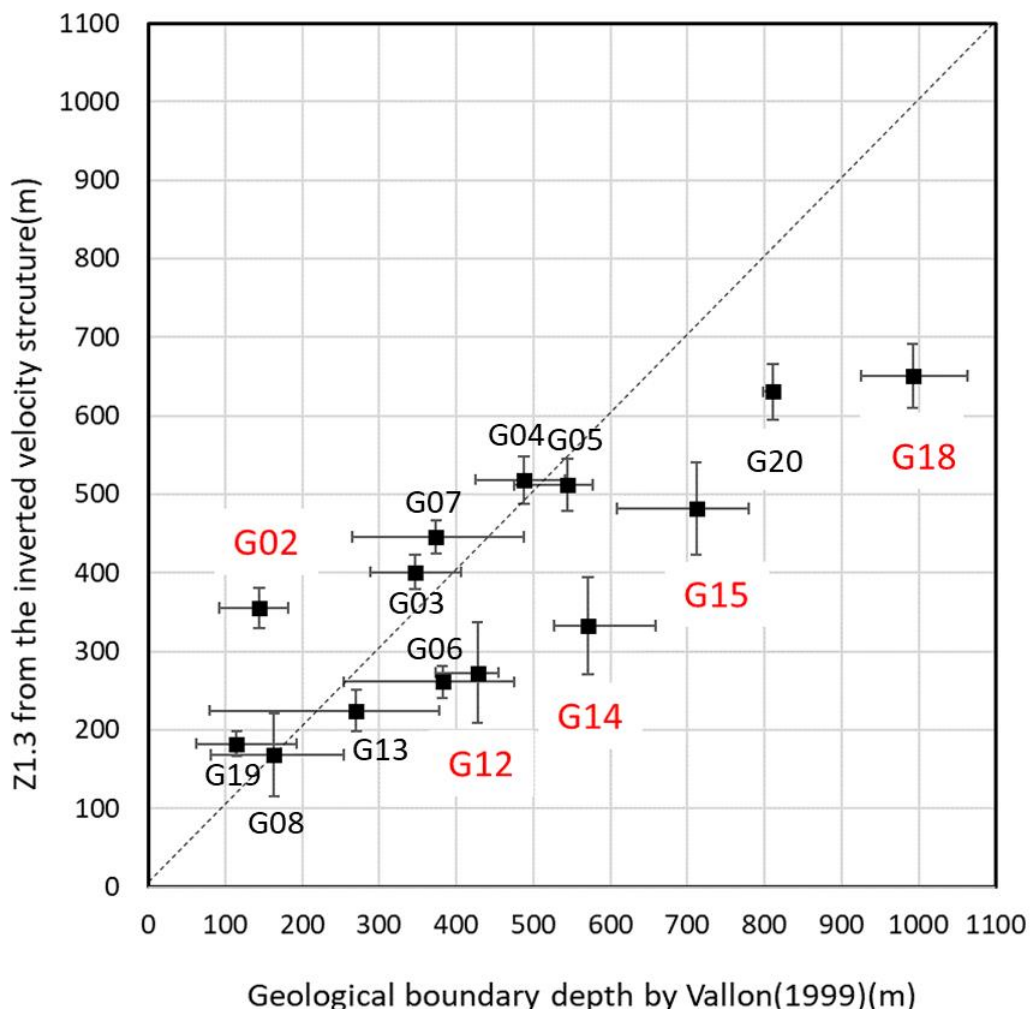


Figure 3.25. Relationship between Z1.3 from the inverted velocity structure and the geological boundary depth by Vallon (1999) at fourteen G-series sites. The square shows Z1.3 from the best-fit model. The bar in the vertical direction shows the average $\pm 1\sigma$ in Z1.3 among ten trials of the inversion and the bar in the horizontal direction shows the error in the geological boundary depth by Vallon (1999) among four nearest sites. The site names in red are those with larger deviation from the 1:1 correlation line.

Some limitations exist in this study. The method proposed in this paper is not applicable to a region where there is no observed earthquake data at all because we first need to compare the pHVSR using EMR for the region with observed eHVSR to check the validity of EMR. We show here that we may need at least a few observed earthquake sites to construct the region-specific EMR. If we do not have earthquake data at all, one can use the Japanese EMR if the region is a tectonically active area or use EMR_G if the region is tectonically similar to the Grenoble area. After more region-specific EMRs are accumulated elsewhere, a data bank of region-specific EMRs would then be available to choose an appropriate EMR based on the tectonic settings of the target region without available region-specific earthquake data.

Another major limitation is that we cannot get the pHVSR similar to the real eHVSR if the microtremor data is contaminated by strong local noise. When we observe microtremors, we need to be careful about placing the sensors and considering their surroundings and local situations because they may make a difference in the amplitude of mHVSR as shown in Guillier et al. (2007) and Molnar et al. (2018). We should also check the stability of mHVSR on the measurement during different times of the day because anthropic noise at high frequency is much higher during the daytime and the weekdays, and so the probability of strong local noise contamination is higher. One important note for the quality check of the observed microtremors is that the microtremor data are not reliable if the peak frequency and amplitude in mHVSR are not close to those of eHVSR. As we have shown for 100 sites in Japan (Kawase, Mori, et al., 2018), the Japanese EMRs in the normalized frequency with respect to the peak frequency of mHVSR are almost always 1 no matter what the peak frequency of mHVSR is.

Because pHVSR originally comes from mHVSR, it may not be as good as eHVSR in restricting the deeper part of the velocity structures in the inversion process. Therefore, our solution in this paper was to introduce several layers in the deeper part of the reference model for the inversion with the averaged characteristics of the inverted structures in the first step, where we reliably determine the velocity structures down to the seismological bedrock from the observed eHVSRs. This is the advantage of having earthquake data even though the number of sites is not large.

The velocity structure obtained from the inversion method may not perfectly reflect the real one, or sometimes may delineate fictitious layers that are not realistic. However, for earthquake disaster reduction due to severe ground shaking as our final goal of the research, the most important thing is to predict the correct site amplification characteristics of S-wave, not a detailed velocity structure itself. In this sense, it is advantageous to use pHVSR, which is very similar to the observed eHVSR, and hence useful to empirically estimate S-wave site amplification factors directly by correcting the vertical amplification functions as shown in Kawase, Nagashima, et al. (2018).

An empirical method for S-wave site amplification factors is especially applicable to the case of a 2D/3D basin like the Grenoble Basin. The presented velocity structures inside the Grenoble Basin are all equivalent 1D structures in which any 2D/3D effects included in the target will be mapped onto these velocity structures as errors. However, we found that the eHVSR from the S-wave portion and the eHVSR from the coda part are remarkably similar to each other inside several soft sedimentary basins in Japan (e.g., Satoh et al., 2001; Kawase, Mori, et al., 2018; Ito et al., 2020). For mHVSR Bonnefoy-Claudet et al. (2006) reported that synthetic mHVSRs in 1D

layered structures show remarkable similarities to each other no matter what is the assumed wavefield of microtremors. If that would be the case for the Grenoble Basin, the delineated 1D structure here at a site would basically reflect the average 1D structure around the site, except for sites very close to the basin edge. The delineation of such equivalent 1D structures from eHVSR or pHVSR will fail when the so-called 2D/3D resonance occurs (Bard and Bouchon, 1985) because we would see only a modal movement of the whole 2D or 3D medium confined by the basin interface and therefore we would see only one common peak frequency all over the basin surface. 2D/3D resonance may occur if the basin is narrow and deep and has a high impedance contrast at the basin interface. Actually, Hobiger (2005) reported the possible 2D resonance phenomena with both observational and theoretical pieces of evidence across a narrow outlet of the Isere River (the Isere Valley) in the northwestern part of the Grenoble Basin, close to G18. However, the majority of the sites inside the Grenoble Basin would not be under the 2D/3D resonance because we have a very consistent spatial correlation of the fundamental peak period with the geological basin depth (Figure 3.3).

As is the case for the delineation of an equivalent 1D structure for a site with 2D/3D effects, similar averaging effects should be expected for the case of a layer with a velocity inversion (i.e., a thin, softer layer inside a thick, stiffer layer or a thin, stiffer layer inside a thick, softer layer). In our current configuration, we do not allow such a velocity inversion (as a matter of choice, not an inherent restriction) and so we obtain a gradually-increasing velocity structure. We choose as such because we occasionally could have a structure with a small and/or thin velocity fluctuation within a thick layer as an artifact due to the poor resolving power of the target. The effect of such a small and/or thin velocity fluctuation on the eHVSR or pHVSR would be quite small so that we need careful scrutiny on the reality of such a delineated velocity inversion. Even if the effects of such a velocity inversion are included in the observed eHVSR or pHVSR, the S-wave site amplification factors can be calculated from them empirically as proposed by Kawase, Nagashima, et al. (2018) and Ito et al. (2020).

3.11 Conclusions and Future Perspectives

We calculate the EMR for the Grenoble Basin (EMR_G) by assuming that the shape of EMR_G should follow the general shapes of Japanese EMRs. We expect to have differences only in the amplitudes, which would be corrected with a modification factor α . By using a two-step grid search for α from 0.1-0.5, we find the optimal α to be 0.28. We find that pHVSRs with α of 0.28 at the five sites in the Grenoble Basin are better matched to observed eHVSRs compared to mHVSRs as well as pHVSRs from the Japanese EMR.

In order to check the validity of pHVSR as a substitute for the observed eHVSR, we inverted velocity structures by the method proposed by Nagashima et al. (2014) for pHVSRs, mHVSRs, and the observed eHVSRs at five sites in the Grenoble Basin using a reference model based on the borehole data at OGFO, which we call the “original reference model”. We find that the velocity structures from the observed eHVSRs were closer to those from pHVSRs than those from mHVSRs.

Then we make an averaged deeper velocity structure from the results of the inversion at five sites in order to constrain velocities in the deeper part for the whole basin inversions. We constructed a new reference model for each site based on the averaged deeper velocity structure and the shallower part of the original reference model in a proportional manner to the depth of the layer with the S-wave velocity of 1.3 km/s (Z1.3). We found that Z1.3 corresponds to the geological boundary depth from the gravity analysis. We use Z1.3 and Z3.2, which are the depths where the S-wave velocities exceed 1.3 and 3.2 km/s, respectively, together with the fundamental peak period T_p , as key parameters to construct a site-specific reference model. We confirm that the inverted velocity structures using the new site-specific reference models are almost identical to those using the original reference model at five sites.

We obtain a clear velocity gradient near the geological boundary defined by the gravity anomaly (Vallon, 1999) and borehole data, which is the most important finding in this study. To show the reality of the velocity gradient and that the inverted velocity structure is well constrained by the targeted pHVSR, we perform a sensitivity analysis for OGFO. We compare the theoretical eHVSR of the velocity structure inverted from pHVSR with that of the borehole data. We check their deviation by varying the model gradually closer to the borehole data. When either the shallower or deeper velocity structure is varied, we find that the closer the model becomes to the borehole data, the worse the matching to the observed eHVSR. This indicates that the velocity gradient near the geological boundary would be real and the inverted velocity structure is well constrained by the target pHVSR. Still, we need further validation of this delineated velocity gradient using the three-dimensional basin response simulation as Chaljub et al. (2009, 2010) performed calculations of the 3D basin synthetics using no-gradient models in the bedrock layer.

Aiming for delineating the whole basin structure in the Grenoble Basin, we calculate pHVSR using EMRG for inversion of the velocity structures at fourteen G-series sites, using a new reference model specific for each site. This means that the new reference models based on the empirical relationship between Z1.3 and T_p are applicable for the inversion at the sites where the observed eHVSRs are not available. Then we compare Z1.3 and the geological boundary depth proposed by Vallon (1999) at each site. The obtained Z1.3s by the proposed method at eight of fourteen sites are closer to those by Vallon (1999). The results at the rest of the sites did not directly match those by Vallon (1999). However, the average ratio between Z1.3 and the geological boundary depth for all the G-series sites is unity, suggesting the overall similarity between them. Therefore, we can safely say that as the first attempt toward the final goal to delineate the whole basin structure, we successfully get an overall picture of the Grenoble Basin from observed microtremors.

For future tasks, we will apply this method to ST-series sites, which are other microtremor recording sites. After getting the velocity structures at ST-series sites, we plan to construct a model of the whole basin structure by interpolating the inverted basin structures at all OG-series, G-series, and ST-series. Then, we will check the validity of the whole basin model by comparing the synthetic eHVSRs obtained by inputting the bedrock ground motion to the bottom of the constructed model with the observed eHVSRs at the strong ground motion observation sites. The effects of 2D/3D amplification in the horizontal and vertical components can be considered by Finite Difference or Spectral Element methods as in Chaljub et al. (2009, 2010).

We also need to check for any discrepancies between the delineated shallow structures determined in this paper at three common sites of Hollender et al. (2018). A preliminary analysis shows mixed results so that we need careful analyses on what would be the source of discrepancy. We would like to perform a full-scale investigation to obtain good simultaneous matching to both eHVSR and the phase velocity from the array microtremor measurements in the near future.

Data and Resources

The Grenoble RAP Network is operated by RESIF - Réseau Sismologique et géodésique Français, Seismic Network (doi:10.15778/RESIF.RA, <http://data.datacite.org/10.15778/RESIF.RA>, last accessed March, 23, 2020). These Grenoble permanent network data were downloaded through ESM Engineering Strong Motion Database (https://esm.mi.ingv.it/DYNAsstage/CadmoDriver?_action_do=1&_page=ACC_redirect_home_page&_rock=INVALID&_state=initial&_tabber=0&_token=NULLNULLNULLNULL, last accessed June, 3, 2020).

In the Appendix, all the digital values of the underground profiles obtained from the inversion at all the OG-series sites in Step-1 and G-series sites in Step-2 are shown in Table A3.1 to A3.3. The average and standard deviation of the eHVSRs from the observed earthquakes at OG-series sites are shown in Figure A3.1. The inversion results at four OG-series sites in Step-1 are shown in Figures A3.2 to A3.5. An example of the application of the scheme to construct the new reference model is shown in Figure A3.6. The inversion results at ten G-series sites in Step-2 are shown in Figures A3.7 to A3.11.

Acknowledgments

We would like to express our gratitude for the discussions and suggestions from Drs. Pierre-Yves Bard and Emmanuel Chaljub of UGA and Alan Yong of USGS. We also appreciate Dr. Fabrice Hollender of CEA for sending us his research material. The incredible efforts to improve the readability of the manuscript by Prof. Sheri Molnar of Western University far beyond the responsibility of the associate editor in charge are highly appreciated. This study was also partially supported by the Core-to-Core Collaborative research program of the Earthquake Research Institute, The University of Tokyo and the Disaster Prevention Research Institute, Kyoto University (ID number:2019-K-02).

References

- Aoi S., K. Obara, S. Hori, K. Kasahara, and Y Okada (2000). New strong-motion observation network: KiK-net. Eos Transactions, AGU 81: 329.
- Bard, P.-Y. and Bouchon, M. (1985). The two-dimensional resonance of sediment-filled valleys,

Bull. Seismol. Soc. Am. 75, 519–541.

Bard, P.-Y. and SESAME Participants (2004), The SESAME project: an overview and main results, In Proc. 13th World Conf. Earth. Engng., Vancouver, August 2004, Paper # 2207.

Bonnefoy-Claudet, S., C. Cornou, P.-Y. Bard, F. Cotton, P. Moczo, J. Kristek, and D. Fäh (2006). H/V ratio: a tool for site effects evaluation. Results from 1-D noise simulations, Geophysics Journal Int., 167, 827–837, doi: 10.1111/j.1365-246X.2006.03154.X

Chaljub, E., C. Cornou, and P.-Y. Bard (2009). Numerical benchmark of 3D ground motion simulation in the valley of Grenoble, French Alps, in ESG 2006, Third Intl. Symposium on the Effects of Surface Geology on Seismic Motion, P.-Y. Bard, E. Chaljub, C. Cornou, F. Cotton, and P. Guéguen (Editors), LCPC Editions, ISSN 1628-4704, Vol. 2, 1365–1375.

Chaljub, E., P. Moczo, S. Tsuno, P.-Y. Bard, J. Kristek, M. Käser, M. Stupazzini, and M. Kristeková (2010). Quantitative comparison of four numerical predictions of 3D ground motion in the Grenoble valley, France, Bull. Seismol. Soc. Am. 100, no. 4, 1427–1455.

Cornou, C. (2002). Traitement d'antenne et imagerie sismique dans l'agglomération grenobloise (Alpes Françaises): Implications pour les effets de site, Ph.D. Thesis, (260 p.p.), Joseph Fourier University, Grenoble (in French).

Cornou, C., P.-Y. Bard, and M. Dietrich (2003a). Contribution of dense array analysis to the identification and quantification of basin-edge induced waves, part I: Methodology, Bull. Seismol. Soc. Am. 93, 2604–2623.

Cornou, C., P.-Y. Bard, and M. Dietrich (2003b). Contribution of dense array analysis to the identification and quantification of basin-edge-induced waves, part II: Application to Grenoble basin (French Alps), Bull. Seismol. Soc. Am. 93, 2624–2648.

Cornou, C., J. Kristek, M. Ohrnberger, G. Di Giulio, E. Schissele, B. Guillier, S. Boonefoy-Claudet, M. Wathelet, D. Faeh, P.-Y. Bard, and P. Moczo, (2004). Simulation of seismic ambient vibrations – II H/V and array techniques for real sites, in Proc. 13th World Conf. Earth. Eng., Vancouver, Canada, August 2004, paper #1130.

Cornou, C., E. Chaljub, and S. Tsuno (2008) Real and synthetic ambient noise recordings in the Grenoble Basin: Reliability of the 3D numerical model, in Proc. 14th World Conf. Earth. Eng., Beijing, China, October 12-17, 2008, paper #P031.

Cornou, C., E. Chaljub, J. Verbeke, J. Converset, C. Voisin, L. Stehly, L. Margerin, S. Tsuno, J.-R. Grasso, P. Guéguen, S. Roussel, P. Roux, S. Hatton, and M. Campillo (2009). Measurement and variability study of site effects in the 3D glacial valley of Grenoble, French Alps, in ESG 2006, Third Intl. Symposium on the Effects of Surface Geology on Seismic Motion, P.-Y. Bard, E. Chaljub, C. Cornou, F. Cotton, and P. Guéguen (Editors), LCPC Editions, ISSN 1628-4704, Vol. 2, 1621–1627.

Dietrich, M., C. Cornou, G. Ménard, F. Lemeille, F. Guyoton, and R. Guiguet (2009). Seismic profiling and borehole measurements in the Isère Valley near Grenoble, France: 1-Data acquisition and processing, in ESG 2006, Third Intl. Symposium on the Effects of Surface Geology on Seismic Motion, P.-Y. Bard, E. Chaljub, C. Cornou, F. Cotton, and P. Guéguen

(Editors), LCPC Editions, ISSN 1628-4704, Vol. 2, p. 1597–1608.

Fukihara K., S. Matsushima, and H. Kawase (2015). Identification of the velocity structure model of Kyoto Basin for strong motion prediction using observed earthquake and microtremor motions, *J. of JAEE*, 15(6): 60-76. (in Japanese with English abstract).

García-Jerez, A., F. Luzón, F.J. Sánchez-Sesma, E. Lunedei, D. Albarello, M.A. Santoyo, and J. Almendros (2013). Diffuse elastic wavefield within a simple crustal model. Some consequences for low and high frequencies, *J. Geophys. Res. Solid Earth*, 118, 5577–5595, doi:10.1002/2013JB010107, 2013.

García-Jerez, A., H. Seivane, F. Luzón, M. Navarro, L. Molina, C. Aranda, J. Piña-Flores, F. Navarro, F. Sánchez-Martos, F. Vidal, A.M. Posadas, F. J. Sánchez-Sesma (2017). 3D model of Campo de Dalías basement from H/V spectral ratio of ambient seismic noise ,19th EGU General Assembly, EGU2017, proceedings from the conference, Vienna, Austria., p.12160.

Gueguen, P., C. Cornou, S. Garambois, and J. Banton (2007). On the Limitation of the H/V Spectral Ratio Using Seismic Noise as an Exploration Tool: Application to the Grenoble Valley (France), a Small Apex Ratio Basin, *Pure and Appl. Geophys.*, 164, 115–134, doi: 10.1007/s00024-006-0151-x

Guillier. B., J. L. Chatelain, S. Bonnefoy-Claudet, and E. Haghshenas (2007). Use of Ambient Noise: From Spectral Amplitude Variability to H/V Stability, *Journal of Earthquake Eng.*, 11:1–18.

Hobiger, M. (2005). Caractérisation expérimentale et numérique des résonances globales de la vallée grenobloise, rapport de stage M1 Physique, Université Joseph Fourier, Grenoble, France, 78 pp (in French).

Hollender, F., C. Cornou, A. Dechamp, K. Oghalaei, F. Renalier, E. Maufroy, C. Burnouf, S. Thomassin, M. Wathélet, P.-Y. Bard, V. Boutin, C. Desbordes, I. Douste-Bacqué, L. Foundotos, C. Guyonnet-Benaize, V. Perron, J. Régnier, A. Rouillé, M. Langlais, and D. Sicilia (2018). Characterization of site conditions (soil class, VS30, velocity profiles) for 33 stations from the French permanent accelerometric network (RAP) using surface-wave methods, *Bull Earthquake Eng.*, 16, 2337–2365, doi:10.1007/s10518-017-0135-5.

Ito, E., K. Nakano, F. Nagashima, and H. Kawase (2020). A Method to Directly Estimate S-Wave Site Amplification Factor from Horizontal-to-Vertical Spectral Ratio of Earthquakes (eHVSRs), *Bull. Seismol. Soc. Am.* (Online only at present), 1–20, doi: 10.1785/0120190315.

Kawase, H (2003) Site effects on strong ground motions, in International Handbook of Earthquake and Engineering Seismology, (edited by W. H. K. Lee, Kanamori, H., Jennings, P. C. and Kisslinger, C.), Chapter 61, Academic Press, pp. 1013-1030.

Kawase H., F. J. Sánchez-Sesma, and S. Matsushima (2011). The optimal use of horizontal-to-vertical spectral ratios of earthquake motions for velocity inversions based on diffuse-field theory for plane waves, *Bull. Seism. Soc. Am.* 101, 2011-2014.

Kawase, H., Y. Mori, and F. Nagashima, (2018). Difference of horizontal-to-vertical spectral

ratios of observed earthquakes and microtremors and its application to S-wave velocity inversion based on the diffuse field concept, *Earth, Planets, and Space* 70, 1, doi:10.1186/s40623-017-0766-4.

Kawase, H., F. Nagashima, K. Nakano, and Y. Mori (2018). Direct evaluation of S-wave amplification factors from microtremor H/V ratios: Double empirical corrections to “Nakamura” method, *Soil Dyn. Earthquake Eng.*, Open Access, doi: 10.1016/j.soildyn.2018.01.049

Kramer, S.L. (1996). *Geotechnical Earthquake Engineering*, Chapter 7, Prentice-Hall International Series in Civil Engineering and Engineering Mechanics, Prentice-Hall International (UK) Limited, London, pp.653, ISBN 0-13-374943-6.

Lebrun, B., D. Hatzfeld, and P. Y. Bard (2001). Site effect study in urban area: Experimental results in Grenoble (France), *Pure Appl. Geophys.*, 158, 2543–2557.

Matsushima, S., T. Hirokawa, F. De Martin, H. Kawase, and F.J. Sánchez-Sesma (2014). The effect of lateral heterogeneity on horizontal-to-vertical spectral ratio of microtremors inferred from observation and synthetics, *Bull. Seism. Soc. Am.*, Vol.104, 381-393, doi:10.1785/0120120321.

Matsushima, S., H. Kosaka, and H. Kawase (2017). Directionally dependent horizontal-to-vertical spectral ratios of microtremors at Onahama, Fukushima, Japan, *Earth, Planets, and Space*, 69:96, 2017, doi:10.1186/s40623-017-0680-9.

Molner, S., J. F. Cassidy, S. Castellaro, C. Cornou, H. Crow, J. A. Hunter, S. Matsushima, F.J. Sánchez-Sesma, and A. Yong (2018). Application of microtremor horizontal-to-vertical spectral ratio (mHVSР) analysis for site characterization: State of the art, *Surv. Geophys.* 39, 613–631, doi: 10.1007/s10712-018-9464-4.

Nagashima, F., S. Matsushima, H. Kawase, F. J. Sánchez-Sesma, T. Hayakawa, T. Satoh, and M. Oshima, (2014). Application of H/V Spectral Ratios of Earthquake Ground Motions to Identify Subsurface Structures at and around the K-NET Site in Tohoku, Japan, *Bull. Seismol. Soc. Am.* 104, 2288-2302, doi:10.1785/0120130219

Nagashima, F., H. Kawase, and S. Matsushima (2017). Estimation of horizontal seismic bedrock motion from vertical surface motion based on horizontal-to-vertical spectral ratios of earthquake motions, Proc 16th World Conf. Earth. Eng., Santiago Chile, January 9 -13, 2017, Paper N°3685.

Sánchez-Sesma F.J., M. Rodríguez, U. Iturrarán-Viveros, F. Luzón, M. Campillo, L. Margerin., A. García-Jerez, M. Suárez, M.A.Santoyo, and A. Rodríguez-Castellanos (2011). A theory for microtremor H/V spectral ratio: Application for a layered medium, *Geophys. J. Int. Exp. Lett.*, 186: 221-225, doi: 10.1111/j.1365-246X.2011.05064.x.

Satoh, T., H. Kawase, and S. Matsushima (2001). Differences between site characteristics obtained from microtremors, S-waves, P-waves, and cudas, *Bull. Seism. Soc. Am.*, Vol.91, No.2, 313–334.

Stupazzini, M., R. Paolucci, and H. Igel (2009). Near-fault earthquake ground motion simulation

in the Grenoble Valley by a high-performance spectral element code, Bull. Seismol. Soc. Am. 99, 286–301.

Traversa P., E. Maufroy, F. Hollender, V. Perron, V. Bremaud, H. Shible, S. Drouet, P. Guéguen, M. Langlais, D. Wolyniec, C. Péquegnat, and I. Douste-Bacque. (2020). RESIF RAP and RLBP dataset of earthquake ground motion in mainland France, Seismol. Res. Lett. XX, 1–16, doi: 10.1785/02201903

Vallon, M. (1999). Estimation de l'épaisseur d'alluvions quaternaires dans la cuvette grenobloise par inversion des anomalies gravimétriques, IPSN/CNRS Report, 33 pages (in French).

Appendix

Tables

Table A3.1

Underground profiles at OG-series sites obtained by the inversion using observed eHVSR (Step-1).

OGDH

Layer No.	Thickness(m)	Depth(m)	Vp(m/s)	Vs(m/s)	Density (10^3 kg/m^3)
1	19.2	19.2	250	1002	1.74
2	6	25.2	274	1018	1.75
3	11.5	36.7	427	1237	1.84
4	19.3	56	461	1529	1.85
5	37.7	93.7	548	1846	1.9
6	461.7	555.4	678	2726	1.95
7	115.3	670.7	1183	3107	2.13
8	213	883.7	1612	4493	2.25
9	1417.9	2301.6	2323	5404	2.42
10	0	2301.6	3200	5637	2.6

OGFO

Layer No.	Thickness(m)	Depth(m)	Vp(m/s)	Vs(m/s)	Density (10^3 kg/m^3)
1	6.6	6.6	246	840	1.73
2	12.3	18.9	438	1370	1.84
3	113.3	132.2	607	1660	1.92
4	109.2	241.5	688	1718	1.96
5	80.5	322	815	2129	2
6	186	508	1025	2538	2.08
7	157.4	665.4	1220	2969	2.14
8	269.9	935.4	1570	3417	2.24
9	310.1	1245.4	2341	4434	2.43
10	0	1245.4	3200	5637	2.6

OGPC

Layer No.	Thickness(m)	Depth(m)	Vp(m/s)	Vs(m/s)	Density (10^3 kg/m^3)
1	0.2	0.2	108	445	1.62
2	12.3	12.5	506	1259	1.88
3	6.7	19.2	804	1730	2
4	13.8	32.9	891	1730	2.03
5	125.9	158.8	1219	2160	2.14
6	141.9	300.7	1219	2503	2.14
7	246.2	547	1336	3104	2.17
8	220.1	767.1	1610	3880	2.25
9	201.8	968.9	2421	4753	2.44
10	0	968.9	3200	5637	2.6

OGPS

Layer No.	Thickness(m)	Depth(m)	Vp(m/s)	Vs(m/s)	Density (10^3 kg/m^3)
1	0.2	0.2	146	490	1.66
2	54.4	54.6	680	1446	1.95
3	128.6	183.2	725	1560	1.97
4	45.3	228.5	805	2006	2
5	111.4	339.9	925	2198	2.04
6	67.8	407.6	1085	2409	2.1
7	73.3	480.9	1314	3096	2.17
8	78.7	559.6	1600	3665	2.25
9	274.1	833.7	2212	4692	2.4
10	0	833.7	3200	5637	2.6

OGCU

Layer No.	Thickness(m)	Depth(m)	Vp(m/s)	Vs(m/s)	Density (10^3 kg/m^3)
1	25.9	25.9	349	1478	1.8
2	29.5	55.5	468	1610	1.86
3	100.2	155.7	677	1823	1.95
4	23.1	178.8	722	1823	1.97
5	144.1	323	868	2487	2.02
6	292.9	615.8	1066	3032	2.09
7	140.8	756.6	1294	3185	2.16
8	139.7	896.3	1612	3846	2.25
9	641.2	1537.6	2302	4548	2.42
10	0	1537.6	3200	5564	2.6

Table A3.2
Underground profiles at OG-series sites obtained by the inversion using pHVSR (Step-1).

OGDH

Layer No.	Thickness(m)	Depth(m)	Vp(m/s)	Vs(m/s)	Density (10^3 kg/m^3)
1	17.7	17.7	200	956	1.7
2	4.7	22.4	304	1205	1.77
3	9.5	31.9	388	1234	1.82
4	26.2	58	581	1929	1.91
5	31.6	89.6	597	2130	1.92
6	411.1	500.7	661	3117	1.94
7	178.6	679.2	988	3635	2.07
8	320.7	999.9	1531	4084	2.23
9	2519.1	3518.9	2247	4724	2.4
10	0	3518.9	3200	5637	2.6

OGFO

Layer No.	Thickness(m)	Depth(m)	Vp(m/s)	Vs(m/s)	Density (10^3 kg/m^3)
1	4.7	4.7	236	679	1.73
2	4.3	9	414	978	1.83
3	129.1	138	603	1851	1.92
4	34.6	172.6	699	2166	1.96
5	67.7	240.3	883	2568	2.03
6	254.2	494.5	883	2983	2.03
7	156.1	650.7	1211	3278	2.14
8	162.8	813.5	1601	4170	2.25
9	453.8	1267.3	2405	5028	2.44
10	0	1267.3	3200	5637	2.6

OGPC

Layer No.	Thickness(m)	Depth(m)	Vp(m/s)	Vs(m/s)	Density (10^3 kg/m^3)
1	2.8	2.8	294	1044	1.76
2	19.3	22.1	639	1853	1.94
3	132	154.2	871	2047	2.03
4	40.5	194.7	994	2365	2.07
5	75.3	270	1103	2585	2.1
6	102.9	372.9	1239	2769	2.15
7	90.4	463.3	1338	3072	2.18
8	158.6	621.9	1599	3650	2.25
9	270.3	892.2	2177	4356	2.39
10	0	892.2	3200	5637	2.6

OGPS

Layer No.	Thickness(m)	Depth(m)	Vp(m/s)	Vs(m/s)	Density (10^3 kg/m^3)
1	0.6	0.6	112	351	1.62
2	1.4	2	273	541	1.75
3	83.6	85.6	613	1376	1.92
4	44.4	129.9	629	1814	1.93
5	70.5	200.4	630	2402	1.93
6	112	312.4	711	2890	1.96
7	184	496.4	1340	3880	2.18
8	32.6	529.1	1435	3962	2.2
9	1326.8	1855.8	2251	4852	2.41
10	0	1855.8	3200	5637	2.6

OGCU

Layer No.	Thickness(m)	Depth(m)	Vp(m/s)	Vs(m/s)	Density (10^3 kg/m^3)
1	59.2	59.2	337	1183	1.79
2	24.2	83.4	407	1822	1.83
3	68.4	151.8	524	1822	1.88
4	301.4	453.1	751	2348	1.98
5	117.6	570.7	1017	3124	2.08
6	195.8	766.5	1237	3381	2.15
7	126.5	893.1	1612	3381	2.25
8	712	1605	2359	4825	2.43
9	0	1605	3200	5564	2.6

Table A3.3

Underground profiles at G-series sites obtained by the inversion using pHVSR (Step-2).

G02

Layer No.	Thickness(m)	Depth(m)	Vp(m/s)	Vs(m/s)	Density (10^3 kg/m^3)
1	17.2	17.2	1126	329	1.78
2	5.1	22.3	1189	436	1.84
3	39.3	61.5	1351	461	1.86
4	19.6	81.1	1351	577	1.91
5	29.6	110.8	1647	733	1.97
6	25.6	136.3	1948	853	2.02
7	92.8	229.1	1979	944	2.05
8	98.5	327.6	2080	1077	2.1
9	94.9	422.5	2991	1319	2.17
10	190	612.5	3447	1598	2.25
11	325.8	938.3	4246	2316	2.42
12	0	938.3	5637	3200	2.6

G03

Layer No.	Thickness(m)	Depth(m)	Vp(m/s)	Vs(m/s)	Density (10^3 kg/m^3)
1	6.5	6.5	595	235	1.72
2	13.7	20.2	1040	295	1.76
3	60.6	80.8	1354	414	1.83
4	25.1	105.9	1354	459	1.85
5	111.8	217.7	1596	676	1.95
6	64.3	282	1837	716	1.97
7	93	375	2211	834	2.01
8	43.3	418.3	2457	1032	2.08
9	87.7	506	2955	1319	2.17
10	172.3	678.2	4061	1598	2.25
11	266.4	944.6	4318	2316	2.42
12	0	944.6	5637	3200	2.6

G04

Layer No.	Thickness(m)	Depth(m)	Vp(m/s)	Vs(m/s)	Density (10^3 kg/m^3)
1	4.6	4.6	653	171	1.68
2	33.9	38.5	1162	414	1.83
3	58.7	97.2	1184	416	1.83
4	11.1	108.2	1494	466	1.86
5	47	155.2	1631	507	1.88
6	117.3	272.5	1973	638	1.93
7	187.7	460.2	2251	841	2.01
8	86.1	546.3	2577	1225	2.14
9	99.6	645.8	3052	1319	2.17
10	219.5	865.3	3839	1598	2.25
11	664.4	1529.8	4393	2316	2.42
12	0	1529.8	5637	3200	2.6

G05

Layer No.	Thickness(m)	Depth(m)	Vp(m/s)	Vs(m/s)	Density (10^3 kg/m^3)
1	54.6	54.6	1151	393	1.82
2	14.5	69.1	1267	393	1.82
3	56.4	125.5	1314	455	1.85
4	34.4	159.9	1499	627	1.93
5	57.6	217.5	1512	713	1.97
6	20.5	238	1850	1031	2.08
7	171.5	409.4	1998	1031	2.08
8	83.5	492.9	2004	1157	2.12
9	145.7	638.6	2497	1319	2.17
10	215.9	854.5	3138	1598	2.25
11	296.4	1150.9	4356	2316	2.42
12	0	1150.9	5637	3200	2.6

G06

Layer No.	Thickness(m)	Depth(m)	Vp(m/s)	Vs(m/s)	Density (10^3 kg/m^3)
1	4.5	4.5	918	211	1.71
2	6.7	11.1	1275	356	1.8
3	134.6	145.7	1567	584	1.91
4	17	162.6	1743	786	1.99
5	15.4	178	1757	786	1.99
6	37.1	215.1	2384	971	2.06
7	243.2	458.2	2396	1092	2.1
8	28.4	486.6	2481	1319	2.17
9	54.7	541.3	2704	1319	2.17
10	78.9	620.2	3609	1598	2.25
11	213.8	834	4276	2316	2.42
12	0	834	5637	3200	2.6

G07

Layer No.	Thickness(m)	Depth(m)	Vp(m/s)	Vs(m/s)	Density (10^3 kg/m^3)
1	4.1	4.1	785	288	1.76
2	2.2	6.3	1080	471	1.86
3	53.3	59.6	1374	554	1.9
4	5.5	65.1	1436	671	1.95
5	72.4	137.5	2046	805	2
6	25.5	163	2067	861	2.02
7	55.6	218.6	2214	1017	2.08
8	57.5	276.1	2931	1181	2.13
9	57.6	333.7	3274	1319	2.17
10	79.4	413.1	3632	1598	2.25
11	169.8	582.9	4266	2316	2.42
12	0	582.9	5637	3200	2.6

G08

Layer No.	Thickness(m)	Depth(m)	Vp(m/s)	Vs(m/s)	Density (10^3 kg/m^3)
1	1.2	1.2	748	411	1.83
2	1.8	3	1307	680	1.95
3	8.6	11.5	1812	884	2.03
4	48.2	59.7	1812	1002	2.07
5	10.6	70.4	1849	1033	2.08
6	37.2	107.6	2328	1152	2.12
7	99.5	207.1	2383	1319	2.17
8	76.1	283.1	2602	1319	2.17
9	67.1	350.2	3003	1319	2.17
10	104.4	454.6	3094	1598	2.25
11	409	863.6	4011	2316	2.42
12	0	863.6	5637	3200	2.6

G12

Layer No.	Thickness(m)	Depth(m)	Vp(m/s)	Vs(m/s)	Density (10^3 kg/m^3)
1	2.6	2.6	913	343	1.79
2	9	11.6	1263	510	1.88
3	66.8	78.4	1263	510	1.88
4	7.5	85.9	1264	511	1.88
5	13.1	99	1662	620	1.93
6	23.8	122.8	1890	917	2.04
7	124	246.8	2637	1102	2.1
8	77.5	324.2	3154	1319	2.17
9	91.4	415.6	3348	1319	2.17
10	148.8	564.4	3894	1598	2.25
11	500	1064.4	4394	2316	2.42
12	0	1064.4	5637	3200	2.6

G13

Layer No.	Thickness(m)	Depth(m)	Vp(m/s)	Vs(m/s)	Density (10^3 kg/m^3)
1	1.4	1.4	581	328	1.78
2	1.5	2.9	1070	618	1.93
3	6.2	9	1123	648	1.94
4	62.7	71.7	1451	684	1.95
5	29.6	101.3	1451	684	1.95
6	2.4	103.7	1682	684	1.95
7	62.4	166.1	1993	684	1.95
8	67.9	234	3072	736	1.97
9	30	264	3072	1319	2.17
10	194.8	458.8	3466	1598	2.25
11	607.2	1066	4278	2316	2.42
12	0	1066	5637	3200	2.6

G14

Layer No.	Thickness(m)	Depth(m)	Vp(m/s)	Vs(m/s)	Density (10^3 kg/m^3)
1	3	3	773	446	1.85
2	0.9	4	1210	680	1.95
3	2.5	6.4	1247	687	1.96
4	53.5	59.9	1971	971	2.06
5	173.4	233.3	2078	1200	2.13
6	2.5	235.8	2078	1200	2.13
7	86.6	322.4	2504	1316	2.17
8	45.7	368	2714	1316	2.17
9	180	548	3242	1319	2.17
10	302.2	850.2	4024	1598	2.25
11	686.9	1537.1	4550	2316	2.42
12	0	1537.1	5637	3200	2.6

G15

Layer No.	Thickness(m)	Depth(m)	Vp(m/s)	Vs(m/s)	Density (10^3 kg/m^3)
1	4.6	4.6	562	181	1.68
2	12.7	17.3	1310	448	1.85
3	70	87.3	1310	480	1.86
4	77.4	164.7	1463	695	1.96
5	29.2	194	1840	794	2
6	74.3	268.3	1840	794	2
7	138.6	406.9	2079	1072	2.09
8	136.3	543.2	2693	1319	2.17
9	202.3	745.4	2995	1319	2.17
10	235.1	980.6	3466	1598	2.25
11	542.8	1523.4	4421	2316	2.42
12	0	1523.4	5637	3200	2.6

G18

Layer No.	Thickness(m)	Depth(m)	Vp(m/s)	Vs(m/s)	Density (10^3 kg/m^3)
1	6.1	6.1	530	240	1.73
2	1.4	7.5	941	541	1.89
3	102.1	109.6	1492	716	1.97
4	98	207.6	1859	743	1.98
5	12.4	220	2008	803	2
6	74.4	294.5	2566	841	2.01
7	184.1	478.6	2870	1059	2.09
8	231.4	709.9	3051	1092	2.1
9	181.8	891.7	3156	1319	2.17
10	206.1	1097.8	3770	1598	2.25
11	557.6	1655.4	4448	2316	2.42
12	0	1655.4	5637	3200	2.6

G19

Layer No.	Thickness(m)	Depth(m)	Vp(m/s)	Vs(m/s)	Density (10^3 kg/m^3)
1	1	1	797	453	1.85
2	0.1	1.1	821	453	1.85
3	2.2	3.3	1417	748	1.98
4	18.4	21.8	1521	748	1.98
5	2.6	24.4	1943	918	2.04
6	144.6	169	2173	1198	2.13
7	26.3	195.3	2232	1198	2.13
8	18.4	213.7	2564	1301	2.16
9	40.8	254.4	3207	1319	2.17
10	146.6	401	3790	1598	2.25
11	124.3	525.4	4097	2316	2.42
12	0	525.4	5637	3200	2.6

G20

Layer No.	Thickness(m)	Depth(m)	Vp(m/s)	Vs(m/s)	Density (10^3 kg/m^3)
1	7.3	7.3	531	256	1.74
2	2.7	9.9	707	372	1.81
3	110.8	120.7	1294	540	1.89
4	27.2	147.9	1537	540	1.89
5	34.3	182.2	1853	667	1.95
6	50.3	232.5	2297	732	1.97
7	256.5	489	2627	732	1.97
8	157.9	646.8	3107	990	2.07
9	101.5	748.3	3235	1319	2.17
10	232.8	981.1	3655	1598	2.25
11	396.4	1377.5	4453	2316	2.42
12	0	1377.5	5637	3200	2.6

Figures

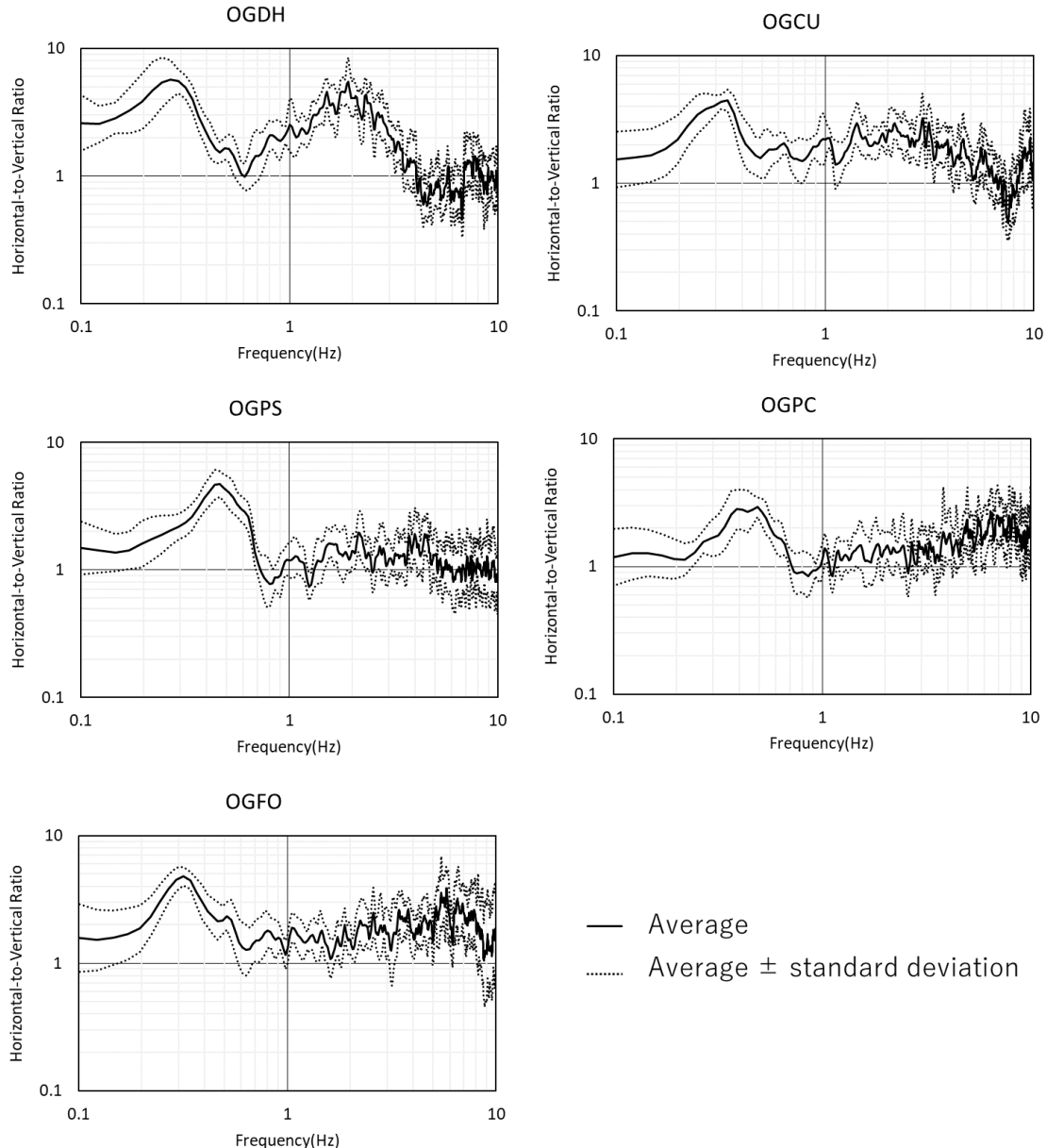


Figure A3.1. Observed eHVSRs at OG-series sites used for calculating EMRG. The black solid line is the average value of eHVSRs calculated from the several earthquakes observed at each site. The black dotted line is the average \pm one standard deviation.

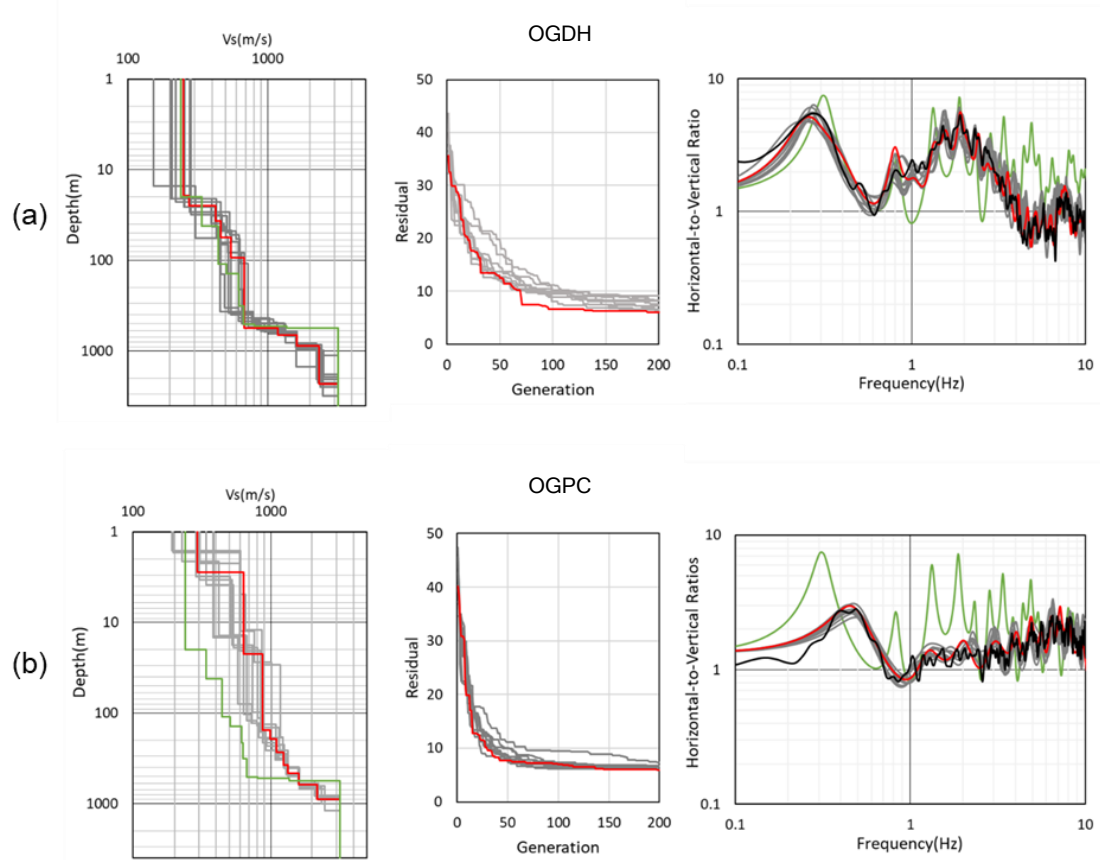


Figure A3.2. Comparison of the obtained S-wave velocities in the left panel, convergence with respect to the generation in HHS in the middle panel, and the best-fit model among ten trials (red line) with the observed eHVSR (black line) used as a target in the right panel. The results of the other nine models are shown in gray lines. The reference model and its theoretical eHVSR are also shown in the left and right panels (green line). (a) OGDH (b) OGPC.

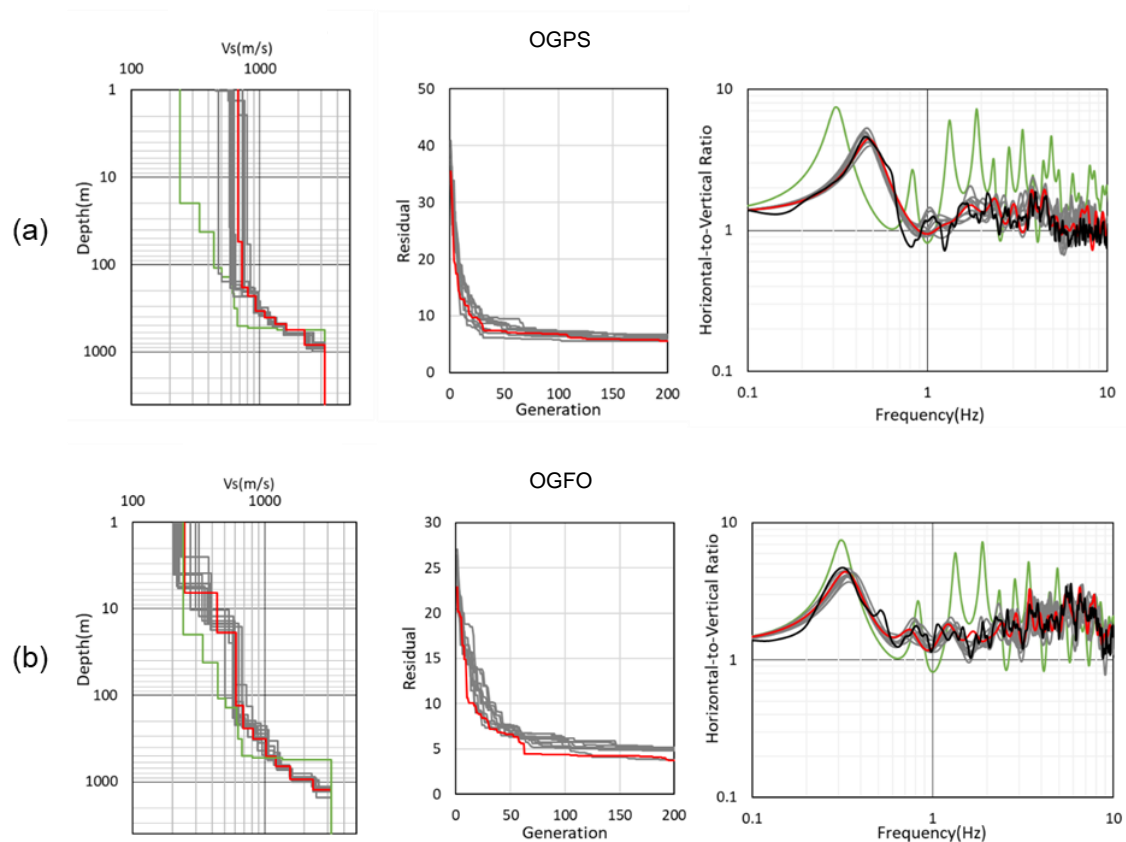


Figure A3.3. Comparison of the obtained S-wave velocities in the left panel, convergence with respect to the generation in HHS in the middle panel, and the best-fit model among ten trials (red line) with the observed eHVSR (black line) used as a target in the right panel, at two sites. The results of the other nine models are shown in gray lines. The reference model and its theoretical eHVSR are also shown in the left and right panels (green line). (a) OGPS (b) OGFO.

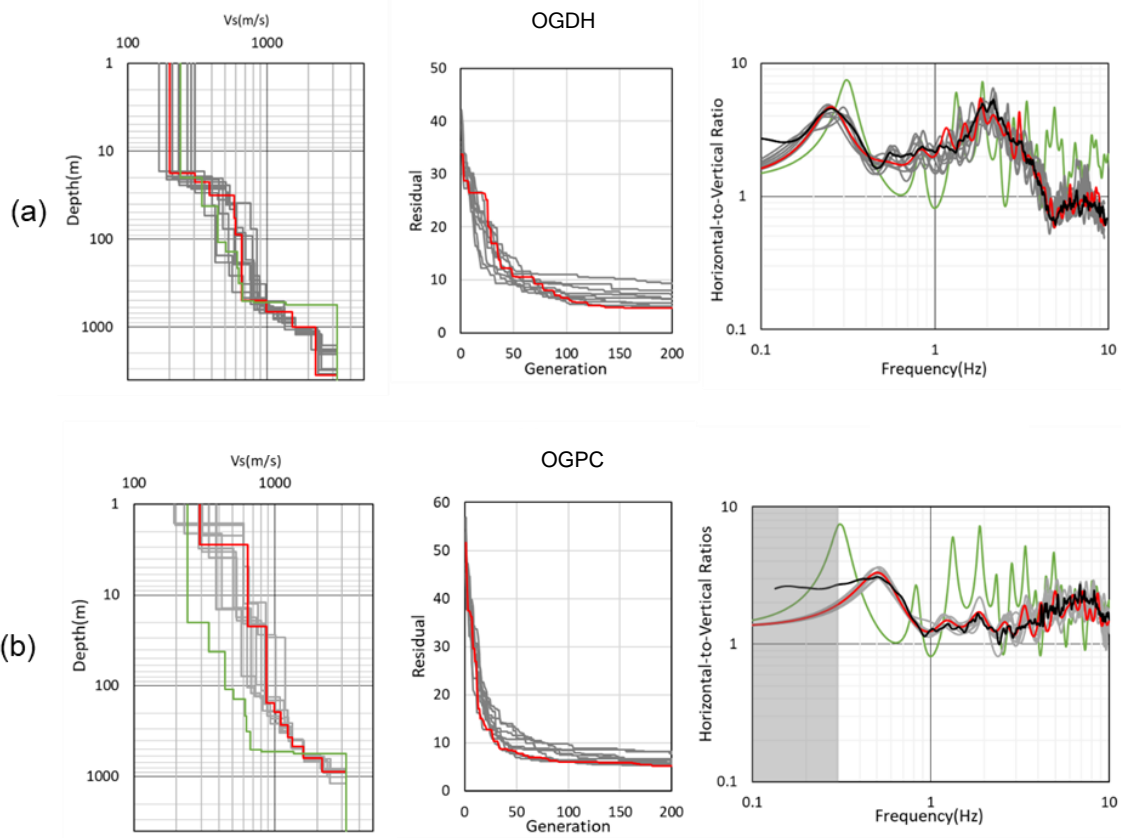


Figure A3.4. Comparison of the obtained S-wave velocities in the left panel, convergence with respect to the generation in HHS in the middle panel, and the best-fit model among ten trials (red line) with the transformed pHVSR (black line) used as a target in the right panel, at two sites. The results of the other nine models are shown in gray lines. The reference model and its theoretical eHVSR are also shown in the left and right panels (green line). (a) OGDH (b) OGPC.

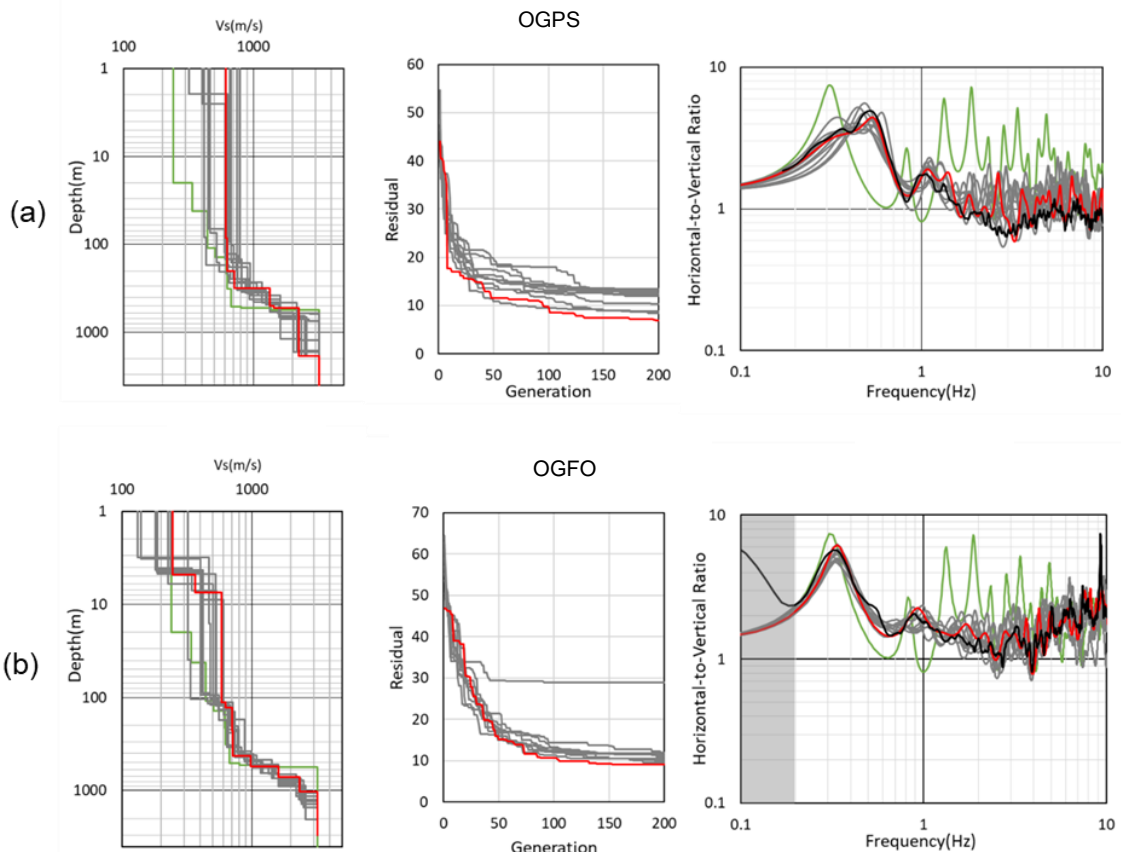


Figure A3.5. Comparison of the obtained S-wave velocities in the left panel, convergence with respect to the generation in HHS in the middle panel, and the best-fit model among ten trials (red line) with the transformed pHVSR (black line) used as a target in the right panel, at two sites. The results of the other nine models are shown in gray lines. The reference model and its theoretical eHVSR are also shown in the left and right panels (green line). (a) OGPS (b) OGFO.

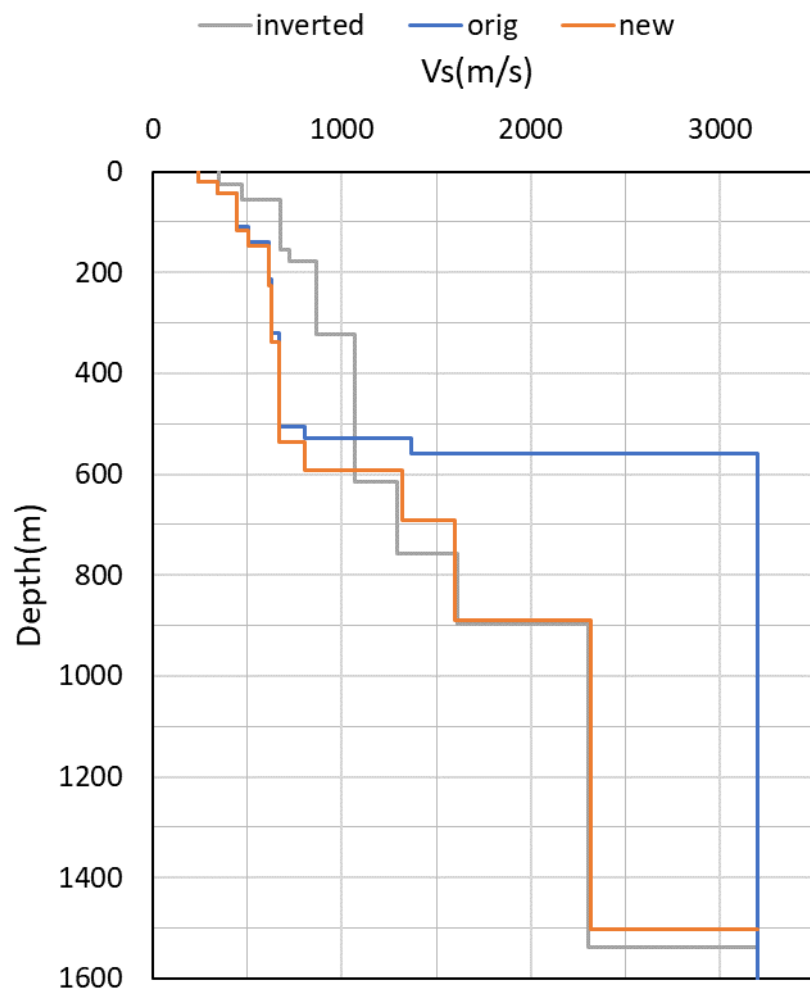


Figure A3.6. The new reference model (orange line) with the original reference model (blue line) and the velocity structure inverted from the original reference model (grey line) in Step-1 at OGCU, as an example of the new reference model calculated from the construction procedure in Figure 15.

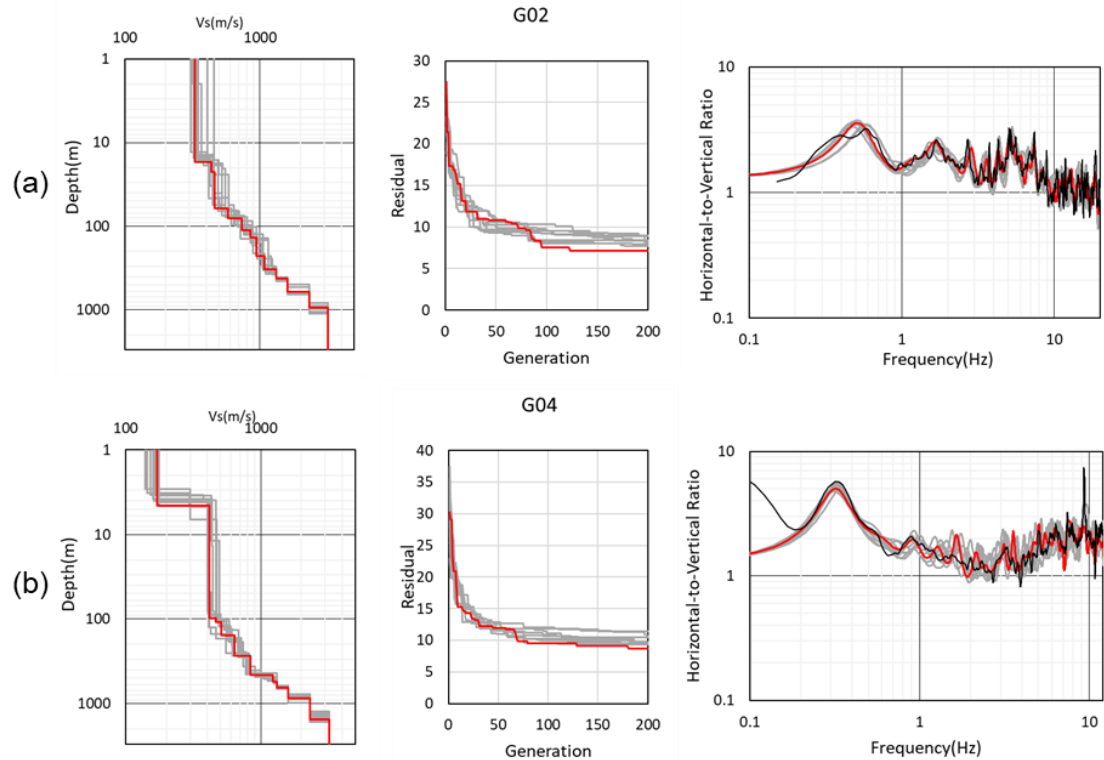


Figure A3.7. Comparison of the obtained S-wave velocities in the left panel, convergence with respect to the generation in the middle panel, and the best-fit model among ten trials (red line) with the transformed pHVSR (black line) in the right panel, at two sites. The results of the other nine trials are shown by gray lines. (a) G02, (b) G04.

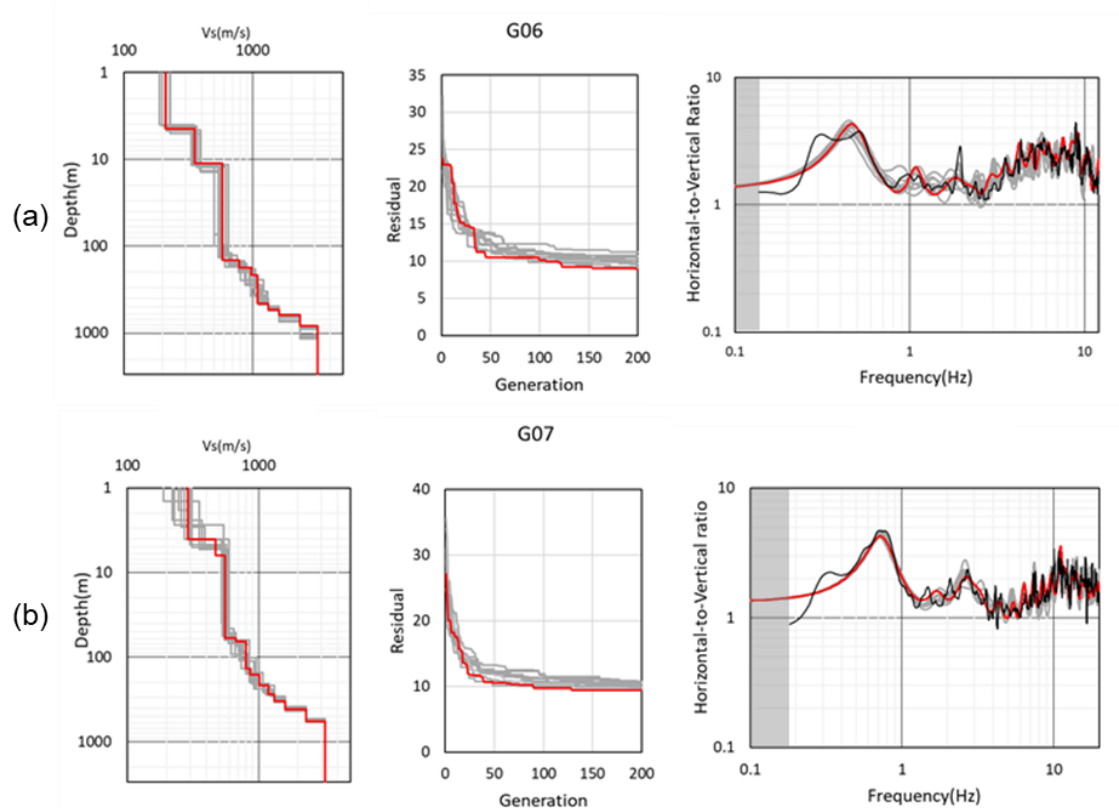


Figure A3.8. Comparison of the obtained S-wave velocities in the left panel, convergence with respect to the generation in the middle panel, and the best-fit model among ten trials (red line) with the transformed pHVSR (black line) in the right panel, at two sites. The results of the other nine trials are shown by gray lines. (a) G06, (b) G07.

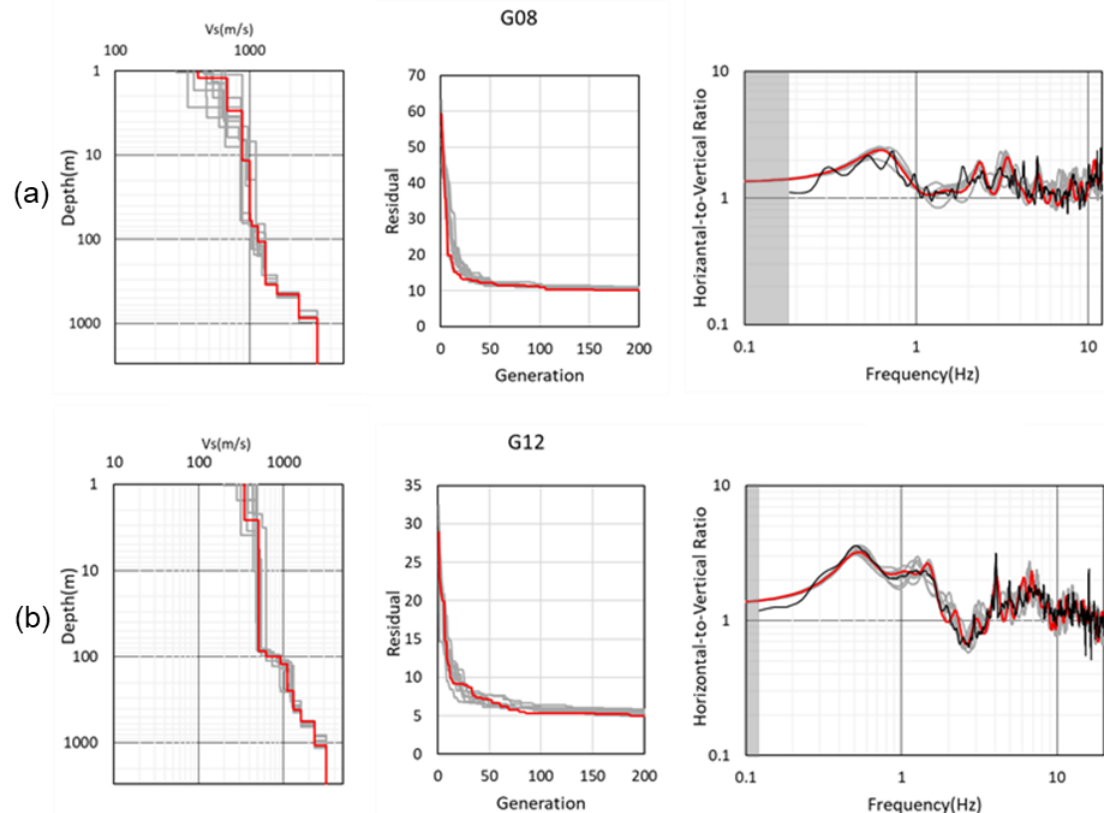


Figure A3.9. Comparison of the obtained S-wave velocities in the left panel, convergence with respect to the generation in the middle panel, and the best-fit model among ten trials (red line) with the transformed pHVSR (black line) in the right panel, at two sites. The results of the other nine trials are shown by gray lines. (a) G08, (b) G12.

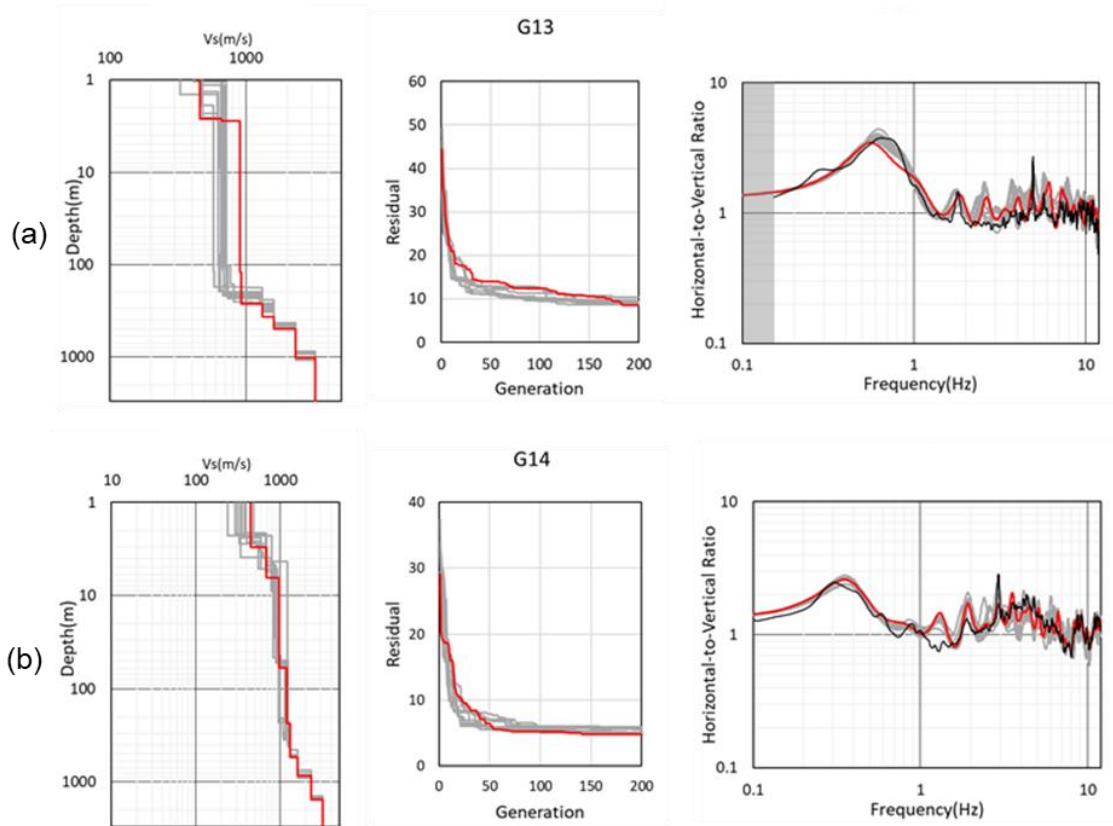


Figure A3.10. Comparison of the obtained S-wave velocities in the left panel, convergence with respect to the generation in the middle panel, and the best-fit model among ten trials (red line) with the transformed pHVSR (black line) in the right panel, at two sites. The results of the other nine trials are shown by gray lines. (a) G13, (b) G14.

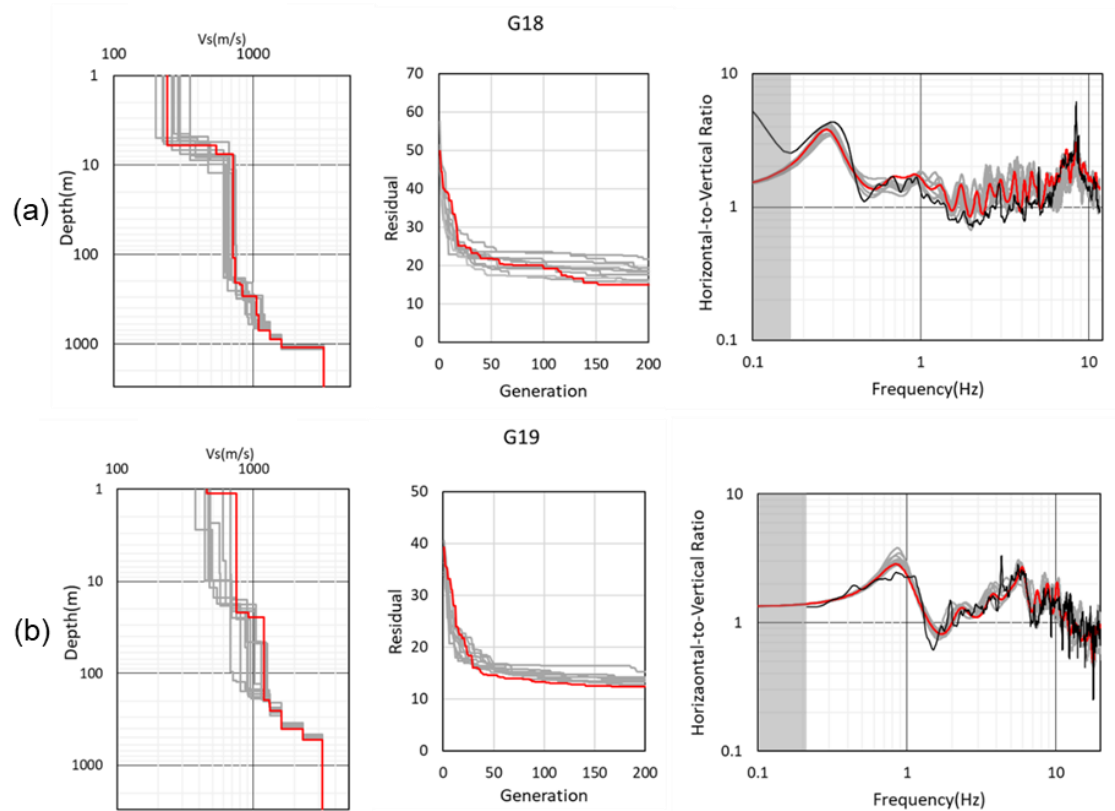


Figure A3.11. Comparison of the obtained S-wave velocities in the left panel, convergence with respect to the generation in the middle panel, and the best-fit model among ten trials (red line) with the transformed pHVSR (black line) in the right panel, at two sites. The results of the other nine trials are shown by gray lines. (a) G18, (b) G19.

Chapter 4

S-Wave Site Amplification Factors from Observed Ground Motions in Japan: Validation of Delineated Velocity Structures and Proposal for Empirical Correction

Abstract

We first derived site amplification factors (SAFs) from the observed strong motions by the Japanese nationwide networks by using the so-called generalized spectral inversion technique. We can use these SAFs for strong motion prediction at these observation sites, however, we need at least observed weak motion or microtremor data for SAF at an arbitrary site. We tested the capability of the current velocity models in Japan whether they can reproduce or not the observed SAFs at the nearest grid of every 250 m as the one-dimensional theoretical transfer functions (TTF). We found that at about one-half of the sites the calculated 1D TTFs show more or less acceptable fit to the observed SAFs, however, the TTFs tend to underestimate the observed SAFs in general. Therefore, we propose a simple, empirical method to fill the gap between the observed SAFs and the calculated TTFs. Validation examples show that our proposed method effectively predict better SAFs than the direct substitute of TTFs at sites without observed data.

4.1 Introduction

The quantitative strong motion prediction with a source- and site-specific scheme is very important for mitigation of earthquake disaster and seismic design of important structures. It is especially true in Japan where large mega-thrust earthquakes are expected to occur within the coming 30 years. That is why we have a couple of nation-wide strong-motion networks in which a considerable number of strong motion records have been accumulated since 1996 (Aoi et al., 2000).

There are several ways to simulate strong-motions as waveforms on the surface at a target site located at an arbitrary position. One is a theoretical Green's function method (TGF) in which wave generation at the source, propagation from the source to the site, and amplification near the site are represented by the numerical modeling for the whole process from the source to the site. In this method we need a physical model of the medium to represent the wave propagation in the whole path. In other words, we need to calculate the theoretical Green's function for a point source on the fault surface. The other is an empirical method in which we use observed ground motions of a small earthquake as a substitute for the Green's function and sum up all the contributions from the elemental sources on the fault surface. It is called the empirical Green's function method (EGF). If there are no appropriate small earthquake records to be used as the empirical Green's function, we first generate synthetic waveforms based on many records of small earthquakes. It is called the statistical Green's function method (SGF). Because the frequency range for the theoretical approach with coherent nature is limited to the lower end, usually below 1 Hz or lower, while the effective frequency range of EGF or SGF with inherent nature of stochasticity should be higher than that, a hybrid scheme with TGF and EGF or TGF and SGF are used naturally, as has been used in the current national project for strong motion predictions with specific sources (NIED, 2020).

After the deployment of the dense national strong motion observation networks, namely K-NET, KiK-net, and JMA Shindo-kei (Instrumental Seismic Intensity) network in Japan, a significant number of data has been accumulated. We can use these data to construct a model of SGF in a broadband frequency range. As long as we can generate the SGF for an arbitrary size of a small earthquake at an arbitrary location of a site in the frequency range of engineering interest, namely from 0.1 Hz to 20 Hz, we need not use a hybrid scheme. Thus we have been analyzing these strong-motion data in Japan by using the generalized spectral inversion technique (GIT) initially developed in 1980's (Andrew, 1986; Iwata and Irikura, 1986) to delineate statistical properties of the three major terms, namely, the source term, path term, and site term (Kawase and Matsuo, 2004; Kawase, 2006; Nakano et al., 2015; Nakano, 2020). The novelty of our approach is that the hypothesized (i.e., extracted) seismological bedrock spectra at a reference site, YM-GH01, are used as a reference to calculate site amplification factors at all the other observed sites. Such a separation of observed spectra into three major terms is sufficient to generate SGF at these observed sites. However, strong-motion simulations for the whole region near the seismogenic fault would be still difficult by SGF because we cannot estimate the site term at an arbitrary location other than the observed sites used in GIT. Thus, we need to develop a method to evaluate the site term at an arbitrary location as precisely as possible.

When we look at the site term as a function of frequency evaluated at K-NET, KiK-net, and JMA Shindo-kei network, we found that they show strong spectral fluctuations from 1 to 10 as a normal range of fluctuations and from 1 to 50 at tens of extraordinary sites with various peak frequencies. Several attempts have been made to correlate the primary characteristics of the observed site amplification factor (SAF) with a site proxy or proxies such as the S-wave velocity (V_s) averaged over top xx m, V_{s_xx} , for example, V_{s30} , or the depth to the layer with the S-wave velocity higher than $y.y$ km/s, $Z_{y.y}$, for example, $Z1.0$ (Borcherdt, 1970; Matsuoka and Midorikawa, 1994; Kawase and Matsuo, 2004; Zhao, 2010; Zhu et al., 2020) trying to reproduce primary characteristics of SAF such as the fundamental peak frequency f_0 and its peak amplitude A_0 . Unfortunately, these extracted characteristics are not sufficient to reproduce synthetic seismograms needed in the SGF summation. We should find a different strategy.

In what follows, we first introduce the fundamental characteristics of the observed SAF in the horizontal component (hSAF) derived from GIT (Nakano et al., 2015; Nakano, 2020). Then, we show comparisons of these hSAFs with the 1D theoretical ones calculated from the recently established unified velocity model (UVM) of the National Research Institute for Earth Science and Disaster Resilience (NIED) in the Kanto and Tokai regions. Next, we obtain the modification ratios to reduce the gap between them at the observation points and propose a scheme to evaluate hSAF at an arbitrary point by using the theoretical hSAF and the interpolated modification ratios, named FMR as the frequency modification ratio and AMR as the amplitude modification ratio. Finally, we propose an interpolation scheme to get hSAF in every 250 m grid point and validate the scheme at selected sites.

4.2 Observed SAF from GIT

In this section, we briefly introduce the observed horizontal SAF (hSAF) and vertical SAF (vSAF) derived from GIT (Nakano et al., 2015; Nakano, 2020). Here we introduce only their basic aspects because we are using their results as a starting point.

They restricted events and sites with the Japan Meteorological Agency (JMA)'s magnitude $M_{JMA} \geq 4.5$; source depth ≤ 60 km; hypocentral distance ≤ 200 km; peak ground acceleration ≤ 2 m/s²; and a number of observation sites triggered simultaneously for one event ≥ 3 . These selection criteria resulted in 150,468 event-station pairs at 2,593 sites for 1,734 events. Only a relatively short duration of acceleration record from the onset of the S-wave was analyzed (5 s if $4.5 < M_{JMA} \leq 6$; 10 s if $6 < M_{JMA} \leq 7$; 15 s if $7 < M_{JMA} \leq 8$). A Parzen window of 0.1 Hz was used for a minimum level of smoothing. As mentioned above, the most important feature of their GIT is that they determined the S-wave velocity structure at the reference site using the transfer function (the spectral ratio and the phase difference) between the surface and the borehole 200 m below and that the observed Fourier spectra on the surface were deconvolved to obtain the hypothesized outcrop spectra on the seismological bedrock with V_s of 3,450 m/s. Nakano et al. (2015) successfully separated the source spectra and path terms as evidenced by their

correspondence to the ω^2 source spectra shapes and Q values similar to the previous studies in Japan.

Figure 4.1 shows examples of the observed hSAF at four sites in the Tokai region. We can see significant differences from site to site. Although we did not show vSAF here, the amplitude and its fluctuation of vSAF is much smaller than hSAF, especially below 3 to 4 Hz. That is why the earthquake horizontal-to-vertical spectral ratio, eHVSR, tends to be similar to hSAF until the fundamental peak frequency of vSAF. However, to get hSAF from eHVSR, we need to correct vSAF, as recently proposed by Ito et al. (2020). Please note that precisely speaking, vSAF in this paper should be referred to as vSAF* as in Ito et al. (2020) because we use the same reference condition for both hSAF and vSAF as the seismological bedrock spectra in the horizontal component so that we need to have correction due to the vertical-to-horizontal spectral ratio on the seismological bedrock on top of the vertical-to-vertical site amplification.

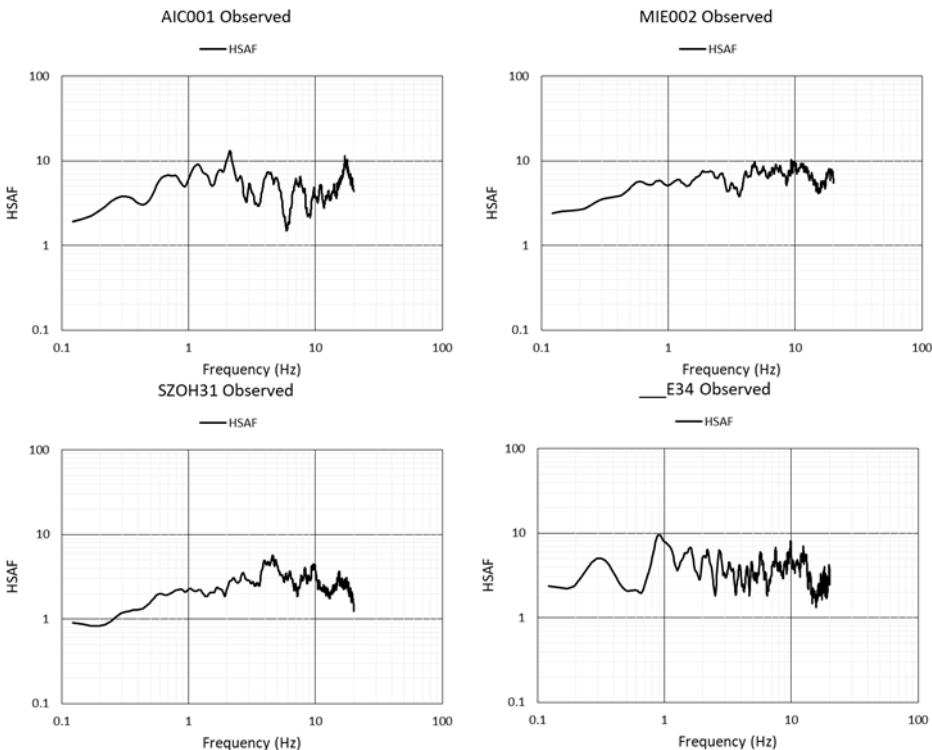


Figure 4.1. Observed horizontal site amplification factor, hSAF, extracted from strong motions at K-NET, KiK-net, and JMA Shindohei network by GIT (Nakano et al., 2015).

4.3 Unified Velocity Model of NIED

To theoretically reproduce the observed hSAF and vSAF* from GIT we need a velocity structure at each site from the seismological bedrock to the surface because they are the spectral ratios with respect to the outcrop spectra on the seismological bedrock. We have been delineating

velocity structures for the deeper- and shallower-parts, separately. The boundary between them is the so-called engineering bedrock, whose Vs would be in between 350 m/s to 450 m/s. However, it is apparent that higher-mode contributions of reverberated S- and P-waves within the whole basin above the seismological bedrock should show up in the frequency range higher than the fundamental peak frequency (Kawase et al., 2018). Therefore, we need a unified velocity model that integrates both shallower- and deeper-parts.

To that end, the National Research Institute for Earth Science and Disaster Resilience (NIED) has developed a unified velocity model (UVM) by integrating shallower- and deeper-parts of the structures above the seismological bedrock in the Kanto and Tokai regions (Senna et al., 2014; Senna et al., 2019; Wakai et al., 2019)

The procedure to develop the model was based on the “concept of creating a subsurface structure model” released by the government agency, the Headquarters for Earthquake Research Promotion (2020). Details of the procedure can be found in the papers referenced above, but the following is a brief description of the procedure.

An initial model of the shallow structure from the ground surface to the engineering bedrock was created based on existing studies and continuously collected SPT values in the boring data. Meanwhile, an initial model of the deep structure from the engineering bedrock down to the seismological bedrock was created based on the velocity models developed in existing studies by HERP. Then, an initial UVM was created by connecting them at the engineering bedrock. Next, the initial UVM was adjusted by using S-wave velocity structures at the strong-motion sites in the regions and those of spatially uniform and dense array microtremor explorations conducted as a part of Japan’s national Strategic Innovation Promotion project. Finally, the adjusted UVM was verified by using earthquake data at the strong-motion sites of NIED.

Examples of the important features of the resultant UVM are shown in Figures 4.2 and 4.3. Figure 4.2 shows the depth to the seismological bedrock with the Vs of 3.1 km/s (Z3.1) in the Tokai region, while Figure 4.3 shows the depth to the engineering bedrock with the Vs of 0.35 km/s (Z0.35), which is the interface between the shallower- and deeper-parts of the UVM in the Tokai region (Wakai et al., 2019). A similar map can be seen for the Kanto region in Senna et al. (2014, 2019). Table 4.1 shows the parameters of layers assumed in the deeper part.

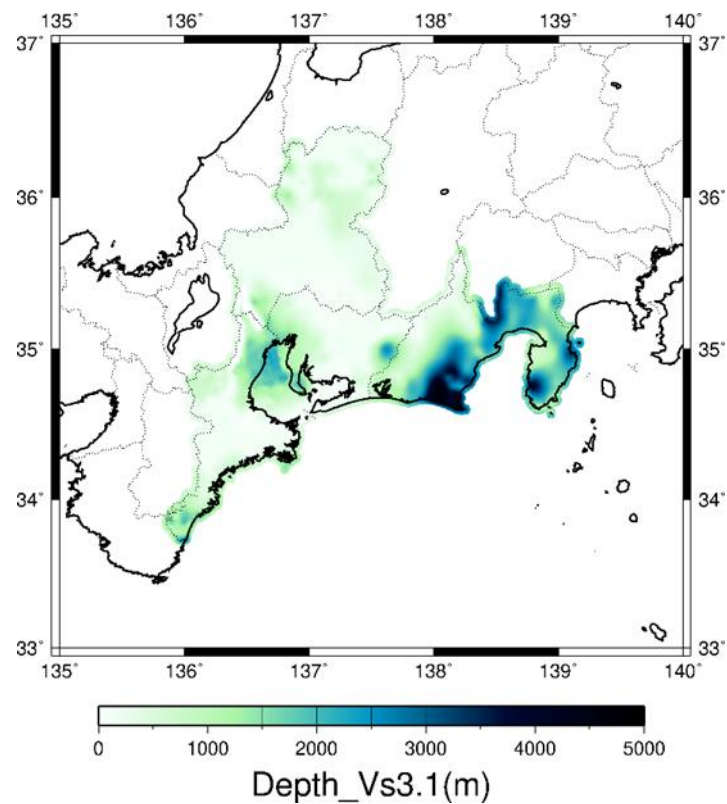


Figure 4.2. Depth contour to the seismological bedrock with Vs of 3.1 km/s in Wakai et al. (2019).

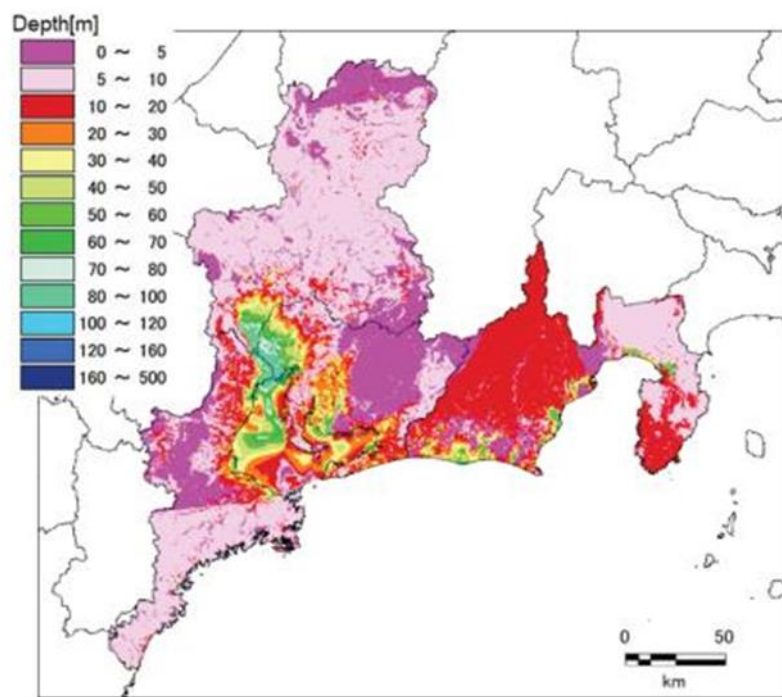


Figure 4.3. Depth contour of the engineering bedrock with Vs of 350 m/s in Wakai et al. (2019).

Table 4.1. Assumed layer profiles for the deeper part of UVM.

No	Vp (m/s)	Vs (m/s)	Ds (kg/m ³)	Q ₀
1	1600	350	1850	70
2	1600	400	1850	80
3	1700	450	1900	90
4	1800	500	1900	100
5	1800	550	1900	110
6	2000	600	1900	120
7	2000	650	1950	130
8	2100	700	2000	140
9	2100	750	2000	150
10	2200	800	2000	160
11	2300	850	2050	170
12	2400	900	2050	180
13	2400	950	2100	190
14	2500	1000	2100	200
15	2500	1100	2150	220
16	2600	1200	2150	240
17	2700	1300	2200	260
18	3000	1400	2250	280
19	3200	1500	2250	300
20	3400	1600	2300	320
21	3500	1700	2300	340
22	3600	1800	2350	360
23	3700	1900	2350	380
24	3800	2000	2400	400
25	4000	2100	2400	420
26	5000	2700	2500	540
27	4600	2900	2550	580
28	5500	3100	2600	620
29	5500	3200	2650	640

Please note that in the following sections when we calculate theoretical one-dimensional (1D) S-wave SAF, we use the following Q values for intrinsic and scattering attenuation:

$$Q=Q_0*0.5 \quad \text{if } f \leq 0.5 \text{ Hz}$$

$$Q=Q_0f \quad \text{if } 0.5 \text{ Hz} < f < 5 \text{ Hz}$$

$$Q=Q_0*5 \quad \text{if } 5 \text{ Hz} \leq f$$

The Q_0 values for the deeper part are listed in Table 4.1, while those for the shallower part we assume $Q_0=Vs/10$.

To connect the bottommost layer of the shallower part Lsb with the topmost layer of the deeper part Ldt, we prioritize the shallower part if the depth Lsb is deeper than Ldt. If there is a gap between the two depths and Vs of Lsb is equal to or larger than Vs of Ldt, we extend Lsb down to Ldt. If Vs of Lsb is much smaller than Vs of Ldt, then we insert three layers with a gentle gradient of increasing Vs.

4.4 Observed and Theoretical SAF

As mentioned in the previous section, the UVM of NIED is considered to be the most reliable velocity model for the strong motion simulation because the UVM combines all the available geophysical information to date related to the velocity structures from the ground surface to the seismological bedrock as densely sampled as possible. From UVM and Q values prescribed above, a theoretical 1D S-wave amplification factor can be easily calculated by a simple multi-reflection theory for a stack of layers (e.g.; Sezawa and Kanai, 1930; Haskell, 1962; Tsai, 1970). However, the actual S-wave SAF at a specific site, as shown in Figure 4.1, can be significantly different from the theoretical one calculated as such. To see the difference, we plot in Figure 4.4 comparisons of the 1D theoretical hSAF with the observed hSAF at the same four sites in Figure 4.1. We connect the shallower-and deeper parts with a priority of the shallower-part, and we use $Q=Q_0f$ where $Q_0=Vs/10$ for the shallower-part and $Q_0=Vs/5$ for the deeper part as shown in Table 4.1. We consider this frequency dependence only in the frequency range from 0.5 Hz to 5 Hz as explained previously. Except for the site SZOH31, the theory tends to underestimate the observation.

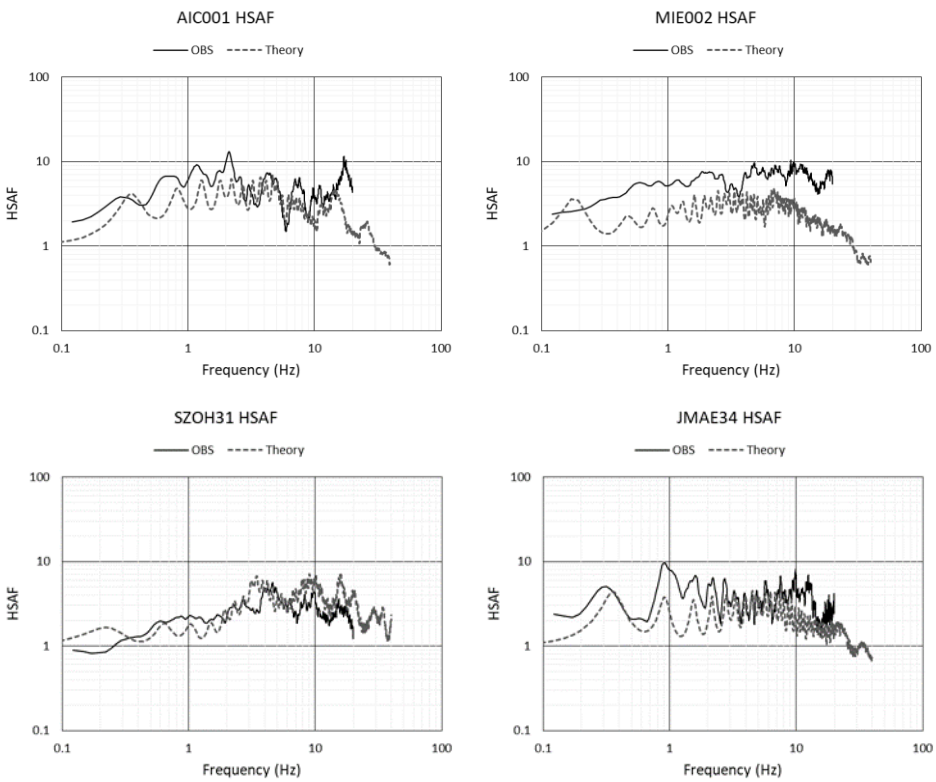


Figure 4.4. Observed hSAF extracted by GIT and 1D theoretical hSAF from UVM (Wakai et al., 2019). Fundamental characteristics are well reproduced, however, the theoretical hSAF tends to underestimate the observed hSAF.

The major reasons for discrepancy are twofold; one is due to an inevitable inaccuracy of the derived velocity structure, and the other is due to a too simplistic assumption of the 1D horizontally-flat layered model. In the former there are two possible causes; one is the inaccuracy of the referenced values to delineate the structure including the assumed Q-values, and the other is the rapid spatial variations within the 250 m grid. In the latter there are two possible causes; one is the additional amplification due to the basin-induced surface waves generated at the edge of two or three-dimensional (2D or 3D) basins (see for example, Bard and Bouchon, 1980; Kawase and Aki, 1989; Kawase, 1996) and the other is the topographic effects near the surface of irregular shapes such as a hill, a valley, or a cliff (see Kawase and Aki, 1990).

To account for the effects of the basin-induced surface waves inside sedimentary basins, Nakano (2020) and Nakano and Kawase (2019) proposed to use an empirical ratio called the whole-wave-to-S-wave ratio (WSR), where the spectral ratios of the whole duration with respect to the S-wave portion with relatively short duration (5 to 15 s depending on the source magnitude as used in GIT) are averaged over all the observed events at a site. They found that the WSR tends to be close to 1 irrespective of frequency for a site on hard rock, whereas it can easily exceed 10 in the lower frequency range for a site inside a soft sedimentary basin. Even for such a site, WSR will converge to 1 in a higher frequency range above a few Hz. Because the spatial variation of WSR at one specific frequency highly correlates with that of the basin depths, as seen in Nakano

and Kawase (2019), Nakano (2020) proposed a scheme to interpolate WSRs to make it possible to calculate a scenario-type hazard map with much higher spatial density than those of strong motion observation sites. This WSR correction is a simple, empirical way to account for the additional amplification due to a basin.

However, other than the basin-induced surface waves, it is difficult to account for the physical cause of the discrepancy between observation and theory at every sites. We have been attempting to fill the gap by inverting the velocity structures from observed horizontal-to-vertical spectral ratios (HVSRs) of earthquakes under the diffuse field assumption (Kawase et al., 2011; Nagashima et al., 2014; Nagashima et al., 2017), which is quite successful to reproduce observed HVSRs (and consequently hSAF, too). This approach can provide us an equivalent 1D structure that will reproduce the observed hSAF at the target site quite precisely, however, the method is valid only for a site with either earthquake or microtremor records. We need a different strategy to evaluate hSAF as precisely as possible at an arbitrary site without any records. Because the velocity structure in the UVM of NIED is obtained with the spatial density of the 250 m grid, we want to reflect the fundamental characteristics of the theoretical transfer function of that structure, yet the resultant hSAF for strong motion simulation should be close enough to the observed hSAF.

4.5 Frequency and Amplitude Modification Ratio

To overcome the difficulty to obtain better velocity models through physical parametrization of the underground structure at the sites without observed records, we would like to propose a different but simple approach here.

Suppose that a theoretical 1D hSAF from the UVM at a certain site deviates from the true hSAF by one of the aforementioned causes or their combination, the difference of the theoretical hSAF would be manifested in both the frequency axis and the amplitude axis. If we have stiffer or thinner layers in reality than the assumed model, then the frequency characteristics would be all shifted towards the higher side. Or if we have a stronger velocity gradient within layers, then the peak amplitudes would be all shifted towards the higher side. Thus, we have two different ways to adjust the theoretical hSAF to make it closer to the observed hSAF, one in the frequency axis and the other in the amplitude axis. Here is a simple way of correction for the theoretical hSAF, $HSAF_{the}$:

$$HSAF_{mod}(f) = AMR * HSAF_{the}(f/FMR), \quad (4.1)$$

where FMR is the frequency modification ratio and AMR is the amplitude modification ratio. $HSAF_{mod}$ is the resultant hSAF after both modifications as a function of frequency f . We need to determine FMR and AMR to make RES , the residual between $HSAF_{mod}$ and the observed hSAF ($HSAF_{obs}$), minimum:

$$RES(FMR, AMR) = \sum_{f=fmin}^{fmax} \frac{|\log_{10}(HSAF_{mod}) - \log_{10}(HSAF_{obs})|}{f} \quad (4.2)$$

where $fmin$ and $fmax$ are the minimum and maximum frequencies of interest and we set them 0.12 Hz and 20 Hz, respectively. Here we use frequency f as a weight because the higher the frequency the denser the data in the linear space.

4.5.1 Grid search scheme

Because the calculation of equation (4.2) is quite easy, we use the grid search to obtain the best FMR and AMR combination. However, after several experiments, we found that the evaluation function in equation (4.2) seems too weak to determine FMR and AMR in a reasonable range because there is a trade-off between them. Therefore, we introduce the correlation function between $HSAF_{mod}$ and $HSAF_{obs}$ as an additional constraint. Then the target function to be maximized, GOF , becomes

$$GOF = RES_{min}/RES(FMR, AMR) * COR(FMR)/COR_{max} \quad (4.3)$$

where RES_{min} is the minimum residual in the searching range, $RES(FMR, AMR)$ is the residual shown in equation (4.2) as a function of FMR and AMR , $COR(FMR)$ is the correlation coefficient between $HSAF_{mod}$ and $HSAF_{obs}$, which is a function of only FMR , not a function of AMR , and COR_{max} is the maximum correlation coefficient in the searching range. Thus 1.0 is the maximum of GOF.

We set the searching range for FMR depending on the original correlation without frequency modulation, which is COR (1.0), as follows:

$$\begin{aligned} & \text{If } 0.6 \leq COR(1.0), \quad 0.80 \leq FMR \leq 1.25 \\ & \text{If } 0.4 \leq COR(1.0) < 0.6, \quad 0.67 \leq FMR \leq 1.50 \\ & \text{If } COR(1.0) < 0.4, \quad 0.50 \leq FMR \leq 2.00 \end{aligned} \quad (4.4)$$

We use these searching ranges because if the correlation of the original model is sufficiently high, we should not modify its frequency characteristics so much. For AMR we set the searching range to be $0.333 \leq AMR \leq 3.00$ irrespective of $COR(1.0)$ because there are a few tens of sites with those amplitude differences as high as 3 times or as low as 1/3 and AMR does not alter $COR(1.0)$. To efficiently search the best FMR and AMR with the precision of two digits, we employ the two-step grid search; first with every 0.1 increments, then with every 0.01 increments around the best FMR and AMR in the first step.

4.5.2 Evaluated *FMR* and *AMR*

Figure 4.5 shows examples of the resultant $HSAF_{mod}$ in comparison with $HSAF_{obs}$ and $HSAF_{the}$ at the same K-NET, KiK-net, or JMA Shindo-kei network sites shown in Figures 4.1 and 4.4. As we can see, $HSAF_{mod}$ determined by the grid search are quite close to $HSAF_{obs}$ in both frequency fluctuations and amplitudes.

Figure 4.6 shows the resultant optimal values of *FMR* and *AMR* at all the 546 sites used. We can see a very weak correlation between them. As for the searching range of *AMR*, namely 1/3 to 3 looks sufficient. On the other hand, we see a significant concentration of sites near the searching range boundary, 1/2 or 2 for *FMR*. This means that we could get better residuals and correlations if we shift frequency more than those limits. However, when we increase the searching range for *FMR* too much, we will see some cases where the reverberated fluctuations by the 1D resonance within the sediments seem to be shifted to the next overtone.

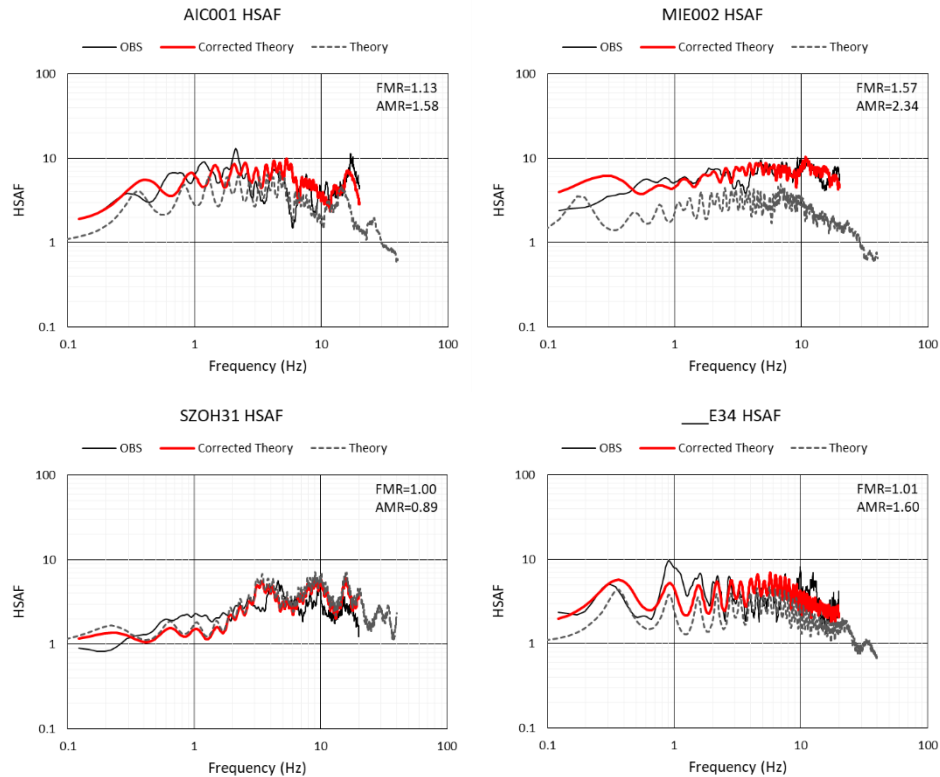


Figure 4.5. Modified hSAF ($HSAF_{mod}$) by using *FMR* and *AMR* in comparison with observed hSAF ($HSAF_{obs}$) extracted by GIT and 1D theoretical hSAF ($HSAF_{the}$) from the velocity structure taken from UVM. The values of *FMR* and *AMR* for each site are shown in the upper-right corner.

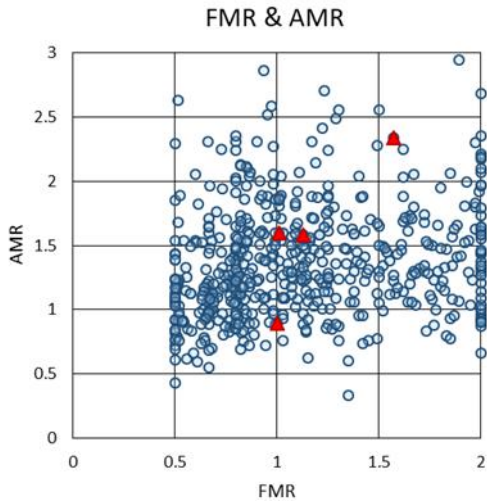


Figure 4.6. Resultant values of FMR and AMR after the grid search for 546 sites in the Kanto and Tokai regions. Red triangles are those for the sites shown in Figure 4.5.

4.5.3 Correlation and residual improvement

If no improvement to the matching with the observed hSAF is achieved, our correction method does not have any merit. Therefore, we need to check if we can see significant improvement or not. Figure 4.7 shows the distributions of the obtained correlation and the averaged residuals between $HSAF_{mod}$ and $HSAF_{obs}$. We can see most of the site shows residuals less than 1.5 and correlations higher than 0.5. Table 4.2 shows the percentage of the sites in different categories in terms of the goodness of fit to $HSAF_{obs}$. When we compare the matching seen in Figure 4.5 and the distribution of these data in Figure 4.7, we can see that the average residual is more important than the correlation in terms of the quality of the modified hSAF because the correlation can be deteriorated easily by small fluctuations in different frequencies.

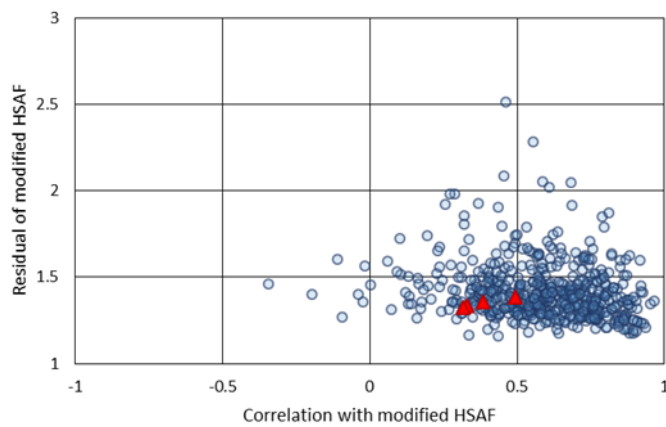


Figure 4.7. Distributions of the correlation of $HSAF_{mod}$ versus the averaged residual (a normal value as a power of 10, that is, the averaged spectral ratio between $HSAF_{mod}$ and $HSAF_{obs}$). Triangles are values at the sites shown in Figure 4.5.

Table 4.2. Residual and correlation improvement between $HSAF_{obs}$ and $HSAF_{the}$ in comparison to those between $HSAF_{obs}$ and $HSAF_{mod}$.

Residual	Original	Modified	Correlation	Original	Modified
<1.25	5	43	<0.0	84	7
1.25-1.50	175	389	0.0-0.4	227	86
1.50-2.00	286	108	0.4-0.6	116	186
2.00-3.00	77	6	0.6-0.8	85	193
3.00<	3	0	0.8-1.0	34	74
Total	546	546	Total	546	546

Figure 4.8 shows significant improvements in correlations from the original ones to the modified ones. There is no data with decreased correlations, however, there still remain 7 sites with correlations less than zero, which was decreased from 84. Figure 4.9 also shows correlation improvements but as a function of FMR . We can see a clear concentration of FMR near the boundaries at 0.8 and 1.25, the boundaries of the searching range if the original correlation is larger than 0.6 as shown in equation (4.4). We can see a smaller improvement in this FMR range for higher correlation sites, in comparison to those with lower correlations.

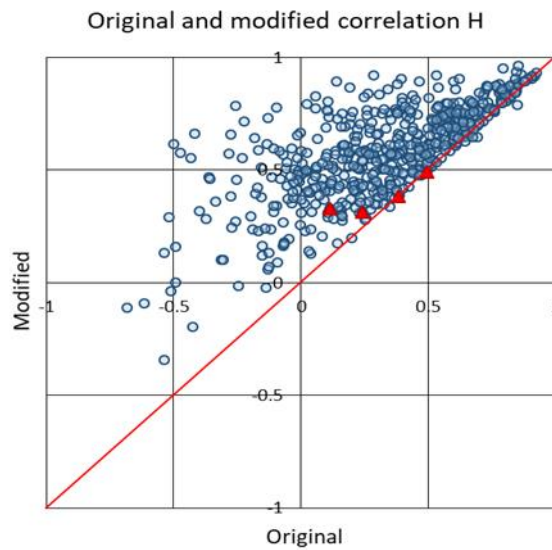


Figure 4.8. Improvement from the original correlations of $HSAF_{the}$ to the modified ones of $HSAF_{mod}$. Triangles are values at the sites shown in Figure 4.5.

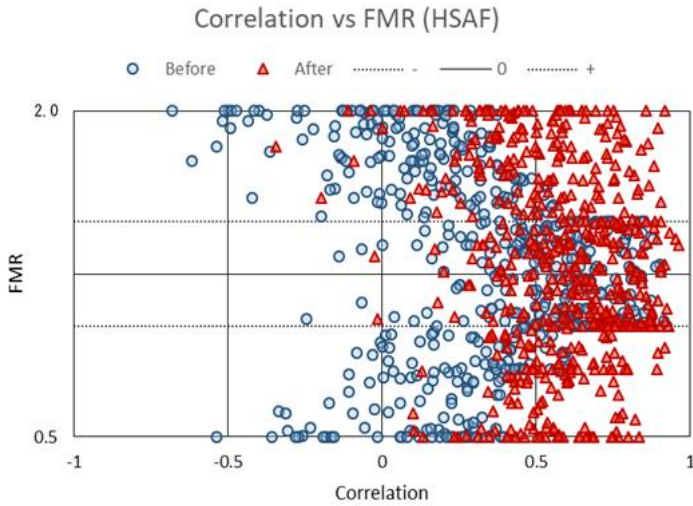


Figure 4.9. Improvement from the original correlations of HSAF to those of HSAFmod as a function of FMR. Data after the correction are concentrated near the boundaries of the searching range when the original correlation is more than 0.6. Note that FMR in this plot is common for both before and after.

4.5.4 Spatial interpolation

Now we have more than 500 sites in the Kanto and Tokai regions where we have determined modification ratios for frequency and amplitude, FMR and AMR . There are various ways to utilize these ratios for the prediction of site amplifications with much denser spatial resolutions based on the UVM in the 250 m grid. One way is to establish relationships of these modification ratios with respect to a site proxy or proxies such as $Vs30$ or $Z1.0$ as mentioned in the introduction. As seen in a lot of previous studies for site effects based on such relationships, however, we need to accept large deviations from the average relationships from site to site because it is the nature of the site amplification. We also face the possibility of the inaccurate choice of a site proxy in UVM for an arbitrary site used for modification ratios.

Therefore, we decide to use a direct spatial interpolation scheme as Nakano (2020) proposed for WSR. In this scheme, we employ first GMT's “surface” function (Smith and Wessel, 1990; Wessel et al., 2013), in which the curvature minimization scheme is used together with the smoothing constraint of an elastic shell with the tension factor of 0.25. In this Step-1 interpolation, we use the 3km equal-spaced grid. Then in Step-2, we use the 250 m grid to interpolate further by using the modified Shepard’s method (Renka, 1999).

Figure 4.10 shows the comparison of interpolated values in Step-1 with those used as targets for (a) FMR and (b) AMR . Interpolation in AMR is better because its spatial variation is smoother than FMR as shown later. Although we see tens of sites in Figure 4.10a away from the 1:1 line, the average deviation from unity for FMR is about 10% (1.1 or 0.9 times) and 91% of the interpolated values are within the range between 1/1.25 and 1.25 times of the original FMR .

The number of outliers is misleading because we use the “blockmedian” command of GMT to refer to only the median value if we have plural sites in the same 3 km grid.

Similarly, Figure 4.11 shows the comparison of interpolated values in Step-2 with those used as targets from Step-1 for (a) *FMR* and (b) *AMR*. In Step-2 the interpolation is performed from the 3 km grid in Step-1 to the 250 m grid. The linearity of interpolation in Step-2 is much higher than that in Step-1 in the case of *FMR*, whereas that of Step-2 is as high as that of Step-1 in the case of *AMR*.

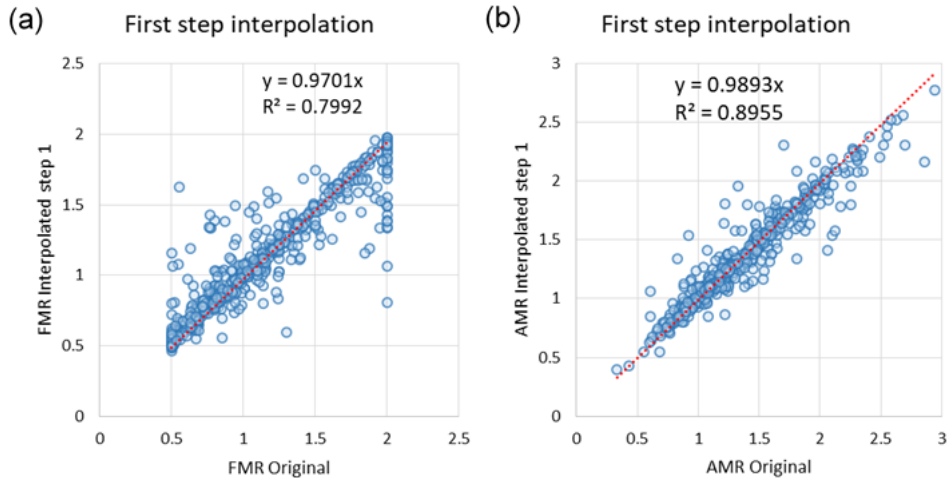


Figure 4.10. Comparison of the original *FMR* and *AMR* used as targets of interpolations and those of interpolated values in Step-1 at strong motion observation sites. Red broken lines are linear regression lines whose inclinations and coefficients of determination are listed inside.

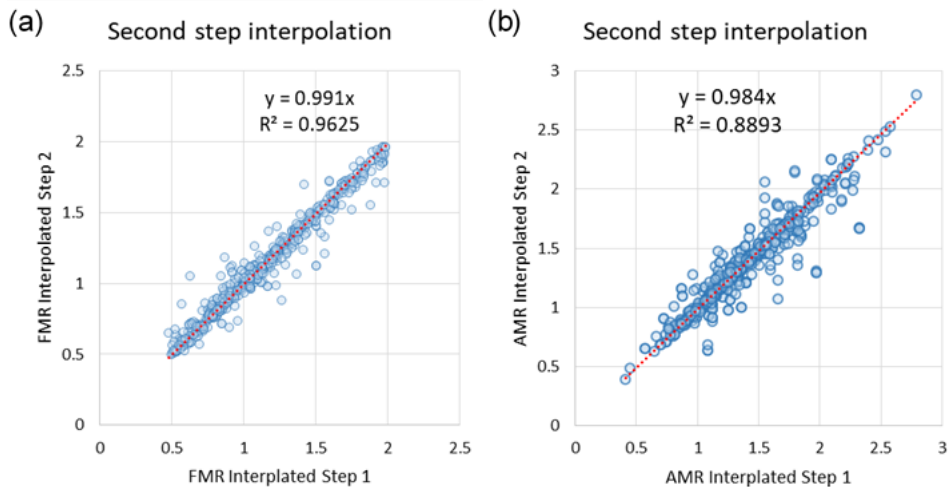


Figure 4.11. Comparison of Step-1 *FMR* and *AMR* used as targets of interpolations in Step-2 interpolation and those of interpolated values in Step-2 at strong motion observation sites. Red broken lines are linear regression lines whose inclinations and coefficients of determination are listed inside.

We can see the spatial stability of the interpolation scheme as a gross picture shown in Figure 4.12 for *FMR* and *AMR*. These are the results of Step-2 with a spatial resolution of 250 m. Apparently, *AMR* is much smoother than *FMR* in terms of spatial variability so that the interpolation for *AMR* should be much easier and precise than *FMR*. On average, the Kanto region needs smaller correction values in *FMR* than those in the Tokai region, although it needs relatively larger correction values in *AMR* inside the whole soft-sedimentary areas in the north of Tokyo Bay.

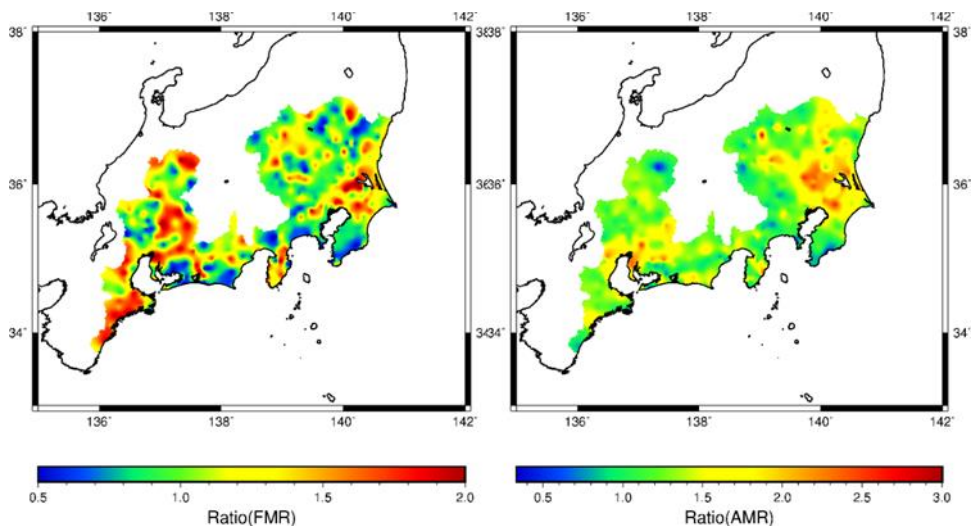


Figure 4.12. Interpolated contour map of *FMR* (left) and *AMR* (right) after the Step-2 interpolation with the spatial resolution of 250 m.

4.5.5 Validation

So far we show that a simple two-step scheme of interpolation works to calculate modification ratios for both frequency and amplitude, namely, *FMR* and *AMR* from 546 strong motion stations in the Kanto and Tokai regions in a grid as small as 250 m. Because the UVM in these regions has a spatial resolution of 250 m, we can directly use these interpolated modification ratios once we calculate 1D theoretical hSAF at any of these grid points. To validate the method, we take four sites shown in Figure 4.5 out from the control points used for interpolation and let the program interpolate the modification ratios there and see how it works.

Figure 4.13 shows contour maps of *FMR* and *AMR* without four points used as examples in Figure 4.5. We can see smooth interpolation is achieved at these four points. Figure 4.14 shows the correspondence of original and interpolated values of *FMR* and *AMR* for the cases with and without four points. In case of *FMR*, the original and interpolated values are close to the 1:1 line and the pure interpolation values at three sites out of four are close to the original ones. In case of *AMR*, the interpolation values without four sites were not as good as those with four sites. Still the deviations from the original values are within the range of 1.5 or 1/1.5 times.

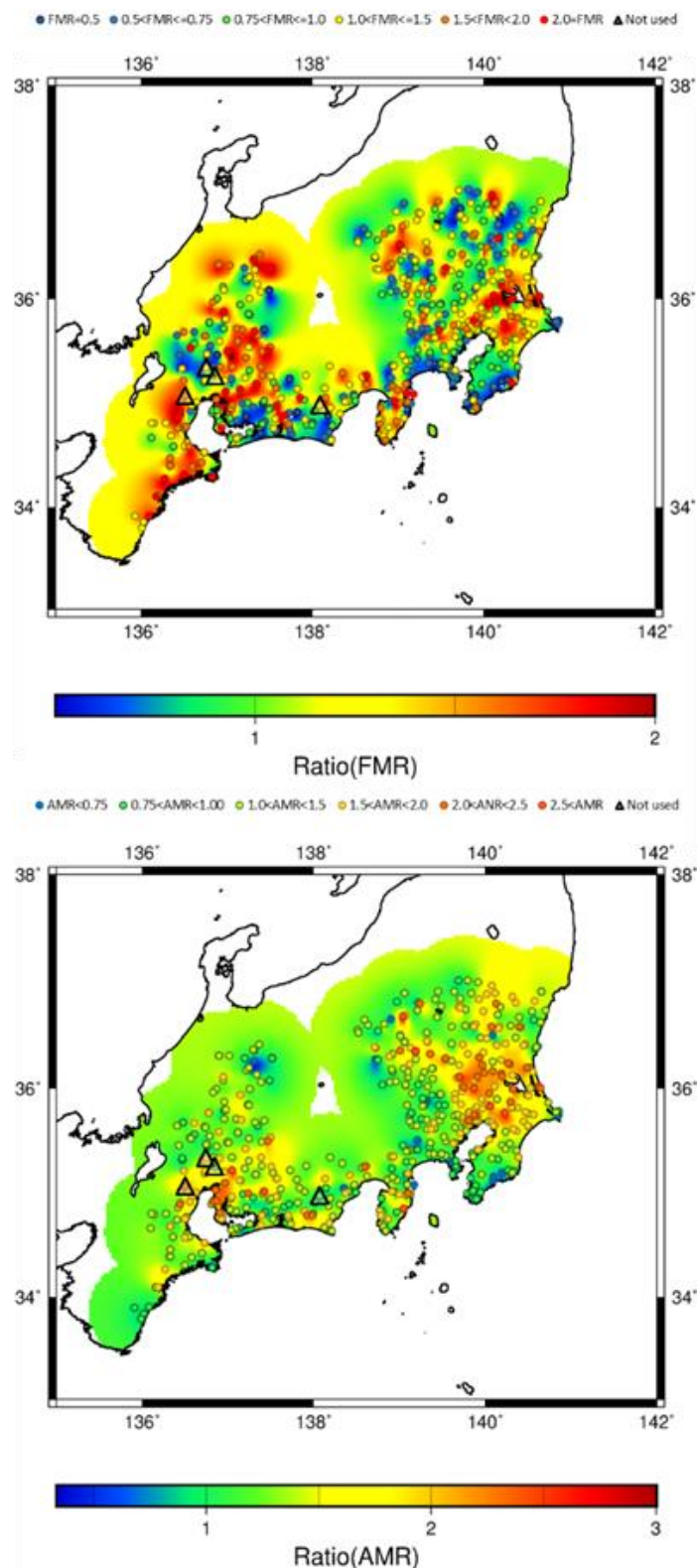


Figure 4.13. Interpolated contour maps of *FMR* (top) and *AMR* (bottom) after the Step-2 interpolation without four points shown by triangles. Inside the triangles interpolated values at these sites are shown by color-coded circles

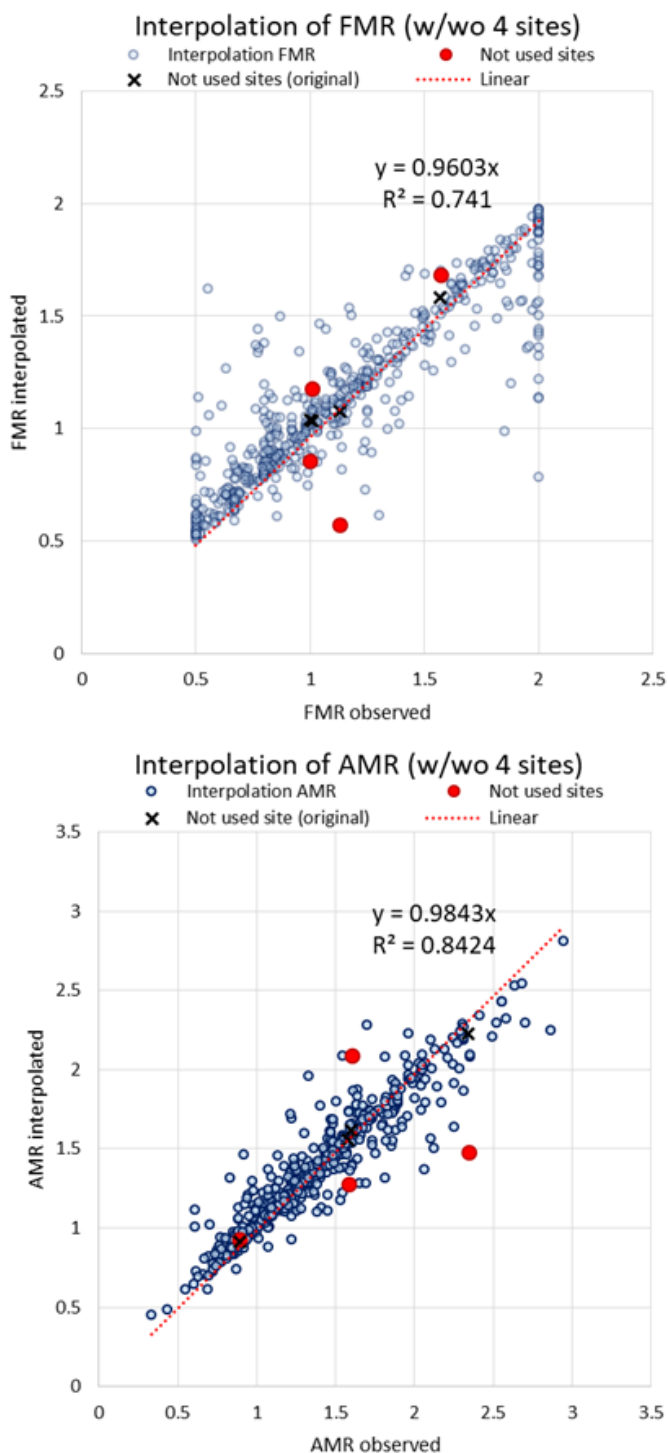


Figure 4.14. Comparison of the original FMR and AMR used as targets of interpolations and those of interpolated values in Step-2 with and without four example sites in Figure 4.5. Black crosses are original values at four sites and red circles are interpolated values without referring to those original values, that is to say, purely interpolated values. Except for one site for FMR our interpolation scheme works.

Finally, we compare the corrected hSAF at those four sites not used in the spatial interpolation as references but used as the targets of the interpolation with the observed hSAF in Figure 4.15. Although the corrections by the original *FMR* and *AMR* seen in Figure 4.5 are much better than the corrections by these interpolated *FMR* and *AMR* in this figure, the interpolated corrections still make theoretical hSAF closer to the observed hSAF.

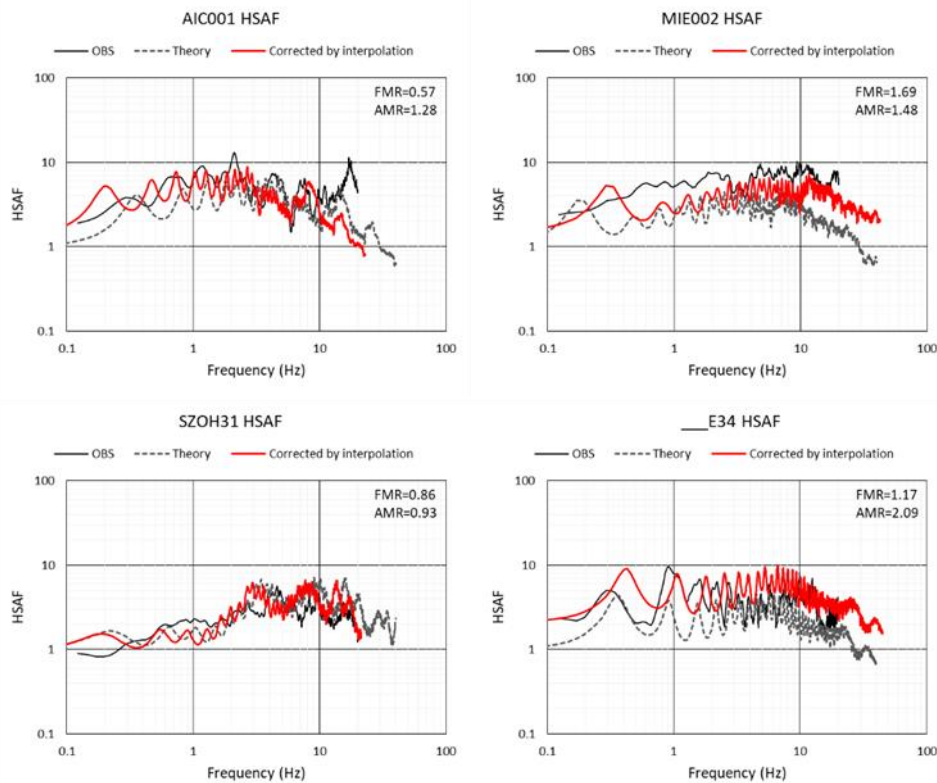


Figure 4.15. Modified hSAF (HSAFmod) by using FMR and AMR after interpolation (without using these four site) in comparison with observed hSAF (HSAFobs) extracted by GIT and 1D theoretical hSAF (HSAFthe) from the velocity structure taken from UVM. The values of FMR and AMR by interpolation for each site are shown in the upper-right corner.

4.6 Conclusions

In order to evaluate an equivalent 1D S-wave site amplification factor at an arbitrary point, we propose an empirical method of correction on to the theoretical site amplification factor calculated from the unified velocity model of NIED for the Kanto and Tokai regions. First, we check how well the current unified velocity model in Japan can reproduce horizontal site amplification factors derived from the observed strong motions in the form of the equivalent 1D S-wave theoretical transfer functions at the nearest grid of every 250 m. We find that at about one-half of the sites the calculated 1D amplification factors show more or less acceptable fit to

the observed ones, however, they tend to underestimate the observed amplifications in general. Therefore, we propose a simple, empirical method to fill the gap between the observed site amplification factors and the calculated ones based on the frequency and amplitude modification ratios. Once we obtain these modification ratios, we can interpolate them in space to obtain them at an arbitrary point. Validation examples show that our proposed method effectively predict better site amplifications than the direct substitute of theoretical amplification factors at a site without observed data.

In the future investigation, we will apply the proposed correction method to the sites where we have observed records of either earthquakes or microtremors but we do not include them in the delineation of the modification ratios in order to further validate the effectiveness of the proposed method.

Acknowledgments

This study has used the strong-motion observation records from the K-NET and KiK-net of the National Research Institute for Earth Science and Disaster Resilience (doi: 10.17598/NIED.0004) as well as the seismic intensity (Shindo-kei) network of the Japan Meteorological Agency (<https://www.jma.go.jp/jma/indexe.html>, last accessed November 2020). A part of this study was supported by the Japan Society for the Promotion of Science (JSPS) Kakenhi Grant-in-Aid for Basic Research (B) Number 19H02405. Continuous support from Hanshin Consultants Co., Ltd is highly appreciated.

References

- Andrew D J: Objective determination of source parameters and similarity of earthquakes of different size, *Earthquake Source Mechanics* (eds. S. Das, J. Boatwright and C. H. Scholz), American Geophysical Union, Washington, D.C., 1986. doi: 10.1029/GM037p0259.
- Aoi S, Obara K, Hori S, Kasahara K, and Okada Y: New strong-motion observation network: KiK-net. *Eos Transactions, AGU*. 2000;81: 329.
- Bard P-Y and Bouchon M: Seismic response of sediment-filled valleys, Part I: The case of incident SH waves, *Bull. Seism. Soc. Am.* 1980;70, 1263–1286.
- Borcherdt R D: Effects of local geology on ground motion near San Francisco Bay, *Bull. Seism. Soc. Am.*, 1970;60, No.1, 29-61.
- Haskell N A: Crustal reflection of plane P and SV waves, *J. Geophy. Res.* 1962;67, 4751-4767.
- The Headquarters for Earthquake Research Promotion: Modeling concept of subsurface structures from seismic bedrock to ground surface, <https://www.jishin.go.jp/evaluation/> strong motion/underground model/ (in Japanese) [accessed November 20, 2020].

- Kawase H, and Aki K: A study on the response of a soft basin for incident S, P, and Rayleigh waves with special reference to the long duration observed in Mexico City, Bull. Seism. Soc. Am., 1989:79, 1361–1382.
- Kawase H and Aki K: Topography effect at critical SV-wave incidence: possible explanation of damage pattern by the Whittier Narrows, California, earthquake of 1 October 1987, Bull. Seism. Soc. Am. 1990:80, 1-22.
- Kawase H: The cause of the damage belt in Kobe: “The basin-edge effect”, Constructive interference of the direct S-wave with the basin-induced diffracted/Rayleigh waves, Seismo. Res. Lett., 1996:67, 25–34.
- Kawase H and Matsuo H: Amplification characteristics of K-NET, KiK-net, and JMA Shindokey network sites based on the spectral inversion technique, 13th World Conf. on Earthquake Engineering, Vancouver, Canada, 2004: Paper No. 454.
- Kawase H and Matsuo H: Relationship of S-wave velocity structures and site effects separated from the observed strong motion data of K-NET, KiK-net, and JMA Network, J. Japan Assoc. Earthq. Eng., 2004:4(4), 126-145 (in Japanese with English abstract).
- Kawase H: Site effects derived from spectral inversion method for K-NET, KiK-net, and JMA strong-motion network with special reference to soil nonlinearity in high PGA records, Bull. Earthq. Res. Inst., Univ. Tokyo, 2006:81, 309–315.
- Kawase H, Sánchez-Sesma F J, and Matsushima S: The optimal use of horizontal-to-vertical spectral ratios of earthquake motions for velocity inversions based on diffuse-field theory for plane waves. Bull. Seism. Soc. Am. 2011:101, 2011–2014.
- Kawase H, Nagashima F, Nakano K, and Mori Y: Direct evaluation of S-wave amplification factors from microtremor H/V ratios: Double empirical corrections to “Nakamura” method, Soil Dyn. Earthq. Eng. 2018:126, doi: 10.1016/j.soildyn.2018. 01.049.
- Ito E, Nakano K, Nagashima F, and Kawase H: A method to directly estimate S-wave site amplification factor from Horizontal-to-Vertical spectral ratio of earthquakes (eHVSRs), Bull. Seism. Soc. Am., 2020:110(6): 2892–2911, doi:10.1785/0120190315.
- Iwata T and Irikura K: Source parameters of the 1983 Japan-Sea earthquake sequence, J. Phys. Earth, 1986:36, 155-184.
- Matsuoka M and Midorikawa S: GIS-based seismic hazard mapping using the digital national land information, Proc. 9th Japan Earthq. Eng. Symp., 1994: E-331-E-336 (in Japanese with English abstract).
- Nagashima F, Matsushima S, Kawase H, Sánchez-Sesma F J, Hayakawa T, Satoh T, and Oshima M: Application of horizontal-to-vertical (H/V) spectral ratios of earthquake ground motions to identify subsurface structures at and around the K-NET site in Tohoku, Japan, Bull. Seism. Soc. Am. 2014:104, 2288-2302, doi: 10.1785/0120130219.
- Nagashima F, Kawase H, and Matsushima S: Estimation of horizontal seismic bedrock motion from vertical surface motion based on horizontal-to-vertical spectral ratios of earthquake

motions, Proc. of 16th World Conf. Earthq. Eng., Santiago Chile, 9–13 January 2017, Paper N°3685.

Nakano K, Matsushima S and Kawase H: Statistical properties of strong ground motions from the generalized spectral inversion of data observed by K-NET, KiK-net, and the JMA Shindo-kei Network in Japan, Bull. Seism. Soc. Am., 2015;105: 2662-2680, doi:10.1785/0120140349.

Nakano K, and Kawase H: Source parameters and site amplifications estimated by generalized inversion technique: Focusing on the 2018 Hokkaido Iburi-Tobu earthquake, Earth Planets Space 2019;71, 66, doi: 10.1186/s40623-019-1047-1.

Nakano K: Strong-motion prediction method based on the spectral inversion, Ph.D. Dissertation, Graduate School of Engineering, Kyoto University, 2020 (in Japanese).

NIED: J-SHIS [Internet]. 2020. Available from: <http://www.j-shis.bosai.go.jp/en/> [Accessed: 2020-11-24]

Renka, R : Algorithm 790: CSHEP2D: Cubic Shepard Method for Bivariate Interpolation of Scattered Data, ACM Transactions on Mathematical Software, 1999;25, No. 1, 70-73, doi:10.1145/305658.305737.

Senna S, Maeda T, Inagaki Y, Suzuki H, Matsuyama H and Fujiwara H: Modeling of the subsurface structure from the seismic bedrock to the ground surface for a broadband strong motion evaluation, J. Disaster Res., 2014;8, No.5, 889-903.

Senna S, Wakai A, Yatagai A, Jin K, Matsuyama H, Suzuki H and Fujiwara H: Modeling of the subsurface structure from the seismic bedrock to the ground surface for a broadband strong motion evaluation in Japan, Proc. of 7th Int. Conf. of Earthquake and Geotechnical Engineering, Malta, 2019.

Sezawa K and Kanai K: Possibility of free oscillations of strata excited by seismic waves, Bull. Earthq. Res. Inst. 1930;8, 1-11.

Smith F H W and Wessel P: Gridding with continuous curvature splines in tension, GEOPHYSICS, 1990;55, Issue 3, doi:10.1190/1.1442837.

Tsai N C: A note on the steady-state response of an elastic half-space, Bull. Seism. Soc. Am., 1970;60, No. 3, 795-808.

Wakai A, Senna S, Jin K, Yatagai A, Suzuki H, Inagaki W, Matsuyama H, and Fujiwara H: Modeling of subsurface velocity structures from seismic bedrock to ground surface in the Tokai region, Japan, for broadband strong ground motion prediction, Journal of Disaster Research 2019;14, No.9, 1140-1153.

Wessel P, Smith W H F, Scharroo R, Luis J F, and Wobbe F, Generic Mapping Tools: Improved version released, EOS Trans. AGU, 2013;94, 409-410.

Zhao J: Geometric spreading functions and modeling of volcanic zones for strong-motion attenuation models derived from records in Japan, Bull. Seism. Soc. Am. 2010;100(2): 712–732.

Zhu C, Pilz M, and Cotton F: Which is a better proxy, site period or depth to bedrock, in modelling linear site response in addition to the average shear-wave velocity?, Bull. Earthq. Eng., 2020:18, 797–820, doi: 10.1007/s10518-019-00738-6.

Part II

Research on Complex Source Modeling for Predicting Realistic Strong Ground Motions

This part explains the method for modeling complex rupture process of source reflected the knowledge accumulated after the 2011 off the Pacific coast of Tohoku Earthquake.

Chapter 5

Strong Motion Simulation for the 1944 Tonankai Earthquake Based on the Statistical Green's Function Method and Stochastic Representation of Complex Source Process

Abstract

The precise evaluation of source, path, and site terms in a broad-band frequency range is indispensable for quantitative prediction of strong motions. We have conducted the generalized spectral inversion on strong motions in Japan to delineate both the spectral amplitude and phase characteristics for statistical Green's functions. To predict mega-thrust earthquakes, we also need to model a kinematic source with stochastic representation of slip and rupture velocity on the fault surface. In this preliminary study we first report the basic features of our statistical Green's functions used for summation. We then show how to construct a kinematic source with distinctive strong-motion generation areas with spatially random slip and rupture velocity variations. After the summation we found that the PGAs and PGVs of synthetics for the M_w8.0 1944 Tonankai earthquake are in good agreement with those of the empirical formula. We see relatively small effects of the random slip distribution.

5.1 Introduction

The quantitative strong motion prediction with a source- and site-specific scheme is very important for mitigation of earthquake disaster and seismic design of important structures. It is especially true in Japan where large mega-thrust earthquakes are expected to occur within coming 30 years along the Nankai Trough on the subduction interface between the Japan Islands and the Philippine Sea Plate. Strong motion prediction in a broad-band frequency range from a large fault is not an easy task because we need to represent complex nature of source, path, and site.

There are several ways to simulate strong motions as waveforms on the surface at a target site located at an arbitrary position. One is the theoretical method in which wave generation at the source, propagation from the source to the site, and local site amplification near the site are represented by the numerical modeling of the medium and wave generation and propagation inside. In this method we need a good physical model of the medium to represent wave propagation phenomena in the whole path from the source to the target site. In other words, we need to calculate first the Green's function for a point source on the fault surface. Because of the limit both on the computational resource and the accuracy of geophysical model that we can use, the frequency coverage of the theoretical method is usually limited in a lower frequency range below 1 Hz, although we have several recent attempts to expand the limit up to 5 Hz (e.g., Roger et al., 2019).

Another method is an empirical one in which we use observed ground motions of a small earthquake as a substitute of the Green's function and sum up all the contributions from the elemental sources on the fault surface. It is called the empirical Green's function method (EGF). EGF has been proved to be good at reproducing the observed mainshocks if we use good aftershock records (e.g., Kamae and Irikura, 1998; Kamae and Kawabe, 2004).

If there are no appropriate small earthquake records to be used as an empirical Green's function, we first generate synthetic waveforms from a lot of small earthquakes and sum up them to represent a large event. It is called the statistical Green's function method (SGF). SGF is very useful for prediction of strong motions for the events that have not occurred yet or those that had not been observed by the strong motion instruments.

Because the frequency range for the theoretical method with coherent nature is limited to the lower end, usually below 1 Hz or lower, whereas the valid range for EGF or SGF with inherent nature of stochasticity should be higher than that, a hybrid scheme for a theoretical method with EGF or SGF are used naturally, as has been used in the current national project for strong motion predictions with specific sources (J-SHIS, 2020).

However, after the deployment of the dense national strong motion observation networks, namely K-NET, KiK-net, and JMA Shindohei network, a significant number of data has been accumulated, and therefore, we can use these data to construct a model of SGF in a broad-band frequency range. As long as we can generate the SGF for an arbitrary size of a small earthquake at an arbitrary location in a frequency range of interest, namely from 0.1 Hz to 20 Hz, we need not to use a hybrid scheme (e.g., Ito and Kawase, 2001; Ho and Kawase, 2007). This means that

we do not need to spend our time to construct a physical model for the complex earth.

Thus, we have been analyzing these strong motion data in Japan by using the generalized spectral inversion technique (GIT, Andrew, 1986; Iwata and Irikura, 1988) to delineate statistical properties of the three major terms, namely, the source term, the path term, and the site term (Kawase and Matsuo, 2004; Nakano et al., 2015; Nakano, 2020). The novelty of our approach is that the hypothesized (i.e., deconvolved) seismological bedrock spectra at a reference site, YMGH01, are used as a reference to calculate site amplification factors at all the observed sites. Such a separation of observed spectra into three major terms is sufficient to generate SGF at these sites.

However, strong motion simulations for a mega-thrust earthquake on the subduction zone need complex source representation for realistic synthetics. Before the 2011 Off the Pacific Coast of Tohoku earthquake of M_w 9.0 we do not have a concrete picture of the source complexity. The source inversions of this earthquake provided us a lot of information useful for the source representation indispensable for broad-band simulations of future earthquakes (e.g., Asano and Iwata, 2012; Kurahashi and Irikura, 2013). Therefore, whenever we predict strong motions for a mega-thrust earthquake after Tohoku event, we must reflect important characteristics on the complex nature of its fault rupture process.

Considering the fact that these mega-thrust events along the Nankai Trough have been occurring periodically (e.g., Ando, 1975), we need to learn from previous experiences as much as we can. Before the nation-wide deployment of strong motion networks, however, delineation of the complex rupture process during the past events are quite difficult because we do not have sufficient constraints from observations. To this end, we would like to use damage statistics of wooden houses, not the seismic intensity, as the physical constraints for the source complexity based on the simulated (reproduced) ground motions together with the structural damage prediction model (e.g., Nagato and Kawase, 2004).

In what follows we first introduce fundamental characteristics of the SGF derived from the GIT applied to the strong motion records by K-NET, KiK-net, and the JMA Shindokey network (Nakano et al., 2015; Nakano, 2020). Then, we introduce a stochastic representation in a kinematic source model for a complex rupture scenario of Tonankai earthquake with the size of 1944 event based on the strong-motion generation areas (SMGAs) with spatially-random perturbation in both slip and rupture velocity. Finally, we calculate synthetic waveforms in the vicinity of the fault area and confirm their appropriateness in term of their average characteristics in the strength indices. We will use these acceleration synthetics to simulate observed damage of wooden houses during the 1944 Tonankai earthquake.

5.2 Statistical Green's function

5.2.1 Outline of GIT

In this section we briefly introduce the observed horizontal site amplification factor (HSAT) and vertical one (VSAT) derived from GIT (Nakano et al., 2015; Nakano, 2020). Here

we only introduce their basic aspects since we are using their results as a starting point.

Based on the ordinary non-parametric GIT concept, the S-wave Fourier spectrum of the horizontal motion, $F_{S_{-}ij}$, of earthquake i observed at site j would be decomposed into the common logarithmic sum of the source term $S_{S_{-}i}$, the path term $P_{S_{-}ij}$, and the horizontal site amplification factor at site j , $H_{S_{-}j}$, as shown in the following equation:

$$\log F_{S_{-}ij} = \log S_{S_{-}i} + \log P_{S_{-}ij} + \log H_{S_{-}j} \quad (5.1)$$

Likewise, the S-wave Fourier spectra of the vertical motion, $G_{S_{-}ij}$, is decomposed into the following equation:

$$\log G_{S_{-}ij} = \log S_{S_{-}i} + \log P_{S_{-}ij} + \log V_B H_B R + \log V_{S_{-}j} \quad (5.2)$$

These equations assume that ground motion is propagated as S-waves until reaching the seismological bedrock immediately below the observation site and then a part of the energy of S-waves is converted to P-waves, which are observed as vertical motion on the ground surface. Here, $V_{S_{-}j}$ is the vertical site amplification factor for site j , whereas the third term in equation (5.2), $V_B H_B R$, is a coefficient for converting horizontal (S-wave) amplitude into vertical (P-wave) amplitude, and theoretically it corresponds to the inverse of the horizontal-to-vertical amplitude ratio of the incident wave at the seismological bedrock, which would be equal to the square-root of the ratio of the P-wave velocity to the S-wave velocity on the seismological bedrock in the diffuse field regime (e.g., Kawase et al., 2011; Nagashima et al., 2014; Ito et al., 2020). This coefficient is needed because the main portion of wave energy consists of the S-waves propagated and scattered through the medium from the hypocenter to the point on the seismological bedrock immediately below the site, while $V_{S_{-}j}$ represents the vertical (P-wave) amplification factor from the seismological bedrock to the surface. Please note that HSAT and VSAT are the general terms referring to the site amplifications in the horizontal and vertical directions, while $H_{S_{-}j}$ and $V_{S_{-}j}$ are the specific terms derived from GIT.

We restricted events and sites with JMA magnitude $M_{JMA} \geq 4.5$; source depth ≤ 60 km; hypocentral distance ≤ 200 km; peak ground acceleration ≤ 2 m/s²; and number of observation sites triggered simultaneously for one event ≥ 3 . These selection criteria resulted in 77,213 event-station pairs at 2,105 sites for 967 events. Only a relatively short duration of acceleration record from the onset of the S-wave is analyzed (5 s if $4.5 < M_{JMA} \leq 6$; 10 s if $6 < M_{JMA} \leq 7$; 15 s if $7 < M_{JMA} \leq 8$). A Parzen window of 0.1 Hz is used for a minimum level of smoothing. As mentioned above, the most important feature of their GIT is that they determined the S-wave velocity structure at the reference site using the transfer function (the spectral ratio and the phase difference) between the surface and the borehole 200 m below and that the observed Fourier spectra on the surface were deconvolved to obtain the hypothesized outcrop spectra on the seismological bedrock with an S-wave velocity of 3,450 m/s. Nakano et al. (2015) and Nakano (2020) successfully separated the source spectra and path terms as evidenced by their

correspondence to the ω^2 source spectra shapes and Q values similar to the previous studies in Japan.

Figure 5.1 shows examples of the separated HSAF and VSAF at four representative sites in Mie Prefecture. We can see significant differences from site to site in HSAF. The amplitude and its fluctuation of VSAF is much smaller than HSAF, especially below 3 to 7 Hz. That is why the earthquake horizontal-to-vertical spectral ratio, eHVSR, tends to be similar to HSAF until the fundamental peak frequency of VSAF. However, to get HSAF from eHVSR, we need to correct VSAF, as recently proposed by Ito et al. (2020). Please note that VSAFs shown in Figure 5.1 are the site amplification factors of the vertical component with respect to the horizontal component on the seismological bedrock, referred to as VSAF* in Ito et al. (2020). Because we are specifically predicting the S-wave spectra radiated from the source, we need to use the relative amplification factors of the vertical component to the S-wave input on the seismological bedrock.

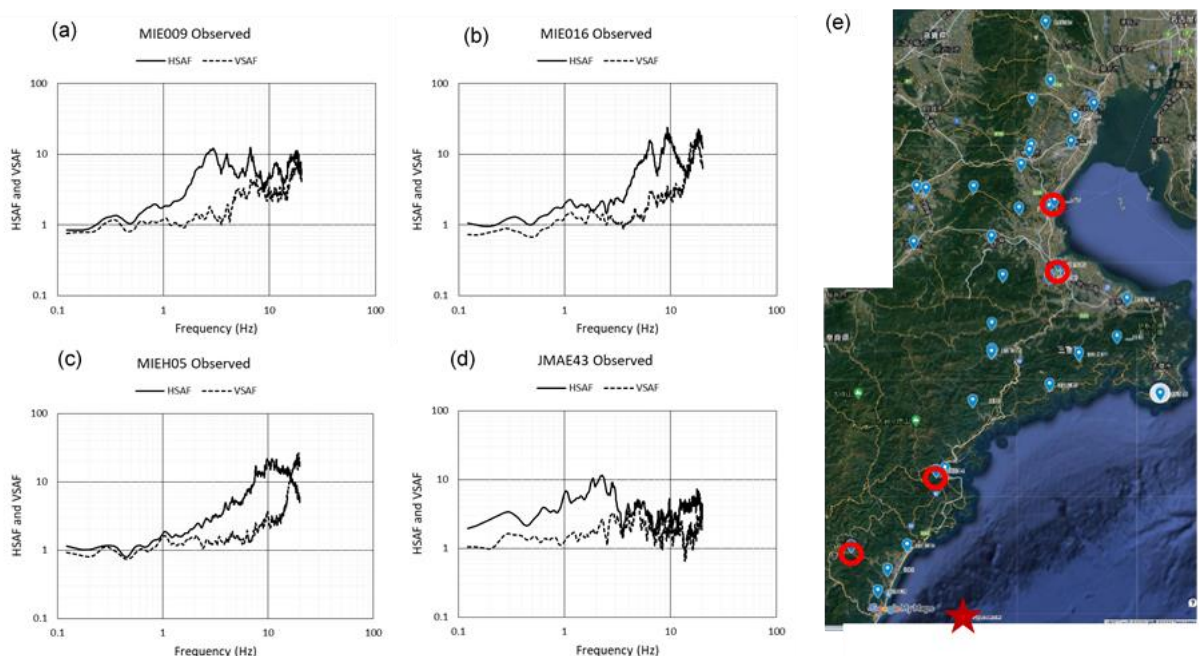


Figure 5.1. Site amplification factors (HSAF and VSAF) extracted from the S-wave portions of records observed at K-NET, KiK-net, and JMA Shindo-kei network used in the SGF simulation (Nakano et al., 2015) at four sites in Mie Prefecture. A map on the right shows their locations, with a rupture initiation point (\star).

5.2.2 WSR to account for basin effects

One of the novelties of our SGF based on GIT is the back calculation of the site factors for the whole duration. When our target sites are located within a sedimentary basin, we see additional amplification due to the basin-induced surface waves generated at the edge of a 2D or

3D basin (e.g., Bard and Bouchon, 1980; Kawase and Aki, 1989; Kawase, 2003). They are quite significant in the lower frequency range below 1 Hz, especially inside soft and large basins. However, if we use directly the whole duration of motion as the target of the GIT analysis, the resultant attenuation would be totally distorted. When we use the whole duration, the Fourier spectra inside a basin but away from the source become larger than those closer to the source but outside of a basin, we cannot see any attenuation in proportion to the distance, and therefore, we will have negative Q values.

To account for the effects of the basin-induced surface waves inside sedimentary basins, Nakano et al. (2019) and Nakano (2020) proposed to use an empirical ratio called the whole-wave-to-S-wave ratio (WSR), where the spectral ratios of the whole duration with respect to the S-wave portion with relatively short duration (5 to 15 s as mentioned above) are averaged over all the observed events at a site. They found that the WSR tends to be close to 1 irrespective of frequency for a site on a hard rock, whereas it can easily exceed 10 in the lower frequency range for a site inside a soft sedimentary basin. Even for such a site, WSR will converge to 1 in the frequency range higher than 1 to 2 Hz. In Figure 5.2 HSAFs for the S-wave portions and those for the whole duration are compared. MIE009, MIE016, and MIEH16 show normal characteristics of the sites outside of a sedimentary basin, whereas JMAE43 shows those inside a basin. Simply WSR is the spectral ratios between red and black lines in this figure.

Because the spatial variation of WSR at one specific frequency highly correlates with that of the basin depths, as seen in Nakano et al. (2019), Nakano (2020) proposed a scheme to interpolate WSRs to make it possible to calculate a scenario-type hazard map with much higher spatial density (in 250 m grid) than those of strong motion observation sites. The interpolation scheme utilized the surface function of GMT (Smith and Wessel, 1990), together with the code developed by Renka (1999). This WSR correction is a simple, empirical way to account for the additional amplifications due to soft sedimentary basins. In Figure 5.3 we plot the original WSRs for HSAF all over Japan and those interpolated based on the scheme proposed by Nakano (2020) at 0.3174 Hz. We can see how the WSR corrections are significant in the lower frequency range inside the large sedimentary basins, especially in the Eastern Japan in the east of the Itoigawa-Shizuoka tectonic line.

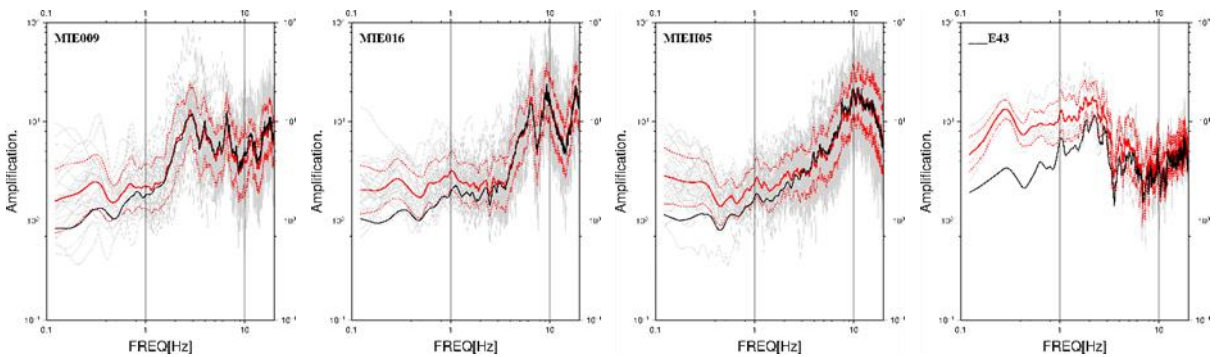


Figure 5.2. HSAFs for the S-wave portion shown in Fig.1 (black lines) and those for the whole duration (red lines), together with its deviations (red dotted lines) and individual ones (Nakano, 2020).

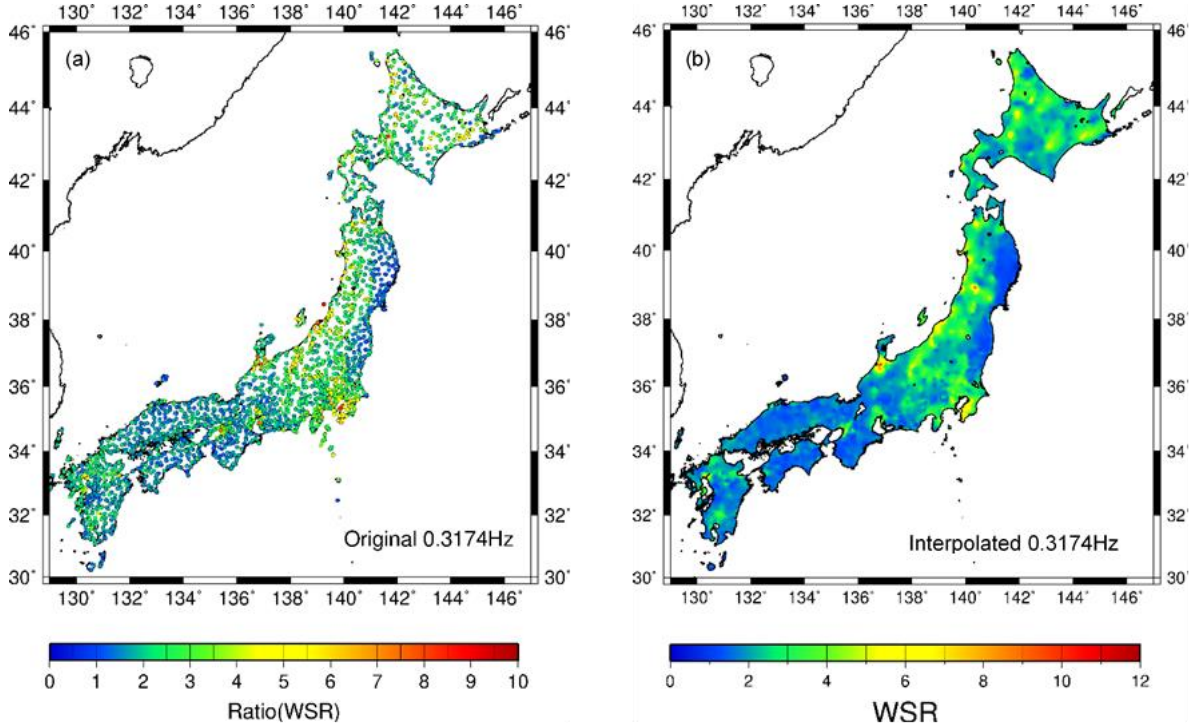


Figure 5.3. Comparison of (a) WSRs calculated from the observed data and (b) those interpolated to higher spatial resolutions (Nakano, 2020).

5.2.3 Tgr modeling

To calculate synthetic waveforms for small to moderate-sized earthquakes as SGFs, we need to specify their phase information or envelope functions to constrain the time-varying characteristics of synthetic SGFs. It is desirable to use phase spectral information because we can account for the frequency dependence of the envelope shape. Thus we follow the procedure of Nakano (2020) to model the group delay time, t_{gr} as:

$$t_{gr} = \frac{d\phi(\omega)}{d\omega}, \quad (5.3)$$

where

$$\phi(\omega) = \tan^{-1}(I(\omega)/R(\omega)), \quad (5.4)$$

and

$$t_{gr} = \frac{R(\omega) \cdot I(\omega)' - R(\omega) \cdot I(\omega)}{R^2(\omega) + I^2(\omega)} \quad (5.5)$$

Then we can model the average and variance characteristics of t_{gr} for the whole duration of observed record $\mu(f)$ and $\sigma(f)$ as

$$\mu_{ij}(f) = \mu^{Source_i}(f) + \sum_k \mu_{ij}^{pass}(f) \cdot X_{ij}^{1.9} + \mu^{Site_j}(f), \quad (5.6)$$

$$\sigma_{ij}(f) = \sigma^{Source_i}(f) + \sum_k \sigma_{ij}^{pass}(f) \cdot X_{ij}^{1.9} + \sigma^{Site_j}(f) \quad (5.7)$$

for the i -th source observed at j -th site.

We show examples of the site terms in equation (5.6) in Figure 5.4 for the same sites shown in Figures 5.1 and 5.2. Only JMAE43 site shows significantly longer durations (rate arrivals), especially in the lower-frequency range.

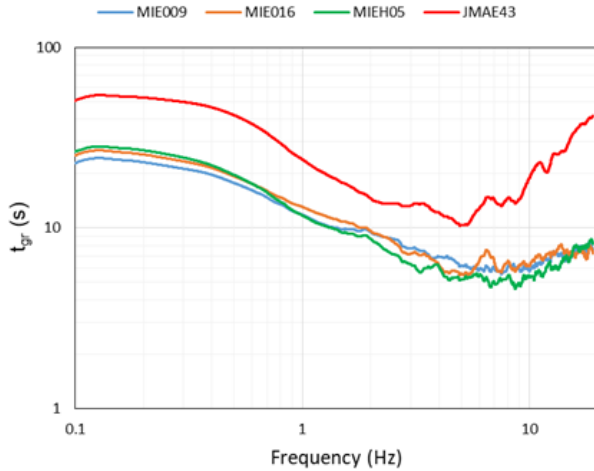


Figure 5.4. Site factors for the average t_{gr} in equation (5.6) extracted by GIT for the whole duration of records.

5.3 Stochastic Source Model

A broadband heterogeneous source model is generated for a plate boundary earthquake along the Nankai Trough by introducing fractal heterogeneity into a characterized source model consisting of a background region and a strong-motion generation region.

The gross ruptured area (i.e., the assumed fault plane) of the fault map of the Central Disaster Management Council (CDMC, 2003) is projected on the upper surface of the Philippine Sea plate of the Japan Integrated Velocity Structure Model (JIVSM; Koketsu et al., 2012) and adjusted the size to be compatible to the fault size of CDMC and to be able to include the strong-motion generation areas (SMGAs) of the Cabinet Office (2015). For the assumed SMGAs here, their areas, moments, stress parameters, rise time, and center positions are adopted from those values by the Cabinet Office (2015) as the basic model (Table 5.1). However, the shape of the SMGA is assumed to be circular, unlike those of the Cabinet Office (2015). We assumed as such because we want to use an automatic generation system for a large number of parametric studies with various locations and areas of SMGA in future. The parameters of the background region of the basic model are based on CDMC (2003). The amount of the average slip is calculated from the total moment and the fault area, similar to the method used by CDMC (2003).

Table 5.1. Fault parameters for the 1944 Tonankai earthquake (After CDMC, 2003)

	Area [km ²]	Moment [Nm]	Mw	Stress parameter [MPa]	Rise time [s]	Center Longitude	Center Latitude
SMGA 1	618.1	1.9e20	7.4	30.0	4.6	135.75	33.20
SMGA 2	619.6	1.9e20	7.4	30.0	4.6	134.90	33.70
SMGA 3	906.8	3.4e20	7.6	30.0	5.6	134.00	33.10
SMGA 4	906.3	3.4e20	7.6	30.0	5.6	133.30	32.70
Background				2.4	10.0		

The broadband source heterogeneity is calculated by randomly adding heterogeneity from about one half of the SMGA areas to several km² in size to the basic source parameter distribution consisting of the background and SMGAs, as described in Sekiguchi and Yoshimi (2010). The amplitude of fluctuation is proportional to the size of heterogeneity. We adjust the power of the fall-off in the spatial distribution of the slip heterogeneity is equal to the value obtained by Mai and Beroza (2002), that is, -1.75. The stress parameter distribution was given in proportion to the variation of the slip distribution. The rupture velocity distribution was started from a uniform distribution of 2.7 km/s and a constant amount of variation regardless of the area of the inhomogeneous patch were added and finally adjusted so that the standard deviation of the spatial variation is equivalent to the level obtained by Miyakoshi and Petukhin (2005) in their analysis of the source-inversion model. The distribution of rupture initiation times at an arbitrary point on the fault was obtained through the wave propagation analysis based on an ordinary two-dimensional finite difference method.

Figure 5.5 shows the assumed shape of the whole ruptured area and the SMGAs, whereas Figure 5.6 shows randomized rupture velocity on the stochastic fault model used for strong motion simulations, the results of which will be shown in the next section.

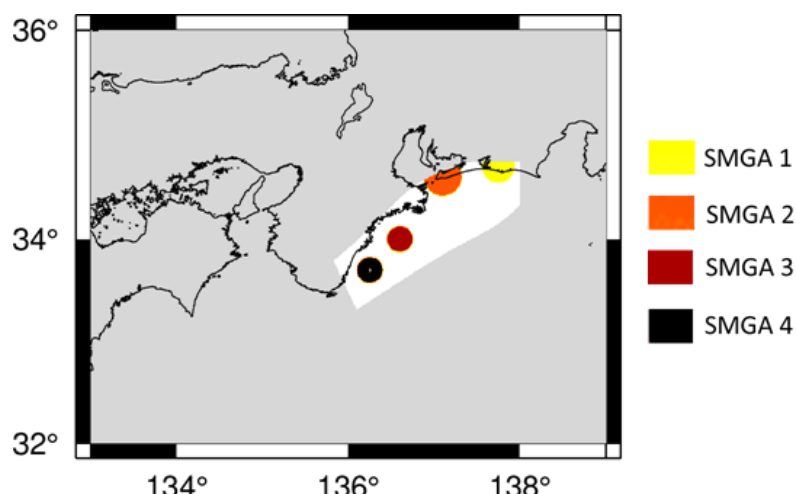


Figure 5.5. Predefined strong motion generation areas (SMGAs) and the whole fault area for the simulation of the 1944 Tonankai earthquake.

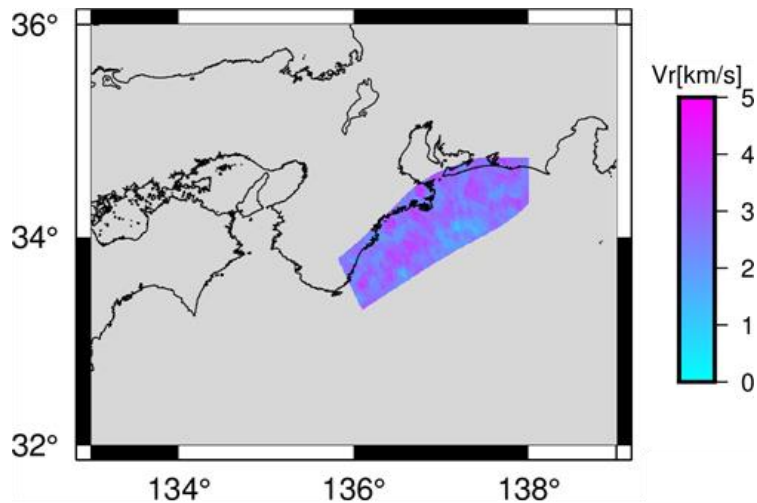


Figure 5.6. Randomized rupture velocity on the stochastic fault model of the 1944 Tonankai earthquake.

5.4 Results of Parametric Study

5.4.1 Scenario with variable slip and constant rupture velocity (CASE1)

A model with variable slip and constant rupture velocity (CASE1) yields strong motion synthetics with PGAs and PGVs that correspond well to the empirical relationship by Morikawa and Fujiwara (2013). As for the deviation, the PGAs are overestimated a little bit while the PGVs are underestimated a little bit. At JMAE43, which is in a basin, the peak of the response spectra are within 0.5~2 second. At MIE016, which is located near the fault, the response spectra are larger than ones of the strong ground motion by Ministry of Construction Notice in the short period at JMAE43.

Figure 5.7 shows attenuation of PGA & PGV in CASE1. Red circle shows PGA and PGV at each site, while the black line shows the empirical relationship from Morikawa and Fujiwara (2013) and the black dotted line shows its standard deviation. Figures 5.8, 5.9, and 5.10 show acceleration waveforms, Fourier spectra, and response spectra at JMAE43, respectively, while Figures 5.11, 5.12 and 5.13 show those at MIE016, respectively. In Figure 5.7, the horizontal axis is the minimum distance from the fault, and the vertical axis is PGA in the upper graph and PGV in the lower graph. In Figure 5.8 and Figure 5.11, the horizontal axis is time and the vertical axis is acceleration. In Figure 5.9 and Figure 5.12, the horizontal axis is frequency and the vertical axis is Fourier spectra. In Figure 5.10 and Figure 5.13, the horizontal axis is period and the vertical axis is response spectra.

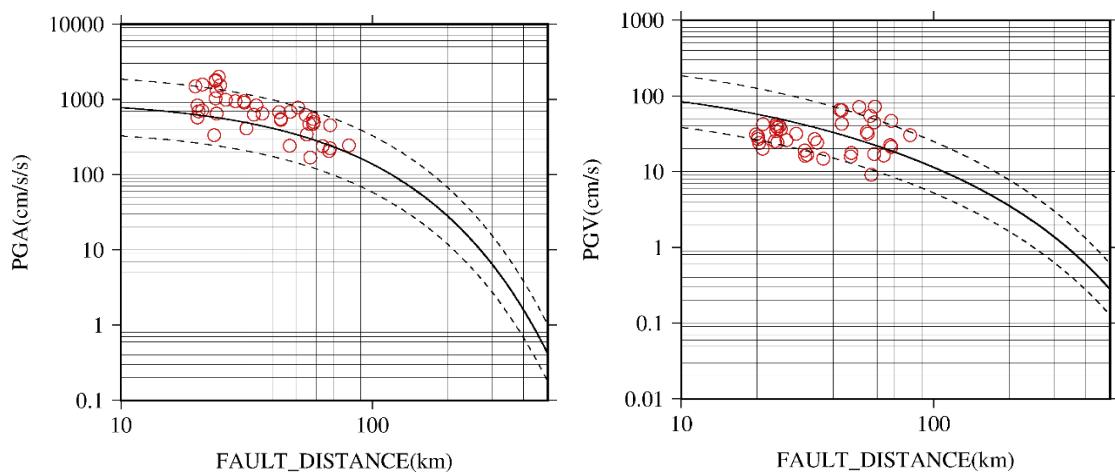


Figure 5.7. Attenuation of PGA & PGV in CASE1

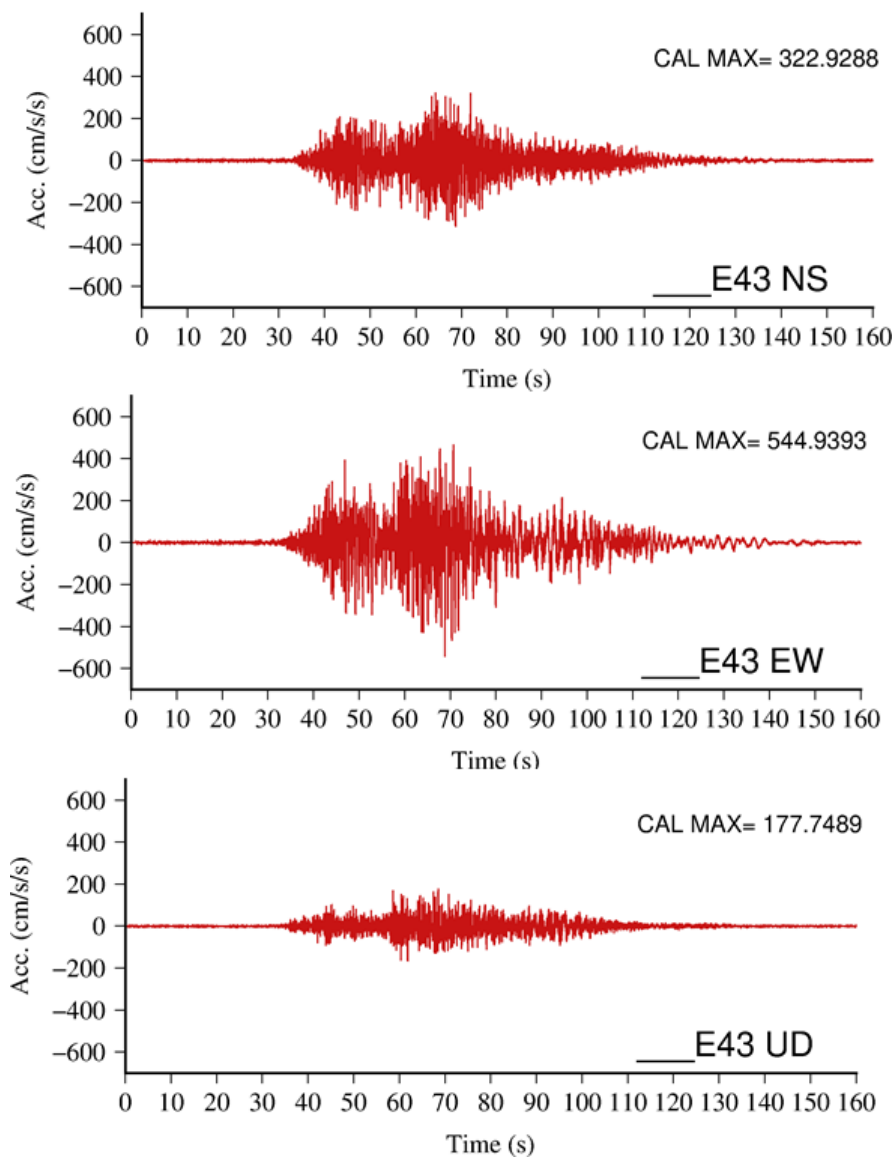


Figure 5.8. Acceleration waveforms at JMAE43 in CASE1

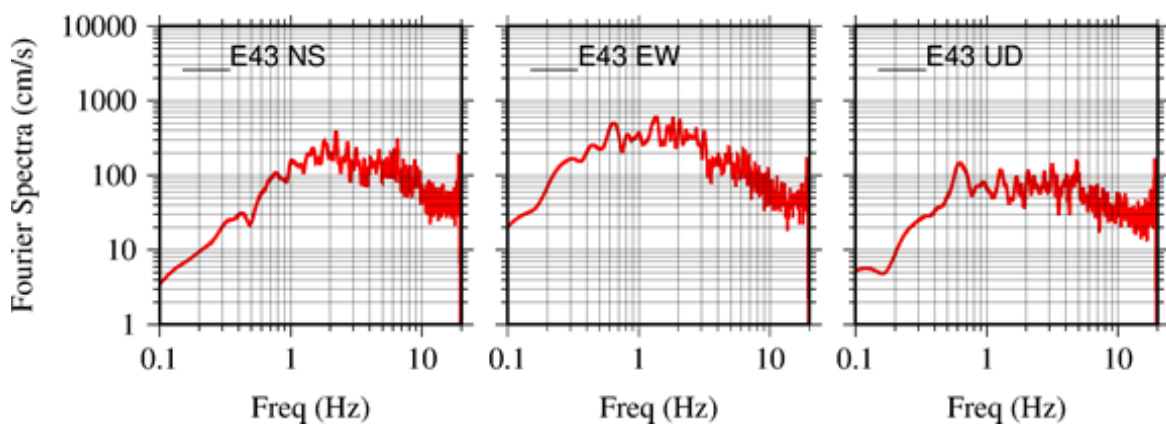


Figure 5.9. Fourier spectra at JMAE43 in CASE1

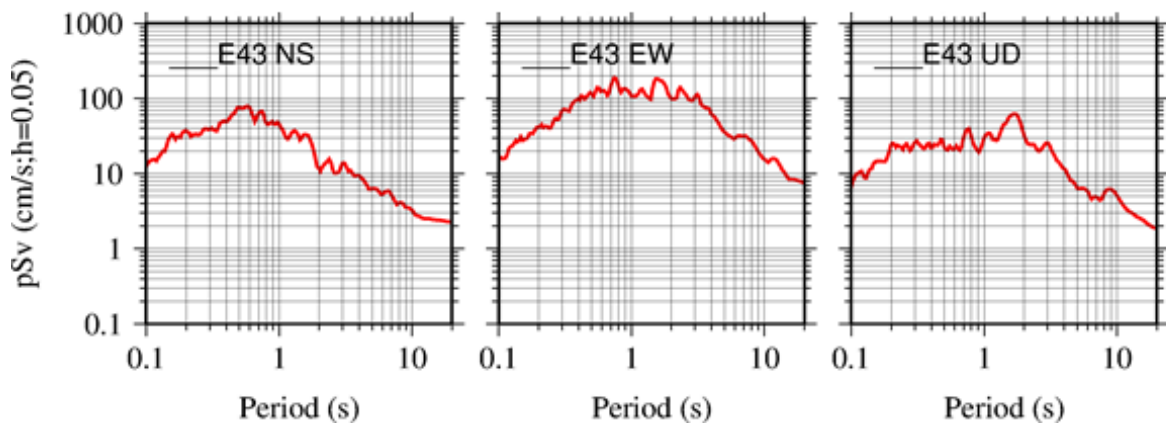


Figure 5.10. Response spectra at JMAE43 in CASE1

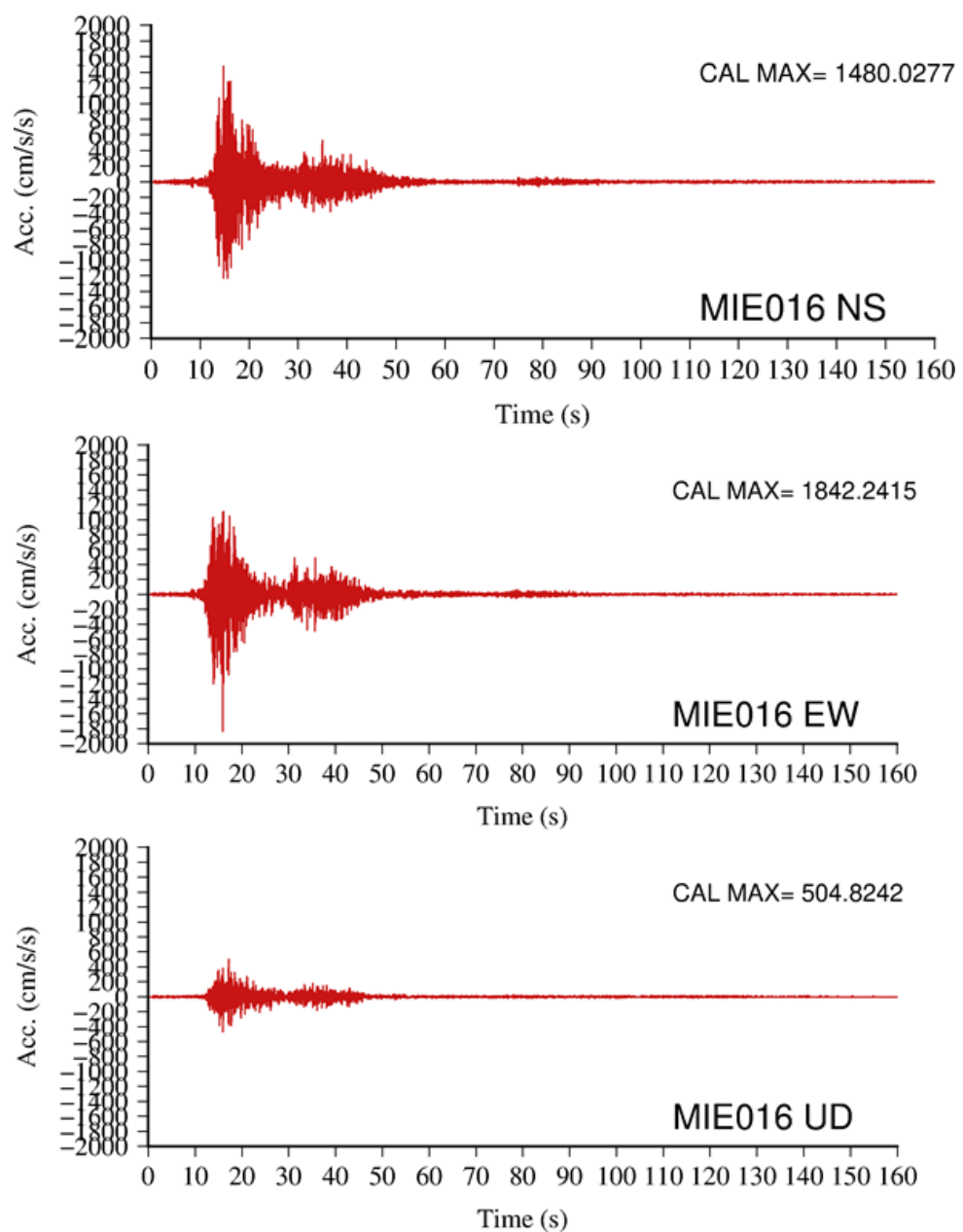


Figure 5.11. Acceleration waveforms at MIE016 in CASE1

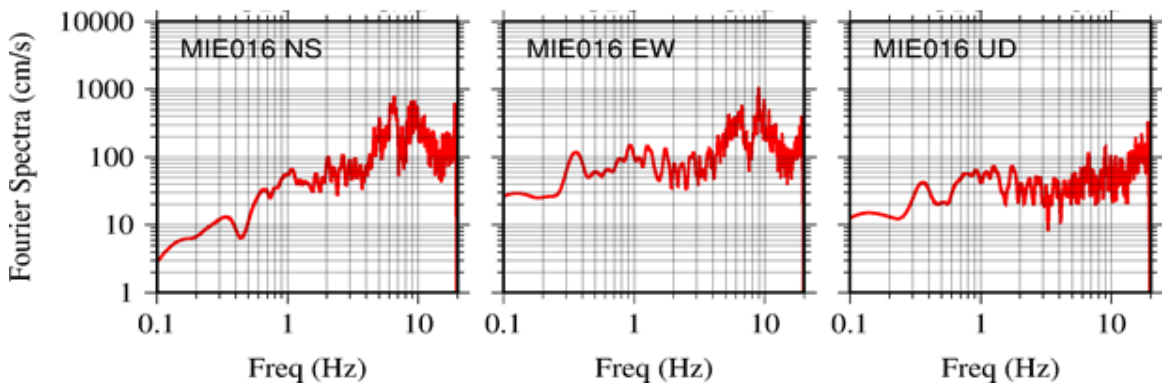


Figure 5.12. Fourier spectra at JMAE43 in CASE1

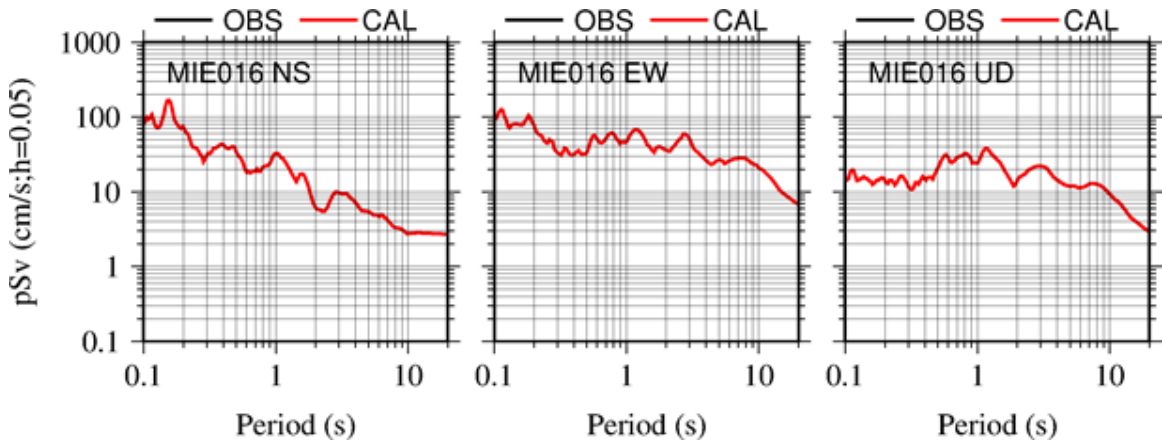


Figure 5.13. Response spectra at JMAE43 in CASE1

5.4.2 Scenario with constant slip and constant rupture velocity (CASE2)

A model with constant slip and constant rupture velocity (CASE2) yields strong motion synthetics with PGAs which correspond with the empirical relationship, but the PGVs are lower than the empirical relationship at sites near the hypocenter. At MIE016, the Fourier spectra are about the half of the one in CASE1 within 0.3~0.4Hz, where the difference between them is the most significant. The response spectra are slightly smaller for CASE2 in almost every period band, with the smallest being about one-half to two-thirds of that of CASE1 at 0.4 to 0.5 s.

Figure 5.14 shows attenuation of PGA & PGV in CASE2. Red circle shows PGA and PGV at each site, while the black line shows the empirical relationship from Morikawa and Fujiwara (2013) and the black dotted line shows its standard deviation. Figures 5.15, 5.16 and 5.17 show acceleration waveforms, Fourier spectra, and response spectra at MIE016. We do not show the results at JMA E43. The differences between CASE1 and CASE1 are not so clear.

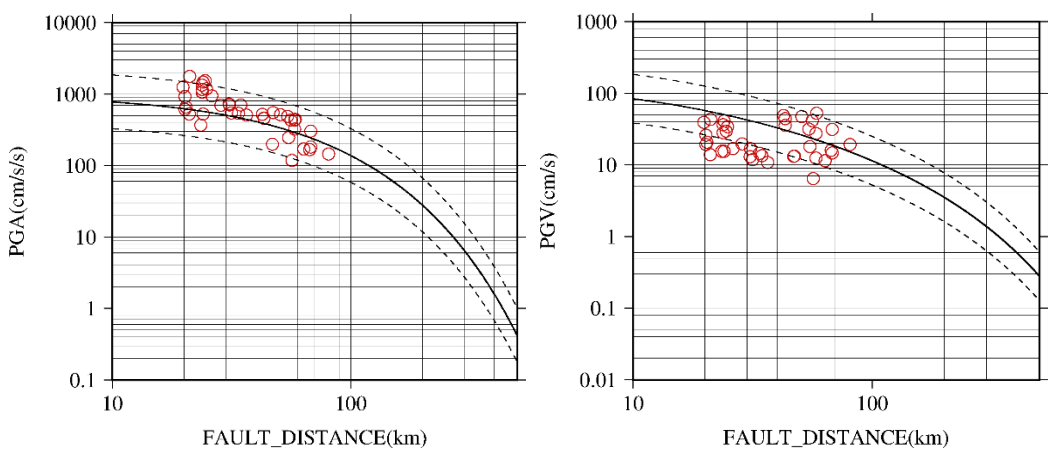


Figure 5.14. Attenuation of PGA & PGV in CASE2

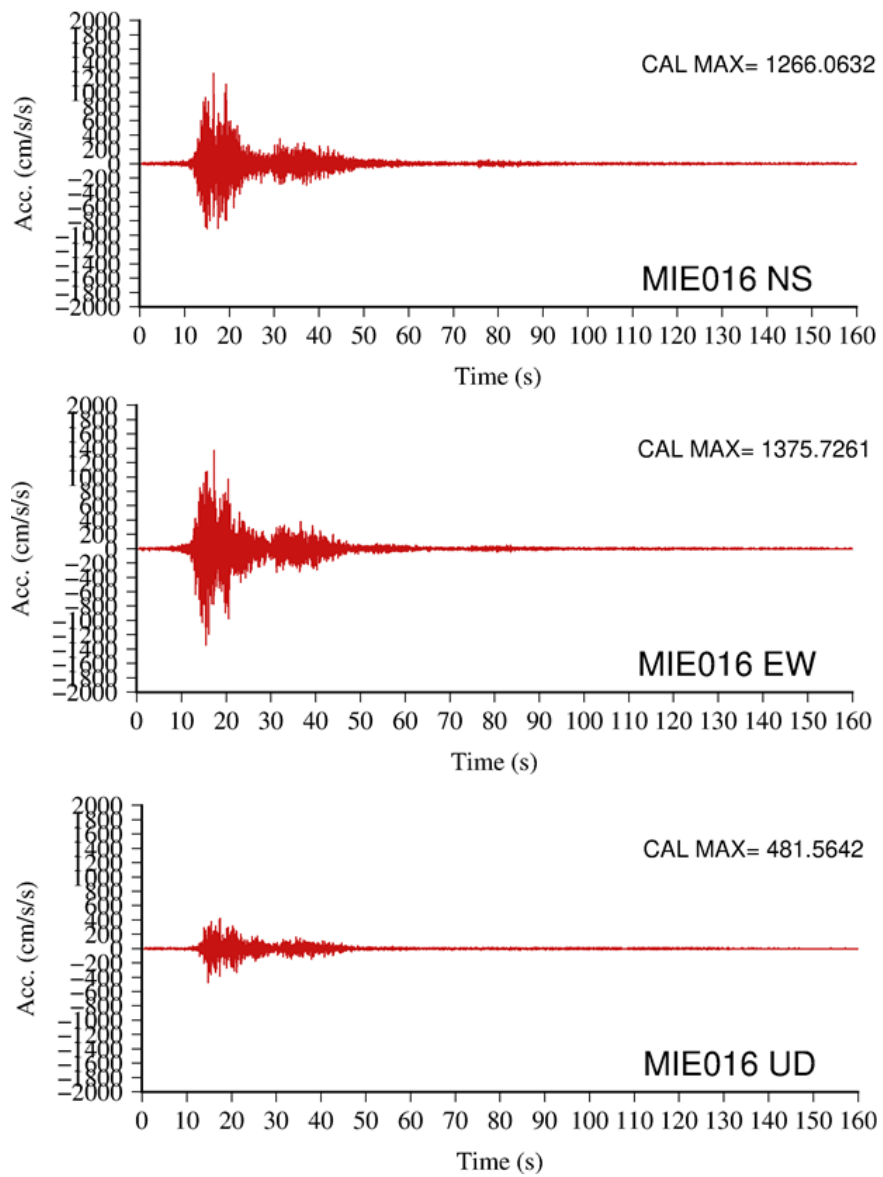


Figure 5.15. Acceleration waveforms at MIE016 in CASE2

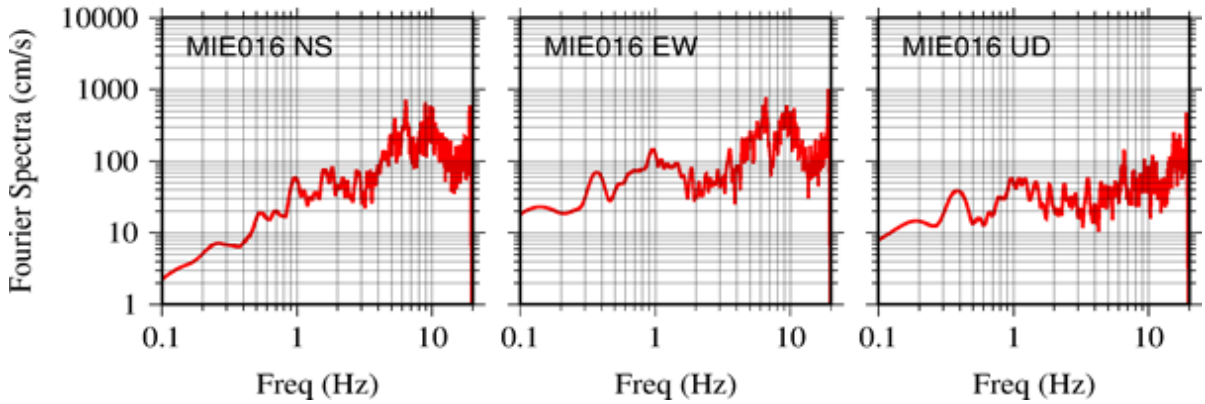


Figure 5.16. Fourier spectra at MIE016 in CASE2

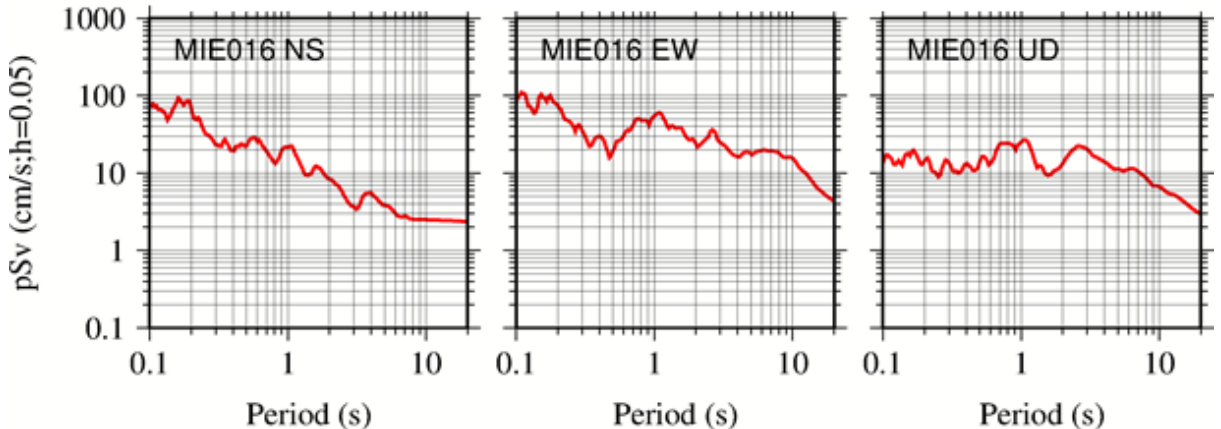


Figure 5.17. Response spectra at MIE016 in CASE2

5.4.3 Scenario with variable slip and variable rupture velocity (CASE3)

A model with variable slip and variable rupture velocity (CASE3) yields strong motion synthetics with PGAs and PGVs that corresponds well to the empirical relationship. In particular, the PGAs show more correspondence with the empirical relationship at sites near the hypocenter than those of CASE1, where the speed of rupture propagation was held constant. In the Fourier spectra, although there are some differences in each frequency, they are at the same level on average. The response spectrum also differs in some periods, but the overall response spectrum is almost the same.

Figure 5.18 shows attenuation of PGA & PGV in CASE3. Red circle shows PGA and PGV at each site, while the black line shows the attenuation curve from Morikawa and Fujiwara (2013) and the black dotted line shows its standard deviation. Figure 5.19, 5.20, and 5.21 show acceleration waveforms, Fourier spectra, and response spectra at MIE016. We do not show the results at JMA E43. The differences between CASE1 and CASE1 are not so clear.

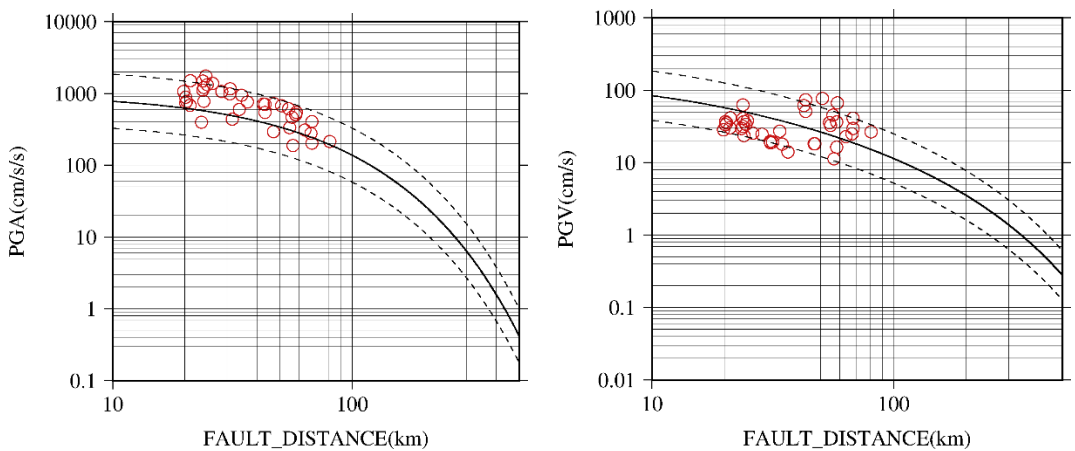


Figure 5.18. Attenuation of PGA & PGV in CASE3

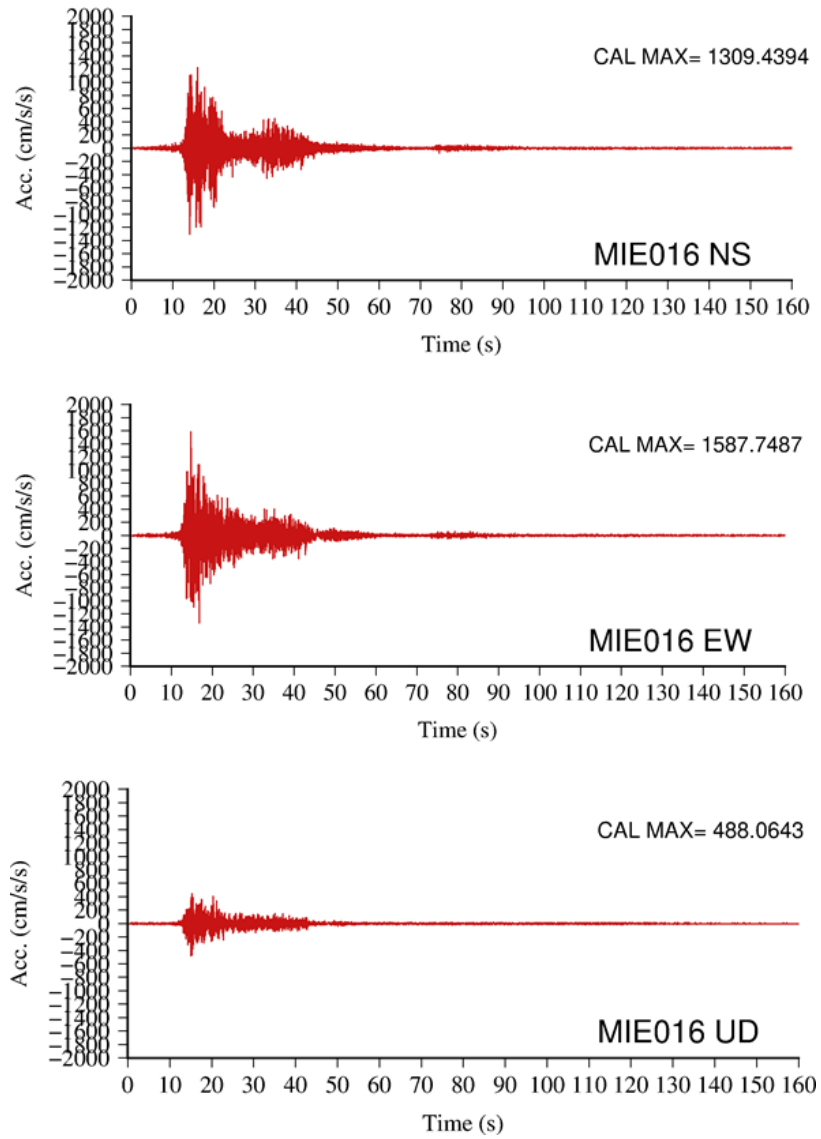


Figure 5.19. Acceleration waveforms at MIE016 in CASE3

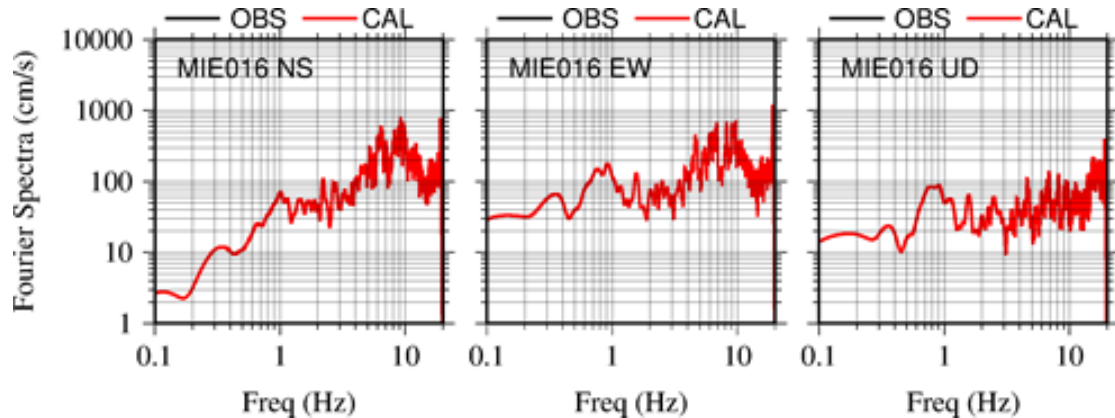


Figure 5.20. Fourier spectra at MIE016 in CASE2

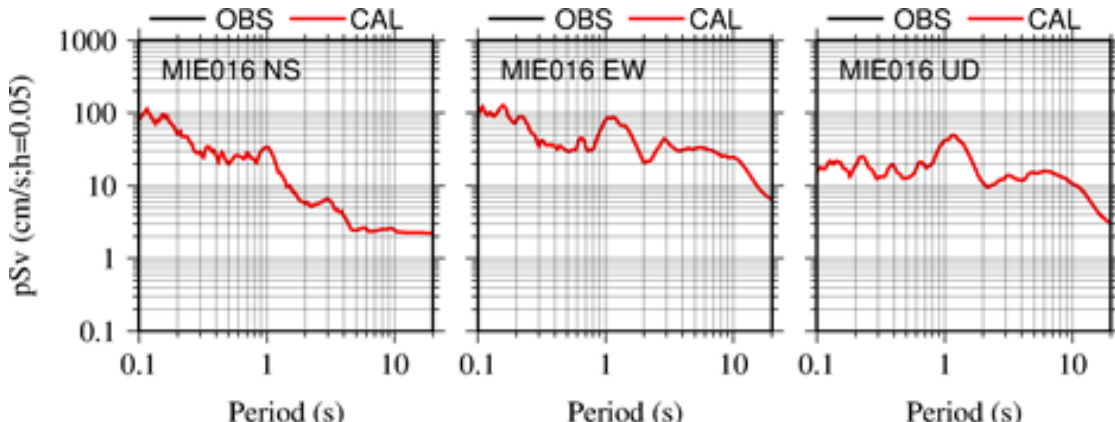


Figure 5.21. Response spectra at MIE016 in CASE2

5.5 Discussion

5.5.1 Effects of slip variation on PGA and PGV

As shown in the Sections 4.1 and 4.2, we can see relatively small difference between the simulated synthetics from CASE1 and those from CASE2 at a selected site (MIE016) near the hypocenter. The difference reflects the effect of the slip variation on the fault. We need to check if it is a universal observation at all the sites analyzed.

Figure 5.22 shows comparisons of PGA and PGV at all 40 sites in Mie Prefecture. It is clear that the PGA from a model with spatial slip variations (CASE1) tends to be slightly higher than the PGA from a model without spatial slip variation (CASE2). For a smooth slip model (CASE2) we see about 15% reduction in PGA in comparison to a variable slip model. On the other hand, the PGVs from a model with spatial slip variations (CASE1) tend to be apparently higher than the PGVs from a model without spatial slip variation (CASE2). For a smooth slip

model (CASE2) we see about 25% reduction in PGVs in comparison to a variable slip model.

These observations may come from the fact that the PGA is primarily controlled by the high frequency component, where the random pulses will overlap in the superposition from each elemental source so that it is difficult to see the effects by the slip variations in individual elements with the size of 5km x 5km, whereas the PGV is controlled in the intermediate frequency component (0.5 to 5 Hz) so that coherent interferences of waves from different elemental sources are taking place so that we can see stronger effects of the slip variation. In our current simulations, we do not assume any spatial fluctuation of the stress drop in the elemental sources which controls the high-frequency radiation level. It may be necessary to consider the spatial fluctuation of the stress drop to understand how it affects the high frequency range of the synthetic waveforms in the future.

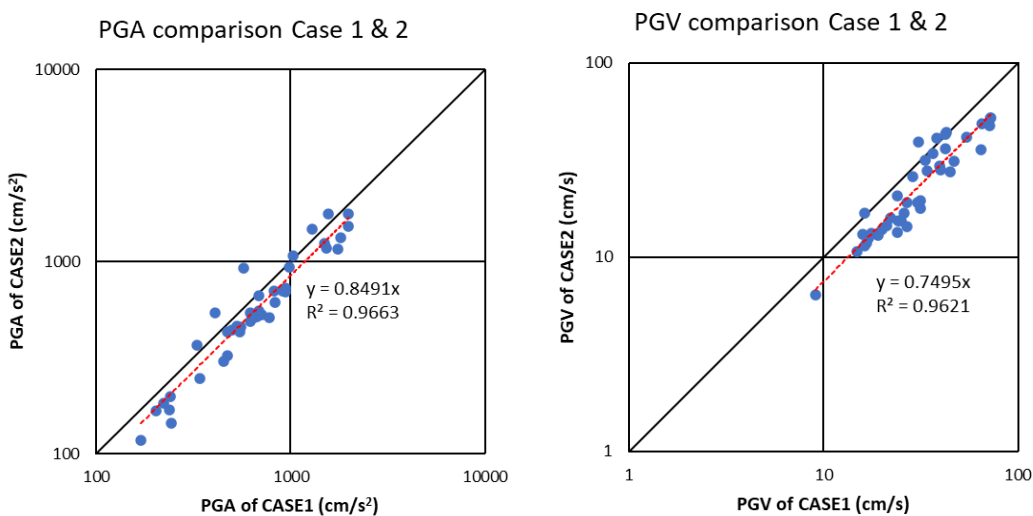


Figure 5.22. Comparisons of PGA and PGV for the calculated synthetics with slip variations (CASE1) and without slip variations (CASE2).

5.5.2 Effects of rupture velocity variation on PGA and PGV

As shown in the Sections 4.1 and 4.3, we can see a minor effect between the simulated synthetics from CASE1 and those from CASE3 at a selected site near the hypocenter. The difference reflects the effect of the rupture velocity variation on the fault. We need to check if it is a universal observation at all the sites analyzed.

Figure 5.23 shows comparisons of PGA and PGV for CASE1 and CASE3 at all 40 sites in Mie Prefecture. It is clear that both the PGAs and PGVs show almost 1:1 correspondence. Although the averaged difference is only 5% for PGA, it is noticeable that higher PGA values in the vicinity of the hypocenter tend to become smaller in CASE3 than in CASE1. This phenomenon can be interpreted as the result of the incoherent rupture directivity in CASE3, in comparison to the coherent rupture directivity in the near-fault regions. When the rupture velocity fluctuates from one elemental source to the other, the forward rupture directivity could become weaker than the constant rupture velocity case.

Please note that these values inevitably fluctuate from site to site even for the same

parameter case since we include random phase component in the elemental-source waveform generation

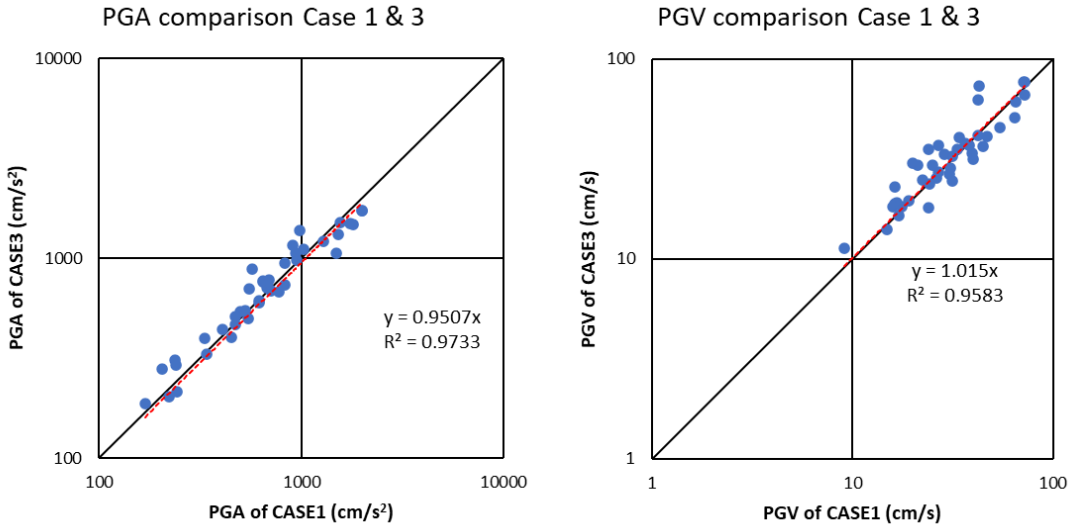


Figure 5.23. Comparisons of PGA and PGV for the calculated synthetics with rupture velocity variations (CASE1) and without rupture velocity variations (CASE3).

5.5.3 Effects of nonlinearity on PGA and PGV

As seen in the simulation results in 5.4, we have high PGV areas inside the Ise Plain where a strong site amplification in the lower frequency range is observed (Figure 5.4). When a strong input of seismic motion is impinged to thick, soft sediments, soil nonlinearity is taking place and we will have a smaller amplitude in the site amplification factor than the linear one (amplitude degradation), and a peak frequency shift. Nakano (2020) proposed two methods to account for the soil nonlinearity in his SGF code; one with only the amplitude degradation, and the other with both the amplitude degradation and the peak frequency shift. In this report we only consider the amplitude degradation for simplicity.

The amplitude degradation curve that Nakano (2020) proposed is based on the collected 174 high PGA and PGV records, together with the Vs₃₀ values (the so-called time-averaged S-wave velocity of top 30 m) at their observation sites. The method follows the one proposed by Yamaguchi and Midorikawa (2014), in which the pseudo-effective shear strain γ'_{eff} is defined as:

$$\gamma'_{eff} = 0.4 \cdot \text{PGV}/\text{Vs30}. \quad (5.8)$$

Then the spectral amplitude degradation $G'(f)$ is modeled as:

$$G'(f) = \alpha(f, \gamma'_{eff}), \quad (5.9)$$

$$\log_{10}\alpha(f, \gamma'_{eff}) = a(f) \times (\log_{10}\gamma'_{eff} - \log_{10}\gamma'_{eff_0}) \quad (5.10)$$

in which $a(f)$ is the regression coefficient for each frequency using a linear function with respect to γ'_{eff} and $\gamma'_{eff_0} = 3.0 \times 10^{-4}$ is the threshold strain level of the linear regime assumed a priori. The regression coefficient $a(f)$ is shown in Figure 5.24 (not as a function of frequency but period $T=1/f$ for comparison with Yamaguchi and Midorikawa, 2014). Nonlinearity will emerge as stronger amplitude degradation in the frequency range between 1 and 10 Hz.

Figure 5.25 shows comparisons of PGA and PGV for CASE1 and CASE1NL calculated by using the spectral nonlinearity shown in the above formula on top of the synthetics calculated under the same assumption as CASE1 at all 40 sites in Mie Prefecture. It shows that the PGA with nonlinearity yields the same PGA level as the linear calculation on the average. However, the PGV higher than 40 cm/s at six sites shows significant reduction. On the average PGVs with nonlinearity are 80% of PGVs with linearity as shown by the linear regression line (red dotted line), although the regression with a power law (blue dotted line) looks better fit to the data. This is rational because equation (5.8) shows that the PGV is the controlling parameter for the degree of nonlinearity, together with Vs30.

If that is the case, the PGAs should also be reduced at those sites with high PGVs, as the reduction shown in Figure 5.24 is taking place in a broad frequency range. When we look at Figure 5.25, the PGAs at the sites with strong reduction of the PGVs show also strong reduction.

On the other hand, the sites with the high PGAs near the hypocenter do not show any significant reductions in their Fourier spectra, as shown in Figure 5.26 for MIE016 as an example. This is so because the effective shear strains in equation (5.8) at these sites were not so large due to both their smaller PGVs and their larger Vs30.

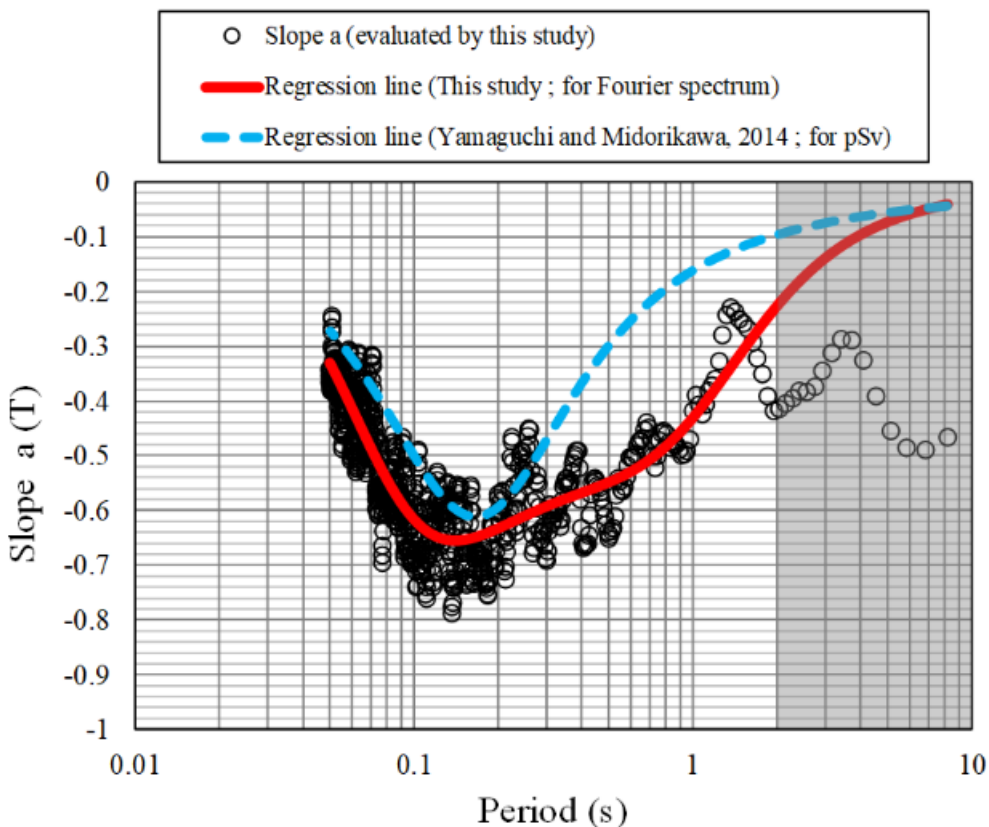


Figure 5.24. Regression coefficients of nonlinearity as a function of period ($1/f$) in the site term in the form of Fourier spectra (circles and red curve as the smoothed average). In comparison, the same regression coefficients for the pseudo-velocity response spectra (pSv) by Yamaguchi and Midorikawa (2014) were also plotted (blue dotted line).

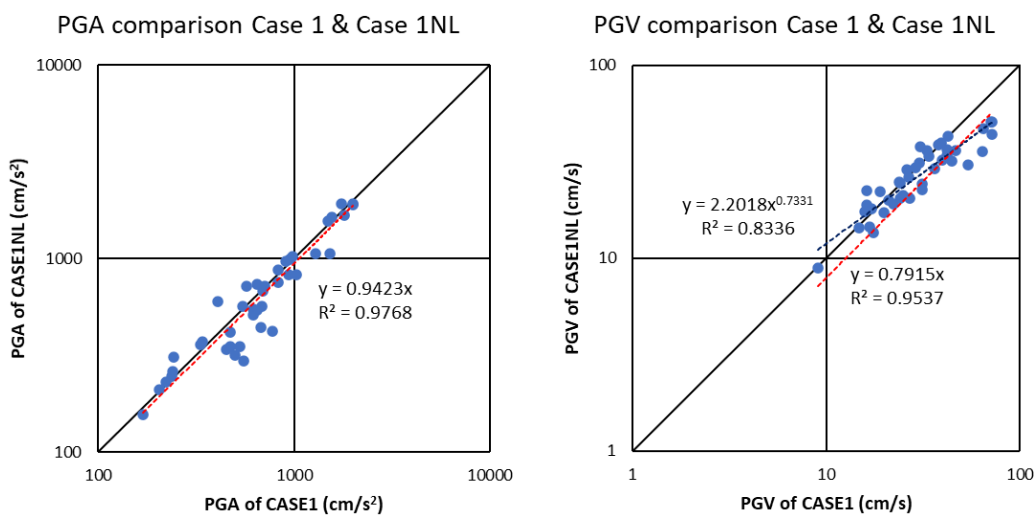


Figure 5.25. Comparisons of PGAs and PGVs for the calculated synthetics without soil nonlinearity (CASE1) and with soil nonlinearity (CASE1NL).

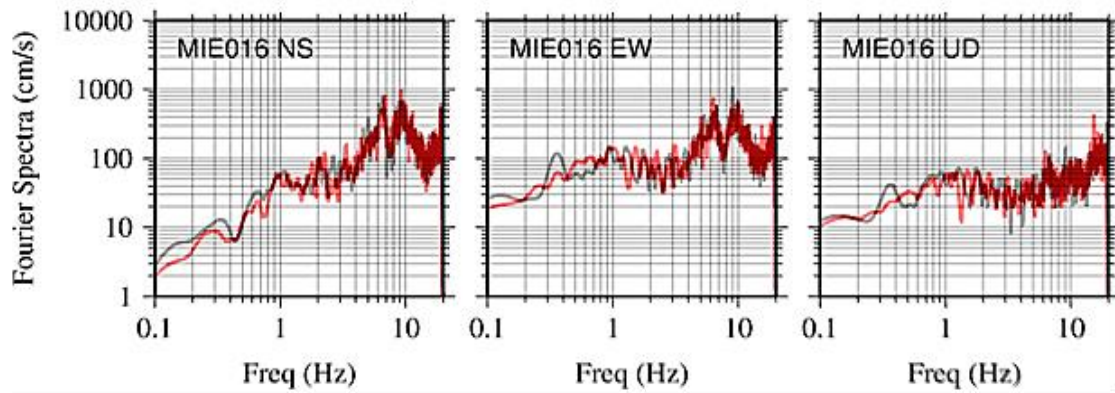


Figure 5.26. Comparison of Fourier Spectra of CASE1 (in black line) with those of CASE1NL (in red line)

Considering these fundamental characteristics of the resultant soil nonlinearity, we think that the empirical approach for soil nonlinearity correction adopted in the current implementation would be usable for large-scale prediction of strong motions as the first-order approximation. We may need further scrutiny for the degree of precision, though.

5.6 Conclusions

We plan to clarify the source process of the past mega-thrust earthquakes, the ground motions of which have not been recorded in the past, by adapting the simulated strong-motion waveforms to the results of the damage survey. For quantitative strong motion synthetics, we need to introduce random spatial heterogeneity in both the slip and rupture propagation velocity, in addition to the presumed strong-motion generation areas. We have developed an effective method to predict strong ground motions over a wide frequency range from 0.1 to 20 Hz by combining such a randomized source model that can represent complex rupture process on the fault and a statistical Green's function that reflects the statistical properties of small and medium-sized earthquakes inverted from a large number of strong-motion observation records in Japan. The method is applied to the 1944 Tonankai earthquake and parametric analysis is performed to investigate the effects of fluctuation in the slip and the rupture propagation velocity. The main results are summarized as follows:

- 1) The standard model with the random slip fluctuation but without rupture velocity perturbation (CASE1) yielded strong motion synthetics with PGAs and PGVs that correspond to the previously-proposed empirical relationship in general. A model with constant slip and constant rupture velocity (CASE2) yields strong motion synthetics with PGAs corresponding with the empirical relationship and the PGVs lower than the empirical relationship at sites near the hypocenter. A model with variable slip and variable rupture velocity (CASE3) yields strong motion synthetics with PGAs and PGVs that correspond well to the empirical relationship. The PGAs show more correspondence with the empirical relationship at sites near the hypocenter than those of CASE1.
- 2) Specifically looked at the deviation, their PGAs tend to be overestimated a little bit whereas

their PGVs tend to be underestimated a little bit, which can be considered as the reflected site effects of the target sites used for calculation.

- 3) The fluctuations of the slip under the current model turned out to increase PGA by 15% and PGV in 25%.
- 4) The variations of the rupture propagation velocity turned out not to change both PGA and PGV significantly, probably because of the stochastic nature in the statistical Green function method adopted here. However, we see systematic reduction of PGAs in the vicinity of the hypocenter, due to the effect of the incoherent rupture in the area with strong forward directivity.
- 5) Empirically-modeled nonlinearity effects will reduce both PGAs and PGVs at the sites with higher PGVs and smaller Vs30, whereas those sites with higher Vs30s, where PGAs were high but PGVs were low, do not show significant reduction.

As the overall characteristics of the calculated synthetics, we found that our current implementation of the complex source model used as a broad-band kinematic source representation and the empirically-determined statistical Green function used as an elemental source of strong motions can be a viable combination for realistic broad-band (0.1 to 20 Hz) strong motion simulations without any hybrid scheme.

For future tasks, we will estimate the building damage by inputting the acceleration waveforms into the wooden building model with construction age for damage estimation, and then search the most realistic source rupture model through a large number of parametric analysis until the estimated damage ratio at each site matches the observed one.

Acknowledgements

Some of the figures presented are created by GMT (Wessel et al, 2013). Satellite image from Google Map is used in Figure 5.1. We use the strong motion records observed at JMA Shindokey network & K-NET and KiK-net (NIED, 2019).

References

- Ando, M. (1975): Source mechanisms and tectonic significance of historical earthquakes along the Nankai trough, Japan, Tectonophysics, 27, 119-140.
- Andrews, D.J. (1986): Objective determination of source parameters and similarity of earthquakes of different size, Earthquake Source Mechanics (eds. S. Das, J. Boatwright and C. H. Scholz), American Geophysical Union, Washington, D.C., 1986. doi: 10.1029/GM037p0259.
- Asano, K. and Iwata, T. (2012): Source model for strong ground motion generation in the frequency range 0.1-10 Hz during the 2011 Tohoku earthquake, Earth Planets Space, Vol.64, 1111-1123.
- Bard, P.Y. and Bouchon, M. (1980). Seismic response of sediment-filled valleys, Part 1: The case of incident SH waves, Bull. Seismol. Soc. Am. 70, 1263-1286.
- Cabinet Office (2015): Report on Long-period Ground Motion Due to a Nankai Trough

- Megaquake, Committee for Modeling a Nankai Trough Megaquake, December 17, 2015, http://www.bousai.go.jp/jishin/nankai/nankaitrough_report.html, (in Japanese, last accessed, 2020/8/29).
- Central Disaster Management Council, (2003): Strong motions and Tsunami heights, Figures and Tables, Vol.3, http://www.bousai.go.jp/kaigirep/chuobou/senmon/tounankai_nankaijishin/16/pdf/siryou3zuhyou_2.pdf (in Japanese, last accessed 2020/08/25).
- Ito, E., Nakano, K., Nagashima, F., and Kawase H. (2020): A Method to Directly Estimate S-Wave Site Amplification Factor from Horizontal-to-Vertical Spectral Ratio of Earthquakes (eHVSRs), Bull. Seismol. Soc. Am. (Online only at present), 1–20, doi: 10.1785/0120190315.
- Iwata, T. and Irikura, K. (1988): Source parameters of the 1983 Japan-Sea earthquake sequence, J. Phys. Earth, 36, 155-184.
- J-SHIS (2020): Japan Seismic Hazard Information Station, NIED, Tsukuba, Japan, <http://www.j-shis.bosai.go.jp/en/> (last accessed 2020/08/25)
- Kamae, K. and Irikura, K. (1998): Source model of the 1995 Hyogo-ken Nanbu earthquake and simulation of near-source ground motion, Bull. Seism. Soc. Am., 88(2), 400–412, 1998.
- Kamae, K. and Kawabe, H. (2004): Source model composed of asperities for the 2003 Tokachi-oki, Japan, earthquake (MJMA=8.0) estimated by the empirical Green's function method, Earth Planets Space, Vol. 56, 323–327.
- Kawase, H. and Aki, K. (1989): A study on the response of a soft basin for incident S, P, and Rayleigh waves with special reference to the long duration observed in Mexico City, Bull. Seismol. Soc. Am., 79, 1361-1382, 1989.
- Kawase, H. (2003): Site effects on strong ground motions, International Handbook of Earthquake and Engineering Seismology, Part B, W.H.K. Lee and H. Kanamori (eds.), Academic Press, London, 1013-1030.
- Kawase, H. and Matsuo, H. (2004): Amplification characteristics of K-NET, KiK-NET, and JMA Shindo-kei network sites based on the spectral inversion technique, 13th World Conf. on Earthquake Engineering, Vancouver, Canada, Paper No. 454.
- Kawase, H., Sánchez-Sesma, F.J., and Matsushima, S. (2011): The optimal use of horizontal-to-vertical spectral ratios of earthquake motions for velocity inversions based on diffuse field theory for plane waves”, Bull. Seismol. Soc. Am., 101, 2001-2014.
- Koketsu K., Miyake H., Suzuki H., (2012) Japan integrated velocity structure model version 1. Proceedings of the 15th world conference on earthquake engineering, Lisbon, Portugal, September, 24-28.
- Kurahashi, S., and Irikura, K. (2013): Short-period source model of the 2011 Mw 9.0 off the Pacific coast of Tohoku earthquake, Bull. Seismol. Soc. Am., Vol.103, 1317-1393.
- Mai, P.M. and Beroza, G.C. (2002): A spatial random field model to characterize complexity in earthquake slip, Journal of Geophysical Research, 107(B11), 2308, doi:10.1029/2001JB000588.
- Miyakoshi, K. and Petukhin, A. (2005): Delineation of rupture velocity of heterogeneous source model extracted from source inversion results of inland earthquakes, Proc. of 2005 Japan Earth and Planetary Science Joint Meeting, May, 22-26, 2005, Chiba, Japan, S046P-002.
- Morikawa, N. and Fujiwara, H. (2013): A new ground motion prediction equation for Japan applicable up to M9 mega-earthquake, J. Disaster Res., Vol. 8, No. 5, 878-888,

doi:10.20965/jdr.2013.p0878.

- Nagato, K and Kawase, H. (2004): Damage evaluation models of reinforced concrete buildings based on the damage statistics and simulated strong motions during the 1995 Hyogo-ken Nanbu earthquake, Earthq. Eng. and Struct. Dyn., Vol.33, No.6, 755-774.
- Nagashima, F., Matsushima, S., Kawase, H., Sánchez-Sesma, F.J., Hayakawa, T., Satoh, T., and Oshima, M. (2014): Application of Horizontal-to-Vertical (H/V) spectral ratios of earthquake ground motions to identify subsurface structures at and around the K-NET Site in Tohoku, Japan, Bull. Seismol. Soc. Am., Vol. 104, No. 5, 2288–2302, doi: 10.1785/0120130219.
- Nakano, K., Matsushima, S. and Kawase, H. (2015): Statistical properties of strong ground motions from the generalized spectral inversion of data observed by K-NET, KiK-net, and the JMA Shindo-kei Network in Japan, Bull. Seismol. Soc. Am., Vol.105, 2662-2680, doi:10.1785/0120140349.
- Nakano, K. and Kawase, H. (2019): Source parameters and site amplifications estimated by generalized inversion technique: focusing on the 2018 Hokkaido Iburi-Tobu earthquake, Earth Planets Space, 71: 66, doi:10.1186/s40623-019-1047-1.
- Nakano, K. (2020): Strong-motion prediction method based on the spectral inversion, Ph.D. Dissertation, Graduate School of Engineering, Kyoto University (in Japanese).
- National Research Institute for Earth Science and Disaster Resilience (2019): NIED K-NET, KiK-net, National Research Institute for Earth Science and Disaster Resilience, doi:10.17598/NIED.0004
- Renka, R. (1999) : Algorithm 790: CSHEP2D: Cubic Shepard Method for Bivariate Interpolation of Scattered Data, ACM Transactions on Mathematical Software, Vol. 25, No. 1, 70-73, doi:10.1145/305658.305737.
- Rodgers, A., Petersson, N.A., Pitarka, A., McCallen, D., Sjogreen B., and Abrahamson, N. (2019): Broadband (0-5 Hz) fully deterministic three-dimensional ground motion simulations of a magnitude 7.0 Hayward Fault earthquake: Comparison with empirical ground motion models and 3D path and site effects from source normalized intensities, Seismol. Res. Lett., 90 (3), 1268-1284, doi: 10.1785/0220180261.
- Satoh, T. (2004): Study on envelope model of ground motions based on inversion of group delay time and scattering theory, J. Struct. Constr. Eng., AJI, No.586, 71-78, doi:10.3130/aijs.69.71_5 (in Japanese with English abstract).
- Sekiguchi, H. and Yoshimi, M. (2010): Broadband Ground Motion Reconstruction for the Kanto Basin during the 1923 Kanto Earthquake, Pure and Applied Geophysics, doi:10.1007/s00024-010-0142-9.
- Smith, F.H.W. and Wessel P.: Gridding with continuous curvature splines in tension, GEOPHYSICS, Volume 55, Issue 3, 1990, doi:10.1190/1.1442837.
- Tsai, N.C. (1970): A note on the steady-state response of an elastic half-space, Bull. Seismol. Soc. Am., Vol.60, No. 3, 795-808.
- Wessel, P., Smith, H.F.W., Scharroo, R., Luis, J.F., and Wobbe, F. (2013): Generic Mapping Tools: Improved version released, EOS Trans. AGU, 94, 409-410, 2013.
- Yamaguchi, M. and Midorikawa, S. (2014): Empirical models for nonlinear site amplification evaluated from observed strong motion records, J. Japan Assoc. Earthq. Eng., Vol.14, No.1, 56-70, doi:10.5610/jaee.14.1_56 (in Japanese with English abstract).

Chapter 6

Complex Source Characterization of the 1944 Tonankai Earthquake from Simulated Damage Ratios based on the Simulated Strong Motions

Abstract

It is indispensable to delineate the detailed rupture process from the existing observed building damage distribution, instead of strong motion records. We reproduce the building damage ratio during the 1944 Tonankai earthquake by inputting the strong motion waveforms into the building damage evaluation models as of 1944. The strong ground motion waveforms are obtained from the statistical Green's function and the heterogeneous source model. The site characteristic is obtained by the method of converting the theoretical S-wave characteristic from the unified velocity model (UVM) by integrating shallower- and deeper-parts of the structures above the seismological bedrock in the Kanto and Tokai regions, to the empirical site characteristics. We prepare the heterogeneous source model with the four asperities as a standard model, and prepare 36 heterogeneous source models in total, of which varying parameters are the location of hypocenters, the location of asperities (SMGAs), and their stress drops. Then we calculate the strong ground motions from the prescribed complex source models and estimate the building damage ratios using the building damage evaluation models, then compared it with the observed damage ratio during the 1944 Tonankai earthquake. Based on the model with the estimated damage ratio best corresponding with the observed one as the new standard model, we investigate additional five heterogeneous source models with different stress drop and area of SMGA No.1 and No.2 to seek the better source model. We found that the case with the second asperity stress drop of 60 MPa from the best model in the first step is the model that best explains the observed building damage ratios. The results show that in order to explain the building damage ratio of more than 40%, it is necessary to consider a source rupture process that would cause stronger forward rupture directivity in the Enshu region. The proposed building damage evaluation model and the distribution of observed damage ratio provide a prospect to clarify the detailed source rupture process of the 1944 Tonankai earthquake.

6.1 Introduction

After the 1995 Hyogo-ken Nanbu earthquake, Southwest Japan is said to have entered an active period, and the mega-thrust earthquake along Nankai Trough and Sagami Trough may occur at any time. In order to mitigate the damage caused by these earthquakes as much as possible, it is necessary to predict the damage level in advance with high accuracy and take appropriate countermeasures. For proper damage estimation of mega-thrust earthquakes, it is necessary to evaluate the three characteristics, i.e., source characteristics, propagation path characteristics, and site amplification characteristics. In particular, as for the source characteristics, a complex model that takes into account the heterogeneity of the source properties is necessary as described in Chapter 5. For the heterogeneity of source model for mega-thrust earthquakes, analyses of the 2011 off the Pacific coast of Tohoku earthquake have shown that there is a large slip area along the trench that contributes to the generation of tsunamis but does not generate short-periods, and that there is a short-period strong motion generation area (SMGA) deeper near the coast, which means two types of heterogeneity are needed to reproduce this type of earthquake(e.g., Asano and Iwata, 2012).If the short-period strong motion generation areas of Tonankai, Nankai, and Kanto earthquakes, which will happen in the near future, are located in the area near the coast, they will be closer to cities than in the case of the 2011 off the Pacific coast of Tohoku earthquake, and the damage will be more severe than predicted. Therefore, it is an urgent issue to grasp the process of short-period generation including the location, size, and amount of stress drop. However, the prediction of damage by strong ground motion and tsunami predictions using M 9 class earthquake scenarios published by the Central Disaster Management Council after the 2011 off the Pacific coast of Tohoku earthquake, does not reflect the latest knowledge on the distribution of short-period strong motion generation areas and rupture propagation on faults, which was obtained from the 2011 off the Pacific coast of Tohoku earthquake.

A detailed understanding of the source rupture process of past earthquakes is important as a basis for predicting damage from future mega-thrust earthquakes. For the three trench earthquakes of the early 1900s, the last seismically active period, namely the Kanto earthquake in 1923, the Tonankai earthquake happened in 1944, and the Nankai earthquake happened in 1946, the long-period ground motion generation areas with periods ranging from a few seconds to 100 seconds are to some extent understood from crustal movements, tsunamis, and records in distant places. On the other hand, short-period ground motion generation areas with a period of two seconds or less that are directly related to building damage have been assumed to be in the long-period generation zone, but their nature has not been fully verified. One reason for this is that there was no building damage evaluation model which reproduced the damage plausibly at the time of the earthquake and the accuracy of the damage assessment was low. Another reason was that since the earthquake occurred before the start of strong-motion waveform observation, there are no observed strong-motion waveforms in the severely damaged areas, so only inversions from the estimated seismic intensities obtained from the post-earthquake building damage survey can be performed, thus areas with a large amount of slip that cannot be considered as a short-period generation area, can be estimated.

In light of this trend, in this study, focusing on the 1944 Tonankai earthquake, we get a

closer look at its detailed picture of the source characteristic. We first create several heterogeneous source models that incorporate the latest findings revealed after the 2011 off the Pacific coast of Tohoku earthquake. Second, we choose the sites where the observed building collapse ratio is greater than or equal to 1% as the sites for calculating the strong ground motions generated from the created multiple sources, and the building damage ratio. Then we calculate the strong ground motions and building damage ratio at these sites by using the recently proposed building damage evaluation models that reflects pre-1930 building characteristics. Finally, we choose the source model of which building damage ratio corresponds to the observed damage ratio best among the created source models as the most realistic model. We apply the site characteristic derived by GIT technique and the interpolation scheme explained in chapter 3 for the choose sites. By obtaining detailed source processes of past earthquakes, quantitative strong-motion evaluation of future scenario earthquakes is possible.

6.2 Reviews of the 1944 Tonankai Earthquake Disaster Reports

Tonankai earthquake, which occurred at 1:00 p.m. on December 7, 1944, at the end of World War II, was a 7.9-magnitude earthquake caused by the subduction of an oceanic plate. It was coincided with school and work hours, resulting in 1,223 deaths, mainly in schools and munitions factories. The death toll also included a number of deaths at a spinning mill that was converted to an airplane assembly plant, neglecting its lack of earthquake resistance. In addition, the Tokai region was an important munitions base at the time and media restrictions were imposed to enhance national prestige, so the full extent of the damage was not disclosed to the public.

In spite of such a situation, damage surveys just after the earthquake were conducted including the report of the Central Meteorological Observatory (the predecessor of Japan Meteorological Agency, 1945), the preliminary report of the Earthquake Research Institute (1945), and Miyamura (1946). In addition to the three survey materials in the immediate aftermath of the earthquake, Aichi Prefecture Disaster Prevention Council (1975) which was a report by Nagoya Regional Meteorological Office and Nagoya Imperial University reprinted several decades after the World War II, Nagoya Local Meteorological Office (1970), and Oba (1957), are the main survey materials.

After that, Iida (1985) vigorously and thoroughly organized the above-mentioned multiple and wide area data and evaluated the distribution of seismic intensity. Because the data in Iida (1985) was thoroughly collected and organized, for a long time there were no papers examining the contents of this literature, but 30 years after Iida (1985), its contents were examined by Takemura and Toraya (2015) for the first time. Since the data in Iida (1985) were grouped by municipality, they assumed that the data in Iida (1985) were enriched by examining, modifying, and adding to the data in Miyamura (1946) from other sources, which was the only one with municipality-specific data in the aforementioned data. Since the data in Iida (1985) were grouped by municipality, they assumed that the data in Iida (1985) were organized by examining, modifying, and adding to the data in Miyamura (1946) by using other sources, which was the only one with municipality-specific data in the aforementioned data. They compare the data in

Miyamura (1946) and in Iida (1985) and clarify how much Iida (1985) complemented the data in Miyamura (1946). They also correct transcription errors in Iida (1985) which must have been made by himself from the data in Miyamura (1946) and estimates the new number of deaths. It also evaluates the estimated seismic intensity based on building damage rates and digitizes the mostly handwritten data in Iida (1985) to make it easier to read. Figure 6.1 shows the evaluated seismic intensity from building damage ratio in Tokai area by Takemura and Toraya (2015).

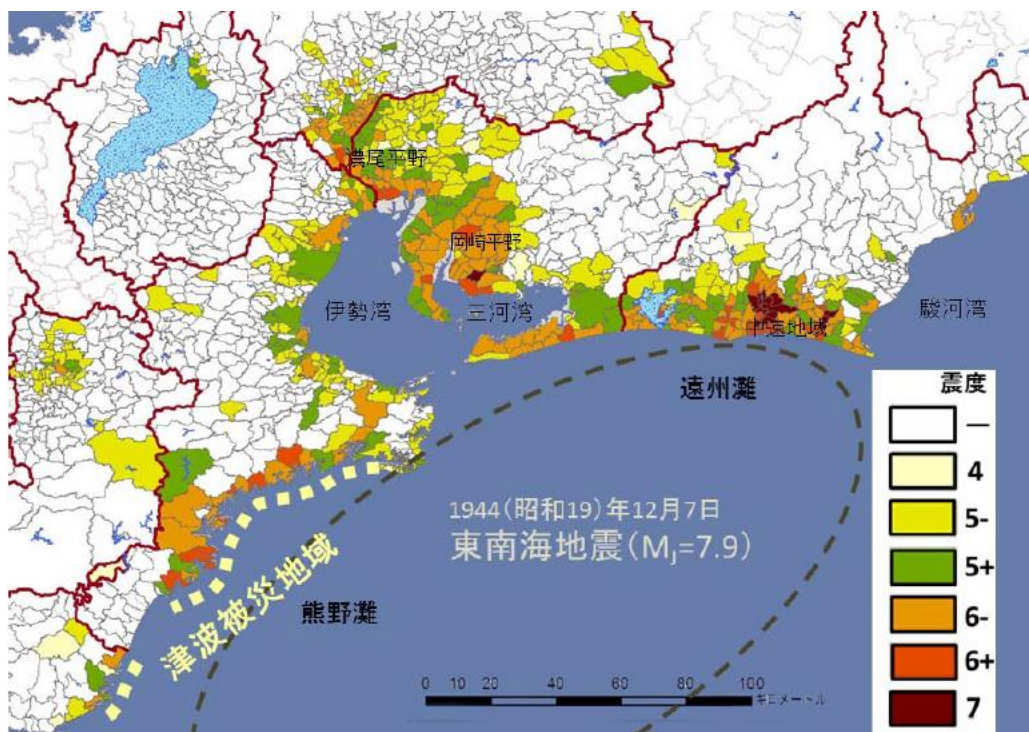


Figure 6.1 Evaluated seismic intensity from building damage ratio in Tokai area by Takemura and Toraya (2015).

Takemura and Toraya (2015) provide detailed data by municipality on the number of households, totally crush ratio, totally and partly crush ratio, assessed seismic intensity, number of totally crushed dwellings, number of totally and partly crushed dwellings, number of totally crushed non-dwellings, number of totally and partly crushed non-dwellings, mortality, population, deaths, injuries, number of swept away buildings, total burned down dwellings, totally burned down dwellings, and totally and partly burned down dwellings as of 1944. Focusing on the “totally crush ratio”, which was used by Iida (1985) for his seismic intensity evaluation, the term of “totally crush” is not currently used in building damage assessment, but Kobayashi (1998) defines it as “the state that the eave touches the ground in the case of a one-story building, and the floor of the second story touches the ground in the case of a two-story building,” which is equivalent to the current definition of “collapse”. Therefore, we extract the “total crush ratio” in Takemura and Toraya (2015) from them and compare it with the collapse ratio calculated from the building damage evaluation model.

6.3 Kinematic Heterogeneous Source Modeling

In order to reproduce the observed collapse ratios shown in Takemura and Toraya (2015), we first prepared three cases for hypocenter, four cases for the locations of four SMGAs, and three cases for stress drop, then by combining these parameters, we calculated 36 cases of source models with various slip and various rupture velocity. The details for each parameter are shown below.

As for the hypocenter, case 1 is where it follows Cabinet Office (2015). Case 2 is where it is moved to the southeast for a length of 30% of the fault width from case 1, and case 3 is where it is moved to the northwest for a length of 30% of the fault width from case 1.

As for the locations of four SMGAs, Case 1 is where they follow Cabinet Office (2015). Case 2 is where the two SMGAs (SMGA 3 and SMGA 4) in the west side are moved to the northwest for a length of 30% of the fault width from case 1. Case 3 is where the two SMGAs (SMGA 1 and SMGA 2) in the east side are moved to the northwest for a length of 30% of the fault width from case 1. Case 4 is where the two SMGAs (SMGA 1 and SMGA 2) in the east side are moved to the northwest for a length of 30% of the fault width from case 3. Here, SMGAs are named SMGA 1, 2, 3, and 4 from the northeast to southwest.

As for the stress drop, case 1 is where the stress drop for each SMGA follows Cabinet Office (2015), which is 30MPa, case 2 is where the stress drop for each SMGA is 24MPa, and case 3 is where the stress drop for each SMGA is 36MPa. Figure 6.2 to 6.13 show the slip, stress drop, rupture velocity and rupture starting time for the 36 cases.

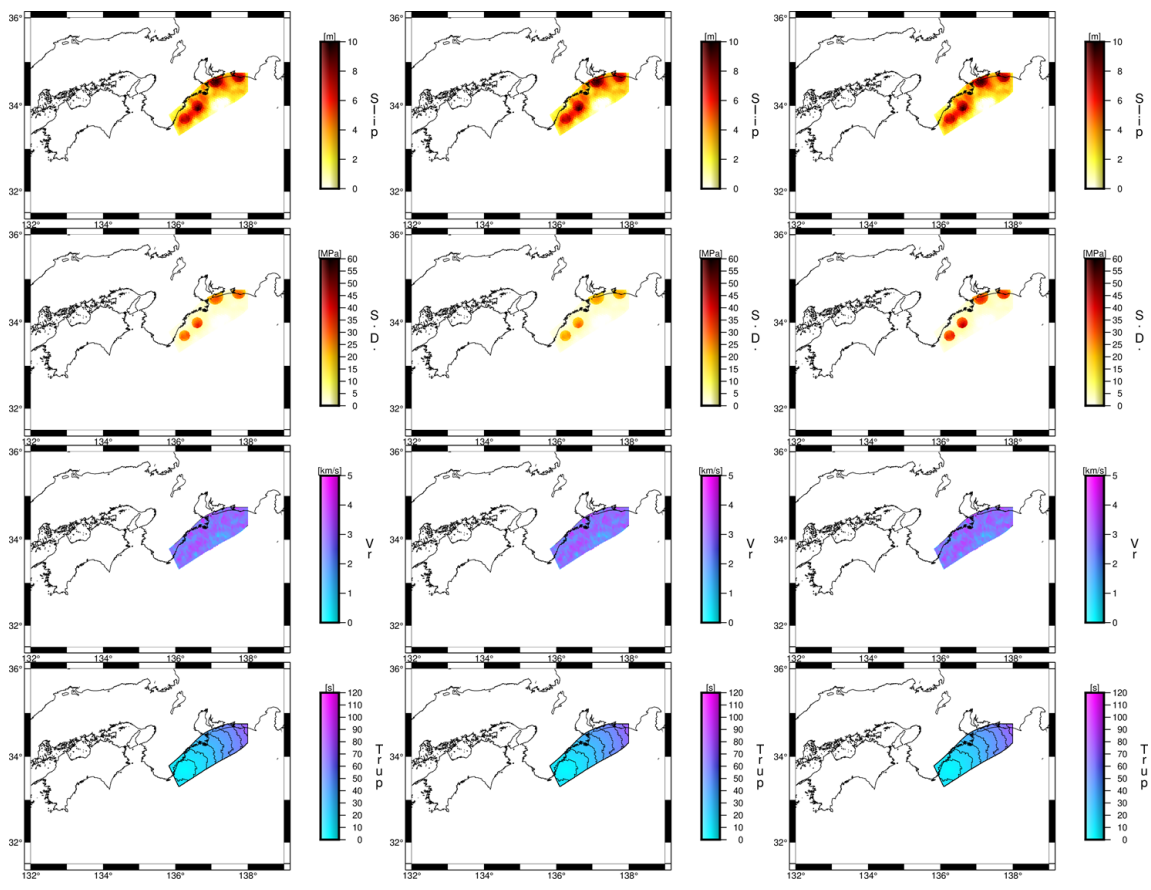


Figure 6.2. The slip, stress drop, rupture velocity and rupture starting time for case 1-1-1 in the left panel, case 1-1-2 in the middle panel and case 1-1-3 in the right panel.

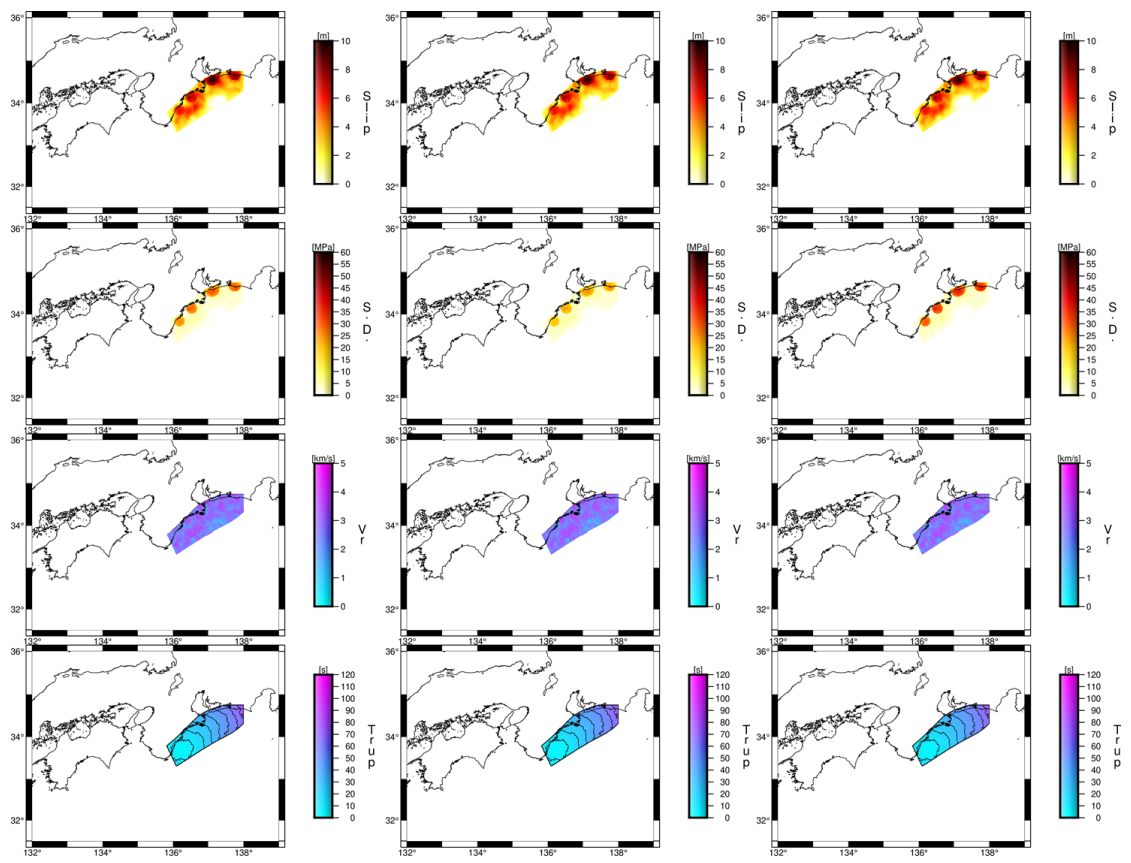


Figure 6.3. The slip, stress drop, rupture velocity and rupture starting time for case1-2-1 in the left panel, case 1-2-2 in the middle panel and case 1-2-3 in the right panel.

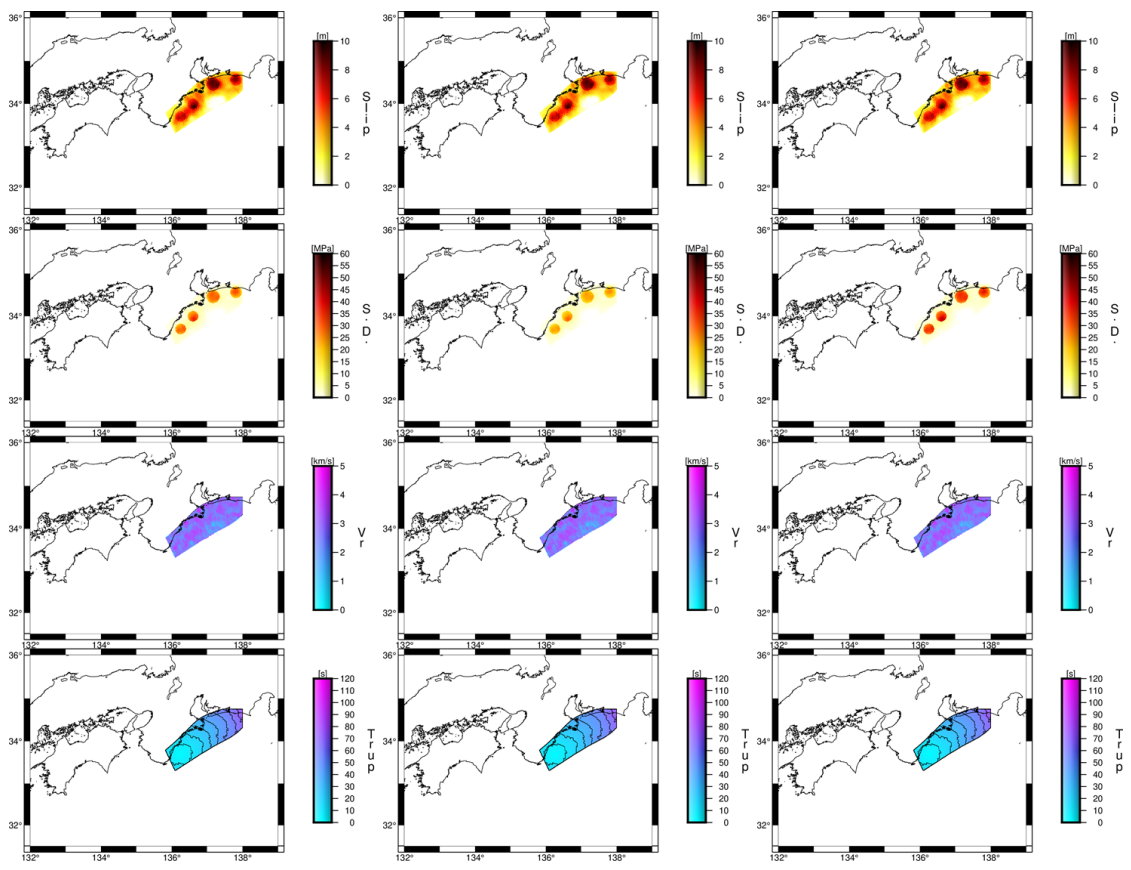


Figure 6.4. The slip, stress drop, rupture velocity and rupture starting time for case 1-3-1 in the left panel, case 1-3-2 in the middle panel and case 1-3-3 in the right panel.

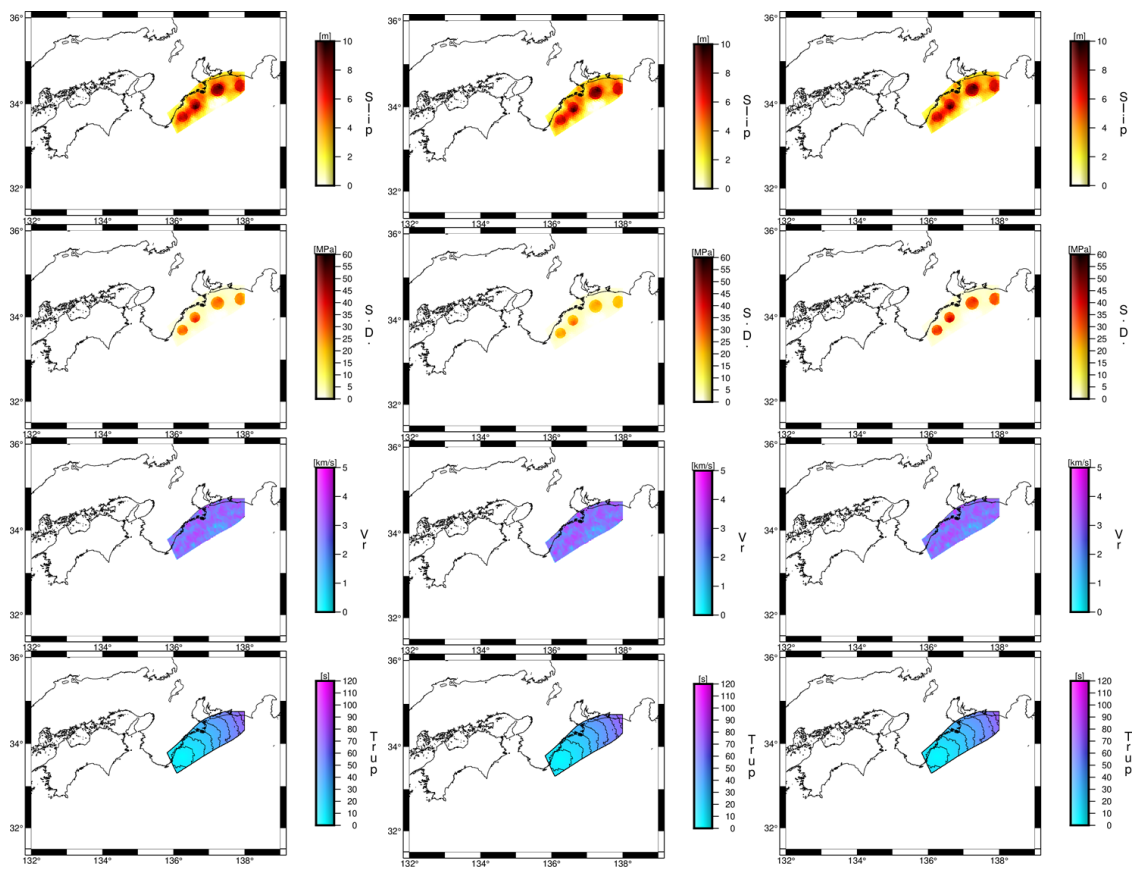


Figure 6.5. The slip, stress drop, rupture velocity and rupture starting time for case 1-4-1 in the left panel, case 1-4-2 in the middle panel and case 1-4-3 in the right panel.

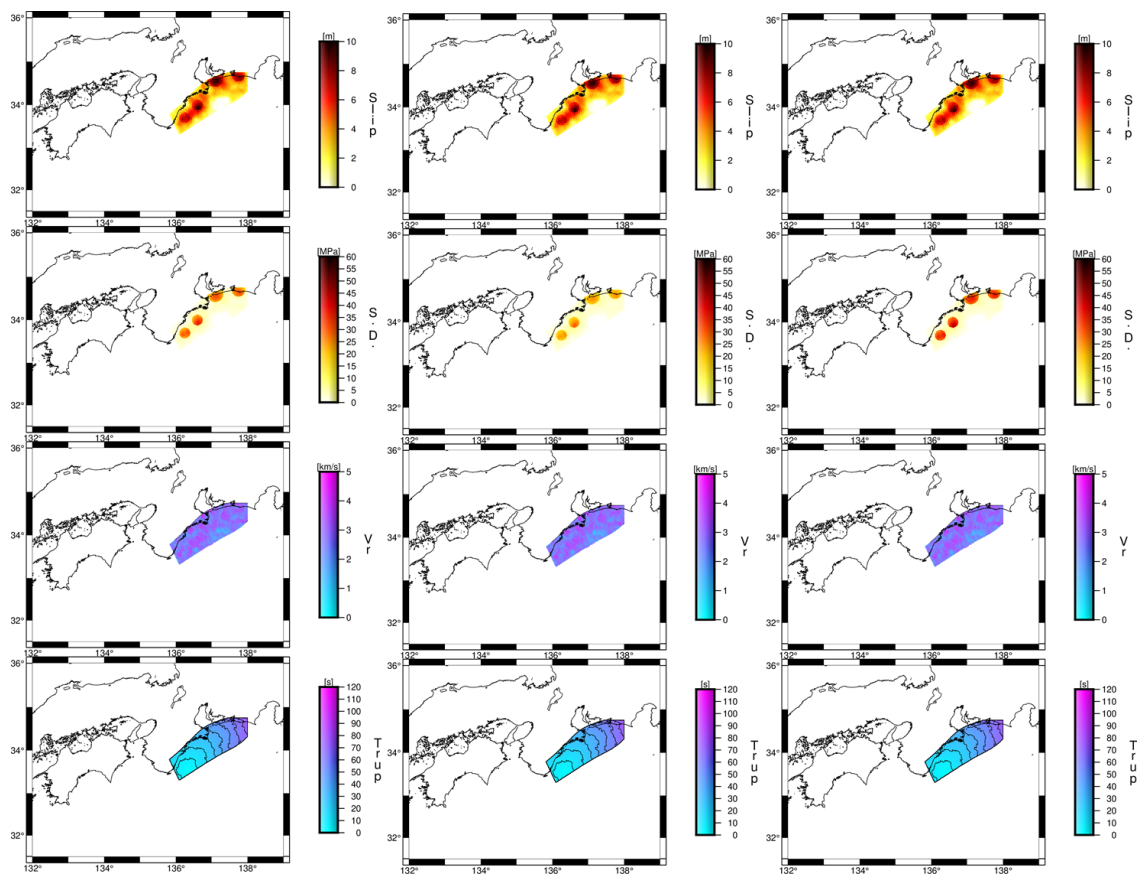


Figure 6.6. The slip, stress drop, rupture velocity and rupture starting time for case 2-1-1 in the left panel, case 2-1-2 in the middle panel and case 2-1-3 in the right panel.

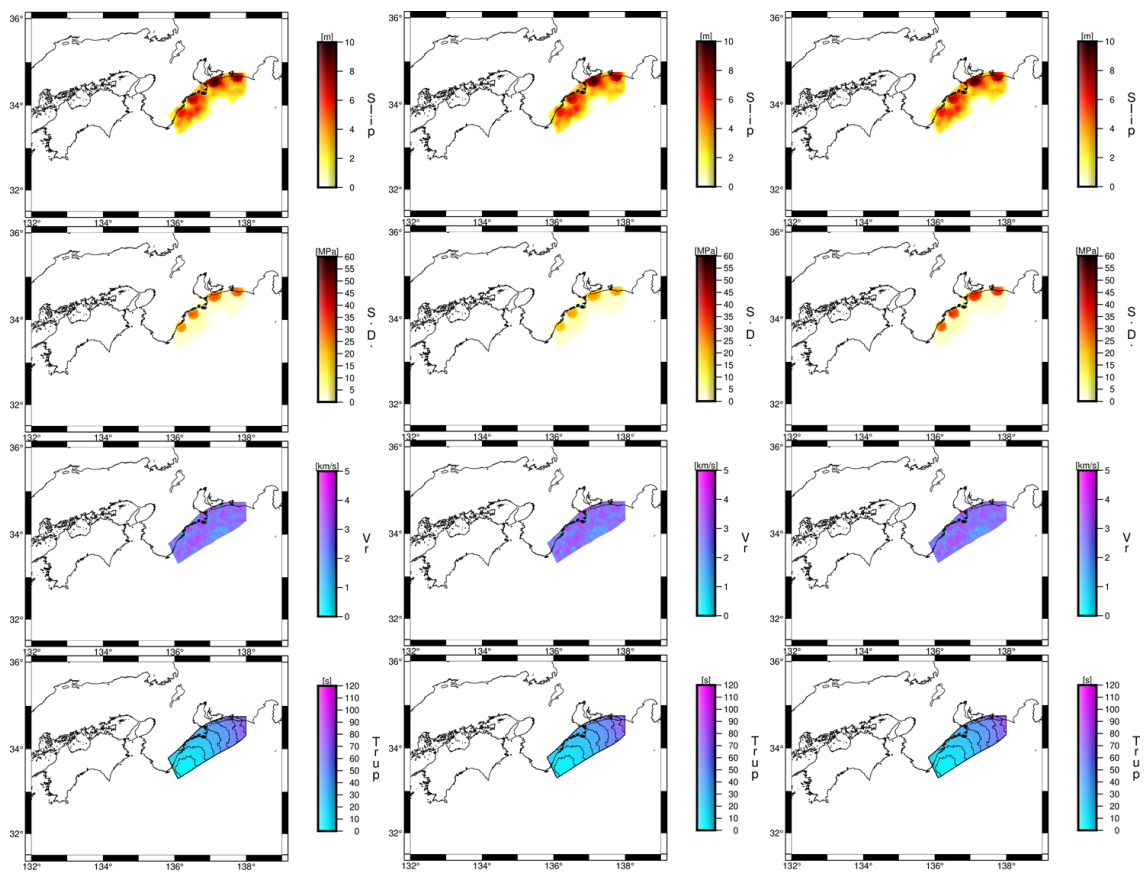


Figure 6.7. The slip, stress drop, rupture velocity and rupture starting time for case 2-2-1 in the left panel, case 2-2-2 in the middle panel and case 2-2-3 in the right panel.

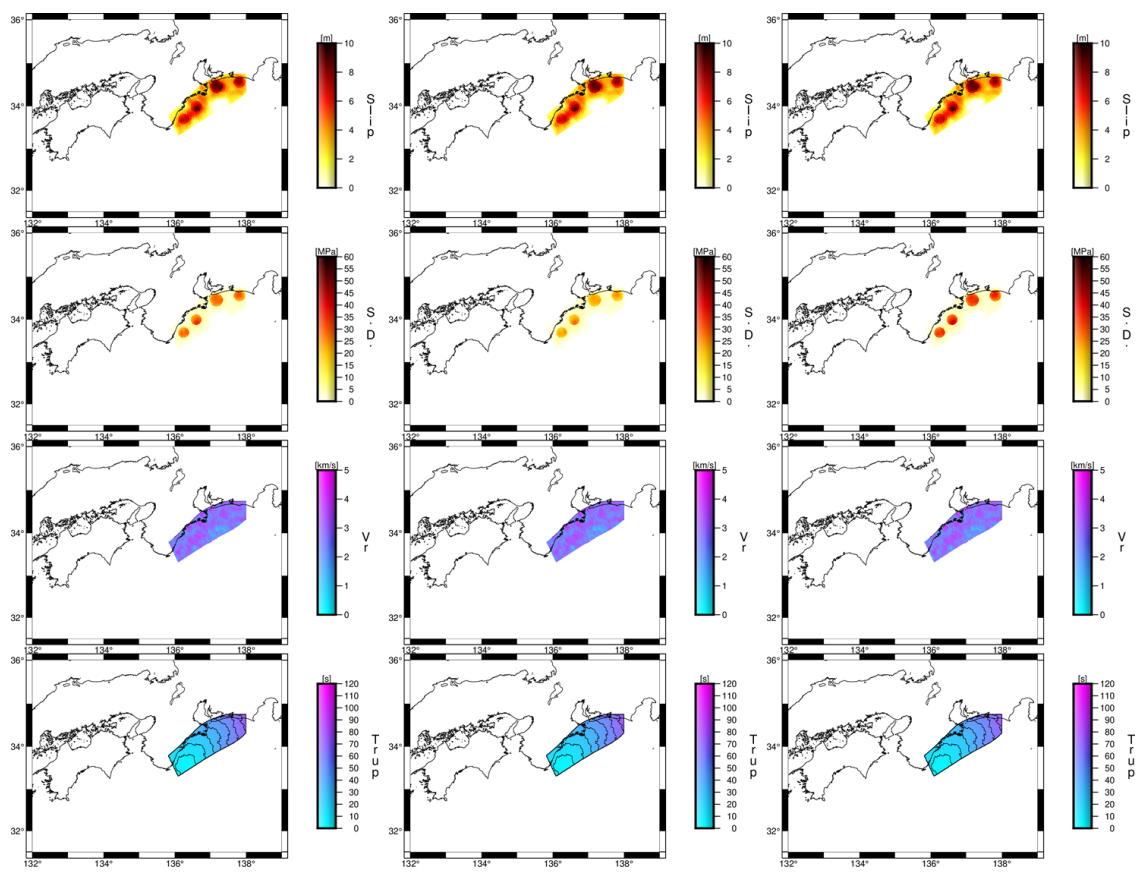


Figure 6.8. The slip, stress drop, rupture velocity and rupture starting time for case 2-3-1 in the left panel, case 2-3-2 in the middle panel and case 2-3-3 in the right panel.

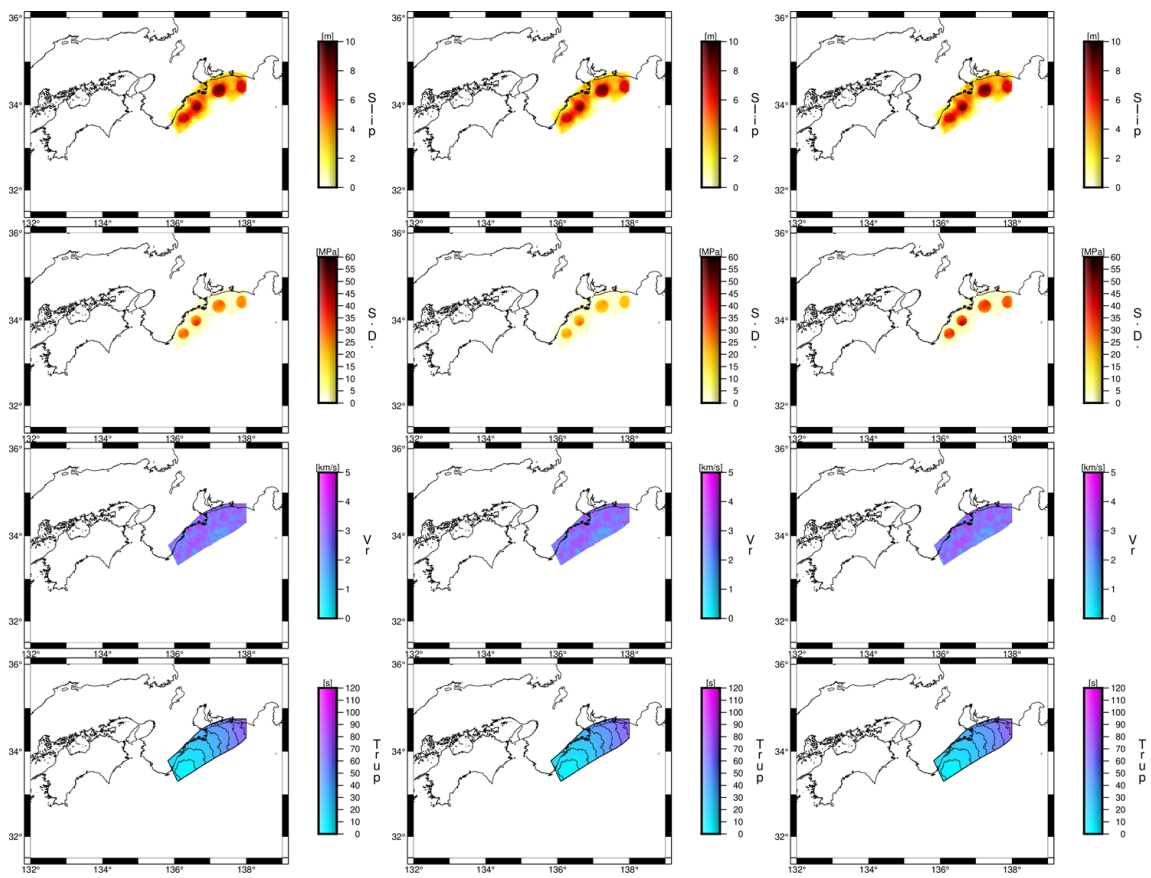


Figure 6.9. The slip, stress drop, rupture velocity and rupture starting time for case 2-4-1 in the left panel, case 2-4-2 in the middle panel and case 2-4-3 in the right panel.

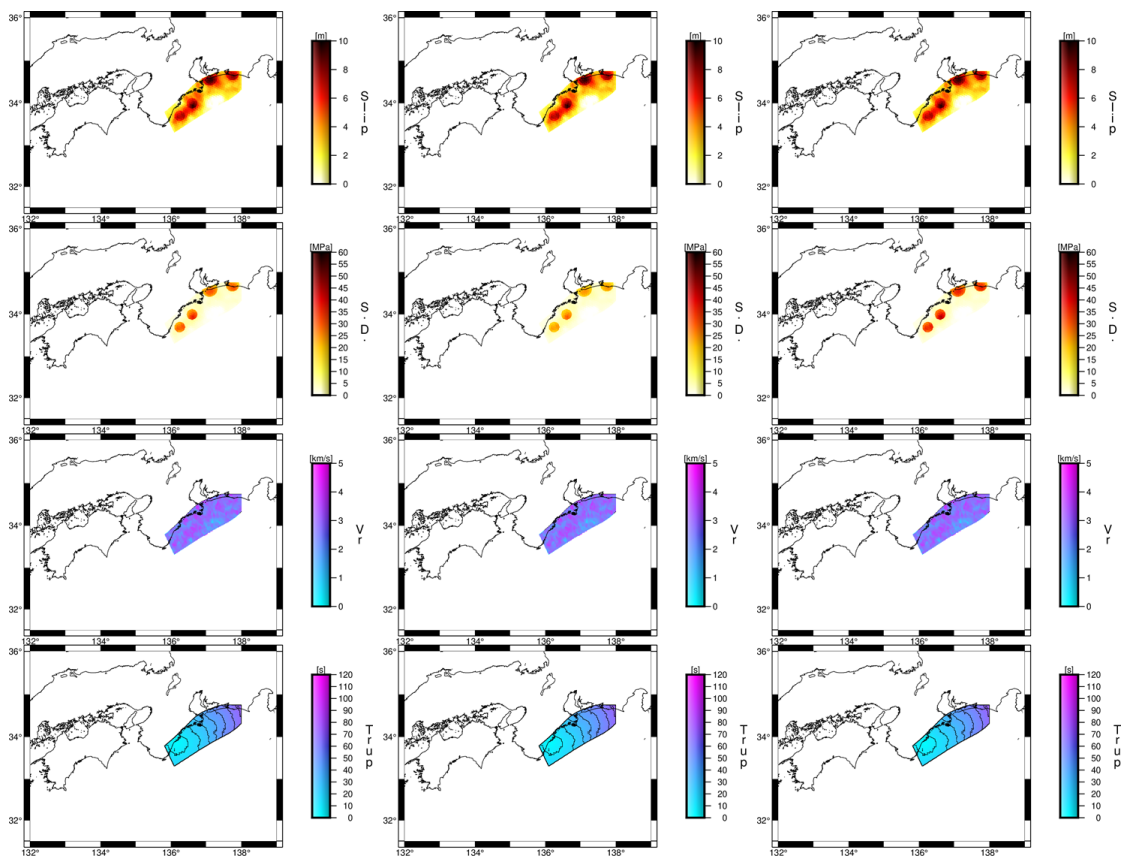


Figure 6.10. The slip, stress drop, rupture velocity and rupture starting time for case 3-1-1 in the left panel, case 3-1-2 in the middle panel and case 3-1-3 in the right panel.

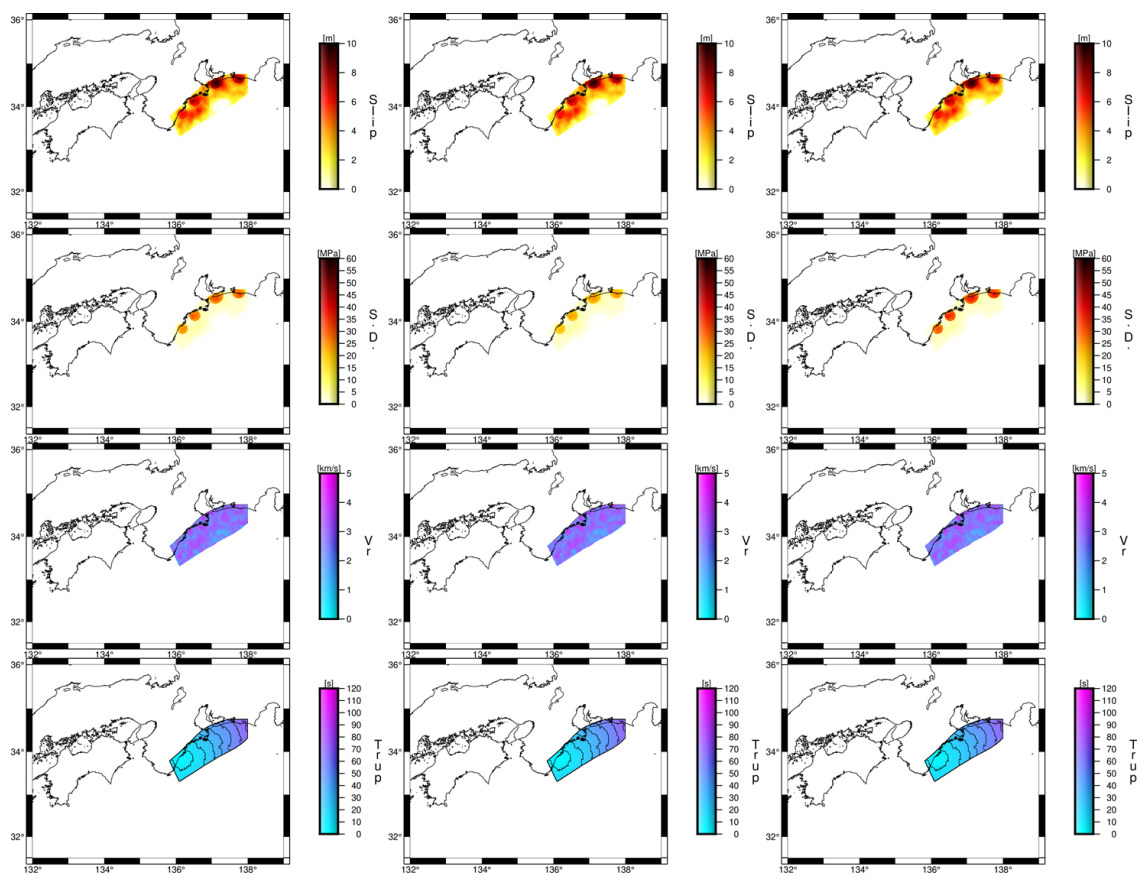


Figure 6.11. The slip, stress drop, rupture velocity and rupture starting time for case 3-2-1 in the left panel, case 3-2-2 in the middle panel and case 3-2-3 in the right panel.

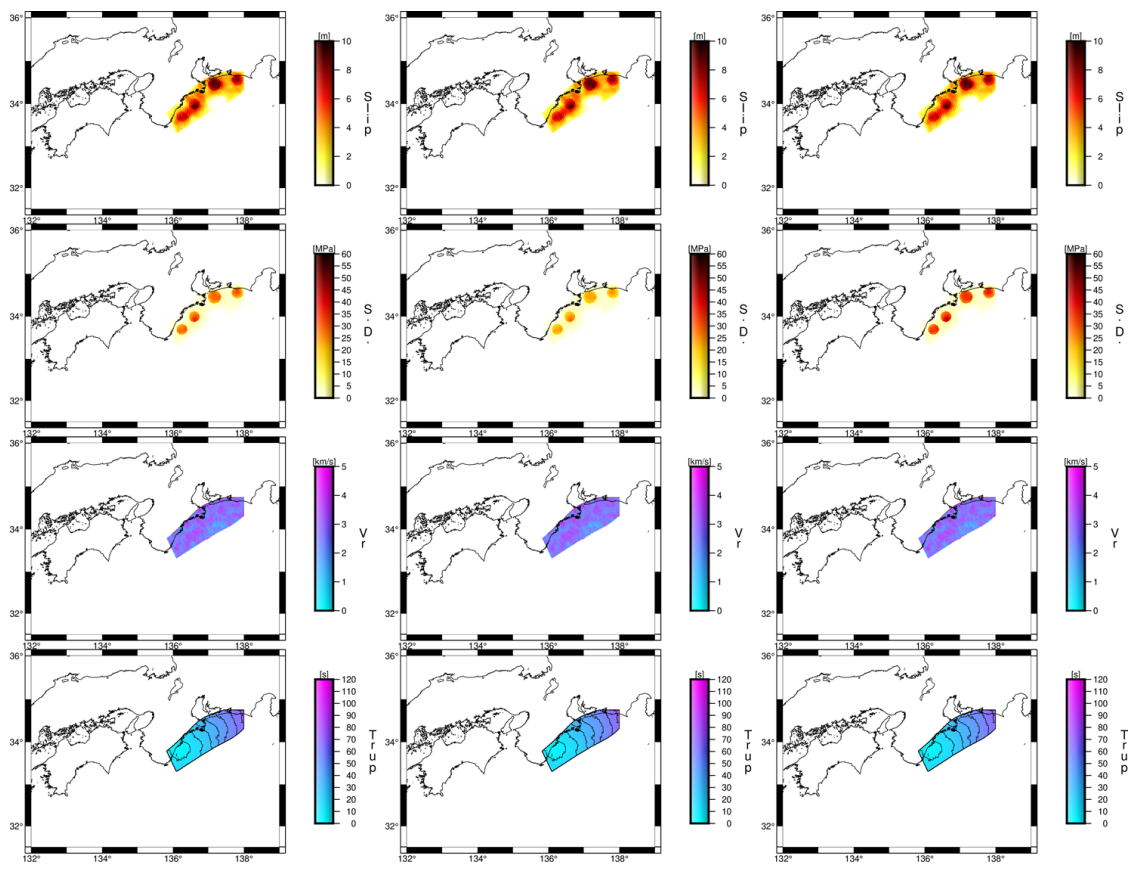


Figure 6.12. The slip, stress drop, rupture velocity and rupture starting time for case 3-3-1 in the left panel, case 3-3-2 in the middle panel and case 3-3-3 in the right panel.

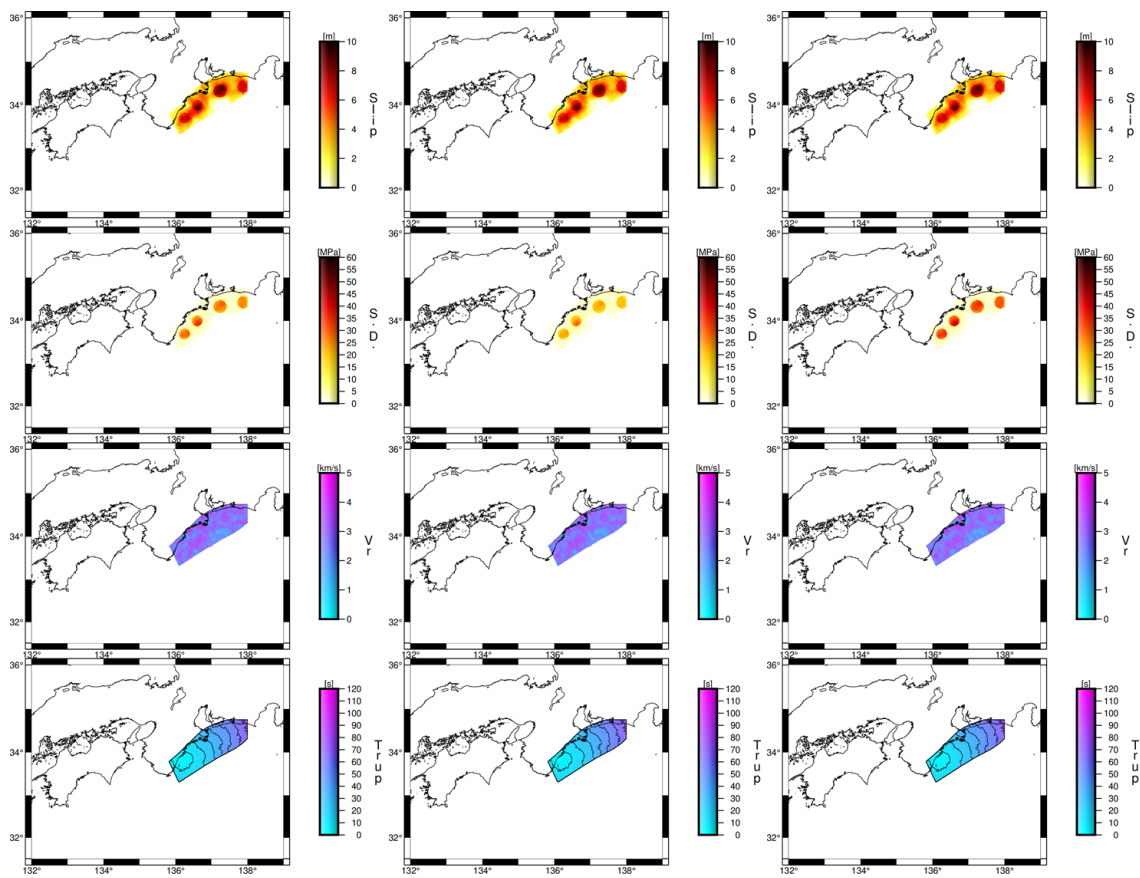


Figure 6.13. The slip, stress drop, rupture velocity and rupture starting time for case 3-4-1 in the left panel, case 3-4-2 in the middle panel and case 3-4-3 in the right panel.

6.4 Reproduced Strong Motions at Damaged Cities and Towns

The final goal of this study is to choose the most realistic source model by comparing the estimated building damage ratio and the observed damage ratio shown in Takemura and Toraya (2015). To the end, we first need to get the target sites for calculating the building damage ratio by using the wooden-house building model which will be explained later, and strong ground motions reproduced from the source models mentioned in the previous section. We extracted the target sites by following the process shown below.

- 1) For municipalities in Takemura and Toraya (2015) with a total collapse rate of 10% or more, the administrative area data as of 1950 by Ministry of Land, Infrastructure, Transport and Tourism (MLIT, 2020) was obtained in QGIS (QGIS development team, 2020) to determine the center of gravity derived from the administrative boundaries, which was used as the representative point for the municipality. For municipalities that existed in 1944 but disappeared in 1950 due to municipal mergers, we converted the data

as of 1944 in Takemura and Toraya to the data as of 1950 by the procedure shown below.

- i. Calculate the number of totally crushed buildings in each municipality and those in the municipality into which they will be merged by 1950, based on the number of households and totally crushed ratio, respectively.
 - ii. The sum of the number of totally crushed buildings of all the municipalities which was merged into one municipality by 1950 divided by the total number of households of all the municipalities is considered to be the total crush ratio in the municipality after the merger.
- 2) For municipalities with a total crush ratio from 1% to less than 10%, the center of gravity of each municipality in Takemura and Toraya (2015) was first obtained in the same way as for the municipalities with total crush ratio over 10%. The municipalities where the strong-motion seismic observation points are located within 2 km from the center of gravity were selected for the comparison of the damage rates in this study. The locations of the strong-motion stations were considered as the sites for calculating the damage ratio. The total number of these sites was 15. Figure 6.14 shows the location of each target site for calculating the building damage ratio.

The interpolation method for site characteristic in chapter 3 was used for the target sites with the totally crush ratio over 10%, and the site characteristics derived by GIT technique explained in chapter 5 at the strong ground motion observation sites were used for the target sites with the totally crush ratio from 1% to less than 10%.

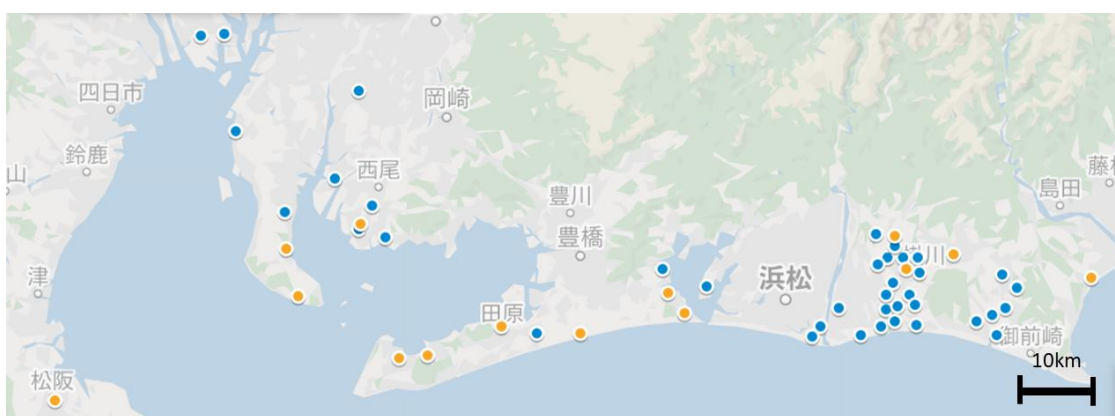
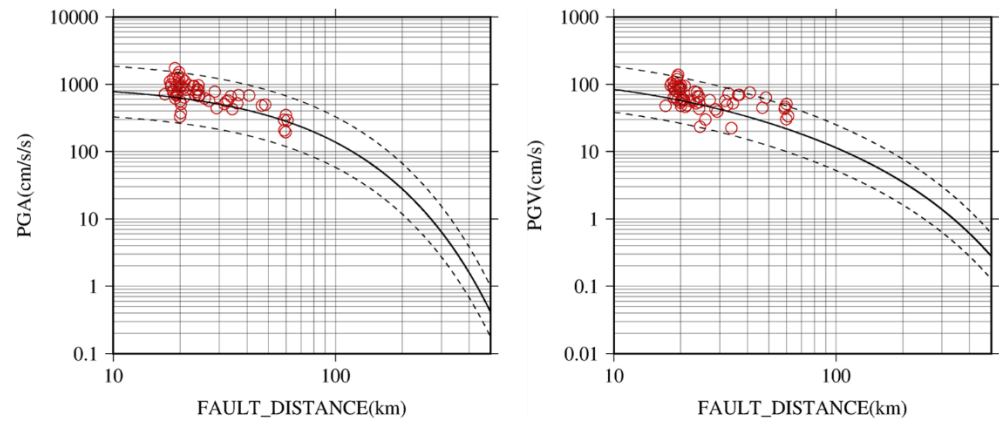


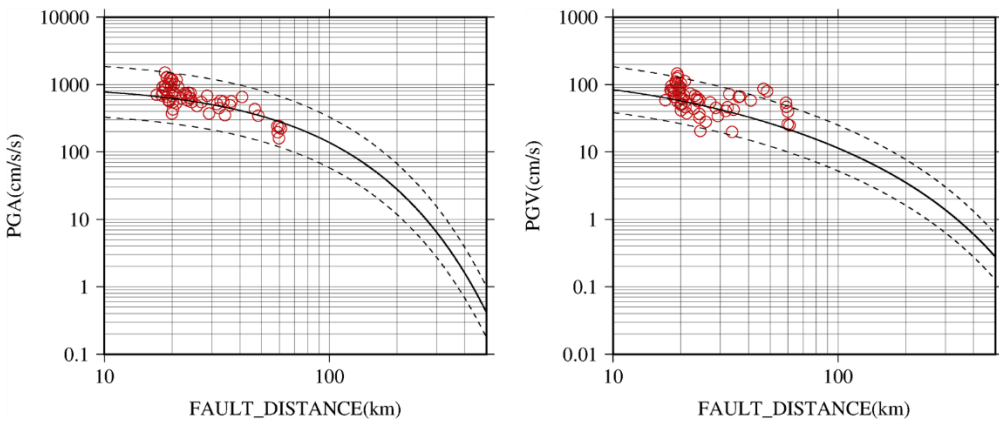
Figure 6.14 Location of each target site. The sites shown in blue circle are those with totally crush ratio are 10% or more, and the sites shown in orange circle are those with totally crush ratio are 1% to less than 10%.

We calculated the strong ground motions at the 53 target sites mentioned above from the 36 different source models. Figures 6.15 to 6.26 show the Relation between PGA and fault distance in the left panel and PGV and fault distance obtained from the PGA and PGV at each target site for all the cases. The blackline and the black dotted line are the attenuation curve and its standard deviation in Morikawa and Fujiwara (2013), respectively.

CASE 1-1-1



CASE 1-1-2



CASE 1-1-3

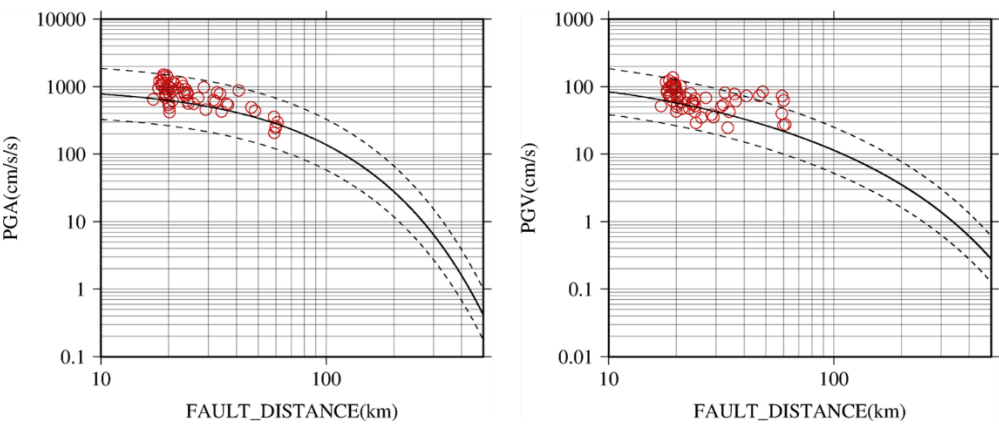
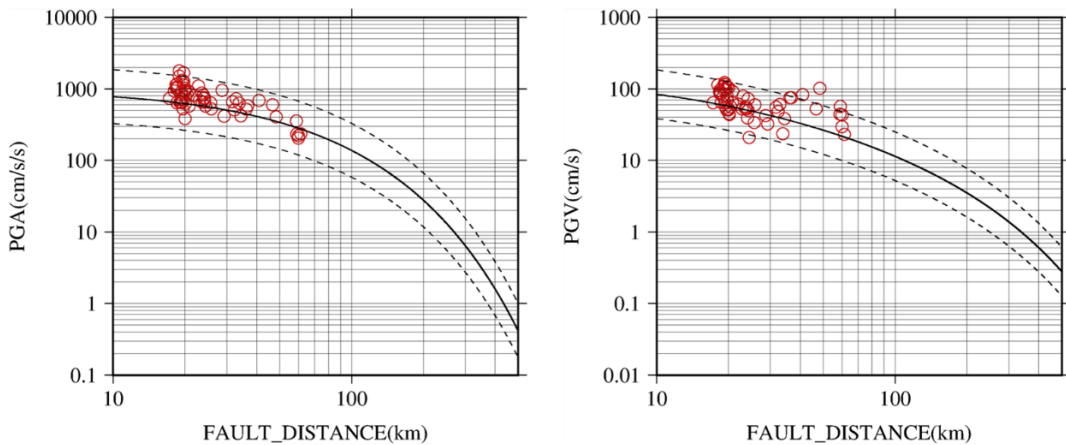
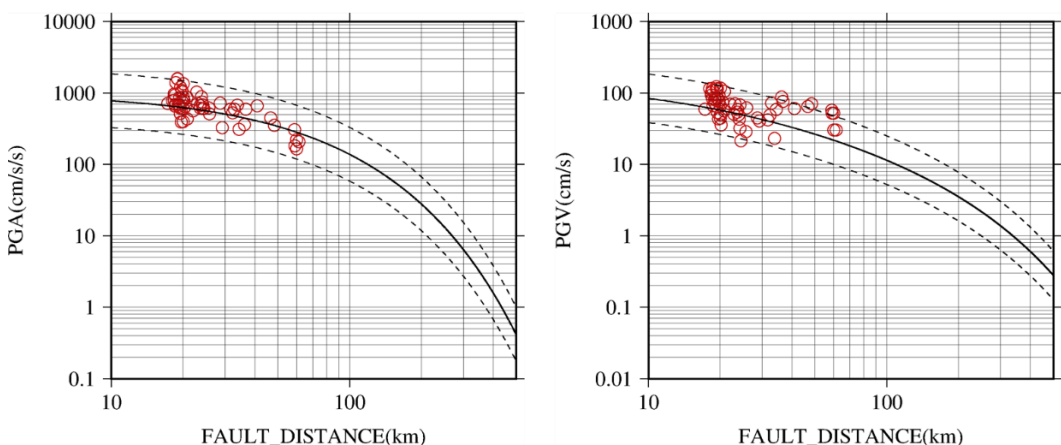


Figure 6.15 Relation between PGA and fault distance in the left panel, and the one between PGV and fault distance in the right panel for case 1-1-1, 1-1-2, and 1-1-3. The blackline and the black dotted line are the attenuation curve and its standard deviation in Morikawa and Fujiwara (2013).

CASE 1-2-1



CASE 1-2-2



CASE 1-2-3

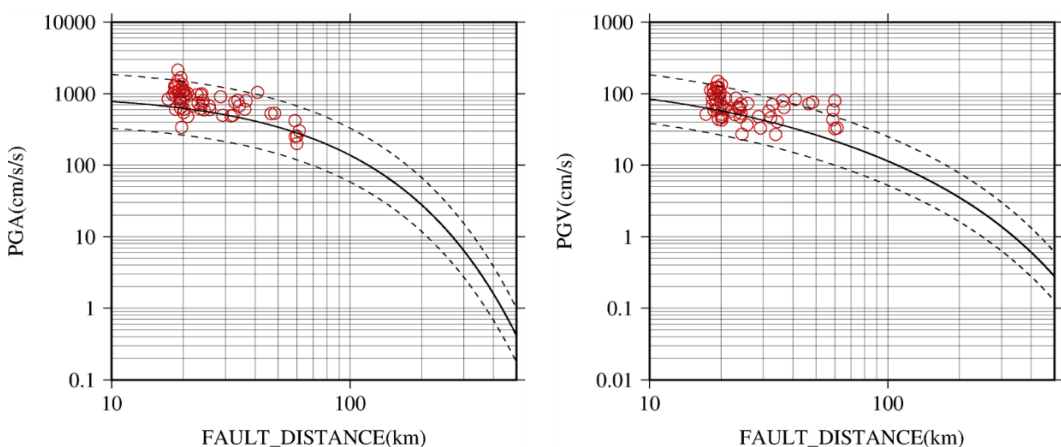
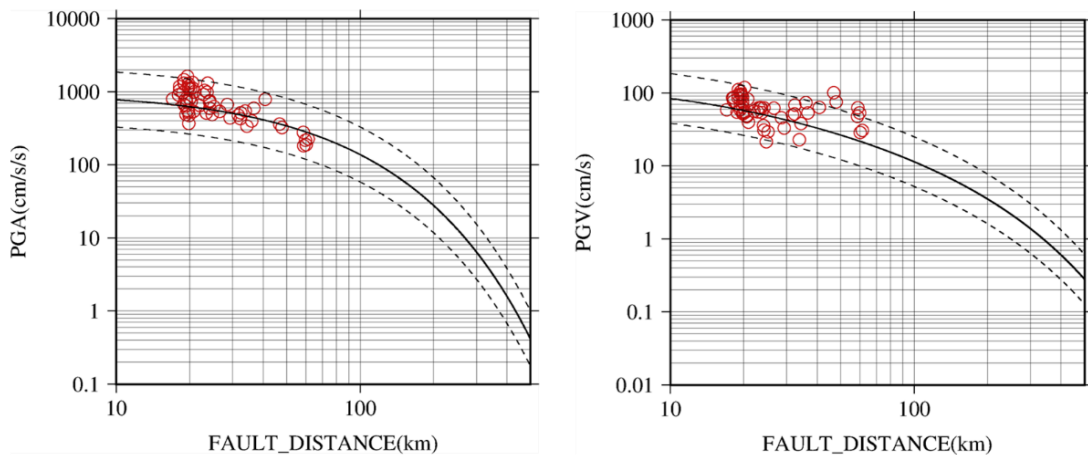
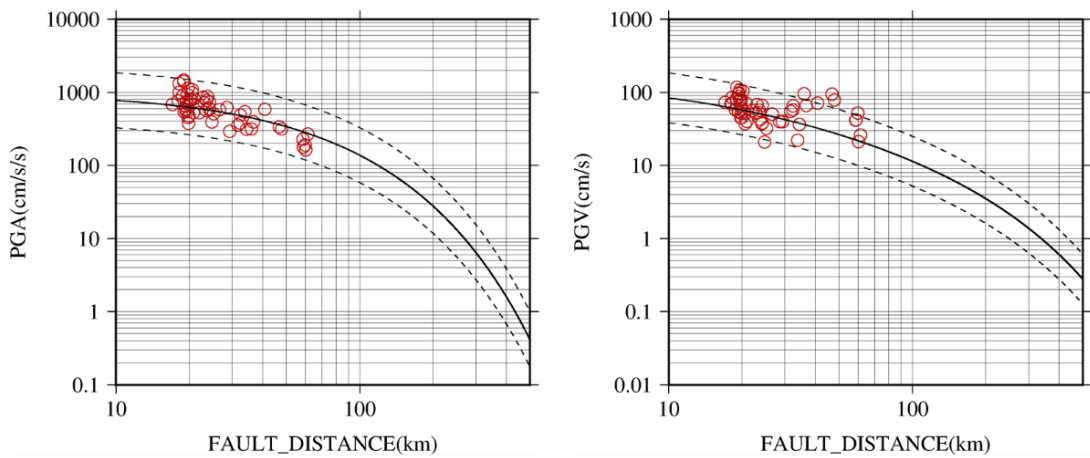


Figure 6.16 Relation between PGA and fault distance in the left panel, and the one between PGV and fault distance in the right panel for case 1-2-1, 1-2-2, and 1-2-3. The blackline and the black dotted line are the attenuation curve and its standard deviation in Morikawa and Fujiwara (2013).

CASE 1-3-1



CASE 1-3-2



CASE 1-3-3

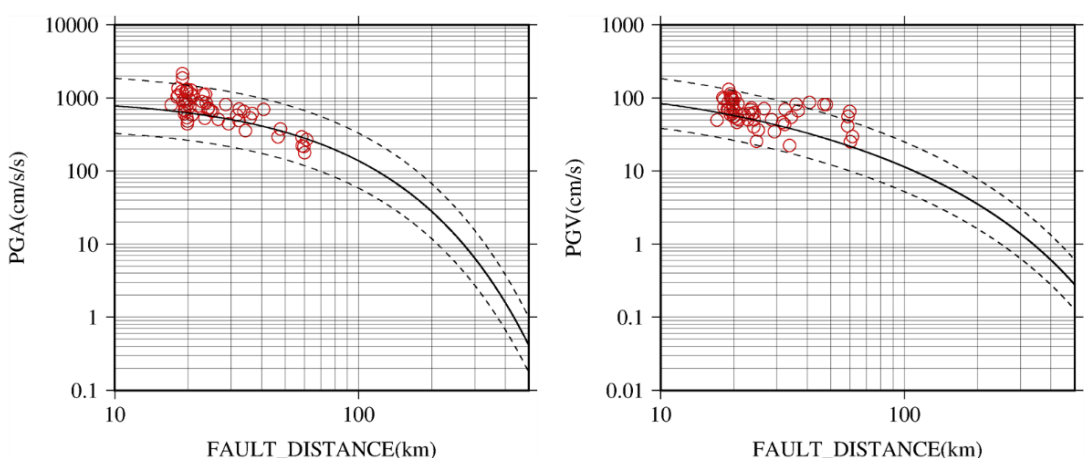
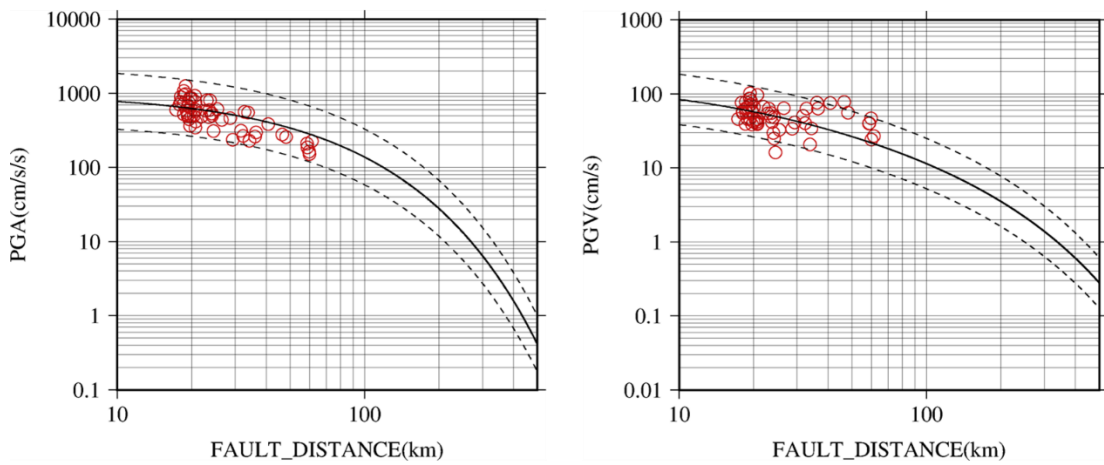
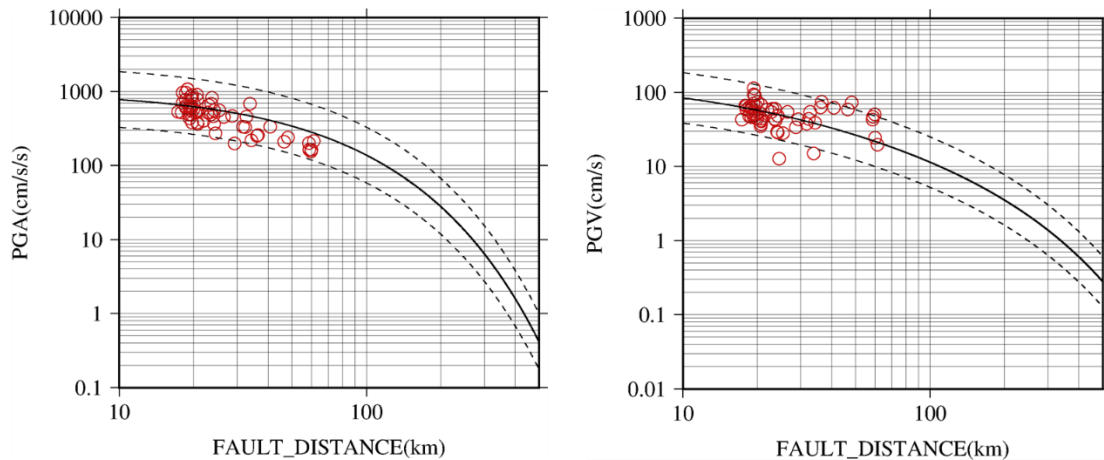


Figure 6.17 Relation between PGA and fault distance in the left panel, and the one between PGV and fault distance in the right panel for case 1-3-1, 1-3-2, and 1-3-3. The blackline and the black dotted line are the attenuation curve and its standard deviation in Morikawa and Fujiwara (2013).

CASE 1-4-1



CASE 1-4-2



CASE 1-4-3

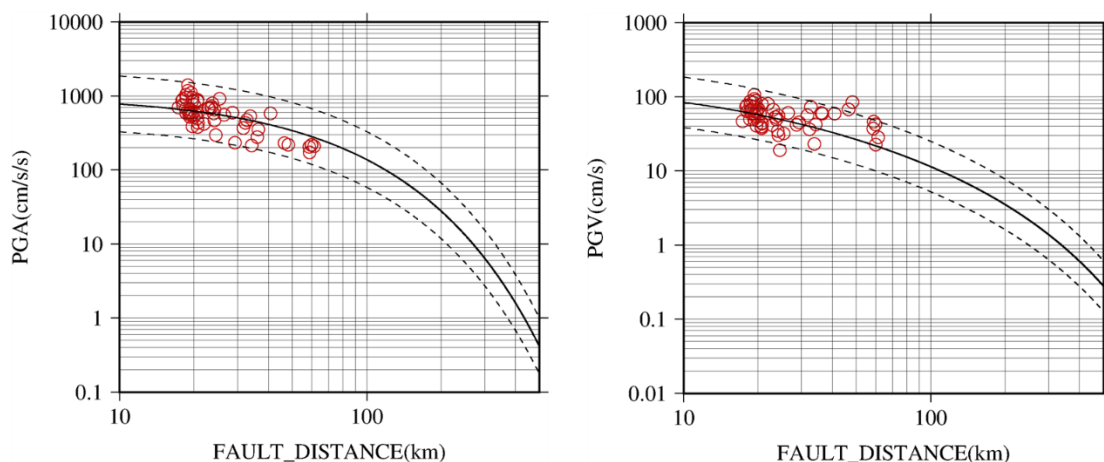
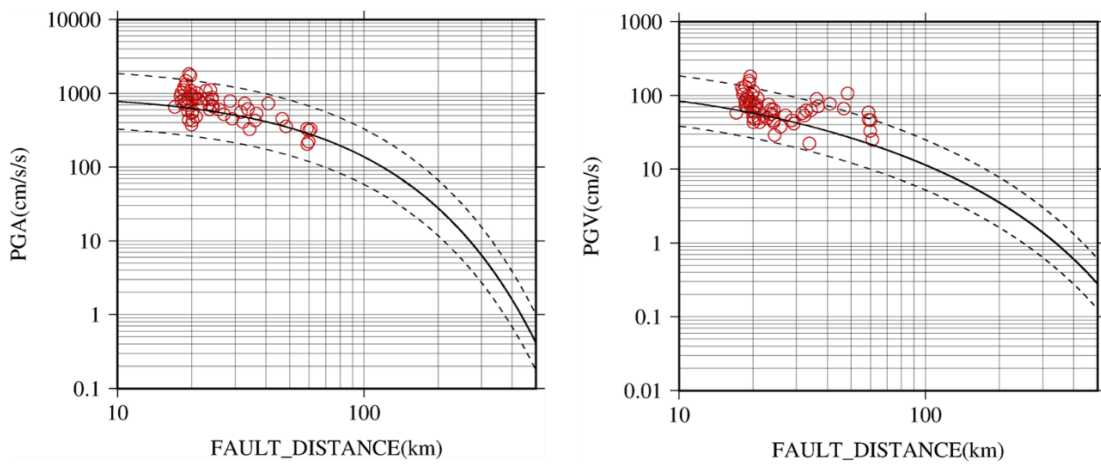
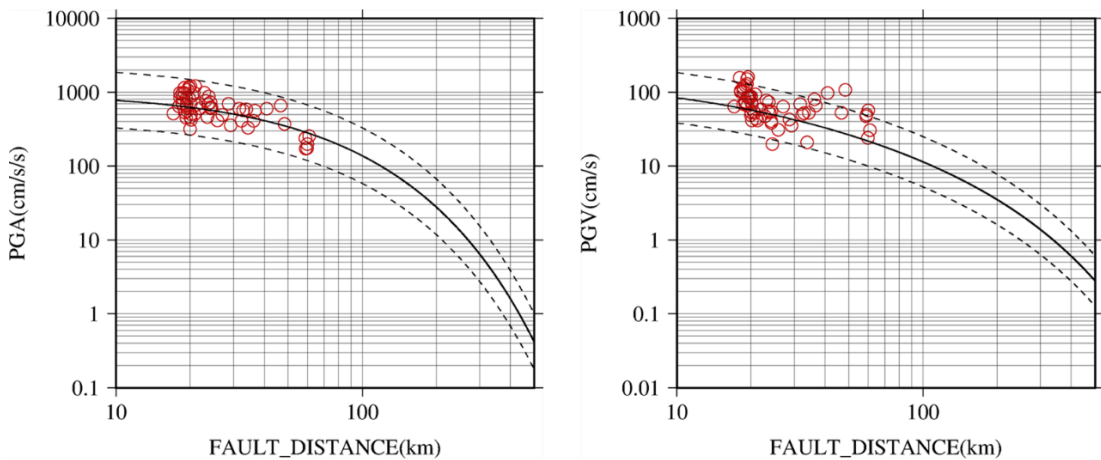


Figure 6.18 Relation between PGA and fault distance in the left panel, and the one between PGV and fault distance in the right panel for case 1-4-1, 1-4-2, and 1-4-3. The blackline and the black dotted line are the attenuation curve and its standard deviation in Morikawa and Fujiwara (2013).

CASE 2-1-1



CASE 2-1-2



CASE 2-1-3

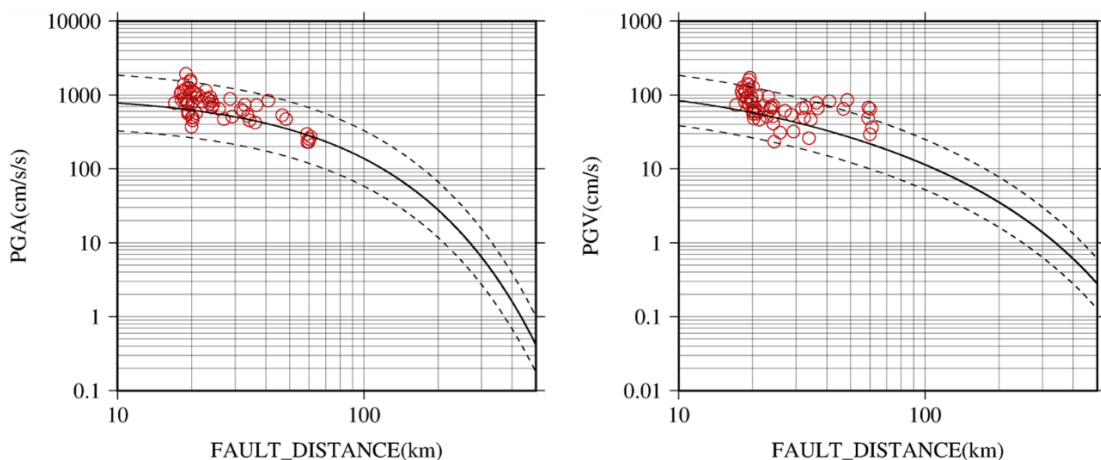
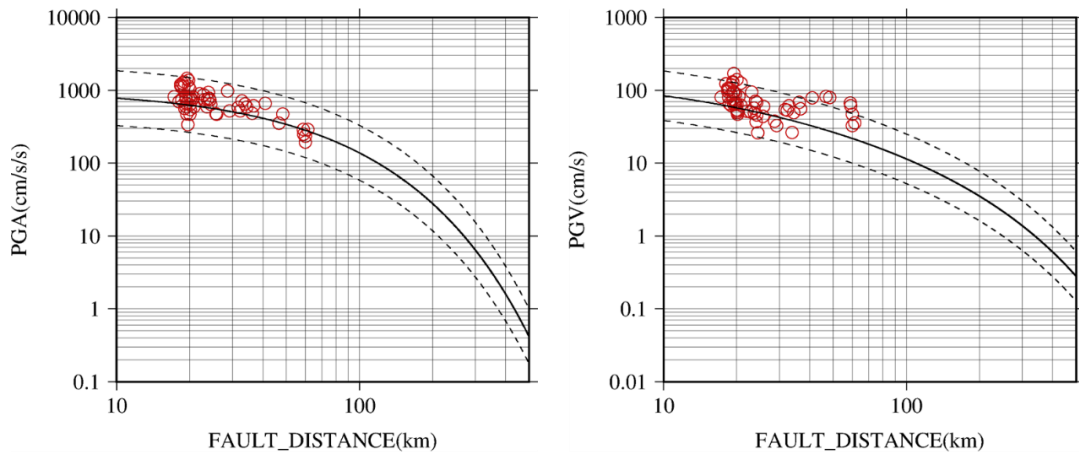
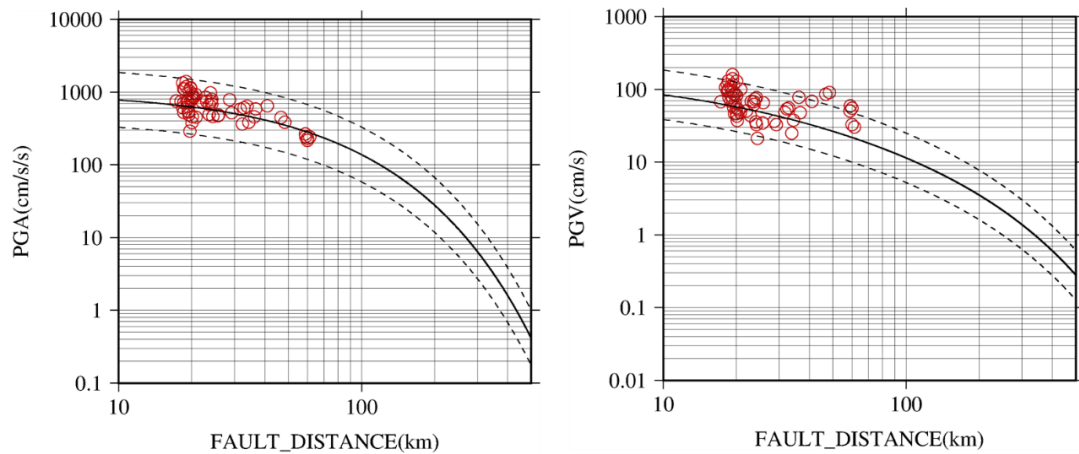


Figure 6.19 Relation between PGA and fault distance in the left panel, and the one between PGV and fault distance in the right panel for case 2-1-1, 2-1-2, and 2-1-3. The blackline and the black dotted line are the attenuation curve and its standard deviation in Morikawa and Fujiwara (2013).

CASE 2-2-1



CASE 2-2-2



CASE 2-2-3

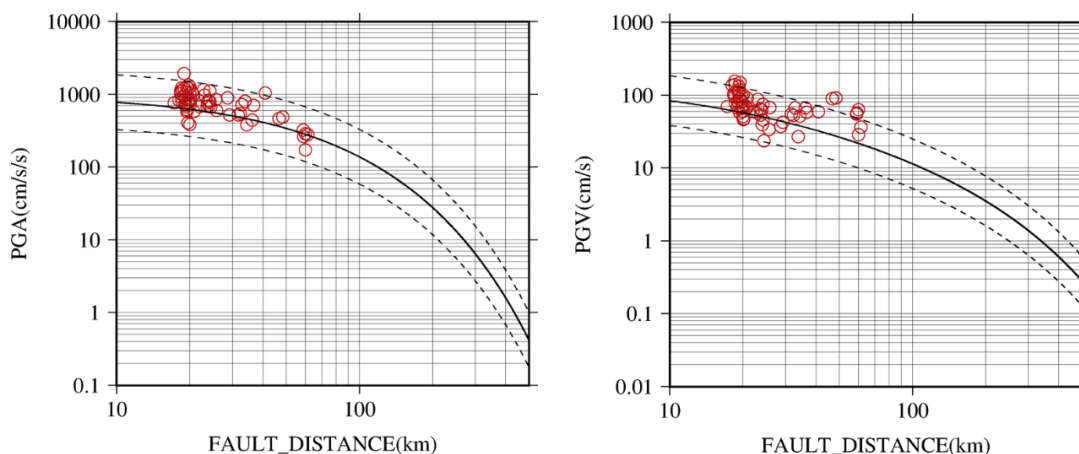
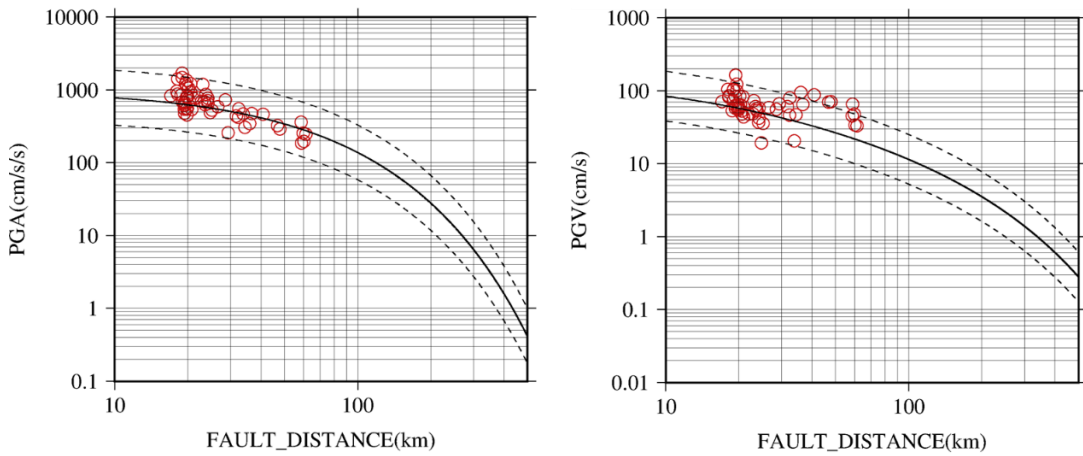
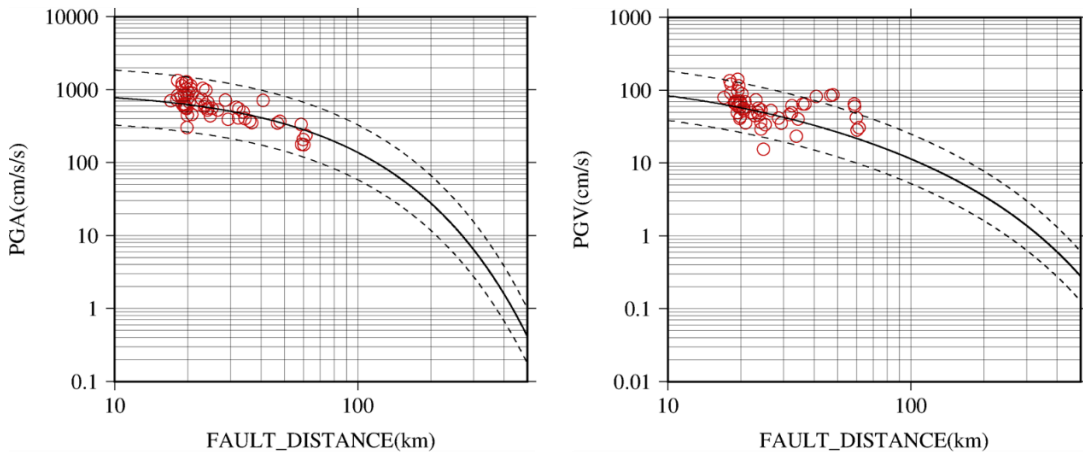


Figure 6.20 Relation between PGA and fault distance in the left panel, and the one between PGV and fault distance in the right panel for case 2-2-1, 2-2-2, and 2-2-3. The blackline and the black dotted line are the attenuation curve and its standard deviation in Morikawa and Fujiwara (2013).

CASE 2-3-1



CASE 2-3-2



CASE 2-3-3

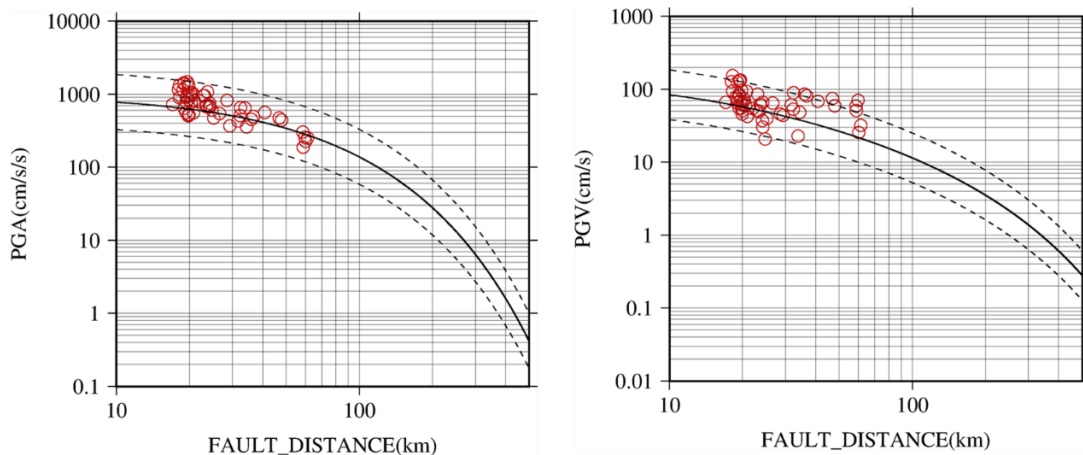
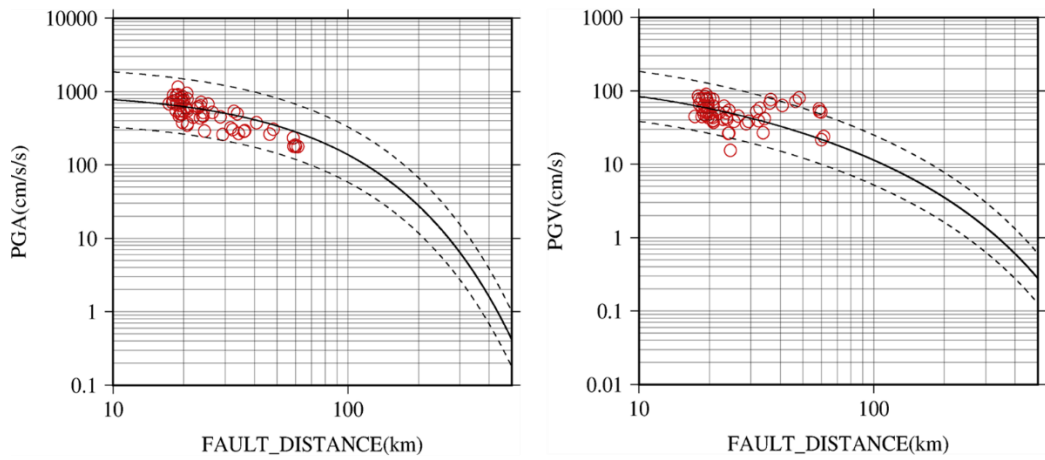
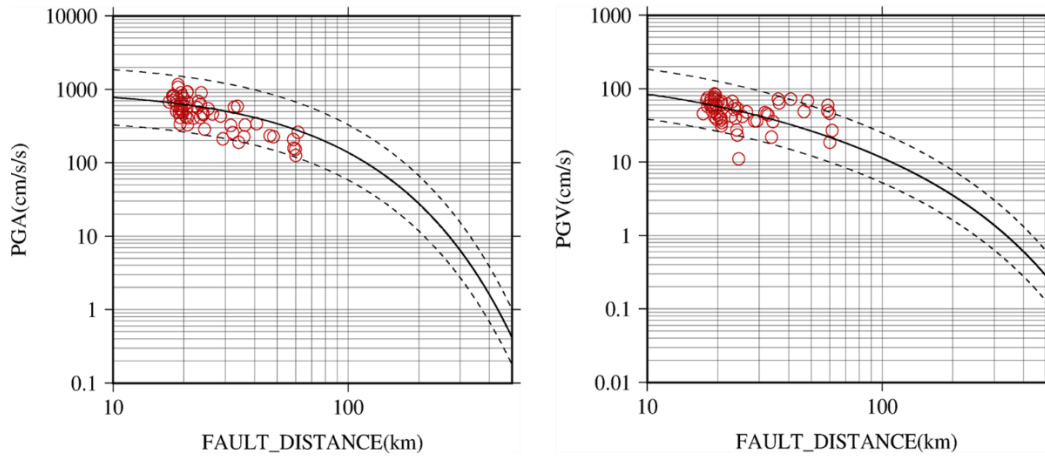


Figure 6.21 Relation between PGA and fault distance in the left panel, and the one between PGV and fault distance in the right panel for case 2-3-1, 2-3-2, and 2-3-3. The blackline and the black dotted line are the attenuation curve and its standard deviation in Morikawa and Fujiwara (2013).

CASE 2-4-1



CASE 2-4-2



CASE 2-4-3

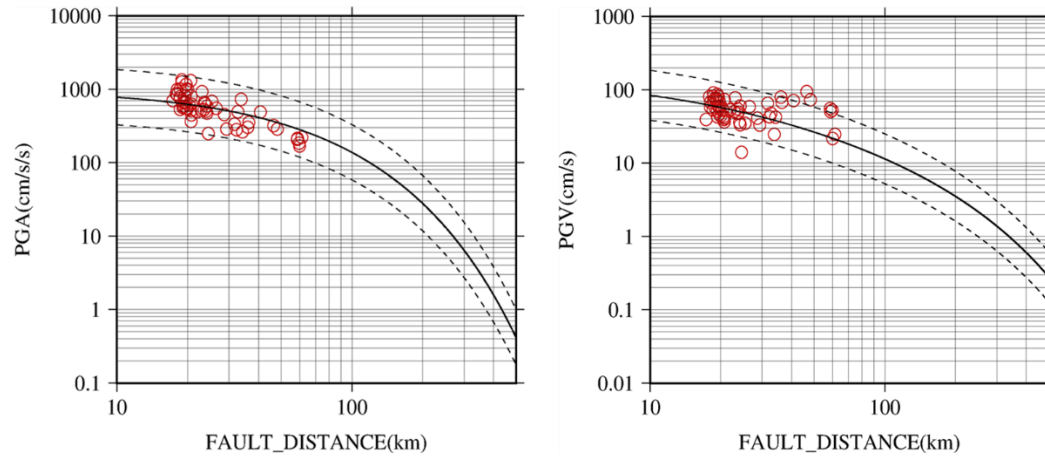
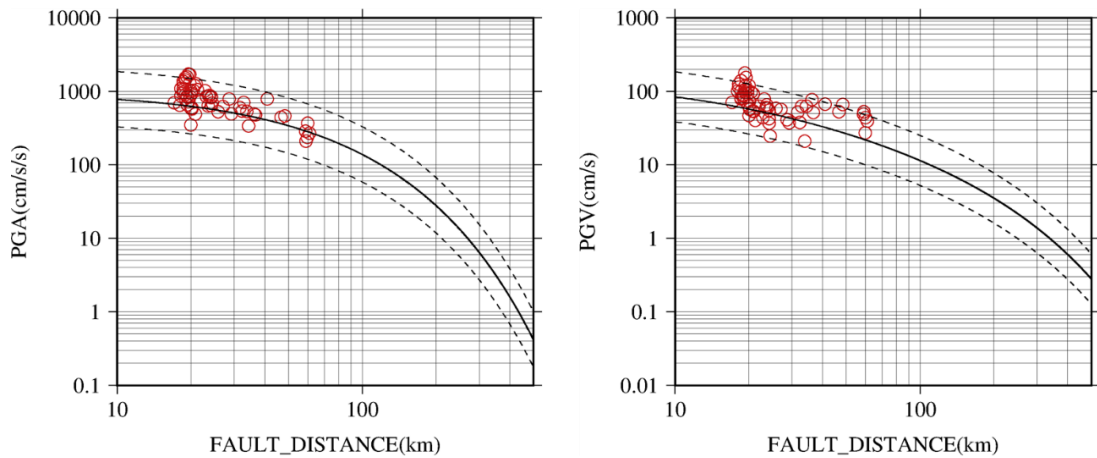
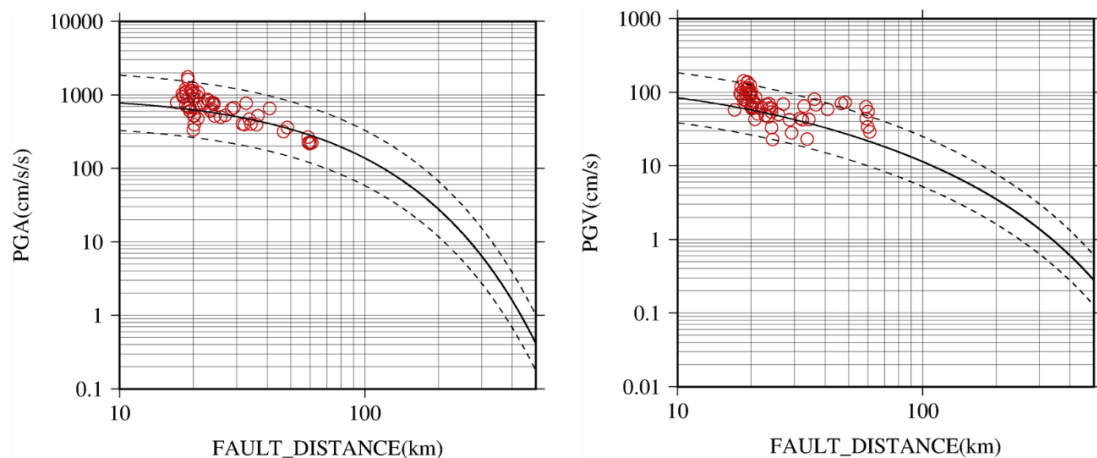


Figure 6.22 Relation between PGA and fault distance in the left panel, and the one between PGV and fault distance in the right panel for case 2-4-1, 2-4-2, and 2-4-3. The blackline and the black dotted line are the attenuation curve and its standard deviation in Morikawa and Fujiwara (2013).

CASE 3-1-1



CASE 3-1-2



CASE 3-1-3

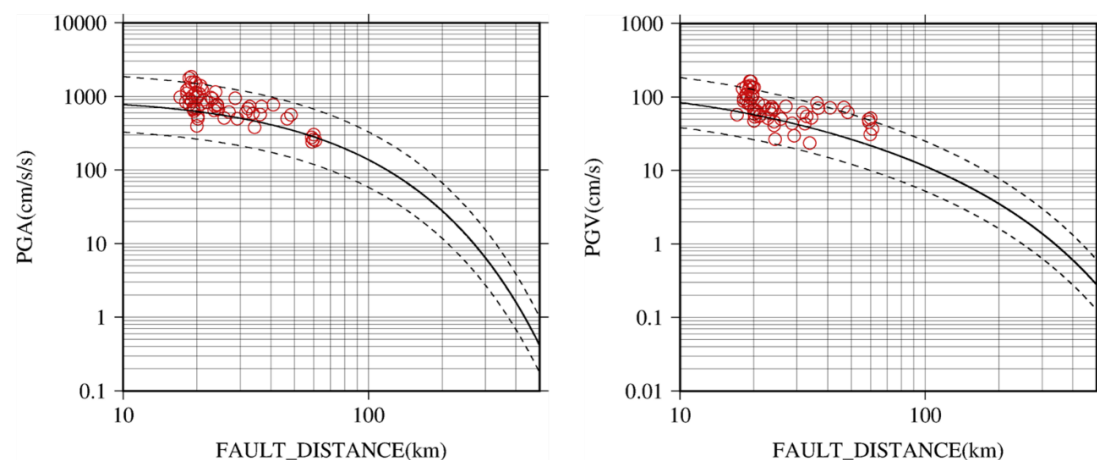
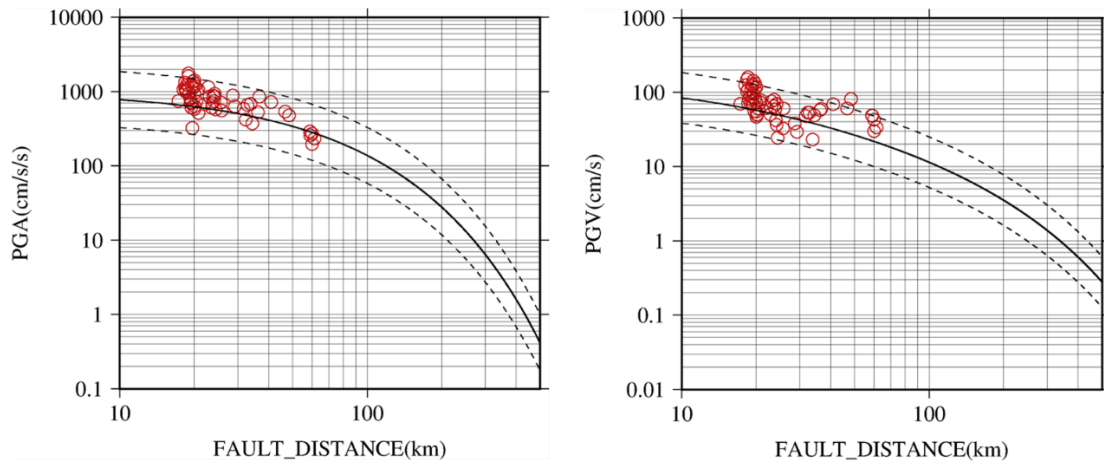
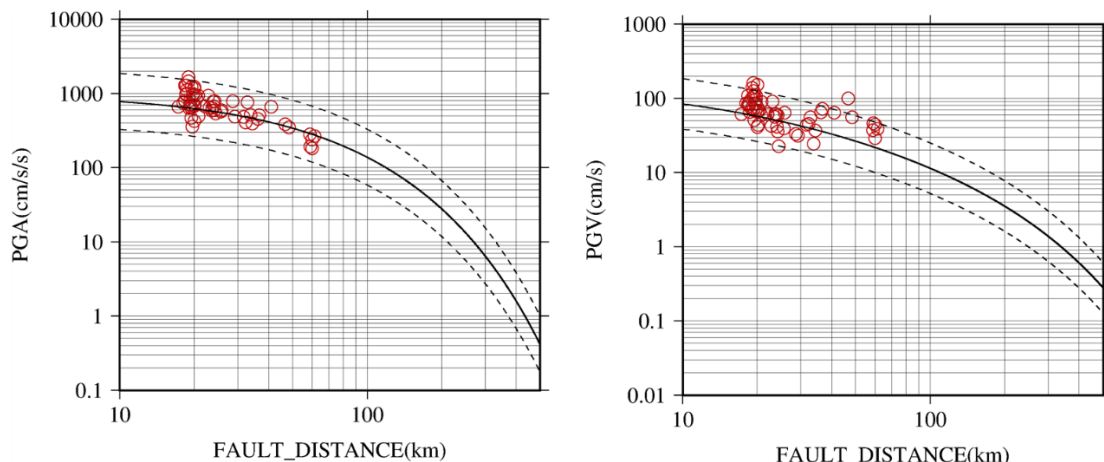


Figure 6.23 Relation between PGA and fault distance in the left panel, and the one between PGV and fault distance in the right panel for case 3-1-1, 3-1-2, and 3-1-3. The blackline and the black dotted line are the attenuation curve and its standard deviation in Morikawa and Fujiwara (2013).

CASE 3-2-1



CASE 3-2-2



CASE 3-2-3

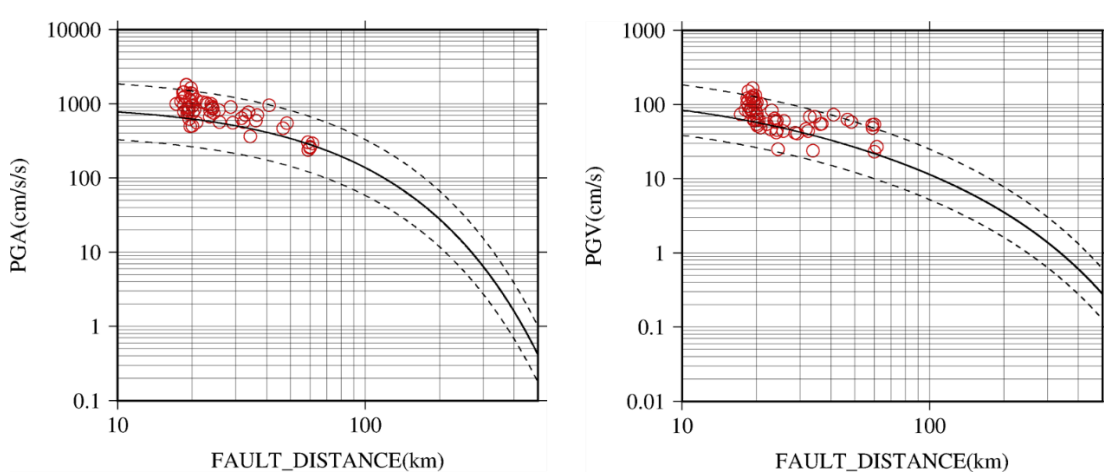
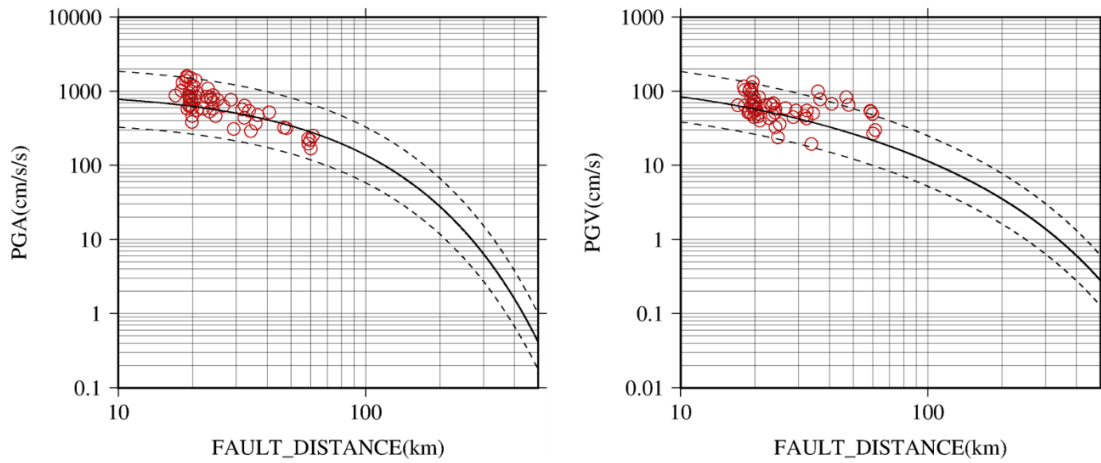
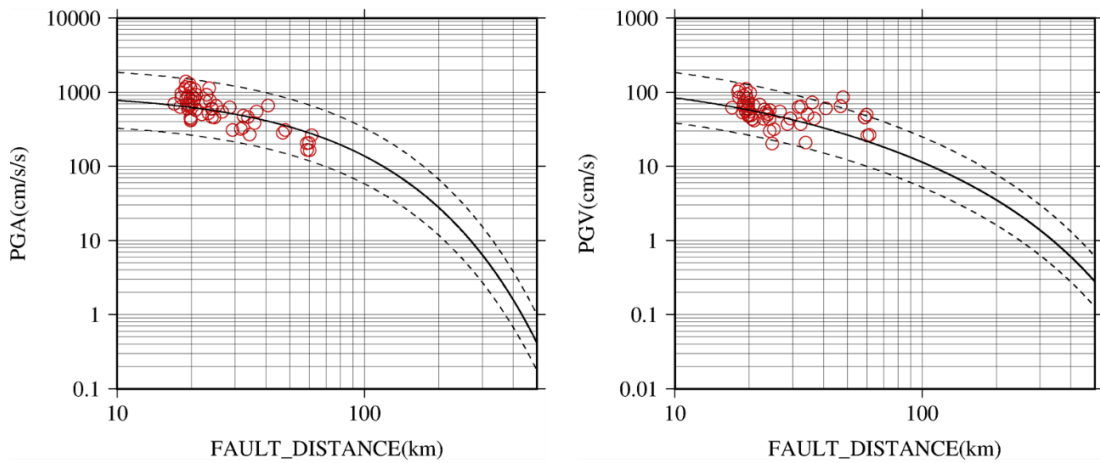


Figure 6.24 Relation between PGA and fault distance in the left panel, and the one between PGV and fault distance in the right panel for case 3-2-1, 3-2-2, and 3-2-3. The blackline and the black dotted line are the attenuation curve and its standard deviation in Morikawa and Fujiwara (2013).

CASE 3-3-1



CASE 3-3-2



CASE 3-3-3

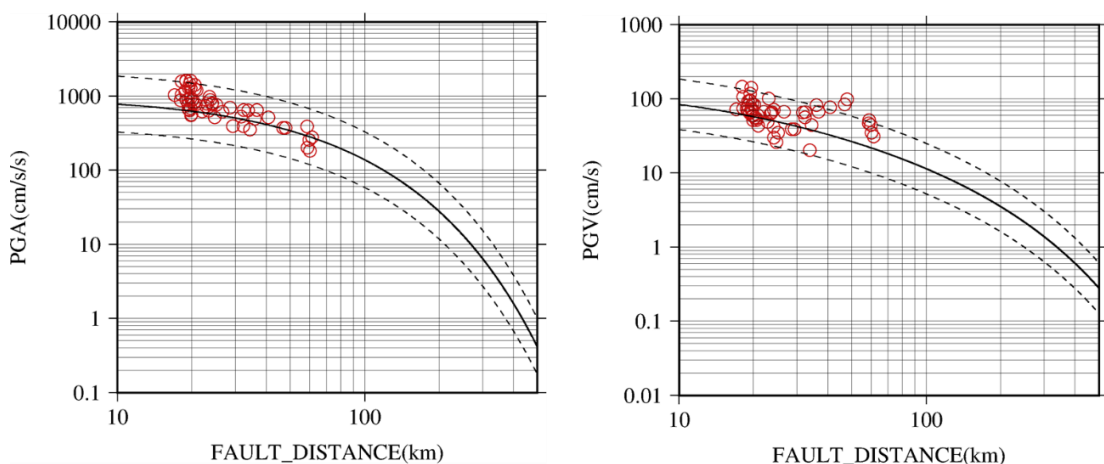
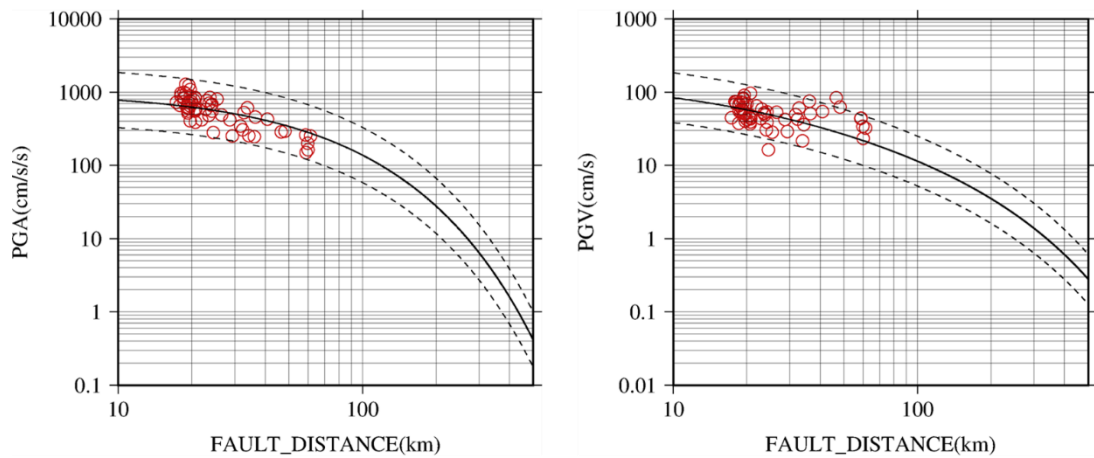
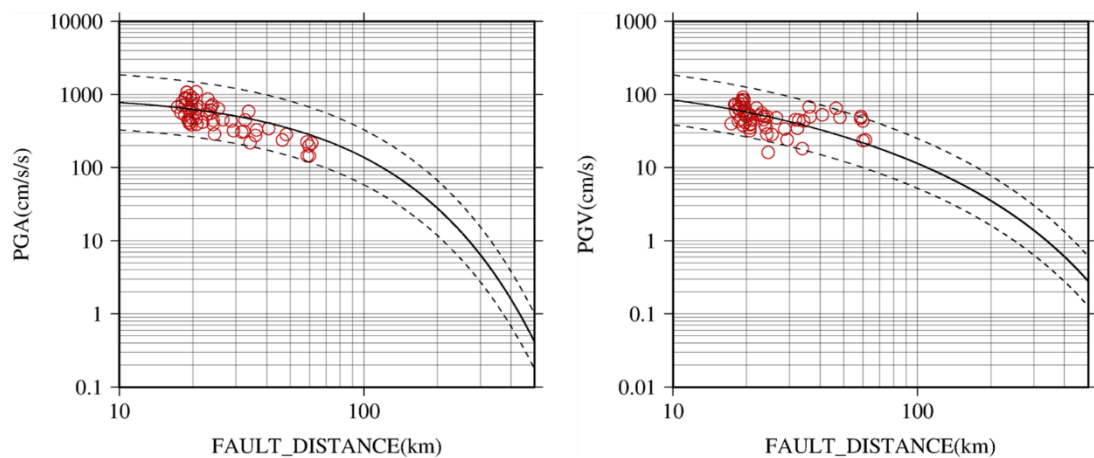


Figure 6.25 Relation between PGA and fault distance in the left panel, and the one between PGV and fault distance in the right panel for case 3-3-1, 3-3-2, and 3-3-3. The blackline and the black dotted line are the attenuation curve and its standard deviation in Morikawa and Fujiwara (2013).

CASE 3-4-1



CASE 3-4-2



CASE 3-4-3

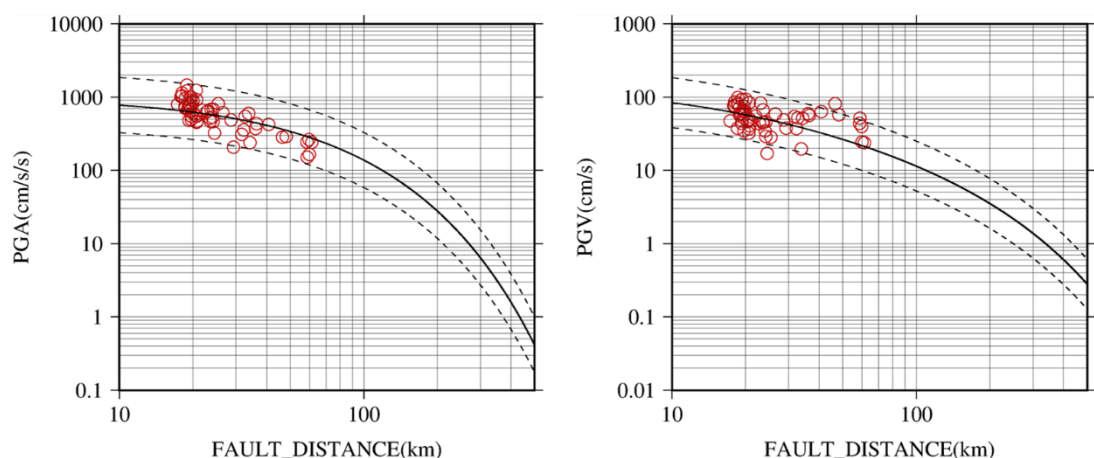


Figure 6.26 Relation between PGA and fault distance in the left panel, and the one between PGV and fault distance in the right panel for case 3-4-1, 3-4-2, and 3-4-3. The blackline and the black dotted line are the attenuation curve and its standard deviation in Morikawa and Fujiwara (2013).

6.5 Damage Evaluation by the Damage Prediction Model of Old Houses

Here we introduce the damage prediction model of those old houses that existed in 1944 when the Tonankai earthquake hit the Tokai region based on the study by Yagi and Kawase (2019). That model is based on the Yoshida model (Yoshida et al., 2004), which was based on the Nagato-Kawase model (Nagato & Kawase, 2002). Thus, we need to describe first the Nagato-Kawase model and then the Yoshida model.

Nagato and Kawase constructed a model for estimating the damage ratio of a wooden houses from observed or simulated ground motions (Nagato & Kawase, 2002). They first calculated the observed damage ratios (ODRs) of heavy damage or collapse based on statistical data in Nada and Higashinada Wards in Kobe City after the 1995 Hyogo-ken Nanbu earthquake. Then they constructed initial two Degree-of-Freedom models by referring to the Japanese building code and the surveyed strength distribution of the damaged houses in Kobe. They assumed that wooden houses are characterized by the degrading trilinear hysteresis type of nonlinear springs combined with a bilinear type of slip model. Subsequently, they analyzed the seismic responses of the initial models and obtained the calculated damage ratios (CDRs) for the theoretical ground motions in every 160 m and 80 m grid reproduced by Matsushima and Kawase (2000). The heavy damage criterion of 1/10 in terms of the calculated story drift in either the first or second story was adopted based on the shaking-table experiments. They compared the ODR and CDR, modified the strength, and performed the analysis again until the difference between the ODR and CDR was sufficiently small. The Nagato-Kawase model proved to successfully reproduce the damage belt caused by the 1995 Hyogo-ken Nanbu earthquake. As a result, they found that Japanese wooden houses would be twice as strong as the minimum requirement by the building standard in 1981 on the average.

The major drawback of the Nagato-Kawase model is that it does not depend on the construction period. Therefore, Yoshida et al. (2004) upgraded the model by following the procedure of the Nagato-Kawase model to consider the four construction periods for a more detailed damage estimation of Japanese wooden houses. They used 24 representative models for the two-floor wooden houses with different strengths. For the first floor, eight representative strength factors relative to the standard strength and the existing ratio were used. These eight strength factors were shown in Figure 6.27. For the second floor, they used a ratio of the second story strength relative to the first story strength to be 1.0, 1.5, and 2.0. The strengths of the standard wooden model were defined by the necessary structural wall quantity for a wooden house according to the Japanese building standard. The necessary structural wall quantity is satisfied when the base shear coefficient is 0.2 at the angle of deformation 1/120 rad. They used the damage statistics for the tax evaluation by municipal governments which provides us the construction period of each house. Based on the comparison between the CDR by the Nagato-Kawase model and the averaged ODR by the tax evaluation, we found that the criterion for the ODR by the tax evaluation (corresponding to the “total damage” level) should be 1/30. Then they set the different parameter α for different construction period, which is the ratio between the structural strength of

a wooden house for a specific construction period and that of the standard wooden model (as the code requirement). Table 6.1 shows those values for four construction periods. They successfully expanded the Nagato–Kawase model to consider different construction periods.

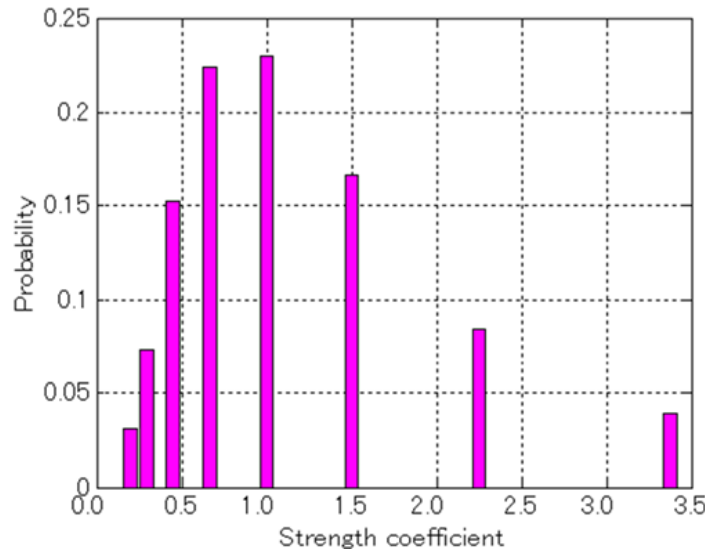


Figure 6.27. Log-normal distribution of existing probability with different strength coefficient (normalized strength with reference to the average) for the two-floor wooden house of the Yoshida model.

Table 6.1. Parameter α for every construction period in the Yoshida model.

Construction Period	1930- 1950	1951-1970	1971-1981	After 1982
α	1.80	2.15	2.90	4.70

In the construction of damage prediction models for old wooden houses before 1930, Yagi and Kawase (2019) first collected the measurement data of natural frequencies for 262 wooden buildings in Japan based on microtremors. The construction method is briefly described below.

- 1) It is assumed that the square of the natural frequency of the wooden house is proportional to its yield strength. Traditional “old” wooden houses are classified into two groups as those built before 1900 and built in between 1900 and 1930. Traditional “new” wooden houses are also classified into the same four groups as the Yoshida model, namely, 1930-1950, 1951-1970, 1971-1981, and 1982 to present.
- 2) Determine the least-square regression equation for estimating the average natural frequencies of wooden houses for each range of the construction period from the relationship between natural frequencies based on microtremor measurements of 262 wooden houses and their

construction years.

- 3) Estimate the yield strength ratio of two old house groups based on the linear relationship between the square of natural frequencies and the yield strength ratios, together with the yield strength ratio of one of the age groups in the Yoshida model used as a reference.
- 4) Assuming that the square of the natural frequencies of each house follows a logarithmic normal distribution, the strength distribution of the old house group before 1900 is calculated from the natural frequencies based on the microtremor measurements of 17 houses built before 1900.
- 5) The damage prediction model for old houses built before 1900 is constructed using the yield strength ratio and yield strength distributions obtained in 3) and 4).

Here is a more detailed description of the procedure. First, we need to determine a formula for estimating the mean natural frequency of wooden houses as a function of their construction years. For houses built after 1900, an approximate curve is determined by the least-squares method based on the relationship between natural frequencies of wooden houses built after 1900 and their years of construction, and we assume that the average natural frequency for each construction period will follow this approximated curve. Because we observed that the variation of natural frequency is small and there was no major technical innovation in the period before 1900, the mean natural frequencies are assumed to be constant regardless of the year of construction so that the mean value of natural frequencies of 17 old houses is adopted. Then, the formula for estimating the average natural frequencies for the year of construction is determined as follows.

$$f'^2 = e^{(0.010709x - 18.077)} \quad (x > 1900) \quad (6.1)$$

$$f'^2 = 7.95 \quad (x \leq 1900) \quad (6.2)$$

From these equations and the representing year of construction for each construction period, we can estimate the square of average natural frequency for each construction period as summarized in Table 6.2.

Table 6.2. Estimated square frequency for each construction period

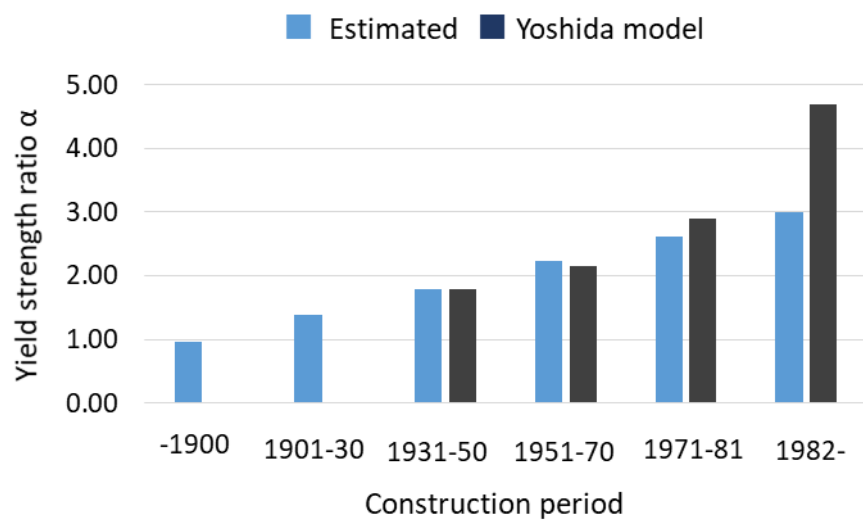
Period	Representative year of construction	$f^2(\text{Hz}^2)$
-1900	-	7.95
1900-30	1915	11.38
1930-50	1940	14.87
1951-70	1960	18.42
1971-81	1975	21.63
1982-	1988	24.86

Next, assuming that the yield strength ratios of each construction-period group of the

Yoshida model are proportional to the square of the mean natural frequency of each age group shown in Table 6.3, the yield strength ratios of each group, including "old house before 1900" and "houses built from 1900 to 1930", are re-evaluated with respect to each of the four age groups in the Yoshida model as a reference. Comparisons of the yield strength ratios of the Yoshida model in the four periods and the re-evaluated yield strength ratios in the same four periods and two additional ones for old houses are shown in Figure 6.28. The yield strength ratios re-evaluated from the yield strength ratio of the construction period after 1982 of the Yoshida model are excluded because they were significantly different from those of other construction periods of the Yoshida model. This may be due to the fact that the formula for estimating average natural frequencies does not adequately reflect the rapid increase in natural frequencies after 1982 due to the revision of the building code, because the formula is determined to fit to the data in a wide range of construction years from 1900 to 2000. On the other hand, the estimated yield strength ratios of the Yoshida model for the periods before 1981 can be stably reproduced if we use one of the construction periods before 1981 as a reference. Therefore, the yield strength ratios of the construction periods before 1900 and between 1900 and 1930 are determined as the average of their yield strength ratios obtained from the three estimates with different reference periods in Figure 6.28. They are given in Equations (6.3) and (6.4).

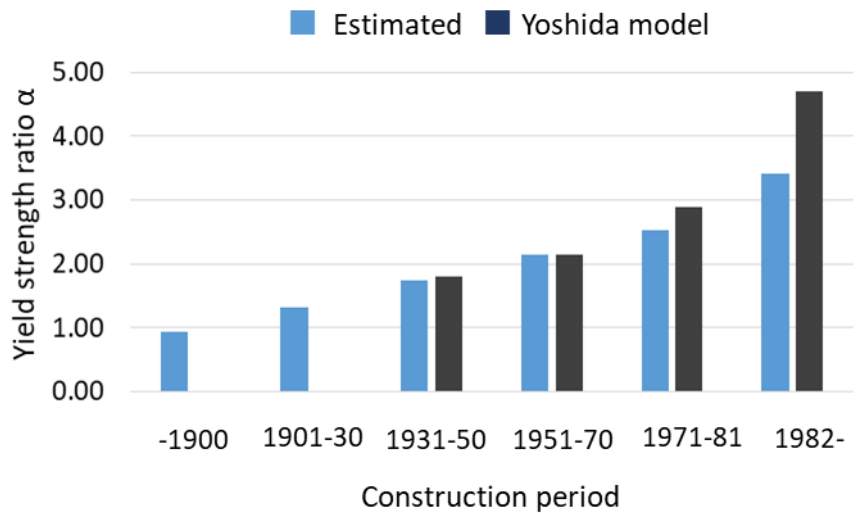
$$-1900 : \bar{\alpha} = 0.99 \quad (6.3)$$

$$1900-1930 : \bar{\alpha} = 1.41 \quad (6.4)$$

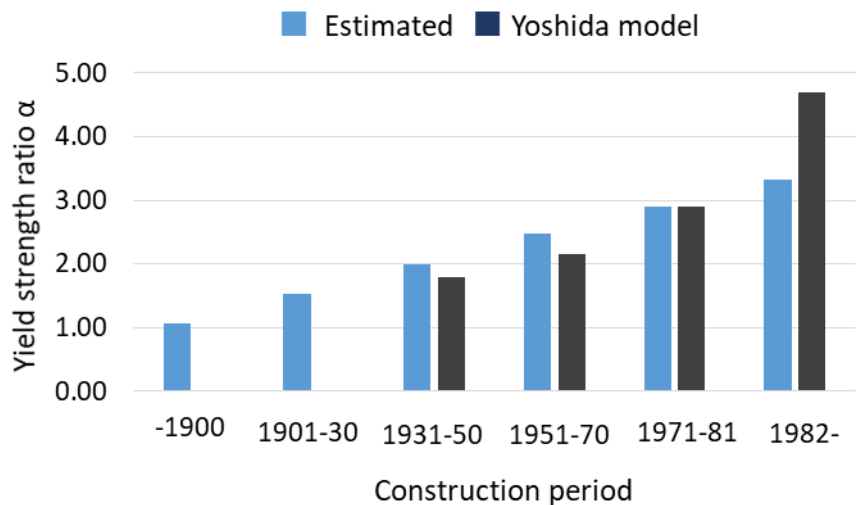


(a) Reference: 1930-1950

Figure 6.28. Estimated yield strength ratios by using three construction-periods in the Yoshida model used as a reference.



(b) Reference: 1951-70



(c) Reference: 1971-81

Figure 6.28. (Cont.) Estimated yield strength ratios by using three construction-periods in the Yoshida model used as a reference.

In the method proposed by Yoshida et al. (2004), the damage ratio is calculated by using the log-normal distribution of the existing ratios with respect to the yield strength. Therefore, it is necessary to calculate the yield strength distribution of old houses in the damage prediction model. Yagi and Kawase (2019) proposed to use the natural frequencies of 17 old houses that have not been relocated. Again assuming that the square of natural frequencies is log-normally distributed, the probability density function is constructed and then used to discretize the distribution into 8 representative values with equal spacing on the logarithmic axis. The existng ratio is obtained as

shown in Table 6.3. However, when we compare these existing ratio distribution with that of the Yoshida model, the distribution of the Yagi-Kawase model is much narrower than that of the Yoshida model. This look strange because houses were built before 1900 without any code specifications so that their variation of the yield strength should be much larger than that of newer houses after the first seismic code implementation in 1929 in Japan. The narrow distribution of squared frequencies in Table 6.3 could come from the fact that only well-constructed houses were survived after hundreds of years. Because it is impossible to sample all kinds of houses with shabby- or well-construction built before 1900, we assumed here the same wide distribution of the yield strength of newer houses as the Yoshida model (Figure 6.27). Therefore, we virtually extend the Yoshida model by replacing only its average yield strength as shown in Equations (3) and (4). In Figure 6.29 we plot the nonlinear base shear coefficient versus shear deformation relationship for the average yield strength model of the construction period before 1900.

Table 6.3. Existing ratios of old houses (~1900) as a function of the yield strength based on the squared natural frequency proposed in Yagi and Kawase (2019).

Yield strength ratio= f^2 ratio to the average	Existing ratio
0.3679	0.0143
0.4724	0.0447
0.6065	0.1152
0.7788	0.2031
1.0000	0.2454
1.2840	0.2031
1.6487	0.1152
2.1170	0.0591

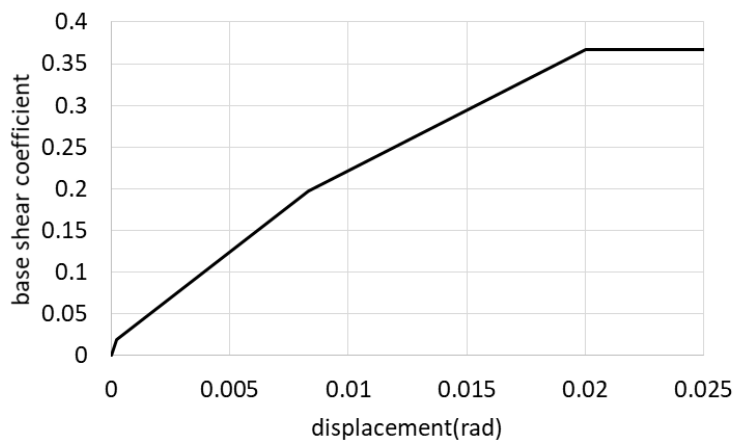


Figure 6.29. Skelton of the nonlinear shear deformation characteristics of the average model for the old period (~1900).

In this study, we compare the estimated collapse ratio with the observed collapse ratio by inputting the strong ground motions obtained from the 36 different source models to the wooden-

house model explained above by following the process below.

First, the term of “totally crushed” in the observed record is changed to “collapse” in this study from now on, considering its definition, which has been already explained. The wooden-house building model can estimate the ratio of sum of “severely damaged” and “collapsed” buildings. In order to obtain the ratio of “collapsed” buildings, we calculated it by multiplying the ratio of sum of “severely damaged” and “collapsed” buildings by 0.58. 0.58 is the ratio of “collapsed” buildings to “severely damaged” buildings and “collapsed” buildings which was obtained from the records of 1995 Hyogo-ken Nanbu earthquake and 2016 Kumamoto earthquake.

For a more accurate estimation of building damage, it is necessary to reflect the percentage of buildings present at the time of construction. We estimated the number of buildings constructed before 1900, within 1900 to 1930, and after 1930, which is the category of the wooden-house building model, by using the survival rate curve and the Housing and Land Statistical Survey as of 1958 found in Koura (1958).

As a result, the ratios of 1900, 1930 and 1950 were 26:60:14. This existence ratio is taken into account to determine the overall collapse rate. Figure 6.30 shows the Survival rate curve shown in Koura (2017).

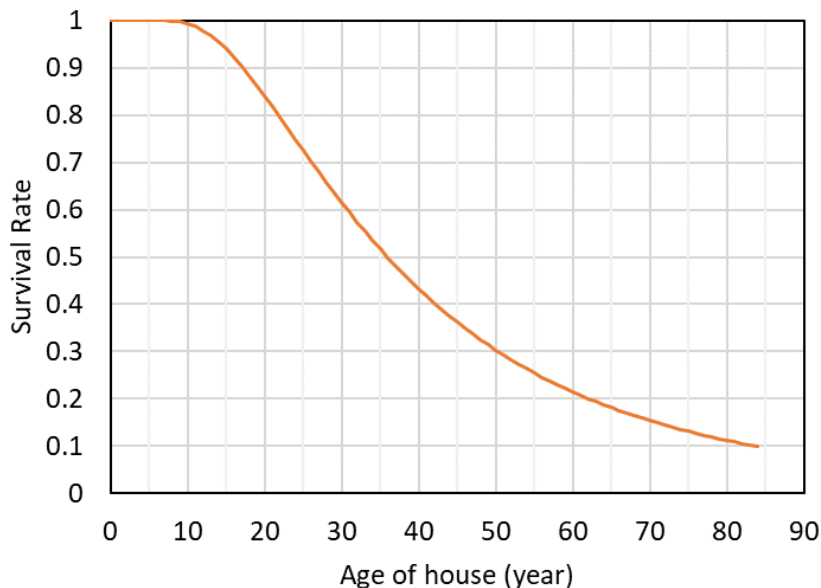


Figure 6.30. Estimated survival curve of buildings in Koura (2017).

We calculated the total collapse building ratio by these existence ratio and collapse ratio of buildings with each construction age which was mentioned above. Figure 6.31 to 6.33 show the distribution of the estimated building collapse ratio. For the areas except for the target sites which were already explained, the estimated building damage is interpolated by the method in GMT (Wessel et al., 2019). Figure 6.34 to 6.36 show the comparison of the estimated collapse ratio by using the wooden-house models with the observed collapse ratio calculated from Takemura and Toraya (2015) for the 36 cases. The linear regression equation (orange line) and its coefficient of

determination R^2 are shown in each figure. The estimated collapse ratio in case 3-2-3 shows the best correlation with the observed collapse ratio among all the cases, which means the source model of case 3-2-3 is the one that reproduces the most feasible strong ground motion for the 1944 Tonankai earthquake.

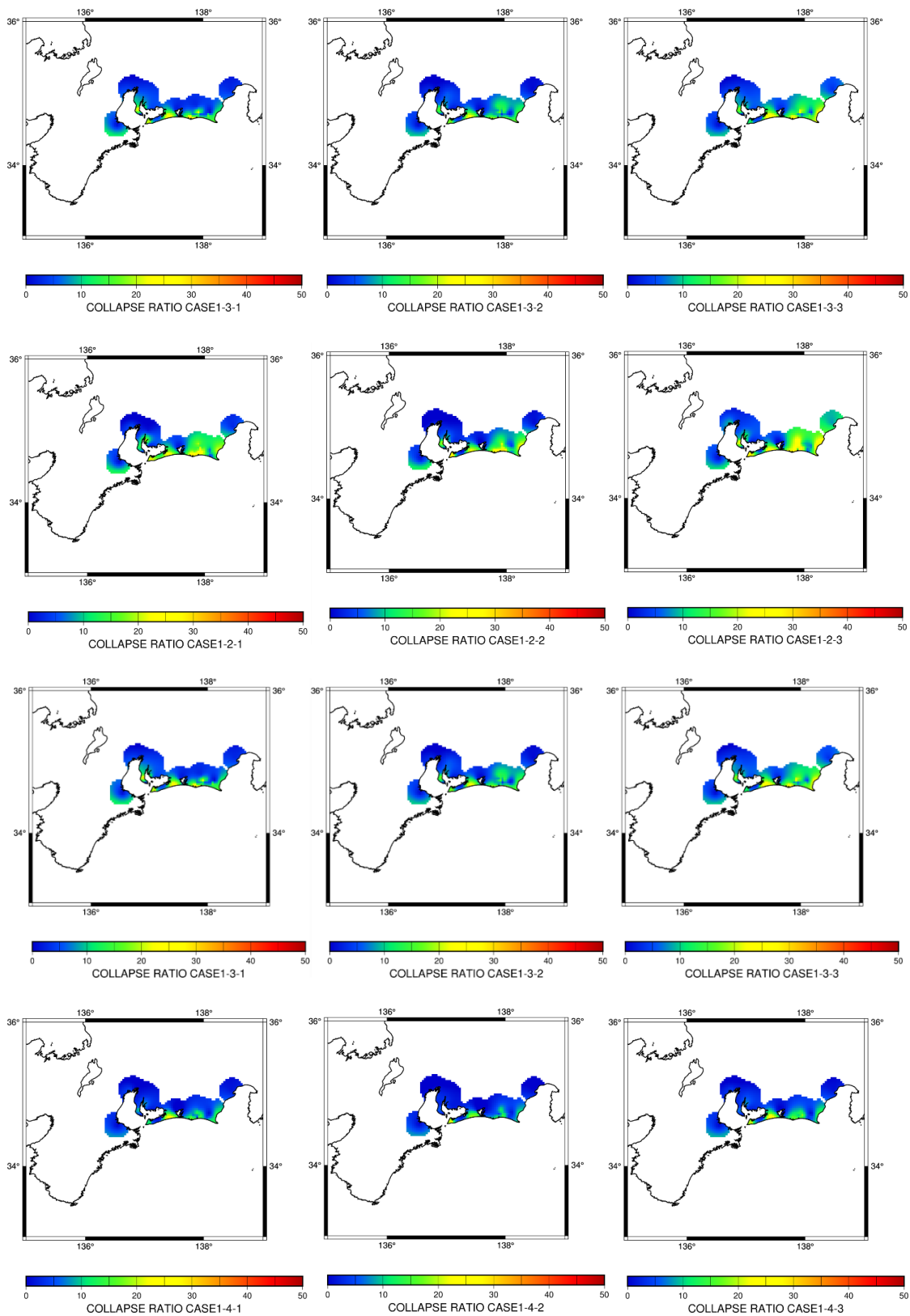


Figure 6.31. Distribution of the estimated building collapse ratio by using the wooden-house models with the interpolation method of GMT for cases from 1-1-1 to 1-4-3.

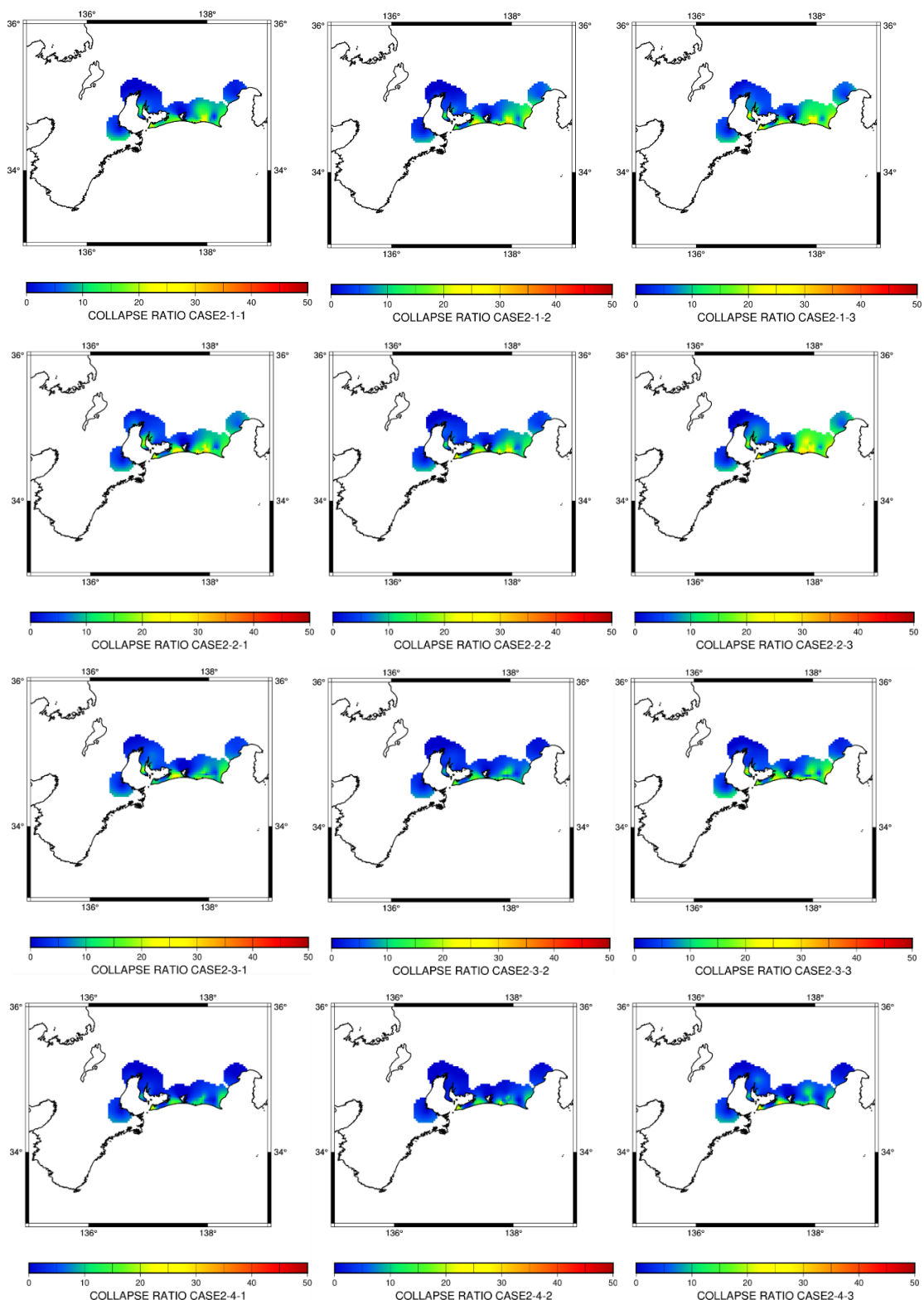


Figure 6.32. Distribution of the estimated building collapse ratio by using the wooden-house models with the interpolation method of GMT for cases from 2-1-1 to 2-4-3.

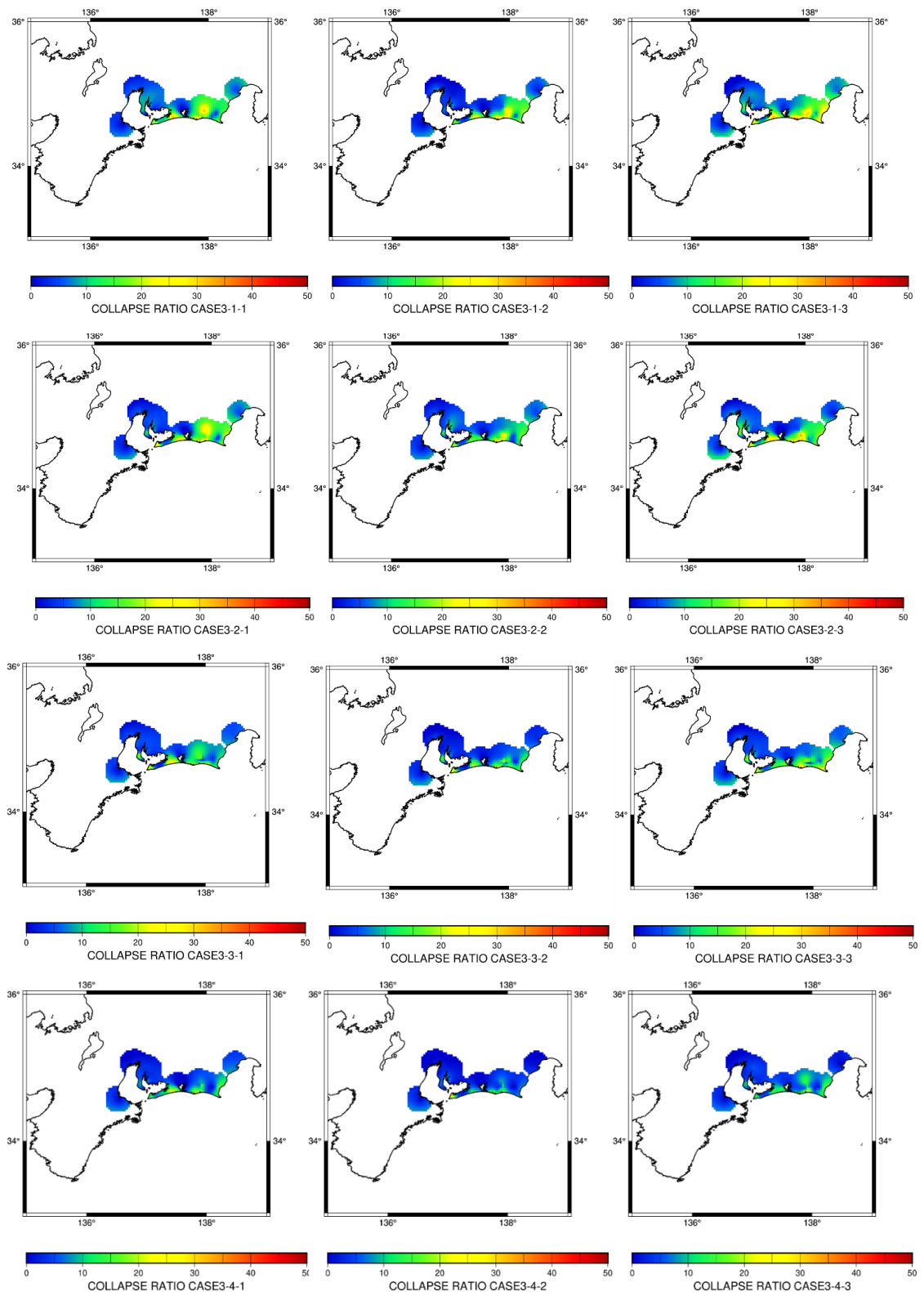


Figure 6.33. Distribution of the estimated building collapse ratio by using the wooden-house models with the interpolation method of GMT for cases from 3-1-1 to 3-4-3.

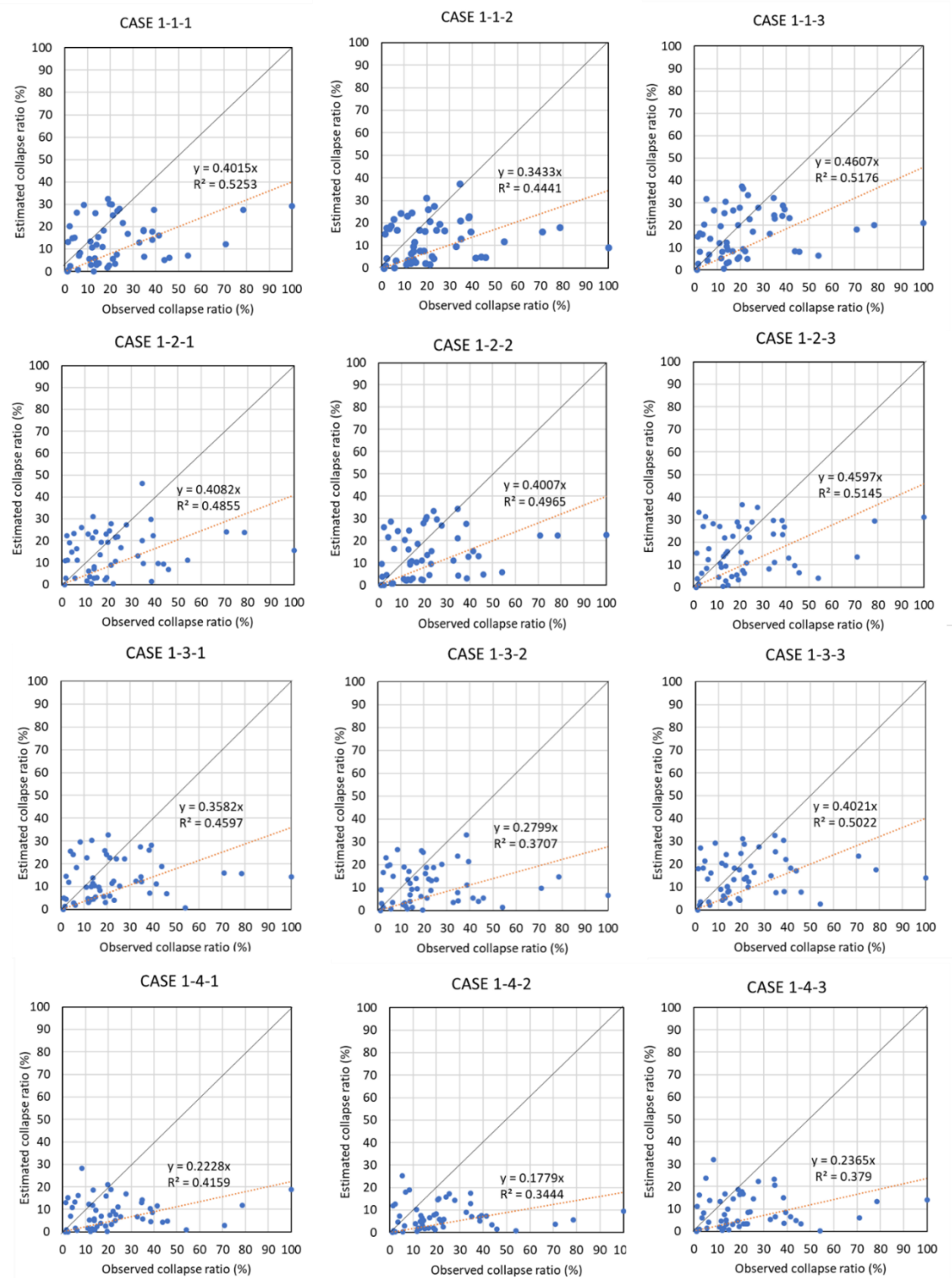


Figure 6.34. Comparison of the estimated collapse ratio by using the wooden-house models with the observed collapse ratio calculated from Takemura and Toraya (2015) for cases from 1-1-1 to 1-4-3.

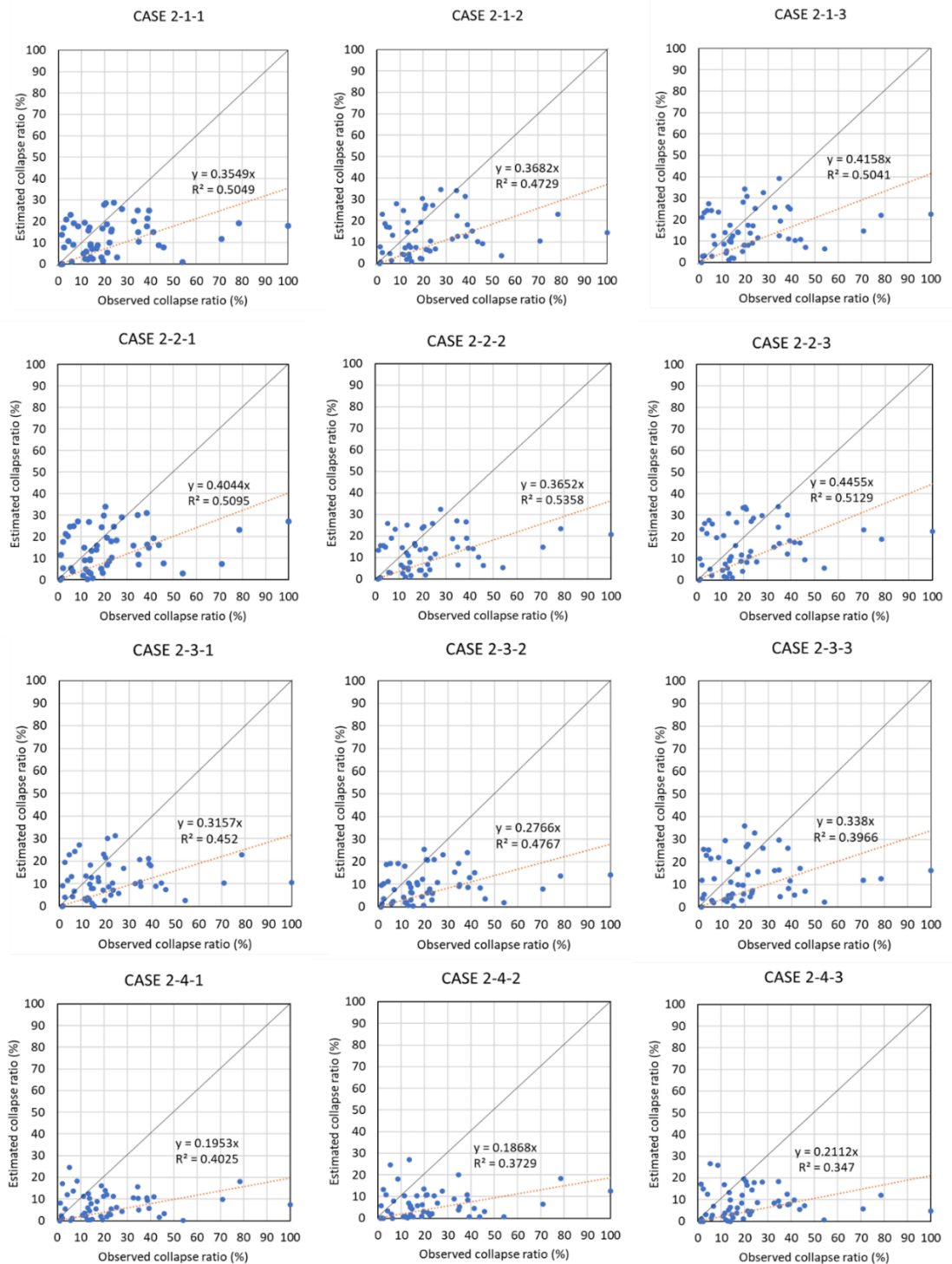


Figure 6.35. Comparison of the estimated collapse ratio by using the wooden-house models with the observed collapse ratio calculated from Takemura and Toraya (2015) for cases from 2-1-1 to 2-4-3.

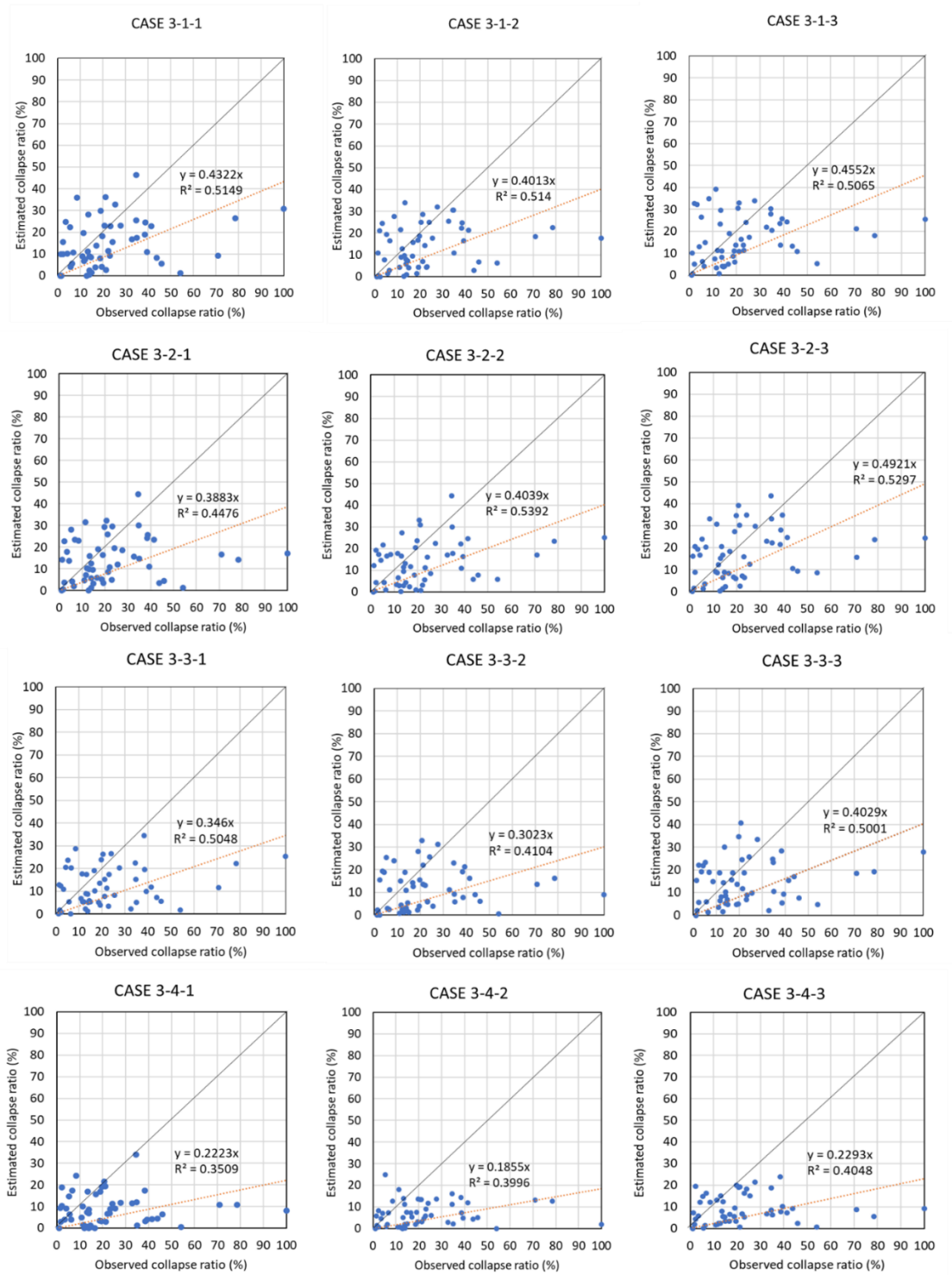


Figure 6.36. Comparison of the estimated collapse ratio by using the wooden-house models with the observed collapse ratio calculated from Takemura and Toraya (2015) for cases from 3-1-1 to 3-4-3.

When looking into the part where the observed collapse ratio is over 40% in case 3-2-3, however, the estimated collapse ratio is significantly underestimated. Therefore, we again prepared other source models with larger stress drop for SMGA1 and SMGA 2, which are located near the sites with observed collapse ratio over 40%. For the hypocenter and the locations of the SMGAs, they are same as those in case 3-2-3. The details of the parameters changed by the new cases are shown in Table 6.4. Figures 6.37 and 6.38 show the slip, stress drop, rupture velocity and rupture starting time for each case.

Table 6.4. Detailed parameters for the case 3-2-4 to 3-2-8.

CASE	SMGA No.	Area (km ²)	Stress Drop (MPa)
3-2-4	1	713.3	60
	2	913.5	36
	3	613.0	36
	4	615.8	36
3-2-5	1	713.3	36
	2	913.5	60
	3	613.0	36
	4	615.8	36
3-2-6	1	713.3	60
	2	913.5	60
	3	613.0	36
	4	615.8	36
3-2-7	1	475.5	60
	2	913.5	36
	3	613.0	36
	4	615.8	36
3-2-8	1	713.3	36
	2	609.0	60
	3	613.0	36
	4	615.8	36

Figure 6.39 shows the distribution of the estimated building collapse ratio with the interpolation method of GMT and Figure 6.40 shows the comparison of the estimated collapse ratio by using the wooden-house models with the observed collapse ratio calculated from Takemura and Toraya (2015) for the 5 cases. The linear regression equation (orange line) and its coefficient of determination R² are shown in each figure. Looking at only the linear regression

equation, the model with the best regression equation is case 3-2-6. On the other hand, when we look at the correspondence of the estimated collapse ratio with the observed collapse ratio over 40 %, the best fitting model is case 3-2-5. Therefore, we concluded that the case 3-2-5 is the most realistic source model.

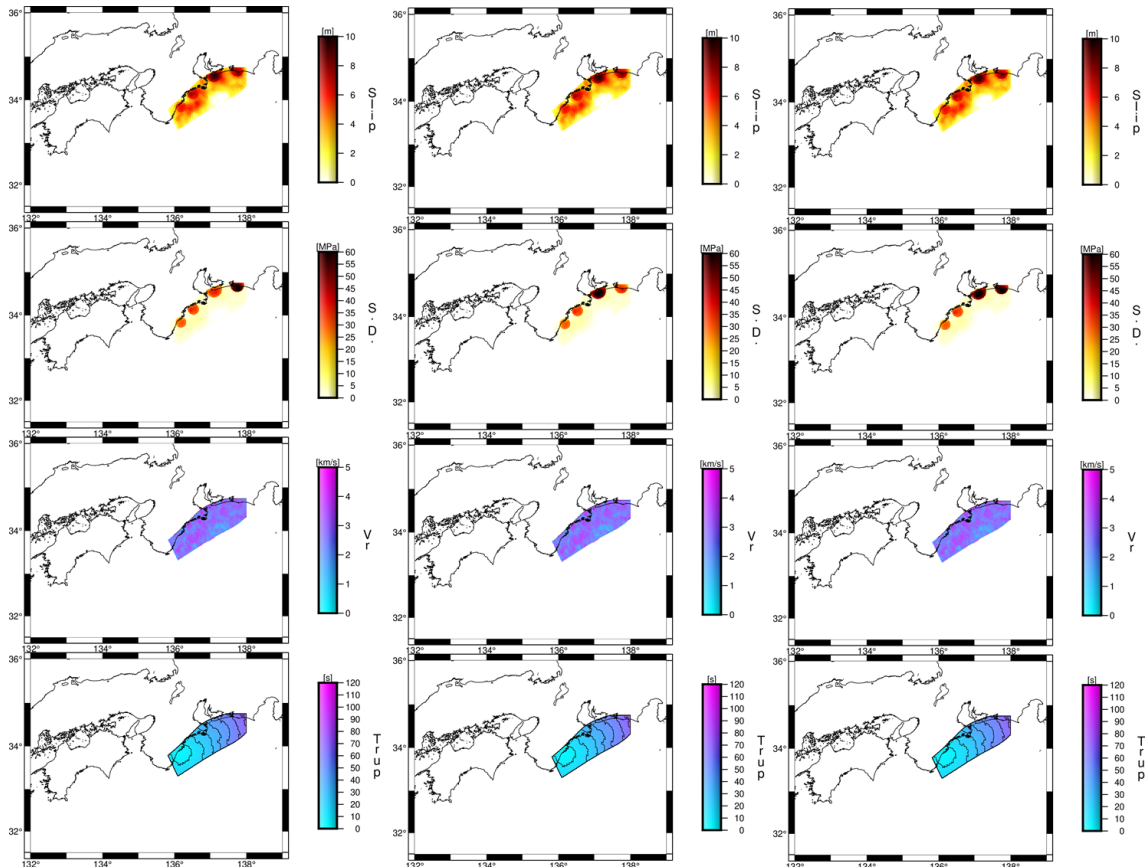


Figure 6.37. Slip, stress drop, rupture velocity and rupture starting time for case 3-2-4 in the left panel, case 3-2-5 in the middle panel, and case 3-2-6 in the right panel.

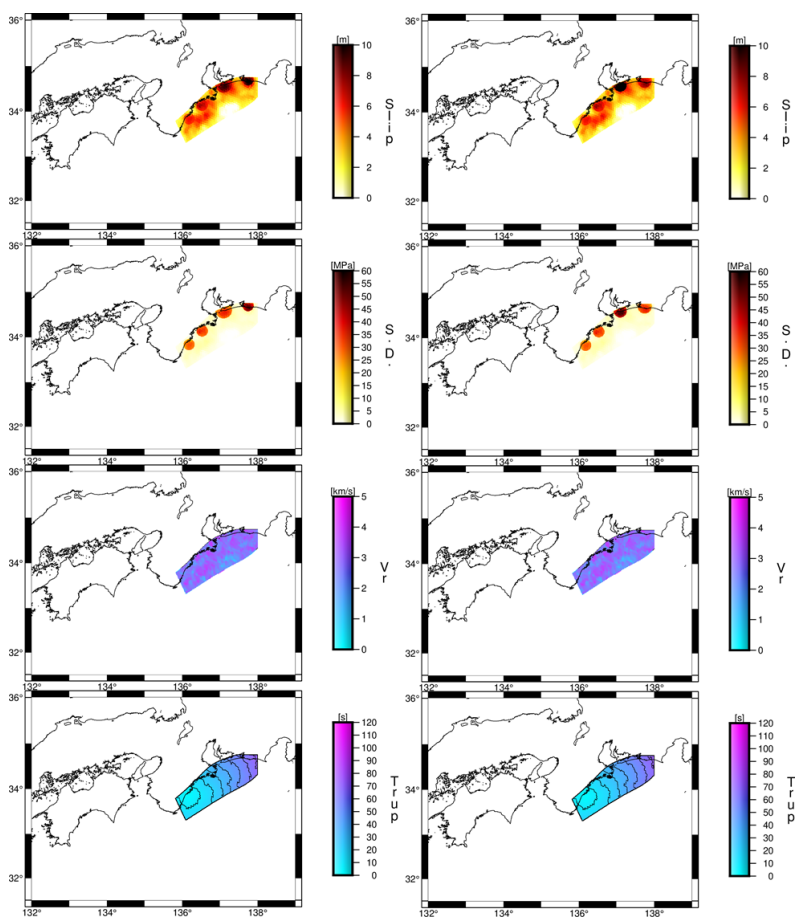


Figure 6.38. Slip, stress drop, rupture velocity and rupture starting time for case 3-2-7 in the left panel, and case 3-2-8 in the middle panel.

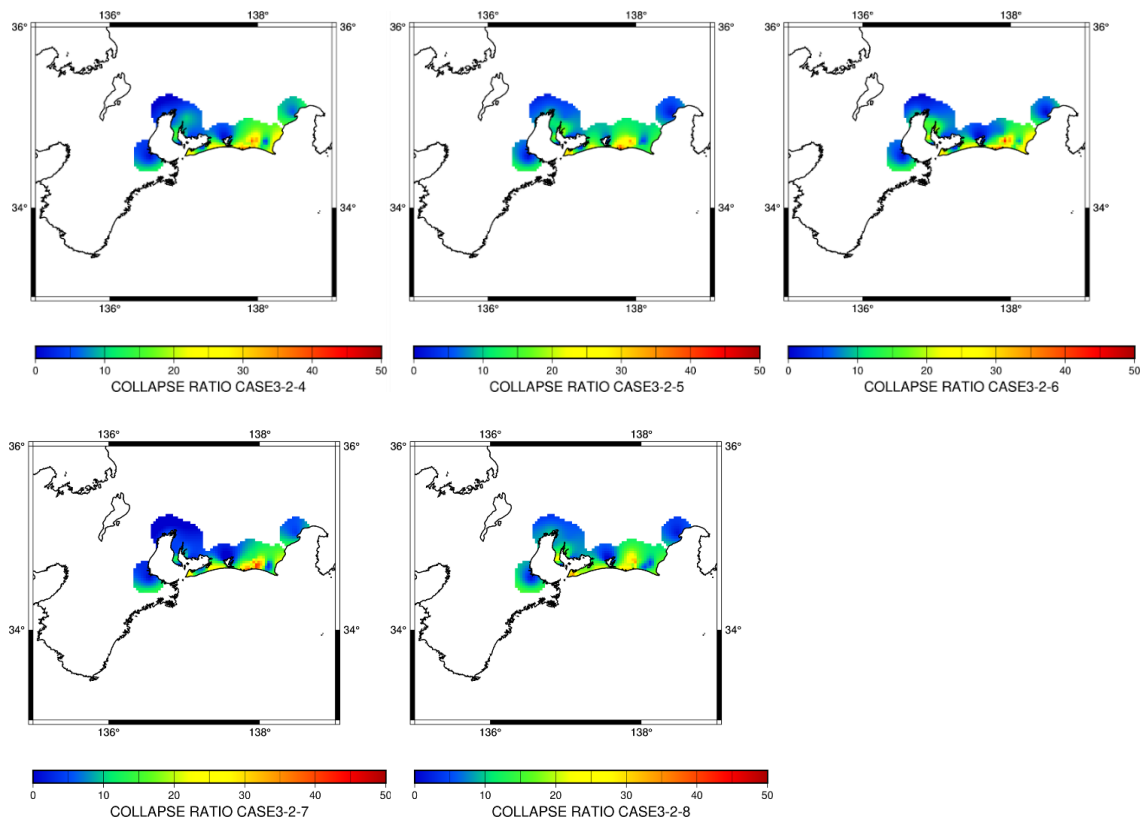


Figure 6.39. Distribution of the estimated building collapse ratio by using the wooden-house models with the interpolation method of GMT for cases from 3-2-4 to 3-2-8.

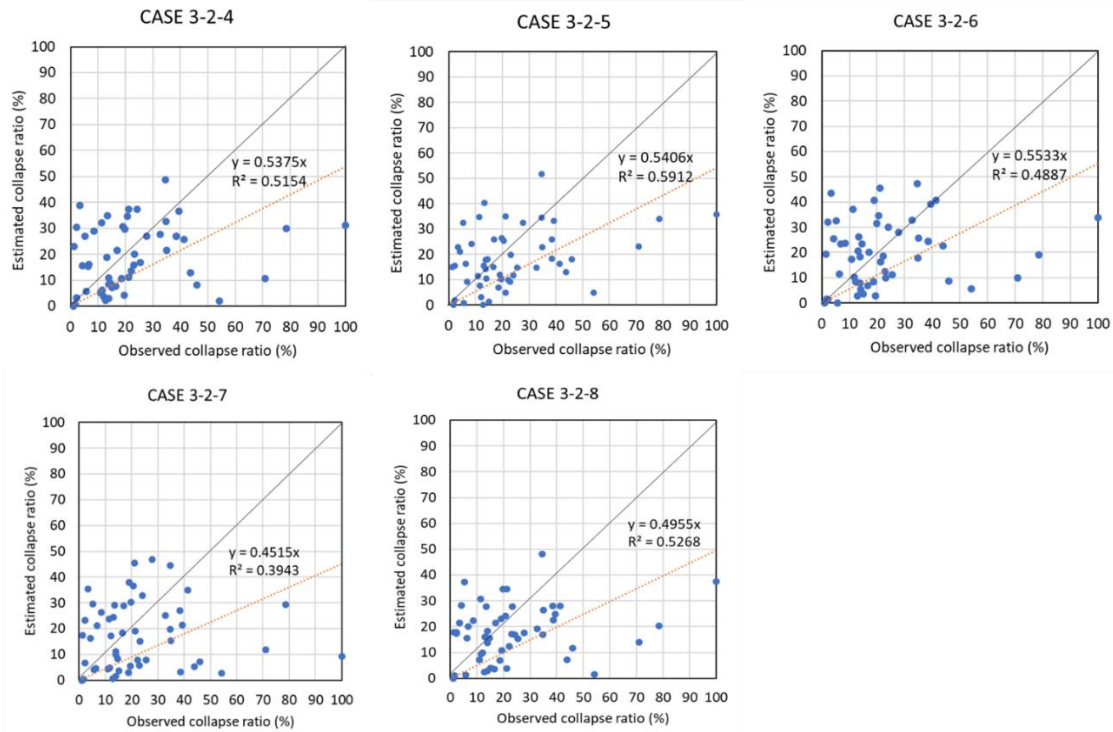


Figure 6.40. Comparison of the estimated collapse ratio by using the wooden-house models with the observed collapse ratio calculated from Takemura and Toraya (2015) for cases from 3-2-4 to 3-2-8.

6.6 Conclusions

In this study, the following analyses were undertaken to elucidate the heterogeneous source rupture propagation process of the 1944 Tonankai earthquake.

We reproduced the building damage ratio during the 1944 Tonankai earthquake by inputting the strong motion waveforms into the building damage evaluation model as of 1944. The strong ground motion waveforms were obtained from the statistical Green's function and the heterogeneous source model. The site characteristic, which is important for the evaluation of the strong ground motion, is obtained by the method of converting the theoretical S-wave characteristic from the unified velocity model (UVM) by integrating shallower- and deeper-parts of the structures above the seismological bedrock in the Kanto and Tokai regions, to the empirical site characteristic.

As the first step, first we prepared the heterogeneous source model with the four asperities as a standard model based on the model of Tonankai segments proposed by the Cabinet Office (2015). Then we prepared additional 35 heterogeneous source models of which parameters were the hypocenter, the location of asperities, and the stress drop. We calculated the strong ground motion from the source model and estimated the building damage ratio using the building damage

evaluation model, then compared it with the observed damage ratio. Seeing the model of which estimated damage ratio best corresponded with the observed one as the new standard model at the 2nd step, we prepared another five heterogeneous source model with different stress drop and area of SMGA 1 and 2. Then we sought to further increase the degree of agreement.

The analysis described above led to the following conclusions:

1. The method proposed in this paper is in good agreement with M8.0-class PGA and PGV, obtained from the empirical model (GMPE), which is supposed to fit well with the observations, and its temporal characteristics also show the characteristics inferred from the fault size and rupture propagation.
2. Parametric analysis revealed that the effect of the first and second asperities on the large amplitudes in the Enshu region of Shizuoka Prefecture due to the forward rupture directivity is significant.
3. The results of the first step of the 36-case parametric study show that the 3-2-3 case is the model that best explains the observed building damage ratio.
4. The results of the second step of the analysis show that the 3-2-5 case with the second asperity stress drop of 60 MPa is the model that best explains the observed building damage ratio.
5. The results show that in order to explain the building damage ratio of more than 40%, it is necessary to consider a source rupture process that would cause stronger forward rupture directivity in the Enshu region.
6. In summary, the proposed building damage evaluation model and the distribution of observed damage ratio provide a prospect to clarify the detailed source rupture process of the 1944 Tonankai earthquake.

References

- Aichi Prefecture Disaster Prevention Council (1975), Report on the December 7, 1944 Tonankai Earthquake, 79pp.
- Asano, K., and T. Iwata (2012), Broadband Strong Ground Motion Simulation of the 2011 Tohoku, Japan, Earthquake, Proc. 15th World Conf. Earthq. Eng., Lisbon, Portugal, paper no. 0934.
- Cabinet Office (2015), Strong Fault Model for Past Earthquakes along the Nankai Trough (Figures and Tables), Report on Long-Period Strong Ground Motions Caused by Mega-Thrust Earthquakes along the Nankai Trough.http://www.bousai.go.jp/jishin/nankai/pdf/jishinnankai20151217_04.pdf, last accessed on December 7, 2020.
- Central Meteorological Observatory (the predecessor of Japan Meteorological Agency, 1945), “Top Secret” Overview of the Survey on the December 7, 1944 Tonakai Earthquake, 94pp.
- Earthquake Research Institute (1945), Quick Report of the Earthquake Research Institute of Tokyo Imperial University, 1945, No. 4, 42pp.
- Iida, K. (1985), Damage and Seismic Intensity Distribution by Tonankai Earthquake Happened on December 7, 1944, Selected Papers of Prof. Kumiji Iida, Historical Record of Disasters by Earthquakes and Tsunamis in Tokai Region, pp.449-570.

- Kobayashi, H. (1998), Fukui Earthquake 1948 and Earthquake Engineering, Earthquake Engineering Promotion Society News, No.161, pp.6-9.
- Koura, K. (2017), Determination Method of Residual Rate Curve Using "Housing and Land Satatising Survey" and Applocation to Estimation of Building Year, Journal of Architecture and Planning (Transactions of AIJ) 82(741):2907-2913. DOI: 10.3130/aija.82.2907
- Matsushima, S. and Kawase, H. (2000) Multiple Asperity Source Model of the Hyogo-ken Nanbu Earthquake of 1995 and Strong Motion Simulation in Kobe, J. of Struct. Constr. Eng., AIJ, 534, 33-40.
- Midoriwaka, N., and Fujiwara, H. (2013), A New Ground Motion Prediction Equation for Japan Applicable up to M9 Mega-Earthquake, Journal of Disaster Research 8(5):878-888. DOI: 10.20965/jdr.2013.p0878
- Ministry of Land, Infrastructure, Transport and Tourism (MLIT, 2020), Administrative Area data as of 1950. https://nlftp.mlit.go.jp/ksj/gml/datalist/KsjTmplt-N03-v2_3.html, last accessed on December 7, 2020.
- Miyamura, S. (1946), Distribution of the damage by Tokaido earthquake (Part.1), Report of Earthquake Research Institute, the University of Tokyo, Vol.24, pp.99-134.
- Nagato, K. and Kawase, H. (2002) A Set of Wooden House Models for Damage Evaluation Based on Observed Damage Statistics and Non-Linear Response Analysis and Its Application to Strong Motions of Recent Earthquakes, Proc. of 11th Japan Earthq. Eng. Symp., 2002.
- Nagoya Local Meteorological Office (1970), Aichi Prefecture Disaster Diary, 548pp.
- Oba, S. (1957), Relation between the distribution of house damage and the ground characteristic in the Totoumi Region by the December 7, 1944 Tonankai Earthquake, Report of Earthquake Research Institute, the University of Tokyo, Vol.35, pp.201-205.
- QGIS Development Team (2009), QGIS Geographic Information System. Open Source Geospatial Foundation Project. <http://qgis.osgeo.org>", last accessed on December 7, 2020.
- Takemura, M. and Toraya, K. (2015), Re-Evaluation of Seismic Intensity Distribution from the1944 Tonankai Earthquake and Its Disaster Characteristics, Journal of Japan Association for Earthquake Engineering, Special Issue, Volume 15 Issue 7 Pages 7_2-7_21. DOI: https://doi.org/10.5610/jaee.15.7_2
- Yagi T. and Kawase, H. (2019) A Construction of the Model of Traditional Wooden Houses Based on the Pull-Down Experiment and Microtremor Measurements for Earthquake Damage Prediction, Proc. of Annual Meeting of AIJ, Vol. B-2, Structure II, 323-324.
- Yoshida K, Hisada Y, and Kawase, H. (2004) Construction of Damage Prediction Model for Wooden Buildings Considering Construction Age, Hokkaido: the 2004 Architectural Institute of Japan, 2004.
- Wessel, P., Luis, J. F., Uieda, L., Scharroo, R., Wobbe, F., Smith, W. H. F., and Tian, D. (2019). The Generic Mapping Tools version 6. *Geochemistry, Geophysics, Geosystems*, 20, 5556–5564. <https://doi.org/10.1029/2019GC008515>.

Part III

Research on Tsunami Evacuation Simulation

This part explains three different approaches for evaluating human loss by using agent-based tsunami evacuation simulation, two of which consider building damage due to strong ground motions.

Chapter 7

Tsunami Evacuation Simulation Considering Road Blockage by Collapsed Buildings Evaluated from Predicted Strong Ground Motion

Abstract

Tsunami evacuation simulations are often used to determine necessary countermeasures that will reduce human loss effectively after earthquakes and subsequent tsunamis. However, so far there has been no simulation for the estimated building damage using up-to-date knowledge of seismic engineering. In this study, in order to clarify the effect of building damage to a tsunami evacuation, we first predicted building damage based on the nonlinear response analysis for a realistic strong ground motion and then simulated a tsunami evacuation considering road blockage due to the collapsed buildings. We used one district in Tanabe City in Wakayama Prefecture in Japan where we expect to have a 12 m of tsunami height after an earthquake along the Nankai Trough plate boundary. We found that the prepared capacity of evacuation sites is not enough to let everyone evacuate and that the number of survivors increases by 3 to 4% if all of the buildings and houses are seismically reinforced. Considering this, plus 1% of expected casualties inside the collapsed houses, it appears to be not as efficient to reinforce buildings and houses to prevent human loss in comparison to increasing the capacity of tsunami evacuation sites in the target district. However, the damage to building and houses will cause a lot of side effects which are not considered here but will prolong the evacuation time. Thus, we concluded that we need to reinforce the buildings and houses as well as consider the appropriate placement, number, and capacity of the evacuation sites.

7.1 Introduction

Given the imminent occurrence of an earthquake or earthquakes along the Nankai Trough plate boundary, developing effective countermeasures has become an urgent priority on the southwestern side of Japan. However, the finances of local governments are constrained, making this a difficult goal to achieve. At the same time, local residents are of an older age and often lack a concrete understanding of the looming disaster or else they feel a sense of defeat about it (that is to say, they are driven to despair). To keep motivation within residents inside the tsunami inundation areas for tsunami evacuation activities immediately after the large mega-thrust earthquake, we need to interact with them through dissemination of information and discussion on what will happen when the mega-thrust earthquake occur offshore of their city or town and stimulate their imagination through a concrete picture of tsunami disaster scenarios that should be expected based on scientifically rational (i.e., evidence-based) simulations (e.g., Nakai et al. 2014).

As far as we have surveyed, one of the first papers related to tsunami evacuation simulation using agents seems to be Usuzawa et al. (1997). They performed the tsunami evacuation simulation in the area damaged by the 1993 Hokkaido Nansei-Oki earthquake for future evacuation planning and they showed that the result was validated by the detailed surveys just after the earthquake. Since then, many papers have been published, mainly focusing on the parameters used in the simulation in order to make them more realistic. For instance, the interaction between pedestrians and motorcycles or cars has been considered (Goto et al. 2012; Mas et al. 2012, 2013; Makinoshima et al. 2016). Among them, Goto et al. (2012) assumed that the walking speed as well as the motorcycle speed decreased with increased density and then simulated the cases with different ratios between pedestrians and motorcycles. They also presented the simulation to the elementary, middle, and high school students in the target area as a course of disaster education and proved that their simulations made easy for students to understand the appropriate evacuation procedure. Mas et al. (2012) introduced a new approach to model the starting time of evacuation based on the sigmoid curve, as they thought that the starting time may have a significant effect on congestions and bottlenecks during evacuation. Thus, progress of tsunami evacuation simulation has been made and these simulations provides various tools for the evacuation planning. Based on such progress, Hori et al. (2015) considered that there remains uncertainty in these tsunami evacuation simulations and suggested a way to evaluate the quality of the simulation.

As for the effects of building damage on evacuation routes, we found only a few reports of the tsunami simulation considering building collapse and subsequent road blockage. For example, Sato et al. (2002) adopted the vulnerability function developed by Murao et al. (1999) for the damage estimate. Tamura et al. (2005) adopted a probability distribution model that predicts the width of the debris depend on the JMA seismic intensity estimated by Akakura et al. (2000). Later Sakata and Teraki (2009) predicted in their tsunami evacuation simulations which buildings would collapse by surveying their ages or observing building exteriors. They proposed a model that can vary the rubble flow distance based on the probabilistic distribution of collapsed directions (i.e., randomly distributed to all directions).

In these pioneering studies, their focus was not primarily on the quantification of expected building damage. The structural damage that buildings are likely to incur depends on a

complex combination of multiple factors, including the building's vibration characteristics, seismic input motion characteristics, and the softness of the surrounding ground. Damages should therefore be quantitatively estimated using an up-to-date technology in earthquake engineering. Since traditional methods have not considered the seismic motion characteristic and the ground characteristics, it is likely that the real outcome will differ from the simulation results. In contrast to the Great East Japan Earthquake of 2011, in which building damages were relatively small (e.g., Baoyintu et al. 2013), there is a concern that building damages caused by seismic motion will be greater for an earthquake along the Nankai Trough, due to the fact that the hypocentral region will be closer to the shore (e.g., Central Disaster Prevention Council 2003; Ho and Kawase 2008). Road blockages caused by collapsed buildings are expected to pose a greater obstacle for residents trying to evacuate before the tsunami hits.

If the estimates of building damages used in an evacuation simulation undertaken for the purpose of disaster impact analysis and subsequent development of countermeasures for disaster reduction deviates greatly from the actual outcome, countermeasures based on that inaccurate estimate may not be quite effective. In order to avoid this, the tsunami evacuation simulations undertaken in the present study predicted building damage by incorporating three major factors—the buildings themselves, ground characteristics, and input ground motions—using the knowledge available in earthquake engineering.

Strong ground motion simulations based on the physics-based methodology with a scenario-type representation of the source process are getting popular in recent years, as evidenced by the institutional activities in Japan as well as in the United States (National Research Institute for Earth Science and Disaster Resilience 2013; Southern California Earthquake Center 2018). As for the Nankai-Trough mega-thrust earthquakes, the Central Disaster Prevention Council released multiple-scenarios with different source sizes and rupture patterns, where structural damages as well as human losses are estimated based on both strong ground motions and tsunami inundation heights (Central Disaster Prevention Council 2003, 2011). The most recent rupture scenario of the Nankai-Trough earthquakes by the Central Disaster Prevention Council is a Magnitude 9.1 four-segment-rupture scenario in which an extraordinarily large length, width, and slip amount are assumed (Central Disaster Prevention Council 2012). Probability of occurrence for such an extraordinary source scenario should be close to null. More plausible scenarios based on the source parameters for the earthquakes in the past are used by several researchers in their quantitative strong motion simulations (e.g., Kamae and Irikura 1994; Ho and Kawase 2008; Baoyintu 2014), whose ground motions are reasonably smaller than those by Central Disaster Prevention Council (2012).

Structural damage predictions should also be physics-based in order to fully utilize the characteristics of the simulated ground motions. This means that we need to construct structural response models used for structural damage predictions. In the current practice of structural damage predictions, we usually use a vulnerability function of a specific level of damage such as total damage, half damage, and partial damage, obtained empirically from the damage statistics of previous earthquakes (e.g., Murao and Yamazaki 2002). The largest problem with this vulnerability function approach is the ignorance of the effects of the difference in ground motion characteristics for crustal earthquakes and subduction-zone earthquakes. The current empirical vulnerability functions in Japan are primarily determined by the damage statistics from the 1995 Hyogo-ken Nanbu (Kobe) earthquake and therefore should not be used for the damage prediction of the Nankai-Trough plate boundary earthquakes. As described later we use structural response

analysis of multi-degree-of-freedom models specific for different types of buildings and different construction years (Nagato and Kawase 2001, 2002a, b).

This study simulated tsunami evacuations in which we considered that collapsed wooden houses would block escape routes in order to evaluate the effectiveness of the current evacuation sites in terms of their locations and capacities. It aimed to quantitatively demonstrate the effects of earthquake-resistant reinforcements on evacuation speed, and thus provide vital information for selecting the most effective countermeasures for mega-thrust earthquakes along the Nankai Trough plate boundary.

7.2 Target District for This Study

For this study, we chose a district comprising 1-, 2-, and 3-Chome of Kamiyashiki and a part of Katamachi, located along the coastline of Tanabe City, Wakayama Prefecture. The district is shown in Figure 7.1 (red area). The population is approximately 1,250 people in 641 households (Tanabe City 2013a). The predicted maximum JMA seismic intensity in the district is 7, in the event of a simultaneous rupture with three consecutive segments, with a 12 m tsunami estimated to arrive approximately 15 minutes at earliest after the earthquake. Here, JMA seismic intensity is the one determined by the Japanese Meteorological Agency which is an index to categorize the intensity of local ground shaking into 10 categories (but 7 is the highest) indicated by the logarithm of peak ground acceleration. Please refer to Karim and Yamazaki (2002) on how to calculate JMA intensity.

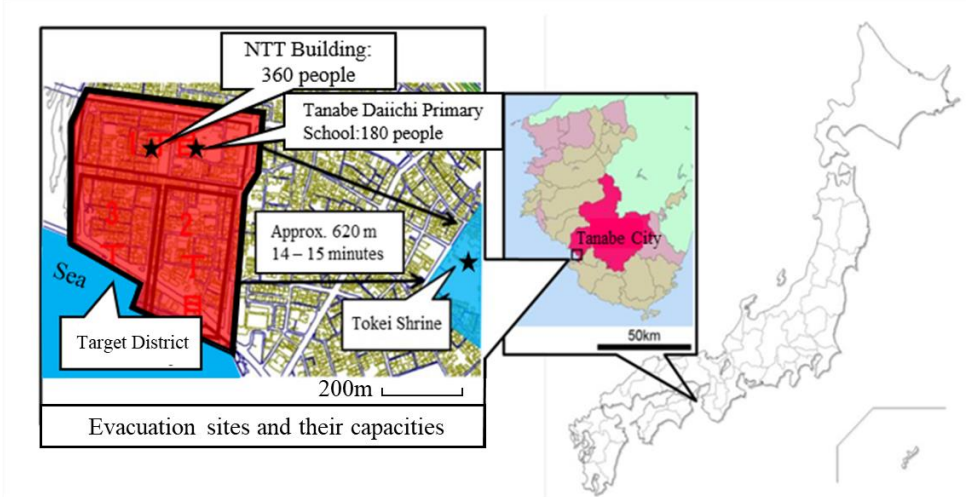


Figure 7.1 The target district for this study, in the southwestern side of Tanabe City, Wakayama Prefecture, Japan. Two evacuation sites, namely the NTT Building and the Tanabe Daiichi Primary School, inside of the target district and one evacuation site outside, Tokei Shrine, are shown by star symbols.

Figure 7.2 shows the final inundation area around the target district (Tababe City 2014). On the map, the Nippon Telegraph and Telephone Corporation (NTT) building and the Tanabe

Daiichi Primary School (hereafter “the Primary School”) are the designated tsunami evacuation buildings, and Tokei Shrine, which is next to a small hill with the capacity for all the people in the target district, has also been designated as an evacuation area (These tsunami evacuation buildings and the evacuation area are shown as black stars in Figures 1 and 2). Hereafter we refer to this evacuation site of a small hill behind Tokei Shrine simply as “Tokei Shrine”. However, Tokei Shrine is at least 620 m away from Kamiyashiki, meaning that it would take residents 14–15 minutes to reach the shrine on foot and is too far away for elderly persons. The district also has many traditional wooden houses remaining.

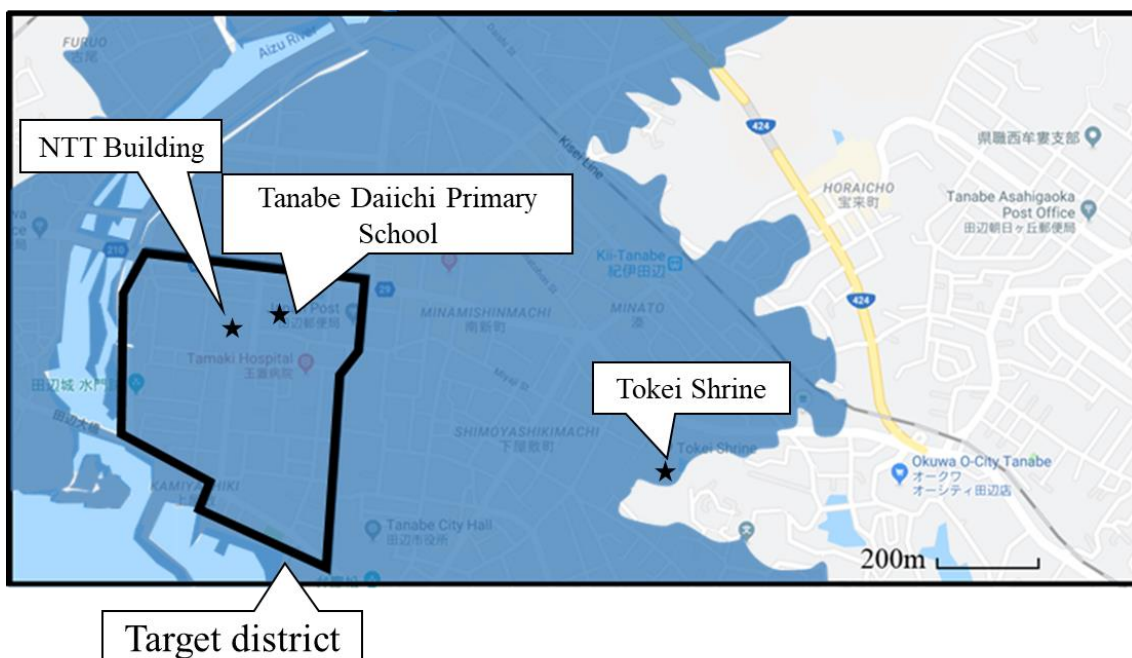


Figure 7.2 A map of the expected inundation area of tsunami around the target district (Tanabe City 2014).

In the event of an earthquake, it is important to escape from houses and start to evacuate as soon as possible in order to avoid the tsunami that follows. For this, however, it is a prerequisite that houses will maintain their integrity and safety after the earthquake. When we asked a city official of Tanabe City about the awareness of the residents to the earthquake, he told us that many of them did not realize that safe evacuation might be delayed or rendered impossible if non-earthquake-resistant houses were heavily damaged during an earthquake.

Tanabe City developed and published an earthquake-resistance countermeasure plan based on predictions of heavy building damage during a Nankai Trough earthquake. The old plan aimed to halve the number of non-earthquake-resistant houses between 2006 and 2015, raising the proportion of earthquake-resistant houses from 56% in 2005 to 80% by 2015. The current plan aims to raise the proportion of earthquake-resistant houses from 75% as of the end of 2015 to 95% by the end of 2020 (Tanabe City 2016). The city committed to providing free earthquake-resistance diagnoses and partial financial assistance for seismic reinforcement design and retrofitting implementation for those houses that scored less than 1.0 in the diagnosis, as well as

commissioning workers to affix furniture for elderly and handicapped residents. However, according to Tanabe City, the number of buildings that can be made earthquake-resistant annually is only approximately 1% of all the non-earthquake-resistant buildings. At this rate, it would be difficult to meet the goals within the allocated timeframe.

7.3 Predicting Building Collapse

As mentioned in the Introduction, building damage predictions have usually been made using a “vulnerability function approach,” which depends on an empirically identified correlation between the strength index of the observed ground motion such as the peak ground acceleration or the seismic intensity and the damage level around the observation point, that is, the ratio of numbers of heavily damaged or collapsed buildings with respect to those of the total buildings inside the designated area. However, it is difficult to observe ground motions at locations where damage ratios are high because strong motion observation sites are still sparse, and therefore it is difficult to measure accurate vulnerability functions in locations with severely damaged structures, where they are of utmost importance. It is also difficult to determine the most appropriate size of the areas used for evaluating damage ratios. Furthermore, vulnerability functions are calculated with respect to one of the strength indices of ground motion, which could not fully represent the structural impact of ground motions from different types of sources, namely crustal earthquakes and subduction-zone earthquakes. Taking these limitations into consideration, Nagato and Kawase (2001, 2002a, b) developed a new damage prediction method founded on nonlinear response analysis of buildings that does not depend on such preconditions, and demonstrated that the model was sufficiently practicable. They reported that the model successfully approximated actual recorded damages during the 2005 West off Fukuoka earthquake (Kawase 2007) and the 2011 Tohoku earthquake (Baoyintu et al. 2013). The latter is important to the present study, as the Tohoku earthquake had a long duration of motion, similar to what is expected during the Nankai Trough mega-thrust earthquakes. Their prediction methodology is briefly described below (please refer to the cited articles for further details).

Nagato and Kawase’s model (Nagato and Kawase 2001, 2002a, b) was constructed through the following procedure.

First, a story-wise multiple shear spring-mass model with nonlinear behavior was constructed as a single column model. Next, multiple models of which the yield strength vary in the specific building category were prepared for different building types and number of floors, and their existence ratios were estimated based on the log-normal distribution from the investigation of numbers of buildings in the past. Their existence ratio distribution with respect to yield strength is important to reproduce the observed damage ratio at the target point from a single input motion there.

Reproduced strong motions (Matsushima and Kawase 2000) were applied to the models at every 60 m by 120 m grids, and the damage ratio was calculated as the sum of the ratio of the models that suffered major damage according to a given criteria. Then the average yield strength was estimated in order to reproduce the average of the observed building damage ratio in the Nada-Ku and Higashi Nada-Ku districts during the Hyogo-ken Nanbu (Kobe) earthquake of 1995. Please note that the damage ratio here was the one surveyed by the structural experts of

Architectural Institute of Japan based on Rank 4 and Rank 5 shown in Okada and Takai (2004), which corresponds to the damage level as “severely damaged” (Rank 4) or “collapsed” (Rank 5). The following conditions were assumed for reinforced concrete (RC) and steel construction:

- 1) The shape of the yield strength distribution (the average of the distribution was estimated through calculation) is log-normal with a fixed standard deviation.
- 2) Destruction criteria (any floor exceeding the threshold was deemed heavily damaged or collapsed) is assumed based on laboratory experiments.
- 3) The vertical shear-stiffness distribution was given by the “ A_i ” distribution in the current building code. The value “ A_i ” is the coefficient of the shear force coefficient with respect to the base-shear coefficient as a function of the floor height, which reflects the vertical distribution of the shear force coefficient in each floor for design.
- 4) Any soil-structure interaction was ignored due to cancellation with soil amplification.

These assumptions were different for wooden houses in 1) and 3), where the detailed statistics of actual wooden houses in Kobe were used.

In order to accurately reproduce the effect of the natural period of the building to the response, four models were created for RC structure (3, 6, 9, and 12 story buildings for both buildings with older earthquake resistance standards, and those with new standards after the large code modification in 1981), and three models were created for steel construction (3, 4, and 5 stories, also divided into old and new standards). For wooden construction, only a two-story model with no age differentiation was used, as this model was representative of the majority of wooden construction houses in the target district. A group of models was thus created based on these assumptions. Matsushima and Kawase’s reproduced strong ground motions (Matsushima and Kawase 2000) were input into the models, and damage ratios were computed and compared to the observed damage ratios. By repeatedly changing the average yield strength, each model’s ability to accurately reproduce the damage ratios was attained.

Figure 7.3 shows the ratio of the optimized yield strength for each building category with respect to the yield strength of the standard building (corresponding to the yield strength as the minimum requirement of the design code in 1981). For the two-storied wooden building with no age differentiation, this ratio was 1.95. The yield strengths thus obtained for the group of building models were considerably larger than those of standard building models in the case of wooden and low-story RC constructions. Nagato and Kawase (2001, 2002a, b) attributed this to the contribution of non-structural elements of buildings to their yield strengths. On the other hand, the yield strengths for low-storied steel construction buildings were almost the same as those of the standard building models, and it could be said for steel construction buildings to be comparatively more vulnerable.

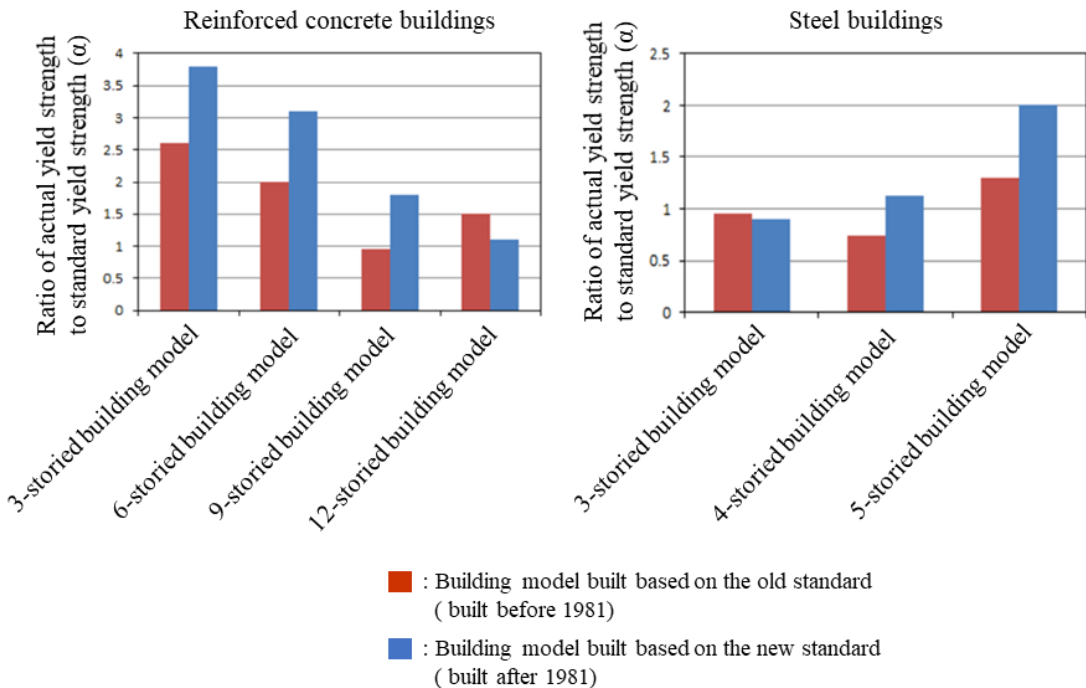


Figure 7.3 Ratios of the actual yield strength with respect to the standard (code required) yield strength for models that can reproduce observed damage ratios in Kobe during the 1995 Hyogo-ken Nanbu (Kobe) earthquake for reinforced concrete buildings (left) and steel buildings (right). Apparent differences in the yield strengths can be seen between buildings built before and after 1981 when a large code modification took place, except for 12 storied RC building models and 3 storied steel building models. After Nagato and Kawase (2001, 2002a, b)

The validity of the building models has been confirmed as follows: when the reproduced seismic wave was applied, the maximum inter-story drift angle distribution matched well with those observed during the Hyogo-ken Nanbu (Kobe) earthquake of 1995, and the calculated damage ratio distribution matched the observed distribution in the Nada-ku and Higashi Nada-Ku districts of Kobe City.

In the present study, the time history wave of the ground motion predicted for the target district in the event of a consecutive rupture scenario for three Nankai-Tonankai-Tokai segments (Baoyintu 2014) of M8.7 was applied to the building models, and the damage ratios were computed. The amplification factor for the surface subsoil in the target district was generally homogenous (between 1.4 and 1.6 according to J-SHIS amplification factor (National Research Institute for Earth Science and Disaster Resilience 2013)); therefore, the seismic wave was not corrected for the effect of surface subsoil at different ground points. In districts where there is considerable spatial variation in the shallow subsoil structure, amplitude corrections must be made based on an index for the spatial variation in the shallow subsoil structure such as Vs30, an average S-wave velocity from the surface to a depth of 30 meters.

The diagrams here show the amplification factor for the target district (Figure 7.4) based on the J-SHIS (National Research Institute for Earth Science and Disaster Resilience 2013) and

the damage ratios obtained by applying the predicted input waves (Figure 7.5). Note that the “damage ratio” here is the percentage of buildings that suffered heavy damage or collapsed.

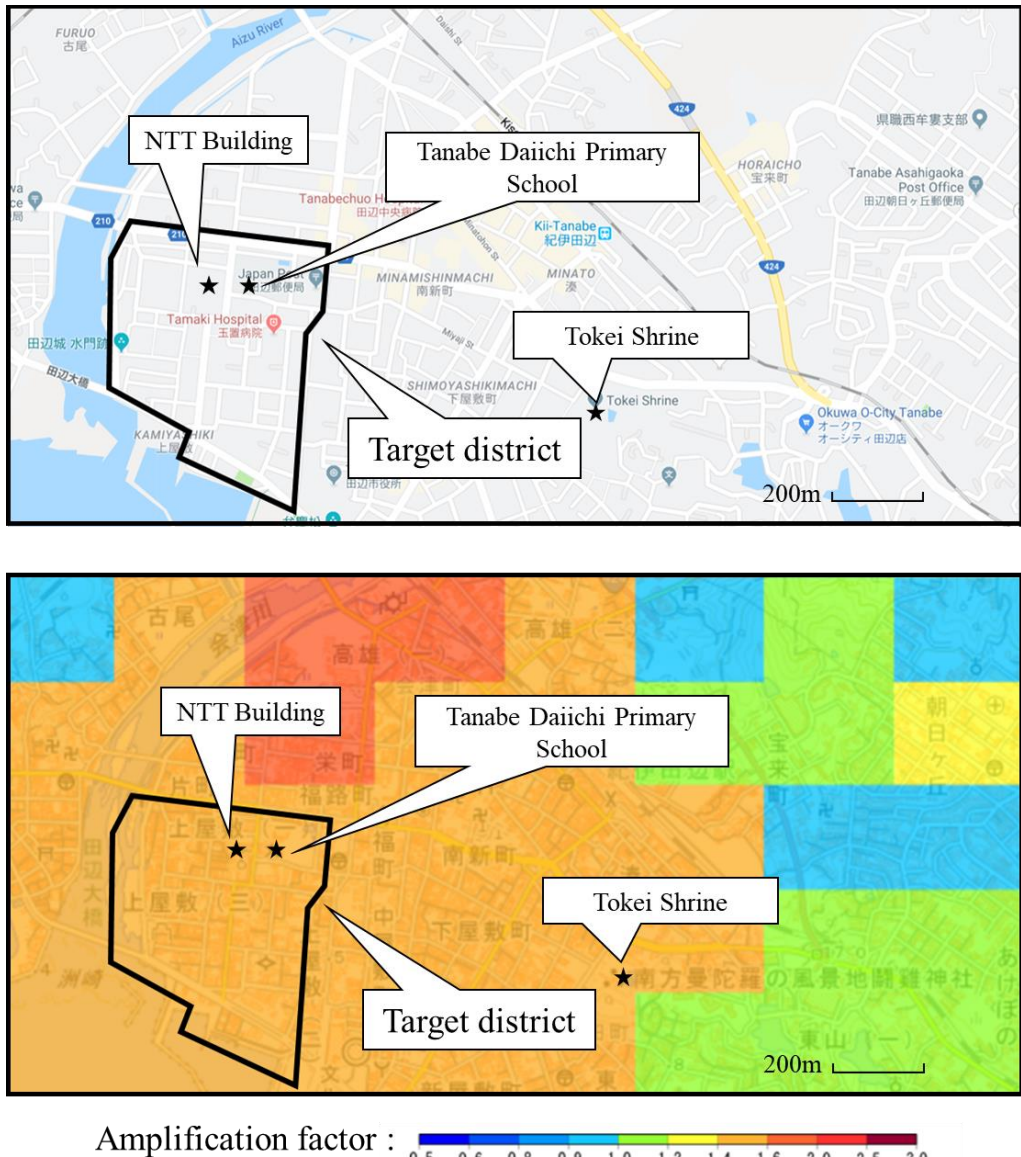


Figure 7.4 The soil amplification factor in the target district (National Research Institute for Earth Science and Disaster Resilience 2013; Baoyintu 2014).

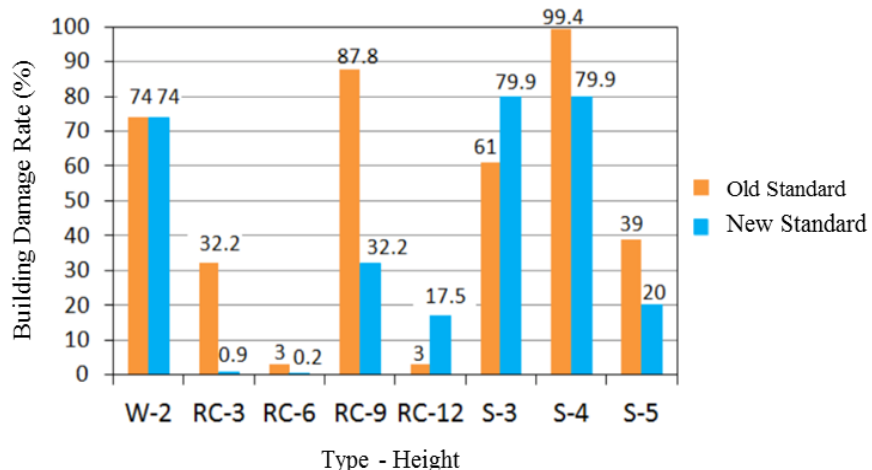


Figure 7.5 Predicted damage ratios for different building types (w: wooden houses, RC: reinforced concrete, S: steel), number of stories, and old/new standards using the damage prediction code (Nagato and Kawase 2001, 2002a, b). No difference for construction years is considered in wooden houses.

7.4 Tsunami Evacuation Simulation Using Agent Methodology

7.4.1 Summary of the tsunami evacuation evaluation system

An agent-based simulator (hereafter “simulator”) was used for tsunami evacuations, and the space-time geographic information system (hereafter “space-time GIS”) was structured in such a way as to share the same database. The former was constructed on a multi-agent platform “Aritsoc” (Kaneda 2010) developed and distributed by Kozo Keikaku Engineering Inc. and the latter was built on “DiMSIS” (Hatayama 1999), a space-time GIS system developed by Disaster Prevention Research Institute, Kyoto University. The only agents in this platform are people, and the underlying data is provided from a database. The data comprises the basic attributes of the residents, information collected from site surveys, and the geographic characteristics of the target district. The geographic characteristics, based on publicly available data, are organized on the space-time GIS system and stored in the database.

The position and direction of motion of the agents at each simulation step are incorporated into the space-time GIS system and overlaid with the tsunami inundation simulation. The movements of the agents are then collated and evaluated, and finally visualized as space-time data. In our study, the residents’ basic attributes were configured as follows:

- 1) Initial positions of agents: night-time was assumed, and agents were initialized inside their homes. Agents were generated based on a register containing population and household data by town (Tanabe City 2012) and the population records by town and age (Tanabe City 2013b) published on Tanabe City’s website. The resident register is broken down by block, gender, and age in five-year increments. Using this information, average households and family members were constructed and randomly distributed among buildings in the target district.
- 2) Evacuation speeds: based on interviews the Ministry of Land, Infrastructure and Transport

conducted with tsunami evacuees of the 2011 Great East Japan Disaster (Ministry of Land, Infrastructure, Transport and Tourism 2012), an average walking speed of 2.65 km per hour was assumed for residents between 10 and 69 years of age, and 1.88 km per hour for residents younger than 10 or older than 70, and 1.96 km per hour in case that residents between 10 and 69 years are evacuating with children under 10 or elderly people over 70.

- 3) Time required to start evacuation: we allowed for three minutes during the earthquake when residents cannot move (two minutes for shaking to settle and one minute to prepare for evacuation) and added two minutes as best effort required, totaling five minutes. The five-minutes for best effort was set by taking into consideration the testimonies regarding the time required to commence evacuation from survivors of the Great East Japan Disaster (Geospatial Information Authority of Japan 2013). The starting point of evacuation was assumed to be the road in front of each house.
- 4) Initial direction: the initial direction was set as the direction of the first destination node, which was dependent on the location of the evacuee's house.
- 5) Method of transportation: for the purpose of this study, we assumed that no cars would be used, and all evacuees would be moving on foot.

The main purpose of this study is not to evaluate the effects of each parameter assumed in the simulation, but to evaluate the effects of damaged buildings and the arrangement of evacuation sites. For that purpose, each parameter above is the most plausible one where we consider the simplest case, that is, the case when the residents are trained enough to start evacuation immediately after the earthquake, and they fully understand the risk of using cars for their evacuation.

7.4.2 Geographical space information

The 1:2500 scale fundamental geospatial data provided by the Geographical Survey Institute (Ministry of Land, Infrastructure, Transport and Tourism, 2011) was used as the base map. The resolution of the map is 5 m in both horizontal and vertical directions. In order to generate evacuation routes, “road curbs” and “buildings” corresponding to residential areas were extracted from the map, and the remaining information was used as the background of the presentation map. Evacuation routes can be divided into intersections and the segments that connect the intersections (“movement path section”), along which agents can move. The curbs at both sides of the routes were marked with dots in approximately every 50 cm increments to digitally enclose the path. Representative nodes at each intersection were assigned node numbers (Figure 7.6).

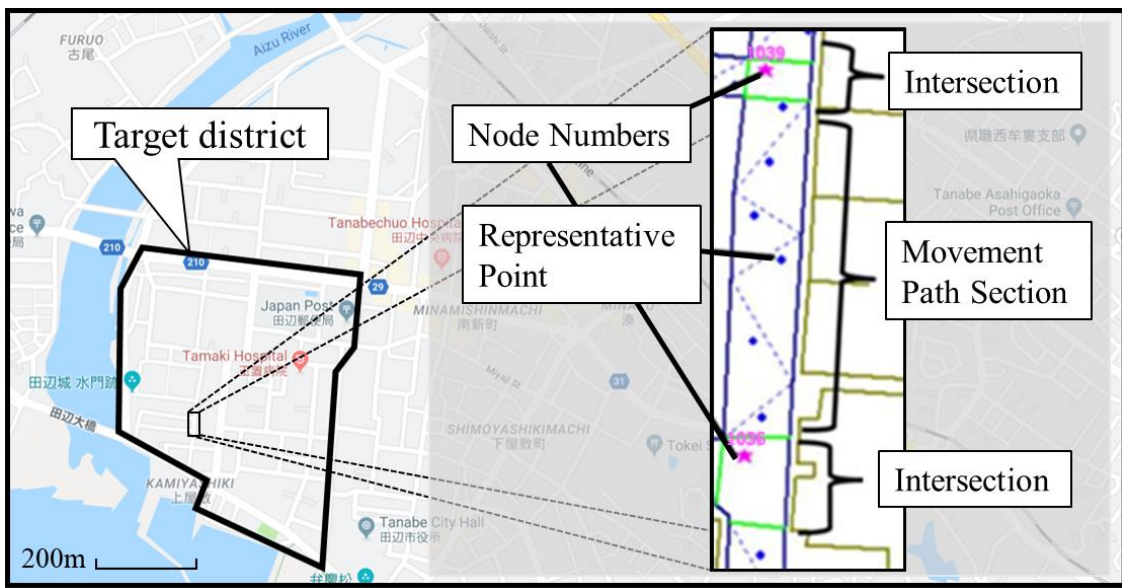


Figure 7.6 An example of the evacuation path in DiMSIS, the space-time GIS used for simulation. The movement path section is defined as the path between two intersections with node numbers, and it is divided into small triangles in which one representative point is placed to give an attribute for forward and backward directions of motion.

For the movement path segments, first we divided the segment into small triangles and then a representing point was placed near one side of the triangle. Its attribute was assigned so that agents would allow movement toward the next intersection, that is to say, the movement in the forward direction along the path. “Forward direction” here refers to the direction from one intersection to the next, from the smaller node number to a larger node number. Data was prepared so that by specifying the final destination node at each starting node (i.e., for evacuees starting from that node), the data would show the next node toward which each evacuee should head. These routes were determined by a shortest-path finding algorithm (Nakai and Hatayama 2013a, b). Simulation results (Suzuki et al. 2011) for an M8.7 consecutive rupture scenario for three Nankai-Tonankai-Tokai segments following the assumptions made by the Central Disaster Prevention Council (Central Disaster Prevention Council 2011) were used to simulate tsunami motion. Figure 7.7 illustrates the example of the tsunami evacuation simulation at one lapse time, 23 minutes after the earthquake.

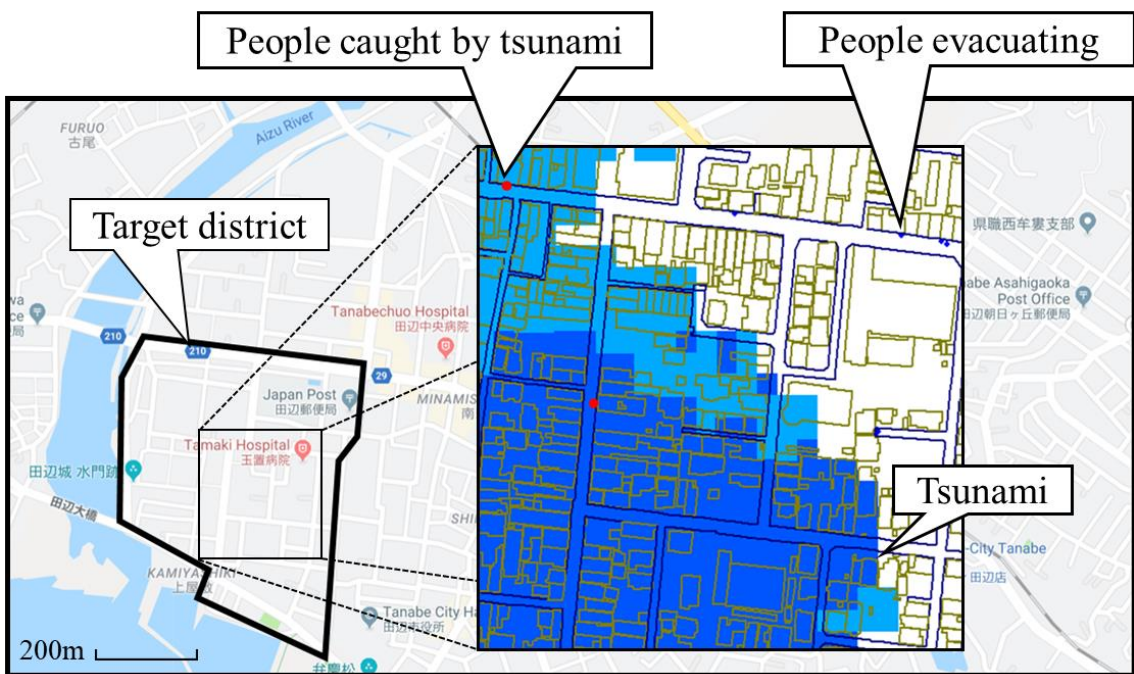


Figure 7.7 A tsunami evacuation simulation example. Dots on the streets represent evacuees.

7.5 Summary of the Tsunami Evacuation Simulation

After preparing the prerequisite information as outlined in Section 4 above and taking into consideration the building damage ratios predicted in Section 3, a tsunami evacuation simulation was performed. Parameters used for the simulation were as follows: tsunami data, number and initial positions of residents, position and capacity of evacuation sites, walking speed, and number and locations of collapsed buildings. The simulation outcome averaged three trials for each of the 210 patterns, comprising the combination of two patterns of the evacuation sites described below and fifteen road blockage patterns, each with a proportion of earthquake-resistant buildings assumed at 0%, 10%, 30%, 50%, 70%, 90%, and 100%. In each of the three trials, routes of individual agents to the evacuation sites were varied, because we selected priority of evacuees by different random numbers at each path at each time and the different selection will be made whenever the number of evacuees exceeded the path capacity. However, in all 210 simulations, variations of the number of the successful evacuees between three trials were small. This may be so because the occurrence of the exceeding path capacity was not so frequent. The parameters for the tsunami evacuation simulation are described in detail below.

7.5.1 Patterns for evacuation sites

The first simulation was performed assuming that both residents in Kamiyashiki 3-Chome, which is situated furthest from the elevated ground and therefore deemed most difficult to evacuate, and residents in the southern part of Kamiyashiki 2-Chome, which the tsunami will hit first, would evacuate to the NTT building and the Primary School. Remaining residents would

evacuate to Tokei Shrine. This simulation was designed to help determine whether the capacity, number, and locations of the evacuation sites would be sufficient. The evacuation plan was deemed the most ideal according to the current circumstances, and it is referred to as Case 1.

Next, another scenario, in which everyone was evacuated to Tokei Shrine was simulated to determine the effectiveness of the capacity and position of the evacuation buildings, namely the NTT building and the Primary School used in Case 1. This is referred to as Case 2.

7.5.2 Road blockages caused by collapsed buildings

In the simulations, the number of collapsed buildings was calculated using the building damage simulation program introduced in Chapter 7.3, together with the approximated ratio of 4:3, which is the number of buildings that were severely damaged versus the number of buildings that collapsed or disintegrated, as per the investigation report by the Architecture and Earthquake Investigation Committee for Chuo-Ku, Kobe City (Central Disaster Prevention Council 2003). Since buildings suffered from severe damage (Rank 4 level in Okada and Takai (2004) criteria) can still stand upright after the earthquake, we should exclude them in the road blockage estimation. The schemes for determining the buildings that would collapse and for generating the patterns of road blockages are described below.

- 1) Buildings that could be determined to be wooden or non-wooden construction using Google Earth and onsite surveys were categorized accordingly and then numbered. Wooden construction buildings were numbered from 1 to 257, and non-wooden buildings were numbered from 1 to 106. Buildings for which construction could not be determined were numbered from 1 to 268 (Figure 7.8).
- 2) For the collapsed buildings, the number of each type of building was multiplied by the damage ratio from Nagato and Kawase's simulation program in order to determine the number of buildings that would suffer major damages or collapse. This number was then multiplied by 3/7, which is the estimated proportion of buildings that would collapse among buildings that suffered major damages and higher, in order to compute the total number of collapsed buildings. Table 7.1 shows these numbers. Note that (a) the number of each type of non-wooden construction buildings (i.e., RC or steel) was computed by multiplying the ratio of the respective building type as recorded on the Tanabe City taxation roll (Tanabe City 2008) by the total number of buildings, 106; and (b) the damage ratios shown in Figure 7.5 were used to calculate damages to wooden and non-wooden construction buildings. For buildings of unknown construction type, the total damage ratio of 70.94% was used. This ratio was derived by multiplying Nagato and Kawase's damage ratio by the building group model and adding the results together.
- 3) The buildings that collapsed were selected using a random number generator across the number of buildings of each construction type (wooden, non-wooden, and unknown), as the one building collapse pattern. By doing the same process 14 times, we got the 15 building collapse patterns. The buildings that collapsed at each level of earthquake resistance were also chosen by randomly selecting assigned numbers.
- 4) After the shapes of the buildings chosen in step 3) were determined using DiMSIS, road blockages were created. Three levels of road blockage were assumed based on the road width

as follows:

- a. Roads with the widths less than 3 m: complete blockage if one of the houses on either side of the road collapsed.
- b. Roads with widths greater than 3 m but less than 6 m: roads were not completely blocked if a house on one side of the road collapsed, but were blocked completely if two opposing houses collapsed.
- c. Roads with widths greater than 6 m: no effect on passage even if houses on both sides of the road collapsed.

Construction	(a) Total	(b) Damage rate (%)	(c) Collapse rate (%)	(d) Number of collapsed buildings $= (a) \times (c) \times 1/100$
Wooden	257	74.0		82
Non-Wooden (RC, Old Standard)	11	32.2		1
Non-Wooden (RC, New Standard)	12	0.9	(b)×3/7	0
Non-Wooden (S, Old Standard)	27	61.0		7
Non-Wooden (S, New Standard)	56	79.9		19
Unknown Construction	268	70.9		81

Table7.1. Numbers of collapsed buildings for different construction types estimated by Nagato and Kawase's model (2001, 2002a, b).



Figure 7.8 Locations of non-wooden buildings and wooden houses in the district. Although the construction age, built before and after 1981, in both non-wooden buildings and wooden houses is distinguished in the database, the letter is not referred to in this study.

The above standard was based on a rubble flow distance of 3 m. Since we were unable to find a quantitative source for rubble flow distance, it was assumed to be 3 m when the first floor of a two-story building, which is the most typical in the target district for this study, collapsed. Furthermore, the direction of the flow was assumed to be frontal. Sakata and Teraki (2009) mentioned that it is theoretically very difficult to uniquely determine the rubble flow direction as a function of two horizontal components of ground motions and so they considered rubble flow direction probabilistically. For the present study, given that most buildings have openings in the front, and there are often structures on the other three sides which would help the structure to withstand collapse in those directions, it was assumed that the collapse would occur frontally, which is the worst possible direction with respect to road blockages.

Since we assumed that collapsed buildings would cause 3 m of blockage regardless of its height, we presumed that buildings that stand further than 3 m from the road would not cause road blockage even if they collapse.

7.5.3 Time required for evacuation

In our simulations, we estimated the number of successful evacuees by determining how soon after the evacuees would need to reach either the evacuation sites inside the area or the exit points to the external evacuation site, that is, Tokei Shrine. The reason why we need to set the exit

points in the eastern side of the target district is as follows: In this simulation we exclude the area between the eastern side of the target district and Tokei Shrine. Therefore, we first calculate the required time to go to Tokei Shrine from these points and estimated the time to get out of these points. When evacuating to Tokei Shrine, we assumed that it would be 27 minutes after the earthquake before the tsunami reached the area surrounding the shrine and that the evacuee may take 14 minutes to reach to the shrine after getting out from the target district and additionally 2 minutes to climb up to the sufficiently elevated ground. Therefore, the evacuee must reach the exit point by 11 minutes after the earthquake. The time required to reach the shrine (14 minutes) was calculated based on the distance from the western end of the target district to the shrine, approximately 620 m, divided by 2.65 km/h, the average walking speed of residents older than 10 and younger than 70. In order to evacuate to buildings inside (the NTT building or the Primary School), we assumed that it would require two minutes to reach the roof of each building, so $t - 2$ is the time limit for evacuation, where t represents the time when the tsunami reaches the building, that is, 17 minutes for the NTT building and 19 minutes for the Primary School. The time limits for successful evacuation are summarized in Figure 7.9.

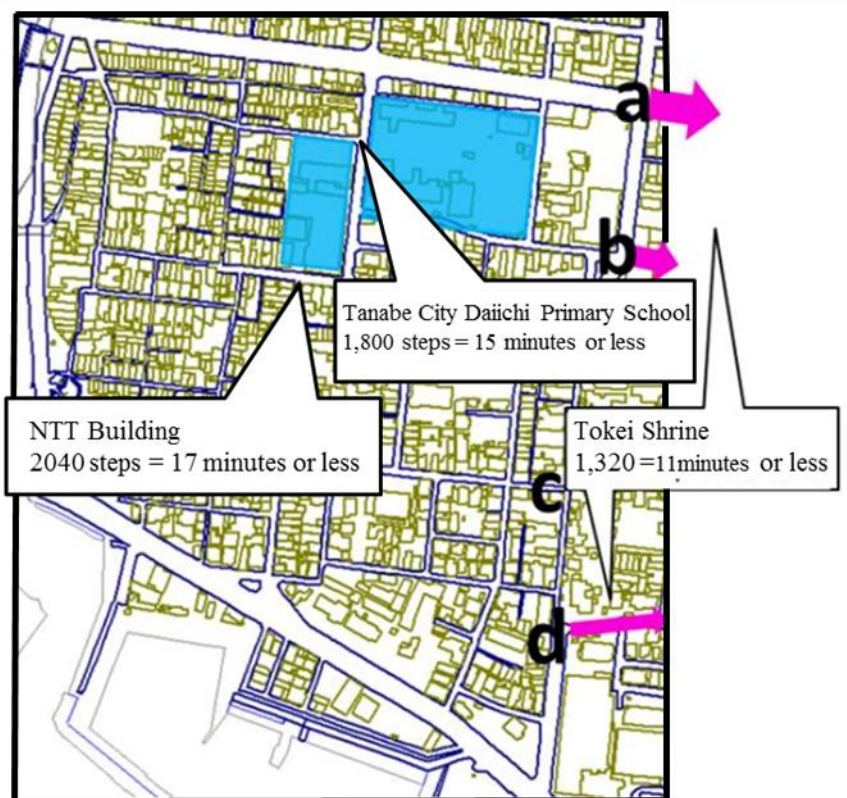


Figure 7.9 The elapsed time from the beginning of the earthquake at each evacuation site for successful evacuation from the tsunami front. Four exit points on the eastern side of the target district, a to d, are defined for the outside evacuation site, Tokei Shrine.

7.6 Tsunami Evacuation Simulation Results and Discussions

7.6.1 Evaluation of designated evacuation sites

First, the performance of the designated evacuation sites at present was evaluated under the assumption that there would be no building collapsed. By adding the evacuation buildings inside, namely, the NTT building and the Primary School, 333 additional people, which is 27% of the whole residents, would be able to evacuate to these locations. However, 391 people, or 31.4% of the residents, would not be able to evacuate in time (Figure 7.10). Thus, the current evacuation plan was found to be inadequate. It is necessary to consider additional evacuation sites in terms of numbers, locations, and their capacities to save all the residents in time. When we see the progress of evacuation in our simulation (Figure 7.11), we found universal congestion around the three-storied RC building circled in red. Therefore, this building seems to be appropriate as an additional tsunami evacuation building to increase the number of successful evacuees.

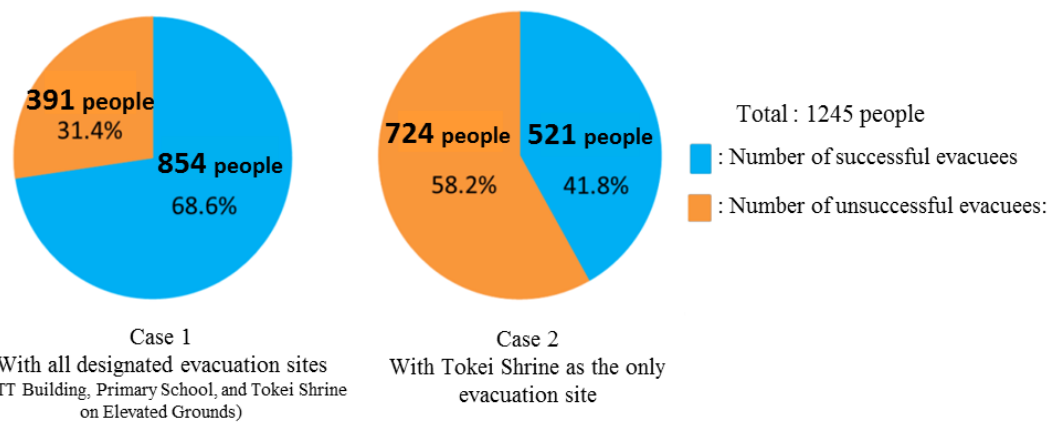


Figure 7.10 Comparison of successful evacuation rate with (Case 1) and without (Case 2) the current evacuation sites inside the target district.

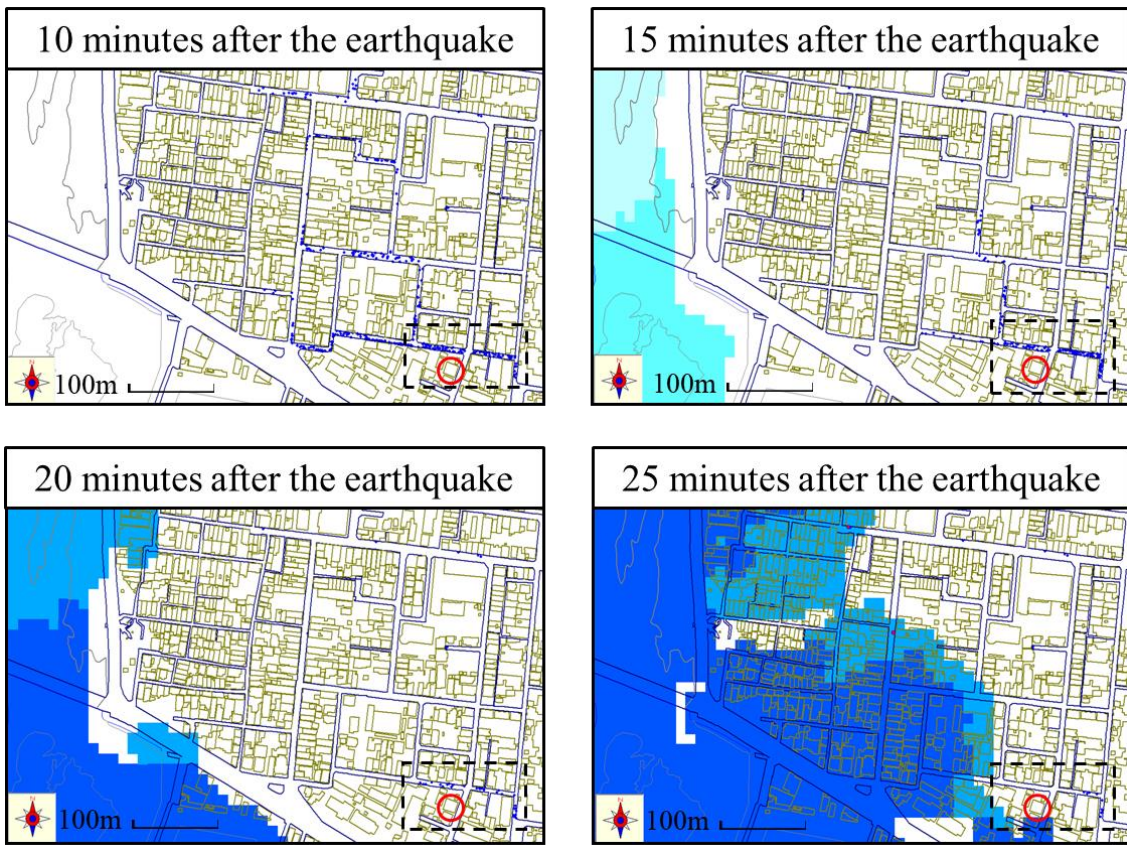


Figure 7.11 Snapshots of the evacuation process for every 5 minutes from 10 minutes after the earthquake. Small dots on the streets represent evacuees. We definitely needed one or more evacuation sites in the southeastern side of the district, as shown by a rectangular with broken lines, in order to save evacuees in that area before the tsunami hit. A three-storied RC building circled in red can be a candidate for an additional evacuation site.

7.6.2 Change in the number of successful evacuees as earthquake resistance reinforcement rates improve

By improving the proportion of earthquake-resistant houses from 0% to 100%, road blockages due to building collapse were eliminated. It was found that an additional 3% of residents could successfully evacuate for Case 1, or an additional 3.6% for Case 2 (Figure 7.12). In this figure, the legends “Shrine a”, “Shrine b”, “Shrine c”, and “Shrine d” respectively refer to the group of residents who passed through the exit points a, b, c, and d to Tokei Shrine as shown in Figure 7.9. The legends “School” and “NTT” refer to the residents that evacuated to these buildings. Please note that there was no one who passed the point “d” in Case 1. The aim here was to calculate the number of people originally who would take too much time to evacuate due to road blockages caused by collapsed houses and be caught by the tsunami despite having successfully escaped their homes, and would be saved thanks to measures to increase earthquake resistance of houses inside the target district.

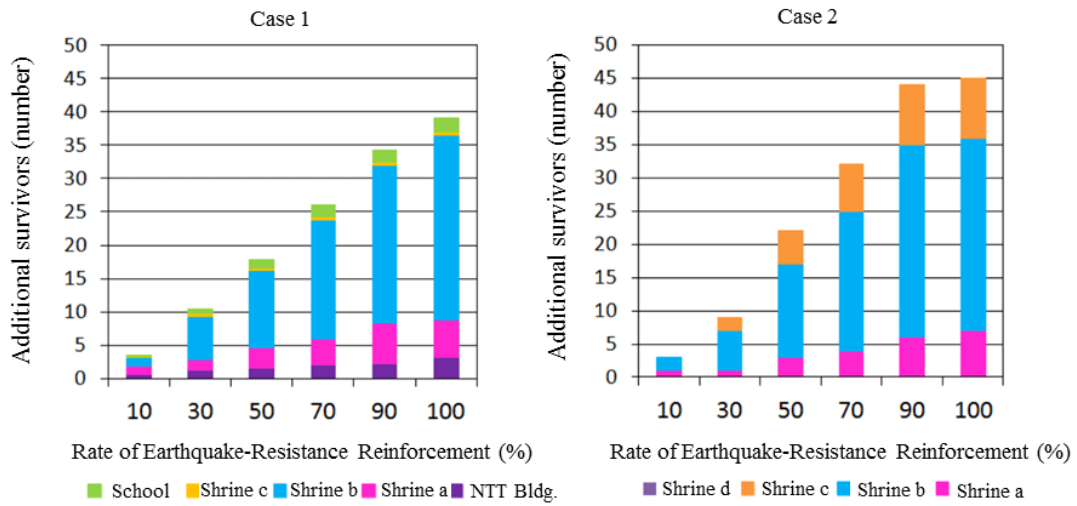


Figure 7.12 Increase in the numbers of successful evacuees with increased earthquake-resistant reinforcement rates for Case 1 and Case 2. We can see that the additional survivors by the reinforcement would be 45 or 4% of the total evacuees at most.

The study did not consider the number of people who may have died directly due to houses collapsing—either crushed to death or trapped until the tsunami arrived. With regard to this last point, the Central Disaster Management Council made the following estimate (Ministry of Construction 1996):

$$\begin{aligned} &\text{Numbers of fatalities due to collapsed wooden houses} \\ &= \text{numbers of totally collapsed wooden houses} \times 6.7\% \end{aligned} \quad (7.1)$$

$$\begin{aligned} &\text{Numbers of fatalities due to collapsed non-wooden houses} \\ &= \text{numbers of totally collapsed non-wooden houses} \times 6.7\% \times \text{correction factor} \\ &(0.0155/0.0629) \end{aligned} \quad (7.2)$$

Applying Equation 1 to 257 houses that were identified to be of wooden construction, where the number of total collapsed houses is 257×0.74 (see Sub-section 5.2), the total number of fatalities due to wooden building collapse would be $257 \times 0.74 \times 0.067 = 12$. The number of buildings that collapsed completely in the above formula was assumed to be equivalent to the number of heavily damaged or collapsed buildings here, based on the criteria defined and used by the Ministry of Construction's Building Research Institute (1996). Less than one fatality would be calculated from Equation 2 for non-wooden houses. Please note that the effect of these immediate fatalities on the number of initial evacuees is negligibly small.

Based on the above, the fatality rate directly or indirectly caused by building collapse can be obtained by adding 12 (derived using Equation 1) and the number of failed evacuees derived from the simulations. For Case 1, this would be $12 + 38 = 50$, which corresponds to 4%

of the total population in the district. For Case 2, this would be $12 + 45 = 57$, or 4.6% of the population. If we also take into account collapsed buildings of unknown construction, the number of fatalities related to building collapse would be higher. Thus, fatalities would decrease if the number of earthquake-resistant buildings were improved. These figures, 3 to 4 % by road blockage plus 1 % by collapsed buildings are not so large compared to the number of additional people that could be saved by increasing or improving the evacuation sites as noted in 6.1. Furthermore, Figure 7.12 shows that the number of successful evacuees increases almost linearly with the increased rate of earthquake-resistant reinforcement. This is mainly due to the fact that the soil amplification factor is homogenous in this district, and wooden construction buildings are evenly distributed, causing the number of collapsed buildings to vary inversely with respect to the percentage of earthquake-resistant houses.

7.6.3 Change in the time required to complete the evacuation of 90% of the population by improving the earthquake resistance

In this section, we examine the delay in arrival at evacuation sites caused by building collapses and how improvement in the proportion of earthquake-resistant buildings might reduce the time required for evacuation, by investigating the average elapsed time after the earthquake until 90% of residents complete evacuation. The reason why 90% was chosen, rather than 100%, is because this is when the increase in the number of successful evacuees converges. This is because after 90% of residents complete evacuation, the remaining evacuees tend to be separated from each other inside the trapped areas and so the time interval to complete evacuation between one person and the next is getting larger and larger.

While we see some variation in the outcome depending on the evacuation sites, the time required for evacuation was reduced by approximately 30 to 60 seconds by improving the rate of earthquake-resistant houses from 0 to 100% (Figure 7.13). Since residents must reach the evacuation site within 11 minutes after the onset of the earthquake if evacuating to Tokei Shrine, 15 minutes to the Primary School, and 17 minutes to the NTT Building for successful evacuation, the reduction in evacuation time of 30 to 60 s did not significantly increase the number of survivors as seen in Figure 7.12. The influence of reinforcing buildings and houses on the number of successful evacuees is not so significant that increasing the capacity of evacuation sites looks more effective to reduce tsunami casualties. However, we did not consider any side effects of building damage to the speed of evacuation. If we have severe damage to the residential structure, first the start-up time of evacuation for residents will be increased because they need time to check the security of all the family members. Second, debris inside and outside of the damaged buildings will prevent smooth evacuation. Third, injuries to the residents inside the damaged buildings may cause further delay in their evacuation. If we combine these side effects into our simulation, the effects of building reinforcement would be more rewarding than the direct influence considered in this paper.

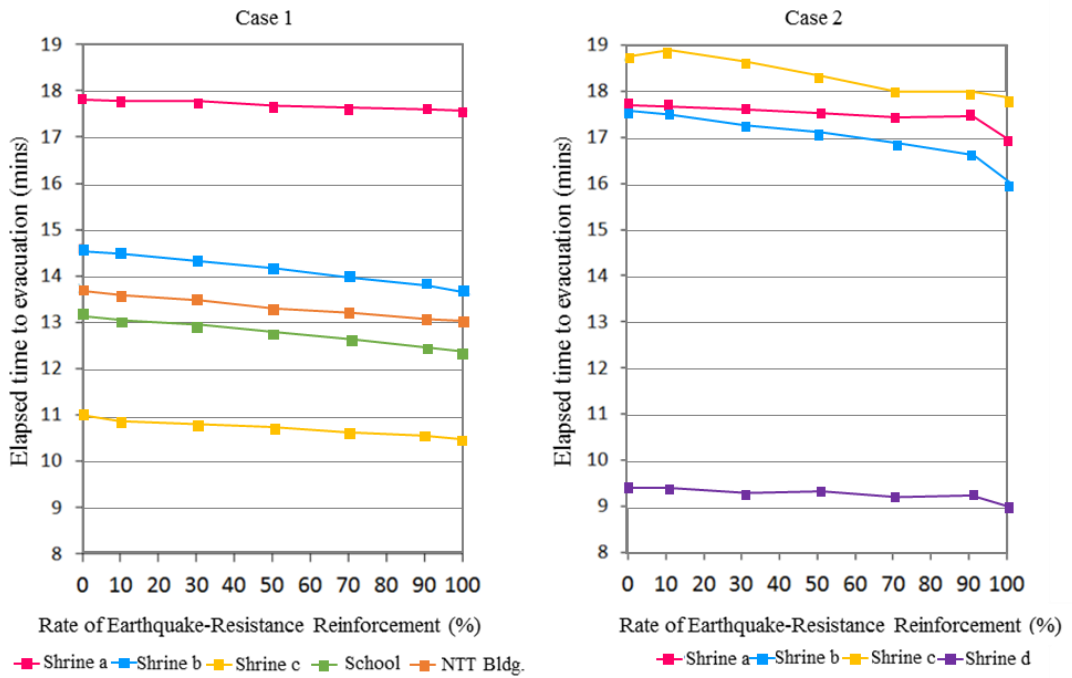


Figure 7.13 Decrease in the elapsed times required for evacuation (for 90% of the total evacuees) with increased earthquake-resistant reinforcement rates for Case 1 and Case 2. We can see that the gain by the reinforcement would be around 60 s at most.

From the above results, it has been quantitatively determined that increasing the number of evacuation sites at appropriate locations is the highest priority. After having improved the numbers and locations of evacuation sites, increasing the percentage of houses with earthquake-resistant reinforcement would have a certain level of effectiveness as well.

7.7 Summery and Future Tasks

In this study, the building collapse ratio simulation program developed by Nagato and Kawase (2001, 2002a, b) was used to predict building collapses in the Tanabe City district in Wakayama Prefecture, where it is expected to have significant damage from both earthquake and tsunami during the earthquake scenario with the whole Tokai, Tonankai, and Nankai segments ruptured. Tsunami evacuation simulation was undertaken assuming road blockages from the predicted building collapses. We found that the prepared countermeasures are not enough to let everyone evacuate and that the number of survivors increases by 3 to 4% if all the houses were seismically reinforced. Considering this plus, only 1% of expected casualties inside the collapsed houses, it appears as though it is not as efficient to reinforce buildings and houses to prevent human loss in comparison to increasing the capacity of tsunami evacuation sites in the target district. However, the damage to building and houses will cause a lot of side effects which are not considered here but must prolong the evacuation time. Thus, we concluded that we need to reinforce the houses as well as considering the appropriate placement, number, and capacity of

the evacuation sites.

Even in the target district where relative consciousness towards disaster prevention is higher than in other districts, and evacuation planning is deemed more advanced, it was found that there are unresolved issues. As discussed in the building collapse prediction in this evacuation simulation, although fatalities from the collapsed buildings themselves and the effect of injuries on evacuation speed remained to be set as a parameter in the simulation, this study was able to quantify the risk of collapsed buildings in the evacuation process through the use of a building collapse ratio simulation program. This is a significant contribution to future studies and disaster prevention planning. We hope to continue to investigate evacuation predictions by extending the model that incorporates the direction of building collapse, variation in initiation time of evacuation, interaction between evacuees and cars and/or motorcycles, and fire breakout and subsequent spreading after the earthquake. We also hope to expand the size of the target district and perform more realistic simulations, thereby enhancing evacuation planning and residents' awareness.

Acknowledgements

A part of this study was supported by the Ministry of Education, Culture, Sports, Science and Technology's special expense," Research Project for the Formation of the Next Generation Disaster Prevention and Mitigation in Preparation for Massive Disasters of Earthquakes and Tsunami" (P.I.: K. Yamori) and JSPS's Grand-in-Aid (Kaken-hi) for Basic Research (A) No.26242034 (P.I.: H. Kawase). The information provided by the officials of Tanabe City and the waveform provided by Dr. Baoyintu are highly appreciated.

References

- Akakura Y, Takahashi H, Nakamoto T (2000) An attempt to model street blockage for prediction of earthquake damage in urban coastal area, Report of Port and Harbor Research Institute, Vol.39, No.4, pp.19-41 [in Japanese].
- Baoyintu (2014) Study regarding the quantitative damage estimation for a massive earthquake in southwest japan and countermeasures, Dissertation, Graduate School of Engineering, Kyoto University [in Japanese].
- Baoyintu, Kawase H, Matsushima S (2013) Strong motion observed during the 2011 Great East Japan earthquake and its destructive powers, Architectural Institute of Japan, Papers from the Great East Japan Earthquake 2nd Anniversary Symposium pp. 293–298 [in Japanese].
- Central Disaster Prevention Council (2003) Disaster estimations for Tonankai-Nankai Earthquake and the summary of estimation methodologies, http://www.bousai.go.jp/kaigirep/chuobou/senmon/tounankai_nankaijishin/6/pdf/siryou3.pdf, Accessed 20 June 2018 [in Japanese].
- Central Disaster Prevention Council (2011) Regarding Tokai, Tonankai, and Nankai Earthquakes, <http://www.bousai.go.jp/jishin/nankai/model/1/pdf/2.pdf>, Accessed 20 June 2018 [in Japanese]
- Central Disaster Prevention Council (2012) Regarding Tokai, Tonankai, and Nankai Earthquakes (Second report), <http://www.bousai.go.jp/jishin/>

- nankai/model/pdf/20120829_2nd_report01.pdf, Accessed 20 June 2018 [in Japanese].
- Geospatial Information Authority of Japan (2013) Maps and Geospatial Information Webpage, <http://www.gsi.go.jp/kiban/index.html>, Accessed 20 June 2018.
- Goto Y, Affan M, Agussabti, Nurdin Y, Yuliana DK, Ardiansyah (2012) Tsunami evacuation simulation for disaster education and city planning, Journal of Disaster Research, Vol.7, No.1, pp.92-101.
- Hatayama M (1999) Development of space-time geographic information systems DiMSIS, GIS – Theory and application, 7/2, pp.25–33 [in Japanese].
- Ho N and Kawase H (2008) Damage prediction and earthquake risk management strategy for environmental load by the next Nankai earthquake, Comprehensive Journal of AIJ, No.6, 87-92 [in Japanese with English abstract].
- Hori M, Suematsu T, Araki H, Okumura Y, Dohi Y (2015) Verification and validation of tsunami evacuation simulation models, J of Japan Association for Earthquake Engineering, Vol.15, No.4, 2015, pp.144-157 [in Japanese with English abstract].
- Kaneda T (2010) Introduction to pedestrian agent simulation using Artisoc: from principle and methodology to space design and management for safety and crowd”, Kozo Keikaku Engineering Inc., Shoseki Kobo Hayama Publishing [in Japanese].
- Kamae K and Irikura K (1994) Strong ground motion evaluation in the near source and the surrounding area at the time of the 1946 Nankai earthquake ($M_w=8.1$), Journal of Structural and Construction Engineering (Transactions of AIJ), No. 455, 61-71 [in Japanese with English abstract].
- Karim KR and Yamazaki F (2002) Correlation of JMA instrumental seismic intensity with strong motion parameters, Earthquake Eng. Struct. Dyn. 31:1191–1212 (DOI: 10.1002/eqe.158).
- Kawase H (2007) Strong motion data of intensity seismometer (Shindo-kei) during the West off Fukuoka earthquake of 2005 and their structural damage potential, J. of Japan Assoc. Earthq. Eng., Vol.7, No.2, 190-204 [in Japanese with English abstract].
- Makinoshima F, Imamura F, Abe Y (2016) Behavior from tsunami recorded in the multimedia sources at Kesennuma City in the 2011 Tohoku tsunami and its simulation by using the evacuation model with pedestrian-car interaction, Coastal Engineering Journal, Japan Society of Civil Engineers, Vol. 58, No. 4, pp.1640023-1-28.
- Mas E, Suppasri A, Imamura F, Koshimura S (2012) Agent-based Simulation of the 2011 Great East Japan earthquake/tsunami evacuation: An integrated model of tsunami inundation and evacuation, Journal of Natural Disaster Science, Vol. 34, No. 1, 2012, pp.41-57.
- Mas E, Suppasri A, Srivihok P, Koshimura S (2013) Feasibility of evacuation at the Pakarang Cape in Thailand based on tsunami inundation model and human evacuation simulation, 10th International Conference on Urban Earthquake Engineering, Tokyo, Japan, pp.1-6.
- Matsushima S and Kawase H (2000) Multiple asperity source model of the Hyogo-Ken Nanbu earthquake of 1995 and strong motion simulation in Kobe, Journal of Structural and Construction Engineering (Transactions of AIJ), No. 534, pp.33-40 [in Japanese with English abstract].
- Ministry of Construction, Building Research Institute (1996) Final Report on the Survey of Damages from the 1995 Hyogo-ken Nanbu Earthquake, BRI, Tsukuba [in Japanese].
- Ministry of Construction, Committee for Investigating the Earthquake Disaster and Architecture (1995) Interim Report on the Survey of Damages from 1995 Hanshin-Awaji Great Earthquake, Ministry of Construction, Tokyo, 1995 [in Japanese].

- Ministry of Land, Infrastructure, Transport and Tourism, City Bureau, Urban Transport Facilities Division, City Planning Division (2011) Great East Japan Earthquake tsunami damage field survey (Stage 3 Report)—Field study of tsunami evacuation (bulletin), MLIT, Tokyo, p.6 [in Japanese].
- Ministry of Land, Infrastructure, Transport and Tourism, City Department, Survey on the method for restructuring the cities suffered from the tsunami (Summary), MLIT, Tokyo, 2012 [in Japanese].
- Murao O (1999) Study on the vulnerability function based on the observed damage statistics in 1995 Hyogoken Nambu earthquake, Dissertation, the University of Tokyo, <http://hdl.handle.net/2261/51136> [in Japanese].
- Murao O and Yamazaki F (2002) Building Fragility Curves for the 1995 Hyogoken-Nanbu Earthquake based on CPIJ & AIJ's Survey Results with detailed Inventory, Journal of Structural and Construction Engineering (Transactions of AIJ), No. 555, 185-192 [in Japanese with English abstract].
- Nagato K and Kawase H (2001) Damage evaluation models of reinforced concrete buildings based on the building damage statistics and simulated strong motions, Journal of Structural and Construction Engineering (Transactions of AIJ), No. 554, pp.31–37 [in Japanese].
- Nagato K and Kawase H (2002a) A set of dynamic models of steel buildings for damage evaluation, Journal of Structural and Construction Engineering (Transactions of AIJ), No. 559, pp.101–106 [in Japanese with English abstract].
- Nagato K and Kawase H (2002b) A set of wooden house models for damage evaluation based on observed damages statistics and non-linear response analysis and its application to strong motions of recent earthquakes, Japan Earthquake Engineering Symposium, Japan Association for Earthquake Engineering, No.11, vo.2, pp.1315-1320 [in Japanese with English abstract].
- Nakai F and Hatayama M (2013a) Development of agent-based simulation system for tsunami evacuation estimation, Presentations of the Committee of Infrastructure Planning and Management Vol. 47, CD-ROM [in Japanese].
- Nakai F and Hatayama M (2013b) Evaluation of Evacuation Plan Through an Analysis of Evacuation Behavior and Resident Coordination: A Case Study Examining Disaster Risk Communication in Kuroshio City, Kochi Prefecture, Presentations of the Committee of Infrastructure Planning and Management Vol. 47, CD-ROM [in Japanese].
- Nakai F, Hatayama M, Yamori K (2014) A study on evaluation for community based planning process of tsunami evacuation using agent based simulation, Information Processing Society of Japan, SIG Notes, No.127, 2014.3, 1-9 [in Japanese].
- National Research Institute for Earth Science and Disaster Resilience (2013) Japan Seismic Hazard Information Station, <http://www.j-shis.bousai.go.jp/>, Accessed 20 June 2018.
- Okada S and Takai N (2004) Damage index functions of wooden buildings and reinforced buildings for seismic risk Management, 13th W. Conf. Earthq. Eng., Vancouver, B.C., Canada, August 1-6, 2004, Paper No. 727.
- Sakata T and Teraki A (2009) A study about simulations for road blockage considering directions of rubble flow, Proceedings from the Institute of Social Safety Science, No. 25, 2009 [in Japanese].
- Sato H, Murakami H, Shimada T, Kozuki Y, Kurata K, Otani H (2002) A study on the evacuation from tsunami considering building collapses by the earthquake, Coastal Engineering

- Journal, Japan Society of Civil Engineers, Vol.49, 2002, pp.311-315 [in Japanese].
- Southern California Earthquake Center (2018) Working Group: Unified Structural Representation (USR), <https://www.scec.org/research/usr/>, Accessed 20 June 2018.
- Suzuki S, Furubayashi T, Okumura Y, Kawada Y (2011) Tokai, Tonankai, Nankai earthquake and tsunami simulation considering sliding near trench axis, Proceedings from the 30th Symposium of the Japan Society for Natural Disaster Science No. 30, pp. 65–66 [in Japanese].
- Tamura T, Nishihata T, Moriya Y, Takimoto K, Miura F (2005) Application of evacuation simulation method during tsunami inundation considering road blockage, Coastal Engineering Journal, Japan Society of Civil Engineers, Vol.52, 2005, pp.1286-1290 [in Japanese].
- Tanabe City (2012) Resident Basic Register: Population and Households by Town, Tanabe City [in Japanese].
- Tanabe City (2013a) Tanabe City Statistics, <http://www.city.tanabe.lg.jp/kikaku/toukei/>, Accessed 20 June 2018.
- Tanabe City (2013b) Resident Basic Register: Population by Town and Age (in 5 year-intervals), Tanabe City [in Japanese].
- Tanabe City (2014) Tanabe City Tsunami Hazard Map, http://www.city.tanabe.lg.jp/bousai/files/tsunami_p04-p05_shinsuishin.pdf, Accessed 20 June 2018.
- Tanabe City (2016) Tanabe City Earthquake Resistant Reinforcement Promotion Plan, <http://www.city.tanabe.lg.jp/kenchiku/kenchiku/files/tanabesitaisinkaisyusokusinkeikaku.pdf>, Accessed 20 June 2018.
- Usuzawa H, Imamura F, Shuto N (1997) Development of the method for evacuation numerical simulation for tsunami events, Annual Meeting of the Tohoku Branch Technology Research Conference, Japan Society of Civil Engineers, pp.430–431 [In Japanese].

Chapter 8

Detailed Estimation of Strong Ground Motion Using Microtremor Observation and Tsunami Evacuation Simulation Considering Road Blockage by Collapsed Houses in a Village with Stiff Soil Layers

Abstract

We chose a village in Japan, where high-frequency amplification due to relatively stiff soil layers is expected. We identified the underground soil structures of the 32 microtremor observation points by using microtremor H/V spectral ratios and estimated the surface ground motions by performing earthquake response analyses of one-dimensional soil structures. We found that the PGAs were larger in the area close to the mountain than in the area along the river or near the coast, and the difference in PGAs in the village is significant while that in PGVs is marginal because of the thin, soft sediments there. Microtremor observations for wooden houses were also conducted inside 38 wooden houses. The yield strength ratio and its distribution for different construction period in the district were obtained. A model of the group of wooden houses in the district was established based on the observed natural period distribution for building damage prediction. The average yield strength ratio of houses constructed before 1981 was higher than those in Kobe, which is reflected in the damage prediction models. We also notice that the yield strength distribution was more concentrated around the mode. From these models and input motions we estimated the building damage in detail. In the end, the number of collapsed or overturned buildings was about 2% of the total buildings in the district. Finally, tsunami evacuation simulations were performed incorporated the number of damaged buildings obtained in the previous investigations. Simulations for 21 patterns were conducted. As a result, the number of successful evacuees 20 minutes after the earthquake was larger in most cases. However, the number of successful evacuees after 20 minutes was larger for the case of starting at 15 minutes than for the case of 10 minutes in 3 patters out of 10 patterns. One reason for this result is that a larger spread in evacuation start time of residents leads to less congestion in roads, allowing everyone to smoothly reach to an evacuation center along the narrow roads of the target district.

8.1 Background of This Study

It has been often reported that when a big earthquake happened, there was a big difference in the extent of damage to each building in a small area, even though they had almost the same strength. This result was estimated to be caused by the difference in the underground soil structures.

Therefore, identifying the ground structures and estimating the strong ground motions in detail is important to estimate the expected damage of each building in an area. It is also important to estimate human loss when an earthquake happens for evacuation planning, considering the building damage by using the knowledge of earthquake engineering, as mentioned in chapter 7.

In this study we choose a village along the coast of Kii Peninsula in Wakayama prefecture, Japan. In this area, high-frequency amplification due to relatively stiff soil layers is expected because the site is located between the seashore and hillside, and they are taking measures in advance to decrease damages to the buildings and residents when a mega-thrust earthquake or earthquakes along the Nankai Trough happens.

We identify the velocity structures of each points using the microtremor records of each observation point, and then estimated the strong ground motion with the aim to estimate the building damage.

We calculate the damage ratio (collapse ratio and severely damaged ratio) through response analysis by applying the strong round motion to each point to the building group model, incorporating characteristics of the district for wooden buildings, and the three-story steel structure model by Kawase and Nagato for non-wooden buildings (Nagato and Kawase 2002a,b; Yoshida 2004).

We reflect the number of damaged (collapsed and severely damaged) buildings in each dominated region on GIS and simulation parameters. Simulations for 21 patterns are conducted (1 pattern without and 20 patterns with building damage), and the results are analyzed.

8.2 Microtremor Observation and Analysis

8.2.1 Microtremor observation

We firstly observed microtremors at 32 points within a radius of 500m in the area we mentioned above, using the SMAR-6A3P by Mitutoyo Corporation, a portable three-component acceleration seismograph with a 0.1–10,000× amplifier, and the DATAMARK LS8800 by Hakusan Corporation, a data acquisition device. The sampling frequency was 200 Hz, the amplifier was set to 500×, and GPS was used for time calibrations. Figure 8.1 shows the 32 microtremor observation points.



Figure 8.1. 32 microtremor observation points in the research area.

8.2.2 Analysis for observation recordings

In waveform analysis, observation recordings were divided into 40.96-s segments with a 50% overlap. We calculated the H/V ratios (Horizontal-to-Vertical ratios, referred to as HVRs) of each segment and defined the average HVRs of all the segments as the observed HVRs.

We minimized the effect of unsteady noise by extracting unsteady noise segments from all the recorded waveforms, and then calculating the average HVRs of the rest of the segments.

S_x , S_y , S_z are defined as power spectrums of each component smoothed by Parzen-windows of 0.1 Hz, which compose HVRs defined as Equation 8.1.

$$\text{HVRs} = \sqrt{\frac{S_x + S_y}{S_z}} \quad (8.1)$$

The 1st peak frequencies of HVRs can be regarded as the resonant amplification frequencies of underground soil structures except for some sites with very low impedance contrast.

Figure 8.2 shows the HVRs at the primary school, and Figure 8.3 shows the distribution of the peak frequencies.

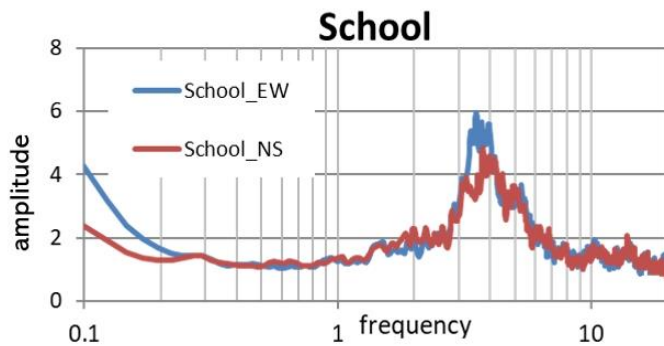


Figure 8.2. The HVRs at the primary school

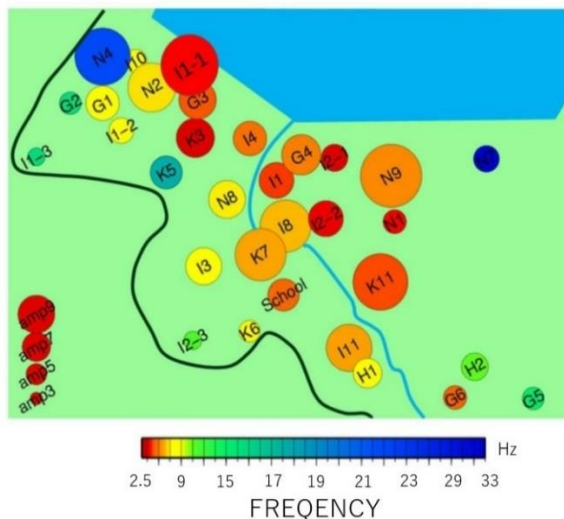


Figure 8.3. The distribution of the peak frequencies in the area.

8.3 Identification of the ground structure

8.3.1 Identification of the initial velocity structure model

We estimated the underground soil structure at the nearby primary school based on the boring data and Equation 8.2-4. Equation 8.2 was proposed by Ota & Goto (1978), and Equation 8.3 and 4 were proposed by Ludwig (1970).

$$V_s = 62.48N^{0.218}H^{0.228}F \quad (8.2)$$

where V_s = S wave velocity; N = N-value; H = depth; and F = coefficients depending on the soil category.

$$V_p(\text{km/sec}) = 0.9409 + 2.0947V_s - 0.8206V_s^2 + 0.2683V_s^3 - 0.0251V_s^4 \quad (8.3)$$

$$\rho(\text{g/cm}^3) = 1.6612V_p - 0.4721V_p^2 + 0.0671V_p^3 - 0.0043V_p^4 + 0.000106V_p^5 \quad (8.4)$$

where V_p = P wave velocity; and ρ = density.

This model has 5 layers, composed by the 1 layer at the bottom and the 4 layers on the bottom layer. Table 8.1 shows the estimated velocity and density of each layer based on the boring data and Equation 8.2-4.

Table 8.1. The estimated velocity and density based on the boring data and Equation 8.2-4.

Layer	thickness	V_p	V_s	ρ
1	3.45	1549.65	137.24	1.54
2	4.00	159.64	159.73	1.56
3	4.00	1730.24	272.68	1.67
4	6.63	1807.64	330.73	1.73
5	----	2770.01	1270.00	2.17

By fitting the peak frequency of the observed HVR of microtremor to that of the theoretical HVR, we modified the velocity model (referred to as “the initial model”).

Here we modified only the S wave velocity (without changing the thickness) of all five layers following Equation 8.5, based on the relation between wavelengths and peak frequencies. Table 8.2 shows the estimated velocity and density calculated from the result showed in Table 8.1 and Equation 8.5.

$$V_{s-after} = \frac{f_{target}}{f_{before}} V_{s-before} \quad (8.5)$$

where $V_{s\text{-before}}$ = S wave velocity before modified; $V_{s\text{-after}}$ = S wave velocity after modified; f_{before} = the peak frequency of the primary school; and f_{target} = the peak frequency of the target site.

Table 8.2. The estimated velocity and density calculated from the result showed in Table 8.1 and Equation 8.5.

Layer	thickness	V_p	V_s	ρ
1	3.45	1223.55	138.22	1.44
2	4.00	1265.85	160.88	1.47
3	4.00	1467.80	274.64	1.61
4	6.63	1565.31	333.10	1.68
5	----	2768.91	1269.00	2.17

We obtained the theoretical HVRs defined as Equation 8.6, which is calculated by the program developed by Sánchez-Sesma et al. (2008), based on the new theory assuming the completely diffuse wave field.

$$\frac{H}{V}(\omega) = \sqrt{\frac{\text{Im}[G_{11}(x, x; \omega)] + \text{Im}[G_{22}(x, x; \omega)]}{\text{Im}[G_{33}(x, x; \omega)]}} \quad (8.6)$$

where x = position vector of excitation point and receiving point; ω = circular frequency; and $G_{ij}(x, x, \omega)$ = Green function equivalent to the displacement at x in direction i by a unit harmonic load in direction j .

Figure 8.4 shows the comparison of the theoretical HVRs based on Equation 8.6 with the observed HVRs at the primary school.

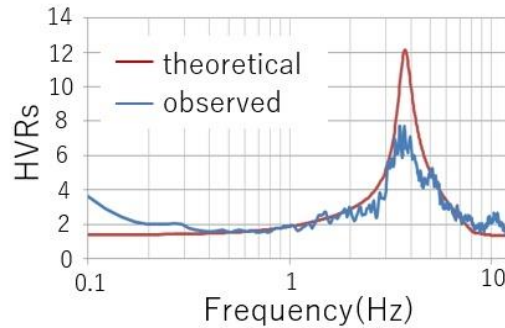


Figure 8.4. The comparison of the theoretical HVRs with the observed HVRs at the primary school.

8.3.2 Identification of the modified velocity structure models

We construct the same velocity structure models for each observation site referring the initial model. This time we modified only the thickness of the initial model following Equation 8.7, as the theoretical frequencies are agreed with the observed peak of each site, which is also based on the relation between wavelengths and peak frequencies. Figure 8.5 shows the microtremor measurement lines and the ground structures for the 3 measurement lines of all, which were identified by using the initial model and Equation 8.7.

$$H_{after} = \frac{f_{target}}{f_{before}} H_{before} \quad (8.7)$$

where H_{before} = the thicknesses of each layer of the initial model; H_{after} = the thicknesses of each layer at the target point; f_{before} = the peak frequency of the primary school; and f_{target} = the peak frequency of the target point. Although we do not have any supporting evidence, we can expect there are inclined deposits of the same S-wave velocity considering that these soft sediments were formed on top of the inclined engineering bedrock.

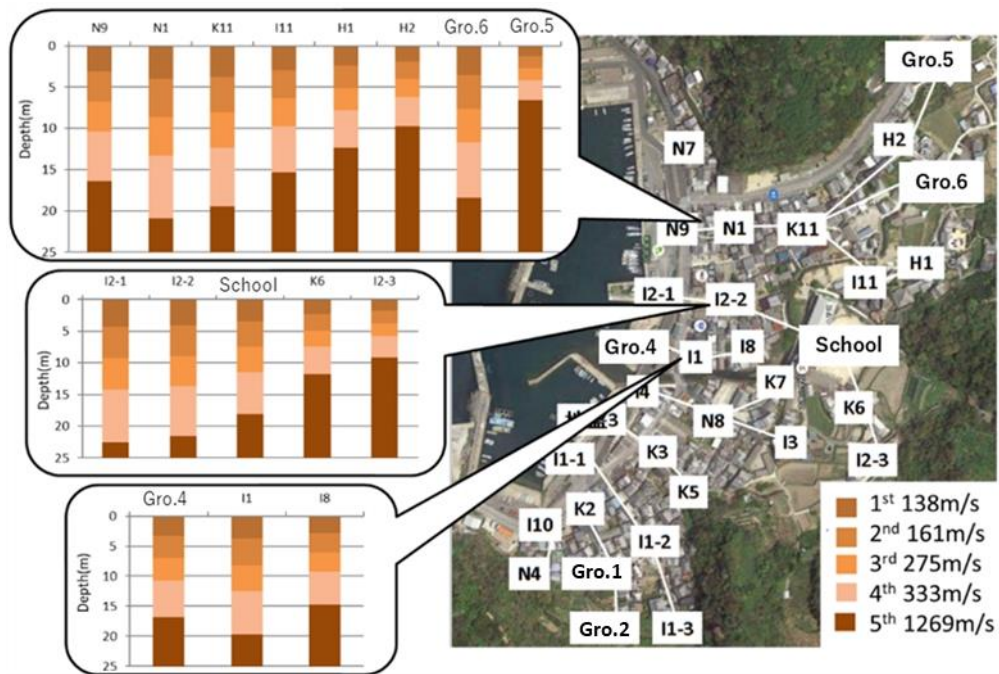


Figure 8.5. The microtremor measurement lines and the identified ground structures for the 3 measurement lines of all.

We found that the peak frequency of the observation points in the mountain side were higher than those along the river and the coast. It indicates that the depth of the engineering bedrock was shallower at the mountain area than the area along the river and the coast.

8.4 Estimation of the Strong Ground Motions

In order to estimate the building damage in detail and evaluate the vulnerability to earthquake in this area, we estimated the strong ground motions of each observation site.

First, we estimated the strong ground motion in this area at the engineering bedrock by removing the effect of the subsurface layers from the strong ground motion of Nankai Trough earthquake, which had been estimated by Bao (2014) at the nearest K-NET site to this area.

Figure 8.6 shows the acceleration wave estimated at the engineering bedrock.

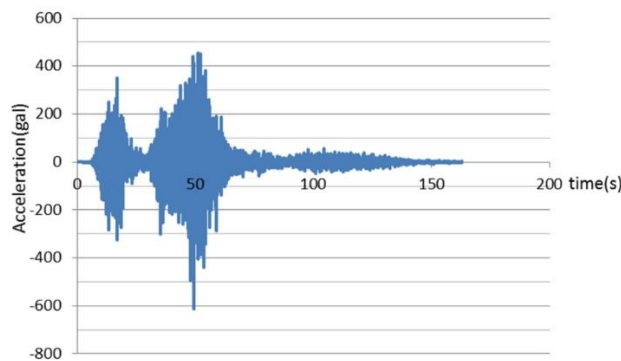


Figure 8.6. The estimated acceleration wave at the engineering bedrock.

We performed earthquake response analysis of one-dimensional soil structure by inputting the strong ground motion at the engineering bedrock, and estimated the surface ground motion of each observation point. Here we used Dyneq, which is the program that can perform non-linear response analysis developed by Yoshida (1996). Figure 8.7 shows the constitutive model (Ministry of Construction, 2000) As for the materials in the velocity structure models used for earthquake response analysis, we regarded the 1st and 2nd layer as clay, 3rd layer as sand, and 4th and 5th layer as elastic, based on the boring data at the primary school. Figure 8.8 and Figure 8.9 show the acceleration waves at the primary school and N1. Figure 8.10 and 11 show 5%-damped pseudo velocity response spectrum at the primary school and N1. N1 is the point where the depth of the engineering bedrock was estimated to be deepest among all the observation points. These results were obtained by performing earthquake response analysis using the estimated acceleration wave at the engineering bedrock (Figure 8.6). Figure 8.12 and Figure 8.13 show the estimated PGAs and PGVs of each observation point.

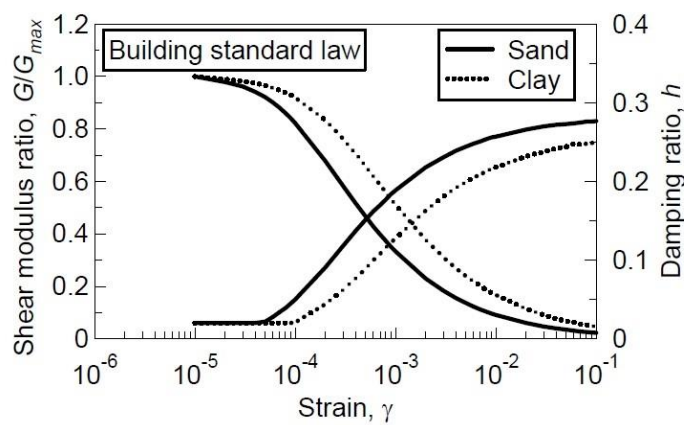


Figure 8.7. The constitutive model used for earthquake response analysis.

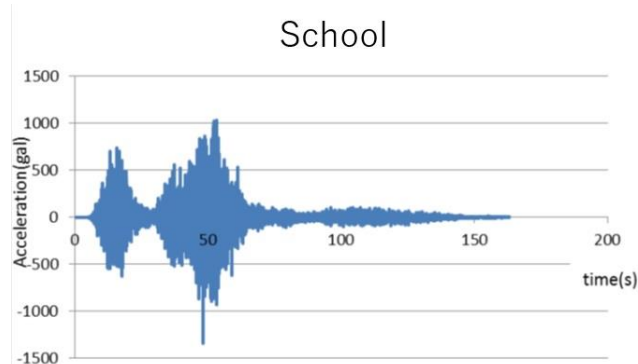


Figure 8.8. The acceleration wave at the primary school.

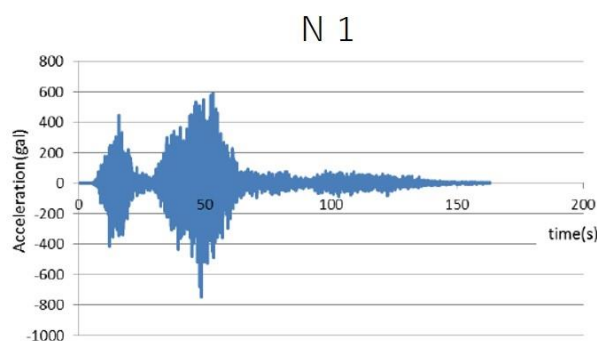


Figure 8.9. The acceleration wave at N1.

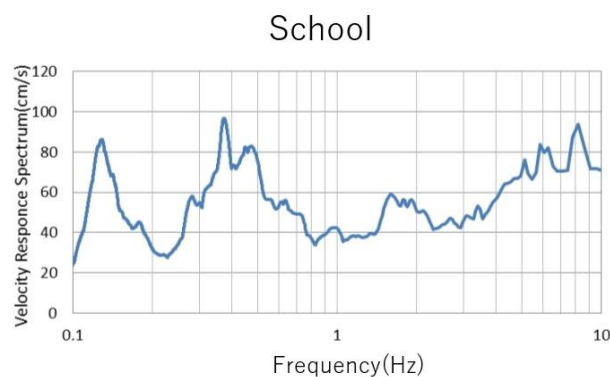


Figure 8.10. The 5%-damped pseudo velocity response spectra at the primary school.

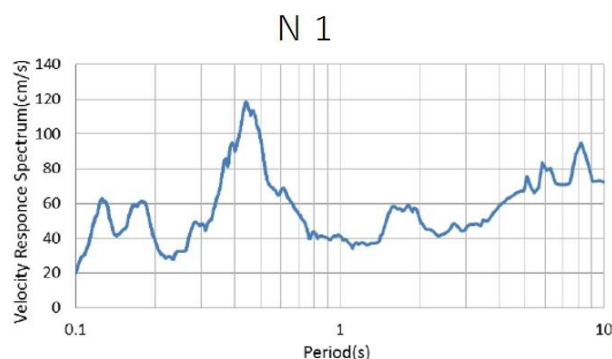


Figure 8.11. The 5%-damped pseudo velocity response spectra at N1.

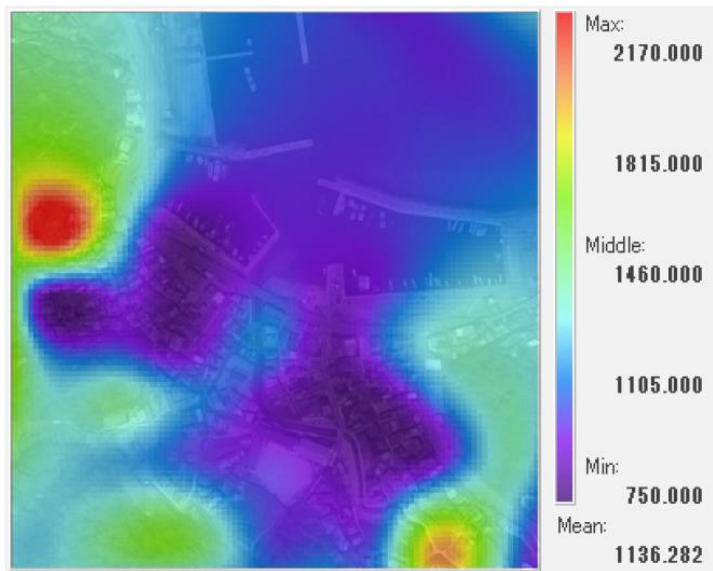


Figure 8.12. The distribution of estimated PGAs (gal).

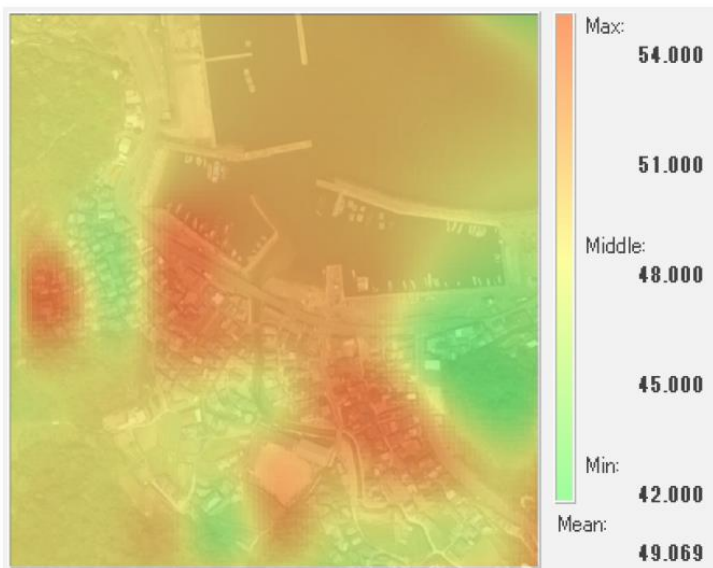


Figure 8.13. The distribution of estimated PGVs (kine).

We found that the PGAs were larger in the area close to the mountain than in the area along the river or near the coast. The difference in PGAs in the village is significant while the difference in PGVs is marginal because of the thin soft sediments there.

8.5 Prediction of Collapse of Wooden Houses

8.5.1 Outline of building damage prediction method

As a first step towards damage prediction of wooden buildings in the target research district, nonlinear earthquake response analyses were conducted on the wooden building group model using the 36 predicted earthquake waveforms (waves 1-36). Similar analyses for non-wooden buildings were conducted using the steel frame three-story building model by Nagase and Kawase (2002a).

8.5.2 Building damage prediction method

Figures 8.14 and 8.15 show the damage prediction results obtained using building models in each prediction location. Figures 8.14 and 8.15 are the ratio of damaged wooden and non-wooden buildings, respectively (units in %, left and right panels are the severely damaged and collapsed buildings, and collapsed buildings, respectively). The number of severely damaged buildings was obtained by first calculating the number of buildings with heavy or severe damage and using the ratio of (severely damaged and collapsed buildings) : (collapsed buildings) in the 1995 Southern Hyogo Prefecture Earthquake, which was approximately 4:3 (Central Disaster Prevention Council 2003).

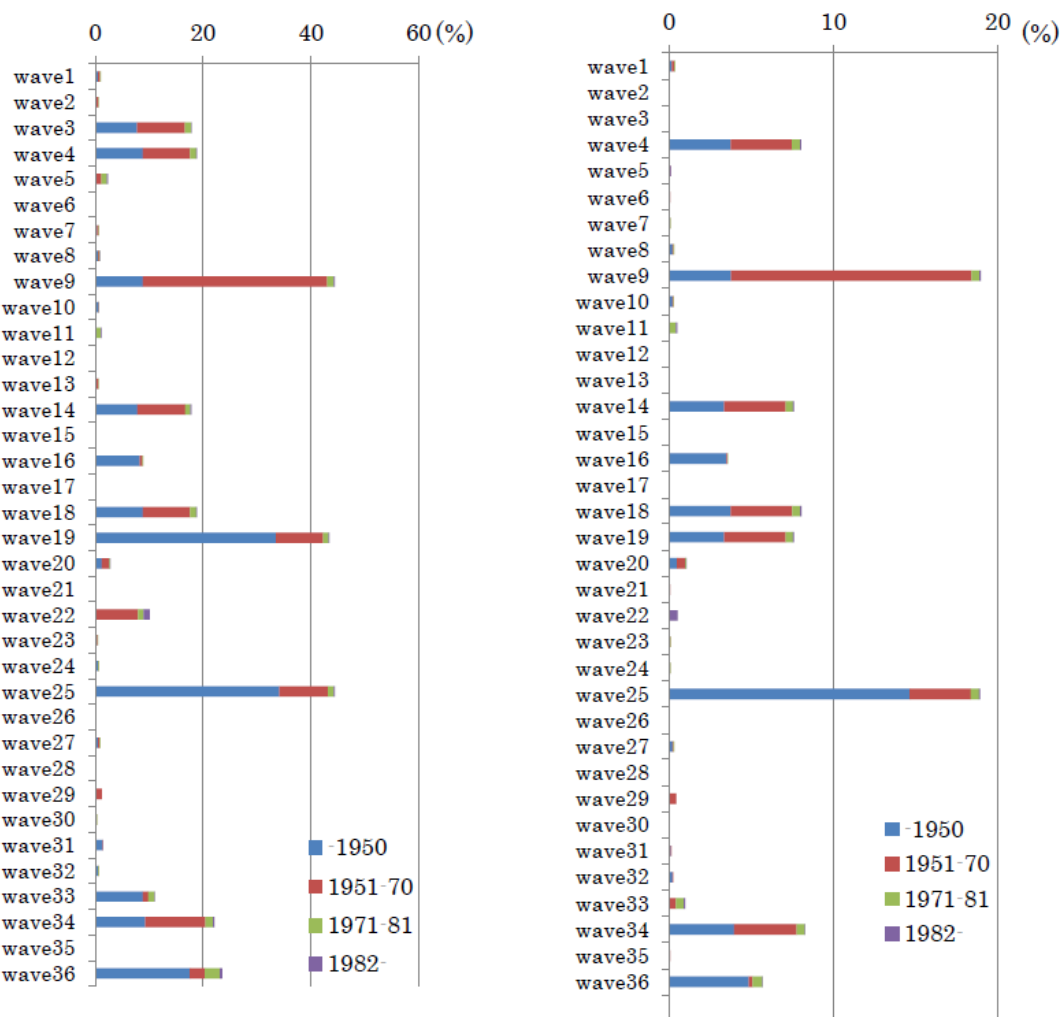


Fig. 8.14. Severely damaged (left) and collapsed (right) ratios of wooden buildings in each location (%). Each color shows the construction age.

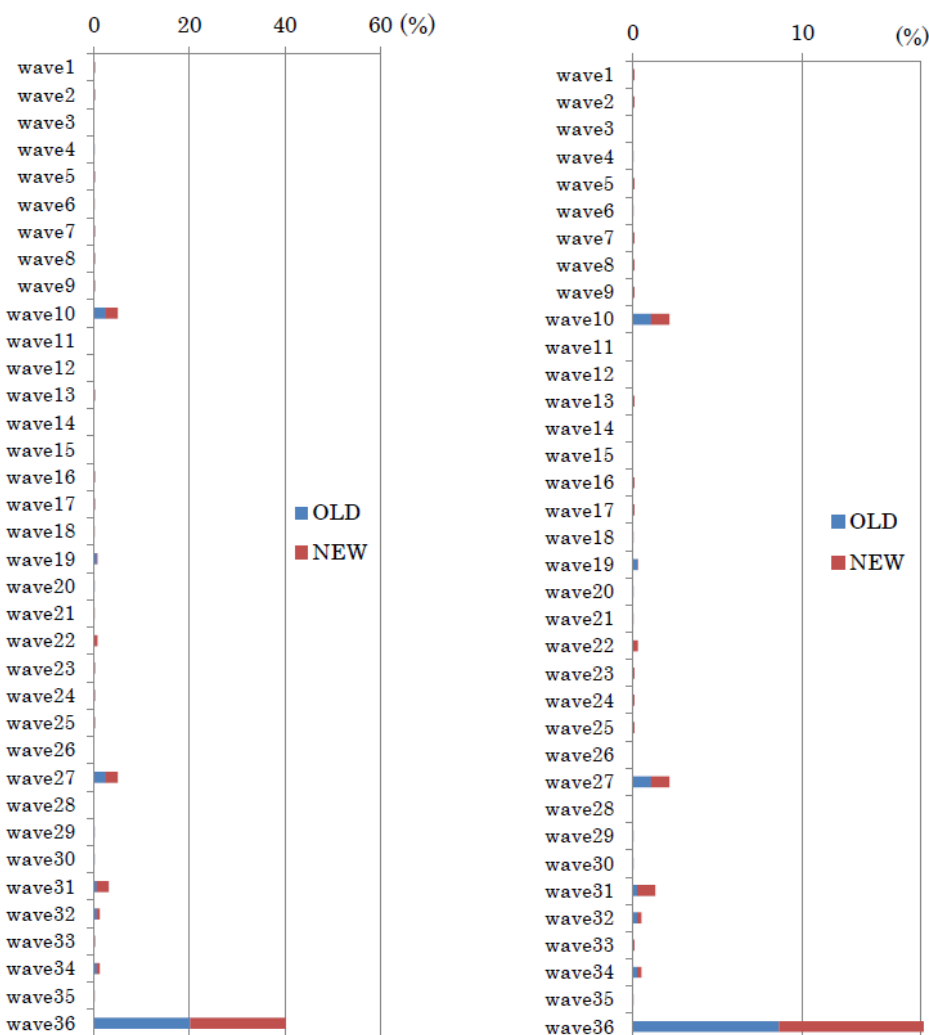


Fig. 8.15. Severely damaged (left) and collapsed (right) ratios of non-wooden buildings in each location (%). Each color shows the construction age.

8.5.3 Damage ratio in the entire target research district

Tsunami evacuation simulations were conducted after determining parameters based on the assumption of evacuation delays to residents in collapsed buildings and limitations to evacuation routes in consideration of road blockage from severely damaged buildings.

To estimate the location of buildings and residents facing evacuation delays as well as road blockades, the positions of damaged buildings are determined using the following procedure.

First, regions in the target research district dominated by the 36 strong ground motion wave types were determined. The centers between microtremor measurement points were connected to obtain the dominant regions centered around a microtremor measurement point. When a building lies on the boundary between regions, the building was assigned to the region where the area of the building in the region is the largest.

Next, the number of buildings in the dominant region of each strong ground motion wave was counted according to attributes, and the number of damaged buildings in a dominant region was calculated by multiplying the damage ratio (total and partial collapse rate) .

The obtained numbers indicate the number of buildings that are damaged in one earthquake. The simulations in this study assumed building damage locations of 10 patterns, i.e., cases where 10 earthquakes occur. Therefore, the cumulative number of damaged buildings after 10 earthquakes was obtained by multiplying the aforementioned number of damaged buildings by 10. The number of damaged buildings in each pattern was reevaluated using the cumulative number of damaged buildings. For example, if the number of damaged buildings obtained by multiplying the number of buildings in the dominant region and the damage ratio was 0.2, buildings were assumed to be damaged 2 out of 10 times. The assignment of 2 earthquakes causing damage among the 10 earthquakes was made randomly.

Damaged buildings were determined according to distribution of attributes. Road blockades were set-up in roads in front of buildings judged to be severely damaged. Delays were assigned to evacuation starting times of residents living in buildings regarded to collapse. Figure 8.16 shows the dominant region of each strong ground motion wave, and Figs. 8.17 and 8.18 give the number of damaged wooden and non-wooden buildings, respectively (left and right panels show the collapse and severely damaged rate, respectively). Bar graph colors indicate the difference in the year of construction.



Fig. 8.16. Dominant region of each strong ground motion wave.

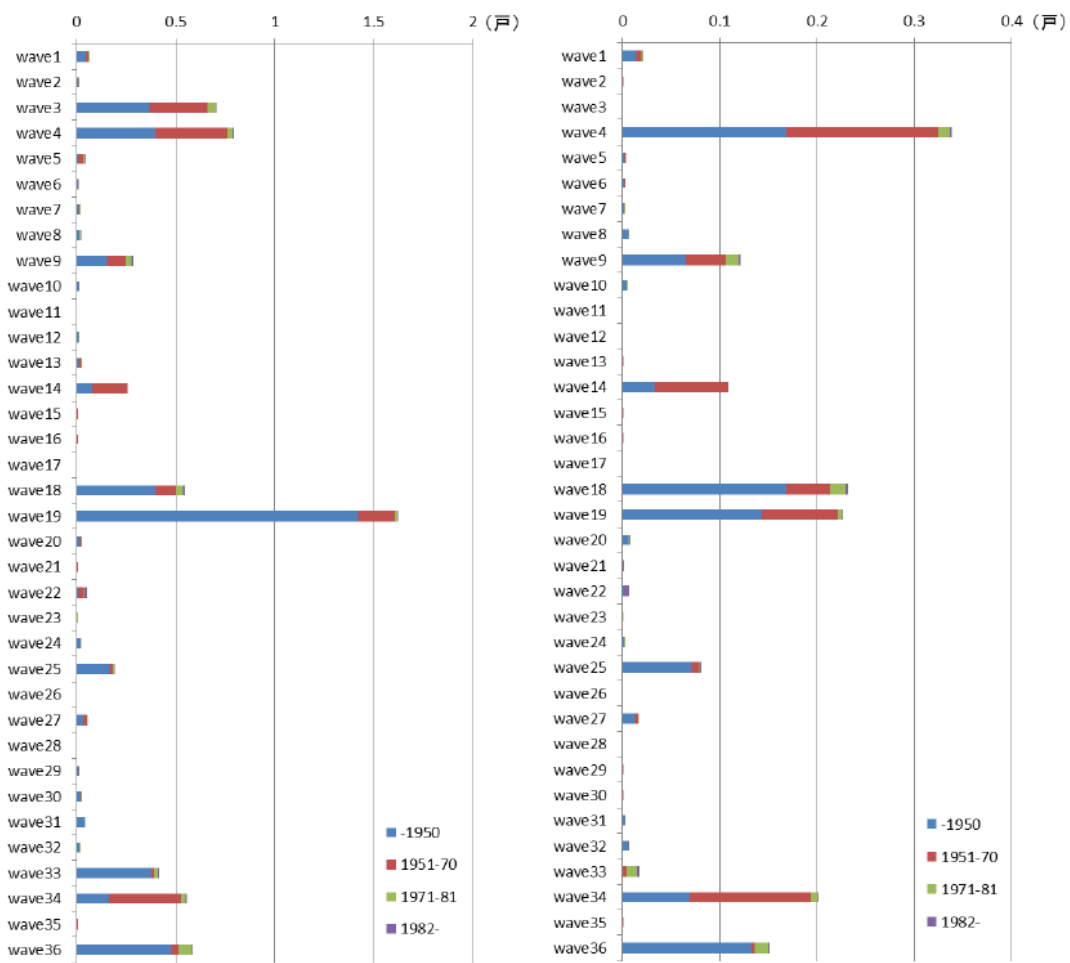


Fig. 8.17. Number of severely damaged (left) and collapsed (right) wooden buildings in the dominant region of each strong ground motion wave). Each color shows the construction age.

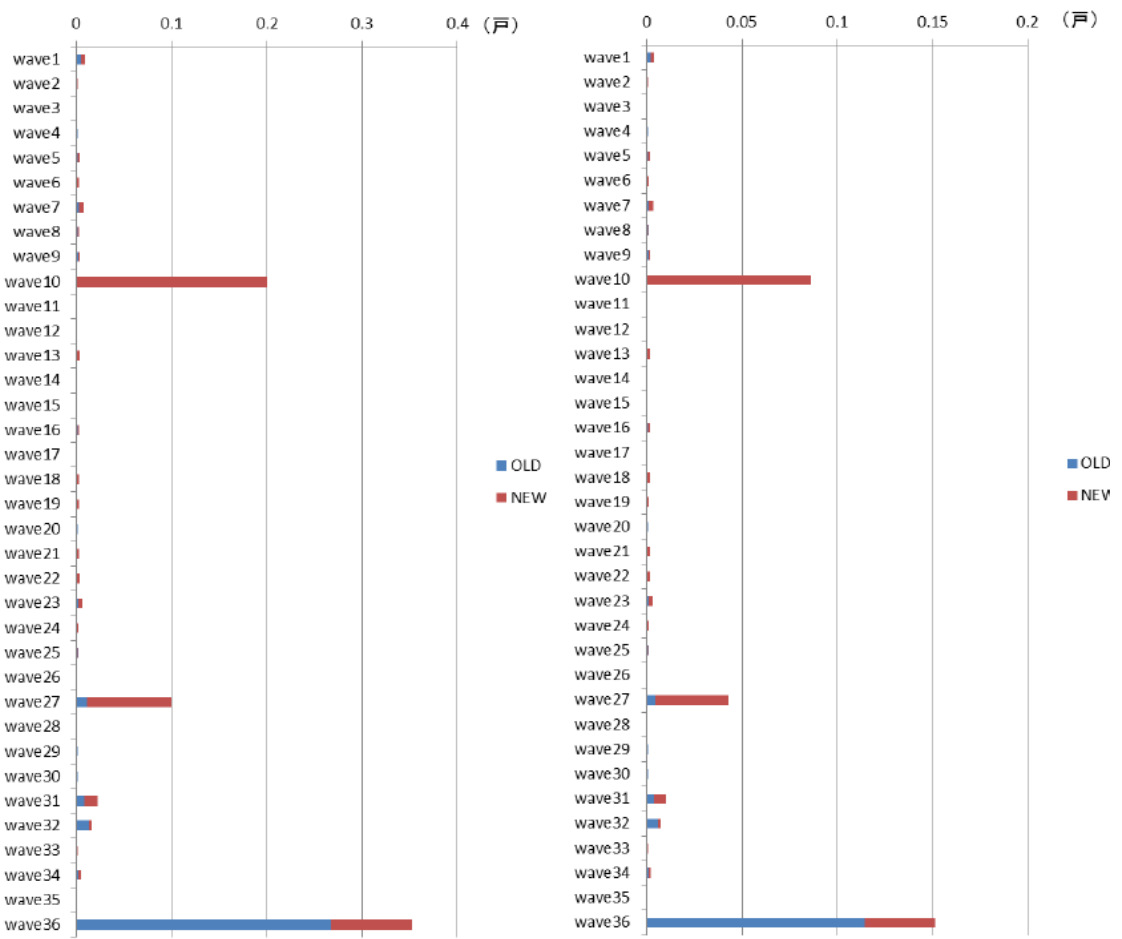


Fig. 8.18. Number of severely damaged (left) and collapsed (right) non-wooden buildings in the dominant region of each strong ground motion wave.

8.6 Tsunami Evacuation Simulation Using Agent Methodology

8.6.1 Overview of simulation system

8.6.1.1 Simulation system

The simulation system employed in this study is composed of an agent-based simulator (hereafter “simulator”), a spatio-temporal geographic information system (GIS), and a database shared by the simulator and GIS. The former was built on the multiagent platform Artisoc provided by Kozo Keikaku Engineering (Kaneda 2010), and the latter on DiMSIS, a GIS licensed by the Disaster Prevention Research Institute, Kyoto University (Hatayama 1999). Agents handled in the simulations were people only, and the fundamental data, which was supplied by the database, consisted of basic attributes of residents, information obtained during field surveys, and geographical characteristics of the target district. The geographical characteristics were based on openly available data, which were organized in the GIS and accumulated in the database. The position and direction of agents in each simulation step shown in the results were loaded into the GIS through the database and then overlaid on tsunami simulation results. The aggregation and evaluation of agent motion was conducted at this stage and finally visualized as spatio-temporal information. The 1:2500 fundamental geospatial data (Geospatial Information Authority of Japan 2013) was used as the base map. From this fundamental geospatial data, road edge and building area information were extracted to generate evacuation route and building regions, respectively, and other information was used for the GIS background.

Evacuation routes were separated into intersection and evacuation path zones. Representative points were set with a pitch around 50 cm. Intersection node numbers were assigned to representative points in each intersection zone. Each representative point in the evacuation path had attribute information allowing agents to move toward the target intersection. The evacuation path was split into triangles that included road edges and attributes were assigned from the angle of the road edge toward the forward direction. A number was assigned to each link connecting neighboring intersections. The forward direction between two linked intersections was the direction from the smaller node number intersection to the larger node number. Data was organized such that the next node to head to can be obtained once the final destination node is given. The route was derived from a shortest path search algorithm (Nakai and Hatayama 2013a, b).

8.6.1.2 Simulation conditions

The following conditions were used in the tsunami evacuation simulations.

- 1) Position information: a nighttime scenario was considered where all residents were at home. Information on the initial position was supplied by Prof. Takayuki Hirata of Wakayama University. The position information was based on the address of the residents’ home.
- 2) Evacuation speed: the average walking speed was set to 2.56 km/h for people aged 10 to 69, 1.88 km/h for those aged 9 and under or 70 and above, and 1.96 km/h when evacuating together with a child or senior citizen. These values were based on interview surveys of

tsunami evacuees of the 2011 Tohoku Earthquake by the Ministry of Land, Infrastructure, Transport and Tourism.

- 3) Aseismic properties of residences: Damage from less earthquake-proof buildings affected the evacuation starting time or caused road blockades.
- 4) The initial position on the road after exiting the residence was the position of the entrance.
- 5) Initial direction: the direction of the node to be reached from the initial position on the evacuation path was determined by the evacuation goal.
- 6) Means of evacuation: all evacuees walked without using a car in this study.
- 7) Evacuation shelter: the closest evacuation goal from the initial position was designated based on a shortest route search. Fig. 8.19 shows the position of evacuation shelters in the district.

This simulation considered the behavior of 482 residents, comprising 554 residents who had recently lived in the district minus 72 residents who were living in a clearly safe place.

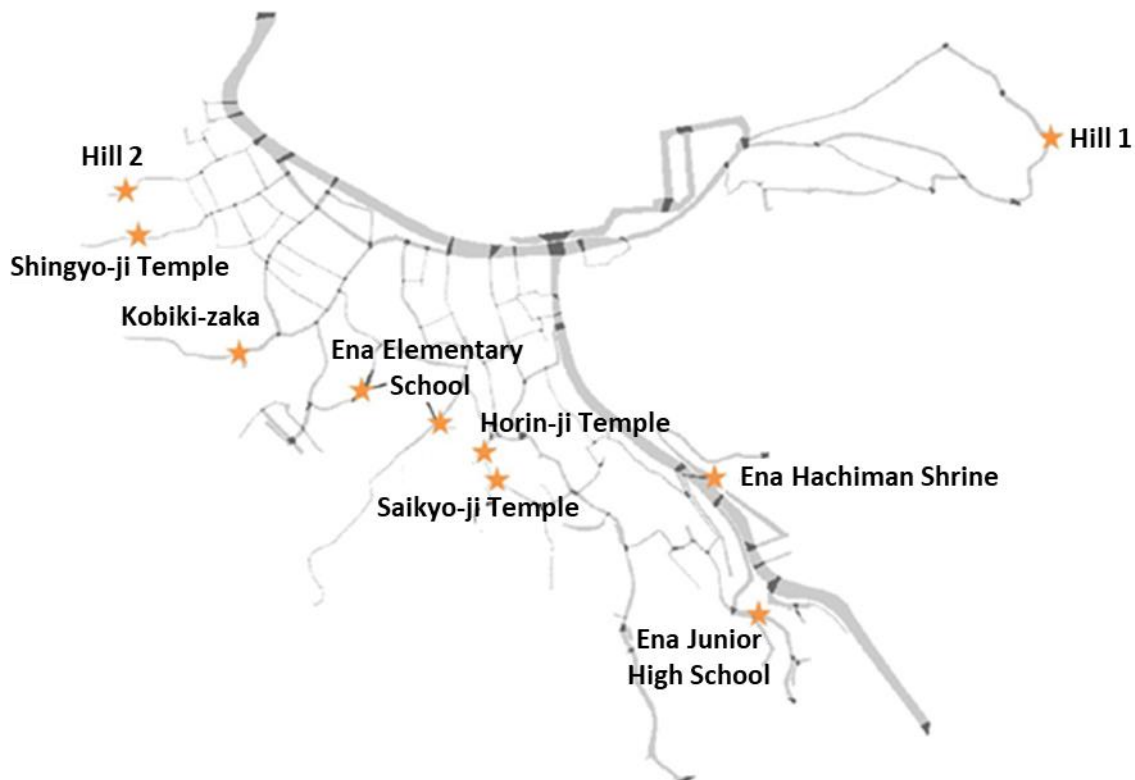


Fig. 8.19 Evacuation shelters (shown in orange star) in the district.

8.6.1.3 Setting of parameters

The building damage prediction was incorporated in parameter settings for tsunami evacuation simulations as follows.

The time before the start of evacuation for residents in severely damaged or collapsed buildings was set to either 10 or 15 minutes after the earthquake. If there was a severely damaged building, the number of seriously injured people was obtained using the estimation equation below from the Central Disaster Prevention Council (2013). The positions of seriously injured people were set based on the positions of severely damaged buildings, and the walking speed of the entire family including seriously injured persons was set to 1.96 km/h, which was the same for evacuations with a child or senior citizen.

$$(\text{Number of seriously injured people}) = 0.1 \times (\text{Totally collapsed buildings})$$

8.6.1.4 Simulation patterns

One simulation pattern prepared did not consider any direct damage to buildings. A total of 20 patterns that considered damage to buildings were prepared, which was a combination of 10 patterns of hypothesized building damage locations and 2 patterns of evacuation start time for residents of collapsed buildings. Table 8.3 shows the number of buildings that severely damaged or collapsed and, among these buildings, severely damaged buildings causing road blockades in each hypothesized building damage location pattern.

Table 8.3 Number of damaged buildings in each hypothesized building damage location pattern.

Pattern	Number of severely damaged and collapsed buildings	Number of collapsed buildings
1	6	1
2	8	1
3	8	4
4	6	1
5	7	3
6	6	1
7	6	2
8	5	1
9	10	1
10	6	2

8.6.2 Simulation results

The simulations of the patterns mentioned above were conducted three times each. The average number of people that successfully evacuated at 10, 15, and 20 minutes after the earthquake is shown in Fig. 8.20. The spread between the three simulations was three people at

most. A and B indicate the results when residents in collapsed buildings started evacuation 10 and 15 minutes after the earthquake, respectively. These are denoted hereafter as evacuation start time A and B, respectively. In all patterns, more than 95% of the local residents in the simulation (460 people) completed evacuation at 20 minutes after the earthquake. In patterns 3 and 5, the number of successful evacuees was larger for evacuation start time B than A at 5 and 20 minutes after the earthquake. In pattern 7, the number of B was also larger than A at 20 minutes after the earthquake. Additionally, B was slightly larger at 5 minutes after the earthquake in pattern 2.

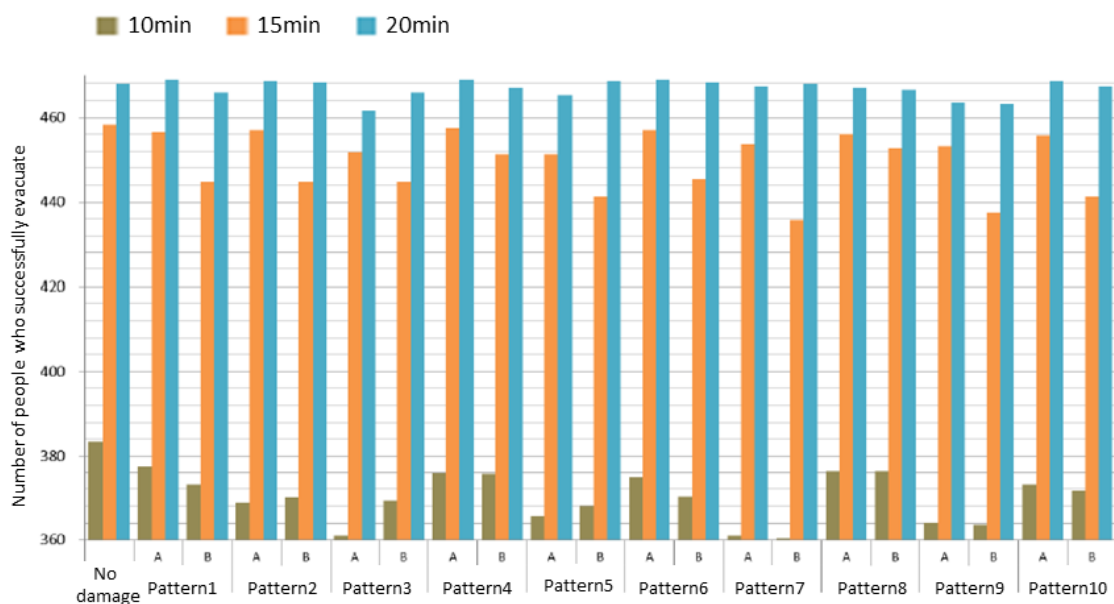


Fig. 8.20. Average number of successful evacuees in each pattern obtained by simulations.

8.6.3 Analysis of simulation results

The number of successful evacuees at 20 minutes from the earthquake was larger in evacuation start time B than A in patterns 3, 5, and 7. These patterns coincided with the three largest numbers of severely damaged buildings, which was also equal to the number of road blockades.

A possible reason for smoother evacuation in B is that there was less congestion of people on roads due to larger delay in evacuation start time (those not affected by building damage began evacuation 5 minutes after the earthquake).

The number of severely damaged buildings is not that large in pattern 2, but the position of severely damaged buildings was close to an evacuation shelter able to accommodate most of the

people in the district. Therefore, the mass of people caused a congestion near the road blockade location for evacuation start time A. In contrast, for B the difference in evacuation start time between people affected and not affected by building damage was larger, and procedures in the evacuation were performed smoothly as observed in patterns 3, 5, and 7.

8.7 Conclusions

This study aimed to understand tremors from earthquakes focused along the Nankai Trough and vulnerability to tsunamis after an earthquake, providing a guide for future evacuation planning. For the target region of Ena district, Yura Town, Hidaka County, Wakayama Prefecture, building damage prediction was conducted based on observed data, and tsunami evacuation simulations were performed.

We estimated the underground soil structures in Ena district in Wakayama prefecture, Japan, where high-frequency amplification due to relatively stiff soil layers is expected, in order to evaluate the vulnerability to an earthquake in this area. Microtremor measurements were conducted with 3-components accelerometers at 32 observation points within a radius of 500m in the area. We constructed the underground soil structure models for all the observation points using the peak frequencies of HVRs, and then estimated the strong ground motion of each observation point.

We found that the peak frequency of the points in the mountain side were higher than those along the river and the coast, and that the difference in PGAs in the village was significant while that in PGVs was marginal. This is because of thin, soft sediments there.

We calculated the damage ratio (collapse ratio and severely damaged ratio) through response analysis by applying the strong round motion to each point to the building group model, incorporating characteristics of the district for wooden buildings, and the three-story steel structure model by Kawase and Nagato for non-wooden buildings. The number of severely damaged or collapsed buildings was slightly less than 2% of the total buildings in the district.

The dominant region of each strong ground motion wave in the district was determined, and the number of damaged buildings in each region was obtained by multiplying the number of buildings with each attribute in the district with the corresponding damage ratio.

We incorporated the number of damaged (collapsed and severely damaged) buildings in each dominated region into GIS and simulation parameters. Simulations for 21 patterns were conducted (1 pattern without and 20 patterns with building damage), and the results were analyzed.

Regarding patterns that considered building damage, 10 road blockade patterns were hypothesized and the evacuation start time of residents in collapsed buildings was set to either 10 or 15 minutes after the earthquake (evacuation start time A and B, respectively). All other residents were presumed to start evacuation five minutes after the earthquake.

The number of successful evacuees 10, 15, and 20 minutes after the earthquake was then totaled.

In the results, the number of successful evacuees 20 minutes after the earthquake was larger for evacuation start time A than B in most cases. However, the number of successful evacuees after 20 minutes was larger for B than A in the 3 (among 10) patterns with the largest number of road blockades. Moreover, the number of successful evacuees after 10 minutes was larger for B in patterns which had fewer road blockades but one near an evacuation shelter with large capacity. One reason for these results is that a larger spread in evacuation start time of residents leads to less congestion in roads, allowing everyone to smoothly head to an evacuation center along the narrow roads of the target district.

As discussed above, this study is one part of a preemptive restoration measure in one fishing district. Building damage was predicted by first estimating the subsoil structure and then evaluating the vulnerability of the district to earthquakes and tsunamis using tsunami evacuation simulations based on subsoil structure. As a result, the ratio of buildings damaged by a Nankai-Tonankai-Tokai triple earthquake was found to be of a few percent.

The tsunami evacuation simulations showed that 95% of residents can complete evacuation within 20 minutes after the earthquake, and hence starting evacuation five minutes after the earthquake has a high probability of mitigating danger of being caught in a tsunami. As mentioned above, the building damage in this district from a triple earthquake is considered to be not severe, thus the assumption that evacuation can start five minutes after the earthquake is realistic.

Moreover, the number of successful evacuees was larger when the evacuation start time of residents in collapsed buildings was delayed because the shift in evacuation start time mitigated congestion in very narrow roads and near road blockades.

Therefore, one approach to smoothen evacuation behavior in the target research district encumbered by narrow roads and susceptibility to congestion is to shift the evacuation start time between blocks in the district beforehand. A road blockade near a major evacuation shelter causes delays to evacuation even if the number of severely damaged buildings in the district as a whole is small. Therefore, according to the results, seismic reinforcement should be prioritized in buildings near evacuation centers.

Future tasks of the study include reporting of the research results, particularly estimation of proof stress of buildings based on microtremor observations, to residents and deepen their awareness of the buildings they live in as well as earthquakes and tsunamis in their district. Another is to suggest as a part of their evacuation plan when a tsunami arrives, that evacuation can be accelerated if residents agree in advance to shift the evacuation start time between blocks and assign evacuation routes so people do not concentrate in certain subdistricts and evacuation shelters.

References

- Architectural Institute of Japan Building Economics Committee Fixed Asset Valuation Subcommittee Working Group in Architectural Institute of Japan (1998), Survey on Building Damage in Higashinada Ward, Nada Ward, and Awaji Island Hokutan-cho during the 1995 Hyogo-ken Nanbu earthquake [in Japanese].
- Bao, Y. 2014. Study regarding the quantitative damage estimation for a massive earthquake in southwest Japan and countermeasures. *Doctoral Thesis, Graduate School of Engineering, Kyoto University* [in Japanese].
- Central Disaster Prevention Council (2003), the investigation report by the Architecture and Earthquake Investigation Committee for Chuo-Ku, Kobe City .
- Central Disaster Prevention Council (2013), Overview of items and method of estimating building damage and human loss by Nankai mega-thrust earthquake.
http://www.bousai.go.jp/jishin/nankai/taisaku/pdf/2_2.pdf
- Geospatial Information Authority of Japan (2013) Maps and Geospatial Information Webpage,
<http://www.gsi.go.jp/kiban/index.html>.
- Hatayama M (1999) Development of space-time geographic information systems DiMSIS, GIS – Theory and application, 7/2, pp.25–33 [in Japanese].
- Kaneda T (2010) Introduction to pedestrian agent simulation using Artisoc: from principle and methodology to space design and management for safety and crowd”, Kozo Keikaku Engineering Inc., Shoseki Kobo Hayama Publishing [in Japanese].
- Ludwig, W. J., J. E. Nafe, and C. L. Drake. : Seismic refraction, in The Sea, A. E. Maxwell, (Editor) Vol. 4, Wiley-Interscience, New York, pp.53–84, 1970
- Ministry of Construction, Building Research Institute (1996) Final Report on the Survey of Damages from the 1995 Hyogo-ken Nanbu Earthquake, BRI, Tsukuba [in Japanese].
- Ministry of Construction (currently, Ministry of Land, Infrastructure, Transport, and Tourism). 2000. Ministry of construction notification based on building standard law #1457 of 2000. *Ministry of Construction*. [in Japanese]
- Nagato K and Kawase H (2001), Damage evaluation models of reinforced concrete buildings based on the building damage statistics and simulated strong motions, Journal of Structural and Construction Engineering (Transactions of AIJ), No. 554, pp.31–37 [in Japanese].
- Nagato K and Kawase H (2002a), A set of dynamic models of steel buildings for damage evaluation, Journal of Structural and Construction Engineering (Transactions of AIJ), No. 559, pp.101–106 [in Japanese with English abstract].
- Nagato K and Kawase H (2002b), A set of wooden house models for damage evaluation based on observed damages statistics and non-linear response analysis and its application to strong motions of recent earthquakes, Japan Earthquake Engineering Symposium, Japan Association for Earthquake Engineering, No.11, vo.2, pp.1315-1320 [in Japanese with English abstract].

- Nakai F and Hatayama M (2013a), Development of agent-based simulation system for tsunami evacuation estimation, Presentations of the Committee of Infrastructure Planning and Management Vol. 47, CD-ROM [in Japanese].
- Nakai F and Hatayama M (2013b), Evaluation of Evacuation Plan Through an Analysis of Evacuation Behavior and Resident Coordination: A Case Study Examining Disaster Risk Communication in Kuroshio City, Kochi Prefecture, Presentations of the Committee of Infrastructure Planning and Management Vol. 47, CD-ROM [in Japanese].
- Ota, Y. & Goto, N. (1978), An empirical formula to estimate the velocity of transverse waves and its physical background. *Physical Exploration* 31(1): 8-17. [in Japanese]
- Sánchez-Sesma F. J., Pérez-Ruiz J. A., Luzón F., Campillo M. and Rodoríguez-Castellanos A. (2008), Diffuse fields in dynamic elasticity, Wave Motion 45, pp.641-654, 2008 18
- Wakayama Prefecture (2014), 2014 State of Aging in Wakayama Prefecture [in Japanese].
<http://www.pref.wakayama.lg.jp/prefg/040300/siryo/aging26/H26.pdf>
- Wakayama prefecture (2015), Fixed Assets Ledger in Ena district, Yura-cho, Hidaka-gun.
- Yoshida, K. (2004), Construction of Dynamic Models of Japanese Wooden Houses for Evaluating Earthquake Damage by Considering Building Age and Proposal of the Destructive Power Index, Summery of master thesis of Department of Architecture, Graduate School of Engineering, Kogakuin University [in Japanese with English abstract].
- Yoshida, N. & Suetomi, I. (1996), A computer program for dynamic analysis of level ground based on equivalent linear method. *Reports of Engineering Research Institute, Sato Kogyo Co., Ltd.*: 61-70. [in Japanese].

Chapter 9

A Method to Extract Difficult-to-Evacuate Areas by Using Tsunami Evacuation Simulation and Numerical Analysis

Abstract

Extracting the area where people have difficulty evacuating (hereafter difficult-to-evacuate areas, DEA) when tsunamis hit after an earthquake is important for taking more effective disaster mitigation measures. The DEA was conventionally extracted simply based on the distance calculated by multiplying walking speed and the time that can be used for evacuation. However, evaluating the DEA based on the simple idea mentioned above is insufficient because the behavior of residents and the road conditions to the evacuation destinations after an earthquake are not sufficiently considered. On the other hand, agent-based tsunami evacuation simulations can reflect the behavior of residents and the real-time changes in the situation, thus DEA can be intuitively captured. Therefore, adopting agent-based simulations for DEA designation is highly effective. However, providing ad-hoc improvement evacuation plans by extracting issues intuitively by images of the simulation within the limited analysis time will not lead to substantial improvements if the number of casualties is already below a certain level in the already completed analysis. This is because the reason why evacuation is hampered may vary by location or there are multiple reasons, and therefore extraction of issues from only images would be difficult. This study conducts agent-based tsunami evacuation simulations on Zihuatanejo, Guerrero, Mexico, which is a major sightseeing destination in Mexico, and investigates each possible evacuation destination distribution model. Numerical analyses that examine three different ways for understanding evacuation difficulties is conducted on simulation results of the best model, and the DEA is comprehensively extracted from the result of these analyses. The procedure is summarized toward application of the proposed method to other areas.

9.1 Introduction

Extracting the area where people have difficulty evacuating (hereafter DEA, difficult-to-evacuate area) when tsunamis hit after an earthquake and setting appropriate tsunami evacuation facility plans for DEA is important for taking more effective disaster mitigation measures. Tsunami evacuation facilities, such as buildings and towers for tsunami evacuation, are effective in increasing the number of people in DEA that successfully evacuate. To the best of our knowledge, the first tsunami evacuation facility in Japan was constructed in 1998 reflecting lessons from the 1993 Southwest-off Hokkaido Earthquake. In the 2000s, the newly proposed tsunami damage estimate from the next Nankai Trough Earthquake significantly exceeded the previous estimate; therefore, the Cabinet Office started to designate tsunami evacuation facilities in 2005. After the 2011 Great East Japan Earthquake, which caused devastating damage in the Tohoku region in Japan, related legislatures were rapidly enacted or revised in areas susceptible to tsunami damage all over Japan. In light of this trend, studies on evaluating the safety of each district using the existing evacuation destination distribution and studies on evaluating the distribution itself began to appear in the 2000s.

Ministry of Land, Infrastructure, Transport, and Tourism (MLIT) (2013) outlined the following procedure to extract the DEA, which is the fundamental information for evacuation destination planning. First, the “time available for evacuation” is simply calculated by subtracting the “time unavailable for evacuation”, which is the time where people cannot move because of the shaking of an earthquake, from the estimated tsunami arrival time after the earthquake happens. The “maximum evacuation distance” is obtained by multiplying the “time available for evacuation” and the walking speed of evacuees, and the DEA is defined as areas where there is no evacuation destination within the maximum evacuation distance. Minato et al. (2016) studied the 1993 Southwest-off Hokkaido Earthquake. The “time unavailable for evacuation” because of shaking by the earthquake was derived in detail using the characteristics of the strong ground motion, and the maximum evacuation distances from 112 representative sites were obtained using walking experiments. The DEA was identified by combining this information and the estimated tsunami arrival time, and the validity of the method was evaluated by comparing it with the record. However, people will most likely be confused immediately after the occurrence of an earthquake in a real situation, thus the evacuation time will be longer than the minimum time necessary for evacuation calculated based on the simple relation between the distance and walking speed, or the time necessary for evacuation from walking experiments at normal times. Indeed, Minato et al. (2016) concluded that, based on comparison of their result with geological distribution of actual casualties, a “margin” time is necessary in addition to the time necessary for evacuation based on walking experiments. Walking experiments are more realistic than the minimum time necessary for evacuation obtained from geometrical relations, but collecting participants with various walking speeds in an experiment is difficult even though there are evacuees with various walking speeds in a real evacuation situation.

Therefore, agent-based simulations that can reflect the behavior of evacuees during evacuation and the variability in walking speeds would be effective for extracting DEA for planning evacuation destinations.

To evaluate the safety for each district, Minamoto (2009) focused on the evacuation process that can only be grasped through simulations. They calculated the “tsunami evacuation

safety index” of each area from the shape of temporal changes in the evacuation completion ratio, and compared the evacuation safety of each district. Osaragi (2012) established a simulation model that reflects existing evacuation plans, and the results were used to calculate detailed evacuation difficulty ratios at the neighborhood level.

As studies to evaluate the existing evacuation destination distribution using simulations, Ohata et al. (2007) investigated a city that spread across seaside plains, where evacuation to land with high elevation is difficult, while Takeuchi (2003) compared and analyzed cases when the floor area ratio of evacuation destinations was and was not considered. Hamada et al. (2005) combined results of Takeuchi (2003) with the results of questionnaires to residents to capture the estimated time to start evacuation as well as the direction and destination. As a result, more realistic simulation parameters were derived. They extracted the DEA by repeatedly conducting simulations in consideration of the evacuation destinations that they newly proposed under conditions from the questionnaires, then evaluated the proposed evacuation destinations. On the other hand, Ito et al. (2020) estimated the strong ground motion wave at the target area considering the characteristics of the underground structure using the knowledge from earthquake engineering, which was then input to a building model for estimating the building collapse rate, and conducted tsunami evaluation simulations considering road blockade from collapsed buildings.

Evaluation of existing evacuation destination distributions outside of Japan is mostly focused on Indonesia, which suffered great tsunami damage from the 2004 Indian Ocean earthquake and tsunami. For example, Asher et al. (2014) claimed that Padang City, which is an Indonesian city susceptible to tsunami hazards, has 13 temporary evacuation shelters (TES) but is far from sufficient in terms of both capacity and distribution. Therefore, 14 potential TES (P-TES) were considered, and buffer analysis of geographic information systems (GIS) was used to investigate how the area where evacuation is possible before tsunami arrival (service area in their terminology) incrementally increases as the number of P-TES increases from one to 14.

However, to the best of our knowledge, we are aware of very few studies evaluating evacuation destinations outside of Japan and Indonesia even though there are many regions worldwide that are threatened by tsunamis. This implies that the practice of designating evacuation destinations by the local government is far from common.

In consideration of the situation, this research first explores plans to improve evacuation destinations in the central area of Zihuatanejo in Mexico, where there are no guidelines for tsunami evacuation, using agent-based tsunami evacuation simulation methods. Afterwards, DEA is extracted under comprehensive judgment using multiple numerical analyses for grasping evacuation difficulty so that we can effectively draft the improved evacuation destination distribution. Important observations from these attempts were re-organized and discussed. This provides a set of standard procedures for developing evacuation destinations from scratch in areas where evacuation destinations have not been designated yet.

9.2 Target Area for Tsunami Evacuation Simulation

We choose the central area of Centro in Zihuatanejo as an area for tsunami evacuation simulation, which belongs to Zihuatanejo de Azua in the Mexican state of Guerrero. Recently many earthquakes have been observed at the sites along the Pacific coast, but there is an area

where an earthquake has not been observed yet in Guerrero. This area is called the “Guerrero gap”, which indicates that there is a high possibility that a big earthquake happens in the future and the area targeted in this study has the possibility of being damaged by the earthquake and resultant tsunami (Cruz-Atienza et al. 2018; Kostoglodov et al, 2003; Miyashita et al, 2020). Figure 9.1 shows the location of the target area.

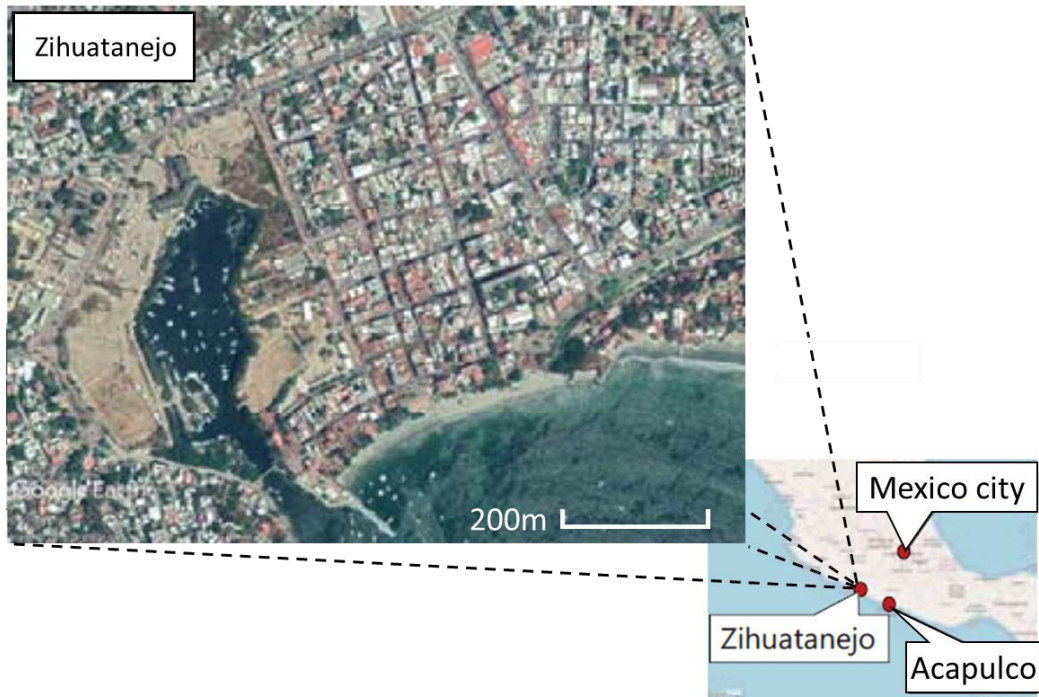


Figure 9.1. Location of the target area in this study.

9.2.1 Vulnerability of the target area to an earthquake and tsunami

The target area is below 5 m in altitude and the low, flat plane spreads from the shoreline to the hills surrounding the target area, which are over 5 m in altitude. The distance between the shoreline and the hill area is about 700 m so it takes about 15 minutes for adults to move on foot. These geological environments make this area vulnerable to the resultant tsunami from earthquakes that occur in the Guerrero gap.

The target area remains a traditional townscape. Many buildings are two stories or less except for the hotels. There are arcades made of wood along the buildings in the streets. There are many tourists, who are not familiar with the area, in high season. These characteristics of the area also make the evacuation situation more difficult.

The awareness of tsunami was low in Zihuatanejo before Japanese researchers began to provide disaster education for evacuation from tsunami as a part of a project in cooperation with Civil Protection (Nakano et al., 2020). During the field survey in the project, hearings were done at the Civil Protection and the Department of Tourism. There, the Japanese researchers showed a trial tsunami evacuation simulation. After showing the simulation, one of the staff members mentioned vertical evacuation, which was not included in the trial simulation. Reflecting on his

suggestion, Hatayama et al. (2018) included a simulation with vertical simulation, which means evacuation to the hotels. They also performed tsunami evacuation simulations assuming that the residents are assigned as the leading evacuees and solved the problem unique to the tourist spot, which has tourists who are not familiar with the target area. In the current real situation, however, the use of the hotels in the evacuation situation needs to be explained well to the hotel owners since they cannot easily accept strangers to their hotels because of potential security problems. Therefore, it can be said that the authority still has a long way to go for planning of the tsunami evacuation facilities in Zihuatanejo.

9.2.2 Estimation of tsunami inundation area for the tsunami evacuation planning

We conducted a tsunami inundation simulation for the Pacific coast of Mexico including the target area. Then, we used the result of the worst-case scenario for the target area in this study as the information used for distributing the evacuation destinations in the tsunami evacuation simulation, which will be explained in detail in section 9.5. Here, we explain the process of estimating the tsunami inundation area and the result.

Mori et al. (2017) conducted a Probabilistic Tsunami Hazard Analysis (PTHA) for the Pacific coast of Mexico. As a result, the source that generated the highest tsunami in Zihuatanejo Bay was selected for tsunami modeling at a fine resolution. In the PTHA, several slip distribution realizations were used to define the worst-case scenario within the Guerrero Gap in Mexico. The moment magnitude of the event was Mw 8.35. The bathymetric data was generated from nautical charts of Mexico. The offshore data (NC521-2) has an average spacing of 900 m, while the near-shore data (NC5213, NC512-4) has an average spacing of 100 m.

The topographic data was provided by Instituto Nacional de Estadística y Geografía (hereafter INEGI) of Mexico. This is a Digital Surface Model (DSM) with a 5 m resolution. The DSM incorporates building heights as part of the land elevation. Due to the high resolution of the computation grids a DSM is convenient over a Digital Elevation Model (DEM) that represents only the terrain without buildings (Muhari et al, 2011 and Mori et al, 2017).

As for the computational domains, we divided the simulation area into six domains intertwined as a nested grid system (Figure 9.2). The details of each domain are shown in Table 9.1. Cell size means the grid size of each domain. Columns and Rows are the number of grids in horizontal axis and vertical axis, respectively. An actual width of each domain can be calculated by multiplying Columns and Cell size, and an actual length can be calculated by multiplying Row and Cell size. XLL and YLL are latitude and longitude of the low-left point of each domain in WGS 84 coordinate system. These parameters are needed for inputting geographic data in raster format in calculation of tsunami numerical simulation. The model used for tsunami propagation and run-up simulation was the Tohoku University's numerical analysis model for the investigation of the Near-Field tsunami No. 2 (TUNAMI-N2) model (Imamura, 1996). TUNAMI-N2 is based on nonlinear shallow water equations, which is a two-dimensional approximation of the three-dimensional Naiver-Stokes equations for fluid motion.

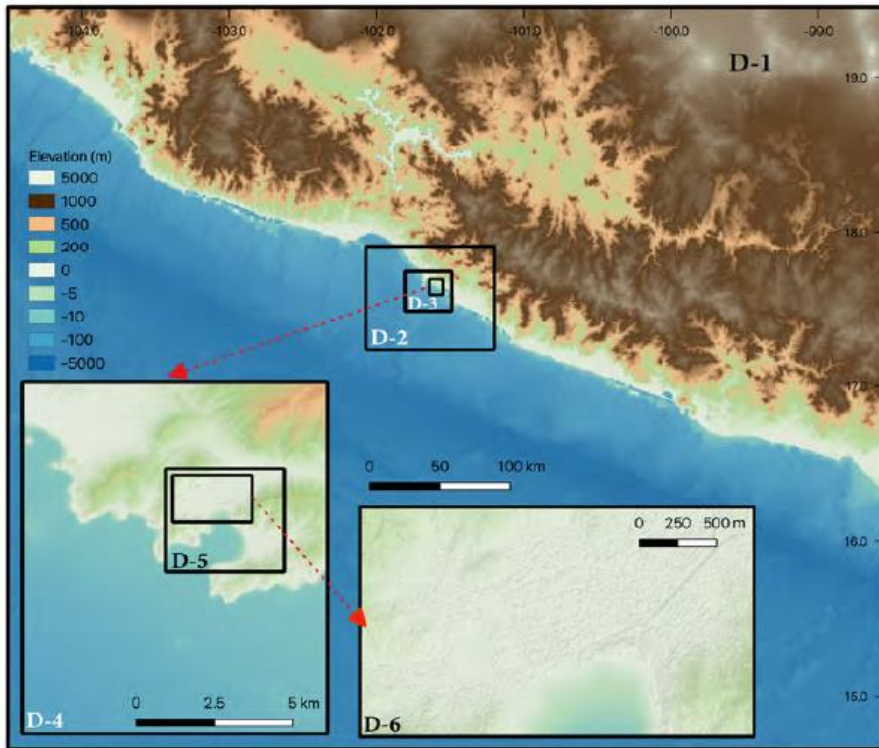


Figure 9.2. Computational domains.

Table 9.1. Computational domains for tsunami numerical simulation.

No.	Cell size (m)	Columns	Rows	XLL (deg.)	YLL (deg.)
D-1	1215	514	436	-104.357393	14.60252
D-2	405	226	184	-102.032973	17.211656
D-3	135	247	214	-101.774215	17.464088
D-4	45	217	250	-101.613167	17.572344
D-5	15	253	220	-101.570617	17.61964
D-6	5	511	298	-101.568843	17.634023

The slip distribution of the tsunami source was selected from the worst-case of tsunami height obtained in the PTHA conducted by Miyashita et al. (2020), which followed the methods introduced by Mori et al. (2017). The cumulative distribution function (CDF) of tsunami heights at Zihuatanejo was obtained from the stochastic simulation during the PTHA. The scenario with maximum tsunami height at 10 m depth offshore Zihuatanejo was selected as the worst-case scenario for detailed simulations. Figure 9.3 shows the slip distribution of the worst-case for the Zihuatanejo. In Miyashita et al. (2020), the PTHA assessment was conducted using data from the General Bathymetric Chart of Oceans (GEBCO) interpolated to 30 m resolution in the smallest domain. In this case, higher resolution data was used to observe the tsunami characteristics in the shallower areas of the bay. As input for the tsunami numerical modeling, the initial sea floor displacement is calculated using the equations proposed by Okada (1992) to solve the surface displacement on rectangular dislocations within an elastic half-space.

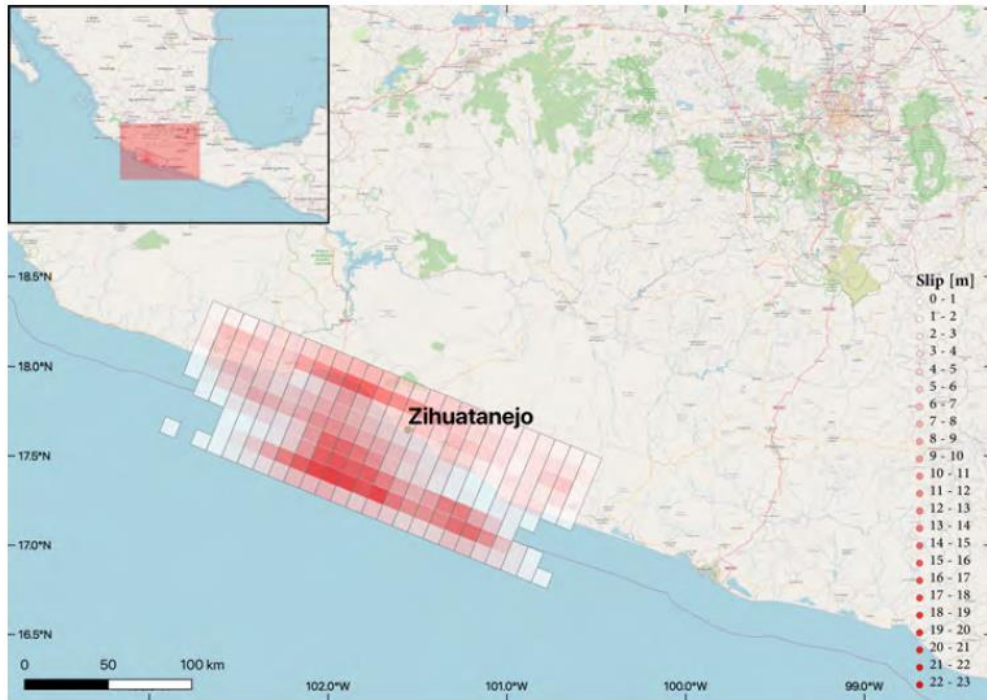


Figure 9.3. The slip distribution of a Mw 8.35 earthquake offshore Zihuatanejo

The resultant inland inundation at Zihuatanejo Bay is shown in Figure 9.4. The areas with the maximum tsunami inundation depth, nearly 18 m, are “La Madera” beach and “La Ropa” beach, located in the east and in the southeast in Figure 9.4, respectively. Compared to these areas, the target area for the tsunami evacuation simulation in this study, which is located in the north in Figure 9.4, has a lower tsunami inundation depth but a larger inundation area than these areas because of its low flat plane. In the target area, the horizontal inundation distance is calculated to be approximately 600 m from the coastline to a maximum run-up point of 7.9 m and a maximum of 14 m depth near the coast and the Zihuatanejo dock is expected in the worst-case scenario.

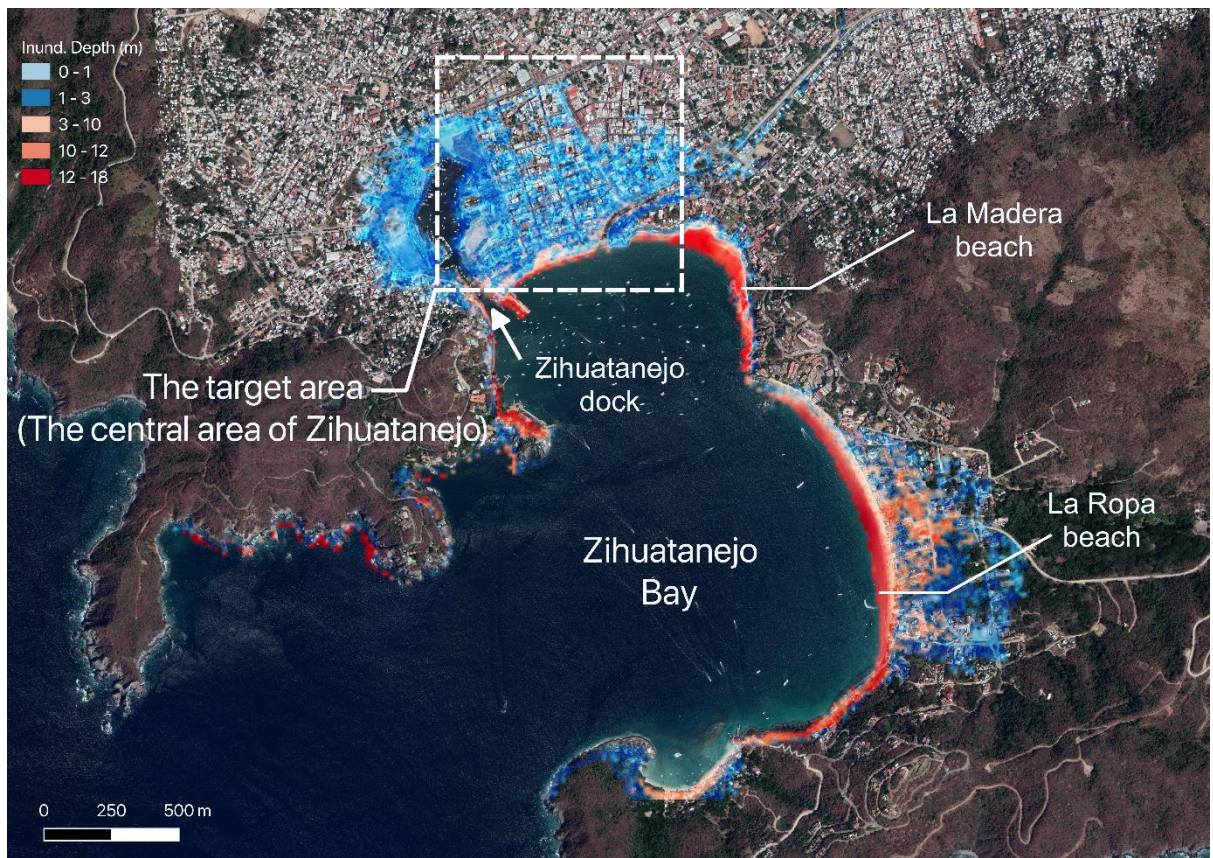


Figure 9.4. Maximum inland inundation depth inside the Zihuatanejo bay.

As for the tsunami arrival, the first wave comes into the Zihuatanejo bay about 8 minutes after the earthquake, then the second wave comes about 10 minutes after the earthquake and begins to inundate the “La Ropa” beach 12 minutes after the earthquake, but it does not inundate the target area. The third wave, which inundates the target area comes into the Zihuatanejo bay 11.5 minutes after the earthquake and begins to inundate the area about 13.5 minutes after the earthquake. Video1 is the tsunami simulation animation of the worst-case scenario for Zihuatanejo (<http://www.regid.irides.tohoku.ac.jp/shared/publications/videos/ZihuatanejoM8.5.mp4>).

We set the distribution of the evacuation destinations in and around the target area by considering the estimated inundation area shown in Figure 9.4. The detailed distribution of the evacuation destinations will be explained in section 9.5.

9.3 Evaluation System for Tsunami Evacuation

The simulation system for this study is composed of the space-time geographic information system (hereafter “GIS”) and a multi-agent simulator (hereafter MAS). The GIS was built on “DiMSIS” (Hatayama 1999) developed by the Disaster Prevention Research Institute,

Kyoto University. The MAS was built on a multi-agent simulation platform “Artisoc” (Kaneda 2010) developed and provided by Kozo Keikaku Engineering Inc.

The source data including the geographic characteristics and the attributes of the residents, who are the only agents in this simulation, are stored in the database. The positions of the agents at each simulation step are computed on MAS and returned to the GIS, then the movements of the agents are evaluated and visualized on the GIS.

As for the data source for the GIS, the road data was acquired from INEGI (2016), and the altitude data was acquired from INEGI (2008). The horizontal resolution of the digital elevation model data is 5 m, and the vertical resolution is 1 m.

To build the data on the GIS, evacuation routes are extracted from the boundary lines acquired from the road and block data of INEGI (2016). Evacuation routes are divided into intersection parts and road parts. Each intersection has a node number. The direction from the smaller node number to the larger node number is defined as the positive direction. For road parts, after they are divided into triangles including the boundary lines as one side, representative points are placed near one side of the triangles. The interval of each representative point is about 50 cm. Each representative point has its own attribute, which is the angle of the boundary line to the positive direction. This attribute allows the agents to move to the next node. The next node to which the agents should go is computed for each road, and agents acquire the next node information at each intersection.

9.4 Simulation Settings

Here we introduce the settings for the simulations in this study. The settings are the same as Hatayama et al. (2018) except for the evacuation destinations.

9.4.1 Environmental settings

In the simulations in this study, the road blockade caused by the collapsed buildings were not considered. Some buildings may collapse when a big earthquake happens, but the possibility that the collapsed building blocks the roads is estimated to be low because almost all the roads are wider than 6 m, and this width is too wide to be blocked by the collapsed buildings.

The time and the season when the targeted earthquake happen is set to be daytime and the high season, respectively. It is expected that the number of the victims is the largest in daytime of the high season because many people, especially tourists, who are not familiar with the area, go out of the buildings or are in the seaside area.

For the evacuation destinations, we newly consider the possible evacuation destinations and facilities because they have not been designated yet in the target area. We chose the hills over 5 m in altitude and the buildings more than two stories, which corresponds to about 5 m, because 5 m is estimated to be high and safe enough in consideration of the estimated tsunami inundation height as shown in Figure 9.2. There are few buildings which have more than two stories, and if any, many of them are not open to the public. Among the taller buildings in the target area, hotels can be considered as relatively open to the public because of their business nature. Therefore, in this study, we chose the hotels as the possible evacuation facilities. The location information of the hotels was obtained from INEGI (2015) and the field survey we conducted in November 2017.

We counted the height of each hotel in the field survey and from Google Street View. Then we chose the hotels which are taller than 5 m. As a result, 37 hotels were chosen. These hotels are over 3 stories or 2 stories with a roof-top floor. Figure 9.5 shows the location of each hotel. After choosing these hotels, we calculated the capacity for the evacuees following the equation below.

$$\begin{aligned} \text{Capacity} &= \text{Area} * (\text{Floor}-2) * 0.2 / 1.0 + \text{Area} * \text{Roof} * 0.8 / 1.0 \\ &= \text{Area} / 1.0 * ((\text{Floor}-2) * 0.2 + \text{Roof} * 0.8) \end{aligned}$$



Figure 9.5. Distribution of the hotels in the target area.

Here we assumed that the evacuees could get into the hallways, but they could not get into each room. “Area” is the projected area of a hotel calculated by QGIS based on an aerial photo from Google Earth. “Floor” is the number of stories of the hotel, therefore “Floor-2” is the number of floors above the second story, of which height is estimated to be great enough considering the tsunami height. Area * 0.2 is the estimated area of the hallways per floor. By referring to the floor map of a hotel in Zihuatanejo, we assumed the ratio of the hallways to the floor was 0.2. “Roof” means the number of roof-top floors. If a hotel has a roof-top floor, then “roof” is 1, otherwise it is 0. The denominator “1.0” is the effective occupied area per person.

In the simulation, basically, evacuees try to evacuate to a high place. When they find a hotel on their way, they can go to the hotel if the capacity of the hotel is not full. Otherwise, they decide to go to the nearest high place.

In this study, we did not consider collapsed hotels, assuming that the old hotels were earthquake-resistant, and the new hotels are resistant enough to a big earthquake. Considering the real situation that many buildings were collapsed when the big earthquake happened on 17th September 2017, there is a possibility that some of the hotels that are picked as the tsunami evacuation facilities will collapse in the next big earthquake. However, to estimate the strength of the hotels, we need the construction age of each hotel and need to construct the vulnerability function of the buildings in Zihuatanejo, and it takes much time to do so. Therefore, considering the earthquake-resistance of the hotels should be a future task for a more realistic tsunami evacuation situation.

9.4.2 Parameters for agents

The basic attributes of the people, which are the only agents in the simulations, were configured as follows:

I. Population of agents by each attribute

In this simulation, all the population data is for the daytime. According to INEGI (2010), the number of residents is 804. The residents are categorized into three groups according to their ages, which are 0 to 7 years old, 8 to 59 years old, and over 60 years old. The number of residents at each category is 587, 117, and 100, respectively. The number of employees working in the targeted area is 3568, which is obtained from INEGI (2015). The seaside area is the tourist area, and according to the municipal officer, the number in the tourist area in the daytime on weekends is 2000. There is an elementary school in the target area, which is also the main place for disaster education, and it has 100 students.

These numbers may be larger than the actual numbers because there is a possibility that the same person is categorized into more than two categories, but in this study, we set the number of all people above as agents in the simulations for the evaluation to be on the safe side.

II. Initial position and distribution of the agents

Residents are distributed in the buildings in each block by referring to Google Earth. Employees are put at their economic unit, which was provided by INEGI (2015). Students are put at their school. Tourists are randomly distributed in the tourist area, which is the seaside area. The initial position of each agent is their own neighborhood road.

III. Direction of the evacuation

Basically, every agent has two possible nodes that it heads for. The distance from the two nodes to the destination is calculated, then the node that has the shorter distance is defined as the initial direction. In the case where the initial position of an agent is on a dead-end road, the initial direction is the direction to another road which connects with the dead-end road.

IV. Means of transportation

In this study, we assumed that the agents were educated to evacuate only on foot and all the people followed it. It is better to set such a simple boundary condition because the main purpose of the study is not to see the effect of the different parameter settings of the agents, but to extract the area where the evacuation may be difficult. In the targeted area, it is expected that using a car for evacuation is not appropriate. The cars are always parked on either side of the many roads, which causes congestion, and there are many one-way roads. It is also expected that abandoned cars also prevent the other cars from going through the roads in the evacuation situation, which makes many people finally give up using their cars. Further consideration of the means of transportation is another future task.

V. Walking speed

The walking speed of 0.5 m/s is assumed for the residents younger than 7 or older than 60 years old, and 1.0 m/s for the residents between 8 to 59 years old. The walking speed for the employees and tourists is assumed to be 1.0 m/s. There is no survey for the age structure of the employees and tourists, but according to the municipal officer, the employee and tourists coming

to this area are mainly healthy adults. Each walking speed here was based on the guideline for tsunami evacuation plan provided by Fire and Disaster Management Agency, Japan (FDMA, 2002).

VI. Behavior of agents depending on the awareness of the tsunami risk

In a real situation, it is expected that the residents and the employees, who are familiar with the area, can choose an appropriate direction for evacuation, while the tourists will not know where to go. It is also expected that some of the residents who are very aware of the vulnerability of this area can evacuate immediately and trigger the evacuation of the other people. Reflecting on this situation, Hatayama et al. (2018) prepared three categories for agents related to evacuation behavior. In this study, we also categorized the agents to the three categories as shown below, based on Hatayama et al. (2018).

i. Leading evacuees

Leading evacuees are those who are well aware of the vulnerability of this area to the tsunami and can evacuate immediately because they are well prepared for evacuation in advance. There are 17 people out of the residents and employees that are categorized in this attribute. Hatayama et al. (2018) simulated the model where the number of the leading evacuees were 193. In a research after we published Hatayama et al. (2018), the models with fewer leading evacuees were simulated, and it turned out that there was almost no difference in the number of victims between the models with 193 leading evacuees and the one with 17 leading evacuees, if the leading evacuees were put on all the roads appropriately in the targeted area. In other words, 17 is the minimum and the most effective for reducing the number of the victims. We are planning to ask the residents for their cooperation in becoming the leading evacuees, and this number can be a feasible number for cooperation. In this study, we performed the simulations under the assumption that the 17 residents were assigned to be leading evacuees by mutual agreement and they were well prepared for the evacuation.

ii. Basic evacuees

Basic evacuees are those who are familiar with the area but are not well aware of the tsunami risk. Therefore, they need more time to be prepared for the evacuation than the leading evacuees. They start to evacuate 5 minutes after the shake of the earthquake stops. Residents and employees except for those who are assigned to be the leading evacuees are categorized in this attribute.

iii. Following evacuees

Following evacuees are those who do not know the appropriate destination or the evacuation routes. Tourists are categorized in this attribute. They start to evacuate when they see the others evacuate within 15 m from them. They follow the other evacuees and go to the same destination as the other evacuee they follow.

They do not react to the other evacuees in the different links or on the different nodes from them even if they see the other evacuees within 15 m.

X. Starting time to evacuate

We assumed that the time evacuees cannot move because of the shake of the earthquake is 1.5

minutes, based on the experience of the Great East Japan Earthquake that happened in 2011. We set the start time of the simulation 1.5 minutes after the earthquake. The starting time to evacuate differs depending on the attributes of the evacuees that was mentioned above. Leading evacuees start to evacuate at the start time of simulation while basic and following evacuees start five minutes after the start time of simulation. Some following evacuees (tourists), who see the leading evacuee, start to evacuate earlier than the basic evacuees (residents and evacuees). This situation may seem to be somehow strange, but actually it is natural because the residents or employees except for the leading evacuees need several minutes to look for their valuables in their house or their office, while the tourists must always have their valuables with them when they go out and they can immediately follow the other evacuees. Figure 9.6 shows the time to start evacuation for all the evacuees.

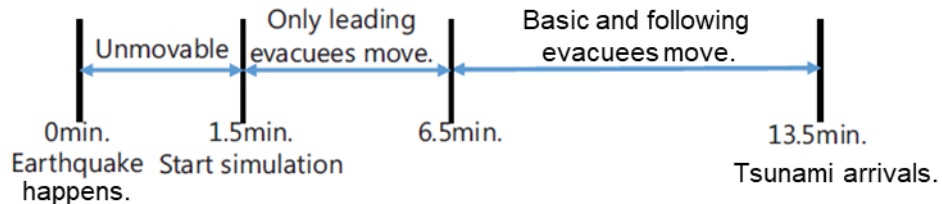


Figure 9.6. Time to start evacuation for all the evacuees. The start time of the simulation is set to 1.5 minutes after the earthquake happens.

9.5 Simulation Models and Results

Tsunami evacuation simulations were conducted using the parameters explained above. We first drafted the initial model, then two series of models, A and B, were drafted while considering whether actual implementation is possible. The definition of “casualties” in this study is the number of evacuees that could not complete evacuation to the intended destination within 12 minutes after the start of a simulation by considering the estimated tsunami arrival time of 13.5 minutes which was explained in section 9.2.2 and the unmovable time of 1.5 minutes which was explained in section 9.4.2. If temporal simulated tsunami data is available, more accurate evaluation of whether evacuation for each agent is successfully completed or not would be possible by overlapping the temporal tsunami data with the position of evacuees at each moment on a GIS. However, such data was not available in this study, thus casualties were defined as mentioned above. This is also a future task for this study, but the ultimate goal in this study is to extract areas that are relatively difficult to evacuate in the target area. Therefore, a comparison of the number of people that could not complete evacuation 12 minutes after the start of the simulation, which is defined as the number of casualties, over all simulation cases would be sufficient. Each model was simulated for three trials, and the number of casualties in this paper is the average of three trials. The difference in casualties within each model was significant, which will be explained below. In ad-hoc searching as is employed in this study, evaluation and comparison of many models through trial and error is more important than obtaining highly converged results in each model, thus simulation for three trials is sufficient.

I. Initial model

In the initial model, hotels, hills that surround and spread to the east and north of the target area, and a bridge adjacent to the sea to the southwest of the target area are designated as the tsunami evacuation destinations. Figure 9.7(A) shows the locations of the evacuation destinations. Hotels are shown in red circles, and the node number adjacent to a hill is shown in red letters. The area near the node numbers at the east and north is higher than 5 m in altitude, therefore it is not included in the tsunami inundation area. Node number 2 in the southwest is where there is a bridge connected to a hill. Hills could be reached just after crossing this bridge, hence the node number near this bridge is considered as an evacuation destination. Figure 9.8(A) shows the distribution of evacuees 12 minutes after the start of the simulation. As is evident in the figure, many casualties are found heading to the hills to the east and via the bridge to the south.

II. A-1 model

In the A-1 model, additional evacuation measures in the main avenue in front of the eastern hills are taken in addition to the hotels in the initial model. This is because many casualties in the initial model were evacuees that evacuated to the eastern hills. Figure 9.7(B) shows all evacuation destinations in the A-1 model. The node numbers in red filled boxes are evacuation destinations newly added in the A-1 model. As for the implementation of the additional evacuation measure, there are a few options, and in reality, the evacuation measure with the best cost performance will be selected after cost evaluation. In this study, we only designate locations with the evacuation measure and do not set the specific kind of measure. The number of casualties was 549, thus many lives are saved compared to the initial model. However, there are still casualties in the area just in front of the main avenue, and there is congestion at the southern bridge. Therefore, a model to save these people was drafted in the next A-2 model. Figure 9.8(B) shows the casualty distribution.

III. A-2 model

In the A-2 model, a tsunami evacuation tower A is set to be constructed in addition to the hotels, hills, and main avenue measures in the A-1 model. Figure 9.7(C) shows all evacuation destinations in the A-2 model. The location of the newly added evacuation tower is shown with a black rectangular frame. The casualties at the southern bridge in the A-1 model evacuate for a relatively longer distance compared to other evacuees. Therefore, tsunami evacuation tower A was set to be located at the center of the seaside area (node number 52), which has vacant space and is easier to access than the southwestern bridge at node number 2. The number of casualties was 195. There was a decrease in the number of evacuees who failed to evacuate because of congestion while evacuating to the bridge south of node number 2. On the other hand, there are still casualties just in front of the eastern main avenue. Figure 9.8(C) shows the casualty distribution.

IV. B-1 model

In the B-1 model, in addition to the hotels and hills, a pier to the south-east of this area, which connects to land with elevation higher than the inundation height, is considered as an evacuation destination. This reflects the result where there were many casualties that tried to evacuate to the eastern hills in the initial model. Figure 9.7(D) shows all evacuation destinations.

The pier newly added as an evacuation destination, which lead to the higher land, is located at node number 152. The node number is considered as a goal in this model. There were 645 casualties, and the main reason why the evacuees failed to evacuate is the congestion in the roads leading to the pier. Moreover, the congestion near node number 2, which is the southwestern bridge, was not resolved. Figure 9.8(D) shows the casualty distribution. The next model aimed to save these people.

V. B-2 model

In the B-2 model, tsunami evacuation tower B is set to be constructed at a location where the hotels, hills, and pier to higher land cannot sufficiently accommodate evacuees. Figure 9.7(E) shows the evacuation destinations in the B-2 model. The added tsunami evacuation tower B was set to be located close to node number 34. Figure 9.7(E) shows its location with a black rectangular frame. The reason for adding tsunami evacuation tower B at node number 34 is as follows. By tracking the motion of people stuck in congestion at the pier in the B-1 model, it turned out that evacuees that were relatively distant from the pier failed to evacuate. Therefore, a tsunami evacuation tower near the yacht harbor at the western main avenue was added as an evacuation destination. The number of casualties was 181. The congestions at the pier at node number 152 and the southern bridge at node number 2 were significantly mitigated. However, there were casualties near tsunami evacuation tower B, which was newly added near node number 34, and around the eastern hills. Figure 9.8(E) shows the casualty distribution.

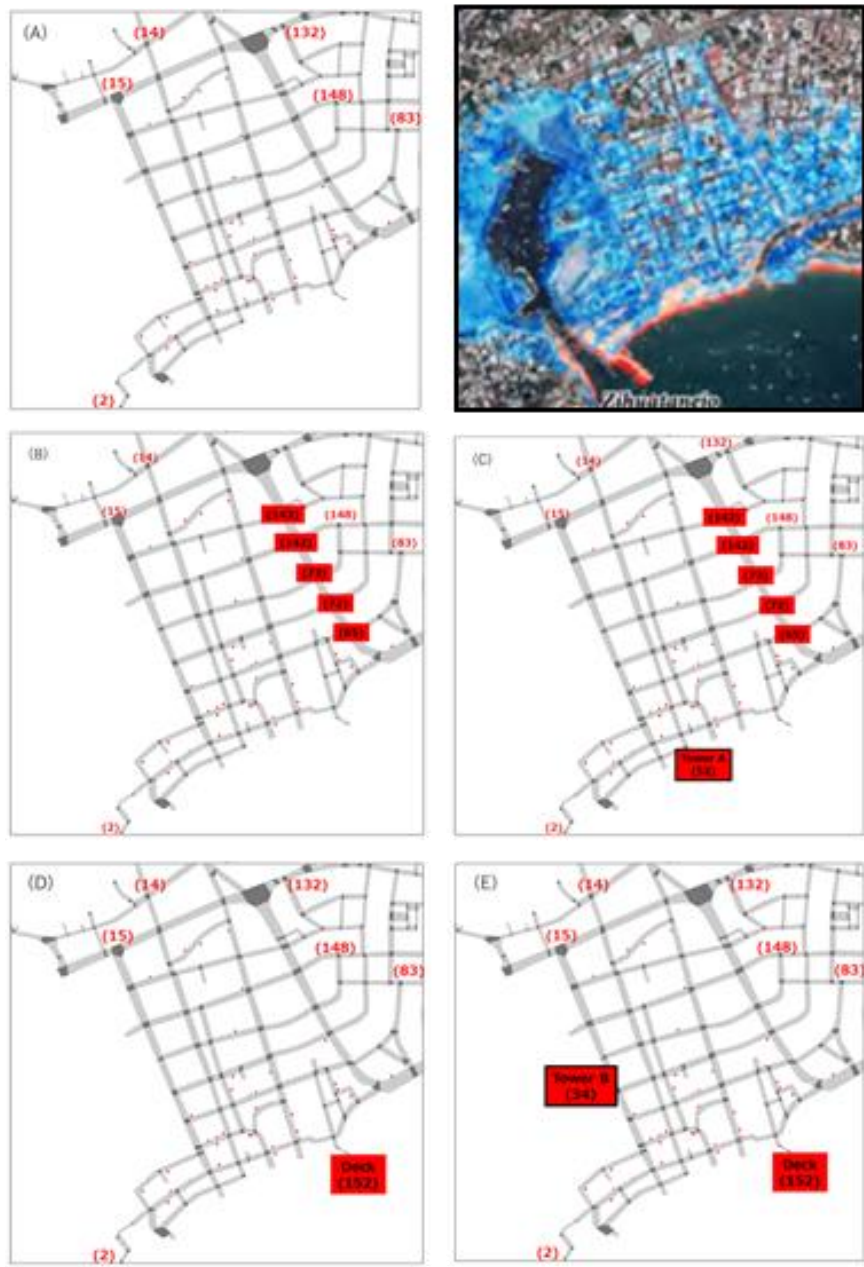


Figure 9.7. The estimated inundation area (top right) and evacuation destination distribution of each model. The small red circles indicate hotels. The numbers in brackets are the node number adjacent to hills that are used as evacuation destinations. The initial, A-1, A-2, B-1, and B-2 models are shown as (A), (B), (C), (D), and (E), respectively. The node numbers of evacuation destinations newly added in the A-1 and B-1 models are shown in red filled boxes, while those of the evacuation destinations newly added in the A-2 and B-2 models are shown in a black rectangular frame (Tower A and B, respectively).

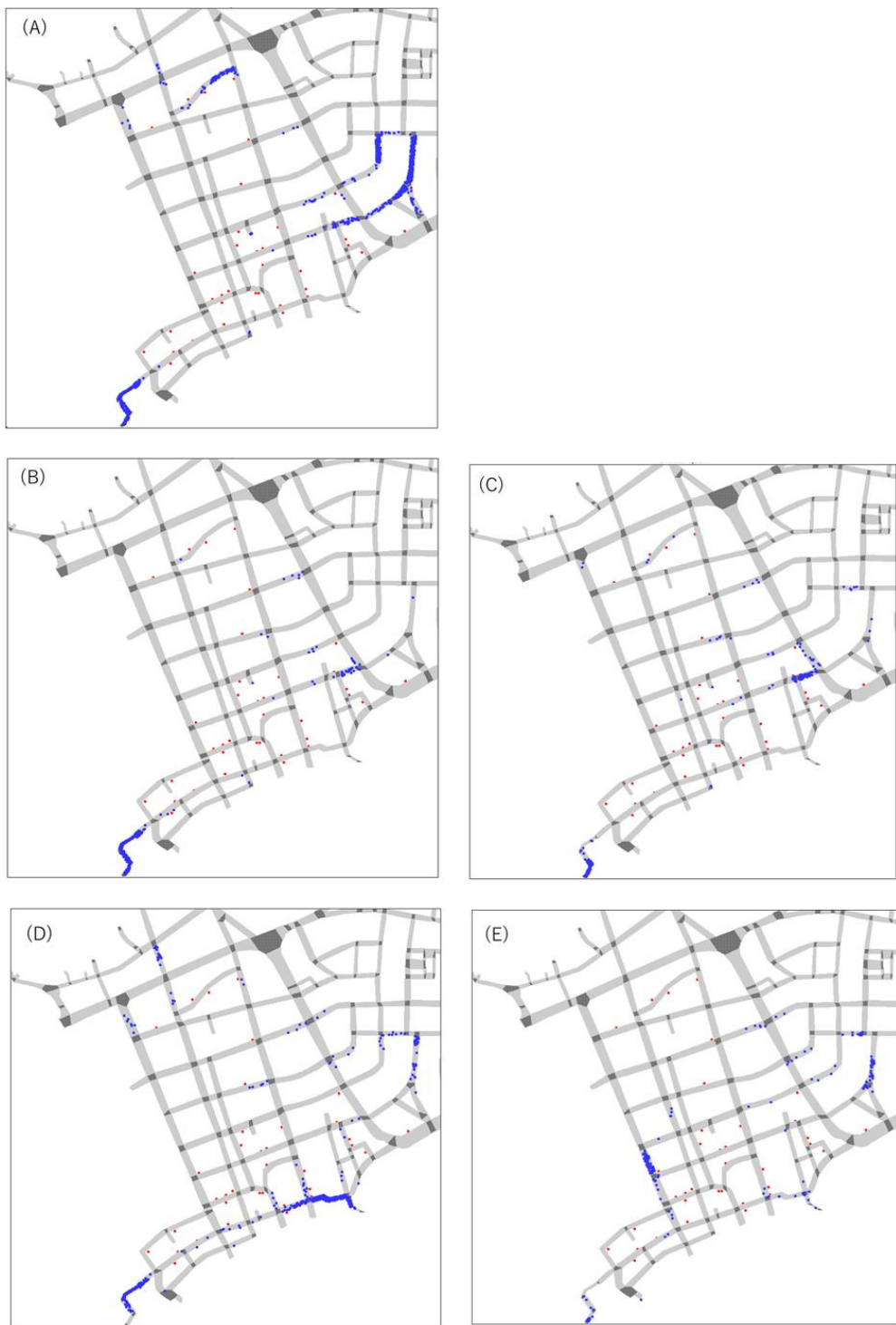


Figure 9.8. Casualty distribution at the tsunami arrival time in each case (one example out of three trials). The small red circles are hotels designated as tsunami evacuation facilities, and the blue points are failed evacuees.

In the A-2 and B-2 models a tsunami evacuation tower was set to be constructed at an appropriate location because construction of a tsunami evacuation tower is feasible with the

support of city officials and local residents. The capacity of the hills is estimated to be sufficiently larger than the number of people in the target area, therefore is not explicitly considered. The capacity of the tsunami evacuation tower is also not explicitly considered. After performing the simulations, it turned out that tower A and tower B accommodate 473 evacuees and 448 evacuees on average in three trials, respectively. Considering there is a tsunami evacuation tower that accommodates up to 600 evacuees in Japan, these numbers of evacuees accommodated into tower A and tower B are feasible. As mentioned above, generally in this study, the capacities for evacuation destinations other than hotels are not considered, but there is no significant effect on the results. This is because the results from several repeated simulations revealed that evacuees who evacuate to destinations other than hotels fail because of evacuation time rather than the capacity of the tsunami evacuation destinations. On the other hand, the evacuation time is not the decisive factor for hotels because these are located inside the target area and they are accessible within 12 minutes after the start of the simulation. Instead, the capacity is the more decisive factor and must be considered.

The number of casualties decreased to less than 200 in both the A and B models by improvement in two steps from more than 1200 in the initial model. Of course, a comprehensive combination of these models can yield the best model. However, constructing two evacuation towers is unrealistic when the construction cost is taken into account. Also, it is not economical because the number of casualties in the models A-2 and B-2, where the first tower is constructed, is already small compared to the total population of the target area. Rather, it would be wise to first analyze in detail the best model among the models drafted so far and extract the district that does not benefit from the measures in the best model, then to focus on and take measures on such a district.

Therefore, three different types of numerical analyses were performed to grasp the evacuation difficulty for each small district using the A-2 model, which is more feasible and has the fewer casualties and is considered as the best model among all the models,

Before the analyses, first the A-2 model was simulated for 10 trials to obtain more stable results, and the initial position of the casualties in each simulation was obtained. Figure 9.9 shows the initial position of the casualties in the first trial.



Figure 9.9. Initial position of casualties in the first trial of the A-2 model. Orange circles show the position of the casualties while blue circles show those who evacuated successfully in the first trial of the simulation.

To extract issues in more detail, the target area was separated into nine subdistricts based on the obtained initial position distribution of the casualties. Figure 9.10 shows the splitting into subdistricts, and Table 9.2 shows the total population of each subdistrict.

After these preparations, as the first analysis, the total number of casualties was obtained, which is the fundamental information for evaluating the evacuation difficulty of a subdistrict. Next, the ratio of casualties to the population in each subdistrict was calculated as the second analysis. Figure 9.11 shows the number of casualties in each subdistrict. The vertical axis is the average number of casualties from 10 trials, while the horizontal axis is the subdistrict number. Figure 9.12 shows the ratio of casualties to the total population in each subdistrict. The vertical axis is the ratio obtained by dividing the number of casualties, which is the average number for 10 trials in Figure 9.11, by the population of the subdistrict in Table 9.2. The horizontal axis is the subdistrict number.

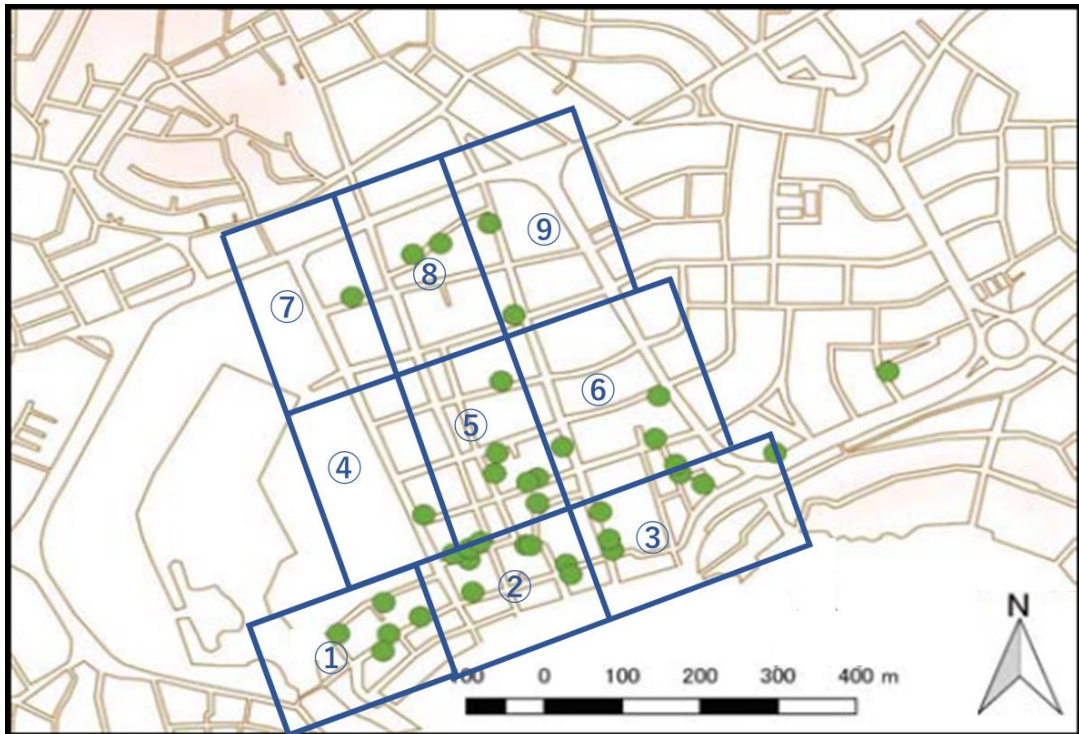


Figure 9.10. Splitting of the target area. The boundary of each subdistrict is shown by blue lines, and the number within the blue boxes is the subdistrict number. Green circles indicate the locations of the hotels designated as evacuation destinations.

Table 9.2. The total population of each subdistrict.

Subdistrict number	1	2	3	4	5	6	7	8	9
Number of people	926	1169	1144	265	441	1266	230	405	641

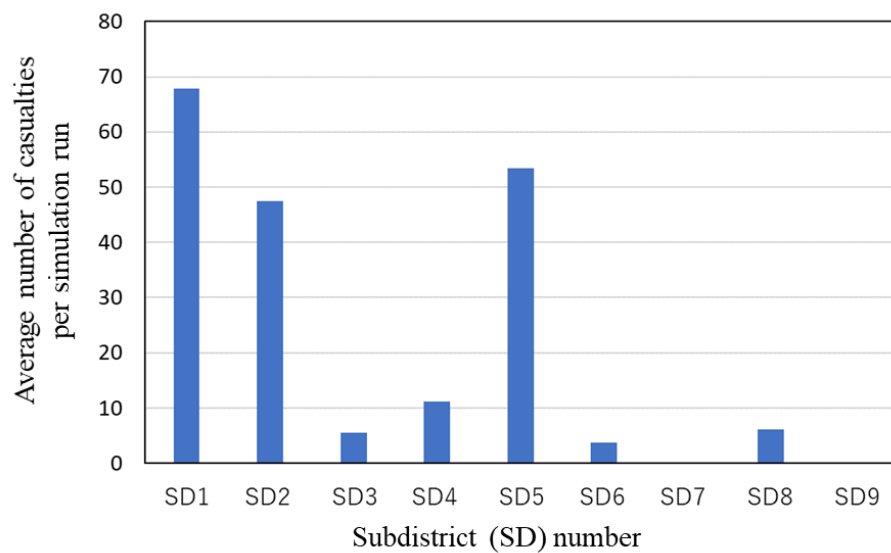


Figure 9.11. Average number of casualties per run in each subdistrict. SD in the horizontal axis stands for subdistrict.

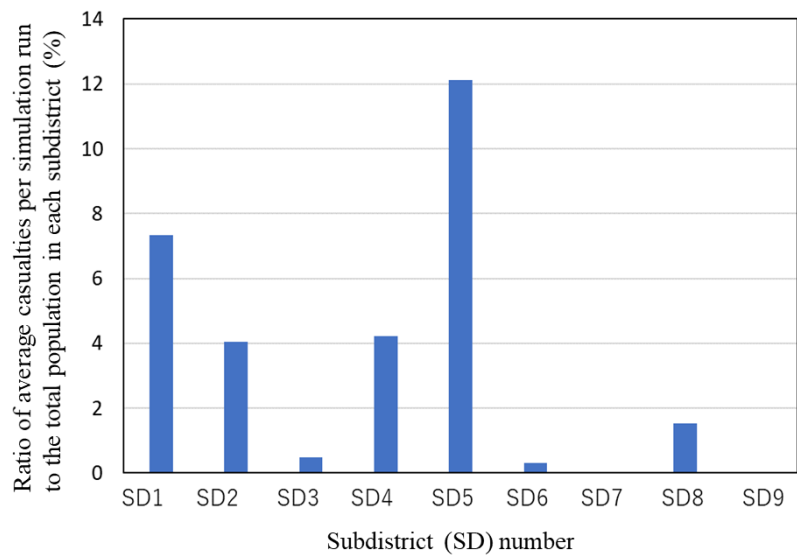


Figure 9.12. Ratio of average casualties per simulation run in Figure 9.11 to the total population in each subdistrict.

Then, to grasp the behavior of each casualty in detail, as the third analysis, the number of failed evacuations among the 10 simulations were calculated for an agent, and the number of agents that failed for the same time was counted in each subdistrict, the result of which is shown in Figure 9.13. Most of the failed agents failed all 10 times in subdistricts 5 and 2, while the number of failures of agents in subdistricts 1 and 4 were scattered. A pinpoint measure is effective when the same agent tends to fail at a high probability.

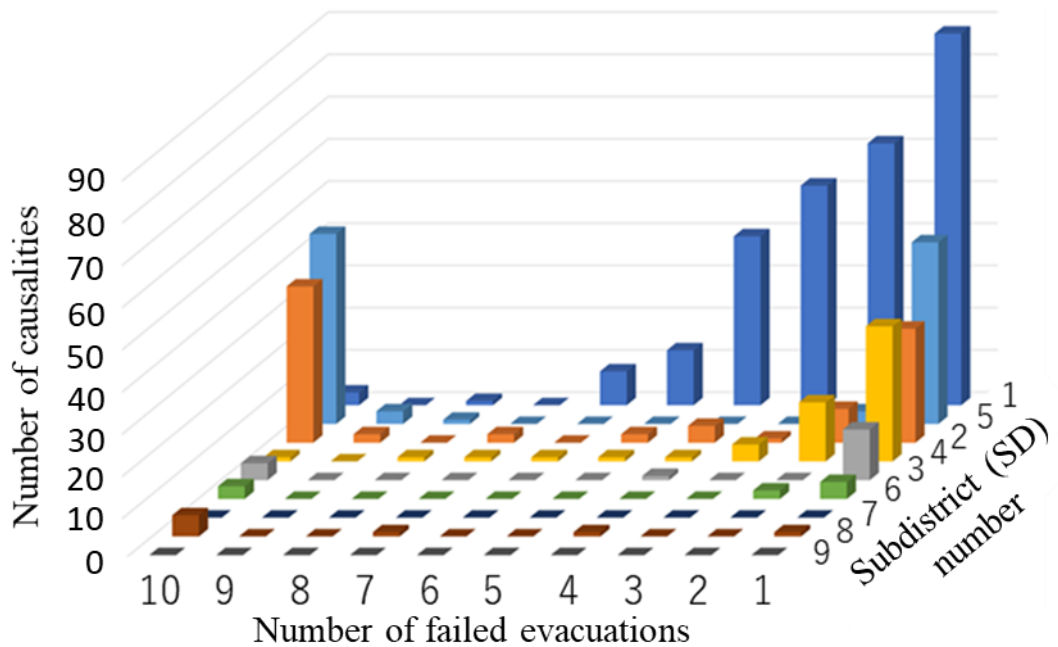


Figure 9.13. The distribution of the number of failures for agents that become casualties in each subdistrict. The depth axis is the subdistrict number. The horizontal axis is the number of failed evacuations among 10 trials for an agent, and the vertical axis is the number of agents with the same number of failures. In other words, the number of a bar shows the number of agents, where the initial position is in the corresponding subdistrict, that fail for the number of times in the horizontal axis among 10 trials. Different agents become casualties in subdistrict 1, while the same agent repeatedly fails in different trials and there are many such agents in subdistricts 5 and 2.

Finally, the evacuation difficulty of subdistricts was comprehensively evaluated based on the above three analyses. Subdistricts 5 and 1 have consistently high evacuation difficulties in Figure 9.9, 11, 12, and 13. Subdistrict 5 has more agents that always fail compared to subdistrict 1, thus investment in subdistrict 5 has higher priority in the case a pinpointed measure is taken.

9.6 Summary of the Whole Simulation Procedure

Section 9.5 explained the whole procedure on how to extract the DEA using tsunami evacuation simulations. In section 9.5 we explained the detailed procedure on how to extract the DEA by using tsunami evacuation simulation. In this section, we summarize the procedure again, provide the significance of each step, and give a few key points to apply the proposed procedures to areas other than the target area in this study. From here on, step 1 is defined as the process up to improvement of the models using simulation images at the tsunami arrival time, and step 2 is defined as the process of the numerical analyses using the A-2 model, which is more feasible and has fewer casualties within the models in step 1.

In step 1, the initial model was drafted, and the position of casualties was captured from

simulation images when the tsunami arrives. The new models with the possible evacuation measures were drafted from the initial model. The important point in step 1 is to build many different models and not to put much effort into improving convergence of each model, thus each model was simulated for three trials. Out of the total population of 6487, the number of casualties was 1290, 549, 195, 645, and 181 in the initial, A-1, A-2, B-1, and B-2 models, respectively. Each improvement of the model resulted in a substantial decrease of the number of casualties. This significant difference in the number of casualties between models suggests that the result from three trials would be sufficient at this stage. The results also imply that, when there are still many casualties, proposing a new evacuation model that reflects the situations visually obtained from the simulation image is still effective.

The number of casualties in the A-2 and B-2 models, which were the improved models in step 1, was just a few percent of the district. The A-2 or B-2 model is the best plan if the improvement of plans is stopped in consideration of the investment cost of the measure. However, there is no doubt that the ultimate goal of a disaster mitigation plan is to save every life, and having a model with as few casualties as possible is important to motivate city officials and residents participating in evacuation drills. Therefore, for further improvement of the model with minimum cost, the three numerical analyses for evaluating the evacuation difficulty were adopted to grasp the current movement patterns of evacuees and to comprehensively extract the DEA.

In step 2, focusing on the A-2 model, which is considered as the best model in Step 1 in terms of the feasibility and low casualties, we performed the three types of numerical analysis mentioned above for revealing the characteristics of the casualty, then extracted the DEA by comprehensively evaluating the result of the analysis. Before the analysis, first the A-2 model was simulated for 10 trials because results from our multi-agent simulator was found to sufficiently stabilize after 10 trials. The number of trials depend on the number of people in the district, complexity of conditions, and the randomness of the simulator. Therefore, confirming the stability of the results is important. Second, the initial positions of casualties in each trial were obtained. Then the area was divided into nine subdistricts based on the initial positions of the casualties to make the differences between each subdistrict more apparent. If the district can be physically divided by geographical features, this division can be used instead of the proposed method. Division by administrative district is an option, if the size is appropriate. Dividing into subdistricts with similar number of evacuees is another possible method, although we still need to decide arbitrarily to draw lines between subdistricts.

After these preparations, the DEA was comprehensively extracted using the following three indices from the numerical analyses for grasping the evacuation difficulty in each subdistrict. The first index is the absolute number, which is the most fundamental index when estimating the evacuation difficulty of one district. However, evaluating only by the absolute number alone is not sufficient because it picks up only the area with the largest number of casualties. Therefore, the second index, the relative number, which is the ratio of casualties to the total number of evacuees in the subdistrict, is needed for an appropriate evaluation. By using the relative number, we can extract the area where there is a high possibility for evacuees to fail to evacuate, in other words, the area where a measure would effectively reduce the casualties. Using the relative number only, however, is also insufficient because it may not pick the area with the largest number of casualties. Evaluation by using both absolute and relative number makes the evaluation more comprehensive.

The third index, which is the number of times that the same agent failed to evacuate

among 10 simulation trials, was counted, and the number of agents with each number of failures was tabulated by subdistrict. The goal of this analysis is to observe the “chance of becoming a casualty” of each agent, which can provide the reason why evacuation is hampered in this subdistrict. This information is valuable when drafting improvement plans. In subdistricts where many agents fail to evacuate for most of the 10 trials, a possible reason for failed evacuations is that the distance to an evacuation destination is too long for the agent. In contrast, in subdistricts where there is scattering in the number of agents that failed to evacuate for a certain number of times among 10 trials, there may be several reasons that hamper evacuation in the subdistrict instead of a single cause such as “distance”. For the former subdistrict, a single measure enacted in the subdistrict would effectively reduce the casualties. For the latter, taking relatively low-cost measures in multiple locations could be more appropriate than one intensive measure.

Finally, the evacuation difficulty was evaluated by comprehensively comparing subdistricts based on the indices obtained from the three numerical analyses. Using multiple indices improves the accuracy of DEA extraction. In the simulations in this study, subdistricts 5 and 1 were evaluated as the two that are most difficult to evacuate. The absolute number of casualties, the first index, was largest in subdistrict 1, while the relative number and the ratio of agents likely to fail for a large number out of 10 trials, the second and third index, respectively, were large in subdistrict 5. Subdistricts 2 and 4 were also found to be the area where it is relatively difficult to evacuate. As a result, DEAs with different characteristics were quantitatively extracted from three indices.

To summarize the whole procedures mentioned above, the proposed method in this study and a few key points in case of applying the method to other areas is as follows:

- I. Draft the improved simulation models reflecting the findings from the simulation images at the tsunami arrival time. Various models in consideration of the feasibility should be drafted with minimum number of trials in simulation after validating the randomness of the simulator.
- II. Choose the best model among the improved models and perform the simulations. Additional trials in new simulations are needed until the results converge to get more accurate results.
- III. Divide the target area into subdistricts. Possible dividing methods are a) dividing by seeing the distribution of casualties, b) dividing into the subdistricts with similar number of evacuees, c) dividing by the geological features, and d) dividing by the administrative district.
- IV. Perform the three types of numerical analyses for grasping the evacuation difficulty in each subdistrict and extract the DEA among the subdistricts by comprehensively considering the results from the analyses.
- V. Propose an appropriate measure on the DEA in consideration of the feasibility and financial situation in the target area. Tangible and intangible measures can be considered depending on the situation in the target area.

9.7 Discussion

One significant feature of this study is to extract the DEA not by using the simple relation

between the distance to the evacuation destination, time needed for evacuation, and walking speed, but by conducting the simulations using the multi agent simulator which can reflect the congestion of the road and the behavior of the agents. By adopting the simulation to extract the DEA, we can grasp a more realistic situation of the casualties and then can take appropriate measures based on the result of the simulation. To recognize the difference between the two methods mentioned above, we first categorized the casualties in the A-2 model by the time needed for evacuation calculated by the simple relation between the distance to the evacuation destination and walking speed, which is the basic idea often used for extracting DEAs as shown in the abstract. Here we call the time needed for evacuation calculated above “minimum evacuation time”. Then we compared the minimum evacuation time with the estimated tsunami arrival time (12 minutes after the start of the simulation), and checked if there are any casualties with a minimum evacuation time that is less than 12 minutes. Figure 9.14 shows the distribution of the number of casualties categorized by each minimum evacuation time. In Figure 9.14, the estimated tsunami arrival time, 12 minutes, is also shown so that it can be compared with the minimum evacuation time. The number of the casualties comes from the result in the third run of the simulations among 10 trials and here we show this figure as an example of 10 trials. In Figure 9.14, it turned out that the minimum evacuation time of a considerable number of the casualties is less than 12 minutes. It means that they are estimated to evacuate successfully in the case of the evaluation by the evacuation time from the simple relation between the distance to the destination and walking speed. Therefore, we can say that the result about the casualties from the simulation is evaluated on a safe side.

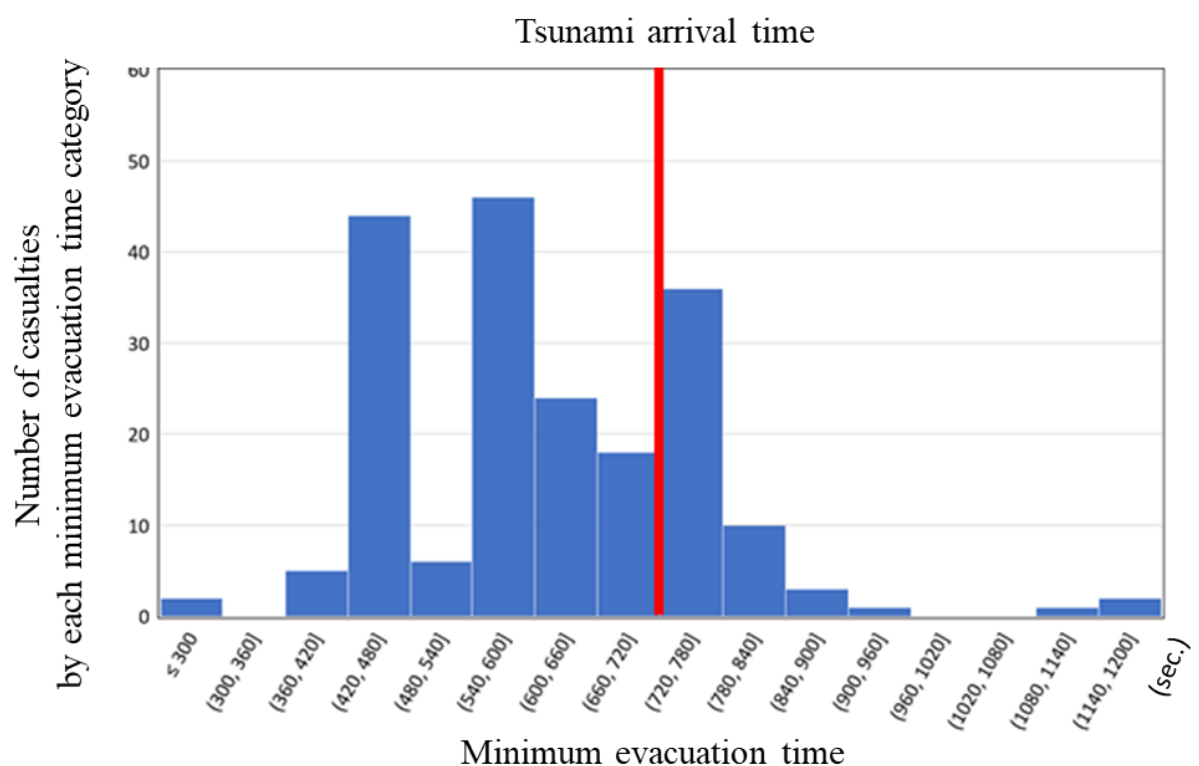


Figure 9.14. Distribution of the number of casualties categorized by each minimum evacuation

time with an interval of 120 seconds. The estimated tsunami arrival time, 12 minutes (720 seconds) is also shown on the figure. All the time is counted from the starting time of the simulation. The horizontal axis is the minimum evacuation time. The vertical axis is the number of casualties in each minimum evacuation time category.

Another important feature of this study is that we extracted the DEA by using the three types of numerical analyses for grasping the evacuation difficulty. From these analyses, subdistrict 5 was evaluated as the district where priority measures should be taken. Reflecting the evaluation above, we simulated a new simulation model with the additional tsunami evacuation facility so that we can verify the evaluation from the proposed method. In subdistrict 5, there is a municipal tax office with three stories and a roof floor. It was constructed relatively recently and has sufficient floor space. In the new simulation model, we designated this building as an additional tsunami evacuation facility. Other evacuation destinations follow the A-2 model. Figure 9.15 shows the distribution of the evacuation destinations in the new simulation model. The reason why we considered designating the municipal tax office as an evacuation facility is feasible is as follows: As explained in section 9.2.1, the reason why we may have difficulty designating the tsunami evacuation facilities in the target area is that owners do not want to let strangers enter their property because of potential security problems. However, the municipal city office is a public building, so it could be designated to be a tsunami evacuation facility with the cooperation of the authorities. Other measures, for example, creating a new tourist spot in other safer subdistricts to prevent too many tourists from coming into subdistrict 5, can be considered, but here we adopted a tangible measure to designate a new tsunami evacuation facility as an example to check the validity of the evacuation from the proposed method.

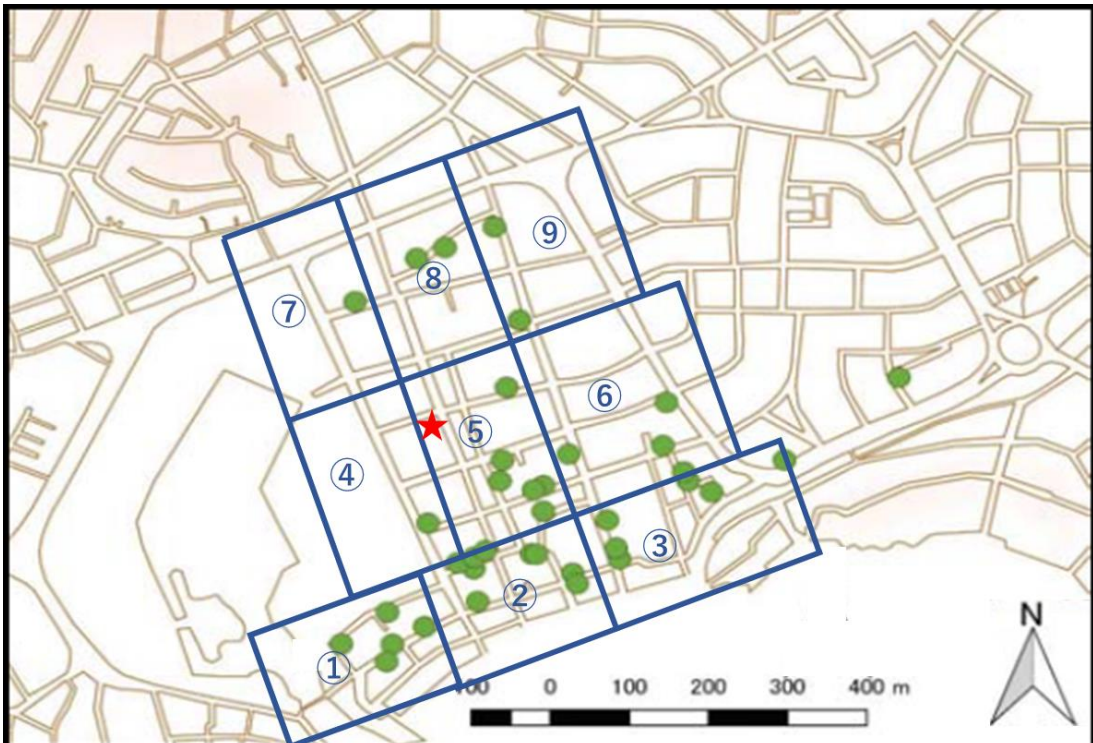


Figure 9.15. The location of the municipal tax office newly considered as a tsunami evacuation facility (red star symbol). Green circles are hotels that were designated as tsunami evacuation facilities from the initial model. The boundary of each subdistrict is shown in blue lines, and the number within the blue boxes is the subdistrict number.

Before conducting the simulation, the floor space of the municipal tax office was estimated based on a satellite image, and the capacity was calculated to be 553 people based on the formula to calculate the hotel capacity shown in section 9.4. Then, the simulations of the new model were conducted for 10 trials. Figure 9.16 shows the comparison of the average number of casualties in the new model with the A-2 model from ten trials. The average number of casualties in the whole target area was 101, which is about half of that in the A-2 model, 195, as shown in section 5. Focusing on the result in each subdistrict, in subdistrict 5 the number of casualties was nine while it was 53 in the A-2 model, which corresponded to 2% and 12.1% of the total number in the district, respectively. Positive effects were also found in subdistricts 2 and 4. From this result, the evaluation from the three types of numerical analyses for grasping the evacuation difficulty is reasonable.

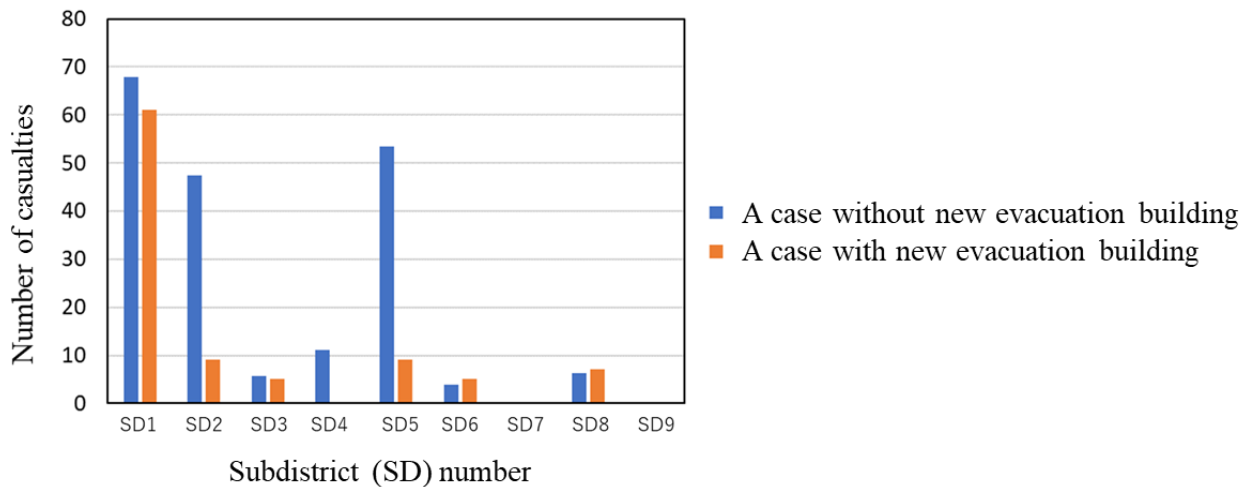


Figure 9.16. Comparison of the average number of casualties in each subdistrict from 10 trials of the A-2 model and the model where the tsunami evacuation facility in Figure 9.15 is newly added.

9.8 Conclusions

This study conducted tsunami evacuation simulations to extract the DEA (difficult-to-evacuate area) from tsunami on Zihuatanejo, Mexico, where there is still insufficient awareness on evacuation among residents and administrative agencies are still investigating evacuation plans.

In step 1, the initial model was drafted and the location of casualties at the estimated tsunami arrival time was captured by using the simulation images, and improved models were drafted by repeatedly adding evacuation destinations while considering the feasibility.

In step 2, The detailed analyses were performed on the A-2 model, which is the more feasible and has fewer causality among the models in step 1. The target area was divided into nine subdistricts and three numerical analyses for grasping the evacuation difficulty of each subdistrict were performed. The evacuation difficulty of each subdistrict was comprehensively evaluated from the resultant three indices, and the DEAs were extracted. Subdistrict 5 which is the central district in the target area, was estimated to be the area where a measure should be taken. Then, steps 1 and 2 were reviewed and the significance of each step was provided toward application of the proposed method to other areas.

In the discussion, the time needed for evacuation, minimum evacuation time, which is simply calculated from the relation between the distance to the evacuation destination and the walking speed for each agent, and the estimated tsunami arrival time (12 minutes), were compared for agents who failed to evacuate in the A-2 model in our simulation. From the comparison, it turned out that a considerable number of evacuees with minimum evacuation time less than 12 minutes failed to evacuate in our simulation. This means that simple geometrical “minimum evacuation time” evaluates on the danger side.

Reflecting on the result from the analyses in step 2 that prioritized measures should be taken in subdistrict 5—the new model where the municipal tax office located in subdistrict 5 was selected as a tsunami evacuation facility was simulated. The casualties of subdistrict 5 became 44 fewer than in the A-2 model, which resulted in a decrease of the ratio of casualties to the total

population of 2% from 12% in the A-2 model.

As for the future tasks, we first need to verify the proposed method for extracting DEA for the other three ways to divide the target area which were not adopted in this study. This study targeted an area with intermediate size where the population is about 6000 people and the area is approximately 0.4 km². We wish to evaluate whether the proposed method for extracting DEA is effective in tsunami evacuation simulations of districts with a larger population and area.

Road blockage due to collapsed buildings was not taken into account in the tsunami evacuation simulations conducted to identify the DEA in this study, as have done in Chapters 7 and 8. Buildings in Mexico are considered to be less earthquake-resistant than those in Japan, and many of them are expected to collapse in an event of a mega-thrust earthquake. Therefore, the additional future task is to construct a building damage prediction model that reflects the building characteristics of Mexico, especially in Zihuatanejo, based on the Japanese building model used in this thesis reflecting the field survey results of buildings, calculate the building damage ratio due to an assumed earthquake, and identify more realistic DEAs based on the evacuation simulation with consideration of road blockage due to collapsed buildings.

Acknowledgment

We thank Prof. Nobuhito Mori from Kyoto University for providing the tsunami source used in this tsunami simulation. The bathymetric and topographic data for the worst-case scenario simulation was kindly provided by the Department of Atmospheric Sciences of the National Autonomous University of Mexico (Special thanks to Dr. Jorge Zavala Hidalgo).

Funding

This research was supported by the Science and Technology Research Partnership for Sustainable Development project, “The Project for Hazard Assessment of Large Earthquakes and Tsunamis in the Mexican Pacific Coast for Disaster Mitigation” (JPMJSA1510).

References

- Ashar, F., Amaralunga, D., and Haigh, R. (2014), The analysis of tsunami vertical shelter in Padang city, Procedia Economics and Finance, 18 (2014), 916 - 923.
- Cruz-Atienza, V. M., Ito, Y., Kostoglodov, V., Hjörleifsdóttir, V., Iglesias, A., Tago, J., Calò, M., Real, J., Husker, A., Ide, S., Nishimura, T., Shinohara, M., Mortera-Gutierrez, C., García, S., and Kido, M. (2018), A Seismogeodetic Amphibious Network in the Guerrero Seismic Gap, Mexico. Seismological Research Letters; 89 (4): 1435–1449. doi: <https://doi.org/10.1785/0220170173>
- Cruz-Atienza, V. M., Y. Ito, V. Kostoglodov, V. Hjörleifsdóttir, A. Iglesias, J. Tagø, M. Calò, et al. 2018. “A Seismogeodetic Amphibious Network in the Guerrero Seismic Gap, Mexico.” Seismological Research Letters 89 (4): 1435–1449.doi:10.1785/0220170173.
- Fire and Disaster Management Agency (2002), Guideline for Tsunami Evacuation Plan Development in Municipalities (Chapter 2), Report on the development of the manual for

- promoting the countermeasures for tsunami [in Japanese].
https://www.fdma.go.jp/singi_kento/kento/items/kento106_01_p00.pdf
- Hamada, Y., Kondo, A., Watanabe, K., Takeuchi, T., and Yamaguchi, M. (2005), Planning of Allocation of Evacuation Facilities based on Residents Awareness of Disaster Prevention; A Case Study in Susaki City, Infrastructure Planning Review, Japan Society of Civil Engineers, Vol. 22, pp.315-323[in Japanese].
- Hatayama, M. (1999), Development of Space-Time Geographic Information Systems DiMSIS, GIS – Theory and Application, 7/2, pp.25–33 [in Japanese].
- Hatayama, M., Kosaka, T., and Hernández-Hernández, A. (2018), Analysis on Tsunami Evacuation Options with Agent-based Simulation in Tourist Area, 2018 5th International Conference on Information and Communication Technologies for Disaster Management (ICT-DM)
- Imamura, F. (1996), Review of tsunami simulation with a finite difference method, In H. Yeh, P. Liu, & C. E. Synolakis (Eds.), Long-Wave Runup Models, pp.25-42, Singapore: World Scientific Publishing Co.
- Instituto Nacional de Estadística y Geografía (INEGI) (2008), Modelo digital de elevación de alta resolución Lidar 2008, cited 27 October 2017.
- Instituto Nacional de Estadística y Geografía (INEGI) (2010), Censo de Población y Vivienda 2010, cited 11 September 2017. <http://www.beta.inegi.org.mx/proyectos/ccpv/2010/>
- Instituto Nacional de Estadística y Geografía (INEGI) (2015), Cartografía geoestadística urbana, Cierre de los Censos Económicos 2014, DENU," 2015, cited 27 October 2017. <https://datos.gob.mx/busca/dataset/cartografia-geoestadistica-urbana-cierre-de-los-censos-economicos-2014-denu-01-2015>
- Instituto Nacional de Estadística y Geografía (INEGI) (2016), Cartografía Geoestadística Urbana y Rural Amanzana. Junio 2016, cited 12 September 2017. <http://www3.inegi.org.mx/sistemas/biblioteca/ficha.aspx?upc=702825218799>
- Ito, E., Kawase, H., Matsushima, S., Hatayama, M. (2020), Tsunami evacuation simulation considering road blockage by collapsed buildings evaluated from predicted strong ground motion, Nat Hazards 101, 959–980. <https://doi.org/10.1007/s11069-020-03903-2>
- Kaneda, T. (2010), Introduction to Pedestrian Agent Simulation using Artisoc: from Principle and Methodology to Space Design and Management for Safety and Crowd”, Kozo Keikaku Engineering Inc., Shoseki Kobo Hayama Publishing [in Japanese].
- Kostoglodov, V., S. K. Singh, J. A. Santiago, S. I. Franco, K. M. Larson, A. R. Lowry, and R. Bilham. 2003. “A Large Silent Earthquake in the Guerrero Seismic Gap, Mexico.” Geophysical Research Letters 30 (15): 1–4.
- Minamoto, T., Nariyuki, Y., Fujiwara, Y., and Mikami, A. (2009), Development of tsunami evacuation simulation system and its application to assessment of area refuge safety, Journal of Japan Society of Civil Engineers, Ser. A1 (Structural Engineering & Earthquake Engineering) Vol.65, No.1, pp. 757-767 [in Japanese].
- Minato, F., Hata, Y., Nakashima, T., Koyama, M., Kuwata, Y., Yamada, M, and Tokida, K. (2016), Evaluation of difficult area for tsunami evacuation in Aonae district Okushiri Island, Japan, based on strong ground motion estimation and walking experiment during the 1993 Southwest Hokkaido earthquake, Journal of Japan Society of Civil Engineers, Ser. B3 (Ocean Engineering), Vol.72, no.2, I_509-I_514 [in Japanese].

- Ministry of Land, Infrastructure, Transport, and Tourism (MLIT) (2013), A guideline for community planning for tsunami disaster mitigation [in Japanese].
<https://www.mlit.go.jp/common/001000488.pdf>
- Miyashita, T., Mori, N., and Goda, K. (2020), Uncertainty of probabilistic tsunami hazard assessment of Zihuatanejo (Mexico) due to the representation of tsunami variability. Coastal Engineering Journal, 62(3), 413-428.
<https://doi.org/10.1080/21664250.2020.1780676>
- Mori, N., Muhammad, A., Goda, K., Yasuda, T., and Ruiz-Angulo, A. (2017), Probabilistic Tsunami Hazard Analysis of the Pacific Coast of Mexico: Case Study Based on the 1995 Colima Earthquake Tsunami. Frontiers in Built Environment, 3(34), 1-16.
<https://doi.org/10.3389/fbuil.2017.00034>
- Muhari, A., Imamura, F., Koshimura, S., and Post, J. (2011), Examination of three practical run-up models for assessing tsunami impact on highly populated areas, Natural Hazards and Earth System Science, 11(12), 3107-3123.
- Nakano, G., Yamori, K., Miyashita, T., Urra, L., Mas, E., and Koshimura, S. (2020), Combination of school evacuation drill with tsunami inundation simulation: Consensus-making between disaster experts and citizens on an evacuation strategy, International Journal of Disaster Risk Reduction, 101803. <https://doi.org/10.1016/j.ijdrr.2020.101803>
- Ohata, D., Takai, N., and Kagami, H. (2007), Spatial Evaluation of Tsunami Refuge Facilities in the Central Kushiro City: Simulation of evacuation behavior from Tsunami utilizing multi agent system Part 2, Journal of Architecture and Planning, AIJ, Vol. 72 No.612, pp.87-91 [in Japanese].
- Okada, Y. (1992), Internal deformation due to shear and tensile faults in a half space, Bulletin of the Seismological Society of America, 82(2), 1018-1040.
- Osaragi, T. and Oki, T. (2012), Difficulty of Evacuation in Densely Built-Up Area In The Aftermath of A Large-Scale Earthquake, Journal of Architecture and Planning, AIJ, Vol. 77 No.68, pp.2561-2567 [in Japanese].
- Takeuchi, T., Kondo, A., Yamaguchi, M., and Hamada, Y. (2003), Empirical Analysis on Evaluation of Refuge Facilities from Tsunami in Consideration of the Capacity; A Case Study in Susaki City-, Infrastructure Planning Review, Japan Society of Civil Engineers, Vol.20, No.2, pp.345-354 [in Japanese].

Chapter 10

General Conclusions

This study aims to propose an integrated risk evaluation system for mega-thrust earthquake based on the information of past earthquakes, damage surveys, geophysical surveys, and observed data, considering the urgent needs to be solved toward more quantitative risk evaluation for future mega-thrust earthquakes. To that end, the potential of the proposed techniques for evaluating the site characteristic, source characteristic, building damage, and human loss by tsunamis are addressed, all of which are indispensable and tightly connected to each other for evaluating the clear and present risk of mega-thrust earthquakes. The conclusions and remarks from each chapter are summarized as follows:

In Chapter 1, the background and purpose of this study were introduced. First, it was addressed that all disasters are complex, and inevitably their prediction can only be accomplished through the integrated use of technologies that cross many different disciplines. The importance of reducing the human casualties from earthquakes by sophisticating the evaluation method of the characteristics of strong motion, building damage, and human casualties and by integrating them into effective countermeasures were emphasized. The current progress of each evaluation method was reviewed and explained how they can be sophisticated and integrated in this study. The challenges that we are facing in the integrated earthquake risk assessment were found, which can be described in detail as:

- 1) Establish a method for quantitatively predicting strong motions of future mega-thrust earthquakes based on the observed records;
- 2) Take into account realistic spatial variability characteristics of fault parameters in setting up rupture scenarios on the fault plane;
- 3) In setting the spatial variability characteristics, extract the source information of past mega-thrust earthquakes and utilize them for prediction;
- 4) For site characteristics that have a significant impact on the prediction of strong ground motions, establish effective and accurate evaluation methods for a wider range of frequency bands based on observed records and subsurface structural information;
- 5) Conduct a realistic tsunami evacuation simulation analysis for tsunami damage reduction and use it for planning countermeasures.

Based on the urgent needs for the integrated earthquake risk evaluation as identified above, their solutions were addressed as follows:

- 1) The statistical Green's function was used, which reflects the characteristics of the observed ground motions over a wide frequency range, to calculate the strong-motion waveforms of mega-thrust earthquakes in a wide area using the conventional waveform summation method.

- 2) Either asperities or SMGAs, which contribute to moderate- to long-period ground motions radiated from a fraction of areas in the large fault plane, and the random variations inside and outside of the asperities, which contribute to short-period ground motions, are taken into account in setting up the rupture on the fault plane.
- 3) The source properties of past giant trench earthquakes are clarified by matching the estimated damage rates of buildings from the strong-motion waveforms reproduced by the above prediction method with the observed damage rates.
- 4) A couple of new methods for quantitative site amplification evaluation using the vertical amplification correction function, the theoretical amplification factor correction, and the region-specific earthquake-to-microtremor HVR correction.
- 5) Evacuation simulation analyses of building damage due to strong ground motion considering site amplification characteristics are carried out which should be reflected in the integrated risk assessment.

In Chapter 2, a simple method to deduce the horizontal site amplification factor (HSAF) in the S-wave portion directly from the EHVR of observed earthquake ground motion was proposed. In this method, a correction procedure based on formulas from the diffuse field concept and GIT was formulated; the adequacy of the used reference condition as the seismological bedrock was confirmed; observation records from 1,678 sites where ten or more earthquakes have been observed in the strong-motion networks of K-NET, KiK-net, and JMA seismic intensity network were focused on; the GIT results to determine the vertical site amplification factor VSAF (to be precise, $VSAF^* = VSAF \times V_B H_B R$) were used; and then all 1,678 sites were averaged to obtain the empirical vertical amplification correction function (VACF). The major findings obtained are as follows:

- 1) The vertical-to-horizontal spectral ratio at the reference observation site ($V_B H_B R$) was nearly unity and agreed with the theoretical solution of 0.76 within the range of variation.
- 2) The amplitude of the VSAF, on average, was 30% to 40% of the HSAF obtained by GIT. While there was a weak correlation between the EHVR and HSAF, the EHVR was obviously smaller than the HSAF in amplitude. Using the EHVR with no correction in place of the HSAF will result in underestimation of HSAF.
- 3) It was possible to obtain the VACF on a very stable basis by reading out the peak amplitude and peak frequency of the EHVR at each site and averaging the data in the corresponding category; there were only negligible differences due to peak amplitude; there were relatively small differences due to peak frequency; the amount of correction increased as the peak frequency decreased; and the VACF was the largest when EHVR peak frequency was 1 Hz or less, where the factor of about 3 was needed.
- 4) Data in each category classified based on the peak amplitude and peak frequency of the EVHR were averaged to obtain nearly identical average values, except for a category having too small amount of data. For the sake of simplicity, a single VACF value by averaging the data of all 1,678 sites without categorization was deduced. The resultant uncategorized VACF shows a linearly increasing amplitude up to 1.0 Hz, above which it shows a constant amplitude of about 2.0 up to 15 Hz. This VACF can be used to correct EHVR considering the variability of 1.5 times.
- 5) The obtained VACF was applied to 103 sites, which have not been used in the averaging. As a result, the observed HSAF has been successfully reproduced at 86% of the sites, although a couple of sites have shown nearly doubled the differences.

In summary, this chapter proposes a new simple method for site amplification, in which

the main S-wave part of earthquake ground motion is extracted, the average horizontal-to-vertical spectral ratio of this portion is determined, and this ratio is multiplied by the empirical correction function to obtain the horizontal S-wave site amplification factor. The method is capable of evaluating site effects of S-waves based on observed values in a wide frequency range from 0.12 to 15 Hz. It should be noted that the proposed method obtains the horizontal S-wave amplification factor from the seismological bedrock, rather than the engineering bedrock, to the ground surface. For the sake of reliability, it is advisable to determine the average horizontal-to-vertical ratio of at least about ten earthquakes.

In Chapter 3, it was attempted to extend the method of the earthquake-to-microtremor ratio of HVSR (EMR) to a basin in the region tectonically different from Japan. The target site is the Grenoble Basin, France. It was assumed that the shape of EMR specific to the Grenoble Basin (EMR_G) should follow the general shape of the Japanese EMR. It is assumed that differences only appear in the amplitudes, which would be corrected with a modification factor α . By using a two-step grid search, the optimal α was found to be 0.28. It was found that pHVSRs with α of 0.28 at the five sites in the Grenoble Basin are better matched to observed eHVSRs compared to mHVSRs as well as pHVSRs from the Japanese EMR. Then, velocity structures from pHVSRs, mHVSRs, and the observed eHVSRs at five sites were inverted and were found that the velocity structures from the observed eHVSRs were closer to those from pHVSRs than those from mHVSRs.

Then, an averaged deeper velocity structure from the results of the inversion at five sites were constructed in order to constrain velocities in the deeper part for the whole basin inversions. A new reference model for each site were constructed based on the averaged deeper velocity structure and the shallower part of the original reference model in a proportional manner to the depth of the layer with the S-wave velocity of 1.3 km/s (Z1.3). It was found that Z1.3 corresponds to the geological boundary depth from the gravity analysis. We use Z1.3 and Z3.2, which are the depths where the S-wave velocities exceed 1.3 and 3.2 km/s, respectively, together with the fundamental peak period T_p , as key parameters to construct a site-specific reference model.

A clear velocity gradient was obtained near the geological boundary defined by the gravity anomaly and borehole data, which is the most important finding in this study. To show the reality of the velocity gradient and strong constraint by the targeted pHVSR, a sensitivity analysis for OGFO was performed. It indicates that the velocity gradient near the geological boundary would be real and the inverted velocity structure is well constrained by the target pHVSR. Still, further validation of this delineated velocity gradient using the three-dimensional basin response simulation is necessary.

Aiming for delineating the whole basin structure in the Grenoble Basin, pHVSRs using EMR_G for inversion of the velocity structures at fourteen G-series sites were calculated, using a new reference model specific for each site. Then Z1.3 and the geological boundary depth from gravity were compared at each site. The obtained Z1.3s by the proposed method at eight of fourteen sites are closer to those by the gravity. The results at the rest of the sites did not directly match, however, the average ratio between Z1.3 and the geological boundary depth for all the G-series sites is unity, suggesting the overall similarity between them. Therefore, as the first attempt toward the final goal to delineate the whole basin structure in a tectonically different environment from Japan, an overall picture of the Grenoble Basin from observed microtremors were successfully derived by using a new scheme proposed here.

In Chapter 4, in order to evaluate an equivalent 1D S-wave site amplification factor at an

arbitrary point, an empirical method of correction on to the one-dimensional (1D) theoretical site amplification factor calculated from the unified velocity model of NIED for the Kanto and Tokai regions was proposed. First, it was confirmed how well the current unified velocity model in Japan can reproduce horizontal site amplification factors derived from the observed strong motions in the form of the equivalent 1D S-wave theoretical transfer functions at the nearest grid of every 250 m. It was found that at about one-half of the sites the theoretical 1D amplification factors show more or less acceptable fit to the observed ones, however, they tend to underestimate the observed amplifications in general. Therefore, a simple, empirical method was proposed to fill the gap between the observed site amplification factors and the calculated ones based on the frequency and amplitude modification ratios. Once these modification ratios are obtained, they can be interpolated in space to obtain the S-wave site amplification factor at an arbitrary point. Validation examples showed that our proposed method effectively predict better site amplifications than the direct substitute of 1D theoretical amplification factors at a site without observed data.

In the future investigation, the proposed correction method will be applied to the sites where we have observed records of either earthquakes or microtremors but we do not include them in the delineation of the modification ratios in order to further validate the effectiveness of the proposed method.

In Chapter 5, it was intended to clarify the source process of the past mega-thrust earthquakes, the ground motions of which have not been recorded in the past, by adapting the simulated strong-motion waveforms to the results of the damage survey. To that end, it was necessary to use good source models and good damage prediction models. For quantitative strong motion synthetics, it was necessary to introduce random spatial heterogeneity in both the slip and rupture propagation velocity, in addition to the presumed strong-motion generation areas. An effective method to predict strong ground motions over a wide frequency range from 0.1 to 20 Hz was developed by combining such a randomized source model that can represent complex rupture process on the fault and a statistical Green's function that reflects the statistical properties of small and medium-sized earthquakes inverted from a large number of strong-motion observation records in Japan. The method is applied to the 1944 Tonankai earthquake and parametric analyses are performed to investigate the effects of fluctuation in the slip and the rupture propagation velocity. The main results are summarized as follows:

- 1) The standard model with the random slip fluctuation but without rupture velocity perturbation (CASE1) yielded strong motion synthetics with PGAs and PGVs that correspond to the previously-proposed empirical relationship in general. A model with constant slip and constant rupture velocity (CASE2) yields strong motion synthetics with PGAs corresponding with the empirical relationship and the PGVs lower than the empirical relationship at sites near the hypocenter. A model with variable slip and variable rupture velocity (CASE3) yields strong motion synthetics with PGAs and PGVs that correspond well to the empirical relationship. The PGAs show more correspondence with the empirical relationship at sites near the hypocenter than those of CASE1.
- 2) Specifically looked at the deviation, their PGAs tend to be overestimated a little bit whereas their PGVs tend to be underestimated a little bit, which can be considered as the reflected site effects of the target sites used for calculation.
- 3) The fluctuations of the slip under the current model turned out to increase PGA by 15% and PGV in 25%.
- 4) The variations of the rupture propagation velocity turned out not to change both PGA and

PGV significantly, probably because of the stochastic nature in the statistical Green function method adopted here. However, a systematic reduction of PGAs in the vicinity of the hypocenter for a source with velocity perturbations were found, due to the effect of the incoherent rupture in the area with strong forward directivity.

- 5) Empirically-modeled nonlinearity effects will reduce both PGAs and PGVs at the sites with higher PGVs and smaller Vs30 values, whereas those sites with higher Vs30s with high PGAs but low PGVs do not show significant reduction by nonlinearity.

As the overall characteristics of the calculated synthetics, it was found that the current implementation of the complex source model used as a broad-band kinematic source representation and the empirically-determined statistical Green function used as an elemental source of strong motions can be a viable combination for realistic broad-band (0.1 to 20 Hz) strong motion simulations without any hybrid scheme.

In Chapter 6, the following analyses were undertaken to elucidate the heterogeneous source rupture propagation process of the 1944 Tonankai earthquake. The building damage ratio during the 1944 Tonankai earthquake was reproduced by inputting the strong motion waveforms into the building damage evaluation model as of 1944. The strong ground motion waveforms were obtained from the statistical Green's function and the heterogeneous source model by the method proved to be valid in Chapter 5. The site characteristic, which is important for the evaluation of the strong ground motion, is obtained by the method of converting the theoretical S-wave characteristic from the unified velocity model (UVM) by integrating shallower- and deeper-parts of the structures above the seismological bedrock in the Kanto and Tokai regions, to the empirical site characteristics presented in Chapter 4.

First the heterogeneous source model with the four asperities was prepared as a standard model based on the model of Tonankai segments as proposed by the Cabinet Office. Then additional 35 heterogeneous source models were prepared of which parameters were the location of hypocenter, the location of asperities (SMGAs), and the stress drops of each asperity. The strong ground motions from the source models were calculated and the building damage ratios using the building damage evaluation model were estimated, and then compared with the observed damage ratio. The model that best reproduces the observed damage ratio were considered as the new standard model in the second step, and additional five heterogeneous source models with different stress drops and the areas of asperity (SMGA) No.1 and No.2 were assumed to search for the source model which reproduces the observed damage ratio best. The series of analyses described above led to the following conclusions:

- 1) The method proposed in this paper is in good agreement with M8.0 class PGA and PGV, obtained from the empirical model (GMPE), which is supposed to fit well with the observations, and its temporal characteristics also show the characteristics inferred from the fault size and rupture propagation.
- 2) Parametric analysis revealed that the effect of the first and second asperities near the coast is significant on the large amplitudes in the Enshu region of Shizuoka Prefecture due to the forward rupture directivity.
- 3) The results of the first step of the 36-case parametric study show that the case with a deeper hypocenter, moderate stress drops, and deeper asperities is the model that best explains the observed building damage ratios.
- 4) The results of the second step of the analysis show that the case with the second asperity stress drop of 60 MPa from the best model in the first step is the model that best explains the observed

building damage ratios.

- 5) The results show that in order to explain the building damage ratio of more than 40%, it is necessary to consider a source rupture process that would cause stronger forward rupture directivity in the Enshu region.
- 6) In summary, the proposed building damage evaluation model and the distribution of observed damage ratio provide a prospect to clarify the detailed source rupture process of the 1944 Tonankai earthquake.

In Chapter 7, focusing on an urbanized area, tsunami evacuation simulations were performed by considering building damage ratios from the building damage prediction model, and evaluate the human loss considering the effects of collapsed buildings during the tsunami evacuation in the target area. The target area is the downtown district of Tanabe City, Wakayama Prefecture, where it is expected to have significant damage from both earthquake and tsunami during the worst-case earthquake scenario with the whole Tokai, Tonankai, and Nankai segments ruptured. Tsunami evacuation simulation was undertaken assuming road blockages from the predicted building collapses. It was found that the prepared countermeasures were not enough to make everyone successfully evacuate and that the number of survivors increases by 3 to 4% if all the houses were seismically reinforced. Considering this plus, only 1% of expected casualties inside the collapsed houses, it appears as though it is not as efficient to reinforce buildings and houses to prevent human loss in comparison to increasing the capacity of tsunami evacuation sites in the target district. However, the damage to building and houses will cause a lot of side effects which are not considered here but must prolong the evacuation time. Thus, it was concluded that it is necessary to reinforce the houses as well as considering the appropriate placement, number, and capacity of the evacuation sites.

Even in the target district where relative consciousness towards disaster prevention is higher than in other districts, and evacuation planning is deemed more advanced, it was found that there are unresolved issues. As discussed in the building collapse prediction in this evacuation simulation, although fatalities from the collapsed buildings themselves and the effect of injuries on evacuation speed remained to be set as a parameter in the simulation, this study was able to quantify the risk of collapsed buildings in the evacuation process through the use of a building collapse ratio simulation program. This is a significant contribution to future studies and disaster prevention planning.

In Chapter 8, focusing on a village with stiff soil layers, tsunami evacuation simulations were performed considering the building damage ratios obtained by the building damage prediction model specific for the area and explore the best strategy of the evacuation plan in the target area. The target region of the damage and evacuation simulation was the Ena district, Yura Town, Hidaka County, Wakayama Prefecture. The underground soil structures were estimated in the district, where high-frequency amplification due to relatively stiff soil layers is expected, in order to evaluate the disaster risk to the mega-thrust earthquakes in this area as precise as possible. Microtremor measurements were conducted with 3-components accelerometers at 32 observation points within a radius of 500 m in the area.

First the underground soil structure models were constructed for all the observation points using the peak frequencies of MHVRs, and then estimated the strong ground motion of each observation point by using the predicted ground motion defined on the engineering bedrock. Microtremor observations were conducted over three days at 12 subsoil points and 38 wooden houses. The yield strength ratio and its distribution for different construction period in the district

were obtained. A model of the group of wooden houses in the district was established based on the observed natural period distribution and the nonlinear models of Nagato and Kawase for building damage prediction. The average yield strength ratio of houses constructed before 1981 was higher than those in Kobe, which is reflected in the damage prediction models. It was also noticed that the yield strength distribution was more concentrated around the mode.

Then, the initial velocity profile was built from available boring data in observation sites, and the subsoil structure was identified by comparing the observed MHVR with the theoretical one through the method of Sánchez-Sesma and others. From the initial velocity profile and the fundamental peak frequency of MHVR, the same velocity structure was shrunk or expanded to obtain a good matching with theory at all the sites. Detailed seismic waves at each observation point were obtained by applying the input seismic waves at the engineering bedrock to the subsoil structure at the observation points, derived from MHVR, and conducting equivalent linear seismic response analysis. The peak ground acceleration (PGA) and peak ground velocity (PGV) in the region was ranging in 750-2,100 cm/s² and 42-54 cm/s, respectively. It was found that the peak frequency of the points in the mountain side were higher than those along the river and near the coast, and that the difference in PGAs in the village was significant reflecting the shallow sediment thickness variations, while that in PGVs was marginal because the sediments are too thin to amplify intermediate-period (~1 s) waves. The building damage were estimated in detail based on the results shown above, and evaluated the difference in the extent of damage between each building in this area. In the end, the number of collapsed or overturned buildings was about 2% of the total buildings in the district.

Finally, tsunami evacuation simulations were performed incorporated the number of damaged (collapsed and overturned) buildings obtained in the previous investigations. Simulations for 21 patterns were conducted (1 pattern without the building damage and 20 patterns with building damage), and the results were analyzed. Regarding patterns that considered building damage, 10 road blockade patterns were hypothesized, and the evacuation start time of residents in collapsed buildings was set to either 10 or 15 minutes after the earthquake. All other residents were presumed to start evacuation five minutes after the earthquake. The number of successful evacuees within 10, 15, and 20 minutes after the earthquake was then totaled. As a result, the number of successful evacuees 20 minutes after the earthquake was larger in most cases. However, the number of successful evacuees after 20 minutes was larger for the case of starting at 15 minutes than for the case of 10 minutes in 3 patters out of 10 patterns with the largest number of road blockades. One reason for this result is that a larger spread in evacuation start time of residents leads to less congestion in roads, allowing everyone to smoothly reach to an evacuation center along the narrow roads of the target district. The tsunami evacuation simulations showed that 95% of residents can complete evacuation within 20 minutes after the earthquake, and hence starting evacuation in five minutes after the earthquake has a high probability of mitigating danger of being caught in a tsunami. The observation that the number of successful evacuees was larger when the evacuation start time of residents in collapsed buildings was delayed because the shift in evacuation start time mitigated congestion in very narrow roads and near road blockades. Therefore, one approach to smoothen evacuation behavior in the target research district encumbered by narrow roads and susceptibility to congestion is to shift the evacuation start time between blocks in the district beforehand. A road blockade near a major evacuation shelter causes delays to evacuation even if the number of overturned buildings in the district as a whole is small. Therefore, according to the results, seismic reinforcement should be prioritized in buildings near evacuation centers.

In Chapter 9, tsunami evacuation simulations were conducted to extract the DEA (difficult-to-evacuate area) from tsunami on Zihuatanejo, Mexico, where there is still insufficient awareness on evacuation among residents and administrative agencies are still investigating evacuation plans. In Step 1, the initial model was drafted and the location of casualties at the estimated tsunami arrival time was captured by using the simulation images, and improved models were delineated by repeatedly adding evacuation destinations while considering the feasibility of the evacuation destination settlement. In Step 2, the detailed analyses were performed on the A-2 model, which is the more feasible and has fewer causality among the models tested in Step 1. The target area was divided into nine subdistricts and three numerical analyses for grasping the evacuation difficulty of each subdistrict were performed. The evacuation difficulty of each subdistrict was comprehensively evaluated from the resultant three indices, and the DEAs were extracted. Subdistrict 5, which is the central district in the target area, was estimated to be the area where a measure should be taken with the highest priority. Then, Steps 1 and 2 were reviewed and the features of each step was summarized toward application of the proposed method to other areas.

In the discussion, the time needed for evacuation or the minimum evacuation time, which is simply calculated from the relation between the distance to the evacuation destination and the walking speed for each agent, and the estimated tsunami arrival time (12 minutes in our case) were compared for agents who failed to evacuate in the A-2 model. From the comparison, it turned out that a considerable number of evacuees with minimum evacuation time less than 12 minutes actually failed to evacuate in our simulation. This means that simple geometrical “minimum evacuation time” evaluates on the danger side. Reflecting on the result from the analyses in Step 2 that prioritized measures should be taken in subdistrict 5, the new model was tested in which the municipal tax office located in subdistrict 5 was selected as an additional tsunami evacuation facility. The casualties of subdistrict 5 became 44 fewer than in the A-2 model, which resulted in a decrease of the ratio of casualties to the total population of 2% from 12% in the A-2 model.

Road blockage due to collapsed buildings was not taken into account in the tsunami evacuation simulations conducted to identify the DEA in this study. In the future study the more realistic DEA will be identified by performing tsunami evacuation simulations which reflect the road blockage caused by the collapsed building, after constructing a building damage prediction model that reflects the building characteristics of Mexico and calculating the damage ratio.

Throughout the course of my studies, I would like to emphasize again the importance of the integrated approach for the earthquake disaster risk evaluation based on the physical modeling of the multiple phenomena that control the final outcomes strongly connected to the damage impact, namely, a complex source rupture process, a strong site amplification, a highly-variable building damage probability, and unpredictable human behavior during the tsunami evacuation. Because of the strong link between them, the overall accuracy of the earthquake risk evaluation cannot be improved unless the accuracies of prediction are improved successfully in every aspect of this chain of events. The whole course of systematic investigations toward more quantitative prediction of future disaster risks from the mega-thrust earthquakes has been established, however, it should be considered to set just the starting point from which we will quantify deterministic and probabilistic risks for developing mitigation measures for future earthquake disasters. Specifically, we need to study the plausible complex rupture process for the 1946 Nankai and 1923 Kanto earthquakes from their damage surveys in the same way as I did for the 1944 Tonankai earthquake in this thesis. After the investigations for three major earthquakes in the past, together with the knowledge from the 2011 Tohoku event, we may construct a scaling law of SMGAs in the mega-

thrust earthquakes along the Pacific Coast of Japan, with which we can predict structural damage and human loss with sufficient accuracy.

It is also necessary to quantitatively evaluate the improvement of the risk evaluation by the methods proposed in this thesis. The improvement in accuracy that was achieved as a result of using the proposed methods in this thesis against the conventional risk evaluation methods for mega-thrust earthquakes has not been quantified. For example, the strong ground motions in Chapters 7 and 8 were estimated by the conventional method and not by the new method proposed in Part 2 of this thesis. Therefore, it shall be demonstrated how the new method can benefit the risk evaluation by predicting the strong ground motion based on the proposed method, predicting the building damage by inputting the strong ground motion to the building damage prediction model, and conducting tsunami evacuation simulation considering the road blockage caused by the collapsed buildings.